

Biomaterials with the regulation of reactive oxygen/nitrogen species for biomedical applications

Edited by

Qihui Zhou, Brandon W. Peterson, Yong Liu and Huihua Yuan

Published in

Frontiers in Bioengineering and Biotechnology



FRONTIERS EBOOK COPYRIGHT STATEMENT

The copyright in the text of individual articles in this ebook is the property of their respective authors or their respective institutions or funders. The copyright in graphics and images within each article may be subject to copyright of other parties. In both cases this is subject to a license granted to Frontiers.

The compilation of articles constituting this ebook is the property of Frontiers.

Each article within this ebook, and the ebook itself, are published under the most recent version of the Creative Commons CC-BY licence. The version current at the date of publication of this ebook is CC-BY 4.0. If the CC-BY licence is updated, the licence granted by Frontiers is automatically updated to the new version.

When exercising any right under the CC-BY licence, Frontiers must be attributed as the original publisher of the article or ebook, as applicable.

Authors have the responsibility of ensuring that any graphics or other materials which are the property of others may be included in the CC-BY licence, but this should be checked before relying on the CC-BY licence to reproduce those materials. Any copyright notices relating to those materials must be complied with.

Copyright and source acknowledgement notices may not be removed and must be displayed in any copy, derivative work or partial copy which includes the elements in question.

All copyright, and all rights therein, are protected by national and international copyright laws. The above represents a summary only. For further information please read Frontiers' Conditions for Website Use and Copyright Statement, and the applicable CC-BY licence.

ISSN 1664-8714
ISBN 978-2-8325-1900-4
DOI 10.3389/978-2-8325-1900-4

About Frontiers

Frontiers is more than just an open access publisher of scholarly articles: it is a pioneering approach to the world of academia, radically improving the way scholarly research is managed. The grand vision of Frontiers is a world where all people have an equal opportunity to seek, share and generate knowledge. Frontiers provides immediate and permanent online open access to all its publications, but this alone is not enough to realize our grand goals.

Frontiers journal series

The Frontiers journal series is a multi-tier and interdisciplinary set of open-access, online journals, promising a paradigm shift from the current review, selection and dissemination processes in academic publishing. All Frontiers journals are driven by researchers for researchers; therefore, they constitute a service to the scholarly community. At the same time, the *Frontiers journal series* operates on a revolutionary invention, the tiered publishing system, initially addressing specific communities of scholars, and gradually climbing up to broader public understanding, thus serving the interests of the lay society, too.

Dedication to quality

Each Frontiers article is a landmark of the highest quality, thanks to genuinely collaborative interactions between authors and review editors, who include some of the world's best academicians. Research must be certified by peers before entering a stream of knowledge that may eventually reach the public - and shape society; therefore, Frontiers only applies the most rigorous and unbiased reviews. Frontiers revolutionizes research publishing by freely delivering the most outstanding research, evaluated with no bias from both the academic and social point of view. By applying the most advanced information technologies, Frontiers is catapulting scholarly publishing into a new generation.

What are Frontiers Research Topics?

Frontiers Research Topics are very popular trademarks of the *Frontiers journals series*: they are collections of at least ten articles, all centered on a particular subject. With their unique mix of varied contributions from Original Research to Review Articles, Frontiers Research Topics unify the most influential researchers, the latest key findings and historical advances in a hot research area.

Find out more on how to host your own Frontiers Research Topic or contribute to one as an author by contacting the Frontiers editorial office: frontiersin.org/about/contact

Biomaterials with the regulation of reactive oxygen/nitrogen species for biomedical applications

Topic editors

Qihui Zhou — University of Health and Rehabilitation Sciences, China

Brandon W. Peterson — University Medical Center Groningen, Netherlands

Yong Liu — University of Chinese Academy of Sciences, China

Huihua Yuan — Nantong University, China

Citation

Zhou, Q., Peterson, B. W., Liu, Y., Yuan, H., eds. (2023). *Biomaterials with the regulation of reactive oxygen/nitrogen species for biomedical applications*.

Lausanne: Frontiers Media SA. doi: 10.3389/978-2-8325-1900-4

Table of contents

- 05 **Editorial: Biomaterials with the regulation of reactive oxygen/nitrogen species for biomedical applications**
Qihui Zhou, Brandon W. Peterson, Yong Liu and Huihua Yuan
- 08 **Preparation of Fucoidan-Based Electrospun Nanofibers and Their Interaction With Endothelial Cells**
Yiwen Chen, Huilin Zhu, Yuanping Hao, Zhanyi Sun, Peili Shen and Qihui Zhou
- 18 **Extracellular Vesicles as Natural Delivery Carriers Regulate Oxidative Stress Under Pathological Conditions**
Hongzhao Qi, Yingruo Wang, Shunxin Fa, Changqing Yuan and Lijun Yang
- 25 **Nanosonosensitizers With Ultrasound-Induced Reactive Oxygen Species Generation for Cancer Sonodynamic Immunotherapy**
Danling Cheng, Xiaoying Wang, Xiaojun Zhou and Jingchao Li
- 33 **Development of A Decahedral Nanoenzyme Capable of Overcoming Hypoxia to Facilitate the Iodine-125 Radiosensitization of Esophageal Cancer**
Dechao Jiao, Kunpeng Wu, Kaihao Xu, Yiming Liu, Deyao Zhao, Xinwei Han and Ruitai Fan
- 42 **Nanotechnologies for Reactive Oxygen Species“Turn-On” Detection**
Hongfei Jiang, Qian Lin, Zongjiang Yu, Chao Wang and Renshuai Zhang
- 49 **Nanomedicine for the Diagnosis and Therapy of COVID-19**
Yingruo Wang, Yuanping Hao, Shunxin Fa, Weiping Zheng, Changqing Yuan and Wanchun Wang
- 56 **Preparation and Evaluation of Starch Hydrogel/Contact Lens Composites as Epigallocatechin Gallate Delivery Systems for Inhibition of Bacterial Adhesion**
Lianghui Zhao, Hongwei Wang, Chengcheng Feng, Fangying Song and Xianli Du
- 65 **Reactive Oxygen Species in Anticancer Immunity: A Double-Edged Sword**
Jie Wang, Ning Liu, Hongfei Jiang, Qian Li and Dongming Xing
- 72 **An Antioxidant Enzyme Therapeutic for Sepsis**
Feifei Li, Ran Yan, Jun Wu, Zeren Han, Meng Qin, Chaoyong Liu and Yunfeng Lu
- 84 **Reactive Oxygen Species-Based Biomaterials for Regenerative Medicine and Tissue Engineering Applications**
Muhammad Shafiq, Yujie Chen, Rashida Hashim, Chuanglong He, Xiumei Mo and Xiaojun Zhou

- 93 **Hybrid Hydrogel Composed of Hyaluronic Acid, Gelatin, and Extracellular Cartilage Matrix for Perforated TM Repair**
Yili Wang, Feng Wen, Xueting Yao, Lulu Zeng, Jiaming Wu, Qinzhong He, Huaqiong Li and Lian Fang
- 103 **Reactive Oxygen Species (ROS)-Responsive Biomaterials for the Treatment of Bone-Related Diseases**
Xiaoxiang Ren, Han Liu, Xianmin Wu, Weizong Weng, Xiuhui Wang and Jiacaan Su
- 109 **Light-Triggered Adhesive Silk-Based Film for Effective Photodynamic Antibacterial Therapy and Rapid Hemostasis**
Tingting Huang, Zhihao Zhou, Qiaoyuan Li, Xiaoxuan Tang, Xiaoli Chen, Yifan Ge and Jue Ling
- 118 **Bioengineered Zinc Oxide Nanoparticle-Loaded Hydrogel for Combinative Treatment of Spinal Cord Transection**
Sen Lin, Hao-sen Zhao, Chang Xu, Zi-peng Zhou, Da-hao Wang, Shu-rui Chen and Xi-fan Mei
- 127 **Osseointegration Effect of Micro-Nano Implants Loaded With Kaempferol in Osteoporotic Rats**
Anyue Wang, Wenhong Yuan, Yu Song, Yanjun Zang and Yanling Yu
- 137 **A Transcriptome Sequencing Study on Genome-Wide Gene Expression Differences of Lung Cancer Cells Modulated by Fucoidan**
Yanjie Zhao, Xinmei Li, Heng Zhang, Mingzhe Yan, Mengmeng Jia and Qihui Zhou
- 147 **Comparative Study of Traditional Single-Needle Electrospinning and Novel Spiral-Vane Electrospinning: Influence on the Properties of Poly(caprolactone)/Gelatin Nanofiber Membranes**
Qi Xu, Wei Liu and Bingcheng Yi
- 156 **Preparation of Novel ICT-CMC-CD59sp Drug-Loaded Microspheres and Targeting Anti-Tumor Effect on Oral Squamous Cell Carcinoma**
Xiang Gao, Wanchun Wang and Meihua Gao
- 165 **Porous Se@SiO₂ Nanoparticles Enhance Wound Healing by ROS-PI3K/Akt Pathway in Dermal Fibroblasts and Reduce Scar Formation**
Bo-Yu Yang, Zhi-Yuan Zhou, Shi-Yun Liu, Ming-Jun Shi, Xi-Jian Liu, Tian-Ming Cheng, Guo-Ying Deng, Ye Tian, Jian Song and Xuan-Hao Li
- 175 **The potential of oxygen and nitrogen species-regulating drug delivery systems in medicine**
Michał Sottan, Dorota Bartusik-Aebischer and David Aebischer



OPEN ACCESS

EDITED AND REVIEWED BY
Hasan Uludag,
University of Alberta, Canada

*CORRESPONDENCE

Qihui Zhou,
qihuizhou@qdu.edu.cn
Brandon W. Peterson,
b.w.peterson@umcg.nl
Yong Liu,
y.liu@ucas.ac.cn
Huihua Yuan,
yuanhh@ntu.edu.cn

SPECIALTY SECTION

This article was submitted to
Biomaterials,
a section of the journal
Frontiers in Bioengineering and
Biotechnology

RECEIVED 29 October 2022

ACCEPTED 07 November 2022

PUBLISHED 25 November 2022

CITATION

Zhou Q, Peterson BW, Liu Y and Yuan H
(2022), Editorial: Biomaterials with the
regulation of reactive oxygen/nitrogen
species for biomedical applications.
Front. Bioeng. Biotechnol. 10:1083727.
doi: 10.3389/fbioe.2022.1083727

COPYRIGHT

© 2022 Zhou, Peterson, Liu and Yuan.
This is an open-access article
distributed under the terms of the
[Creative Commons Attribution License](#)
(CC BY). The use, distribution or
reproduction in other forums is
permitted, provided the original
author(s) and the copyright owner(s) are
credited and that the original
publication in this journal is cited, in
accordance with accepted academic
practice. No use, distribution or
reproduction is permitted which does
not comply with these terms.

Editorial: Biomaterials with the regulation of reactive oxygen/nitrogen species for biomedical applications

Qihui Zhou^{1,2*}, Brandon W. Peterson^{3*}, Yong Liu^{4*} and
Huihua Yuan^{5*}

¹Department of Stomatology, Institute for Translational Medicine, The Affiliated Hospital of Qingdao University, Qingdao University, Qingdao, China, ²School of Rehabilitation Sciences and Engineering, University of Health and Rehabilitation Sciences, Qingdao, China, ³Department of Biomedical Engineering, University of Medical Center Groningen, Groningen, Netherlands, ⁴Wenzhou Institute, University of Chinese Academy of Sciences, Wenzhou, China, ⁵School of Life Sciences, Nantong University, Nantong, China

KEYWORDS

reactive oxygen species, reactive nitrogen species, biomaterials, anti-bacteria, anticancer, tissue repair and regeneration

Editorial on the Research Topic

Biomaterials with the regulation of reactive oxygen/nitrogen species for biomedical applications

In recent years, reactive oxygen/nitrogen species (ROS/RNS), as “two-faced” products, have garnered increasing interest in biomedical research (Patel et al., 1999; Pizzimenti et al., 2010; Sies and Jones, 2020). As is well-known, ROS/RNS can result in oxidative/nitrosative stress or the imbalance of redox homeostasis, damaging cellular macromolecules (e.g., lipids, protein, and DNA) and leading to the development of diseases (Patel et al., 1999; Checa and Aran, 2020). On the other hand, locally enhanced ROS/RNS can be used in the management of bacteria/virus infection and cancer (Dharmaraja, 2017; Yu et al., 2020; Tang et al., 2022). The precise regulation of ROS/RNS in living organisms and their surrounding microenvironment plays a crucial role in the treatment of diseases as well as in tissue repair and regeneration. The rational design and manufacture of advanced biomaterials has led them to emerge as a new ROS/RNS modulators, with significant potential in biomedical applications. In this Research Topic, 20 articles were published, focusing on the principles and applications of biomaterials for the regulation of ROS/RNS in the biomedical field.

In one of several reviews in this Research Topic, Shafiq et al. outlined the underlying mechanism of ROS formation in the cell/tissue microenvironment, and presented ROS-responsive biomaterials for tissue repair and regeneration applications. The authors highlighted the design and processing of ROS-scavenging functional biomaterials and their roles in both mediating oxidative stress and the damaged tissue/organ

microenvironment for accelerating tissue repair. Ren et al. reviewed the role of ROS in the bone microenvironment and outlined ROS-responsive biomaterials for the management of bone-related diseases. The authors proposed that bone-targeting biomaterials with ROS-responsive features and their accurate, controlled release should be particular areas of focus. Qi et al. and Li et al. summarized the regulation properties of extracellular vesicles (EVs) and PEGylated catalases for ROS and oxidative stress, directly and indirectly. EVs containing antioxidant substances or oxidants can be delivered to receptor cells to accelerate or slow down oxidative stress. Meanwhile, regulators of oxidative stress-related signaling pathways can be mediated by EVs for delivery to receptor cells, allowing indirect regulation of oxidative stress. PEGylated catalases effectively modulated cytokine production by activating leukocytes, and inhibited elevated TNF- α and IL-6 levels in mice, inducing sepsis and considerably improving mouse survival rates. Furthermore, Softan et al. presented the main pathways of ROS/RNS regulation in tissue microenvironments and summarized recent advances in ROS/RNS-controlled biomaterials used in medicine. Jiang et al. summarized recent advances in nanomaterials with the capacity for ROS “turn-on” responses. Future work on the development of ROS “turn-on” detection nanomaterials should concentrate on enhancing the sensing capacity, detection limit, cytocompatibility, living cell imaging, and even the ability to sample *in vivo*.

In an original research article in this Research Topic, regarding the regulation of biomaterial-mediated ROS for tissue repair and regeneration, Yang et al. designed porous Se@SiO₂ nanoparticles which were applied to promote wound healing by mediating the ROS-PI3K/Akt pathway to suppress the generation of ROS, modulating the behaviors of fibroblasts and reducing scar formation. Lin et al. developed a skeletal muscle-derived adhesive hydrogel containing ZnONPs (ZnONPs-Gel), which exhibited excellent biocompatibility, significantly inhibited ROS formation, and suppressed cell apoptosis, thereby accelerating the function recovery in spinal cord injury. In addition to the ROS-mediated inorganic nanoparticles used, Wang et al. reported the fabrication of biomimetic hyaluronic acid methacryloyl/gelatin methacryloyl/extracellular cartilage matrix hydrogels for the repair of damaged, perforated tympanic membrane. The introduction of hyaluronic acid methacryloyl generated a high water content and elasticity and it scavenged ROS. The addition of an extracellular cartilage matrix promoted the chondrogenic differentiation of stem cells. A typical marine polysaccharide fucoidan exhibiting an antioxidant function was reported to possess the ability to remove ROS. Fucoidan-based nanofibers, as a bioactive scaffold, were developed by Chen et al.

In contrast, ROS-inducing biomaterials have been commonly used in antimicrobial and cancer applications. For antimicrobial

research, Huang et al. developed a light-responsive silk-based hemostatic film containing a photodynamic agent (Chlorin e6) for effective photodynamic antibacterial therapy *via* forming ROS upon near-infrared (NIR) irradiation, which offers great promise in treating infected wounds and related diseases. Wang et al. reviewed recent advances in nanomaterials for COVID-19 therapy through generating ROS/RNS. For anticancer research, Cheng et al. summarized recent progress in nanosensitizers, with ultrasound-induced ROS formation for cancer sonodynamic immunotherapy (CSI). The challenges and outlook for clinical use of nanosensitizer-based CSI were further discussed. Wang et al. reviewed the “two-faced” effects of ROS on anticancer immunity, including macrophage polarization, immune checkpoint blocking (ICB) therapy, T cell activation and expansion, as well as the induction of immunogenic cell death. Designing smart biomaterials to mediate dynamic changes in ROS/RNS for specific biomedical purposes is critical for biomedical applications.

In summary, the appropriate regulation of ROS/RNS in organisms and their surrounding microenvironment plays a critical role in treating infection/cancer-related diseases, as well as tissue repair and regeneration. In future, the rational design and preparation of ROS-responsive smart biomaterials could offer enormous potential in advanced biomedical applications.

Author contributions

QZ wrote the editorial which was revised, proofread, and accepted by all authors.

Acknowledgments

The Editors deeply acknowledge the authors of all contributions composing this Research Topic. They also acknowledge all reviewers' constructive comments and engagement, and editorial support from Frontiers throughout the publication process.

Conflict of interest

The authors declare that the research was conducted in the absence of any commercial or financial relationships that could be construed as a potential conflict of interest.

Publisher's note

All claims expressed in this article are solely those of the authors and do not necessarily represent those of their affiliated

organizations, or those of the publisher, the editors and the reviewers. Any product that may be evaluated in this article, or

claim that may be made by its manufacturer, is not guaranteed or endorsed by the publisher.

References

- Checa, J., and Aran, J. M. (2020). Reactive oxygen species: Drivers of physiological and pathological. *J. Inflamm. Res.* 13, 1057–1073. doi:10.2147/jir.s275595
- Dharmaraja, A. T. (2017). Role of reactive oxygen species (ROS) in therapeutics and drug resistance in cancer and bacteria. *J. Med. Chem.* 60, 3221–3240. doi:10.1021/acs.jmedchem.6b01243
- Patel, R. P., McAndrew, J., Sellak, H., White, C. R., Jo, H., Freeman, B. A., et al. (1999). Biological aspects of reactive nitrogen species. *Biochimica Biophysica Acta - Bioenergetics* 1411, 385–400. doi:10.1016/s0005-2728(99)00028-6
- Pizzimenti, S., Toaldo, C., Pettazzoni, P., Dianzani, M. U., and Barrera, G. (2010). The "two-faced" effects of reactive oxygen species and the lipid peroxidation product 4-hydroxynonenal in the hallmarks of cancer. *Cancers (Basel)* 2, 338–363. doi:10.3390/cancers2020338
- Sies, H., and Jones, D. P. (2020). Reactive oxygen species (ROS) as pleiotropic physiological signalling agents. *Nat. Rev. Mol. Cell Biol.* 21, 363–383. doi:10.1038/s41580-020-0230-3
- Tang, S., Zhang, H., Mei, L., Dou, K., Jiang, Y., Sun, Z., et al. (2022). Fucoidan-derived carbon dots against *Enterococcus faecalis* biofilm and infected dentinal tubules for the treatment of persistent endodontic infections. *J. Nanobiotechnol.* 20, 321–416. doi:10.1186/s12951-022-01501-x
- Yu, Z., Li, Q., Wang, J., Yu, Y., Wang, Y., Zhou, Q., et al. (2020). Reactive oxygen species-related nanoparticle toxicity in the biomedical field. *Nanoscale Res. Lett.* 15, 115. doi:10.1186/s11671-020-03344-7



Preparation of Fucoidan-Based Electrospun Nanofibers and Their Interaction With Endothelial Cells

Yiwen Chen^{1,2†}, Huilin Zhu^{1,2†}, Yuanping Hao¹, Zhanyi Sun³, Peili Shen³ and Qihui Zhou^{1,2*}

¹Department of Stomatology, Institute for Translational Medicine, The Affiliated Hospital of Qingdao University, Qingdao University, Qingdao, China, ²School of Stomatology, Qingdao University, Qingdao, China, ³State Key Laboratory of Bioactive Seaweed Substances, Qingdao Bright Moon Seaweed Group Co., Ltd., Qingdao, China

OPEN ACCESS

Edited by:

Yilong Cheng,
Xi'an Jiaotong University, China

Reviewed by:

Shixian Lv,
University of Washington,
United States

Jue Ling,
Nantong University, China

*Correspondence:

Qihui Zhou
qihuizhou@qdu.edu.cn

[†]These authors have contributed
equally to this work

Specialty section:

This article was submitted to
Biomaterials,
a section of the journal
Frontiers in Bioengineering and
Biotechnology

Received: 10 July 2021

Accepted: 23 August 2021

Published: 06 September 2021

Citation:

Chen Y, Zhu H, Hao Y, Sun Z, Shen P
and Zhou Q (2021) Preparation of
Fucoidan-Based Electrospun
Nanofibers and Their Interaction With
Endothelial Cells.
Front. Bioeng. Biotechnol. 9:739209.
doi: 10.3389/fbioe.2021.739209

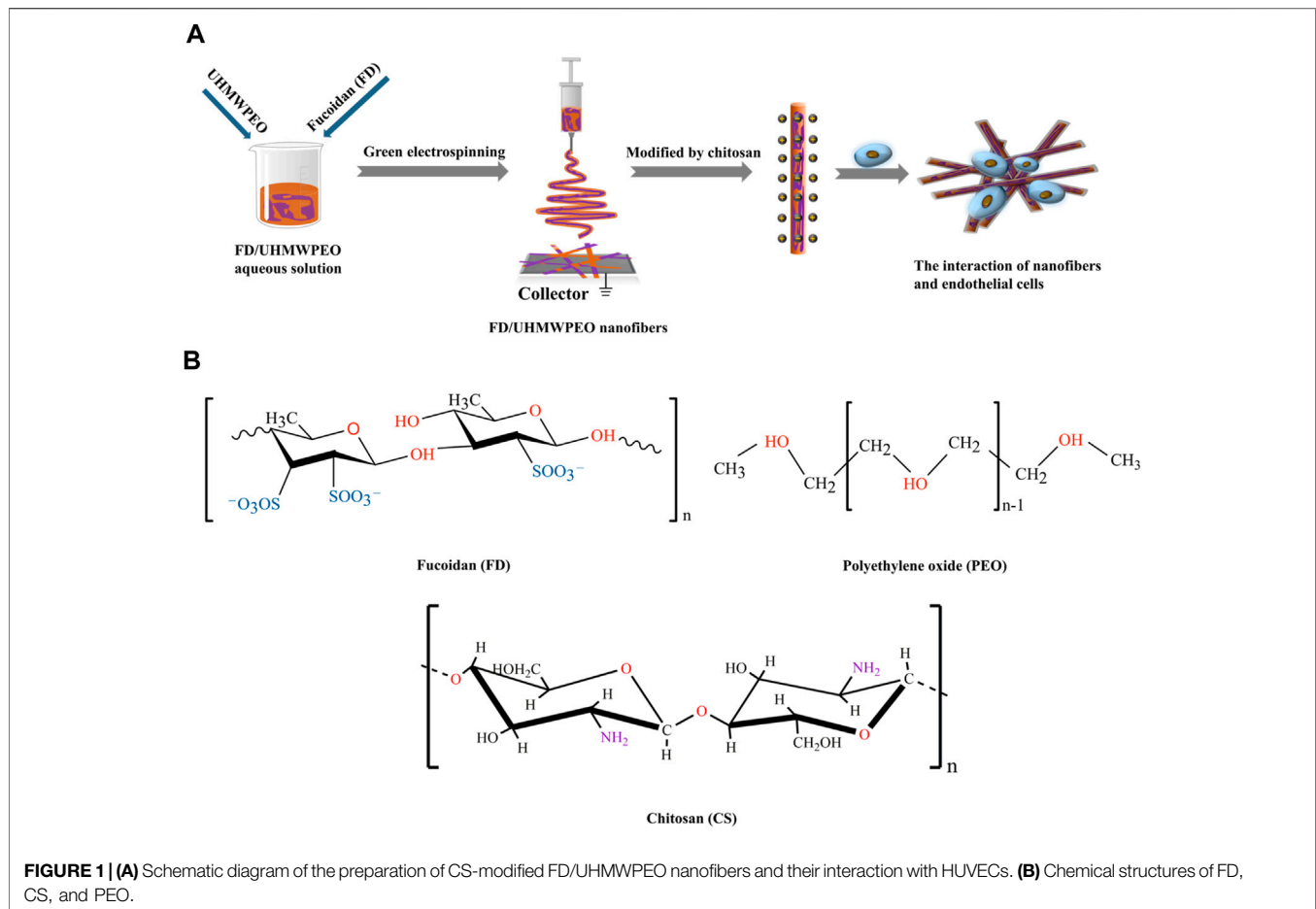
Sulfated polysaccharide fucoidan (FD) is widely applied in biomedical applications owing to its outstanding bioactivities. In addition to the biochemical features, the architecture of biomaterials plays a critical role in tissue repair and regeneration. Particularly, nanofibers have elicited great interest due to their extracellular matrix-like structure, high specific surface area, and favorable biological properties. Herein, chitosan-modified FD/ultra-high molecular weight polyethylene oxide (UHMWPEO) nanofibers are developed via green electrospinning and electrostatic interaction for studying their interaction with endothelial cells. The appropriate solvent is screened to dissolve FD. The electrospinnability of FD/UHMWPEO aqueous solutions is greatly dependent on the weight ratios of FD/UHMWPEO. The incorporation of UHMWPEO significantly improves the electrospinnability of solution and thermo-stability of nanofibers. Also, it is found that there is good miscibility or no phase separation in FD/UHMWPEO solutions. *In vitro* biological experiments show that the chitosan-modified FD/UHMWPEO nanofibers greatly facilitate the adhesion of endothelial cells and inhibit the attachment of monocytes. Thus, the designed FD-based nanofibers are promising bio-scaffolds in building tissue-engineered blood vessels.

Keywords: fucoidan, electrospun nanofibers, extracellular matrix, endothelial cells, biointerface, cell-material interface

INTRODUCTION

In the past few decades, marine polysaccharides have gained increasing attention in the area of diversified biomedical applications owing to their inherent (bio)physicochemical features, such as biocompatibility, biodegradability, favorable bioactive, biomechanical properties, and structural functionalities (Bidarra et al., 2014; Fernando et al., 2019; Hao et al., 2020; Jana et al., 2020; Yin et al., 2021; Zheng et al., 2021). Particularly, sulfated polysaccharide fucoidan, extracted from marine brown seaweed, has been well-known to possess various biological activities, e.g., antibacterial, antiviral, antioxidant, anticoagulant, anti-inflammatory, antitumor, antithrombotic, antifibrotic, and immunomodulatory activities, facilitating the generation of angiogenesis and fibrillar collagen matrix (Li et al., 2008; Senthilkumar et al., 2017; Oka et al., 2020; Yao et al., 2020). These unique characteristics make them remarkable candidates for blood vessel tissue engineering, which has not been examined closely.

Besides the biochemical properties, their biophysical structure can significantly mediate cell attachment, shape, viability, the differentiation or pluripotency of stem cells, and even tissue repair



and regeneration (Li et al., 2018; Cui et al., 2020; Yu et al., 2020; Yu et al., 2021; Zhou et al., 2020; Liu et al., 2021; Yang et al., 2021a; Yang et al., 2021b). Recently, the development of nanofibrous materials has received increasing attention in tissue engineering and regenerative medicine due to their outstanding properties, such as their favorable biological properties, sufficient mechanical strength, highly porous mesh with interconnectivity, extremely high specific surface area, and aspect ratio (Zhou et al., 2015; Zhou et al., 2017; Kenry and Lim, 2017; Xue et al., 2019; Ahmadi et al., 2021). In addition, nanofibers can mimic the natural extracellular matrix (ECM) structure in the blood vessel and have been widely used as a blood vessel tissue-engineering scaffold (Xu et al., 2004; Devolder et al., 2011). In the recent 2 decades, the electrospinning technique has been widely used to prepare polymeric fibers with diameters typically ranging from tens of nanometers to several micrometers (Zhang et al., 2005; Xue et al., 2019; Daraeinejad and Shabani, 2021; Fetz et al., 2021; Peng et al., 2021). However, the electrospinning of fucoidan (FD) remains a challenge due to its low viscoelasticity and solubility issues. It was reported that other nature polymers [e.g., chitosan (CS), cellulose, sodium alginate, protein] with a small amount of ultra-high molecular weight polymer (UHMWP) [e.g., polyethylene oxide (PEO), polyvinyl alcohol (PVA), polyvinyl pyrrolidone (PVP)] can

allow their preparation in nanofibers *via* electrospinning (Zhang et al., 2008; Li et al., 2015). In this sense, the combination of FD and UHMWP could also be considered to address the issue of spinnability.

Vascular endothelial cells (VECs) are the predominant cell type and generate a continuous inner monolayer of blood vessels, which are responsible for regulating inflammation and vascular homeostasis in healthy blood vessels (Coultas et al., 2005). Also, the attachment of monocytes to VECs is vital for the occurrence of atherosclerosis and inflammation (Rajendran et al., 2013; Yang et al., 2019; Li et al., 2021a; Li et al., 2021b; Zong et al., 2021). Herein we hypothesize that FD-based nanofibers would be able to exhibit favorable physicochemical properties to mediate VEC responses in engineering vascular tissues. To test the hypothesis, FD/UHMWPEO nanofibrous films were fabricated using green electrospinning. **Figure 1A** displays the overall strategy to develop CS-modified FD/UHMWPEO nanofibers and their interaction with VECs. H₂O and a small amount of UHMWPEO were selected as the solvent and co-spinning polymer for electrospinning of FD. Then, positively charged CS was selected to interact with negatively charged FD *via* the electrostatic interaction. The chemical structures of FD, UHMWPEO and CS used are shown in **Figure 1B**. The physicochemical features of FD-based nanofibers,

i.e., morphology, crystallization, and thermal properties, were systematically tested by different characterization techniques. Further, FD-based nanofibers were seeded with human umbilical VECs (HUVECs) to investigate the effects of material physicochemical properties on cellular attachment and the adhesion of monocytes to HUVECs.

MATERIALS AND METHODS

Materials

Fucoidan (FD, Mw = 276 kDa, sulfate: 29.65%) was provided by Qingdao Bright Moon Seaweed Group Co., Ltd. (Qingdao, China). UHMWPEO (Mv = ~6,000,000 g/mol⁻¹), chitosan (CS, Mv = 300 kDa and deacetylation degree ≥90%), and acetic acid (HAc, purity ≥99.8%) were supplied by Shanghai Macklin Biochemical Co., Ltd. (Shanghai, China). Both the human umbilical vein endothelial cells (HUVECs) and human acute monocytic leukemia cells (THP-1) were bought from the Shanghai Institutes for Biological Sciences (Shanghai, China). Dulbecco's Modified Eagle Medium/Nutrient Mixture F-12, RPMI 1640 media, and fetal bovine serum were supplied by Biological Industries (Israel). FITC phalloidin and DAPI were provided by Solarbio (Beijing, China). Cell Counting Kit-8 was purchased from Absin Bioscience Inc. (China). Carboxyfluorescein diacetate succinimidyl ester was provided by MedChemExpress (Shanghai, China). Other chemical reagents were of analytical grade and used without further purification. Ultrapure water used in all experiments was obtained with a Milli-Q apparatus (Millipore, Bedford, MA, USA).

Preparation of Electrospun FD-Based Nanofibers

The FD aqueous solutions were doped with a small amount of UHMWPEO (i.e., FD/UHMWPEO = 100/0, 98/2, 97/3, 96/4, 95/5, 94/6, 93/7, 92/8, 91/9, and 90/10). The mixed solutions were stirred for ~6 h at room temperature prior to processing to ensure thorough mixing. The solution was loaded into a 20 ml plastic syringe attached with a 25-gauge blunt-ended needle as the spinneret which was charged at a high electric potential of 10–15 kV by a high voltage power supply (Tianjin Dongwen High Voltage Power Supply Plant, China). The solution feeding rate (0.3–1 ml/h) was precisely controlled by a syringe pump (Baoding Longer Precision Pump Co., Ltd., China). The FD-based nanofibers were collected onto an aluminum foil-covered collector placed 15 cm away from the needle tip. Electrospinning processes were performed on a horizontal electrospinning setup at 20–25°C with an ambient humidity of 30–35%.

Modification of FD-Based Nanofibers by CS

FD-based nanofibers prepared from FD/PEO (90/10) were particularly selected for modification with CS. First, 1% CS was dissolved in an aqueous mixed solvent system consisting of 30, 60, and 90 wt% HAc, respectively. The FD-based nanofibers were immersed in the CS/HAc solution for ~60 s. All modified samples were dried for 2–3 days in a vacuum oven

(DZF-6050AB, Beijing, China) at 35°C to remove any potential residual solvent.

Characterization

The morphological structure of the prepared nanofibers was observed using a scanning electron microscope (SEM) (VEGA3, TESCAN, Czech) operated at an acceleration voltage of 8–10 kV. Prior to observation, samples were sputter-coated with gold for 120 s to increase the electronic conductivity. The mean diameter of nanofibers was identified by randomly detecting at least 50 fibers from various SEM images for each type of sample using Image J software.

The rheometer (MCR301, Anton Paar, China) equipped with a parallel plate (20 mm) was used to measure the viscous property of FD/PEO aqueous solutions.

A Nicolet iN10 FTIR spectrometer (Thermo Fisher Scientific, Waltham, MA, USA) was used to characterize Fourier transform-infrared (FTIR) spectra of the samples over the range of 500–4,000 cm⁻¹ at a scanning resolution of 2 cm⁻¹ during 32 scans.

X-ray diffraction (XRD) spectroscopy was performed by DX2700 (Dandong, China) to measure the crystal structures of nanofiber samples. The samples were tested between 10 and 80° (2θ) at a scanning rate of 0.05° (2θ) per min operating with voltage 40 kV and current 30 mA equipped with Cu Kα radiation (λ = 1.5418 Å).

Thermogravimetric analysis on the nanofiber samples was conducted in a thermogravimetric analyzer (NETZSCH, Germany) at a scan range from 0 to 800°C with continuous nitrogen flow.

Differential scanning calorimetry (DSC, TA, USA) was used to measure the thermal properties of the electrospun FD-based nanofibers. A nitrogen atmosphere (flow rate = 50 ml/min) was used throughout. All samples were first quenched to -80°C with liquid nitrogen and then heated at a rate of 10°C/min to 180°C.

Cellular Assays

HUVECs (passage: 3–5) were cultured in Dulbecco's Modified Eagle Medium/Nutrient Mixture F-12 (Biological Industries, Israel) supplemented with 10% fetal bovine serum (Biological Industries, Israel) and 1% Penicillin-Streptomycin Liquid (Biological Industries, Israel) in a humidified incubator of 5% CO₂ at 37°C. THP-1 cells were cultured in RPMI 1640 media (Biological Industries, Israel) supplemented with 10% FBS in a humidified 37°C and 5% CO₂ incubator. THP-1 cells were used in the following experiments.

All substrates (Ø14 mm) were immersed into 75% ethanol for 2 min and then irradiated with UV for 1 h, placed in 24-wells, and washed by PBS. After that, HUVECs were incubated on the substrates in 24-well plates at a density of 3 × 10⁴ cells/well for cell adhesion. All plates were stored in an incubator at 37°C and 5% CO₂ for 24 h. Then, HUVECs were fixated by 4% paraformaldehyde (Solarbio, Beijing, China) for 20 min. Subsequently, the cell membrane was permeabilized with 0.5% Triton X-100 (Sigma) solution for 3 min. Finally, the cells were stained by FITC phalloidin and DAPI for 30 and 10 min, respectively (Solarbio, Beijing, China). The images were captured by Fluorescence Microscopy (Nikon A1 MP, Japan).

TABLE 1 | The solubility of FD in different solvents.

H ₂ O	DCM	EA	DMSO	TCM	DMF	Diox	CCl ₄	CAN	Hex	THF
+	–	–	–	–	–	–	–	–	–	–

DCM, Dichloromethane; EA, Ethyl acetate; DMSO, Dimethyl Sulphoxide; TCM, Trichloromethane; DMF, Dimethyl Formamide; Diox, Dioxane; CCl₄, Carbon Tetrachloride; CAN, Acetonitrile; Hex, Hexyl hydride; THF, Tetrahydrofuran. “–” means insolubilization; “+” means solubilization.

HUVECs were seeded onto the sterilized substrate (Ø14 mm) in 24-well plates at a density of 5×10^4 cells/well for forming cell monolayers. After 1 day, THP-1 cells (1.5×10^5 cells/well) stained by Carboxyfluorescein diacetate succinimidyl ester (CFSE, MCE, China) were seeded onto HUVEC monolayer, and co-cultured for 4 h. Afterward, each well was washed with PBS three times and counted the number of THP-1 adhered by HUVECs using the Fluorescence Microscopy (Nikon A1 MP, Japan).

Statistical Analysis

All data were expressed as mean \pm SD. Statistical analysis was performed using Origin 9.0. All the data were analyzed using one-way analysis of variance (ANOVA) with Tukey's test to determine differences between groups. A value of $p < 0.05$ was considered to be statistically significant.

RESULTS AND DISCUSSION

Solubility of FD in Various Solvents

It was demonstrated that the selection of solvent is critical to determine material solubility, viscoelasticity, electrical conductivity and electrospinnability of the solution, as well as the productivity and morphology of nanofibers (Zhou et al., 2013; Casasola et al., 2014). However, no studies have been performed to find out which solvents FD could dissolve in. In our study, FD was first dispersed into 11 solvents as shown in **Table 1** under magnetic stirring at room temperature. After 12 h, it was found that FD was only dissolved in the water (**Table 1**), which formed a hazel homogeneous solution (data not shown). The maximum solubility of FD in the water at room temperature is 10%. When water was heated to 40°C, FD dissolved faster and the amount of dissolved FD significantly increased. Therefore, in the following experiment water was used as a solvent to prepare FD nanofibers *via* electrospinning. Also, water-based electrospinning, also named “green electrospinning,” has several advantages of being environmentally friendly, non-toxic, and non-flammable. It was reported that organic solvents remaining in the fibers had a negative effect on cellular adhesion and proliferation both *in vitro* and *in vivo* (Mooney et al., 1996; Lv et al., 2018). The water-based electrospinning strategy here for preparing FD nanofibers is a safe and versatile route to numerous applications in biology, medicine, and pharmacy.

Preparation of FD-Based Electrospun Nanofibers

To obtain the adequate viscosity of FD solution, the maximum FD concentration (10% w/v) at room temperature was used in the

following experiment. However, when 10% w/v FD aqueous solution was used for electrospinning, only droplets were formed as shown in **Figure 2A**, probably because the used FD solution still did not have enough viscosity.

As reported, the electrospinnability of naturally derived polymer solutions can be greatly improved by introducing a small amount of UHMWPEO (Zhang et al., 2008; Li et al., 2015). As shown in **Figure 2B**, with the decrement of the weight ratios of FD/PEO from 100:0 to 98:2, FD/PEO microbeads were fabricated. When the mass ratio of FD/PEO was further decreased from 97:3 to 91:9, the nanofibers with bead-string morphology were generated, the microspheres were elongated, and the average diameter of nanofibers decreased (**Figures 2C–E**). The defect-free nanofibers with an average diameter (560 ± 88 nm) were prepared in the electrospinning of the FD/PEO (90:10) solution (**Figure 2F**). **Figure 2G** showed the variation in viscosity with the weight ratios of FD/PEO solutions. By adding PEO with different ratios relative to FD (FD/PEO = 98/2, 95/5, and 90/10), it was found that the viscosity of solutions was increased from 0.0114 to 0.0879 Pa·s. It was reported that the chain entanglements caused by the increased polymer concentration can play a vital role in fiber formation during electrospinning (Shenoy et al., 2005; Zhou et al., 2013).

Quantification shows that the fiber diameter first decreased and then increased with increasing the amount of PEO (**Figure 2H**). The size of microbeads initially increased with increasing the amount of PEO and then was relatively independent of the amount of PEO. The increased chain entanglements can serve to stabilize the electrospinning jet by inhibiting jet breakup, which elongated beads (Shenoy et al., 2005). These results indicate that the morphology and diameter of electrospun FD/PEO nanofibers greatly depended on the weight ratios of FD/PEO. Also, UHMWPEO as the co-spinning polymer significantly improved the spinnability of FD.

It was well-demonstrated that the diameter of nanofibers can affect the drug release, modulate cell adhesion, migration, proliferation, differentiation, siRNA uptake, and gene silencing, as well as even tissue repair and regeneration (Jaiswal and Brown, 2012; Higgins et al., 2015; Pelipenko et al., 2015; Yau et al., 2015). As depicted in **Figures 3A,B**, the diameter of FD/PEO nanofibers slightly increased and then decreased with increasing the applied voltage and collecting distance. The nanofiber diameter remained unchanged with the increment of feed rate (**Figure 3C**).

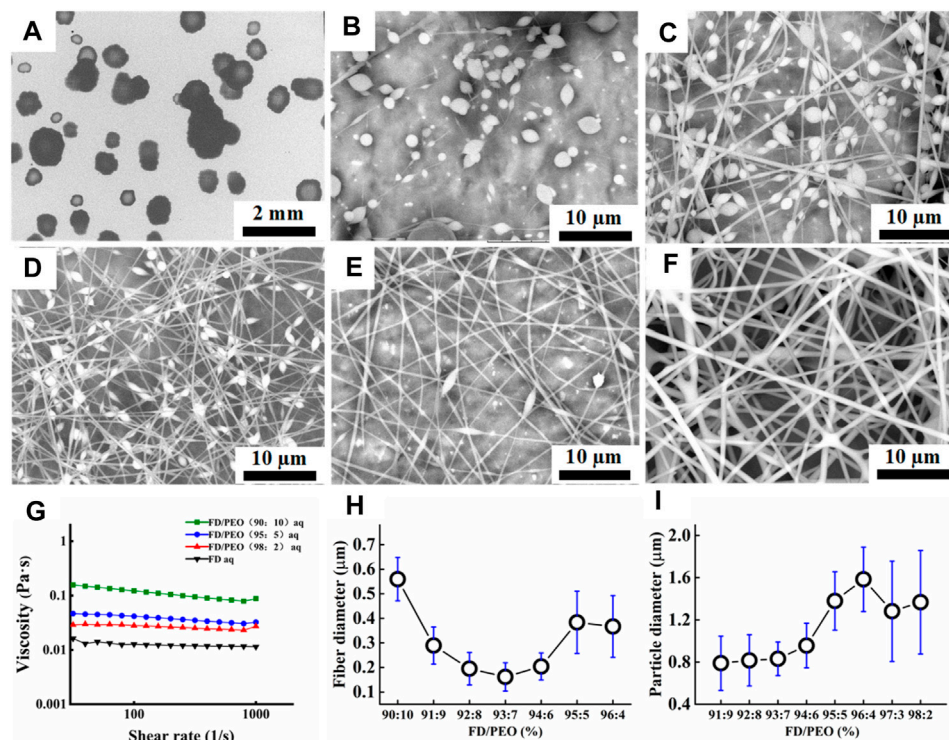


FIGURE 2 | (A–F) SEM images of FD/PEO electrospun nanofibers with different weight ratios of FD/PEO (i.e., 100/0, 98/2, 97/3, 93/7, 91/9, and 90/10). **(G)** The viscosity of FD/PEO solutions with different weight ratios. **(H, I)** Dependence of fiber diameter and microbead size on different weight ratios of FD/PEO, respectively.

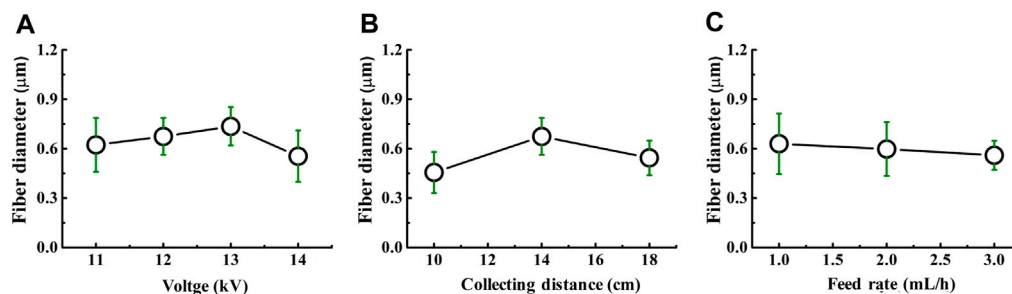


FIGURE 3 | Dependence of the fiber diameter on **(A)** voltage, **(B)** collecting distance, and **(C)** feed rate.

Characterization of the FD-Based Nanofibers

FT-IR spectra were performed to ascertain the molecular interactions in FD/PEO nanofibers (**Figure 4A**). PEO revealed a relatively sharp peak at $2,938\text{ cm}^{-1}$, which is attributed to —CH_2 stretching (Shariful et al., 2017). And its typical peaks at $1,148$ and $1,110\text{ cm}^{-1}$ correspond to C-O-C vibration. In addition, FD showed absorption bands at $3,434\text{ cm}^{-1}$ (O-H stretching), $1,642\text{ cm}^{-1}$ (C=O stretching), $1,232\text{ cm}^{-1}$ (S=O bending), and 833 cm^{-1} (C-O-S bending). The absorption band associated with C-O-C disappeared in FD/PEO nanofibers, probably because C-O-C is a proton acceptor and may form hydrogen bonding with the OH group in FD molecules (Kondo et al., 1994).

Figure 4B displays the XRD patterns of raw materials and the beaded nanofibers (FD/PEO = 95:5), nanofibers (FD/PEO = 90:10). The PEO powder showed two characteristic diffraction peaks at 19.2 and 23.3° , corresponding to (120) and (112) planes, respectively. Pure FD powder at 23° displayed low overall crystallinity, which suggests that it is a semicrystalline polymer, which is consistent with other reports (Saravana et al., 2016). The XRD patterns of FD-based nanomaterials were similar to that of FD. There were no significant differences between nanomaterials with different ratios. Also, the diffraction peaks of PEO were largely depressed in the nanomaterials probably due to a small amount of added PEO and/or good miscibility between FD and PEO.

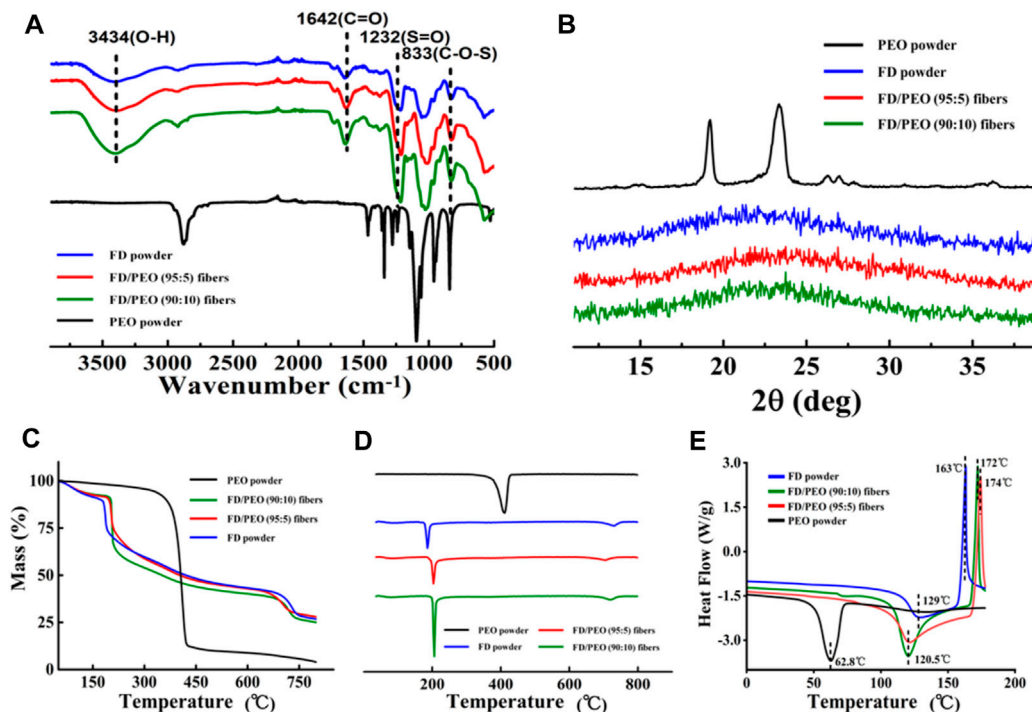


FIGURE 4 | (A) FT-IR spectra, **(B)** XRD diffraction patterns, **(C)** Raw TGA thermograms and **(D)** their first-order derivative curves, and **(E)** DSC curves of FD powder, PEO powder, FD/PEO (95/5) beaded nanofibers, and FD/PEO (90/10) nanofibers.

Raw TGA thermograms and their first-order derivative curves are shown in **Figures 4C,D**. It was found that the pure PEO is found to thermally decompose at 375°C and decomposed completely at 433°C. The FD powder showed a weight loss of approximately 28% between 35 and 200°C and a continuous weight loss until the temperature reaches 800°C. The thermal behavior of FD/PEO nanomaterials displayed a similar trend to that of FD powder. The first stage of weight loss (<100°C) was due to moisture evaporation. The second stage exhibited a sharp decrease in weight owing to the decomposition of FD. With an increased amount of PEO, the maximum decomposition rate of FD/PEO nanomaterials slightly increased from 186 to 206°C. The reason may be due to a small amount of added PEO in composite nanofibers. Also, the introduction of PEO increased the thermal stability of FD/PEO nanomaterials.

Moreover, DSC analysis of the prepared FD/PEO nanomaterials displayed shifts in glass transition temperature with the incorporation of PEO to FD. No extra transition signals appeared as compared to the DSC curve of FD. Taken together, these results indicate that there was good miscibility or no obvious phase separation between FD and PEO.

FD/PEO Nanofibers Modified by CS

Because PEO and FD have a high solubility in water, the structure of prepared FD/PEO fibrous membranes in the aqueous environment can be destroyed. To maintain the structure of FD/PEO nanofibers in the cell culture medium, it is necessary to modify the nanofiber surface with an H₂O-insoluble polymer.

Here, positively charged CS was selected which could interact with negatively charged FD *via* the electrostatic interaction. The FD/PEO nanofibers were soaked in 2 wt% CS solutions with various HAc/H₂O percentages (i.e., 30, 60, and 90%). Representative SEM images of FD/PEO nanofibers before and after modification are shown in **Figure 5**. After the treatment of CS solution in HAc/H₂O = 30 wt%, the integrity of the fiber structure was retained (**Figure 5A**). After the modification of CS solution in HAc/H₂O = 60 and 90 wt%, the fibers swelled largely and the fiber structure was disappeared (**Figures 5B,C**). Next, CS-modified FD/PEO nanofibers were soaked in water for 30 min and their fiber morphology remained. However, the nanofibers had obvious swelling and adhesion (**Figure 5D**). Although chemical crosslinking has been widely used to make natural polymers stable, the crosslinkers used are cytotoxic. Meanwhile, the chemical crosslinking of fucoidan has been not reported. Therefore, positively charged CS was selected which could interact with negatively charged FD *via* the electrostatic interaction.

HUVEC Attachment and Their Interactions With Monocytes

HUVECs were selected because they are the main cell type and play a critical role in the function of the blood vessel (Yang et al., 2017; Kang et al., 2019; Rocha et al., 2020). Cell attachment is regarded as the first and critical response of cells with their surrounding bio-scaffold, which precedes all

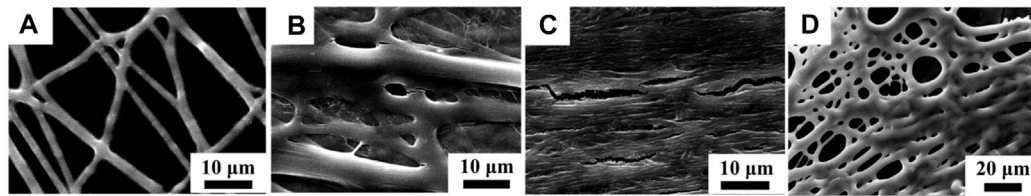


FIGURE 5 | SEM images of CS-modified FD nanofibers with different weight ratios of HAC/H₂O [i.e., (A) 30%, (B) 60%, and (C) 90%]. (D) The SEM image of CS-modified FD-based nanofibers in HAC/H₂O = 30% after infiltrating with H₂O.

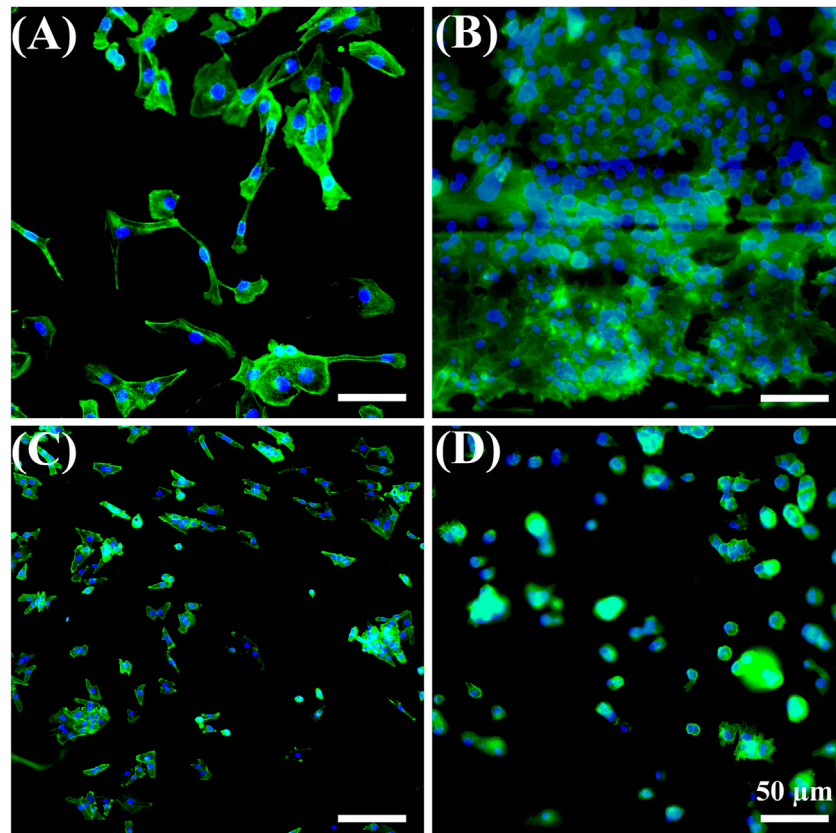


FIGURE 6 | Fluorescent images of HUVECs for 1 day on the (A) coverslip control, (B) CS-modified FD/UHMWPEO nanofibers, (C) CS/UHMWPEO nanofibers, and (D) FD/CS/UHMWPEO nonfibrous film. Scale bars = 50 μ m.

other cellular events, e.g., survival, viability, function, and differentiation (Zhou et al., 2015; Zhou et al., 2020). As shown in **Figure 6**, HUVEC adhesion in all samples after 1 day of cell culture was studied with a double-label fluorescence staining of the nucleus (blue) and actin cytoskeleton (green). More adhered cells were found on the CS-modified FD/UHMWPEO nanofibers compared to the CS/UHMWPEO nanofibers and FD/CS/UHMWPEO nonfibrous films, indicating that FD and fiber structure could greatly promote cell adhesion. This result suggests that the CS-modified FD/UHMWPEO nanofibers possessed excellent cytocompatibility as a bio-scaffold for blood vessel tissue engineering.

The adhesion and migration of monocytes to endothelial cells is a process of the inflammatory response, which is mediated by specific molecules on endothelial cells and monocytes (Ross, 1999; Bian et al., 2017; Lin et al., 2018; Liu et al., 2020). THP-1 cells were seeded on HUVECs exposed to different materials. As shown in **Figure 7A**, the number of adhered monocytes on HUVECs cultured on the CS-modified FD/UHMWPEO nanofibers was less than those of other groups, indicating that the CS-modified FD/UHMWPEO nanofibers could inhibit the inflammatory response. Quantification shows that there were no significant differences among the samples.

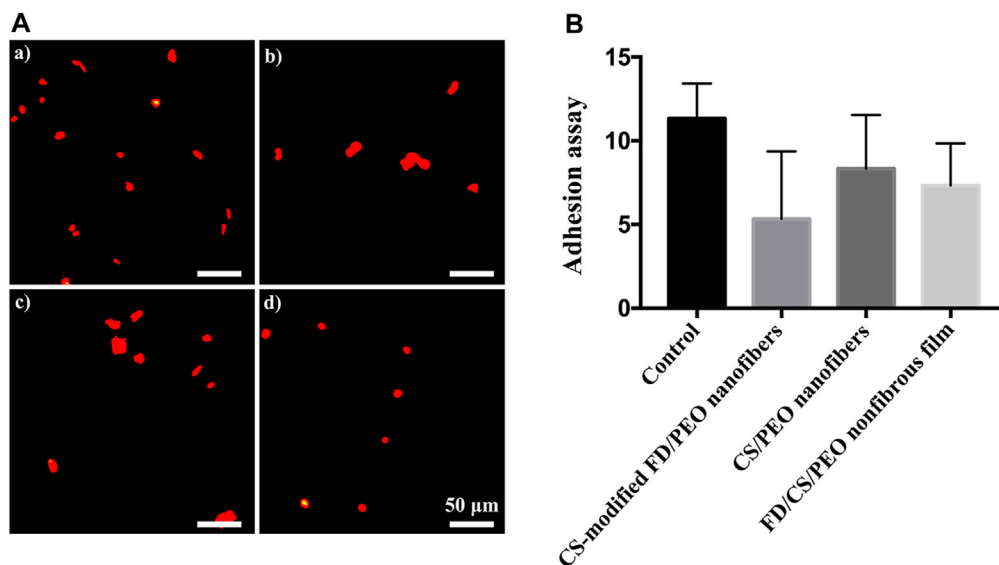


FIGURE 7 | (A) Fluorescent images of THP-1 cells on HUVECs cultured on the (a) the coverslip control, (b) CS-modified FD/UHMWPEO nanofibers, (c) CS/UHMWPEO nanofibers, and (d) FD/CS/UHMWPEO nonfibrous film. Scale bar = 50 μm. **(B)** The number of THP-1 cells on HUVECs cultured on different samples.

CONCLUSION

In summary, chitosan-modified FD/UHMWPEO nanofibers were fabricated using green electrospinning. Water was screened and used as a solvent to dissolve FD. The defect-free nanofibers with an average diameter (560 ± 88 nm) were prepared in the electrospinning of the FD/UHMWPEO (90:10) solution. The addition of UHMWPEO greatly improved the electrospinnability of the solution and thermo-stability of nanofibers. Cellular experiments demonstrated that the chitosan-modified FD/UHMWPEO nanofibers facilitate HUVEC adhesion and suppressed the attachment of monocytes. Thus, the developed FD-based nanofibers display great potential for vascular tissue engineering.

DATA AVAILABILITY STATEMENT

The original contributions presented in the study are included in the article/Supplementary Material, further inquiries can be directed to the corresponding author.

REFERENCES

- Ahmadi, A., Ahmadi, P., Sani, M. A., Ehsani, A., and Ghanbarzadeh, B. (2021). Functional Biocompatible Nanocomposite Films Consisting of Selenium and Zinc Oxide Nanoparticles Embedded in Gelatin/cellulose Nanofiber Matrices. *Int. J. Biol. Macromolecules* 175, 87–97. doi:10.1016/j.ijbiomac.2021.01.135
- Bian, T., Li, H., Zhou, Q., Ni, C., Zhang, Y., and Yan, F. (2017). Human β -Defensin 3 Reduces TNF- α -Induced Inflammation and Monocyte Adhesion in Human Umbilical Vein Endothelial Cells. *Mediators Inflamm.* 2017, 8529542. doi:10.1155/2017/8529542
- Bidarra, S. J., Barrias, C. C., and Granja, P. L. (2014). Injectable Alginate Hydrogels for Cell Delivery in Tissue Engineering. *Acta Biomater.* 10, 1646–1662. doi:10.1016/j.actbio.2013.12.006

AUTHOR CONTRIBUTIONS

QZ contributed to the conception and design of the study. YC, HZ, YH, ZS, and PS performed the experiment. YC and HZ analyzed the data and performed the statistical analysis. YC and HZ wrote the first draft of the manuscript. QZ revised the manuscript. All authors contributed to manuscript revision, read, and approved the submitted version.

FUNDING

The authors are very grateful for the financial support of the National Natural Science Foundation of China (Grant No. 31900957), Shandong Provincial Natural Science Foundation (Grant No. ZR2019QC007), Innovation and technology program for the excellent youth scholars of higher education of Shandong province (Grant No. 2019KJE015), and China Postdoctoral Science Foundation (Grant No. 2019M652326).

- Casasola, R., Thomas, N. L., Trybala, A., and Georgiadou, S. (2014). Electrospun Poly Lactic Acid (PLA) Fibres: Effect of Different Solvent Systems on Fibre Morphology and Diameter. *Polymer* 55, 4728–4737. doi:10.1016/j.polymer.2014.06.032
- Coultas, L., Chawengsaksohak, K., and Rossant, J. (2005). Endothelial Cells and VEGF in Vascular Development. *Nature* 438, 937–945. doi:10.1038/nature04479
- Cui, C., Chen, X., Ma, L., Zhong, Q., Li, Z., Mariappan, A., et al. (2020). Polythiourethane Covalent Adaptable Networks for Strong and Reworkable Adhesives and Fully Recyclable Carbon Fiber-Reinforced Composites. *ACS Appl. Mater. Inter.* 12, 47975–47983. doi:10.1021/acsami.0c14189
- Darajinejad, Z., and Shabani, I. (2021). Enhancing Cellular Infiltration on Fluffy Polyaniline-Based Electrospun Nanofibers. *Front. Bioeng. Biotechnol.* 9, 641371. doi:10.3389/fbioe.2021.641371

- Devolder, R. J., Bae, H., Lee, J., and Kong, H. (2011). Directed Blood Vessel Growth Using an Angiogenic Microfiber/microparticle Composite Patch. *Adv. Mater.* 23, 3139–3143. doi:10.1002/adma.201100823
- Fernando, I. P. S., Kim, D., Nah, J.-W., and Jeon, Y.-J. (2019). Advances in Functionalizing Fucoidans and Alginates (Bio)polymers by Structural Modifications: A Review. *Chem. Eng. J.* 355, 33–48. doi:10.1016/j.cej.2018.08.115
- Fetz, A. E., Wallace, S. E., and Bowlin, G. L. (2021). Electrospun Polydioxanone Loaded with Chloroquine Modulates Template-Induced NET Release and Inflammatory Responses from Human Neutrophils. *Front. Bioeng. Biotechnol.* 9, 268. doi:10.3389/fbioe.2021.652055
- Hao, Y., Zhao, W., Zhang, L., Zeng, X., Sun, Z., Zhang, D., et al. (2020). Bio-Multifunctional Alginate/Chitosan/Fucoidan Sponges with Enhanced Angiogenesis and Hair Follicle Regeneration for Promoting Full-Thickness Wound Healing. *Mater. Des.* 193, 108863. doi:10.1016/j.matdes.2020.108863
- Higgins, A. M., Banik, B. L., and Brown, J. L. (2015). Geometry Sensing through POR1 Regulates Rac1 Activity Controlling Early Osteoblast Differentiation in Response to Nanofiber Diameter. *Integr. Biol.* 7, 229–236. doi:10.1039/c4ib00225c
- Jaiswal, D., and Brown, J. L. (2012). Nanofiber Diameter-Dependent MAPK Activity in Osteoblasts. *J. Biomed. Mater. Res.* 100A, 2921–2928. doi:10.1002/jbm.a.34234
- Jana, S., Gandhi, A., and Roy, C. (2020). “Marine Biomaterials-Based Systems,” in *Marine Biomaterials-Based Systems*. Editor S.-K Kim (John Wiley & Sons Ltd), 1141–1174. doi:10.1002/9781119143802.ch47
- Kang, P. L., Huang, H. H., Chen, T., Ju, K. C., and Kuo, S. M. (2019). Angiogenesis-promoting Effect of LIPUS on hADSCs and HUVECs Cultured on Collagen/hyaluronan Scaffolds. *Mater. Sci. Eng. C* 102, 22–33. doi:10.1016/j.msec.2019.04.045
- Kenryand Lim, C. T. (2017). Nanofiber Technology: Current Status and Emerging Developments. *Prog. Polym. Sci.* 70, 1–17. doi:10.1016/j.progpolymsci.2017.03.002
- Kondo, T., Sawatari, C., Manley, R. S. J., and Gray, D. G. (1994). Characterization of Hydrogen Bonding in Cellulose-Synthetic Polymer Blend Systems with Regioselectively Substituted Methylcellulose. *Macromolecules* 27, 210–215. doi:10.1021/ma00079a031
- Li, B., Lu, F., Wei, X., and Zhao, R. (2008). Fucoidan: Structure and Bioactivity. *Molecules* 13, 1671–1695. doi:10.3390/molecules13081671
- Li, Q., Wang, X., Lou, X., Yuan, H., Tu, H., Li, B., et al. (2015). Genipin-crosslinked Electrospun Chitosan Nanofibers: Determination of Crosslinking Conditions and Evaluation of Cytocompatibility. *Carbohydr. Polym.* 130, 166–174. doi:10.1016/j.carbpol.2015.05.039
- Li, W., Yan, Z., Ren, J., and Qu, X. (2018). Manipulating Cell Fate: Dynamic Control of Cell Behaviors on Functional Platforms. *Chem. Soc. Rev.* 47, 8639–8684. doi:10.1039/c8cs00053k
- Li, D., Yang, Y., Wang, S., He, X., Liu, M., Bai, B., et al. (2021a). Role of Acetylation in Doxorubicin-Induced Cardiotoxicity. *Redox Biol.* 46, 102089. doi:10.1016/j.redox.2021.102089
- Li, X., Yang, Y., Wang, Z., Jiang, S., Meng, Y., Song, X., et al. (2021b). Targeting Non-Coding RNAs in Unstable Atherosclerotic Plaques: Mechanism, Regulation, Possibilities, and Limitations. *Int. J. Biol. Sci.* 17, 3413–3427. doi:10.7150/ijbs.62506
- Lin, Z., Jin, J., Bai, W., Li, J., and Shan, X. (2018). Netrin-1 Prevents the Attachment of Monocytes to Endothelial Cells via an Anti-inflammatory Effect. *Mol. Immunol.* 103, 166–172. doi:10.1016/j.molimm.2018.08.021
- Liu, Y., Deng, W., Yang, L., Fu, X., Wang, Z., van Rijn, P., et al. (2020). Biointerface Topography Mediates the Interplay between Endothelial Cells and Monocytes. *RSC Adv.* 10, 13848–13854. doi:10.1039/d0ra00704h
- Liu, L., Han, Z., An, F., Gong, X., Zhao, C., Zheng, W., et al. (2021). Aptamer-Based Biosensors for the Diagnosis of Sepsis. *J. Nanobiotechnology* 19, 1–22. doi:10.1186/s12951-021-00959-5
- Lv, D., Zhu, M., Jiang, Z., Jiang, S., Zhang, Q., Xiong, R., et al. (2018). Green Electrospun Nanofibers and Their Application in Air Filtration. *Macromol. Mater. Eng.* 303, 1–18. doi:10.1002/mame.201800336
- Mooney, D. J., Baldwin, D. F., Suh, N. P., Vacanti, J. P., and Langer, R. (1996). Novel Approach to Fabricate Porous Sponges of Poly(D,L-Lactic-Co-Glycolic Acid) without the Use of Organic Solvents. *Biomaterials* 17, 1417–1422. doi:10.1016/0142-9612(96)87284-x
- Oka, S., Okabe, M., Tsubura, S., Mikami, M., and Imai, A. (2020). Properties of Fucoidans Beneficial to Oral Healthcare. *Odontology* 108, 34–42. doi:10.1007/s10266-019-00437-3
- Pelipenko, J., Kocbek, P., and Kristl, J. (2015). Nanofiber Diameter as a Critical Parameter Affecting Skin Cell Response. *Eur. J. Pharm. Sci.* 66, 29–35. doi:10.1016/j.ejps.2014.09.022
- Peng, W., Ren, S., Zhang, Y., Fan, R., Zhou, Y., Li, L., et al. (2021). MgO Nanoparticles-Incorporated PCL/Gelatin-Derived Coaxial Electrospinning Nanocellulose Membranes for Periodontal Tissue Regeneration. *Front. Bioeng. Biotechnol.* 9, 216. doi:10.3389/fbioe.2021.668428
- Rajendran, P., Rengarajan, T., Thangavel, J., Nishigaki, Y., Sakthisekaran, D., Sethi, G., et al. (2013). The Vascular Endothelium and Human Diseases. *Int. J. Biol. Sci.* 9, 1057–1069. doi:10.7150/ijbs.7502
- Rocha, L. A., Gomes, E. D., Afonso, J. L., Granja, S., Baltazar, F., Silva, N. A., et al. (2020). *In Vitro* evaluation of ASCs and HUVECs Co-cultures in 3D Biodegradable Hydrogels on Neurite Outgrowth and Vascular Organization. *Front. Cell Dev. Biol.* 8, 489. doi:10.3389/fcell.2020.00489
- Ross, R. (1999). Atherosclerosis - An Inflammatory Disease. *N. Engl. J. Med.* 340, 115–126. doi:10.1056/nejm199901143400207
- Saravana, P. S., Cho, Y.-J., Park, Y.-B., Woo, H.-C., and Chun, B.-S. (2016). Structural, Antioxidant, and Emulsifying Activities of Fucoidan from *Saccharina Japonica* Using Pressurized Liquid Extraction. *Carbohydr. Polym.* 153, 518–525. doi:10.1016/j.carbpol.2016.08.014
- Senthilkumar, K., Ramajayam, G., Venkatesan, J., Kim, S.-K., and Ahn, B.-C. (2017). “Biomedical Applications of Fucoidan, Seaweed Polysaccharides,” in *Seaweed Polysaccharides*. Editors J Venkatesan, S Anil, and S.-K Kim (Elsevier), 269–281. doi:10.1016/b978-0-12-809816-5.00014-1
- Shariful, M. I., Sharif, S. B., Lee, J. J. L., Habiba, U., Ang, B. C., and Amalina, M. A. (2017). Adsorption of Divalent Heavy Metal Ion by Mesoporous-High Surface Area Chitosan/poly (Ethylene Oxide) Nanofibrous Membrane. *Carbohydr. Polym.* 157, 57–64. doi:10.1016/j.carbpol.2016.09.063
- Shenoy, S. L., Bates, W. D., Frisch, H. L., and Wnek, G. E. (2005). Role of Chain Entanglements on Fiber Formation during Electrospinning of Polymer Solutions: Good Solvent, Non-specific Polymer-Polymer Interaction Limit. *Polymer* 46, 3372–3384. doi:10.1016/j.polymer.2005.03.011
- Xu, C., Inai, R., Kotaki, M., and Ramakrishna, S. (2004). Aligned Biodegradable Nanofibrous Structure: A Potential Scaffold for Blood Vessel Engineering. *Biomaterials* 25, 877–886. doi:10.1016/s0142-9612(03)00593-3
- Xue, J., Wu, T., Dai, Y., and Xia, Y. (2019). Electrospinning and Electrospun Nanofibers: Methods, Materials, and Applications. *Chem. Rev.* 119, 5298–5415. doi:10.1021/acs.chemrev.8b00593
- Yang, J., Hao, X., Li, Q., Akpanyung, M., Nejari, A., Neve, A. L., et al. (2017). CAGW Peptide- and PEG-Modified Gene Carrier for Selective Gene Delivery and Promotion of Angiogenesis in HUVECs *In Vivo*. *ACS Appl. Mater. Inter.* 9, 4485–4497. doi:10.1021/acsami.6b14769
- Yang, L., Han, D., Zhan, Q., Li, X., Shan, P., Hu, Y., et al. (2019). Blood TfR+ Exosomes Separated by a pH-Responsive Method Deliver Chemotherapeutics for Tumor Therapy. *Theranostics* 9, 7680–7696. doi:10.7150/thno.37220
- Yang, L., Pijuan-Galito, S., Rho, H. S., Vasilevich, A. S., Eren, A. D., Ge, L., et al. (2021a). High-Throughput Methods in the Discovery and Study of Biomaterials and Materiobiology. *Chem. Rev.* 121, 4561–4677. doi:10.1021/acs.chemrev.0c00752
- Yang, Y., Zhao, X., Yu, J., Chen, X., Wang, R., Zhang, M., et al. (2021b). Bioactive Skin-Mimicking Hydrogel Band-Aids for Diabetic Wound Healing and Infectious Skin Incision Treatment. *Bioactive Mater.* 6, 3962–3975. doi:10.1016/j.bioactmat.2021.04.007
- Yao, Y., Zaw, A. M., Anderson, D. E. J., Hinds, M. T., and Yim, E. K. F. (2020). Fucoidan Functionalization on Poly(vinyl Alcohol) Hydrogels for Improved Endothelialization and Hemocompatibility. *Biomaterials* 249, 120011–120024. doi:10.1016/j.biomaterials.2020.120011
- Yau, W. W. Y., Long, H., Gauthier, N. C., Chan, J. K. Y., and Chew, S. Y. (2015). The Effects of Nanofiber Diameter and Orientation on siRNA Uptake and Gene Silencing. *Biomaterials* 37, 94–106. doi:10.1016/j.biomaterials.2014.10.003
- Yin, X., Hao, Y., Lu, Y., Zhang, D., Zhao, Y., Mei, L., et al. (2021). Bio-Multifunctional Hydrogel Patches for Repairing Full-Thickness Abdominal Wall Defect. *Adv. Funct. Mater.* 2105614. doi:10.1002/adfm.202105614
- Yu, Z., Li, Q., Wang, J., Yu, Y., Wang, Y., Zhou, Q., et al. (2020). Reactive Oxygen Species-Related Nanoparticle Toxicity in the Biomedical Field. *Nanoscale Res. Lett.* 15, 115. doi:10.1186/s11671-020-03344-7
- Yu, J., Xu, K., Chen, X., Zhao, X., Yang, Y., Chu, D., et al. (2021). Highly Stretchable, Tough, Resilient, and Antifatigue Hydrogels Based on Multiple Hydrogen

- Bonding Interactions Formed by Phenylalanine Derivatives. *Biomacromolecules* 22, 1297–1304. doi:10.1021/acs.biomac.0c01788
- Zhang, Y., Lim, C. T., Ramakrishna, S., and Huang, Z.-M. (2005). Recent Development of Polymer Nanofibers for Biomedical and Biotechnological Applications. *J. Mater. Sci. Mater. Med.* 16, 933–946. doi:10.1007/s10856-005-4428-x
- Zhang, Y., Venugopal, J. R., El-Turki, A., Ramakrishna, S., Su, B., and Lim, C. T. (2008). Electrospun Biomimetic Nanocomposite Nanofibers of Hydroxyapatite/chitosan for Bone Tissue Engineering. *Biomaterials* 29 (32), 4314–4322. doi:10.1016/j.biomaterials.2008.07.038
- Zheng, W., Hao, Y., Wang, D., Huang, H., Guo, F., Sun, Z., et al. (2021). Preparation of Triamcinolone Acetonide-Loaded Chitosan/fucoidan Hydrogel and its Potential Application as an Oral Mucosa Patch. *Carbohydr. Polym.* 272, 118493. doi:10.1016/j.carbpol.2021.118493
- Zhou, Q., Bao, M., Yuan, H., Zhao, S., Dong, W., and Zhang, Y. (2013). Implication of Stable Jet Length in Electrospinning for Collecting Well-Aligned Ultrafine PLLA Fibers. *Polymer* 54, 6867–6876. doi:10.1016/j.polymer.2013.10.042
- Zhou, Q., Xie, J., Bao, M., Yuan, H., Ye, Z., Lou, X., et al. (2015). Engineering Aligned Electrospun PLLA Microfibers with Nano-Porous Surface Nanotopography for Modulating the Responses of Vascular Smooth Muscle Cells. *J. Mater. Chem. B* 3, 4439–4450. doi:10.1039/c5tb00051c
- Zhou, Q., Zhang, H., Zhou, Y., Yu, Z., Yuan, H., Feng, B., et al. (2017). Alkali-Mediated Miscibility of Gelatin/Polycaprolactone for Electrospinning Homogeneous Composite Nanofibers for Tissue Scaffolding. *Macromol. Biosci.* 17, 1–10. doi:10.1002/mabi.201700268
- Zhou, Q., Chen, J., Luan, Y., Vainikka, P. A., Thallmair, S., Marrink, S. J., et al. (2020). Unidirectional Rotating Molecular Motors Dynamically Interact with Adsorbed Proteins to Direct the Fate of Mesenchymal Stem Cells. *Sci. Adv.* 6, eaay2756. doi:10.1126/sciadv.aay2756
- Zong, T., Yang, Y., Lin, X., Jiang, S., Zhao, H., Liu, M., et al. (2021). 5'-tiRNA-Cys-GCA Regulates VSMC Proliferation and Phenotypic Transition by Targeting STAT4 in Aortic Dissection. *Mol. Ther. Acids.* doi:10.1016/j.omtn.2021.07.013

Conflict of Interest: ZS and PS are employed by Qingdao Bright Moon Seaweed Group Co., Ltd.

The remaining authors declare that the research was conducted in the absence of any commercial or financial relationships that could be construed as a potential conflict of interest.

Publisher's Note: All claims expressed in this article are solely those of the authors and do not necessarily represent those of their affiliated organizations, or those of the publisher, the editors and the reviewers. Any product that may be evaluated in this article, or claim that may be made by its manufacturer, is not guaranteed or endorsed by the publisher.

Copyright © 2021 Chen, Zhu, Hao, Sun, Shen and Zhou. This is an open-access article distributed under the terms of the Creative Commons Attribution License (CC BY). The use, distribution or reproduction in other forums is permitted, provided the original author(s) and the copyright owner(s) are credited and that the original publication in this journal is cited, in accordance with accepted academic practice. No use, distribution or reproduction is permitted which does not comply with these terms.



Extracellular Vesicles as Natural Delivery Carriers Regulate Oxidative Stress Under Pathological Conditions

Hongzhao Qi^{1*}, Yingruo Wang², Shunxin Fa^{3,4}, Changqing Yuan³ and Lijun Yang^{5*}

¹Department of Aging Research, Institute of Translational Medicine, The Affiliated Hospital of Qingdao University, College of Medicine, Qingdao University, Qingdao, China, ²Shandong University of Science and Technology, Qingdao, China, ³School of Stomatology, Qingdao University, Qingdao, China, ⁴York School, Monterey, CA, United States, ⁵Qingdao Institute of Bioenergy and Bioprocess Technology, Chinese Academy of Sciences, Qingdao, China

OPEN ACCESS

Edited by:

Huihua Yuan,
Nantong University, China

Reviewed by:

Chaoyong Liu,
Beijing University of Chemical
Technology, China
Xin Hou,
Tianjin University, China
Yu Ren,
Tianjin Medical University, China

*Correspondence:

Hongzhao Qi
qihongzhao@qdu.edu.cn
Lijun Yang
tingjun02101224@126.com

Specialty section:

This article was submitted to
Biomaterials,
a section of the journal
Frontiers in Bioengineering and
Biotechnology

Received: 02 August 2021

Accepted: 26 August 2021

Published: 07 September 2021

Citation:

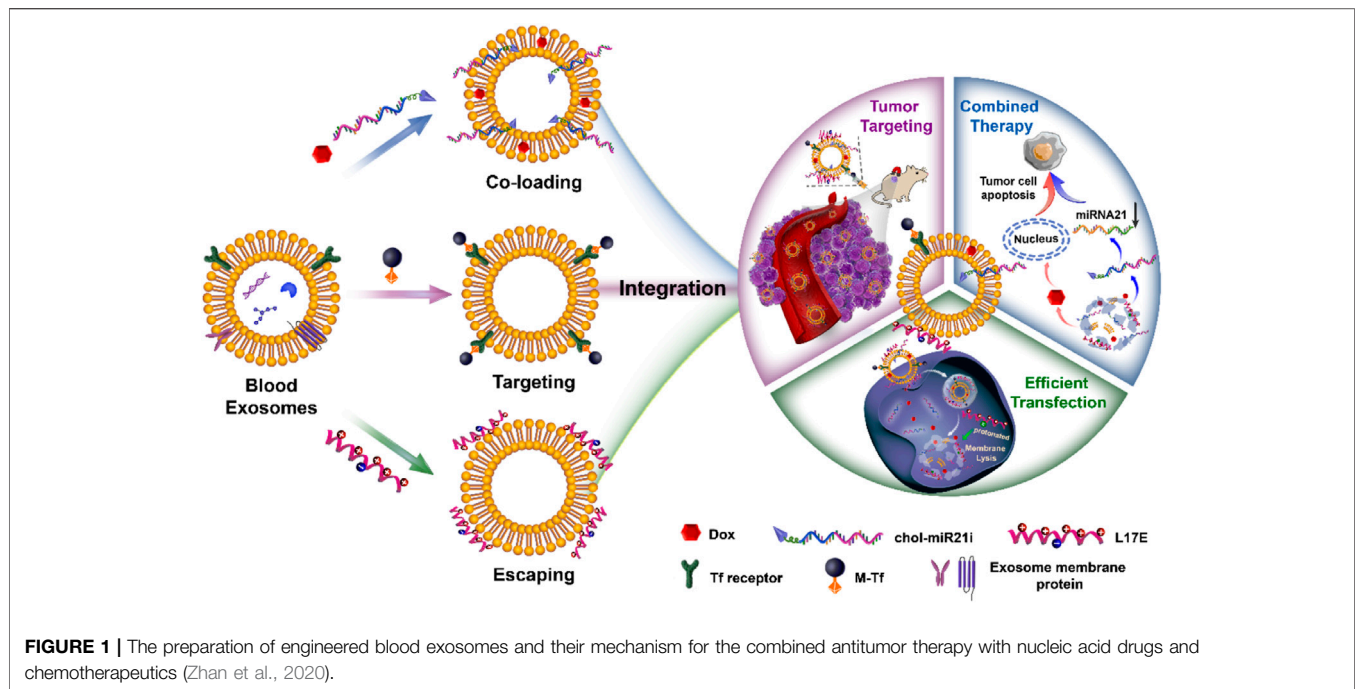
Qi H, Wang Y, Fa S, Yuan C and Yang L
(2021) Extracellular Vesicles as Natural
Delivery Carriers Regulate Oxidative
Stress Under Pathological Conditions.
Front. Bioeng. Biotechnol. 9:752019.
doi: 10.3389/fbioe.2021.752019

Extracellular vesicles are cellular secretory particles that can be used as natural drug delivery carriers. They have successfully delivered drugs including chemotherapeutics, proteins, and genes to treat various diseases. Oxidative stress is an abnormal physiological phenomenon, and it is associated with nearly all diseases. In this short review, we summarize the regulation of EVs on oxidative stress. There are direct effects and indirect effects on the regulation of oxidative stress through EVs. On the one hand, they can deliver antioxidant substances or oxides to recipient cells, directly relieving or aggravating oxidative stress. On the other hand, regulate factors of oxidative stress-related signaling pathways can be delivered to recipient cells by the mediation of EVs, realizing the indirect regulation of oxidative stress. To the best of our knowledge, however, only endogenous drugs have been delivered by EVs to regulate oxidative stress till now. And the heterogeneity of EVs may complicate the regulation of oxidative stress. Therefore, this short review aims to draw more attention to the EVs-based regulation of oxidative stress, and we hope excellent EVs-based delivery carriers that can deliver exogenous drugs to regulate oxidative stress can be exploited.

Keywords: extracellular vesicles, oxidative stress, delivery carriers, direct effects, indirect effects

INTRODUCTION

Extracellular vesicles (EVs) are phospholipid bilayer-encapsulated vesicles that can be secreted by nearly all cell types (Andaloussi et al., 2013). They can be found in cell culture supernatants as well as biological fluids such as saliva (Winck et al., 2015), blood (Arraud et al., 2014), milk (Zonneveld et al., 2014), cerebrospinal fluids (Akers et al., 2016), and malignant ascites (Li et al., 2019). According to their biogenesis, EVs can be generally divided into three distinct categories: exosomes, microvesicles, and apoptotic bodies (Lässer et al., 2018). Exosomes originate from multivesicular bodies (MVBs) formed by the invagination of the limiting membrane of endosomes (Théry et al., 2002). MVBs can fuse with the cellular membrane to release exosomes into the extracellular space. Different from exosomes, microvesicles and apoptotic bodies are both generated from the cell membrane (Akers et al., 2013). Microvesicles derive from direct outward budding of the normal cells membrane, while apoptotic bodies are only secreted by dying cells during their fragmentation. Besides the origination, size is commonly used as a criterion to distinguish between the three types of EVs (Varga et al., 2014). In general, the size of exosomes, microvesicles, and apoptotic bodies is respectively 30–150 nm, 50–1,000 nm, and 50 nm–2 μm. It should be noted that the size range of the three types of EVs is



overlapped due to their severe heterogeneity (Lőrincz et al., 2015). Furthermore, the heterogeneity of EVs may result in the absence of marker proteins belonging to a certain population. The distinguish of different types of EVs, therefore, cannot rely on a single standard, and it needs to comprehensively consider multiple criteria such as size, marker proteins or genes, and specific lipids (Théry et al., 2018). EVs have been recognized as a kind of messengers of intercellular communication during the past several decades. They can transport cargoes including DNA, RNA, proteins, and lipids between neighboring or distant cells (Tkach and Théry 2016). Taking advantage of their cargoes, EVs can perform numerous physiological functions. As an example, EVs can regulate immune responses to participate in the occurrence and development of many diseases such as cancers, cardiovascular diseases, osteoporosis, and central nervous system diseases (Robbins and Morelli, 2014; Yin et al., 2017).

From a material science point of view, EVs are natural drug delivery carriers. Their phospholipid bilayers similar in structure to liposomes endow EVs with the ability of hydrophilic and hydrophobic drugs loading (van der Meel et al., 2014). And the loaded drugs can be effectively protected from degradation. Compared with liposomes, EVs have intrinsic stability owing to their negatively charged surface and the support of skeletal proteins (Frank et al., 2018). Importantly, EVs have many unique properties superior to synthetic drug delivery carriers. They have low immunogenicity and cytotoxicity due to their endogenous source (Elsharkasy et al., 2020). And their lipid composition and protein content endow them with inherent active targeting properties and the capacity to cross multiple biological barriers such as the blood-brain barrier and mucosal barrier (Ashrafian et al., 2019; Matsumoto et al., 2017). Besides endogenous compositions, exogenous drugs can be loaded in EVs and delivered into target cells (Vader et al., 2016). In our previous

researches, we have exploited a series of blood exosome-based delivery systems to efficiently deliver chemotherapeutics for tumor therapy (Qi et al., 2017; Qi et al., 2016; Qi et al., 2018; Yang et al., 2019; Zhan et al., 2020). As shown in **Figure 1**, we take advantage of the structure and properties of the blood exosome membrane to load nucleic acid drugs and chemotherapeutics. The system with the tumor-targeting ability and endosome-escaping capacity realizes the combined antitumor therapy. In general, EVs have been used as carriers to deliver endogenous or exogenous drugs for disease treatment. Oxidative stress is an abnormal physiological phenomenon, and it is defined as “an imbalance between antioxidants and oxidants, resulting in the disruption of redox signaling and the corresponding molecular damage.” To the best of our knowledge, it is associated with nearly all diseases such as cancers (Hayes et al., 2020), cardiovascular diseases (Dubois-Deruy et al., 2020), aortic dissection (Zong et al., 2021), atherosclerosis (Li et al., 2021; Xue et al., 2021), COVID-19 (Li et al., 2021), drug-induced injuries (Li et al., 2021), and diabetes (Zhang et al., 2020). The effective regulation or relief of oxidative stress can potentially prevent many diseases, and EVs play an important role in this process. In this mini-review, we will mainly summarize how oxidative stress under pathological conditions is modulated by EV-mediated drug delivery, and also discuss the influence of oxidative stress on EVs.

EVs MODULATE OXIDATIVE STRESS

As we have mentioned above, EVs derived from different cells have heterogeneity. They may have different sizes, shapes, and compositions. Therefore, EVs may exhibit diverse regulations of oxidative stress, and the modulation mechanism is shown in

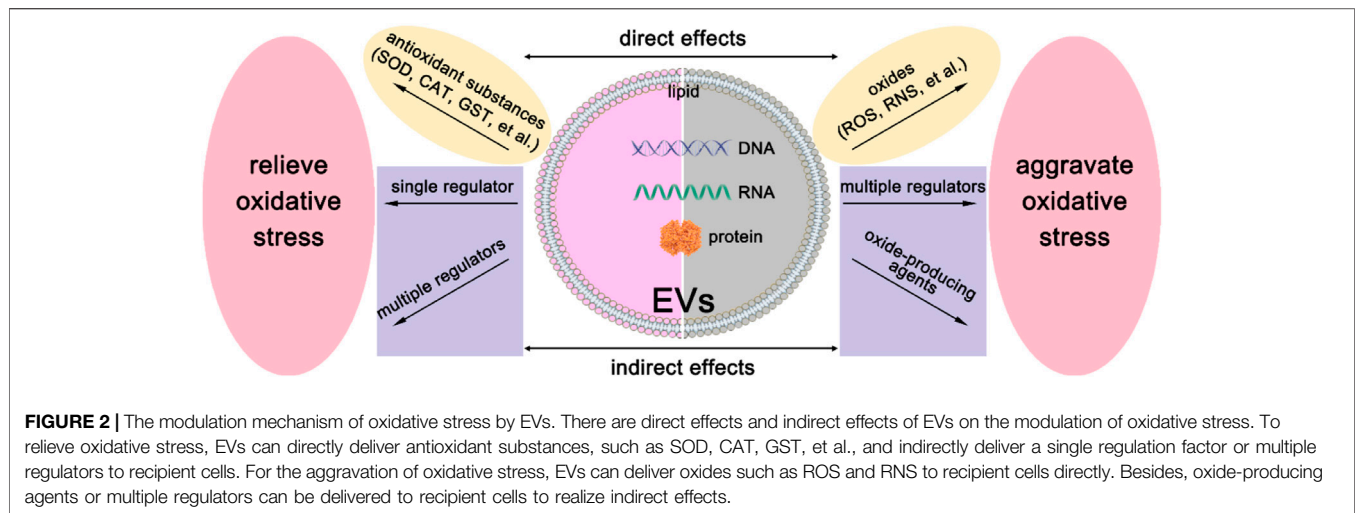


Figure 2. On the one hand, they can deliver reactive oxygen species (ROS) scavengers to relieve oxidative stress. On the other hand, they may produce ROS by their detrimental contents. Below we will discuss these two aspects in great detail.

EVs Relieve Oxidative Stress

Under normal physiological conditions, the production and elimination of ROS are balanced, while oxidative stress is produced when this balance is disturbed (Betteridge, 2000). In eukaryotic cells, antioxidant enzymes are commonly used as ROS scavengers to maintain the balance. EVs could inherently carry antioxidant enzymes, and numerous proteomic analyses have proved that superoxide dismutases (SOD), catalase (CAT), peroxiredoxin (PRDX), glutathione peroxidase (GPX), glutathione S-transferase (GST), and thioredoxin (TRX), et al. can be secreted into EVs (Bodega et al., 2019). These antioxidant enzymes loaded in EVs can directly relieve oxidative stress under various pathological conditions. For example, EVs released from T lymphocytes can deliver antioxidant enzymes, such as SOD isoforms and CAT, to human umbilical vein endothelial cells (HUVECs) and scavenge ROS (Soleti et al., 2012). Compared with other cells, stem cells are one of the main sources of antioxidant enzyme-loaded EVs. EVs derived from human mesenchymal stem cells (hMSCs) can protect hippocampal neurons from oxidative stress by the mediation of CAT (Bodart-Santos et al., 2019). hMSCs can also secrete manganese-SOD (Mn-SOD) into EVs that can reduce oxidative stress in the hepatic ischemia-reperfusion injury (Yao et al., 2018). In addition to antioxidant enzymes, other proteins can also be riched in EVs to relieve oxidative stress. EVs secreted by astroglial cells can transport apolipoprotein D to neurons and reduce oxidative stress damage (Pascua-Maestro et al., 2019). Besides, endothelial EVs carry functional endothelial nitric oxide synthase (eNOS) to regulate eNOS/Akt signaling pathway, protecting against oxidative stress in endothelial cells (Mahmoud et al., 2017). These antioxidant substance-loaded EVs are more like ROS scavengers and they can directly eliminate both intracellular and extracellular ROS to relieve oxidative stress.

Besides the above direct effects, indirect effects on ROS or oxidative stress can be carried out by EVs. They can deliver drugs to target cells and regulate oxidative stress-associated signaling pathways. For example, EVs secreted by H293T cells can deliver microRNA-126 to H₂O₂-treated neonatal rat ventricular cardiomyocytes, attenuating the ROS elevation and reducing the apoptosis by targeting ERRFI1 (Wang et al., 2019). By comparison, stem cell-derived EVs possess a greater regulatory capacity owing to their versatility. EVs derived from hMSCs can mediate the nuclear factor erythroid 2-related factor-2 (Nrf2) signaling pathway to reduce ROS generation in H₂O₂-stimulated keratinocytes or UV-irradiated mice skin (Wang et al., 2020). They can also resist cisplatin-induced oxidative stress by increasing GSH levels and suppressing activation of the p38MAPK pathway (Zhou et al., 2013). Adipose-derived mesenchymal stem cells (ADMSCs)-derived EVs can alleviate LPS induced accumulation of ROS and inflammatory cytokines in macrophages *via* regulating the Nrf2/heme oxygenase-1 (HO-1) signaling pathway (Shen et al., 2021). Besides, they can reduce ischemia/reperfusion injury as well as lung injury by suppressing oxidative stress (Liu et al., 2019; Gao et al., 2021). EVs derived from human placental mesenchymal stem cells (hP-MSCs) can eliminate ROS and reduce the activity of myeloperoxidase (MPO) effectively suppressing oxidative stress (Duan et al., 2020). Human Wharton Jelly mesenchymal stem cells (hWJMSCs)-released EVs can protect the kidney against ischemia/reperfusion injury by suppressing nicotinamide adenine dinucleotide phosphate oxidases 2 (NOX2) expression or enhancing Nrf2/ARE activation and the subsequent alleviation of the oxidative stress (Zhang et al., 2014; Zhang et al., 2016a). These indirect regulation effects may be more lasting. That is because antioxidant substances loaded in EVs for the direct relief of oxidative stress are readily destroyed.

Compound types of EVs such as EVs separated from body fluids also show the capacity of oxidative stress relief. Human milk-derived EVs protect intestinal stem cells (ISCs) from oxidative stress injury mediated *via* the Wnt/ β -catenin signaling pathway (Dong et al., 2020). Blood-derived EVs from

healthy individuals can restore the homeostasis of oxidative stress in the mice model of Parkinson's disease possessing neuroprotective effects (Sun et al., 2020). Camel milk EVs and their related genes ameliorate oxidative stress, normalize the antioxidant status, regulate the inflammatory pattern and improve the immune response in the cyclophosphamide (CTX)-treated animals (Ibrahim et al., 2019). The regulation mechanisms of compound types of EVs are more complicated because different types of EVs may have distinct functions. Furthermore, the ratio of different types of EVs is diverse at each separation resulting in the unstable regulation efficiency of compound types of EVs.

EVs Aggravate Oxidative Stress

In addition to being therapeutics, EVs may also be accomplices of oxidative stress. They can directly load ROS or other oxides and deliver them to recipient cells. EVs derived from hypoxia/reoxygenation-treated HUVECs can deliver ROS into H9C2 cardiomyocytes resulting in ROS overload and subsequent oxidative stress (Zhang et al., 2016b). However, this direct effect mediated by EVs-loaded ROS is rarely reported owing to the extremely short life span of ROS. Similar to indirect relief of oxidative stress, the indirect aggravation of oxidative stress depends on the contents of EVs. On the one hand, EVs may directly produce ROS by the loaded enzymes to aggravate oxidative stress. As an example, endothelial EVs containing NOX subunits produce ROS to involve in endothelial damage (Burger et al., 2016). On the other hand, EVs can regulate target cells to indirectly aggravate oxidative stress. Gene drugs loaded in EVs have multi-target control ability, and they may induce numerous target genes to involve in oxidative stress. For example, EVs from ionizing irradiated mouse embryo fibroblasts (MEFs) can deliver microRNA-34c into unirradiated cells, potentially triggering a cascade of gene expression alterations to increase ROS and inducing bystander oxidative stress (Rastogi et al., 2018). And this radiation-induced bystander effect is also present in the body. EVs originated from mice irradiated with 2-Gy X-rays are intravenously injected into bystander mice, and the circulating reactive oxygen metabolite (ROM) level is increased (Hargitai et al., 2021). Ketamine-injured human uroepithelial cells (SV-HUC-1) cells can secrete EVs containing specific miRNAs. They enhance oxidative stress by mediating P38/NF- κ B pathway (Xi et al., 2020). Besides genes, proteins or other small molecules can also be delivered by EVs. Polycyclic aromatic hydrocarbons-treated hepatocytes release EVs that are enriched in proteins, such as NOX and ferritin, as well as iron (van Meteren et al., 2020). These EVs could induce oxidative stress in recipient cells, thereby resulting in apoptosis.

It should be noted EVs that can aggravate oxidative stress are mainly derived from stimulated cells. The stimulating factors usually cause changes in the redox state of parent cells, and cells would secrete EVs to maintain their redox homeostasis. These EVs contain genes, proteins, and even lipids that can activate or regulate signaling pathways of oxidative stress aggravation. Therefore, these EVs can be thought of as products of the stress response of cells.

This stress response also occurs in the body. EVs derived from body fluids such as blood potentially aggravate oxidative stress. Platelet-derived EVs are the main type of EVs in the blood, and they are readily instigated to increase oxidative stress. In severe sepsis patients, platelet-derived EVs can produce ROS by the mediation of NOX and subsequently induce vascular cell apoptosis (Janiszewski et al., 2004). However, it is also reported that EVs derived from septic shock patients show protective effects on vascular function (Mostefai et al., 2008). This difference is potentially due to different sources of EVs. Besides, EVs from mice with the acetaminophen-induced liver injury can cause the allogeneic mice plasma ROS elevation inducing *in vivo* toxicity (Cho et al., 2018). Body fluids of different individuals are significant heterogeneity, and corresponding EVs may differ in origin, composition, and structure. Different from EVs from a specific type of cells, therefore, EVs separated from body fluids may show diverse functions.

OXIDATIVE STRESS MODULATE EVS

As drug delivery carriers, EVs can modulate oxidative stress by their contents. While the contents of EVs are readily changed under different pathological conditions. Cells with or without the treatment of oxidative stress secrete EVs with heterogeneity, and these diverse EVs may possess positive or negative effects on their adjacent or distant cells and tissues.

Oxidative Stress Educates EVs

Under oxidative stress, cells may secrete EVs with positive effects. Firstly, oxidative stress-educated EVs may have the anti-oxidative ability. These EVs can relieve the cell's oxidative stress as well as the oxidative stress of other cells or tissues. EVs derived from the non-pigmented ciliary epithelium (NPCE) which are exposed to oxidative stress can deliver protecting messages to activate major antioxidant genes and enhance SOD and CAT activity, protecting the trabecular meshwork (TM). Mouse mast cells exposed to oxidative stress release EVs, and these EVs transport mRNA to recipient cells providing them with resistance against oxidative stress (Tailleux et al., 2010). Besides relieving oxidative stress, other beneficial physiological effects can also be realized through oxidative stress-educated EVs. Retinal pigment epithelium (RPE) cells release higher amounts of EVs when they are exposed to oxidative stress. These EVs have a higher expression of vascular endothelial growth factor receptors (VEGFRs) in the surface membrane and have VEGFR mRNA in their internal cavity, promoting angiogenesis in endothelial cells (Atienzar-Aroca et al., 2016). Besides, oxidative stress-educated EVs can also involve in the muscle regeneration process. EVs released from oxidatively challenged myotubes have an increased loading of nucleic acid. They can decrease the diameter of the myotube, the mRNA levels of myogenin, and the expression of myosin heavy chain, leading to the proliferation of recipient myoblast (Guescini et al., 2017). EVs derived from stem cells often show beneficial effects, and oxidative stress may enhance these effects. The angiogenic and antimicrobial protein content of EVs derived

from H₂O₂-treated ADMSCs was altered (Mayo et al., 2019). These EVs can enhance the viability of flaps and increase capillary density, improving tissue recovery. Taken together, these oxidative stress-educated EVs can be used as compensatory measures to minimize damage caused by oxidative stress.

Oxidative Stress Miseducates EVs

Whether *in vitro* or *in vivo*, the cells can interact with each other, and EVs are important media of the interaction. Under pathological conditions, oxidative stress cause damage to cells, while these cells would expand the damage to other cells by their miseducated EVs. To date, immune cells are the main victims of oxidative stress-miseducated EVs, and immunosuppressive EVs are often released under oxidative stress. It has been reported that Jurkat and Raji cells release EVs containing NKG2D relative mRNA and proteins under thermal or oxidative stress. These EVs can reduce the cytotoxicity mediated by natural killer cell group 2D (NKG2D) receptor-ligand system and thus impair the functions of natural killer (NK) cells (Zimmer et al., 2011). Besides the specific type of cells, the body fluids of patients also contain immunosuppressive EVs. EVs separated from the blood of patients with rheumatoid arthritis contain oxidized phospholipids. These EVs can stimulate cells expressing Toll-like receptor 4 (TLR4), involving in inflammatory diseases (Manček-Keber et al., 2015). In addition, EVs have an important role in feto-maternal communication. Under oxidative stress, fetal cells-derived EVs can deliver unique cargos to parturition-associated uterine cells, inducing inflammation (Shahin et al., 2021). The effects of oxidative stress-miseducated EVs on the immune system need to be taken seriously since the immune system involves in nearly all pathological diseases. Furthermore, how to effectively avoid the effects is also worth study.

FUTURE AND PROSPECT

Genes, proteins, and even lipids loaded in EVs can all be used as regulatory factors. In recent researches, however, EVs used to regulate oxidative stress are undecorated products, and it means that regulatory factors are endogenous components of EVs. These crude EVs have low regulation efficiency of oxidative stress. That is because EVs have heterogeneity, and parts of EVs may not have the regulation ability because of their lack of endogenous regulatory factors. Furthermore, it is complicated to adjust endogenous components of EVs for the regulation of oxidative stress. To improve the regulation efficiency, therefore, exogenous drugs possessing the efficient

regulation ability of oxidative stress should be loaded into EVs. Numerous methods, such as electroporation and surfactant incubation, have been applied to load exogenous drugs into EVs. But it is still difficult to efficiently load macromolecular drugs into EVs, and there is a great need to exploit new drug loading methods. Moreover, it should be noted that EVs should not be oxidated during the drug loading process because oxidative stress potentially miseducates these EVs rendering opposite functions.

The sources of EVs applied for oxidative stress regulation should be carefully selected. As we have mentioned above, once parent cells are subjected to oxidative stress, EVs are potentially miseducated, and they may have side effects. To improve the safety of EVs, an appropriate source of EVs should be identified, and parent cells should not be under pathological conditions. *In vitro* cells are readily influenced by culture conditions, and corresponding EVs can be miseducated to a large extent. Therefore, the body fluids of healthy individuals are outstanding sources of EVs. As an example, EVs separated from the blood of healthy individuals show excellent biosafety and can be used for the delivery of chemotherapeutics. However, EVs separated from body fluids are often compound. Homogeneous types of EVs should be separated from the source, potentially minimizing the heterogeneity. Furthermore, we should make full use of the characteristics of EVs for different diseases. For example, specific types of EVs can target specific types of diseases, facilitating their loading of exogenous drugs to regulate oxidative stress.

In conclusion, EVs can be used as carriers to deliver endogenous or exogenous drugs for the modulation of oxidative, but the source and loading drugs of EVs should be charily selected. And how to reduce the impact of the heterogeneity of EVs should also be carefully considered.

AUTHOR CONTRIBUTIONS

HQ and LY: conceptualization. HQ and YW: original draft preparation. SF and CY: review and editing. LY: supervision. All authors contributed to the manuscript and approved the submitted version.

FUNDING

This work was supported by the National Nature Science Foundation of China (No. 52103170) and the Nature Science Foundation of Shandong Province (No. ZR2019BC020).

REFERENCES

- Akers, J. C., Gonda, D., Kim, R., Carter, B. S., and Chen, C. C. (2013). Biogenesis of Extracellular Vesicles (EV): Exosomes, Microvesicles, Retrovirus-Like Vesicles, and Apoptotic Bodies. *J. Neurooncol.* 113, 1–11. doi:10.1007/s11060-013-1084-8
- Akers, J. C., Ramakrishnan, V., Nolan, J. P., Duggan, E., Fu, C.-C., Hochberg, F. H., et al. (2016). Comparative Analysis of Technologies for Quantifying Extracellular Vesicles (EVs) in Clinical Cerebrospinal Fluids (CSF). *PLoS One* 11, e0149866. doi:10.1371/journal.pone.0149866
- Andaloussi, S., Mäger, I., Breakefield, X. O., and Wood, M. J. A. (2013). Extracellular Vesicles: Biology and Emerging Therapeutic Opportunities. *Nat. Rev. Drug Discov.* 12, 347–357. doi:10.1038/nrd3978

- Arraud, N., Linares, R., Tan, S., Gounou, C., Pasquet, J.-M., Mornet, S., et al. (2014). Extracellular Vesicles from Blood Plasma: Determination of Their Morphology, Size, Phenotype and Concentration. *J. Thromb. Haemost.* 12, 614–627. doi:10.1111/jth.12554
- Ashrafi, F., Shahriari, A., Behrouzi, A., Moradi, H. R., Keshavarz Azizi Raftar, S., Lari, A., et al. (2019). Akkermansia Muciniphila-Derived Extracellular Vesicles as a Mucosal Delivery Vector for Amelioration of Obesity in Mice. *Front. Microbiol.* 10, 2155. doi:10.3389/fmicb.2019.02155
- Atienzar-Aroca, S., Flores-Bellver, M., Serrano-Heras, G., Martinez-Gil, N., Barcia, J. M., Aparicio, S., et al. (2016). Oxidative Stress in Retinal Pigment Epithelium Cells Increases Exosome Secretion and Promotes Angiogenesis in Endothelial Cells. *J. Cel. Mol. Med.* 20, 1457–1466. doi:10.1111/jcmm.12834
- Betteridge, D. J. (2000). What Is Oxidative Stress? *Metabolism* 49, 3–8. doi:10.1016/S0026-0495(00)80077-3
- Bodart-Santos, V., de Carvalho, L. R. P., de Godoy, M. A., Batista, A. F., Saraiva, L. M., Lima, L. G., et al. (2019). Extracellular Vesicles Derived from Human Wharton's Jelly Mesenchymal Stem Cells Protect Hippocampal Neurons from Oxidative Stress and Synapse Damage Induced by Amyloid- β Oligomers. *Stem Cel Res. Ther.* 10, 1–13. doi:10.1186/s13287-019-1432-5
- Bodega, G., Alique, M., Puebla, L., Carracedo, J., and Ramirez, R. M. (2019). Microvesicles: ROS Scavengers and ROS Producers. *J. Extracellular Vesicles* 8, 1626654. doi:10.1080/20013078.2019.1626654
- Burger, D., Turner, M., Munkonda, M. N., and Touyz, R. M. (2016). Endothelial Microparticle-Derived Reactive Oxygen Species: Role in Endothelial Signaling and Vascular Function. *Oxidative Med. Cell Longevity* 2016, 1–10. doi:10.1155/2016/5047954
- Cho, Y.-E., Seo, W., Kim, D.-K., Moon, P.-G., Kim, S.-H., Lee, B.-H., et al. (2018). Exogenous Exosomes from Mice with Acetaminophen-Induced Liver Injury Promote Toxicity in the Recipient Hepatocytes and Mice. *Sci. Rep.* 8, 1–13. doi:10.1038/s41598-018-34309-7
- Dong, P., Zhang, Y., Yan, D.-y., Wang, Y., Xu, X., Zhao, Y.-c., et al. (2020). Protective Effects of Human Milk-Derived Exosomes on Intestinal Stem Cells Damaged by Oxidative Stress. *Cel Transpl.* 29, 096368972091269. doi:10.1177/0963689720912690
- Duan, L., Huang, H., Zhao, X., Zhou, M., Chen, S., Wang, C., et al. (2020). Extracellular Vesicles Derived from Human Placental Mesenchymal Stem Cells Alleviate Experimental Colitis in Mice by Inhibiting Inflammation and Oxidative Stress. *Int. J. Mol. Med.* 46, 1551–1561. doi:10.3892/ijmm.2020.4679
- Dubois-Deruy, E., Peugnet, V., Turkieh, A., and Pinet, F. (2020). Oxidative Stress in Cardiovascular Diseases. *Antioxidants* 9, 864. doi:10.3390/antiox9090864
- Eldh, M., Ekström, K., Valadi, H., Sjöstrand, M., Olsson, B., Jernäs, M., et al. (2010). Exosomes Communicate Protective Messages during Oxidative Stress; Possible Role of Exosomal Shuttle RNA. *PLoS One* 5, e15353. doi:10.1371/journal.pone.0015353
- Elsharkasy, O. M., Nordin, J. Z., Hagey, D. W., de Jong, O. G., Schiffelers, R. M., Andaloussi, S. E., et al. (2020). Extracellular Vesicles as Drug Delivery Systems: Why and How? *Adv. Drug Deliv. Rev.* 159, 332–343. doi:10.1016/j.addr.2020.04.004
- Frank, J., Richter, M., de Rossi, C., Lehr, C.-M., Fuhrmann, K., and Fuhrmann, G. (2018). Extracellular Vesicles Protect Glucuronidase Model Enzymes during Freeze-Drying. *Sci. Rep.* 8, 1–8. doi:10.1038/s41598-018-30786-y
- Gao, Y., Huang, X., Lin, H., Zhao, M., Liu, W., Li, W., et al. (2021). Adipose Mesenchymal Stem Cell-Derived Antioxidative Extracellular Vesicles Exhibit Anti-Oxidative Stress and Immunomodulatory Effects under PM2.5 Exposure. *Toxicology* 447, 152627. doi:10.1016/j.tox.2020.152627
- Guescini, M., Maggio, S., Ceccaroli, P., Battistelli, M., Annibali, G., Piccoli, G., et al. (2017). Extracellular Vesicles Released by Oxidatively Injured or Intact C2C12 Myotubes Promote Distinct Responses Converging toward Myogenesis. *Int. J. Mol. Sci.* 18, 2488. doi:10.3390/ijms18112488
- Hargitai, R., Kis, D., Persa, E., Szatmári, T., Sáfrány, G., and Lumniczky, K. (2021). Oxidative Stress and Gene Expression Modifications Mediated by Extracellular Vesicles: An *In Vivo* Study of the Radiation-Induced Bystander Effect. *Antioxidants* 10, 156. doi:10.3390/antiox10020156
- Hayes, J. D., Dinkova-Kostova, A. T., and Tew, K. D. (2020). Oxidative Stress in Cancer. *Cancer cell* 38, 167–197. doi:10.1016/j.ccell.2020.06.001
- Hedlund, M., Nagaeva, O., Kargl, D., Baranov, V., Mincheva-Nilsson, L., and Mincheva-Nilsson, L. (2011). Thermal- and Oxidative Stress Causes Enhanced Release of NKG2D Ligand-Bearing Immunosuppressive Exosomes in Leukemia/lymphoma T and B Cells. *PLoS One* 6, e16899. doi:10.1371/journal.pone.0016899
- Ibrahim, H. M., Mohammed-Geba, K., Tawfic, A. A., and El-Magd, M. A. (2019). Camel Milk Exosomes Modulate Cyclophosphamide-Induced Oxidative Stress and Immuno-Toxicity in Rats. *Food Funct.* 10, 7523–7532. doi:10.1039/c9fo01914f
- Janiszewski, M., Do Carmo, A. O., Pedro, M. A., Silva, E., Knobel, E., and Laurindo, F. R. M. (2004). Platelet-derived Exosomes of Septic Individuals Possess Proapoptotic NAD(P)H Oxidase Activity: A Novel Vascular Redox Pathway*. *Crit. Care Med.* 32, 818–825. doi:10.1097/01.ccm.0000114829.17746.19
- Lässer, C., Jang, S. C., and Lötvall, J. (2018). Subpopulations of Extracellular Vesicles and Their Therapeutic Potential. *Mol. Aspects Med.* 60, 1–14. doi:10.1016/j.mam.2018.02.002
- Li, Y., Zhou, J., Zhuo, Q., Zhang, J., Xie, J., Han, S., et al. (2019). Malignant Ascite-Derived Extracellular Vesicles Inhibit T Cell Activity by Upregulating Siglec-10 Expression. *Cancer. Manag. Res.* 11, 7123–7134. doi:10.2147/CMAR.S210568
- Li, D., Yang, Y., Wang, S., He, X., Liu, M., Bai, B., et al. (2021). Role of Acetylation in Doxorubicin-Induced Cardiotoxicity. *Redox Biol.* 46, 102089. doi:10.1016/j.redox.2021.102089
- Li, X., Yang, Y., Wang, Z., Jiang, S., Meng, Y., Song, X., et al. (2021). Targeting Non-coding RNAs in Unstable Atherosclerotic Plaques: Mechanism, Regulation, Possibilities, and Limitations. *Int. J. Biol. Sci.* 17, 3413–3427. doi:10.7150/ijbs.62506
- Li, X., Yin, D., Yang, Y., Bi, C., Wang, Z., Ma, G., et al. (2021). Eosinophil: A Nonnegligible Predictor in COVID-19 Re-Positive Patients. *Front. Immunol.* 12, 690653. doi:10.3389/fimmu.2021.690653
- Liu, Z., Xu, Y., Wan, Y., Gao, J., Chu, Y., and Li, J. (2019). Exosomes from Adipose-Derived Mesenchymal Stem Cells Prevent Cardiomyocyte Apoptosis Induced by Oxidative Stress. *Cell Death Discov.* 5, 1–7. doi:10.1038/s41420-019-0159-5
- Lorincz, A. M., Schütte, M., Timár, C. I., Veres, D. S., Kittel, A., McLeish, K. R., et al. (2015). Functionally and Morphologically Distinct Populations of Extracellular Vesicles Produced by Human Neutrophilic Granulocytes. *J. Leukoc. Biol.* 98, 583–589. doi:10.1189/jlb.3VMA1014-514R
- Mahmoud, A. M., Wilkinson, F. L., McCarthy, E. M., Moreno-Martinez, D. M., Langford-Smith, A., Romero, M., et al. (2017). Endothelial Microparticles Prevent Lipid-Induced Endothelial Damage via Akt/eNOS Signaling and Reduced Oxidative Stress. *FASEB j.* 31, 4636–4648. doi:10.1096/fj.201601244RR
- Manček-Keber, M., Frank-Bertoncelj, M., Hafner-Bratkovič, I., Smole, A., Zorko, M., Pirher, N., et al. (2015). Toll-Like Receptor 4 Senses Oxidative Stress Mediated by the Oxidation of Phospholipids in Extracellular Vesicles. *Sci. Signal.* 8, ra60. doi:10.1126/scisignal.2005860
- Matsumoto, J., Stewart, T., Banks, W. A., and Zhang, J. (2018). The Transport Mechanism of Extracellular Vesicles at the Blood-Brain Barrier. *Curr. Pharm. Des.* 23, 6206–6214. doi:10.2174/1381612823666170913164738
- Mayo, J. S., Kurata, W. E., O'Connor, K. M., and Pierce, L. M. (2019). Oxidative Stress Alters Angiogenic and Antimicrobial Content of Extracellular Vesicles and Improves Flap Survival. *Plast. Reconstr. Surg. - Glob. Open* 7, e2588. doi:10.1097/gox.0000000000002588
- Mostefai, H. A., Meziani, F., Mastronardi, M. L., Agouni, A., Heymes, C., Sargentini, C., et al. (2008). Circulating Microparticles from Patients with Septic Shock Exert Protective Role in Vascular Function. *Am. J. Respir. Crit. Care Med.* 178, 1148–1155. doi:10.1164/rccm.200712-1835OC
- Pascua-Maestro, R., González, E., Lillo, C., Ganfornina, M. D., Falcón-Pérez, J. M., and Sanchez, D. (2019). Extracellular Vesicles Secreted by Astroglial Cells Transport Apolipoprotein D to Neurons and Mediate Neuronal Survival upon Oxidative Stress. *Front. Cel. Neurosci.* 12, 526. doi:10.3389/fncel.2018.00526
- Qi, H., Liu, C., Long, L., Ren, Y., Zhang, S., Chang, X., et al. (2016). Blood Exosomes Encoded with Magnetic and Targeting Properties for Cancer Therapy. *ACS Nano* 10, 3323–3333. doi:10.1021/acsnano.5b06939
- Qi, H., Jia, H., Sang, J., Ren, Y., Zhao, J., Hou, X., et al. (2017). Using Endogenous Ligands for Direct Superparamagnetic Nanoparticle Cluster-Based Body Fluid Exosome Separation. *RSC Adv.* 7, 2926–2933. doi:10.1039/C6RA24937J
- Qi, H., Yang, L., Li, X., Zhan, Q., Han, D., Zhao, J., et al. (2018). Exosomes Separated Based on the "STOP" Criteria for Tumor-Targeted Drug Delivery. *J. Mater. Chem. B* 6, 2758–2768. doi:10.1039/C8TB00355F

- Rastogi, S., Hwang, A., Chan, J., Wang, J. Y. J., and Luo, K. (2018). Extracellular Vesicles Transfer Nuclear Abl-Dependent and Radiation-Induced miR-34c into Unirradiated Cells to Cause Bystander Effects. *Mol. Biol. Cell.* 29, 2228–2242. doi:10.1091/mbc.E18-02-0130
- Robbins, P. D., and Morelli, A. E. (2014). Regulation of Immune Responses by Extracellular Vesicles. *Nat. Rev. Immunol.* 14, 195–208. doi:10.1038/nri3622
- Shahin, H. I., Radnaa, E., Tantengco, O. A. G., Kechichian, T., Kammala, A. K., Sheller-Miller, S., et al. (2021). Microvesicles and Exosomes Released by Amnion Epithelial Cells under Oxidative Stress Cause Inflammatory Changes in Uterine Cells. *Biol. Reprod.* 105, 464–480. doi:10.1093/biolre/iob088
- Shen, K., Jia, Y., Wang, X., Zhang, J., Liu, K., Wang, J., et al. (2021). Exosomes from Adipose-Derived Stem Cells Alleviate the Inflammation and Oxidative Stress via Regulating Nrf2/HO-1 axis in Macrophages. *Free Radic. Biol. Med.* 165, 54–66. doi:10.1016/j.freeradbiomed.2021.01.023
- Soleti, R., Lauret, E., Andriantsitohaina, R., and Carmen Martínez, M. (2012). Internalization and Induction of Antioxidant Messages by Microvesicles Contribute to the Antiapoptotic Effects on Human Endothelial Cells. *Free Radic. Biol. Med.* 53, 2159–2170. doi:10.1016/j.freeradbiomed.2012.09.021
- Sun, T., Ding, Z.-X., Luo, X., Liu, Q.-S., Cheng, Y., and Hassanzadeh, K. (2020). Blood Exosomes Have Neuroprotective Effects in a Mouse Model of Parkinson's Disease. *Oxidative Med. Cell Longevity* 2020, 1–14. doi:10.1155/2020/3807476
- Théry, C., Zitvogel, L., and Amigorena, S. (2002). Exosomes: Composition, Biogenesis and Function. *Nat. Rev. Immunol.* 2, 569–579. doi:10.1038/nri855
- Théry, C., Witwer, K. W., Aikawa, E., Alcaraz, M. J., Anderson, J. D., Andriantsitohaina, R., et al. (2018). Minimal Information for Studies of Extracellular Vesicles 2018 (MISEV2018): A Position Statement of the International Society for Extracellular Vesicles and Update of the MISEV2014 Guidelines. *J. Extracell. Vesicles* 7, 1535750. doi:10.1080/20013078.2018.1535750
- Tkach, M., and Théry, C. (2016). Communication by Extracellular Vesicles: Where We Are and where We Need to Go. *Cell* 164, 1226–1232. doi:10.1016/j.cell.2016.01.043
- Vader, P., Mol, E. A., Pasterkamp, G., and Schiffelers, R. M. (2016). Extracellular Vesicles for Drug Delivery. *Adv. Drug Deliv. Rev.* 106, 148–156. doi:10.1016/j.addr.2016.02.006
- van der Meel, R., Fens, M. H. A. M., Vader, P., Van Solinge, W. W., Eniola-Adefeso, O., and Schiffelers, R. M. (2014). Extracellular Vesicles as Drug Delivery Systems: Lessons from the Liposome Field. *J. Controlled Release* 195, 72–85. doi:10.1016/j.jconrel.2014.07.049
- van Meteren, N., Lagadic-Gossman, D., Pouchard, N., Gobart, D., Gallais, I., Chevanne, M., et al. (2020). Extracellular Vesicles Released by Polycyclic Aromatic Hydrocarbons-Treated Hepatocytes Trigger Oxidative Stress in Recipient Hepatocytes by Delivering Iron. *Free Radic. Biol. Med.* 160, 246–262. doi:10.1016/j.freeradbiomed.2020.08.001
- Varga, Z., Yuana, Y., Grootemaat, A. E., Van der Pol, E., Gollwitzer, C., Krumrey, M., et al. (2014). Towards Traceable Size Determination of Extracellular Vesicles. *J. Extracellular Vesicles* 3, 23298. doi:10.3402/jev.v3.23298
- Wang, W., Zheng, Y., Wang, M., Yan, M., Jiang, J., and Li, Z. (2019). Exosomes Derived miR-126 Attenuates Oxidative Stress and Apoptosis from Ischemia and Reperfusion Injury by Targeting ERFF1. *Gene* 690, 75–80. doi:10.1016/j.gene.2018.12.044
- Wang, T., Jian, Z., Baskys, A., Yang, J., Li, J., Guo, H., et al. (2020). MSC-derived Exosomes Protect against Oxidative Stress-Induced Skin Injury via Adaptive Regulation of the NRF2 Defense System. *Biomaterials* 257, 120264. doi:10.1016/j.biomaterials.2020.120264
- Winck, F. V., Prado Ribeiro, A. C., Ramos Domingues, R., Ling, L. Y., Riaño-Pachón, D. M., Rivera, C., et al. (2015). Insights into Immune Responses in Oral Cancer through Proteomic Analysis of Saliva and Salivary Extracellular Vesicles. *Sci. Rep.* 5, 1–13. doi:10.1038/srep16305
- Xi, X. J., Zeng, J. J., Lu, Y., Chen, S. H., Jiang, Z. W., He, P. J., et al. (2020). Extracellular Vesicles Enhance Oxidative Stress through P38/NF- κ B Pathway in Ketamine-induced Ulcerative Cystitis. *J. Cel. Mol. Med.* 24, 7609–7624. doi:10.1111/jcmm.15397
- Xue, Q., He, N., Wang, Z., Fu, X., Aung, L. H. H., Liu, Y., et al. (2021). Functional Roles and Mechanisms of Ginsenosides from Panax Ginseng in Atherosclerosis. *J. Ginseng Res.* 45, 22–31. doi:10.1016/j.jgr.2020.07.002
- Yang, L., Han, D., Zhan, Q., Li, X., Shan, P., Hu, Y., et al. (2019). Blood Tfr+ Exosomes Separated by a pH-Responsive Method Deliver Chemotherapeutics for Tumor Therapy. *Theranostics* 9, 7680–7696. doi:10.7150/thno.37220
- Yao, J., Zheng, J., Cai, J., Zeng, K., Zhou, C., Zhang, J., et al. (2018). Extracellular Vesicles Derived from Human Umbilical Cord Mesenchymal Stem Cells Alleviate Rat Hepatic Ischemia-Reperfusion Injury by Suppressing Oxidative Stress and Neutrophil Inflammatory Response. *FASEB j.* 33, 1695–1710. doi:10.1096/fj.201800131RR
- Yin, P., Lv, H., Li, Y., Deng, Y., Zhang, L., and Tang, P. (2017). Exosome-mediated Genetic Information Transfer, a Missing Piece of Osteoblast-Osteoclast Communication Puzzle. *Front. Endocrinol.* 8, 336. doi:10.3389/fendo.2017.00336
- Zhan, Q., Yi, K., Qi, H., Li, S., Li, X., Wang, Q., et al. (2020). Engineering Blood Exosomes for Tumor-Targeting Efficient Gene/chemo Combination Therapy. *Theranostics* 10, 7889–7905. doi:10.7150/thno.45028
- Zhang, G., Zou, X., Miao, S., Chen, J., Du, T., Zhong, L., et al. (2014). The Anti-Oxidative Role of Micro-Vesicles Derived from Human Wharton-Jelly Mesenchymal Stromal Cells through NOX2/gp91(phox) Suppression in Alleviating Renal Ischemia-Reperfusion Injury in Rats. *PLoS One* 9, e92129. doi:10.1371/journal.pone.0092129
- Zhang, G., Zou, X., Huang, Y., Wang, F., Miao, S., Liu, G., et al. (2016a). Mesenchymal Stromal Cell-Derived Extracellular Vesicles Protect against Acute Kidney Injury through Anti-oxidation by Enhancing Nrf2/ARE Activation in Rats. *Kidney Blood Press. Res.* 41, 119–128. doi:10.1159/000443413
- Zhang, Q., Shang, M., Zhang, M., Wang, Y., Chen, Y., Wu, Y., et al. (2016b). Microvesicles Derived from Hypoxia/reoxygenation-Treated Human Umbilical Vein Endothelial Cells Promote Apoptosis and Oxidative Stress in H9c2 Cardiomyocytes. *BMC Cel Biol.* 17, 25. doi:10.1186/s12860-016-0100-1
- Zhang, P., Li, T., Wu, X., Nice, E. C., Huang, C., and Zhang, Y. (2020). Oxidative Stress and Diabetes: Antioxidative Strategies. *Front. Med.* 14, 583–600. doi:10.1007/s11684-019-0729-1
- Zhou, Y., Xu, H., Xu, W., Wang, B., Wu, H., Tao, Y., et al. (2013). Exosomes Released by Human Umbilical Cord Mesenchymal Stem Cells Protect against Cisplatin-Induced Renal Oxidative Stress and Apoptosis *In Vivo* and *In Vitro*. *Stem Cel Res. Ther.* 4, 34. doi:10.1186/scri194
- Zong, T., Yang, Y., Lin, X., Jiang, S., Zhao, H., Liu, M., et al. (2021). 5'-tiRNA-Cys-GCA Regulates VSMC Proliferation and Phenotypic Transition by Targeting STAT4 in Aortic Dissection. *Mol. Ther. - Nucleic Acids*. in press doi:10.1016/j.omtn.2021.07.013
- Zonneveld, M. I., Brisson, A. R., van Herwijnen, M. J. C., Tan, S., van de Lest, C. H. A., Redegeld, F. A., et al. (2014). Recovery of Extracellular Vesicles from Human Breast Milk Is Influenced by Sample Collection and Vesicle Isolation Procedures. *J. Extracellular Vesicles* 3, 24215. doi:10.3402/jev.v3.24215

Conflict of Interest: The authors declare that the research was conducted in the absence of any commercial or financial relationships that could be construed as a potential conflict of interest.

Publisher's Note: All claims expressed in this article are solely those of the authors and do not necessarily represent those of their affiliated organizations, or those of the publisher, the editors and the reviewers. Any product that may be evaluated in this article, or claim that may be made by its manufacturer, is not guaranteed or endorsed by the publisher.

Copyright © 2021 Qi, Wang, Fa, Yuan and Yang. This is an open-access article distributed under the terms of the Creative Commons Attribution License (CC BY). The use, distribution or reproduction in other forums is permitted, provided the original author(s) and the copyright owner(s) are credited and that the original publication in this journal is cited, in accordance with accepted academic practice. No use, distribution or reproduction is permitted which does not comply with these terms.



Nanosonosensitizers With Ultrasound-Induced Reactive Oxygen Species Generation for Cancer Sonodynamic Immunotherapy

Danling Cheng^{1†}, Xiaoying Wang^{2†}, Xiaojun Zhou^{1*} and Jingchao Li^{1*}

¹Shanghai Engineering Research Center of Nano-Biomaterials and Regenerative Medicine, College of Chemistry, Chemical Engineering and Biotechnology, Donghua University, Shanghai, China, ²Xuhui District Center for Disease Control and Prevention, Shanghai, China

OPEN ACCESS

Edited by:

Qihui Zhou,
Qingdao University, China

Reviewed by:

Qingqing Miao,
Soochow University, China
Houjuan Zhu,
Institute of Materials Research and
Engineering (A*STAR), Singapore

*Correspondence:

Xiaojun Zhou
zxj@dhru.edu.cn
Jingchao Li
jcli@dhru.edu.cn

†These authors contributed equally to
this work.

Specialty section:

This article was submitted to
Biomaterials,
a section of the journal
Frontiers in Bioengineering and
Biotechnology

Received: 19 August 2021

Accepted: 30 August 2021

Published: 30 September 2021

Citation:

Cheng D, Wang X, Zhou X and Li J
(2021) Nanosonosensitizers With
Ultrasound-Induced Reactive Oxygen
Species Generation for Cancer
Sonodynamic Immunotherapy.
Front. Bioeng. Biotechnol. 9:761218.
doi: 10.3389/fbioe.2021.761218

Immunotherapy is a promising therapeutic strategy for cancer, while it has been demonstrated to encounter the issues of low immune responses and underlying immune-related adverse events. The sonodynamic therapy (SDT) that utilizes sonosensitizers to produce reactive oxygen species (ROS) triggered by ultrasound (US) stimulation can be used to ablate tumors, which also leads to the induction of immunogenic cell death (ICD), thus achieving SDT-induced immunotherapy. Further combination of SDT with immunotherapy is able to afford enhanced antitumor immunity for tumor regression. In this mini review, we summarize the recent development of nanosonosensitizers with US-induced ROS generation for cancer SDT immunotherapy. The uses of nanosonosensitizers to achieve SDT-induced immunotherapy, combinational therapy of SDT with immunotherapy, and combinational therapy of SDT with multiple immunotherapies are briefly introduced. Furthermore, the current concerns and perspectives for the development and further clinical applications of these nanosonosensitizers for SDT-combined immunotherapy of cancer are discussed.

Keywords: reactive oxygen species, nanosonosensitizers, ultrasound, immunotherapy, sonodynamic therapy

INTRODUCTION

Immunotherapy including cancer vaccines, immune checkpoint blockade therapy, and adoptive T-cell therapy has emerged as a promising strategy for cancer treatment (Pardoll, 2012; Kuai et al., 2017; Fraietta et al., 2018). Different from some traditional therapeutic modalities that directly target tumor cells, immunotherapy achieves the treatment of tumors by boosting the body's systemic immune responses and triggering the activation of immune cells (Del Paggio, 2018). In such a unique way, immunotherapy can not only eradicate localized tumors but also remove distant metastatic tumors and even prevent tumor recurrence by forming long-term immune memory (Nam et al., 2019; Li et al., 2021a; Vitale et al., 2021). Currently, immunotherapy has shown ideal antitumor efficacy in a subset of clinical patients, which benefits from the approval of various immunotherapeutic agents by the U.S. Food and Drug Administration (FDA) (Zhang and Pu, 2020). However, only a few patients are currently proven to be responsive to immunotherapy, and a substantial fraction of them receiving treatments will develop immune-related adverse events (irAEs) (Boutros et al., 2016; Chiang et al., 2018; Song et al., 2018; Eun et al., 2019).

It has been extensively demonstrated that other treatment methods (such as chemotherapy, photodynamic therapy, photothermal therapy, and radiotherapy) can also trigger immunity by inducing immunogenic cell death (ICD) with the release of tumor-associated antigens (TAAs) (Ma et al., 2019b; Chen et al., 2019; Jin et al., 2021; Zhao et al., 2021). Moreover, these treatments can convert non-immunogenic “cold” tumor microenvironment to a “hot” one, which contributes to enhanced therapeutic efficacy of immune checkpoint blockade (Irvine and Dane, 2020). Nevertheless, obvious systemic side effects of chemotherapy/radiotherapy and shallow tissue penetration of photodynamic/photothermal therapy limit their efficacy for tumor treatment (Maruoka et al., 2018; Ma et al., 2019c). In contrast, the sonodynamic therapy (SDT) utilizing sonosensitizers to generate reactive oxygen species (ROS) under ultrasound (US) irradiation for tumor ablation shows negligible toxicity to normal tissues and can overcome the tissue penetration limitation due to its tissue penetration depth of >10 cm (Zhang et al., 2016; Li et al., 2018; Ma A. et al., 2019). Therefore, the combination of SDT with immunotherapy has been considered as a promising strategy for cancer treatment. In this regard, a class of nanosonosensitizers (such as small molecular sonosensitizer-based nanoparticles and inorganic nanomaterials) with ROS generation ability have been developed for this purpose.

Herein, we summarize the recent development of nanosonosensitizers with US-induced ROS generation for their application in cancer treatment by combining SDT with immunotherapy. In the following, the key roles of nanosonosensitizer-mediated SDT in inducing ICD and thus promoting antitumor immunity are discussed. The combinations of SDT with different types of immunotherapy for tumor remission are then introduced. A brief discussion of existing concerns and perspectives for the development of nanosonosensitizers toward clinical translation of SDT immunotherapy are also given.

Sonodynamic Therapy–Triggered Antitumor Immunity

In addition to direct ablation of local tumors, SDT can trigger systemic immune responses by eliciting ICD to effectively inhibit distant metastatic tumors and prevent tumor recurrence. ICD has been reported to promote the processes of antigen uptake, processing, and presentation, thus facilitating the production of cytotoxic T cells (Shi and Lammers, 2019). Cai's group constructed a multifunctional nanosonosensitizer by loading a manganese–protoporphyrin complex as a nanosonosensitizer into liposomes with surface modification of folic acid (FA) (Chen et al., 2021). FA is a targeting ligand that specifically binds to FA receptors overexpressed on the surface of many cancer cells (Li et al., 2013). Due to the decreased molecular orbital energy via metal coordination, the $^1\text{O}_2$ generation efficacy of the formed FA–MnPs under US irradiation was greatly enhanced, which was also observed in the mimic tissue up to 8 cm depth. Such a good depth-responded action of FA–MnPs not only efficiently inhibited the growth of superficial tumors but also showed a good

therapeutic effect for deep-seated tumors in 4T1 tumor-bearing mouse models. More importantly, FA–MnP-mediated SDT could repolarize macrophages from immunosuppressive M2 to antitumor M1 phenotypes. In addition, this treatment strategy triggered the activation of dendritic cells (DCs), T lymphocytes, and natural killer (NK) cells by eliciting ICD of tumor cells and reduced the population of regulatory T (Treg) cells. As such, a strong antitumor immunity was evoked in living mice, which resulted in the inhibition of tumor growth. Although this study provided a simple strategy for treatment of deep-seated and metastatic tumors, the tumors were not completely eradicated, and the therapeutic efficacy should be improved.

To induce robust ICD for cancer immunotherapy, Zhang and coworkers recently developed an SDT-based nanoplatfom with continuous CO_2 generation to enforce continuous US-induced inertial cavitation (UIC) for amplifying ROS production (Yin et al., 2021). The nanoplatfoms were constructed by encapsulating CO_2 -adsorbed L-arginine (LA) and protoporphyrin (PpIX) as sonosensitizers into mesoporous organosilica nanoparticles (MONs). The formed nanoplatfom (MON-PpIX-LA- CO_2) could release CO_2 in a continuous manner, thus forming the UIC effect under US irradiation, which enabled massive generation of ROS and afforded multiple enhancements of the SDT effect after a single administration. Such a high-efficiency ROS generation during MON-PpIX-LA- CO_2 -mediated treatment triggered robust ICD of tumor cells, thus promoting the maturation of DCs and activation of effector CD8^+ T cells in 4T1 tumor-bearing mouse models. Meanwhile, the immunosuppressive M2 macrophages were polarized into antitumor M1 phenotypes. Due to the formed systemic antitumor immunity, the growth of both primary and distant metastatic 4T1 tumors was greatly inhibited.

Due to the dependence of oxygen for SDT, its therapeutic efficacy is often compromised by the hypoxic tumor microenvironment and continuous consumption of oxygen (Chen et al., 2017; Pan et al., 2020). By taking advantage of the SDT-aggravated hypoxia tumor microenvironment, Wang and Zhang's group constructed a biomimetic decoy for SDT-induced enhanced ICD and immunotherapy (Zhao et al., 2020). The biomimetic decoy was constructed by encapsulating chlorin e6 (Ce6) as the sonosensitizers and a hypoxia-activated tirapazamine (TPZ) into pH-sensitive liposomes camouflaged by a red blood cell-platelet hybrid membrane. In the view of the immune escape and specific targeting behaviors of surface biomimetic membrane camouflages, the biomimetic decoy showed high accumulation and retention in tumor sites. Under US irradiation, Ce6 generated ROS for SDT and consumed oxygen to aggravate the tumor hypoxic microenvironment, which led to the activation of TPZ and thus achieved a highly effective synergistic therapy. As a result, such decoy-mediated therapy triggered amplified ICD of tumor cells and a strong antitumor immune response to inhibit the growth of B16-F10 tumors in C57BL/6 mice and prevent lung metastasis. Different from other therapeutic nanoagents, the biomimetic decoy retained platelet binding functions and thus could obviously inhibit the danger-associated molecular pattern (DAMP)-mediated tumor metastasis.

In addition to chemotherapy, ferroptosis has been combined with SDT to induce enhanced ICD and antitumor immunity. As an example, manganese porphyrin-based metal-organic frameworks (MOFs) containing metal ion zirconium (Zr) were constructed for SDT/ferroptosis/immunotherapy of hypoxic tumors (Xu et al., 2021). The MOFs showed a catalase-like activity to induce the decomposition of H_2O_2 in the tumor microenvironment to produce oxygen, thereby overcoming tumor hypoxia and enhancing the generation of ROS under US irradiation. In addition, Zr ions within MOFs decreased glutathione (GSH) levels in tumor cells to further promote ROS levels, thus achieving enhanced ROS-generated ferroptosis. Moreover, the MOF-mediated treatment under US irradiation greatly reversed the tumor immune microenvironment by increasing the populations of matured DCs and effector $CD8^+$ T cells and decreasing the population of myeloid-derived suppressor cells (MDSCs) in tumor tissues. As such, the MOFs combined SDT, ferroptosis, and antitumor immunity, showing strong anticancer efficacy in both subcutaneous H22 tumors and metastatic 4T1 tumor models. However, the long-term biocompatibility of MOFs in living animals should be carefully investigated.

COMBINATIONAL THERAPY OF SONODYNAMIC THERAPY WITH IMMUNOTHERAPY

Although SDT can elicit antitumor immunity *via* the ICD effect, the strength is still limited for effective eradication of tumors (Li et al., 2021a). To achieve high therapeutic efficacy, SDT has been combined with different types of immunotherapy. For example, Liu's group fabricated a two-dimensional (2D) coordination nanosheet composed of Zn^{2+} and tetrakis(4-carboxyphenyl) porphyrin (TCPP) with an excellent sonodynamic ROS generation for enhanced antitumor immunotherapy (Zhu et al., 2021). In addition, the 2D Zn-TCPP nanosheets exhibited a high surface area and thus could load cytosine phosphorothioate guanine oligodeoxynucleotide (CpG ODN), a potent toll-like receptor 9 (TLR9) agonist, as the immunotherapeutic agent. In the tumor tissue accumulated with Zn-TCPP/CpG, ROS was generated under US irradiation to induce ICD with the release of tumor debris as TAAs. CpG ODN agonists in nanosheets then worked together with the released TAAs to trigger a strong antitumor immune response. Therefore, Zn-TCPP/CpG nanosheet-mediated therapy could not only destroy primary tumors but also result in antitumor immunity to inhibit the growth of distant tumors in subcutaneous CT26 tumor-bearing mouse models. Such a combinational therapy also built a strong immunological memory effect to prevent tumor recurrence after treatment. Besides the good therapeutic efficacy, a key issue may be the possible leakage of CpG ODN agonists from nanosheets during blood circulation.

Different from TLR agonists, inhibitors of indoleamine 2,3-dioxygenase (IDO) can block important negative regulatory molecules overexpressed in tumor cells and antigen-presenting cells (Peng et al., 2018). Thus, the combination of SDT and IDO

inhibitor-mediated immunotherapy has been adopted for cancer treatment. As demonstrated by Liu's group, the authors developed a biomimetic nanosystem for the treatment of metastatic tumors via the synergetic action of SDT/CO gas therapy and IDO immunotherapy (Zhang D. et al., 2020). In their system, gold nanoparticles (AuNPs) were *in situ* synthesized on black phosphorus quantum dot (BPQD)-doped mesoporous silica frameworks (BMSNs) to form a hybrid nanoplatform (Au-BMSNs) acting as nanosonosensitizers, which were then loaded with CO-releasing molecules and the surface coated with a macrophage cell membrane. Such a biomimetic nanosystem showed an active targeting ability to tumors and thus achieved high tumor accumulation. Under ultrasonic irradiation, 1O_2 was generated and CO was released, resulting in cell apoptosis and mitochondrial dysfunction of tumor cells. In addition, such an SDT/CO therapy could induce ICD of tumor cells and then trigger a potent antitumor immune response and long-term immune memory by combining with the IDO inhibitor-mediated immunotherapy. Such a combinational action effectively inhibited the growth of subcutaneous tumors, suppressed tumor recurrence, and also prevented lung metastasis in 4T1 tumor-bearing mouse models. However, the IDO inhibitors were intraperitoneally injected into mice, and their bioavailability should be further improved.

In addition to IDO inhibitors, the combination of SDT with immune checkpoint blockade using an anti-PD-1 or anti-PD-L1 antibody has emerged as another promising therapeutic strategy for cancer. Zhang and coworkers recently designed a transformable nanosensitizer with tumor microenvironment-activated SDT action and Ca^{2+} release for enhanced cancer immunotherapy (Tan et al., 2021). An acid-degradable CaP was coated onto the surface of titanium dioxide (TiO_2) nanoparticles to form core/shell structured $TiO_2@CaP$ nanoplatforms as the nanosensitizers. In the acidic tumor microenvironment, the CaP shell was dissolved to release Ca^{2+} , which led to mitochondrial dysfunction by overloading intracellular Ca^{2+} . In addition, the disintegrated TiO_2 nanoparticles allowed ROS generation under US irradiation for SDT. Such a cascade action enhanced the death of cancer cells and substantially amplified ICD, leading to enhanced activation and infiltration of tumor-specific cytotoxic T cells into 4T1 tumors of mice. After a combination with anti-PD-1-mediated checkpoint blockade therapy, $TiO_2@CaP$ nanoplatforms triggered a systemic antitumor immunity to inhibit the growth of both primary and distant tumors and suppress lung metastasis. This study indeed provided a smart tumor microenvironment-responsive nanosonosensitizers for effective cancer therapy.

In another study, Park's group developed a necroptosis-inducible nanobubble (NB) to combine SDT and anti-PD-L1 immunotherapy for cancer (Um et al., 2020). Different from apoptosis, necroptosis is a caspase-independent necrosis with the characterizations of intracellular content leakages, plasma membrane integrity loss, and cytoplasmic swelling (Zhang et al., 2009). Necroptosis has been reported to boost antitumor immunity more efficiently than apoptosis (Suntharalingam et al., 2015). The NBs composed of perfluoropentane, carboxymethyl dextran, and Ce6 as the gas precursor, hydrophilic backbone, and hydrophobic sonosensitizer, respectively. Under US irradiation,

NBs primarily induced ROS generation due to the action of Ce6 and then acoustic cavitation of perfluoropentane caused necroptosis by inducing burst-mediated cell membrane disintegration, leading to ICD of tumor cells. Such an action further triggered antitumor immunity by promoting the maturation of DCs and activation of CD8⁺ cytotoxic T cells. By combining with immune checkpoint blockade (anti-PD-L1), the NB-mediated therapy achieved complete regression of the primary tumors and effective inhibition of metastatic tumors in CT26 tumor-bearing mouse models.

To overcome the limitations of SDT, the combination of SDT and chemodynamic therapy (CDT) with immune checkpoint therapy can be adopted. As an example, a multifunctional nanoreactor of polyethylene glycol (PEG)-modified CoFe₂O₄ nanoflowers (CFPs) was synthesized using a typical solvothermal method for an augmented SDT/CDT-elicited robust immune response (Fu et al., 2021). The CFP showed a catalase-like activity to produce a hydroxyl radical ($\cdot\text{OH}$) for CDT and catalyze the decomposition of H₂O₂ in a tumor microenvironment to form O₂ to relieve tumor hypoxia, which enabled the generation of a high level of ¹O₂ under US irradiation to achieve effective SDT. Thus, CFP-mediated SDT/CDT could efficiently induce ICD of tumor cells, which would lead to a boost in antitumor immunity in 4T1 tumor-bearing mice after the combination with immune checkpoint blockade (anti-PD-L1). Such a combinational therapy afforded an excellent efficacy in inhibiting the growth of primary and distant tumors and suppressing lung metastasis. Different from the aforementioned nanosystems, CFP could be used for T₂-weighted magnetic resonance (MR) imaging of tumors and thus achieved the evaluation of tumor accumulation for US irradiation.

In another study, a nanosystem based on L-arginine (LA)-loaded black mesoporous titania (BMT) was fabricated for SDT and gas therapy-combined immunotherapy (Wang et al., 2021). In this system, BMT and LA acted as a sonosensitizer and exogenous NO supplementation to produce ¹O₂ for SDT and NO for gas therapy under US irradiation, respectively. Moreover, more NO was produced because of the oxidation of LA promoted by the generated ¹O₂. The high levels of ¹O₂ and NO led to strong intracellular oxidative stress and DNA double-strand breaks, which induced apoptosis of cancer cells with the release of TAAs. By combining with the immune checkpoint inhibitor (anti-PD-L1), a strong antitumor immune response was induced to effectively treat both primary and distant tumors and inhibit lung metastasis of U14 tumors.

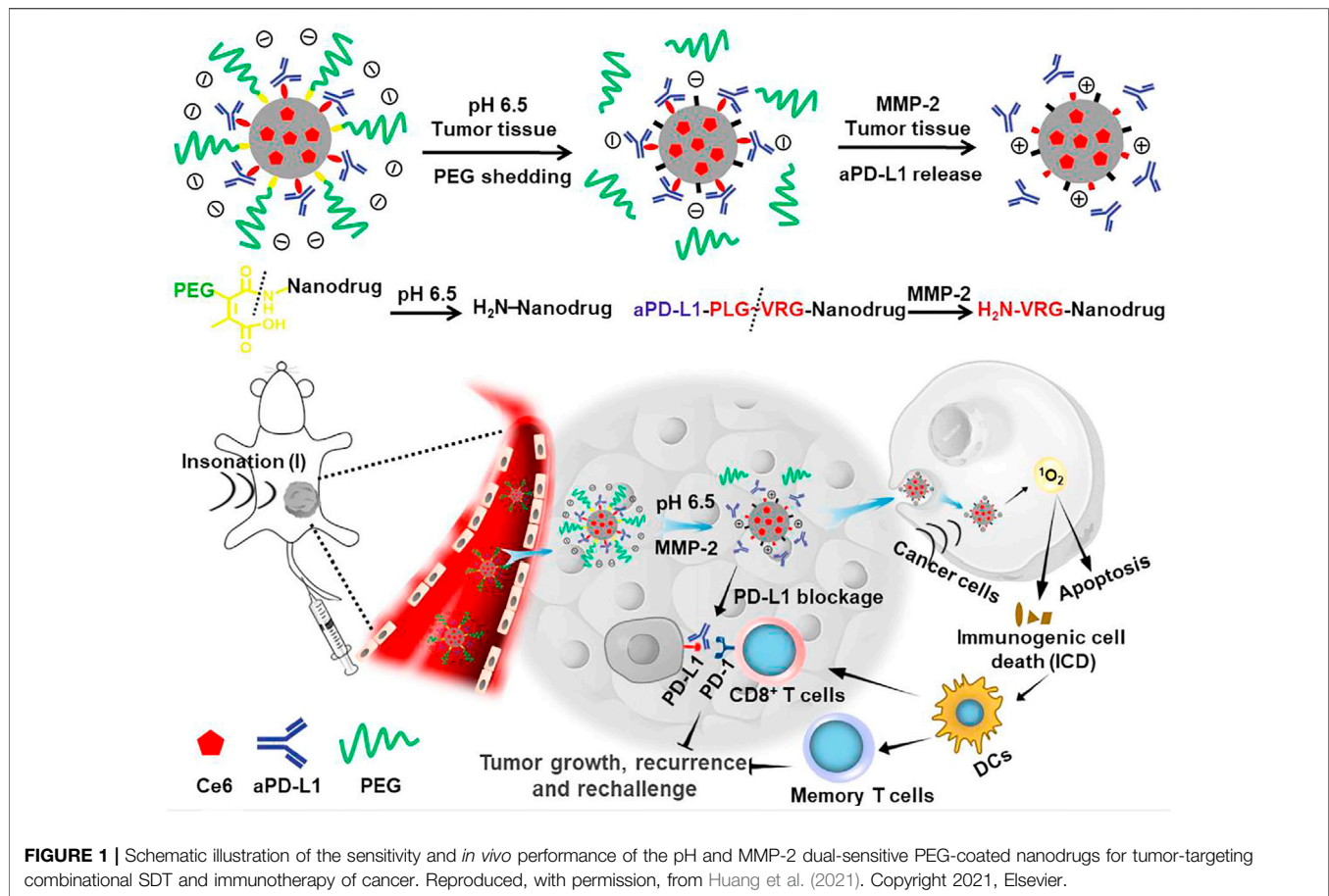
Although the combination of SDT and immunotherapy has achieved ideal antitumor efficacy, the administration of immunotherapeutic agents (such as anti-PD-1 and anti-PD-L1) is conducted via systematic injection. This often leads to insufficient accumulation of immunotherapeutic agents in tumor sites, which greatly inhibits the antitumor efficacy and potentially causes immune-related adverse effects (Wang et al., 2018). To address this concern, Shuai's group developed a tumor microenvironment-responsive nanodrug for combinational SDT/immunotherapy (Huang et al., 2021). Nanodrugs were constructed based on lipid nanocarriers with the encapsulation of Ce6 in the core as the sonosensitizers, a conjugation of an anti-PD-L1 antibody

via MMP-2-cleavable peptides, and PEG chains through an acid-labile amide bond (Figure 1). In acidic tumor tissues, the PEG outer chains were shed from nanodrugs to promote the cellular uptake by tumor cells, and the overexpressed intratumoral MMP-2 cleaved the peptide linkers to trigger the release of anti-PD-L1. In addition, Ce6 within nanodrugs mediated SDT under US irradiation to induce ICD. As a result, the nanodrug-enabled combinational SDT/immunotherapy elicited a robust antitumor immunity and long-term immune memory, resulting in effective inhibition of tumor growth and suppression of tumor recurrence in B16-F10 tumor-bearing mice. Moreover, this therapeutic strategy remarkably reduced systemic immune-related adverse effects and thus showed great promise for cancer therapy.

COMBINATIONAL THERAPY OF SONODYNAMIC THERAPY WITH MULTIPLE IMMUNOTHERAPIES

To obtain better therapeutic efficacies by triggering stronger antitumor immunity, some nanosystems integrating two types of immunotherapeutic agents have been developed for SDT-combined multiple immunotherapies. Wang and coworkers constructed a multifunctional nanosonosensitizer by loading Ce6 and CpG ODN in TiO₂ nanoparticles. Due to the existence of TiO₂-Ce6 for augmented SDT under US irradiation and immune adjuvant CpG to boost the immune response, the nanosonosensitizers (TiO₂-Ce6-CpG) effectively ablated tumors with the release of TAAs and stimulated the immune system to activate the adaptive immune responses. After combining with anti-PD-L1, the TiO₂-Ce6-CpG-mediated therapy induced a strong antitumor immune response to greatly inhibit the growth of treated primary tumors and non-treated distant tumors. Actually, the antitumor efficacy still should be further improved as all the treated mice died after around 80 days.

To achieve the targeting delivery of nanosystems into tumor sites, Yang and coworkers designed a cell membrane-coated biomimetic nanovaccine to combine SDT with multiple immunotherapies (Zhan et al., 2021). The nanovaccine was constructed by integrating manganese porphyrin-based MOF (Mn-MOF) with CpG ODN, followed by surface coating with cell membranes derived from ovalbumin (OVA)-overexpressing melanoma B16 cells. The nanovaccine showed a prolonged blood circulation and enhanced tumor targeting ability to hypoxic tumors, in which the high level of ROS was generated under US irradiation for SDT accompanied by ICD of tumor cells. SDT-induced TAAs and OVA on a cell membrane showed a vaccine-like function and synergized with CpG ODN to trigger a strong tumor-specific immune response by promoting the maturation of DCs and activation of T cells. After combining with the anti-PD-1-mediated immunotherapy, the nanovaccine-triggered therapeutic action induced a stronger systemic immune response and long-term immunological memory function to inhibit the growth of primary and distant tumors and prevent recurrence in subcutaneous B16-OVA tumor-bearing mice. This study indeed provided a promising strategy for the combinational therapy with immune checkpoint inhibitors in hypoxic tumors.



By using a TLR7 agonist, imiquimod (R837), as the immune adjuvant, Chen's group reported nanosonosensitizers to allow SDT, enhanced SDT-based immunotherapy, and anti-PD-L1 for cancer treatment (Yue et al., 2019). The nanosonosensitizers were constructed by loading hematoporphyrin monomethyl ether (HMME) as the sonosensitizer and immune adjuvant (R837) into nano-liposomes. After accumulation in tumor sites, the nanosonosensitizers generated ¹O₂ under US irradiation to induce apoptosis/necrosis and ICD of tumor cells with the release of TAAs (Figure 2). The *in situ* released TAAs showed a vaccine-like function together with R837, leading to the elicitation of antitumor immunity by promoting maturation of DCs, activation of T cells, and secretion of cytokines. The strength of immune response was greatly enhanced after combining with anti-PD-L1-mediated immune checkpoint blockade as the population of tumor-infiltrating CD8⁺ T cells increased. Such a combinational therapy could treat primary tumors and prevent the progression of tumor metastasis in subcutaneous CT26 colorectal cancer and orthotopic 4T1 breast cancer mouse models. In addition, the therapeutic action provided a long-term immunological memory function to protect against tumor recurrence. More importantly, all the major components in nanosonosensitizers are clinically approved for use; this combinational therapeutic strategy is thus highly promising for further clinical translation.

DISCUSSION

Recent development of nanosonosensitizers with US-induced ROS generation to combine SDT with immunotherapy for cancer treatment has been summarized. Although the efficacies of SDT are often limited by a hypoxic tumor microenvironment, different strategies have been adopted to address this issue, such as the production of molecular oxygen (Zhang Y. et al., 2020), supplement of oxygen (Zeng et al., 2020), and depletion of GSH (Dong et al., 2020). In addition to direct ablation of tumors, SDT can induce ICD of tumor cells, thus promoting the activation of immune responses. Further combination of SDT with different types of immunotherapy will lead to obviously enhanced antitumor immunity. As a result, this combinational therapy can afford enhanced therapeutic efficacy in suppressing tumor growth and metastasis, and even preventing tumor recurrence.

Although these are promising results, several concerns of SDT-combined immunotherapy using nanosonosensitizers still need to be considered before the successful translation for clinical trials. First, US has a stronger tissue penetration ability relative to light (Qian et al., 2016), while SDT-combined immunotherapy has not been explored to treat deep-seated tumors in living mice, which should be systematically evaluated in the future. Second, most of immunotherapeutic agents are systemically injected into mice and often have limited accumulation in tumor sites, leading

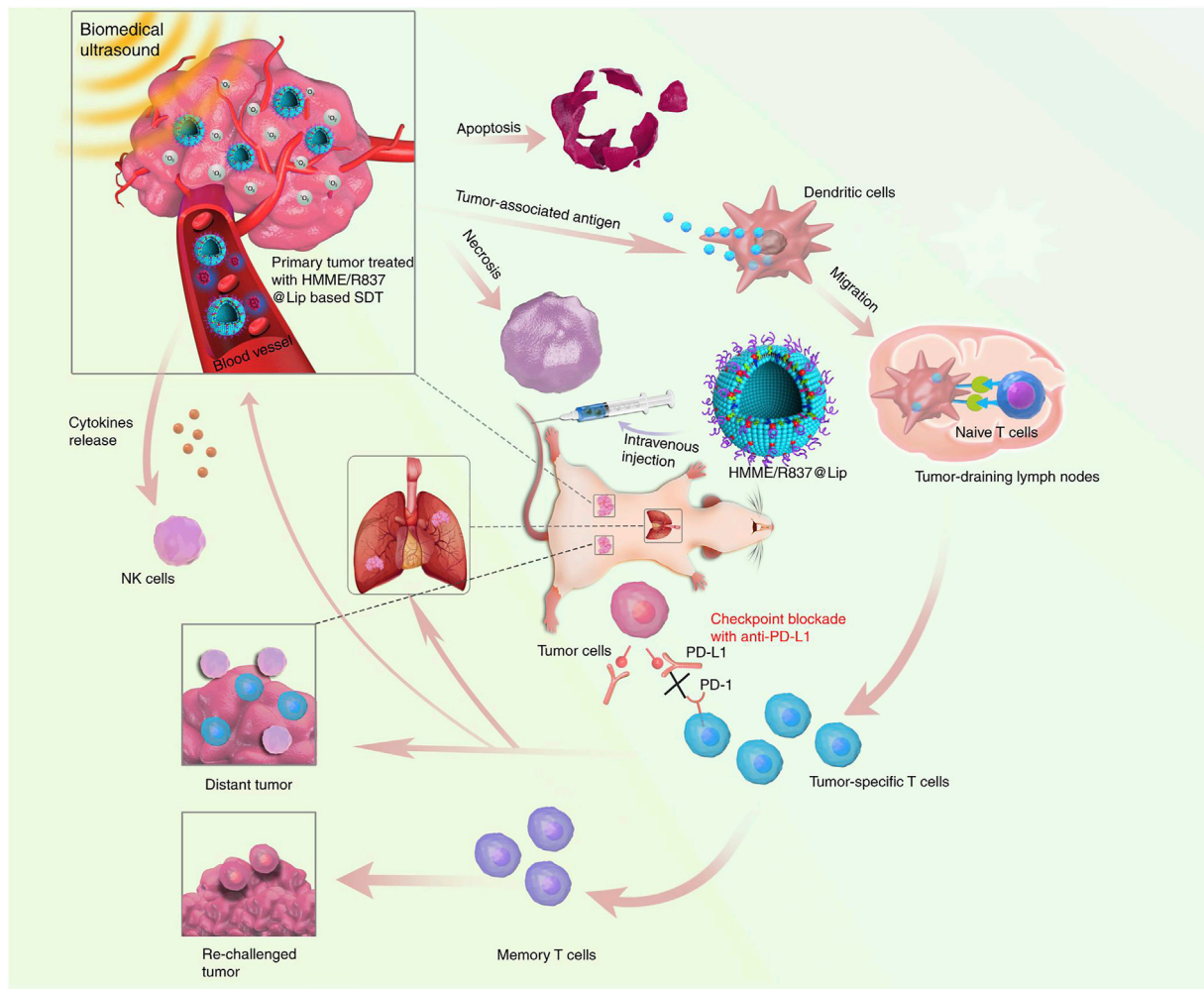


FIGURE 2 | Design principle of nanosonosensitizer-augmented synergistic SDT and immunotherapy. Schematic illustration of antitumor immune responses induced by combined noninvasive SDT with immune adjuvant-contained nanosonosensitizer and checkpoint blockade for effective cancer immunotherapy. Reproduced, with permission, from Yue et al. (2019). Copyright 2019, Nature Publishing Group.

to low therapeutic efficacy and potential immune-related adverse effects. Loading immunotherapeutic agents in nanocarriers to achieve their targeting delivery into tumors can commendably address these issues (Uthaman et al., 2020; Li et al., 2021b). Third, the metabolism and degradation of nanoparticles in living animals should be carefully evaluated to ensure their long-term biosafety. It is of high demand to develop biodegradable or clearable nanoparticles for the therapeutic purposes (Li and Pu, 2019). Fourth, the dynamic monitoring of immune responses in living animals after treatments is necessary to ensure effective therapy, which however is a great challenge. The integration of immune-specific imaging reporters into nanosystems is a feasible method to achieve monitoring of immune activation (He et al., 2020; Ramesh et al., 2020). Fifth, some efforts should be put to combine SDT with cancer vaccines or adoptive T-cell therapy. In addition, the potential applications of SDT-combined immunotherapy using nanosonosensitizers for the treatment of

other diseases such as infectious diseases and autoimmunity can be explored (Pang et al., 2019).

AUTHOR CONTRIBUTIONS

DC and XW wrote the original draft manuscript; XZ and JL reviewed and edited the manuscript. All authors read and approved the final manuscript.

FUNDING

This study was supported by the Fundamental Research Funds for the Central Universities (2232021A-05, 2232021D-10) and Science and Technology Commission of Shanghai Municipality (20DZ2254900).

REFERENCES

- Boutros, C., Tarhini, A., Routier, E., Lambotte, O., Ladurie, F. L., Carbone, F., et al. (2016). Safety Profiles of Anti-CTLA-4 and Anti-PD-1 Antibodies Alone and in Combination. *Nat. Rev. Clin. Oncol.* 13, 473–486. doi:10.1038/nrclinonc.2016.58
- Chen, H., Liu, L., Ma, A., Yin, T., Chen, Z., Liang, R., et al. (2021). Noninvasively Immunogenic Sonodynamic Therapy with Manganese Protoporphyrin Liposomes against Triple-Negative Breast Cancer. *Biomaterials* 269, 120639. doi:10.1016/j.biomaterials.2020.120639
- Chen, Q., Chen, J., Liang, C., Feng, L., Dong, Z., Song, X., et al. (2017). Drug-induced Co-assembly of Albumin/catalase as Smart Nano-Theranostics for Deep Intra-tumoral Penetration, Hypoxia Relieve, and Synergistic Combination Therapy. *J. Controlled Release* 263, 79–89. doi:10.1016/j.jconrel.2016.11.006
- Chen, Q., Chen, J., Yang, Z., Xu, J., Xu, L., Liang, C., et al. (2019). Nanoparticle-enhanced Radiotherapy to Trigger Robust Cancer Immunotherapy. *Adv. Mater.* 31, 1802228. doi:10.1002/adma.201802228
- Chiang, C.-S., Lin, Y.-J., Lee, R., Lai, Y.-H., Cheng, H.-W., Hsieh, C.-H., et al. (2018). Combination of Fucoidan-Based Magnetic Nanoparticles and Immunomodulators Enhances Tumour-Localized Immunotherapy. *Nat. Nanotech* 13, 746–754. doi:10.1038/s41565-018-0146-7
- Del Paggio, J. C. (2018). Cancer Immunotherapy and the Value of Cure. *Nat. Rev. Clin. Oncol.* 15, 268–270. doi:10.1038/nrclinonc.2018.27
- Dong, Z., Feng, L., Hao, Y., Li, Q., Chen, M., Yang, Z., et al. (2020). Synthesis of CaCO₃-Based Nanomedicine for Enhanced Sonodynamic Therapy via Amplification of Tumor Oxidative Stress. *Chem* 6, 1391–1407. doi:10.1016/j.chempr.2020.02.020
- Eun, Y., Kim, I. Y., Sun, J.-M., Lee, J., Cha, H.-S., Koh, E.-M., et al. (2019). Risk Factors for Immune-Related Adverse Events Associated with Anti-PD-1 Pembrolizumab. *Sci. Rep.* 9, 14039. doi:10.1038/s41598-019-50574-6
- Fraietta, J. A., Lacey, S. F., Orlando, E. J., Pruteanu-Malinici, I., Gohil, M., Lundh, S., et al. (2018). Determinants of Response and Resistance to CD19 Chimeric Antigen Receptor (CAR) T Cell Therapy of Chronic Lymphocytic Leukemia. *Nat. Med.* 24, 563–571. doi:10.1038/s41591-018-0010-1
- Fu, S., Yang, R., Ren, J., Liu, J., Zhang, L., Xu, Z., et al. (2021). Catalytically Active CoFe₂O₄ Nanoflowers for Augmented Sonodynamic and Chemodynamic Combination Therapy with Elicitation of Robust Immune Response. *ACS Nano* 15, 11953–11969. doi:10.1021/acsnano.1c03128
- He, S., Li, J., Lyu, Y., Huang, J., and Pu, K. (2020). Near-infrared Fluorescent Macromolecular Reporters for Real-Time Imaging and Urinalysis of Cancer Immunotherapy. *J. Am. Chem. Soc.* 142, 7075–7082. doi:10.1021/jacs.0c00659
- Huang, J., Xiao, Z., An, Y., Han, S., Wu, W., Wang, Y., et al. (2021). Nanodrug with Dual-Sensitivity to Tumor Microenvironment for Immuno-Sonodynamic Anti-cancer Therapy. *Biomaterials* 269, 120636. doi:10.1016/j.biomaterials.2020.120636
- Irvine, D. J., and Dane, E. L. (2020). Enhancing Cancer Immunotherapy with Nanomedicine. *Nat. Rev. Immunol.* 20, 321–334. doi:10.1038/s41577-019-0269-6
- Jin, L., Shen, S., Huang, Y., Li, D., and Yang, X. (2021). Corn-like Au/Ag Nanorod-Mediated NIR-II Photothermal/photodynamic Therapy Potentiates Immune Checkpoint Antibody Efficacy by Reprogramming the Cold Tumor Microenvironment. *Biomaterials* 268, 120582. doi:10.1016/j.biomaterials.2020.120582
- Kuai, R., Ochyl, L. J., Bahjat, K. S., Schwendeman, A., and Moon, J. J. (2017). Designer Vaccine Nanodiscs for Personalized Cancer Immunotherapy. *Nat. Mater* 16, 489–496. doi:10.1038/nmat4822
- Li, J., Luo, Y., and Pu, K. (2021a). Electromagnetic Nanomedicines for Combinational Cancer Immunotherapy. *Angew. Chem. Int. Ed.* 60, 12682–12705. doi:10.1002/anie.202008386
- Li, J., and Pu, K. (2019). Development of Organic Semiconducting Materials for Deep-Tissue Optical Imaging, Phototherapy and Photoactivation. *Chem. Soc. Rev.* 48, 38–71. doi:10.1039/c8cs00001h
- Li, J., Yu, X., Jiang, Y., He, S., Zhang, Y., Luo, Y., et al. (2021b). Second Near-Infrared Thermal Semiconducting Polymer Nanoadjuvant for Enhanced Cancer Immunotherapy. *Adv. Mater.* 33, 2003458. doi:10.1002/adma.202003458
- Li, J., Zheng, L., Cai, H., Sun, W., Shen, M., Zhang, G., et al. (2013). Polyethyleneimine-mediated Synthesis of Folic Acid-Targeted Iron Oxide Nanoparticles for *In Vivo* Tumor MR Imaging. *Biomaterials* 34, 8382–8392. doi:10.1016/j.biomaterials.2013.07.070
- Li, Z., Han, J., Yu, L., Qian, X., Xing, H., Lin, H., et al. (2018). Synergistic Sonodynamic/chemotherapeutic Suppression of Hepatocellular Carcinoma by Targeted Biodegradable Mesoporous Nanosonosensitizers. *Adv. Funct. Mater.* 28, 1800145. doi:10.1002/adfm.201800145
- Ma, A., Chen, H., Cui, Y., Luo, Z., Liang, R., Wu, Z., et al. (2019a). Metalloporphyrin Complex-Based Nanosonosensitizers for Deep-Tissue Tumor Theranostics by Noninvasive Sonodynamic Therapy. *Small* 15, 1804028. doi:10.1002/sml.201804028
- Ma, Y., Zhang, Y., Li, X., Zhao, Y., Li, M., Jiang, W., et al. (2019b). Near-infrared II Phototherapy Induces Deep Tissue Immunogenic Cell Death and Potentiates Cancer Immunotherapy. *ACS Nano* 13, 11967–11980. doi:10.1021/acsnano.9b06040
- Ma, Y., Zhao, Y., Bejjanki, N. K., Tang, X., Jiang, W., Dou, J., et al. (2019c). Nanoclustered Cascaded Enzymes for Targeted Tumor Starvation and Deoxygenation-Activated Chemotherapy without Systemic Toxicity. *ACS Nano* 13, 8890–8902. doi:10.1021/acsnano.9b02466
- Maruoka, Y., Nagaya, T., Sato, K., Ogata, F., Okuyama, S., Choyke, P. L., et al. (2018). Near Infrared Photoimmunotherapy with Combined Exposure of External and Interstitial Light Sources. *Mol. Pharmaceutics* 15, 3634–3641. doi:10.1021/acs.molpharmaceut.8b00002
- Nam, J., Son, S., Park, K. S., Zou, W., Shea, L. D., and Moon, J. J. (2019). Cancer Nanomedicine for Combination Cancer Immunotherapy. *Nat. Rev. Mater.* 4, 398–414. doi:10.1038/s41578-019-0108-1
- Pan, X., Wang, W., Huang, Z., Liu, S., Guo, J., Zhang, F., et al. (2020). MOF-Derived Double-Layer Hollow Nanoparticles with Oxygen Generation Ability for Multimodal Imaging-Guided Sonodynamic Therapy. *Angew. Chem. Int. Ed.* 59, 13557–13561. doi:10.1002/anie.202004894
- Pang, X., Liu, X., Cheng, Y., Zhang, C., Ren, E., Liu, C., et al. (2019). Sono-Immunotherapeutic Nanocapsule to Combat Multidrug-Resistant Bacterial Infections. *Adv. Mater.* 31, 1902530. doi:10.1002/adma.201902530
- Pardoll, D. M. (2012). The Blockade of Immune Checkpoints in Cancer Immunotherapy. *Nat. Rev. Cancer* 12, 252–264. doi:10.1038/nrc3239
- Peng, J., Xiao, Y., Li, W., Yang, Q., Tan, L., Jia, Y., et al. (2018). Photosensitizer Micelles Together with Ido Inhibitor Enhance Cancer Photothermal Therapy and Immunotherapy. *Adv. Sci.* 5, 1700891. doi:10.1002/adv.201700891
- Qian, X., Zheng, Y., and Chen, Y. (2016). Micro/nanoparticle-augmented Sonodynamic Therapy (SDT): Breaking the Depth Shallow of Photoactivation. *Adv. Mater.* 28, 8097–8129. doi:10.1002/adma.201602012
- Ramesh, A., Kumar, S., Brouillard, A., Nandi, D., and Kulkarni, A. (2020). A Nitric Oxide (NO) Nanoreporter for Noninvasive Real-Time Imaging of Macrophage Immunotherapy. *Adv. Mater.* 32, 2000648. doi:10.1002/adma.202000648
- Shi, Y., and Lammers, T. (2019). Combining Nanomedicine and Immunotherapy. *Acc. Chem. Res.* 52, 1543–1554. doi:10.1021/acs.accounts.9b00148
- Song, W., Shen, L., Wang, Y., Liu, Q., Goodwin, T. J., Li, J., et al. (2018). Synergistic and Low Adverse Effect Cancer Immunotherapy by Immunogenic Chemotherapy and Locally Expressed PD-L1 Trap. *Nat. Commun.* 9, 2237. doi:10.1038/s41467-018-04605-x
- Suntharalingam, K., Awuah, S. G., Bruno, P. M., Johnstone, T. C., Wang, F., Lin, W., et al. (2015). Necroptosis-inducing Rhenium(V) Oxo Complexes. *J. Am. Chem. Soc.* 137, 2967–2974. doi:10.1021/ja511978y
- Tan, X., Huang, J., Wang, Y., He, S., Jia, L., Zhu, Y., et al. (2021). Transformable Nanosensitizer with Tumor Microenvironment-Activated Sonodynamic Process and Calcium Release for Enhanced Cancer Immunotherapy. *Angew. Chem. Int. Ed.* 60, 14051–14059. doi:10.1002/anie.202102703
- Um, W., Ko, H., You, D. G., Lim, S., Kwak, G., Shim, M. K., et al. (2020). Necroptosis-Inducible Polymeric Nanobubbles for Enhanced Cancer Sonoimmunotherapy. *Adv. Mater.* 32, 1907953. doi:10.1002/adma.201907953
- Uthaman, S., Pillarisetti, S., Mathew, A. P., Kim, Y., Bae, W. K., Huh, K. M., et al. (2020). Long Circulating Photoactivable Nanomicelles with Tumor Localized Activation and ROS Triggered Self-Accelerating Drug Release for Enhanced Locoregional Chemo-Photodynamic Therapy. *Biomaterials* 232, 119702. doi:10.1016/j.biomaterials.2019.119702

- Vitale, I., Shema, E., Loi, S., and Galluzzi, L. (2021). Intratumoral Heterogeneity in Cancer Progression and Response to Immunotherapy. *Nat. Med.* 27, 212–224. doi:10.1038/s41591-021-01233-9
- Wang, M., Hou, Z., Liu, S., Liang, S., Ding, B., Zhao, Y., et al. (2021). A Multifunctional Nanovaccine Based on L-Arginine-Loaded Black Mesoporous Titania: Ultrasound-Triggered Synergistic Cancer Sonodynamic Therapy/Gas Therapy/Immunotherapy with Remarkably Enhanced Efficacy. *Small* 17, 2005728. doi:10.1002/sml.202005728
- Wang, Y., Wiesnoski, D. H., Helmink, B. A., Gopalakrishnan, V., Choi, K., Dupont, H. L., et al. (2018). Fecal Microbiota Transplantation for Refractory Immune Checkpoint Inhibitor-Associated Colitis. *Nat. Med.* 24, 1804–1808. doi:10.1038/s41591-018-0238-9
- Xu, Q., Zhan, G., Zhang, Z., Yong, T., Yang, X., and Gan, L. (2021). Manganese Porphyrin-Based Metal-Organic Framework for Synergistic Sonodynamic Therapy and Ferroptosis in Hypoxic Tumors. *Theranostics* 11, 1937–1952. doi:10.7150/thno.45511
- Yin, Y., Jiang, X., Sun, L., Li, H., Su, C., Zhang, Y., et al. (2021). Continuous Inertial Cavitation Evokes Massive ROS for Reinforcing Sonodynamic Therapy and Immunogenic Cell Death against Breast Carcinoma. *Nano Today* 36, 101009. doi:10.1016/j.nantod.2020.101009
- Yue, W., Chen, L., Yu, L., Zhou, B., Yin, H., Ren, W., et al. (2019). Checkpoint Blockade and Nanosonosensitizer-Augmented Noninvasive Sonodynamic Therapy Combination Reduces Tumour Growth and Metastases in Mice. *Nat. Commun.* 10, 2025. doi:10.1038/s41467-019-09760-3
- Zeng, Q., Qiao, L., Cheng, L., Li, C., Cao, Z., Chen, Z., et al. (2020). Perfluorohexane-loaded Polymeric Nanovesicles with Oxygen Supply for Enhanced Sonodynamic Therapy. *ACS Biomater. Sci. Eng.* 6, 2956–2969. doi:10.1021/acsbmaterials.0c00407
- Zhan, G., Xu, Q., Zhang, Z., Wei, Z., Yong, T., Bie, N., et al. (2021). Biomimetic Sonodynamic Therapy-Nanovaccine Integration Platform Potentiates Anti-PD-1 Therapy in Hypoxic Tumors. *Nano Today* 38, 101195. doi:10.1016/j.nantod.2021.101195
- Zhang, C., and Pu, K. (2020). Molecular and Nanoengineering Approaches towards Activatable Cancer Immunotherapy. *Chem. Soc. Rev.* 49, 4234–4253. doi:10.1039/c9cs00773c
- Zhang, D.-W., Shao, J., Lin, J., Zhang, N., Lu, B.-J., Lin, S.-C., et al. (2009). RIP3, an Energy Metabolism Regulator that Switches TNF-Induced Cell Death from Apoptosis to Necrosis. *Science* 325, 332–336. doi:10.1126/science.1172308
- Zhang, D., Lin, Z., Zheng, Y., Song, J., Li, J., Zeng, Y., et al. (2020a). Ultrasound-driven Biomimetic Nanosystem Suppresses Tumor Growth and Metastasis through Sonodynamic Therapy, CO Therapy, and Indoleamine 2,3-dioxygenase Inhibition. *ACS Nano* 14, 8985–8999. doi:10.1021/acsnano.0c03833
- Zhang, K., Xu, H., Jia, X., Chen, Y., Ma, M., Sun, L., et al. (2016). Ultrasound-triggered Nitric Oxide Release Platform Based on Energy Transformation for Targeted Inhibition of Pancreatic Tumor. *ACS Nano* 10, 10816–10828. doi:10.1021/acsnano.6b04921
- Zhang, Y., Xu, Y., Sun, D., Meng, Z., Ying, W., Gao, W., et al. (2020b). Hollow Magnetic Nanosystem-Boosting Synergistic Effect between Magnetic Hyperthermia and Sonodynamic Therapy via Modulating Reactive Oxygen Species and Heat Shock Proteins. *Chem. Eng. J.* 390, 124521. doi:10.1016/j.cej.2020.124521
- Zhao, H., Zhao, B., Li, L., Ding, K., Xiao, H., Zheng, C., et al. (2020). Biomimetic Decoy Inhibits Tumor Growth and Lung Metastasis by Reversing the Drawbacks of Sonodynamic Therapy. *Adv. Healthcare Mater.* 9, 1901335. doi:10.1002/adhm.201901335
- Zhao, L., Zheng, R., Liu, L., Chen, X., Guan, R., Yang, N., et al. (2021). Self-delivery Oxidative Stress Amplifier for Chemotherapy Sensitized Immunotherapy. *Biomaterials* 275, 120970. doi:10.1016/j.biomaterials.2021.120970
- Zhu, W., Chen, Q., Jin, Q., Chao, Y., Sun, L., Han, X., et al. (2021). Sonodynamic Therapy with Immune Modulatable Two-Dimensional Coordination Nanosheets for Enhanced Anti-tumor Immunotherapy. *Nano Res.* 14, 212–221. doi:10.1007/s12274-020-3070-8

Conflict of Interest: The authors declare that the research was conducted in the absence of any commercial or financial relationships that could be construed as a potential conflict of interest.

Publisher's Note: All claims expressed in this article are solely those of the authors and do not necessarily represent those of their affiliated organizations, or those of the publisher, the editors, and the reviewers. Any product that may be evaluated in this article, or claim that may be made by its manufacturer, is not guaranteed or endorsed by the publisher.

Copyright © 2021 Cheng, Wang, Zhou and Li. This is an open-access article distributed under the terms of the Creative Commons Attribution License (CC BY). The use, distribution or reproduction in other forums is permitted, provided the original author(s) and the copyright owner(s) are credited and that the original publication in this journal is cited, in accordance with accepted academic practice. No use, distribution or reproduction is permitted which does not comply with these terms.



Development of A Decahedral Nanoenzyme Capable of Overcoming Hypoxia to Facilitate the Iodine-125 Radiosensitization of Esophageal Cancer

Dechao Jiao^{1†}, Kunpeng Wu^{1†}, Kaihao Xu¹, Yiming Liu¹, Deyao Zhao², Xinwei Han^{1*} and Ruitai Fan^{2*}

¹Department of Interventional Radiology, First Affiliated Hospital of Zhengzhou University, Zhengzhou, China, ²Department of Irradiation, The First Affiliated Hospital of Zhengzhou University, Zhengzhou, China

OPEN ACCESS

Edited by:

Huihua Yuan,
Nantong University, China

Reviewed by:

Mingzhen Zhang,
Xi'an Jiaotong University, China
Jingchao Li,
Donghua University, China
Fuyin Zheng,
Beihang University, China

*Correspondence:

Xinwei Han
13592583911@163.com
Ruitai Fan
fccfanrt@zzu.edu.cn

[†]These authors have contributed
equally to this work and share first
authorship

Specialty section:

This article was submitted to
Biomaterials,
a section of the journal
Frontiers in Bioengineering and
Biotechnology

Received: 25 August 2021

Accepted: 22 September 2021

Published: 08 October 2021

Citation:

Jiao D, Wu K, Xu K, Liu Y, Zhao D,
Han X and Fan R (2021) Development
of A Decahedral Nanoenzyme Capable
of Overcoming Hypoxia to Facilitate the
Iodine-125 Radiosensitization of
Esophageal Cancer.
Front. Bioeng. Biotechnol. 9:764531.
doi: 10.3389/fbioe.2021.764531

Radioisotopes have long been leveraged for internal radiotherapy-mediated cancer treatment. However, such therapeutic approaches are associated with serious side effects, and their efficacy is limited by intratumoral hypoxia. Herein, we prepared a folic acid-decorated palladium decahedral platform capable of enhancing the radiotherapeutic efficacy of iodine-125 (¹²⁵I) seed treatment. This decahedral nanoenzyme was able to target tumor regions and catalyze the conversion of intracellular H₂O₂ to O₂, thereby alleviating hypoxia within the tumor microenvironment. In addition, palladium was hypoxia can be alleviated, on the other hand, palladium was able to enhance the radiotherapeutic energy deposition within tumor tissues. The results of this analysis indicated that synthesized decahedral constructs can efficiently target and modify the hypoxic tumor microenvironment while simultaneously enhancing radiation energy deposition therein. Relative to palladium nanodots, the prolonged *in vivo* circulation of these decahedral constructs better enabled them to facilitate sustained radiosensitization. Overall, the results of this study highlight a novel approach to improving the therapeutic utility of ¹²⁵I seed interstitial implantation, thus underscoring an important direction for future clinical research.

Keywords: nanoenzyme, radiotherapy, hypoxia, 125 I, esophageal cancer

INTRODUCTION

Esophageal cancer is among the most common forms of human malignancy and is frequently characterized by progressive dysphagia (Sung et al., 2021). Radiotherapy (RT) is one of the primary treatments for esophageal cancer (Guo et al., 2021), but patients undergoing RT are highly susceptible to esophageal mucosal edema and radiation esophagitis, both of which can aggravate underlying dysphagia and result in serious eating disorders (Su et al., 2016). In addition to hampering the efficacy of RT treatment, this can also result in potentially life-threatening venous thrombosis.

RT is among the most common forms of cancer treatment, relying on localized irradiation as an antitumor modality. Different forms of *in vitro* accelerator therapy and *in vivo* radioisotope therapy can be classified into external beam radiotherapy (EBRT) and internal radioisotope therapy (RIT) strategies (Chao et al., 2018; Xie et al., 2019; Liu et al., 2020) Both EBRT and RIT rely on high-energy

rays (such as X-rays or electron beams), particle beams (such as proton beams), or radioactive isotopes to indirectly or directly damage nuclear DNA *via* the induction of ionizing radiation, thereby inducing tumor cell apoptosis (Pei et al., 2021). While RT has emerged as a primary cancer treatment strategy, it is subject to significant limitations that constrain its utility. In order to kill tumor cells, EBRT must pass through the skin and proximal normal tissues without any tumor-specific targeting, resulting in damage, inflammation, and potential oncogenesis in these otherwise healthy tissues (Dai et al., 2017; Huang et al., 2021a). In contrast, RIT approaches rely upon the intratumoral delivery of radioactive sources using a needle or similar mechanism (Sau et al., 2017). These radioactive sources are typically classified according to the particle type which they emit in the form of ionizing radiation, including α , β , and Auger particle emitters (Maier-Hauff et al., 2011). ^{255}Ac and ^{213}Bi , which emit alpha particles, exhibit a limited penetration depth (28–100 μm) and are thus only suited to the treatment of small or residual tumors after surgery (Zhu et al., 2017). In contrast, β -emitting particles such as ^{125}I and ^{188}Re can penetrate deeper tissues (20–130 mm) while maintaining relatively low cytotoxicity (Yi et al., 2018). Certain radioisotopes (^{123}I –123, ^{125}I –125) achieve optimal therapeutic efficacy only when present within the nucleus, and they exhibit a very low penetration depth (<0.5 μm) (Pirovano et al., 2020; Shen et al., 2020). Relative to EBRT, RIT is better suited to tumor targeting, but as an invasive treatment it can nonetheless damage surrounding normal tissues (Song et al., 2017). The tumor microenvironment (TME) is a highly acidic and hypoxic compartment, and repeated EBRT or RIT can aggravate such hypoxia, resulting in hypoxic radiotherapy tolerance and further reducing RT efficacy (Finley and Popel, 2013; Satterlee et al., 2017). As such, the selection of an excessively high radiation dose that damages healthy tissues or an excessively low dose that fails to induce sufficient tumor cell death can lead to adverse outcomes. Appropriately balancing tissue protection and tumor cell killing remains a major challenge to the effective treatment of cancer patients (Ma et al., 2017).

Rapid advances in the development of nanotechnology have highlighted a range of strategies well-suited to enhancing the therapeutic efficacy of radionuclides. Several studies have indicated that specific nanomaterials can improve RIT sensitivity and associated treatment outcomes (Kwatra et al., 2013; Lomax et al., 2013; Mi et al., 2016), with known RIT sensitizing materials being broadly classified based upon the mechanisms whereby they mediate radiosensitization. Nanomaterials containing elements with a high atomic number can improve the therapeutic effect of RIT (Chao et al., 2018). As the photoelectric effect associated with ionizing radiation is directly proportional to the cubic power of an element's atomic number, an increase in this photoelectric effect will thus enhance RIT radiotherapeutic efficacy. Le Goas et al. prepared a Hybrid Polymer (PMAA-AUNPs) *via* controlled free radical polymerization and determined that the resultant particles were able to increase the radiation dose deposited proximal to this polymer while significantly enhancing the cytotoxic effects of systemic ^{125}I administration on tumor cells, thereby increasing RIT sensitivity (Le Goas et al., 2019). The targeting of radioactive

sources can improve the killing of tumor cells while minimizing healthy tissue damage (Ge et al., 2020). Chen et al. synthesized a hybrid protein nanoreactor (^{125}I -HSA-CAT), that, as it incorporated catalase, was able to catalyze the decomposition of endogenous H_2O_2 while simultaneously delivering ^{125}I to the target tumors, thereby significantly enhancing the efficacy of RIT treatment (Finger and Giaccia, 2010; Chen et al., 2019). Modulating the TME thus represents an attractive approach to increasing the radiosensitivity of tumor cells, thereby maximizing radiation dose utilization. Tao et al. designed a composite nanomaterial (^{125}I -rGO-MnO₂-PEG) in which MnO₂ was able to consume H_2O_2 within the TME to alleviate hypoxia, together with the systemic intravenous administration of ^{125}I along with the nanocarrier-reducing nano-graphene oxide (rGO), enabling the synergistic enhancement of ^{125}I -mediated radiotherapy *via* a thermotherapy approach (Tao et al., 2018). While these current internal radiation sensitizers can effectively improve the treatment effect of RIT, they are nonetheless subject to multiple shortcomings and limitations. For example, the rapid internal circulation *in vivo* can lead to the rapid metabolic processing of these sensitizers such that they are largely discharged or degraded before playing an effective therapeutic role (Semenza, 2016; Yi et al., 2016; Xia et al., 2020). Additionally, the complexities of living systems and the role of the immune system in humans and other animal models can prevent these sensitizers from achieving the desired therapeutic effects (Huang et al., 2021b).

To enhance the therapeutic efficiency of ^{125}I , we herein developed a nanoenzyme platform capable of alleviating intratumoral hypoxia and thereby achieving robust radiosensitization. For this approach, we synthesized a decahedron consisting of palladium (Pd Decahedron), and these decahedral constructs were then decorated with folic acid to yield PD-FA. PD-FA was able to catalyze the conversion of high levels of intratumoral H_2O_2 into oxygen, thus reducing intratumoral hypoxia. Following PD-FA injection *via* the tail vein, it was able to target tumor regions in a folic acid-dependent manner. ^{125}I was then injected intratumorally, releasing γ rays in tumors and thereby inducing indirect or direct DNA damage. The resultant DNA radicals can then be fixed by the generated oxygen. Overall, these PD-FA nanoparticles exhibit promising properties that make them efficient radiosensitizers in the context of ^{125}I treatment.

RESULTS AND DISCUSSION

PD-FA nanoparticles were prepared *via* a two-step process wherein Pd decahedra were initially synthesized and were then coated with folic acid. Pd decahedra synthesis was conducted using a modified version of a previously published method. Briefly, 40 mg of Na_2SO_4 and 80 mg of polyvinyl pyrrolidone were dissolved and mixed in diethylene glycol at 105°C for 30 min, after which 15.5 mg of Na_2PdCl_4 was dissolved in 1 ml of diethylene glycol, and this solution was added to the prepared mixture. This solution was allowed to react for 5 h at 105°C, after which it was quenched with ice. Acetone was then added into the mixture, with was then centrifuged at 16,000 rpm to collect the product. This product was then washed twice with deionized water and dried overnight under vacuum. Folic acid surface

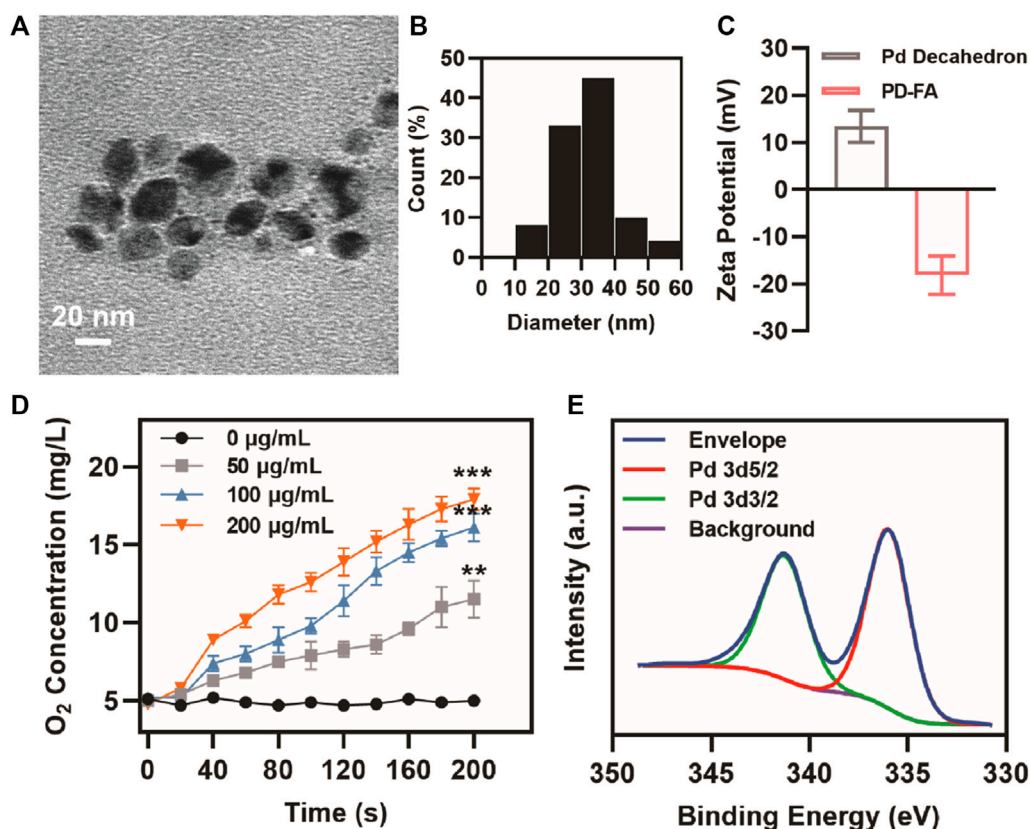


FIGURE 1 | PD-FA characterization. **(A)** TEM images of PD-FA and **(B)** PD-FA size distributions. **(C)** Zeta potential values for Pd decahedra and PD-FA preparations. **(D)** Oxygen content measurements following the addition of H₂O₂ to PD-FA samples at the indicated concentrations. **(E)** XPS spectra corresponding to elemental Pd.

modification was achieved by dispersing folic acid and Pd decahedra in absolute ethanol and stirring for 12 h under ultrasonication. The resultant product was then washed and dried under vacuum to yield PD-FA.

When Pd decahedra were analyzed *via* transmission electron microscopy (TEM), they exhibited a decahedral structure and were ~30 nm in size (**Supplementary Figure S1**). PD-FA TEM images revealed the presence of a thin film surrounding the decahedron (**Figure 1A**). PD-FA size distribution profiles revealed these particles to have an average diameter of 31.9 nm (**Figure 1B**). Pd decahedra exhibited a zeta potential of 13.4 mV, but this shifted to -18.2 mV following folic acid addition, consistent with successful surface modification (**Figure 1C**). Various concentrations of PD-FA were then combined with H₂O₂. The X-ray photoelectron spectrum (XPS) for these preparations exhibited characteristic Pd 3d_{5/2} and Pd 3d_{3/2} bands at 341.1 and 336.0 eV, respectively (**Figure 1E**). The ability of PD-FA to catalyze H₂O₂ conversion into oxygen, confirming that at a PD-FA concentration of 200 µg/ml, the oxygen content reached 17.9 mg/L after 200 s (**Figure 1D**), with this being sufficient to alleviate hypoxia.

Following successful PD-FA preparation, the ability of these nanoparticles to enhance radiosensitivity *in vitro* was assessed by

using them to treat EC109 human esophageal cells. Both PD-FA and Pd decahedrons were labeled with Cy-5 and then cultured with EC109 cells, after which fluorescence was assessed *via* confocal laser scanning microscopy. Cells pretreated with PD-FA exhibited increased fluorescence intensity relative to those treated with Pd decahedrons (**Figure 2A**), consistent with enhanced PD-FA uptake owing to the targeting properties of folic acid. The median fluorescence intensity (MFI) of PD-FA-treated cells was 3.1-fold higher than that for Pd decahedron-treated cells (**Figure 2B**). In light of these promising results, we examined the radiosensitization activity of these cells by assessing EC109 cell apoptosis using Calcein-AM and propidium iodide (PI) to stain for live and dead cells, respectively. No significant cell death was evident in the RT or PD-FA treatment groups (**Figure 2C**), whereas in the presence of PD-FA, significant apoptosis was induced upon subsequent RT treatment. These results were further confirmed *via* a quantitative CCK-8 assay (**Figure 2D**), as RT or PD-FA treatments were associated with limited cellular apoptosis, whereas the viability of cells in the PD-FA + RT group decreased by 42.1%, consistent with the marked radiosensitization ability of PD-FA. B-cell lymphoma-2 (Bcl-2) is an important apoptosis-related gene, and Western blotting further demonstrated that Bcl-2 protein levels in the PD-FA + RT group were reduced relative to other treatment groups

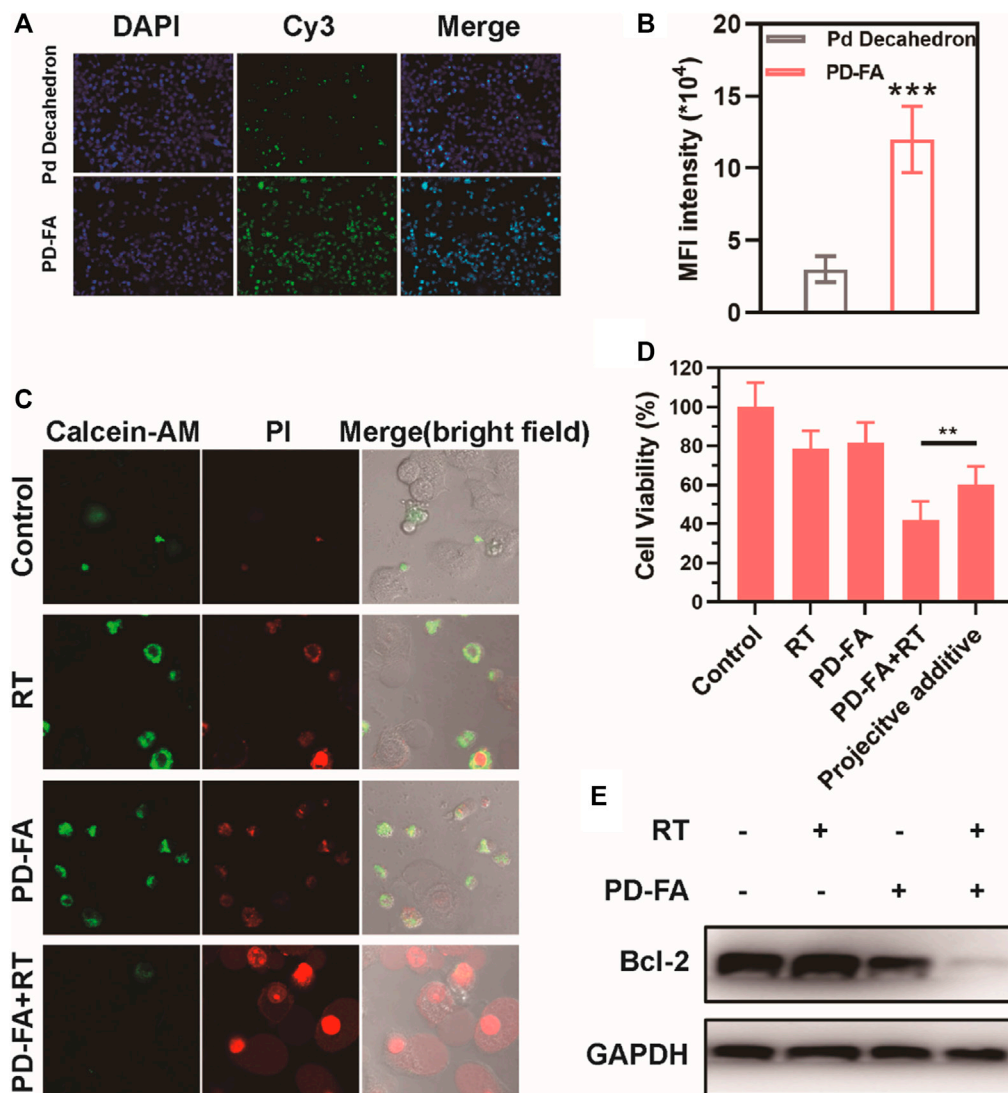


FIGURE 2 | Assessment of the *in vitro* radiosensitization ability of PD-FA *in vitro*. **(A)** CLSM images of cells and **(B)** corresponding quantitative analyses of image fluorescence. **(C)** CLSM images of live and dead cells following the indicated treatments and **(D)** results of CCK-8 assay. **(E)** Western blotting results for cells in the indicated treatment groups.

(Figure 2E), consistent with the increase in apoptotic cell death in this group.

A subcutaneous tumor model was next established to confirm the ability of PD-FA treatment to alleviate intratumoral hypoxia. PA imaging was utilized to measure *in vivo* oxygen content as a function of time in mice that were injected intravenously with PD-FA (Figures 3A,B). Following injection, oxygen levels in tumors rose until 6 h post-injection, and remained at relatively high levels until 24 h post-injection, consistent with the ability of PD-FA to successfully alleviate hypoxia. These results suggested that 6 h post-injection would be the optimal time to conduct RT treatment, given the maximal oxygen levels at this time. The tumor-targeting abilities of PD-FA and Pd decahedrons were additionally evaluated *via* immunofluorescence staining (Figure 3C). In the control group, tumors exhibited extensive

hypoxia that was partially alleviated following Pd decahedron administration, consistent with the ability of these nanoparticles to increase oxygen levels. Importantly, PD-FA treatment significantly reduced hypoxia within these tumors (Figure 3D), with the pimonidazole stained area in control groups being 6.6 times that observed in the PD-FA group.

In order to be clinically viable, the off-target toxicity of novel biomaterials must be assessed to ensure they exhibit satisfactory biocompatibility. To that end, we next intravenously injected nude BALB/c mice with PBS or a suspension of PD-FA in PBS. PD-FA injection was not associated with any apparent lesions in the major organs of injected mice (Supplementary Figure S2), suggesting that it does not induce any significant off-target cytotoxicity. We then assessed the antitumor efficacy of combination PD-FA + RT treatment by randomly assigning

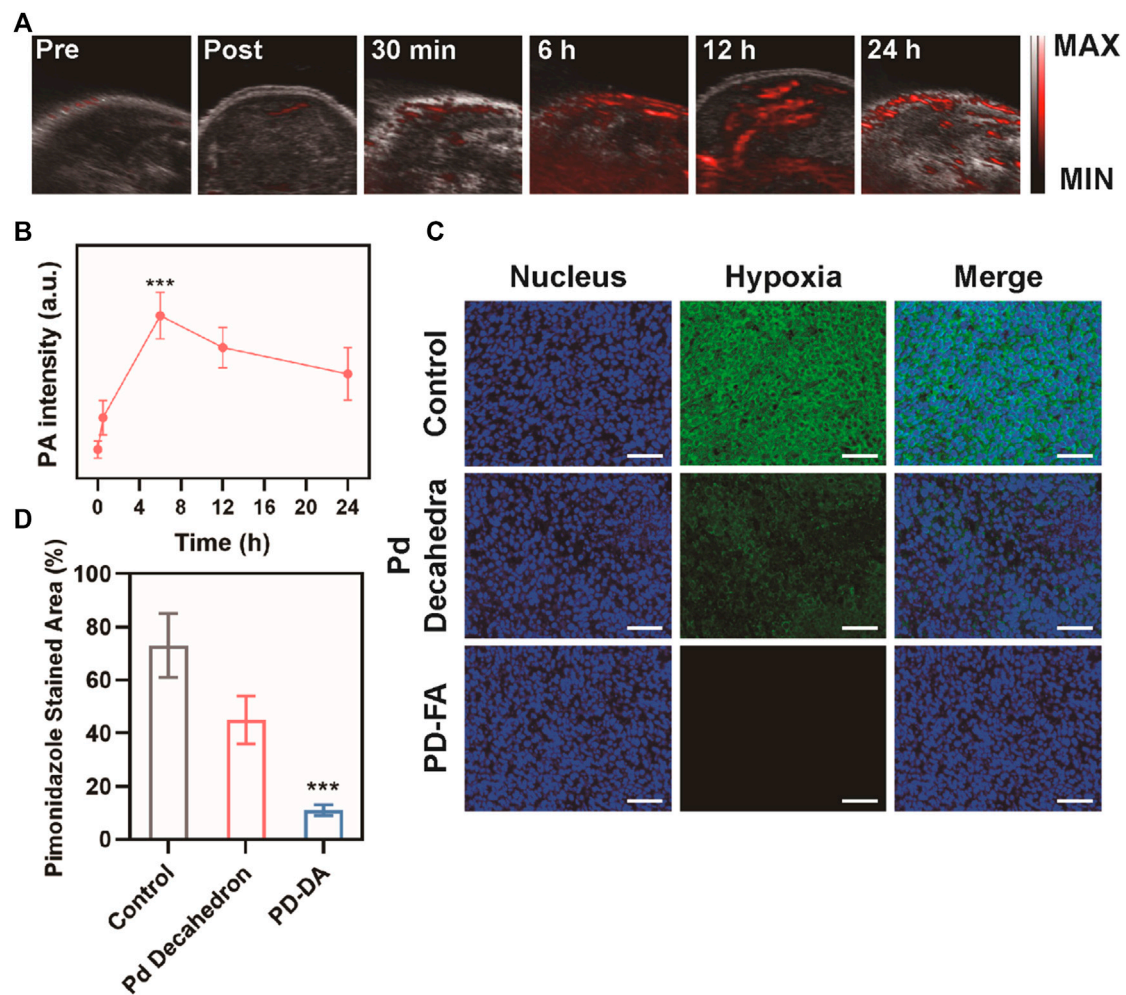


FIGURE 3 | Assessment of the *in vivo* PD-FA-mediated alleviation of intratumoral hypoxia. **(A)** PA images of tumors pre-injection and at 30 min, 6, 12, and 24 h post-injection, with **(B)** corresponding PA signal intensity analysis. **(C)** immunofluorescence-stained tumor sections following the indicated treatments with **(D)** corresponding quantification of pimonidazole fluorescence (scale bar: 50 μ m).

mice bearing EC109 tumors of a similar size into control and treatment groups that were intravenously injected with PBS or PD-FA and intratumorally injected with PBS or implanted with two radioactive ^{125}I particles. Murine body weight and tumor volumes were monitored after treatment, revealing no obvious difference of body weight in all groups (Figure 4C) and sustained tumor growth in control animals only administered PBS (Figure 4D). In contrast, mice in the PD-FA + RT group exhibited the most extensive tumor ablation owing to the precise targeting activity and radiosensitization effects of PD-FA treatment. RT treatment alone was also sufficient to suppress tumor growth to some extent. On day 19, mice were euthanized and tumor tissues were collected. Subsequent hematoxylin and eosin (H&E) staining demonstrated extensive tumor cell apoptosis in the PD-FA + RT group (Figure 4E). Together, these data suggest that PD-FA + RT treatment can lead to near-complete tumor ablation. Corresponding pharmacokinetic

curves (Figure 4A) indicated that these PD-FA nanoparticles are retained in circulation for extended periods owing to the utilized folic acid coating. Inductively coupled plasma-atomic emission spectrometry (ICP-AES) was used to assess Pd in tissue samples from these animals, revealing that PD-FA was associated with enhanced intratumoral accumulation and decreased hepatic and renal accumulation (Figure 4B). As such, these particles may achieve enhanced efficacy while reducing off-target toxicity. RT-PCR analyses further confirmed that HIF-1 α and EGFR expression levels were reduced in the PD-FA + RT group relative to the control group (Figure 4F), while BAX and Caspase-3 expression exhibited the opposite phenotype (Figures 4G,H). Decreased changes in Bcl-2 and PCNA expression were observed in the PD-FA + RT group (Figures 4I,J). Taken together, these results show that PD-FA + RT can induce marked intratumoral cellular apoptosis.

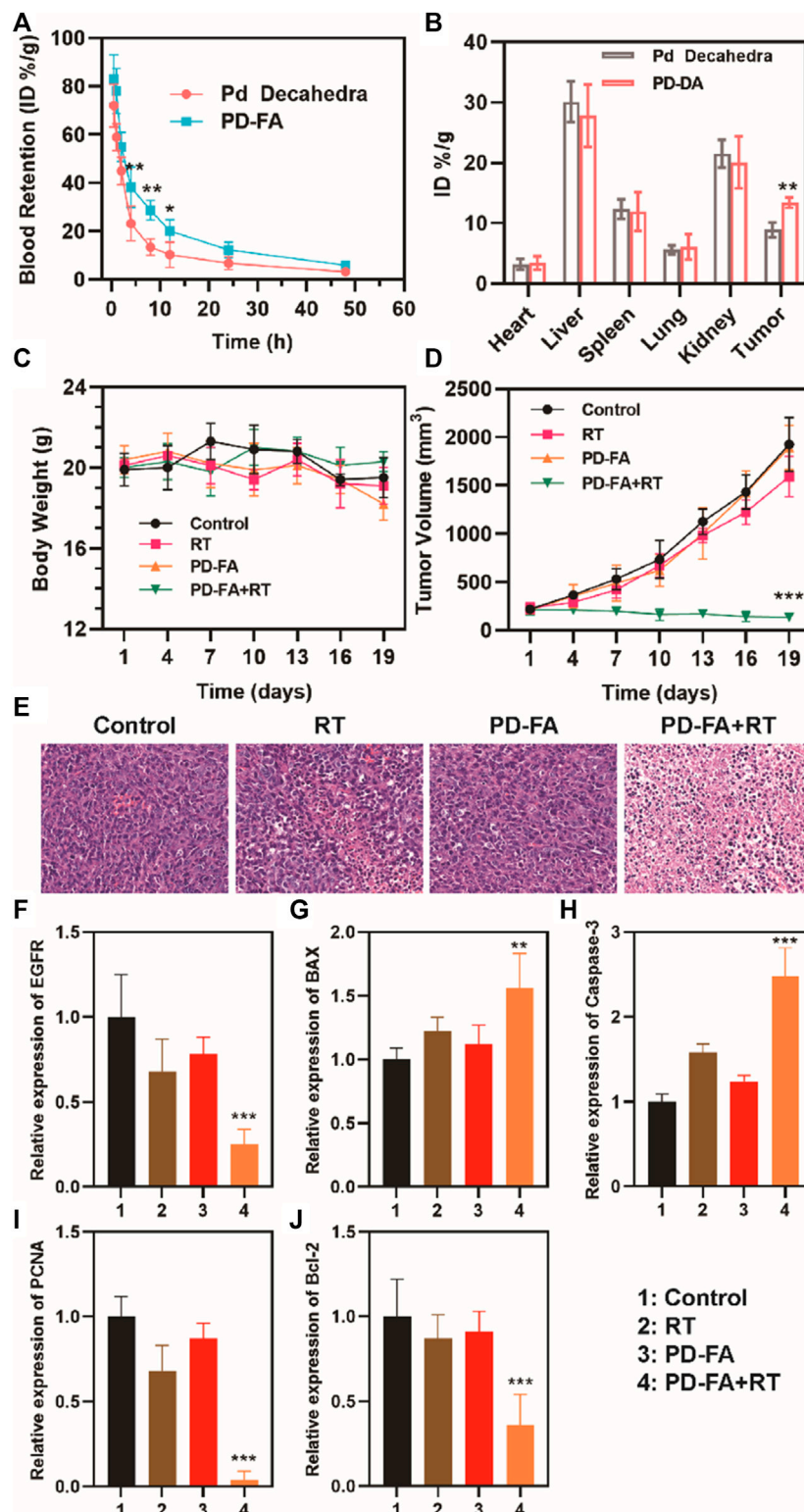
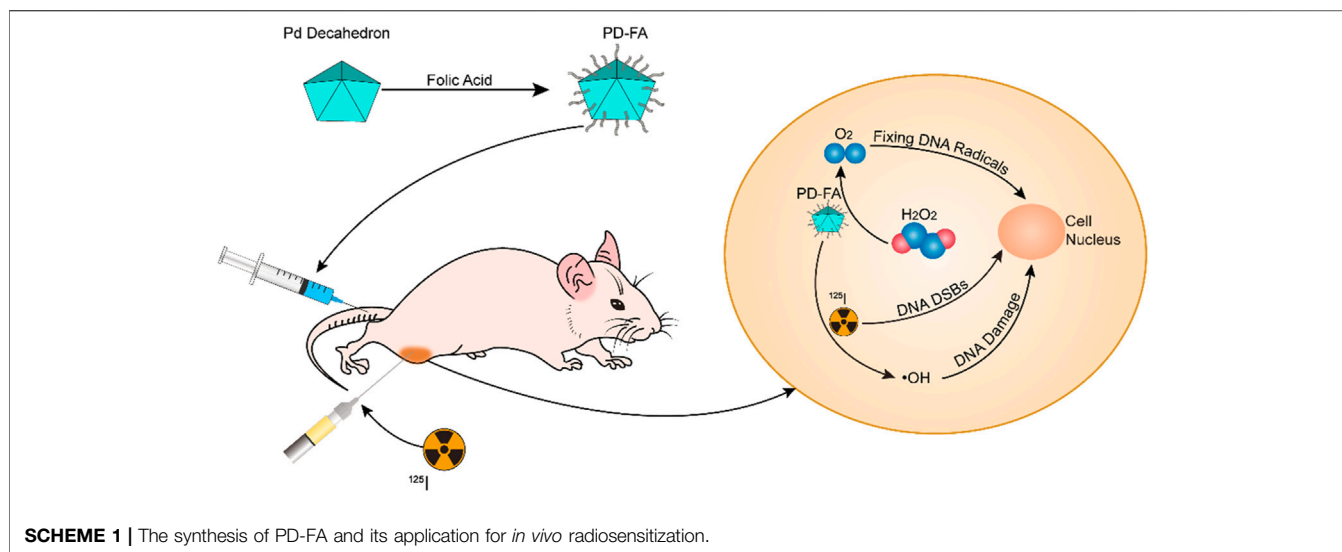


FIGURE 4 | Analysis of antitumor efficacy. **(A)** Pharmacokinetic curves. **(B)** Biodistribution results for the indicated treatment groups. **(C)** Murine body weight and **(D)** tumor volumes in the four treatment groups. **(E)** HE staining of tumors in four groups. Quantitative analyses of the expression of **(F)** EGFR, **(G)** BAX, **(H)** Caspase-3, **(I)** PCNA, and **(J)** Bcl-2 in the indicated groups as assessed via RT-PCR.



CONCLUSION

Hypoxia can impair the therapeutic efficacy of radiotherapy-based antitumor interventions. Herein, we successfully constructed a decahedral PD-FA nanoenzyme and leveraged it for the radiosensitization of RIT using ^{125}I seed. PD-FA was able to efficiently and actively target tumor regions, therein catalyzing the conversion of H_2O_2 to oxygen and thus alleviating intratumoral hypoxia. IN addition, PD-FA was able to enhance ^{125}I seed energy deposition within tumor regions, bolstering the generation of DNA radicals that can be fixed by oxygen cause permanent damage and induce cellular apoptosis. As such, this PD-FA nanoenzyme represents great potential for ^{125}I seed radiosensitization, and exhibits good biocompatibility that warrants further clinical study.

MATERIALS AND METHODS

Pd Decahedron and PD-FA Characterization

Pd decahedron and PD-FA NP morphological characteristics were assessed *via* transmission electron microscopy (TEM; Tecnai G2 F20 S-Twin, FEI, United States) at an acceleration voltage of 100 keV. Surface chemical elements were analyzed *via* XPS (ESCA-Lab250XI, Thermo Fisher Ltd., United States). The zeta potential and zeta-diameter measurements were quantified based upon dynamic light scattering (DLS, Nano-Zen 3,600, Malvern Instruments, United Kingdom).

Oxygen Measurements

To assess the oxygen-generating capacity of PD-FA, we utilized a dissolved oxygen meter to measure oxygen concentrations under a nitrogen atmosphere to assess the impact of different PD-FA concentrations (0, 50, 100, 200 $\mu\text{g}/\text{ml}$) on H_2O_2 at concentration of 30 mM generation.

Cell Culture

Human esophageal EC109 cancer cells (Chinese Academy of Sciences, Shanghai, China) were cultured in RPMI-1640 containing 10% FBS (Hyclone, United States) at 37°C in a humidified 5% CO_2 incubator.

In Vitro Cytotoxicity Analysis

A CCK-8 kit was used to assess *in vitro* EC109 cell killing. Initially, the impact of different PD-FA concentrations on cell survival following co-culture was assessed by plating EC109 cells overnight in 96-well plates (5,000/well), after which different PD-FA concentrations (0, 12.5, 25, 50, 100, 200 $\mu\text{g}/\text{ml}$) were added, and cells were incubated for an additional 24 h. Next, 10 μl of CCK-8 reagent was added per well, and plates were incubated for 2 h, after which a microplate meter (Rayto-6000 system, Rayto, China) was used to measure absorbance at 450 nm as a correlate for cytotoxicity. A CCK-9 kit was also used to assess cytotoxicity as a function of treatment type. Briefly, EC109 cells were plated and incubated overnight as above, after which they were separated into 4 treatment groups (5 wells/group): 1) Control; 2) PD-FA; 3) RT; and 4) PD-FA + RT. The PD-FA concentration for all groups was 50 $\mu\text{g}/\text{ml}$. Cells were treated as appropriate and incubated overnight, after which 10 μl of CCK-8 was added per well for 2 h, and absorbance was measured as above.

Western Blotting

EC109 cells were separated into four treatment groups: 1) Control; 2) PD-FA; 3) RT; and 4) PD-FA + RT, with a PD-FA concentration of 50 $\mu\text{g}/\text{ml}$. Total protein was then isolated from treated cells, and Bcl-2 protein levels therein were assessed *via* Western blotting.

Confirmation of In Vitro Cytotoxicity

To assess the cytotoxic effects of PD-FA treatment, EC109 cells were separated into four treatment groups: 1) control; 2) PD-FA; 3) RT; and 4) PD-FA + RT groups and were treated for 4 h in

60 mm tissue culture dishes. The PD-FA dose for these analyses was 50 µg/ml, while the RT dose was 22 MBq. Following the addition of FDA and PI, cells were rinsed using PBS and examined *via* fluorescence microscope (IX81, Olympus, Japan).

Animal Model Establishment

Female BALB/c nude mice (4–5 weeks old, Vital River Company, Beijing, China) were subcutaneously injected with 1×10^5 EC109 cells in a 100 µl volume on the right side of the abdomen. All the protocols for the procedures were approved by Animal Experiment Center of Wuhan University according to the protocols of the Institutional Animal Care and Use Committee (IACUC).

Assessment of *In Vivo* Oxygenation

The *in vivo* oxygenation activity of PD-FA was assessed by removing the hair from tumor sites in five mice, and then scanning these sites with a Vevo Lazer system (Fujifilm, Visualsonics Inc. Canada) to obtain PA images of blood saturation. Next, 100 µl of PD-FA (200 µg/ml) was injected into the caudal vein, and the tumor site was scanned using this device at 0, 6, and 24 h.

For subsequent immunofluorescent analyses, mice in the control group and mice that had been injected with PD-FA 24 h previously were intraperitoneally injected with pimonidazole hydrochloride (60 mg/kg), after which tumors were collected and frozen. Tumor sections were then stained with anti-pimonidazole and HRP-conjugated rabbit anti-FITC (1:100), while blood vessels were stained with monoclonal rat anti-mouse CD31 (1:200) and a rhodamine-linked donkey anti-rat secondary antibody (1:200). DAPI (1:5,000) was used to stain cellular nuclei, and cells were imaged *via* confocal microscopy.

Assessment of *In Vivo* Antitumor Efficacy

A total of 20 BALB/c nude mice were subcutaneously implanted on the right side of their abdomen with 100 µl of an EC109 cell suspension. When tumors were $\sim 100 \text{ mm}^3$ in size, animals were randomized into four treatment groups (5 mice/group): 1) control; 2) PD-FA; 3) RT; and 4) PD-FA + RT groups. The PD-FA concentration for all animals was 200 µg/ml (100 µl) for once, and the RT dose was 22 MBq by implantation of two ^{125}I particles following the injection. Tumor growth was monitored every 3 days using calipers, and changes in tumor volume and body weight were recorded.

Analyses of Blood Biochemistry

When tumors had grown to $80\text{--}100 \text{ mm}^3$ in size, mice were separated into three groups: 1) control mice, 2) mice injected with

100 µl of Pd decahedrons (200 µg/ml), and 3) mice injected with 100 µl of PD-FA (200 µg/ml) *via* the tail vein. Retroorbital blood samples were collected from these animals at 0.5, 2, 4, 8, 12, and 24 h, post-treatment.

Safety Assessment of PD-FA

Healthy mice were divided into two groups to assess the *in vivo* biocompatibility of PD-FA. Mice of 6-week-old were intravenously administrated with PBS or PD-FA (100 µl; 200 µg/ml). 30 days post the injection, the mice were sacrificed and main organs including heart, liver, spleen, lung and kidney were harvest for further HE staining.

RT-PCR Analysis of Tumor Tissues

After various treatment, mice in each group were sacrificed and tumor tissues were collected for RT-PCR to evaluate mRNA expression of EGFR, BAX, Caspase-3, PCNA, Bcl-2, respectively.

DATA AVAILABILITY STATEMENT

The original contributions presented in the study are included in the article/**Supplementary Material**, further inquiries can be directed to the corresponding authors.

ETHICS STATEMENT

The animal study was reviewed and approved by the Animal Experiment Center of Wuhan University.

AUTHOR CONTRIBUTIONS

DJ, KW, XH, and RF contributed to conception and design of the study. DJ organized the database. KX performed the statistical analysis. DJ wrote the first draft of the manuscript. KW, KX, YL, and DZ wrote sections of the manuscript. All authors contributed to manuscript revision, read, and approved the submitted version.

SUPPLEMENTARY MATERIAL

The Supplementary Material for this article can be found online at: <https://www.frontiersin.org/articles/10.3389/fbioe.2021.764531/full#supplementary-material>

REFERENCES

- Chao, Y., Liang, C., Yang, Y., Wang, G., Maiti, D., Tian, L., et al. (2018). Highly Effective Radioisotope Cancer Therapy with a Non-Therapeutic Isotope Delivered and Sensitized by Nanoscale Coordination Polymers. *ACS Nano* 12 (8), 7519–7528. doi:10.1021/acsnano.8b02400
- Chen, J., Liang, C., Song, X., Yi, X., Yang, K., Feng, L., et al. (2019). Hybrid Protein Nano-Reactors Enable Simultaneous Increments of Tumor Oxygenation and Iodine-131 Delivery for Enhanced Radionuclide Therapy. *Small* 15 (46), e1903628. doi:10.1002/sml.201903628
- Dai, Y., Xu, C., Sun, X., and Chen, X. (2017). Nanoparticle Design Strategies for Enhanced Anticancer Therapy by Exploiting the Tumor Microenvironment. *Chem. Soc. Rev.* 46 (12), 3830–3852. doi:10.1039/c6cs00592f

- Finger, E. C., and Giaccia, A. J. (2010). Hypoxia, Inflammation, and the Tumor Microenvironment in Metastatic Disease. *Cancer Metastasis Rev.* 29 (2), 285–293. doi:10.1007/s10555-010-9224-5
- Finley, S. D., and Popel, A. S. (2013). Effect of Tumor Microenvironment on Tumor VEGF During Anti-VEGF Treatment: Systems Biology Predictions. *JNCI: J. Natl. Cancer Inst.* 105 (11), 802–811. doi:10.1093/jnci/djt093
- Ge, J., Zhang, Q., Zeng, J., Gu, Z., and Gao, M. (2020). Radiolabeling Nanomaterials for Multimodality Imaging: New Insights into Nuclear Medicine and Cancer Diagnosis. *Biomaterials* 228, 119553. doi:10.1016/j.biomaterials.2019.119553
- Guo, D., Huang, Y., Jin, X., Zhang, C., and Zhu, X. (2021). A Redox-Responsive, *In-Situ* Polymerized Polyplatinum(IV)-Coated Gold Nanorod as an Amplifier of Tumor Accumulation for Enhanced Thermo-Chemotherapy. *Biomaterials* 266, 120400. doi:10.1016/j.biomaterials.2020.120400
- Huang, C., Wang, F. B., Liu, L., Jiang, W., Liu, W., Ma, W., et al. (2021). Hypoxic Tumor Radiosensitization Using Engineered Probiotics. *Adv. Healthc. Mater.* 10 (10), e2002207. doi:10.1002/adhm.202002207
- Huang, C., Ding, S., Jiang, W., and Wang, F. B. (2021). Glutathione-Depleting Nanoplatelets for Enhanced Sonodynamic Cancer Therapy. *Nanoscale* 13, 4512–4518. doi:10.1039/d0nr08440a
- Kwatra, D., Venugopal, A., and Anant, S. (2013). Nanoparticles in Radiation Therapy: A Summary of Various Approaches to Enhance Radiosensitization in Cancer. *Translational Cancer Res.* 2 (4), 330–342. doi:10.3978/j.issn.2218-676X.2013.08.06
- Le Goas, M., Paquet, M., Paquirissamy, A., Guglielmi, J., Compin, C., Thariat, J., et al. (2019). Improving ¹³¹I Radioiodine Therapy by Hybrid Polymer-Grafted Gold Nanoparticles. *Int. J. Nanomedicine* 14, 7933–7946. doi:10.2147/ijnm.s211496
- Liu, T., Yang, K., and Liu, Z. (2020). Recent Advances in Functional Nanomaterials for X-ray Triggered Cancer Therapy. *Prog. Nat. Sci. Mater. Int.* 30 (5), 567–576. doi:10.1016/j.pnsc.2020.09.009
- Lomax, M. E., Folkes, L. K., and O'Neill, P. (2013). Biological Consequences of Radiation-Induced DNA Damage: Relevance to Radiotherapy. *Clin. Oncol.* 25 (10), 578–585. doi:10.1016/j.clon.2013.06.007
- Ma, N., Wu, F.-G., Zhang, X., Jiang, Y.-W., Jia, H.-R., Wang, H.-Y., et al. (2017). Shape-Dependent Radiosensitization Effect of Gold Nanostructures in Cancer Radiotherapy: Comparison of Gold Nanoparticles, Nanospikes, and Nanorods. *ACS Appl. Mater. Inter.* 9 (15), 13037–13048. doi:10.1021/acsami.7b01112
- Maier-Hauff, K., Ulrich, F., Nestler, D., Niehoff, H., Wust, P., Thiesen, B., et al. (2011). Efficacy and Safety of Intratumoral Thermotherapy Using Magnetic Iron-Oxide Nanoparticles Combined with External Beam Radiotherapy on Patients with Recurrent Glioblastoma Multiforme. *J. Neurooncol.* 103 (2), 317–324. doi:10.1007/s11060-010-0389-0
- Mi, Y., Shao, Z., Vang, J., Kaidar-Person, O., and Wang, A. Z. (2016). Application of Nanotechnology to Cancer Radiotherapy. *Cancer Nano* 7 (1), 11. doi:10.1186/s12645-016-0024-7
- Pei, P., Liu, T., Shen, W., Liu, Z., and Yang, K. (2021). Biomaterial-Mediated Internal Radioisotope Therapy. *Mater. Horiz.* 8 (5), 1348–1366. doi:10.1039/d0mh01761b
- Pirovano, G., Jannetti, S. A., Carter, L. M., Sadique, A., Kossatz, S., Guru, N., et al. (2020). Targeted Brain Tumor Radiotherapy Using an Auger Emitter. *Clin. Cancer Res.* 26 (12), 2871–2881. doi:10.1158/1078-0432.ccr-19-2440
- Satterlee, A. B., Rojas, J. D., Dayton, P. A., and Huang, L. (2017). Enhancing Nanoparticle Accumulation and Retention in Desmoplastic Tumors via Vascular Disruption for Internal Radiation Therapy. *Theranostics* 7 (2), 253–269. doi:10.7150/thno.16681
- Sau, S., Alsaab, H. O., Kashaw, S. K., Tatiparti, K., and Iyer, A. K. (2017). Advances in Antibody-Drug Conjugates: A new era of Targeted Cancer Therapy. *Drug Discov. Today* 22 (10), 1547–1556. doi:10.1016/j.drudis.2017.05.011
- Semenza, G. L. (2016). The Hypoxic Tumor Microenvironment: A Driving Force for Breast Cancer Progression. *Biochim. Biophys. Acta (Bba) - Mol. Cel. Res.* 1863 (3), 382–391. doi:10.1016/j.bbamcr.2015.05.036
- Shen, C. J., Minn, I., Hobbs, R. F., Chen, Y., Josefsson, A., Brummet, M., et al. (2020). Auger Radiopharmaceutical Therapy Targeting Prostate-Specific Membrane Antigen in a Micrometastatic Model of Prostate Cancer. *Theranostics* 10 (7), 2888–2896. doi:10.7150/thno.38882
- Song, G., Cheng, L., Chao, Y., Yang, K., and Liu, Z. (2017). Emerging Nanotechnology and Advanced Materials for Cancer Radiation Therapy. *Adv. Mater.* 29 (32), 1600096. doi:10.1002/adma.201700996
- Su, H., Lin, F., Deng, X., Shen, L., Fang, Y., Fei, Z., et al. (2016). Profiling and Bioinformatics Analyses Reveal Differential Circular RNA Expression in Radioresistant Esophageal Cancer Cells. *J. Transl. Med.* 14 (1), 225. doi:10.1186/s12967-016-0977-7
- Sung, H., Ferlay, J., Siegel, R. L., Laversanne, M., Soerjomataram, I., Jemal, A., et al. (2021). Global Cancer Statistics 2020: GLOBOCAN Estimates of Incidence and Mortality Worldwide for 36 Cancers in 185 Countries. *CA: A Cancer J. Clinicians* 71 (3), 209–249. accepted. doi:10.3322/caac.21660
- Tao, Y., Zhu, L., Zhao, Y., Yi, X., Zhu, L., Ge, F., et al. (2018). Nano-Graphene Oxide-Manganese Dioxide Nanocomposites for Overcoming Tumor Hypoxia and Enhancing Cancer Radioisotope Therapy. *Nanoscale* 10 (11), 5114–5123. doi:10.1039/c7nr08747k
- Xia, D., Hang, D., Li, Y., Jiang, W., Zhu, J., Ding, Y., et al. (2020). Au-Hemoglobin Loaded Platelet Alleviating Tumor Hypoxia and Enhancing the Radiotherapy Effect with Low-Dose X-ray. *ACS Nano* 14 (11), 15654–15668. doi:10.1021/acsnano.0c06541
- Xie, J., Gong, L., Zhu, S., Yong, Y., Gu, Z., and Zhao, Y. (2019). Emerging Strategies of Nanomaterial-Mediated Tumor Radiosensitization. *Adv. Mater.* 31 (3), e1802244. doi:10.1002/adma.201802244
- Yi, X., Chen, L., Zhong, X., Gao, R., Qian, Y., Wu, F., et al. (2016). Core-shell Au@MnO₂ Nanoparticles for Enhanced Radiotherapy via Improving the Tumor Oxygenation. *Nano Res.* 9 (11), 3267–3278. doi:10.1007/s12274-016-1205-8
- Yi, X., Xu, M., Zhou, H., Xiong, S., Qian, R., Chai, Z., et al. (2018). Ultrasmall Hyperbranched Semiconducting Polymer Nanoparticles with Different Radioisotopes Labeling for Cancer Theranostics. *ACS Nano* 12 (9), 9142–9151. doi:10.1021/acsnano.8b03514
- Zhu, C., Sempkowski, M., Holleran, T., Linz, T., Bertalan, T., Josefsson, A., et al. (2017). Alpha-Particle Radiotherapy: For Large Solid Tumors Diffusion Trumps Targeting. *Biomaterials* 130, 67–75. doi:10.1016/j.biomaterials.2017.03.035

Conflict of Interest: The authors declare that the research was conducted in the absence of any commercial or financial relationships that could be construed as a potential conflict of interest.

Publisher's Note: All claims expressed in this article are solely those of the authors and do not necessarily represent those of their affiliated organizations, or those of the publisher, the editors and the reviewers. Any product that may be evaluated in this article, or claim that may be made by its manufacturer, is not guaranteed or endorsed by the publisher.

Copyright © 2021 Jiao, Wu, Xu, Liu, Zhao, Han and Fan. This is an open-access article distributed under the terms of the Creative Commons Attribution License (CC BY). The use, distribution or reproduction in other forums is permitted, provided the original author(s) and the copyright owner(s) are credited and that the original publication in this journal is cited, in accordance with accepted academic practice. No use, distribution or reproduction is permitted which does not comply with these terms.



Nanotechnologies for Reactive Oxygen Species“Turn-On” Detection

Hongfei Jiang^{1†}, Qian Lin^{1†}, Zongjiang Yu^{2*}, Chao Wang^{1*} and Renshuai Zhang^{1*}

¹Cancer Institute, The Affiliated Hospital of Qingdao University and Qingdao Cancer Institute, Qingdao, China, ²Key Laboratory of Biobased Materials, Qingdao Institute of Bioenergy and Bioprocess Technology, Chinese Academy of Sciences, Qingdao, China

OPEN ACCESS

Edited by:

Huihua Yuan,
Nantong University, China

Reviewed by:

Tao Deng,
Chongqing Medical University, China
Qiuyu Gong,
Independent Researcher, Singapore,
Singapore

*Correspondence:

Zongjiang Yu
yuzj@qibebt.ac.cn
Chao Wang
wangchao@qdu.edu.cn
Renshuai Zhang
zhangrenshuai@qdu.edu.cn

[†]These authors have contributed
equally to this work

Specialty section:

This article was submitted to
Biomaterials,
a section of the journal
Frontiers in Bioengineering and
Biotechnology

Received: 20 September 2021

Accepted: 18 October 2021

Published: 03 November 2021

Citation:

Jiang H, Lin Q, Yu Z, Wang C and
Zhang R (2021) Nanotechnologies for
Reactive Oxygen Species“Turn-
On” Detection.
Front. Bioeng. Biotechnol. 9:780032.
doi: 10.3389/fbioe.2021.780032

Reactive oxygen species (ROS) encompasses a collection of complicated chemical entities characterized by individually specific biological reactivities and physicochemical properties. ROS detection is attracting tremendous attention. The reaction-based nanomaterials for ROS “turn-on” sensing represent novel and efficient tools for ROS detection. These nanomaterials have the advantages of high sensitivity, real-time sensing ability, and almost infinite contrast against background. This review focuses on appraising nanotechnologies with the ROS “turn-on” detection mechanism coupled with the ability for broad biological applications. In this review, we highlighted the weaknesses and advantages in prior sensor studies and raised some guidelines for the development of future nanoprobes.

Keywords: reactive oxygen species, ROS nanotechnology, ROS turn-on detection, detection method, sensor

INTRODUCTION

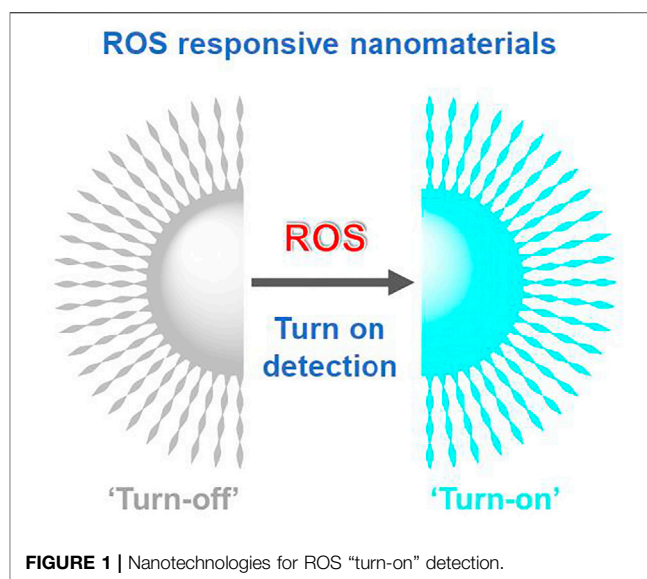
Reactive oxygen species (ROS) is the group of reactive anionic and neutral small molecules which are produced within many cell types. It mainly includes singlet oxygen (¹O₂), superoxide anion (O₂^{•−}), hydroxyl radical (•OH), and hydrogen peroxide (H₂O₂) (Yang et al., 2019). ROS has been confirmed to play a significant role in regulating numerous physiological functions of living organisms. However, ROS overproduction leads to oxidative stress and results in oxidative damage to a number of biomolecules including lipids, nucleic acids, proteins, and carbohydrates (Mattila et al., 2015), which is implicated in various diseases such as cancer, cardiovascular disease, diabetes mellitus, and aging (Valko et al., 2007; Winyard et al., 2011). Therefore, to improve the understanding of redox biology, the source and the stimulation of ROS generation, along with the consequences, we need to monitor and quantify ROS in cells, tissues, and whole organisms. Furthermore, the accurate species needs to be identified for each biological condition to fully understand redox biology.

Joint efforts have been made by chemists and biologists to monitor the locations and concentrations of these highly aggressive species with very short lifetime. Thanks to these precise ROS detection methods, remarkable progress has been witnessed in unveiling the relevant biological mechanisms and uncovering the apparently paradoxical roles of distinct ROS in human health and disease. Small molecule fluorescent probes, especially reaction-based “turn-on” fluorescent probes, are generally useful owing to their high levels of sensitivity and capability to be applied in temporal and spatial sampling for *in vivo* and live cell imaging (Wu et al., 2019; Wang et al., 2020; Zhang et al., 2021). Alternatively, great varieties of nanomaterials with peculiar ROS-regulating abilities have been fabricated to support ROS science in the aspects of ROS generation, depletion, transition, and detection (Zhou Z. et al., 2016); these nanotechnologies finally benefit the ROS-based therapeutic outcomes (Yang et al., 2019; Yu et al., 2020; Zhang et al., 2021; Zheng et al., 2021). Nanoparticles exhibit tunable properties in size, shape, and function that make them flexible in process and product control for a wide range of applications (He et al., 2021; Yang et al., 2021; Yin et al., 2021). Using nanoparticles

as probes, probe vectors, and compartmentalization agents for ROS detection has become more and more popular. Rationally designed nanotechnologies for ROS “turn-on” detection (**Figure 1**) are expected to possess the advantages of tunable functional group control, low cellular toxicity, high levels of sensitivity, and in particular, the capability of temporal and spatial sampling for *in vivo* and living cell imaging (Wu et al., 2019). It is worth mentioning that the benefit of “turn-on” over “turn-off” sensors is that they have almost infinite contrast against background. In principle, nanomaterials for ROS “turn-on” detection include carbon dots, silica nanoparticles, metal–organic framework (MOF), and nanoflakes. Herein, a selection of state-of-the-art nanomaterials for “turn-on” sensing of ROS with demonstrated promising application in biological systems is reviewed. We will appraise in detail these nanotechnologies with exactly demonstrated reaction mechanisms to help researchers choose suitable nanoprobes or inspire the development of future nanotechnologies.

DETECTION OF H₂O₂

H₂O₂ is a reactive species among ROS and is closely related to various physiological processes, such as cell proliferation, apoptosis, differentiation, and other signal transmissions. Therefore, the accumulation of excessive H₂O₂ has been implicated in many diseases. Thus, it is of great significance in monitoring the concentration of H₂O₂ in a physiological environment. As H₂O₂ is the most studied species of ROS, numerous mapping tools including radiative recombination mechanism and “dark” biological processes have been developed for H₂O₂ detection (Wu et al., 2019). Inspired by the successful development of boronic acid-based molecular fluorescent probes for H₂O₂ detection with a “turn-on” mechanism (Bull et al., 2013), several boronic acid functionalized fluorescent nanoprobes have been designed for “turn-on” sensing of H₂O₂. This design relies on the formation of the non-fluorescence boronic acid/boronate ester, which contains an electrophilic boron center; it reacts rapidly with H₂O₂, resulting in accelerated oxidative cleavage to afford the corresponding phenol to “turn on” the fluorescence (**Figure 2A**). Depending on this mechanism, Wu and co-workers developed a fluorescence resonance energy transfer (FRET)-based ratiometric fluorescent probe for the detection of H₂O₂. This nanoparticle uses carbon dots as the energy donor and carrier. The small size (~4 nm) and good *in vivo* utility of this nanoparticle may support its eventual application in clinics (limit of detection (LOD) = 0.5 μM). Higher selectivity has been achieved for the nanoparticle for the detection of H₂O₂ over other ROS and biologically relevant species (Wu et al., 2014). Zhao’s group attached boronate ester to the surface of functional mesoporous silica nanoparticles (MSNPs) for “turn-on” detection of H₂O₂ (LOD = 3.33 μM). Moreover, they fabricated a H₂O₂-triggered drug release system for heart failure therapy. This system exhibits the potential for different variants of heart failure models to target theranostic treatment (Tan et al., 2017). The first MOF for H₂O₂ sensing have been designed by Sk and co-workers. Different from the previous two nanoparticles, the MOF directly uses boronic acid as a functional group attached to a Zr(IV)



MOF for “turn-on” sensing of H₂O₂ in live cells (LOD = 0.015 μM). However, it also has moderate response to some other ROS and biologically relevant species, indicating that the selectivity of this MOF material toward H₂O₂ is a major defect (Sk et al., 2018). Then a boronic acid-functionalized 3D indium MOF was fabricated for H₂O₂ detection. The MOF exhibits an improved selectivity for H₂O₂ with an LOD of 420 nM (Jiang et al., 2021). In general, boronic acid-functionalized nanomaterials are easier for fabrication, while boronate ester nanomaterials possess higher selectivity for H₂O₂.

The carbon dot-based fluorescence “turn-on” probe for H₂O₂ with a photo-induced electron transfer (PET) mechanism was fabricated by Zhang’s group. In this nanoprobe, diphenylphosphine moiety is covalently attached to the surface of the carbon dot; they serve as the PET donor and acceptor, respectively. Subsequently, H₂O₂ can selectively oxidize the diphenylphosphine to produce the target oxide and prevent the PET mechanism; then the fluorescence will “turn on” (**Figure 2B**). The nanoprobe has a fast response to H₂O₂ with a LOD of 84 nM (Lan et al., 2015). Peroxalate-functionalized carbon nanodots are novel near-infrared chemiluminescent nanomaterials for H₂O₂ detection (LOD = 5 nM). Nanointegration of near-infrared carbon nanodots and peroxalate (P-CDs) with amphiphilic triblock copolymer as bridge can serve as “turn-on” sensors for the detection and imaging of H₂O₂ (**Figure 2C**). The high efficiency and large penetration depth of near-infrared photons of P-CDs make this strategy a good choice for bioimaging of H₂O₂ *in vitro* and *in vivo* (Shen et al., 2020).

Ag-based nanomaterials have broad application for H₂O₂ detection. In these designs, Ag materials normally act as a shell and serve as efficient quenchers, while H₂O₂ can prevent the Ag material-mediated quenching mechanism and fulfill the “turn-on” detection of H₂O₂ (**Figure 2D**). Chu’s group utilized DNA-templated Ag nanoparticles (DNA-AgNPs) coupled with NaYF₄:Yb/Tm@NaYF₄ shell upconversion nanoparticles (UCNPs) for the detection of H₂O₂ (LOD = 1.08 μM), in which, UCNPs and DNA-AgNPs serve as donors and

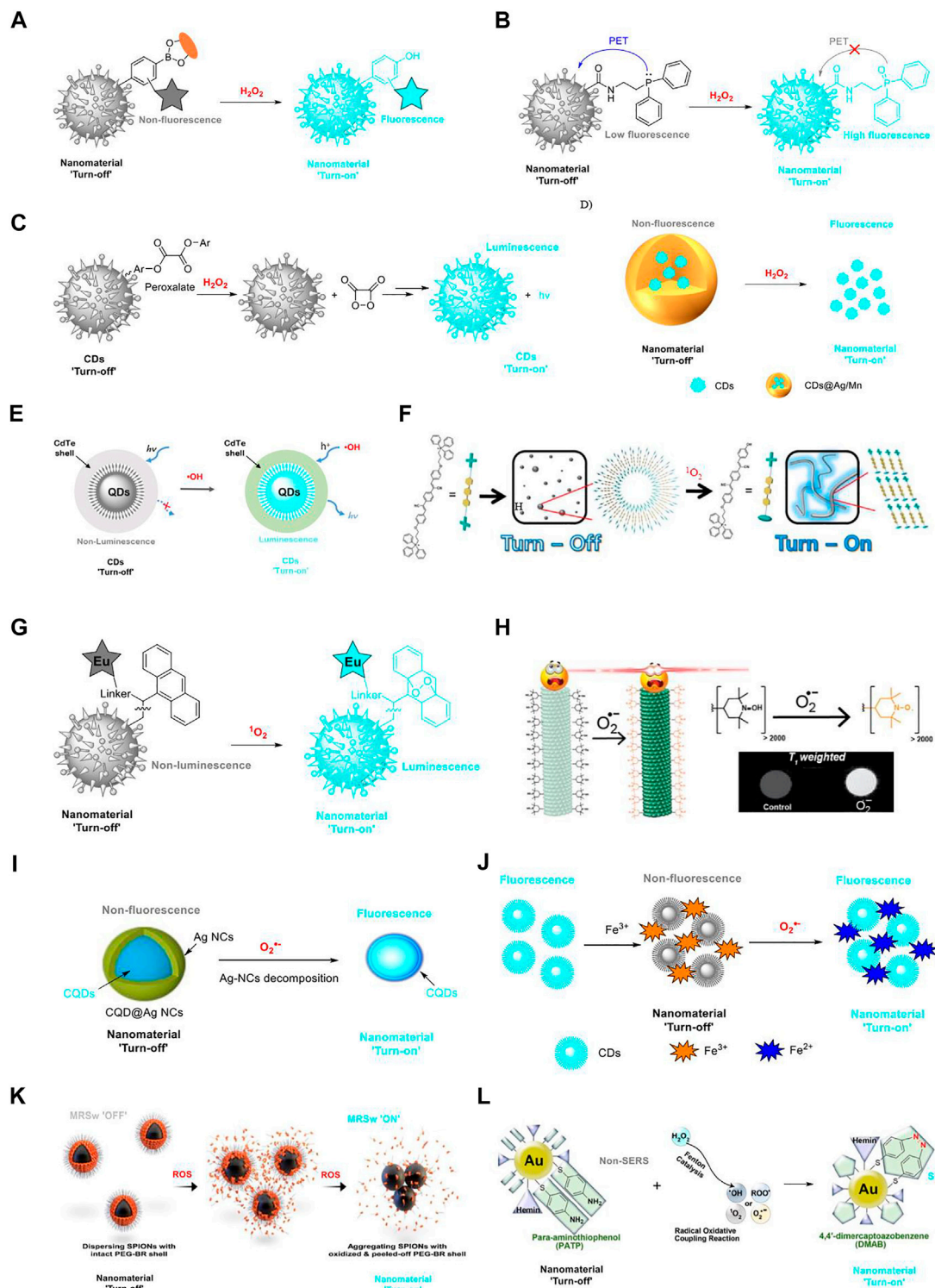


FIGURE 2 | Nanotechnologies for ROS detection with a “turn-on” mechanism. **(A)** Boronic acid/boronate ester-based nanomaterials for H_2O_2 “turn-on” detection; **(B)** carbon dot-based fluorescence “turn-on” probe for H_2O_2 detection with a PET mechanism; **(C)** peroxalate-functionalized carbon nanodots as near-infrared chemiluminescent nanomaterial for H_2O_2 “turn-on” detection; **(D)** Ag- and Mn-based nanomaterials for H_2O_2 “turn-on” detection; **(E)** semiconductor quantum dots as “turn-on” luminescent probes for real-time detection of $\bullet OH$; **(F)** triphenylphosphonium-based self-assembled nanomaterial for 1O_2 “turn-on” detection; **(G)** “turn-on” detection of 1O_2 using a nanostructured porous silicon microcavity through photonic luminescence enhancement strategy; **(H)** metal-free magnetic resonance imaging (MRI) tool for $O_2^{\bullet -}$ “turn-on” detection (copyright 2018 American Chemical Society); **(I)** schematic illustrations of fluorescence “turn-on” detection of $O_2^{\bullet -}$ based on CQD@Ag NCs (copyright 2017 Springer); **(J)** illustration of CDs- Fe^{3+} for the detection of $O_2^{\bullet -}$; **(K)** PEG-BR@SPIONs as the biosensor with a magnetic relaxation switching-based mechanism for ROS “turn-on” detection; **(L)** Au-PATP-Hemin nanoprobe for ROS “turn-on” detection (copyright 2018 American Chemical Society).

quenchers, respectively. This design results in luminescence quenching of UCNP using DNA-AgNPs by luminescence resonance energy transfer (LRET). Upon H_2O_2 introduction, AgNPs can be converted to Ag^+ , leading to the inhibition of the LRET process and inducing the recovery of upconversion luminescence (Wu et al., 2016). In this way, graphene quantum dots (QDs) adopted with the silver shell (GQD@Ag, LOD = 2 μM) (Kong et al., 2017), nitrogen-doped carbon QDs coated with silver nanoparticles (N-CQD/AgNPs, LOD = 4.7 μM) (Walekar et al., 2017), and a novel nanocluster-mediated chemical information processing system (CIPS, LOD information unavailable) (Zhao et al., 2018) have been designed and applied in selective H_2O_2 sensing with a “turn-on” mechanism.

Alternatively, the Mn-mediated nanotechnologies share a similar mechanism with Ag-mediated nanomaterials for H_2O_2 “turn-on” detection but have higher selectivity (Figure 2D). In this process, MnO_2 nanosheets serve as a quencher but can be oxidized by H_2O_2 to fulfill the “turn-on” sensing of H_2O_2 . Depending on this design, Yuan and co-workers fabricated manganese dioxide (MnO_2)-nanosheet-modified UCNP for rapid detection of H_2O_2 (LOD = 0.9 μM). The MnO_2 nanosheets on the surface of UCNP serve as the quencher. Fluorescence of UCNP will be recovered after the addition of H_2O_2 , which can reduce MnO_2 to Mn^{2+} and destroy the structure of the MnO_2 quencher (Yuan et al., 2015). Following this design, Lei and Liu’s group developed a carbon dot- MnO_2 probe (LOD = 0.87 μM) and a three-in-one stimulus-responsive nanoplatform (Au@ MnO_2 @Raman reporter, LOD = 6–7 μM), respectively, for H_2O_2 sensing with relatively improved selectivity or sensitivity (Ning et al., 2020; Zhang et al., 2020). While the Ag and Mn-mediated nanomaterials are utilized for H_2O_2 sensing in solutions, the biocompatibility of such structures is still questionable.

DETECTION OF HYDROXYL RADICAL ($\cdot\text{OH}$)

$\cdot\text{OH}$, the result of the homolytic cleavage of water ($\text{H}_2\text{O} \rightarrow \cdot\text{OH} + \cdot\text{H}$), is the most deleterious and reactive species of ROS. The general reactivity of the main ROS in biological systems decreases in the order of $\cdot\text{OH} > {}^1\text{O}_2 > \text{H}_2\text{O}_2 > \text{O}_2^{\cdot-}$ (Mattila et al., 2015). $\cdot\text{OH}$ can destroy a number of biomolecules including proteins, lipids, and DNA, so as to induce numerous oxidative stress-related diseases. However, at present time, the detailed function of $\cdot\text{OH}$ has seldom been demonstrated owing to the extremely high reactivity and short lifetime (Bai et al., 2019). Therefore, real-time sensing of $\cdot\text{OH}$ in biological samples is of great importance. The use of semiconductor QDs as “turn-on” luminescent probes for real-time detection of $\cdot\text{OH}$ has been developed (LOD = 0.3 μM) (Figure 2E). In this design, metal citrate complexes are adopted on the surfaces of QDs and can act as electron donors, injecting electrons into the lowest unoccupied molecular orbital (LUMO) of the QDs. Interestingly, only $\cdot\text{OH}$ can inject holes into the highest occupied molecular orbital (HOMO) of the QDs. Consequently, the produced electron-hole pairs could emit strong luminescence through electron-hole recombination. This nanotechnology is demonstrated to have an application in detecting the endogenous release of $\cdot\text{OH}$ in living cells (Zhou W. et al., 2016).

Alternatively, Yu’s group fabricated a polyhedral-AuPd nanoparticle-based dual-mode cytosensor (PH-AuPd NPs, LOD information unavailable) with a “turn-on”-enabled signal for $\cdot\text{OH}$ sensing. In this strategy, tetramethylbenzidine (TMB) acting as a functional group on the cytosensor is oxidized to ox TMB, a colored product, and can be monitored through colorimetric analysis. Coupled with a rational design, the nanotechnology has been constructed as a convenient method for the sensitive detection of MCF-7 cells (LOD = 20 cells ml^{-1}) (Wang H. et al., 2018).

DETECTION OF SINGLET OXYGEN

${}^1\text{O}_2$ has raised vital interest recently as a result of its significance in both chemical and biological systems. ${}^1\text{O}_2$ is the lowest excited electronic state of molecular oxygen but is recognized to be highly reactive. Studies have demonstrated that ${}^1\text{O}_2$ is highly toxic and destroys key biological molecules including proteins, DNA, and unsaturated lipids. Depending on a triphenylphosphonium derivative, the self-assembled nanomaterial has been fabricated for ${}^1\text{O}_2$ “turn-on” detection (LOD = 33–56 μM) (Figure 2F). However, these nanoparticles are responsive to both ${}^1\text{O}_2$ and ClO^- (Choi et al., 2018). A strategy for “turn-on” detection of ${}^1\text{O}_2$ using a nanostructured porous silicon microcavity (pSiMC, LOD = 37 nM) through photonic luminescence enhancements has been developed (Figure 2G). The pSiMC is modified with an Eu(III)-linker-anthracene complex. In the presence of ${}^1\text{O}_2$, the formation of an endoperoxide in the 9,10 position of anthracene is confirmed. Changes in the anthracene moiety can result in changes to the emission of the Eu(III) ion so as to induce these nanoprobe to become luminescent (Jenie et al., 2017). Alternatively, a technique for electrical detection of ${}^1\text{O}_2$ on the surface of silver nanoparticle film has been fabricated by Knoblauch and co-workers. Singlet oxygen sensor green (SOSG, LOD information unavailable) in this system functions as a crucial moiety for the fluorescence “turn-on” sensing process. The presence of ${}^1\text{O}_2$ in this system can result in change in the SOSG fluorescence quantum yield, which permits a stronger energy transfer from the SOSG probe to a proximal silver nanoparticle island film located in the near-electric field of the probe. This induces an increase in the target electric current flow, allowing for the sensing of the ${}^1\text{O}_2$ (Knoblauch et al., 2020).

DETECTION OF SUPEROXIDE ($\text{O}_2^{\cdot-}$)

$\text{O}_2^{\cdot-}$ is a by-product of ATP generation processes of the human body microenvironment, which plays a significant role in regulating biochemistry and organic pathology. Furthermore, exposure to excess $\text{O}_2^{\cdot-}$ would oxidize organisms, biological membranes, and tissues and cause diseases such as hepatitis, cancer, and diabetes (Gorrini et al., 2013). Nanomaterials such as carbon dots (Liang et al., 2020; Yue et al., 2021), MOF (Das et al., 2019), and tobacco mosaic virus (TMV) nanoparticles (Dharmarwardana et al., 2018) have been fabricated as selective sensors for “turn-on” sensing of $\text{O}_2^{\cdot-}$. Silver nanoparticle (Ag NP)-coated carbon quantum dot (CQD)

core-shell-structured nanocomposites (CQD@Ag NCs) have been developed for fluorescent sensing of intracellular $O_2^{\bullet-}$ (LOD = 0.3 μ M) (**Figure 2I**). In CQD@Ag NCs, CQDs display a potent blue fluorescence; however, the fluorescence is quenched by Ag NPs. In the presence of $O_2^{\bullet-}$, Ag NPs are oxide-etched, and the fluorescence of CQDs is recovered (Liang et al., 2020). Yue and co-workers fabricated similar carbon dots for $O_2^{\bullet-}$ sensing while the quencher is Fe^{3+} (LOD = 25 pM). The addition of $O_2^{\bullet-}$ can convert Fe^{3+} to Fe^{2+} and recover the fluorescence of carbon dots (Yue et al., 2021) (**Figure 2J**). It is reported that CQD@Ag NCs are successfully utilized in the imaging of $O_2^{\bullet-}$ in MCF-7 cells; however, the biocompatibility of Liang's carbon dots is questionable. The Gassensmith group managed to functionalize the surface of TMV (LOD information unavailable) nanoparticles with 4-hydroxy-tetramethylpiperidine at the protein tyrosine residue. The nanoparticles function as a metal-free magnetic resonance imaging (MRI) tool for $O_2^{\bullet-}$ monitoring (**Figure 2H**). The mechanism of this strategy for $O_2^{\bullet-}$ "turn-on" detection is that 4-hydroxy-tetramethylpiperidine can be oxidized to TEMPO, which has a different T_1 -weighted imaging. TMV nanoparticles can selectively respond to $O_2^{\bullet-}$ without being affected by H_2O_2 and O_2 ; however, no available data show whether other species of ROS, for example, the more reactive $\bullet OH$, can react with TMV nanoparticles (Dharmawardana et al., 2018). However, a MOF material of the UiO family called Zr-UiO-66-NH-CH₂-Py has been fabricated with a clear selectivity toward $O_2^{\bullet-}$ over other ROS (LOD = 0.21 μ M). Enhancement of the fluorescence response of the MOF upon stepwise addition of $O_2^{\bullet-}$ has been recorded. The mechanism of the fluorescence "turn-on" procedure is recognized as follows: the structural collapse of the MOF in the presence of $O_2^{\bullet-}$ can result in the release of the linker (2-((pyridin-4-ylmethyl)amino)terephthalic acid) with the enhancement of the fluorescence intensity of the system (Das et al., 2019).

DETECTION OF COMBINED SPECIES OF ROS

In some conditions, the evaluation of cellular or system total ROS provides helpful information on cell proliferation, metabolism, and tumor detection. Distinct from the design of nanotechnologies for selective sensing of specific species of ROS, these nanomaterials can detect the combined species of ROS by one platform. Several nanomaterials, including PEGylated bilirubin-coated superparamagnetic iron oxide nanoparticles (PEG-BR@SPIONs) (Lee et al., 2020), UCNPs-MoS₂ nanoflakes (Wang F. et al., 2018), multifunctional theranostic nanoprobe (Au-Ag-HM) (Wang et al., 2021), para-aminothiophenol and hemin-decorated gold (Au-PATP-Hemin) nanoprobe (Cui et al., 2018), cyclotriphosphazene-doped graphene quantum dots (C-GQDs) (Xu et al., 2020), ROS-responsive microgel (Liu et al., 2018), and the ionic nanoparticles in a hydrogel microparticle (Liu et al., 2018), are designed under this context. Therein, PEG-BR@SPIONs and Au-PATP-Hemin nanoprobe are promising tools for "turn-on" detection of ROS with demonstrated mechanisms and have potentialities in biological applications.

PEG-BR@SPIONs as a biosensor with a magnetic relaxation switching-based mechanism have been employed for whole-blood ROS sensing (LOD = 30–50 μ M) (**Figure 2K**). The "turn-on" mechanism is actualized by the change of magnetic relaxation signal upon exposure to ROS. Furthermore, these ROS-responsive PEG-BR@SPIONs are utilized in a sepsis-mimetic clinical setting to directly monitor the total concentration of ROS in the blood samples through an explicit change in T_2 magnetic relaxation signals and a "turn-on" signal of fluorescence. The design of a Au-PATP-Hemin nanoprobe is principled upon the discovery that PATP can react with ROS through a radical oxidative coupling mechanism to form 4,4'-dimercaptoazobenzene (DMAB), which can elicit potent characteristic surface-enhanced Raman scattering (SERS) signals at 1,142, 1,386, and 1,432 cm^{-1} and directly enable the detection of ROS through a hemin-catalyzed Fenton reaction (LOD = 26 pM) (**Figure 2L**). Simultaneous detection of five ROS species ($\bullet OH$, $ROO\bullet$, $O_2^{\bullet-}$, 1O_2 , and H_2O_2) has been realized by the Au-PATP-Hemin nanoprobe. In two typical ROS-elevated mice models of allergic dermatitis and tumors, the Au-PATP-Hemin nanoprobe performed well in monitoring inflammation progression and tumor development in a sensitive and quantitative manner.

CONCLUSION

In this short review, nanomaterials with the ability for ROS "turn-on" detection have been deciphered from the aspects of both nanotechnology and chemical reaction mechanisms. In general, "turn-on" nanotechnologies are powerful tools with a low detection limit, real-time sensing ability, and almost infinite contrast against background. Future studies for the design of ROS "turn-on" detection nanomaterials should make efforts to improve selectivity, detection limit, and biocompatibility. Another consideration is the accessibility of these nanomaterials. Reagents for the nanomaterial fabrication are commercially available or can be prepared in simple synthetic steps from commercially available building blocks, which will be greatly in vogue. Continuous efforts are poised to develop more powerful nanotechnologies in this promising field to shed light on critical information of ROS in biological systems.

AUTHOR CONTRIBUTIONS

RZ, CW, and ZY conceived the conceptualization of the manuscript. All authors contributed to the discussion and composition of the content and helped write the manuscript.

FUNDING

This study was supported by the Shandong Provincial Natural Science Foundation, China (No. ZR2020QC081, HJ), and Youth Innovation Team Talent Introduction Program of Shandong Province (20190164, RZ and HJ).

REFERENCES

- Bai, X., Ng, K. K.-H., Hu, J. J., Ye, S., and Yang, D. (2019). Small-molecule-based Fluorescent Sensors for Selective Detection of Reactive Oxygen Species in Biological Systems. *Annu. Rev. Biochem.* 88, 605–633. doi:10.1146/annurev-biochem-013118-111754
- Bull, S. D., Davidson, M. G., van den Elsen, J. M. H., Fossey, J. S., Jenkins, A. T. A., Jiang, Y.-B., et al. (2013). Exploiting the Reversible Covalent Bonding of Boronic Acids: Recognition, Sensing, and Assembly. *Acc. Chem. Res.* 46, 312–326. doi:10.1021/ar300130w
- Choi, W., Lim, N., Choi, H., Seo, M., Ahn, J., and Jung, J. (2018). Self-assembled Triphenylphosphonium-Conjugated Dicyanostilbene Nanoparticles and Their Fluorescence Probes for Reactive Oxygen Species. *Nanomaterials* 8, 1034. doi:10.3390/nano8121034
- Cui, K., Fan, C., Chen, G., Qiu, Y., Li, M., Lin, M., et al. (2018). Para-aminothiophenol Radical Reaction-Functionalized Gold Nanoprobe for One-To-All Detection of Five Reactive Oxygen Species *In Vivo*. *Anal. Chem.* 90, 12137–12144. doi:10.1021/acs.analchem.8b03116
- Das, A., Anbu, N., Sk, M., Dhakshinamoorthy, A., and Biswas, S. (2019). A Functionalized UiO-66 Mof for Turn-On Fluorescence Sensing of Superoxide in Water and Efficient Catalysis for Knoevenagel Condensation. *Dalton Trans.* 48, 17371–17380. doi:10.1039/c9dt03638e
- Dharmarwardana, M., Martins, A. F., Chen, Z., Palacios, P. M., Nowak, C. M., Welch, R. P., et al. (2018). Nitroxyl Modified Tobacco Mosaic Virus as a Metal-free High-Relaxivity MRI and EPR Active Superoxide Sensor. *Mol. Pharmaceutics* 15, 2973–2983. doi:10.1021/acs.molpharmaceut.8b00262
- Gorini, C., Harris, I. S., and Mak, T. W. (2013). Modulation of Oxidative Stress as an Anticancer Strategy. *Nat. Rev. Drug Discov.* 12, 931–947. doi:10.1038/nrd4002
- He, Y., Zhao, W., Dong, Z., Ji, Y., Li, M., Hao, Y., et al. (2021). A Biodegradable Antibacterial Alginate/carboxymethyl Chitosan/kangfuxin Sponges for Promoting Blood Coagulation and Full-Thickness Wound Healing. *Int. J. Biol. Macromol.* 167, 182–192. doi:10.1016/j.ijbiomac.2020.11.168
- Jenie, S. N. A., Plush, S. E., and Voelcker, N. H. (2017). Singlet Oxygen Detection on a Nanostructured Porous Silicon Thin Film via Photonic Luminescence Enhancements. *Langmuir* 33, 8606–8613. doi:10.1021/acs.langmuir.7b00522
- Jiang, X., Fan, R., Zhou, X., Zhu, K., Sun, T., Zheng, X., et al. (2021). Mixed Functionalization Strategy on Indium-Organic Framework for Multiple Ion Detection and H₂O₂ Turn-On Sensing. *Dalton Trans.* 50, 7554–7562. doi:10.1039/d1dt00889g
- Knoblauch, R., Moskowitz, J., Hawkins, E., and Geddes, C. D. (2020). Fluorophore-induced Plasmonic Current: Generation-Based Detection of Singlet Oxygen. *ACS Sens.* 5, 1223–1229. doi:10.1021/acssensors.0c00377
- Kong, R.-M., Yang, A., Wang, Q., Wang, Y., Ma, L., and Qu, F. (2017). Uricase Based Fluorometric Determination of Uric Acid Based on the Use of Graphene Quantum Dot@silver Core-Shell Nanocomposites. *Microchim. Acta* 185, 63. doi:10.1007/s00604-017-2614-4
- Lan, M., Di, Y., Zhu, X., Ng, T.-W., Xia, J., Liu, W., et al. (2015). A Carbon Dot-Based Fluorescence Turn-On Sensor for Hydrogen Peroxide with a Photo-Induced Electron Transfer Mechanism. *Chem. Commun.* 51, 15574–15577. doi:10.1039/c5cc05835j
- Lee, D. Y., Kang, S., Lee, Y., Kim, J. Y., Yoo, D., Jung, W., et al. (2020). Pegylated Bilirubin-Coated Iron Oxide Nanoparticles as a Biosensor for Magnetic Relaxation Switching-Based Ros Detection in Whole Blood. *Theranostics* 10, 1997–2007. doi:10.7150/thno.39662
- Liang, H., Liu, H., Tian, B., Ma, R., and Wang, Y. (2020). Carbon Quantum Dot@silver Nanocomposite-Based Fluorescent Imaging of Intracellular Superoxide Anion. *Microchim. Acta* 187, 484. doi:10.1007/s00604-020-04359-8
- Liu, Y., Wang, Y.-M., Sedano, S., Jiang, Q., Duan, Y., Shen, W., et al. (2018). Encapsulation of Ionic Nanoparticles Produces Reactive Oxygen Species (Ros)-responsive Microgel Useful for Molecular Detection. *Chem. Commun.* 54, 4329–4332. doi:10.1039/c8cc01432a
- Mattila, H., Khorobrykh, S., Havurinne, V., and Tyystjärvi, E. (2015). Reactive Oxygen Species: Reactions and Detection from Photosynthetic Tissues. *J. Photochem. Photobiol. B: Biol.* 152, 176–214. doi:10.1016/j.jphotobiol.2015.10.001
- Ning, K., Xiang, G., Wang, C., Huang, F., Liu, J., Zhang, L., et al. (2020). 'Turn-on' Fluorescence Sensing of Hydrogen Peroxide in marine Food Samples Using a Carbon Dots-MnO₂ Probe. *Luminescence* 35, 897–902. doi:10.1002/bio.3799
- Shen, C. L., Lou, Q., Zang, J. H., Liu, K. K., Qu, S. N., Dong, L., et al. (2020). Near-Infrared Chemiluminescent Carbon Nanodots and Their Application in Reactive Oxygen Species Bioimaging. *Adv. Sci.* 7, 1903525. doi:10.1002/advs.201903525
- Sk, M., Banesh, S., Trivedi, V., and Biswas, S. (2018). Selective and Sensitive Sensing of Hydrogen Peroxide by a Boronic Acid Functionalized Metal-Organic Framework and its Application in Live-Cell Imaging. *Inorg. Chem.* 57, 14574–14581. doi:10.1021/acs.inorgchem.8b02240
- Tan, S. Y., Teh, C., Ang, C. Y., Li, M., Li, P., Korzh, V., et al. (2017). Responsive Mesoporous Silica Nanoparticles for Sensing of Hydrogen Peroxide and Simultaneous Treatment toward Heart Failure. *Nanoscale* 9, 2253–2261. doi:10.1039/c6nr08869d
- Valko, M., Leibfritz, D., Moncol, J., Cronin, M. T. D., Mazur, M., and Telser, J. (2007). Free Radicals and Antioxidants in normal Physiological Functions and Human Disease. *Int. J. Biochem. Cel Biol.* 39, 44–84. doi:10.1016/j.biocel.2006.07.001
- Walekar, L. S., Hu, P., Liao, F., Guo, X., and Long, M. (2017). Turn-on Fluorometric and Colorimetric Probe for Hydrogen Peroxide Based on the *In-Situ* Formation of Silver Ions from a Composite Made from N-Doped Carbon Quantum Dots and Silver Nanoparticles. *Microchim. Acta* 185, 31. doi:10.1007/s00604-017-2545-0
- Wang, F., Qu, X., Liu, D., Ding, C., Zhang, C., and Xian, Y. (2018a). Upconversion Nanoparticles-Mos2 Nanoassembly as a Fluorescent Turn-On Probe for Bioimaging of Reactive Oxygen Species in Living Cells and Zebrafish. *Sens. Actuators B: Chem.* 274, 180–187. doi:10.1016/j.snb.2018.07.125
- Wang, H., Zhou, C., Sun, X., Jian, Y., Kong, Q., Cui, K., et al. (2018b). Polyhedral-AuPd Nanoparticles-Based Dual-Mode Cytosensor with Turn on Enable Signal for Highly Sensitive Cell Evaluation on Lab-On-Paper Device. *Biosens. Bioelectron.* 117, 651–658. doi:10.1016/j.bios.2018.07.004
- Wang, K., Zhang, F., Wei, Y., Wei, W., Jiang, L., Liu, Z., et al. (2021). *In Situ* imaging of Cellular Reactive Oxygen Species and Caspase-3 Activity Using a Multifunctional Theranostic Probe for Cancer Diagnosis and Therapy. *Anal. Chem.* 93, 7870–7878. doi:10.1021/acs.analchem.1c00385
- Wang, K., Ma, W., Xu, Y., Liu, X., Chen, G., Yu, M., et al. (2020). Design of a Novel Mitochondria Targetable Turn-On Fluorescence Probe for Hydrogen Peroxide and its Two-Photon Bioimaging Applications. *Chin. Chem. Lett.* 31, 3149–3152. doi:10.1016/j.ccl.2020.08.039
- Winyard, P. G., Ryan, B., Eggleton, P., Nissim, A., Taylor, E., Lo Faro, M. L., et al. (2011). Measurement and Meaning of Markers of Reactive Species of Oxygen, Nitrogen and Sulfur in Healthy Human Subjects and Patients with Inflammatory Joint Disease. *Biochem. Soc. Trans.* 39, 1226–1232. doi:10.1042/bst0391226
- Wu, G., Zeng, F., Yu, C., Wu, S., and Li, W. (2014). A Ratiometric Fluorescent Nanoprobe for H₂O₂sensing and *In Vivo* Detection of Drug-Induced Oxidative Damage to the Digestive System. *J. Mater. Chem. B* 2, 8528–8537. doi:10.1039/c4tb01432d
- Wu, S., Kong, X.-J., Cen, Y., Yuan, J., Yu, R.-Q., and Chu, X. (2016). Fabrication of a LRET-Based Upconverting Hybrid Nanocomposite for Turn-On Sensing of H₂O₂and Glucose. *Nanoscale* 8, 8939–8946. doi:10.1039/c6nr00470a
- Wu, L., Sedgwick, A. C., Sun, X., Bull, S. D., He, X.-P., and James, T. D. (2019). Reaction-based Fluorescent Probes for the Detection and Imaging of Reactive Oxygen, Nitrogen, and Sulfur Species. *Acc. Chem. Res.* 52, 2582–2597. doi:10.1021/acs.accounts.9b00302
- Xu, A., He, P., Ye, C., Liu, Z., Gu, B., Gao, B., et al. (2020). Polarizing Graphene Quantum Dots toward Long-Acting Intracellular Reactive Oxygen Species Evaluation and Tumor Detection. *ACS Appl. Mater. Inter.* 12, 10781–10790. doi:10.1021/acsami.9b20434
- Yang, B., Chen, Y., and Shi, J. (2019). Reactive Oxygen Species (Ros)-Based Nanomedicine. *Chem. Rev.* 119, 4881–4985. doi:10.1021/acs.chemrev.8b00626
- Yang, L., Pijuan-Galito, S., Rho, H. S., Vasilevich, A. S., Eren, A. D., Ge, L., et al. (2021). High-throughput Methods in the Discovery and Study of Biomaterials and Microbiology. *Chem. Rev.* 121, 4561–4677. doi:10.1021/acs.chemrev.0c00752

- Yin, X., Hao, Y., Lu, Y., Zhang, D., Zhao, Y., Mei, L., et al. (2021). Bio-Multifunctional Hydrogel Patches for Repairing Full-Thickness Abdominal wall Defect. *Adv. Funct. Mater.* 31, 2105614. doi:10.1002/adfm.202105614
- Yu, Z., Li, Q., Wang, J., Yu, Y., Wang, Y., Zhou, Q., et al. (2020). Reactive Oxygen Species-Related Nanoparticle Toxicity in the Biomedical Field. *Nanoscale Res. Lett.* 15, 115. doi:10.1186/s11671-020-03344-7
- Yuan, J., Cen, Y., Kong, X.-J., Wu, S., Liu, C.-L., Yu, R.-Q., et al. (2015). MnO₂-nanosheet-modified Upconversion Nanosystem for Sensitive Turn-On Fluorescence Detection of H₂O₂ and Glucose in Blood. *ACS Appl. Mater. Inter.* 7, 10548–10555. doi:10.1021/acsami.5b02188
- Yue, J., Peng, J., Yu, L., Sun, M., Sun, Z., Tan, H., et al. (2021). Superoxide Anion Turns on the Fluorescence of Carbon Dots-Ferric Complex for Sensing. *Microchemical J.* 168, 106412. doi:10.1016/j.microc.2021.106412
- Zhang, C., Liu, X., Xu, Z., and Liu, D. (2020). Multichannel Stimulus-Responsive Nanoprobes for H₂O₂ Sensing in Diverse Biological Milieus. *Anal. Chem.* 92, 12639–12646. doi:10.1021/acs.analchem.0c02769
- Zhang, W., Chen, L., Xiong, Y., Panayi, A. C., Abududilibaier, A., Hu, Y., et al. (2021). Antioxidant Therapy and Antioxidant-Related Bionanomaterials in Diabetic Wound Healing. *Front. Bioeng. Biotechnol.* 9, 707479. doi:10.3389/fbioe.2021.707479
- Zhao, Y., Liu, H., Jiang, Y., Song, S., Zhao, Y., Zhang, C., et al. (2018). Detection of Various Biomarkers and Enzymes via a Nanocluster-Based Fluorescence Turn-On Sensing Platform. *Anal. Chem.* 90, 14578–14585. doi:10.1021/acs.analchem.8b04691
- Zheng, W., Zhou, Q., and Yuan, C. (2021). Nanoparticles for Oral Cancer Diagnosis and Therapy. *Bioinorg Chem. Appl.* 2021, 9977131. doi:10.1155/2021/9977131
- Zhou, W., Cao, Y., Sui, D., and Lu, C. (2016a). Turn-on Luminescent Probes for the Real-Time Monitoring of Endogenous Hydroxyl Radicals in Living Cells. *Angew. Chem. Int. Ed.* 55, 4236–4241. doi:10.1002/anie.201511868
- Zhou, Z., Song, J., Nie, L., and Chen, X. (2016b). Reactive Oxygen Species Generating Systems Meeting Challenges of Photodynamic Cancer Therapy. *Chem. Soc. Rev.* 45, 6597–6626. doi:10.1039/c6cs00271d

Conflict of Interest: The authors declare that the research was conducted in the absence of any commercial or financial relationships that could be construed as a potential conflict of interest.

Publisher's Note: All claims expressed in this article are solely those of the authors and do not necessarily represent those of their affiliated organizations, or those of the publisher, the editors and the reviewers. Any product that may be evaluated in this article, or claim that may be made by its manufacturer, is not guaranteed or endorsed by the publisher.

Copyright © 2021 Jiang, Lin, Yu, Wang and Zhang. This is an open-access article distributed under the terms of the Creative Commons Attribution License (CC BY). The use, distribution or reproduction in other forums is permitted, provided the original author(s) and the copyright owner(s) are credited and that the original publication in this journal is cited, in accordance with accepted academic practice. No use, distribution or reproduction is permitted which does not comply with these terms.



Nanomedicine for the Diagnosis and Therapy of COVID-19

Yingruo Wang¹, Yuanping Hao², Shunxin Fa^{3,4}, Weiping Zheng^{5,3}, Changqing Yuan^{5,3*} and Wanchun Wang^{2*}

¹Shandong University of Science and Technology, Qingdao, China, ²Qingdao Stomatological Hospital Affiliated to Qingdao University, Qingdao, China, ³School of Stomatology, Qingdao University, Qingdao, China, ⁴York School, Monterey, CA, United States, ⁵Department of Stomatology, The Affiliated Hospital of Qingdao University, Qingdao, China

OPEN ACCESS

Edited by:

Yong Liu,
University of Chinese Academy of
Sciences, China

Reviewed by:

Linzhu Su,
Nankai University, China
Chunxiang Zheng,
Sun Yat-sen University, China

*Correspondence:

Wanchun Wang
kqwwch@126.com
Changqing Yuan
ycq613@163.com

Specialty section:

This article was submitted to
Biomaterials,
a section of the journal
Frontiers in Bioengineering and
Biotechnology

Received: 13 August 2021

Accepted: 03 September 2021

Published: 04 November 2021

Citation:

Wang Y, Hao Y, Fa S, Zheng W,
Yuan C and Wang W (2021)
Nanomedicine for the Diagnosis and
Therapy of COVID-19.
Front. Bioeng. Biotechnol. 9:758121.
doi: 10.3389/fbioe.2021.758121

The coronavirus disease-2019 (COVID-19) pandemics caused by the severe acute respiratory syndrome coronavirus 2 (SARS-CoV-2) has been spreading around the world due to its high infection rate, long incubation period, as well as lack of effective diagnosis and therapy or vaccines, which is tearing global health systems apart. It is an urgent demand for point-of-care diagnosis and effective treatment to prevent the spread of COVID-19. Currently, based on the rapid development of functional materials with unique physicochemical features through advanced fabrication and chemical modification, nanomaterials provide an emerging tool to detect SARS-CoV-2, inhibit the interplay in the virus and host cell interface, and enhance host immune response. In our manuscript, we summarized recent advances of nanomaterials for the diagnosis and therapy of COVID-19. The limitation, current challenges, and perspectives for the nano-diagnosis and nano-therapy of COVID-19 are proposed. The review is expected to enable researchers to understand the effect of nanomaterials for the diagnosis and therapy of COVID-19 and may catalyze breakthroughs in this area.

Keywords: nanomaterials, COVID-19, SARS-CoV-2, theranostic nanomedicine, advanced materials

INTRODUCTION

The coronavirus infectious disease 2019 (COVID-19) was caused by the severe acute respiratory syndrome coronavirus 2 (SARS-CoV-2) with the magnificent nanostructure (**Figure 1**) (Shin et al., 2020; Weiss et al., 2020; Chang et al., 2020a; Kostarelos, 2020a). Since its first discovery in December 2019 in the Wuhan city of China, it has already infected millions of people worldwide and resulted in hundreds of thousands of deaths due to its high infection rate, long incubation period, as well as lack of effective and practical diagnosis and therapy or vaccines, which is tearing global health systems apart (Lai et al., 2020; Dima et al., 2020). The primary symptoms of SARS-CoV-2 infected patients include fever, dry cough, fatigue, and difficulty in breathing or maybe silent carriers (Cui et al., 2019; Chang et al., 2020b). In addition, SARS-CoV-2 has four major structural proteins, i.e., spike (S) protein, nucleocapsid (N) protein, envelope (E) protein, and membrane (M) protein (**Figure 2**) (Schoeman and Fielding, 2019; Phan, 2020; Wang et al., 2020). Particularly, the S protein plays a critical role in affecting cells, because it facilitates SARS-CoV-2 to determine the angiotensin-converting enzyme 2 (ACE2) and thereby invade into the host cell (**Figure 2**) (Gheblawi et al., 2020; Wang et al., 2020; Xia et al., 2020; Yan et al., 2020). Increasing evidence reveals that some patients with COVID-19 show severe organ damage, e.g., heart, liver, kidney, lung, the central nervous system, etc. (Batlle et al., 2020; Li et al., 2020; Zaim et al., 2020).

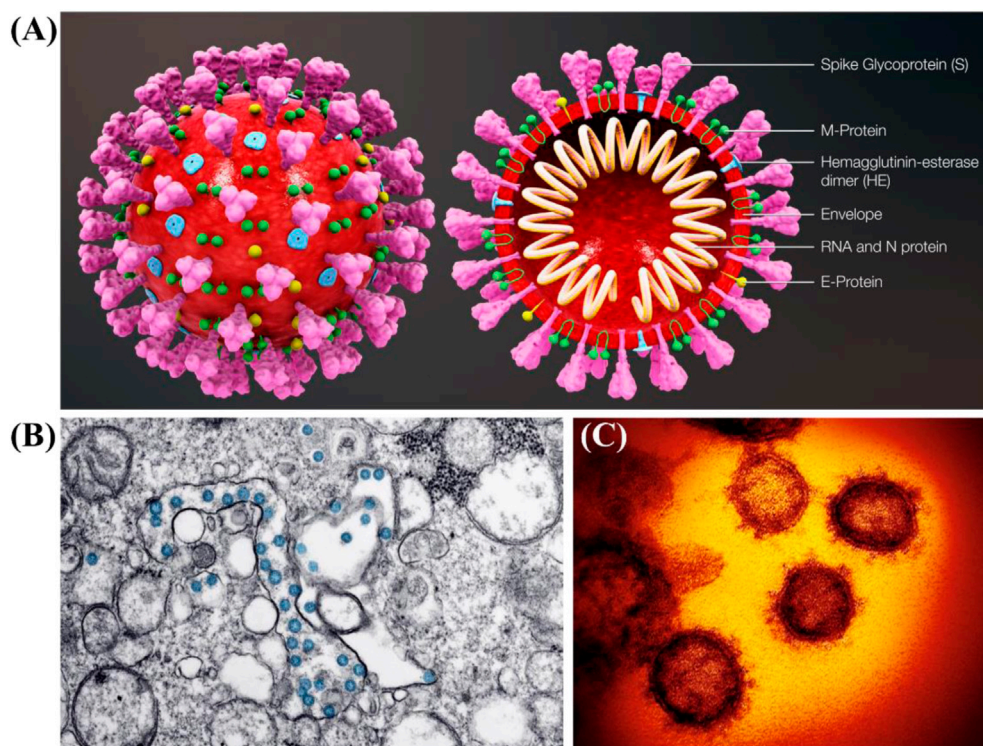


FIGURE 1 | (A) Schematic diagram of SARS-CoV-2 and its cross-sectional representation with proteins (Scientific Animations, 2020). **(B)** Transmission electron microscope image of SARS-CoV-2 (CDC, 2020). **(C)** False colored images of SARS-CoV-2 (Kostarelos, 2020a).

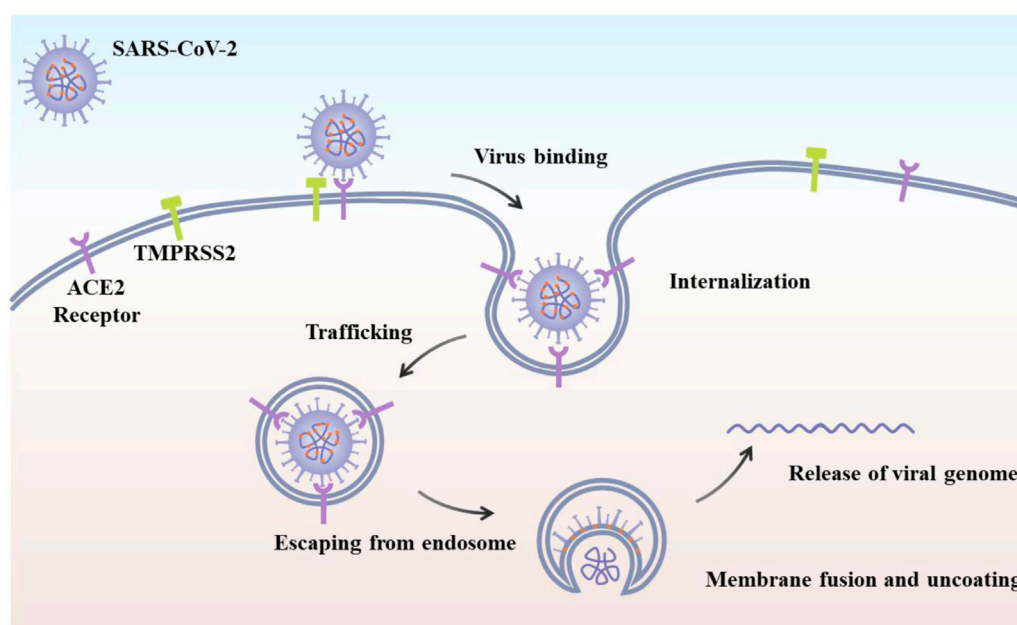


FIGURE 2 | Schematic of SARS-CoV-2 viral life cycle. The initial attachment of SARS-CoV-2 to cells involves specific binding between the viral S glycoprotein and the cellular receptor, ACE2 (Yang et al., 2020).

Its genome sequencing analysis indicates that SARS-CoV-2 has a single-stranded RNA genome (19 sequences), which is very similar to CoV, particularly β -CoVs (Guo et al., 2020; Neogi et al., 2020; Palestino et al., 2020). The availability of SARS-CoV-2 genome sequence is conducive to develop PCR kits to diagnose SARS-CoV-2 infected patients by the real-time reverse transcription-polymerase chain reaction (RT-PCR) (Ravi et al., 2020). Although the RT-PCR strategy is highly sensitive based in the detection of RNA, there are several defects as follows: 1) high cost and time-consuming (2–5 h), 2) sophisticated devices and complicated operation by highly skilled staff, 3) false-negative and false-positive results, and 4) a laboratory with biosafety level 2 or above (Nguyen et al., 2019; Palestino et al., 2020). Further, alternative techniques based on anti-bodies (serological testing) and Clustered Regularly Interspaced Short Palindromic Repeats (CRISPR) have been employed for the diagnosis of the SARS-CoV-2 infection. Chest computed tomography (CT) is also the optional imaging strategy for the detection of COVID-19 (Ye et al., 2020).

This inefficient strategy is exceptionally adverse for COVID-19 emergencies. Abbott designed a kit that achieved a 5-min rapid detection dependent on isothermal amplification of nucleic acid by testing the RNA-dependent RNA polymerase (RdRP) of COVID-19 (Carter et al., 2020). However, test kits developed (e.g., isothermal amplification tests, serological tests, etc.) also have some limitations, especially low accuracy (Lee et al., 2015). Developing rapid point-of-care and reliable diagnostic strategies is highly valuable in community clinics and emergency rooms and further prevents the spread of the SARS-CoV-2.

In addition, for the therapy of COVID-19, researchers are testing various drug formulations to treat SARS-CoV-2 infected patients (Cortegiani et al., 2020; Yang et al., 2020). Although the HIV drug and traditional Chinese medicine (TCM) had a positive effect on the treatment of COVID-19 (Luo et al., 2020; Ren et al., 2020), they still cannot cure COVID-19. Unfortunately, there are no vaccines or therapeutics available approved by the United States Food and Drug Administration (FDA) agency for treating patients with COVID-19. The research and development cycle of vaccines generally requires years before they can be used widely due to the regulatory steps required to ensure their safety and efficacy.

It has been demonstrated that nanomaterials offer an emerging platform for the point-of-care diagnosis carriers for therapeutics, and vaccine development owing to their low toxicity, unique size, tunable charge, chemical modification capabilities, and so on (Adhikari et al., 2020; Chauhan et al., 2020; Mainardes and Diedrich, 2020; Manivannan and Ponnuchamy, 2020; Palestino et al., 2020; Shin et al., 2020; Weiss et al., 2020). For the nano-diagnosis, nanomaterials can bind with target molecules to form a measurable signal, allowing the detection and identification of the virus (Bidram et al., 2021; Rashidzadeh et al., 2021; Vahedifard and Chakravarthy, 2021). The strategy is easy to operate and marketable, possesses stable, accurate, and highly sensitive features, as well as does not require specialized instrumentation. For the therapy, lipid nanoparticles containing mRNA vaccines have already reached Phase II clinical trials (Shin et al., 2020). In this review, we overviewed recent

advances of nanomaterials for the diagnosis and therapy of COVID-19. The current challenges and perspectives for the nano-diagnosis and nano-therapy of COVID-19 are proposed. The review is expected to enable researchers to understand the effect of nanomaterials for the diagnosis and therapy of COVID-19 and may catalyze breakthroughs in this area.

NANOMATERIALS FOR THE DIAGNOSIS OF COVID-19

As mentioned, there are no vaccines or therapeutics available approved by the FDA for treating patients with COVID-19. Thus, rapid point-of-care nano-diagnosis of COVID-19 plays a key role in detecting COVID-19 patients to prevent further infection of the SARS-CoV-2 (Nguyen et al., 2019; Chan, 2020; Chauhan et al., 2020; Sharma et al., 2021). The tunable physicochemical properties of nanomaterials, such as size, shape, charge, and chemical functions (Cheng et al., 2013; Zhu et al., 2013; Liu et al., 2017), make them very useful in the diagnosis of COVID-19.

Previously, it was well-demonstrated that magnetic nanoparticles (MNPs) were valuable as nano-sensors (Mishra et al., 2018). Zhao *et al.* prepared carboxyl polymer-coated MNPs to combine the virus lysis and RNA binding steps into a single step (Zhao et al., 2020). This system can extract viral RNA from several samples within 20 min and 10-copy sensitivity. This method offers a simplified RNA extraction protocol to address the labor-intensive and time-consuming viral RNA extraction steps, and thus shows a promising alternative in the high-throughput molecular diagnosis of SARS-CoV-2. Taking into account the advantages mentioned above, another multifunctional nano-magnetic particle was designed and prepared to be used in RT-PCR for 2019-nCoV viral RNA extraction. Zinc ferrite NPs were prepared using the combustion synthesis method followed by modification with silica and carboxyl-functionalized polyvinyl alcohol (Somvanshi et al., 2020). The simple and cost-effective nature of this strategy may offer a capable substitute for traditional techniques to tackle the tedious time taking procedures and therefore demonstrates the ability of this method in detection of COVID-19.

Recently, the dual-functional plasmonic biosensor is used for the diagnosis of nucleic acid from COVID-19 (Qiu et al., 2020). This system includes the sensing transduction of localized surface plasmon resonance (ISPR) and the effect of the plasmonic photothermal (PPT). One plasmonic chip, which consists of Au-S bonding between thiol-cDNA receptor of RNA-dependent RNA polymerase (RdRp) and two-dimensional gold nanoislands (AuNIs), polyprotein ORF1ab, or the E gene sequence, can develop fast and delicate recognition of nucleic acids by enhancing the hybridization kinetics of matching strands.

To detect and monitor the progression of COVID-19, Chen and co-workers reported a rapid point-of-care lateral flow immunoassay based on lanthanide-doped polystyrene nanoparticles to identify anti-SARV-CoV-2 IgG in human

serum in 10 min (Chen et al., 2020). Importantly, it was found that the outcome satisfies the demand for clinical diagnostic kits. Also, the strategy could be used to monitor the progression of COVID-19 and evaluating the response of SARS-CoV-2 infected patients to treatment.

Further, to avoid interference from other viruses, Moitra and co-workers developed gold nanomaterials combined with the antisense oligonucleotides specific for N-gene of SARS-CoV-2 viral genome to selectively detect positive COVID-19 patients within 10 min by a colorimetric assay (Moitra et al., 2020). Also, the anti-interference performance of the biosensor above was demonstrated that no significant change in absorbance was detected with the Middle East respiratory syndrome (MERS)-CoV RNA. This work describes an accurate, highly sensitive, and naked-eye detection of SARS-CoV-2 without the requirement of any special laboratory facilities.

NANOMATERIALS FOR THE THERAPY OF COVID-19

Nanomaterials provided a powerful platform to neutralize different viral infections, such as SARS or MERS coronaviruses (Abd Ellah et al., 2020; Barar, 2020; Bonam et al., 2020; Shapiro, 2021; Varahachalam et al., 2021). Thus, the use of nanomaterials displays great potential in developing novel therapeutic strategies for the therapy of COVID-19.

As mentioned in the introduction, the S protein of SARS-CoV-2 plays a critical role in its infection mechanism, which is similar to MERS-CoV. Based on the interaction between S protein and ACE2 on the host cell membrane, already existing antiviral nanomaterials can be used to treat COVID-19. For instance, the effective heptad repeat 1 (HR1) peptide inhibitor that is Pregnancy Induced Hypertension (PIH), can interrupt HR1/HR2-mediated membrane fusion between MERS-CoV and host cells. Huang and co-workers demonstrated that PIH released from Au nanomaterials possessed significant enhanced viral inhibitory ability than free PIH (Itani et al., 2020). Furthermore, this PIH/Au nanomaterial display high stability with potential applications for similar coronaviruses. In addition to kill the virus inside the body, nanomaterials can prevent the virus entry into the cells. Also, Łoczechin *et al.* developed boronic acid ligands conjugated with carbon quantum dots (CQDs) to inhibit the interaction between protein S-receptor and host cell membrane, inhibiting the virus entry into the host cells (Łoczechin et al., 2019). Recently, inhaled silver nanoparticles (Ag NPs) were used as a first-line approach for the treatment and prevention of COVID-19 infection progression (Sarkar, 2020; Zachar, 2020). The antiviral effect of Ag NPs may be attributed to the attachment of Ag NPs to RNA virus surface glycoproteins, stopping the virus from integrating into host cells.

Copper is known for its antimicrobial and antiviral activity since ancient times, and more lately, the Cu effectiveness to deactivate coronaviruses recommends possible alike effectiveness towards SARS-CoV-2. The deactivation mechanism is due to damage of viral proteins and lipids (Doremalen, 2020).

Also, increasing evidence demonstrated that nanomaterials served as potential tools for immune modulation to activate the immune response against a pathogen. For example, graphene oxide modified with amino groups mediated the signal path of STAT1/IRF1 interferon in T cells, inducing the expression of T cell chemoattractants (Orecchioni et al., 2017).

As reported, SARS-CoV-2 has a size of approximately 125 nm and be considered as natural nanomaterials (Kostarelos, 2020b). Nanomaterials that mimic the intrinsic immunostimulatory characteristics of viruses, enable the design of next-generation vaccine development. A messenger RNA (mRNA)-lipid nanoparticle vaccine has been tested to fight with SARS-CoV and MERS (Garber, 2018; Jackson et al., 2020). Particularly, McKay *et al.* developed a self-amplifying RNA encoding the SARS-CoV-2 S protein loaded in a lipid nanoparticle as a vaccine to stimulate high neutralizing antibody titers in mice. Their work offers new insight into the development of vaccines and the evaluation of immunogenicity to accelerate the translation of nanomaterial-based vaccines from the bench to the clinic (McKay et al., 2020).

LIMITATION

Although nanomaterials have shown great potential in the diagnosis and therapy of COVID-19, studies have demonstrated that nanomaterials have the actual risk to cause detrimental actions to human health (i.e., nanotoxicology) (Singh et al., 2019; Miller and PolandNanotoxicology, 2020; Yu et al., 2020). One of the most frequently nanomaterial-related toxicities is oxidative stress responses caused by reactive oxygen species (ROS) generation, which can further induce pathophysiological effects, e.g., genotoxicity, inflammation, and fibrosis, etc. (Kim et al., 2015; Lujan and Sayes, 2017). The interactions between nanomaterial interface and cell, mediated by ROS, can damage the cell membrane, denature protein, as well as result in lipid peroxidation and alteration of calcium homeostasis, causing mitochondrial damage, immune cell activation, and nicotinamide adenine dinucleotide phosphate (NADPH) oxidase system (Fu et al., 2014; Lujan and Sayes, 2017; Yang et al., 2019; Yu et al., 2020). Most of nanomaterial intrinsic characterizations can catalyze ROS generation (Yang et al., 2019). Also, the physicochemical features of nanomaterials, e.g., morphology, size, charge, and component, affect the production of ROS and nanomaterial-induced damage (Yang et al., 2019; Yu et al., 2020). In addition to ROS, nanomaterials also result in reactive nitrogen species-mediated damage (Manke et al., 2013; Ferreira et al., 2018). Therefore, in terms of nanotherapeutics for COVID-19, a rigorous regulatory approval process must be performed to ensure safety and efficacy.

CONCLUSION AND OUTLOOK

So far, no FDA-approved drugs are available for combating COVID-19, and particularly vaccines are under clinical trials. Increasing evidence indicates that nanomaterials could offer new

insights to develop novel delivery systems or kill viruses directly. Also, nanomaterials can be used to detect virus-infected patients. In our manuscript, we summarized the recent progress of nanomaterials for the diagnosis and therapy of COVID-19. The inherent chemico-physical properties of nanomaterials, e.g., low toxicity, ultra-small dimension, high specific surface area, chemical modification capabilities, and high reactivity, play a critical role in point-of-care diagnosis and intriguing nanosystems for COVID-19 treatment. With the rapid development of engineered nanomaterials for advanced diagnosis and therapy, it is expected that nanomedicine would have a great impact on the in-depth of COVID-19 in the near future.

However, to accelerate the translation of nanomaterial-based outcomes from the bench to the clinic, more studies are needed to be performed. First, an extensive body of work is required to elicit the underlying mechanisms of the interactions between nanomaterial interface and SARS-CoV-2, tracing a reasonable design of COVID-19 therapeutics. Second, to improve the efficiency of COVID-19 therapeutics *in vitro* and *in vivo*, high-throughput strategies are expected to be designed. This strategy has many advantages, e.g., cost and time-efficiency, combining multi-parameter on a single system, and

minimizing methodological or systematic errors. The big data from high-throughput strategies would provide a better understanding of the interplay between nanomaterial features and SARS-CoV-2. Finally, advanced technologies (e.g., artificial intelligence and other computation tools) could greatly shorten the lengthy process of high-performance nanomaterial discovery against SARS-CoV-2.

AUTHOR CONTRIBUTIONS

YW, CY, and WW contributed to the conception. WZ prepared the figures. YW, YH, and SF wrote the first draft of the manuscript. WW and CY revised the manuscript. All authors read and approved the submitted version.

ACKNOWLEDGMENTS

The authors are very thankful for financial support by Qingdao Key Health Discipline Development Fund. The authors are very grateful for the discussion of Hongzhao Qi.

REFERENCES

- Abd Ellah, N. H., Gad, S. F., Muhammad, K., E Batiha, G., and Hetta, H. F. (2020). Nanomedicine as a promising approach for diagnosis, treatment and prophylaxis against COVID-19. *Nanomedicine* 15, 2085–2102. doi:10.2217/nnm-2020-0247
- Adhikari, S., Adhikari, U., Mishra, A., and Guragain, B. S. (2020). Nanomaterials for diagnostic, treatment and prevention of COVID-19. *Appl. Sci. Technol. Ann.* 1, 155–164. doi:10.3126/asta.v1i1.30295
- Barar, J. (2020). COVID-19 clinical implications: the significance of nanomedicine. *BioImpacts BI* 10, 137. doi:10.34172/bi.2020.16
- Battle, D., Soler, M. J., Sparks, M. A., Hiremath, S., South, A. M., Welling, P. A., et al. (2020). Acute Kidney Injury in COVID-19: Emerging Evidence of a Distinct Pathophysiology. *J. Am. Soc. Nephrol.* 31, 1380, 2020. LP – 1383. doi:10.1681/ASN.2020040419
- Bidram, E., Esmaeili, Y., Amini, A., Sartorius, R., Tay, F. R., Shariati, L., et al. (2021). Nanobased Platforms for Diagnosis and Treatment of COVID-19: From Benchtop to Bedside. *ACS Biomater. Sci. Eng.* 7 (6), 2150–2176. doi:10.1021/acsbomaterials.1c00318
- Bonam, S. R., Kotla, N. G., Bohara, R. A., Rochev, Y., Webster, T. J., and Bayry, J. (2020). Potential immuno-nanomedicine strategies to fight COVID-19 like pulmonary infections. *Nano Today*, 101051. doi:10.1016/j.nantod.2020.101051
- Carter, L. J., Garner, L. V., Smoot, J. W., Li, Y., Zhou, Q., Saveson, C. J., et al. Assay techniques and test development for COVID-19 diagnosis 2020. *ACS Cent. Sci.* 6 (5), 591–605. doi:10.1021/acscentsci.0c00501
- CDC (2020). Details. <https://phil.cdc.gov/Details.aspx?pid=23354> (accessed December 4, 2020).
- Chan, W. C. W. (2020). Nano Research for COVID-19. *ACS Nano* 14 (4), 3719–3720. doi:10.1021/acsnano.0c02540
- Chang, M. C., Baek, J. H., and Park, D. (2020). Lessons from South Korea Regarding the Early Stage of the COVID-19 Outbreak. *Healthcare (Basel)* 8. doi:10.3390/healthcare8030229
- Chang, M. C., Hur, J., and Park, D. (2020). Strategies for the Prevention of the Intra-Hospital Transmission of COVID-19: A Retrospective Cohort Study. *Healthcare (Basel)* 8. doi:10.3390/healthcare8030195
- Chauhan, G., Madou, M. J., Kalra, S., Chopra, V., Ghosh, D., and Martinez-Chapa, S. O. (2020). Nanotechnology for COVID-19: Therapeutics and Vaccine Research. *ACS Nano* 14 (7), 7760–7782. doi:10.1021/acsnano.0c04006
- Chen, Z., Zhang, Z., Zhai, X., Li, Y., Lin, L., Zhao, H., et al. (2020). Rapid and Sensitive Detection of anti-SARS-CoV-2 IgG, Using Lanthanide-Doped Nanoparticles-Based Lateral Flow Immunoassay. *Anal. Chem.* 92, 7226–7231. doi:10.1021/acs.analchem.0c00784
- Cheng, L.-C., Jiang, X., Wang, J., Chen, C., and Liu, R.-S. (2013). Nano-bio effects: interaction of nanomaterials with cells. *Nanoscale* 5, 3547–3569. doi:10.1039/C3NR34276J
- Cortegiani, A., Ingoglia, G., Ippolito, M., Giarratano, A., and Einav, S. (2020). A systematic review on the efficacy and safety of chloroquine for the treatment of COVID-19. *J. Crit. Care* 57, 279–283. doi:10.1016/j.jcrc.2020.03.005
- Cui, J., Li, F., and Shi, Z.-L. (2019). Origin and evolution of pathogenic coronaviruses. *Nat. Rev. Microbiol.* 17, 181–192. doi:10.1038/s41579-018-0118-9
- Dima, A., Balaban, D. V., Jurcut, C., Berza, I., Jurcut, R., and Jinga, M. (2020). Physicians' Perspectives on COVID-19: An International Survey. *Healthcare (Basel)* 8. doi:10.3390/healthcare8030250
- Doremalen, V. (2020). c o r r e s p o n d e n c e Aerosol and Surface Stability of SARS-CoV-2 as Compared with SARS-CoV-1. *Nejm*, 0–2.
- Ferreira, C. A., Ni, D., Rosenkrans, Z. T., and Cai, W. (2018). Scavenging of reactive oxygen and nitrogen species with nanomaterials. *Nano Res.* 11, 4955–4984. doi:10.1007/s12274-018-2092-y
- Fu, P. P., Xia, Q., Hwang, H.-M., Ray, P. C., and Yu, H. (2014). Mechanisms of nanotoxicity: Generation of reactive oxygen species. *J. Food Drug Anal.* 22, 64–75. doi:10.1016/j.jfda.2014.01.005
- Garber, K. (2018). Alnylam launches era of RNAi drugs. *Nat. Biotechnol.* 36, 777–778. doi:10.1038/nbt0918-777
- Gheblawi, M., Wang, K., Viveiros, A., Nguyen, Q., Zhong, J.-C., Turner, A. J., et al. (2020). Angiotensin-Converting Enzyme 2: SARS-CoV-2 Receptor and Regulator of the Renin-Angiotensin System. *Circ. Res.* 126, 1456–1474. doi:10.1161/CIRCRESAHA.120.317015
- Guo, Y.-R., Cao, Q.-D., Hong, Z.-S., Tan, Y.-Y., Chen, S.-D., Jin, H.-J., et al. (2020). The origin, transmission and clinical therapies on coronavirus disease 2019 (COVID-19) outbreak – an update on the status. *Mil. Med. Res.* 7, 11. doi:10.1186/s40779-020-00240-0
- Itani, R., Tobaiqi, M., and Al Faraj, A. (2020). Optimizing use of theranostic nanoparticles as a life-saving strategy for treating COVID-19 patients. *Theranostics* 10, 5932–5942. doi:10.7150/thno.46691
- Jackson, L. A., Anderson, E. J., Roupael, N. G., Roberts, P. C., Makhene, M., Coler, R. N., et al. (2020). An mRNA Vaccine against SARS-CoV-2 — Preliminary Report. *N. Engl. J. Med.* 383 (20), 1920–1931. doi:10.1056/NEJMoa2022483

- Kim, K. S., Lee, D., Song, C. G., and Kang, P. M. (2015). Reactive oxygen species-activated nanomaterials as theranostic agents. *Nanomedicine* 10, 2709–2723. doi:10.2217/nnm.15.108
- Kostarelos, K. (2020). Nanoscale nights of COVID-19. *Nat. Nanotechnol.* 15, 343–344. doi:10.1038/s41565-020-0687-4
- Kostarelos, K. (2020). Nanoscale nights of COVID-19. *Nat. Nanotechnol.* 15, 343–344. doi:10.1038/s41565-020-0687-4
- Lai, C.-C., Shih, T.-P., Ko, W.-C., Tang, H.-J., and Hsueh, P.-R. (2020). Severe acute respiratory syndrome coronavirus 2 (SARS-CoV-2) and coronavirus disease-2019 (COVID-19): The epidemic and the challenges. *Int. J. Antimicrob. Agents* 55, 105924. doi:10.1016/j.ijantimicag.2020.105924
- Lee, H. Y., Jeong, H., Jung, I. Y., Jang, B., Seo, Y. C., Lee, H., et al. (2015). DhTACT: DNA Hydrogel Formation by Isothermal Amplification of Complementary Target in Fluidic Channels. *Adv. Mater.* 27, 3513–3517. doi:10.1002/adma.201500414
- Li, X., Wang, L., Yan, S., Yang, F., Xiang, L., Zhu, J., et al. (2020). Clinical characteristics of 25 death cases with COVID-19: A retrospective review of medical records in a single medical center, Wuhan, China. *Int. J. Infect. Dis.* 94, 128–132. doi:10.1016/j.ijid.2020.03.053
- Liu, Y., Workalemahu, B., and Jiang, X. (2017). The Effects of Physicochemical Properties of Nanomaterials on Their Cellular Uptake *In Vitro* and *In Vivo*. *Small* 13, 1701815. doi:10.1002/smll.201701815
- Lujan, H., and Sayes, C. M. (2017). Cytotoxicological pathways induced after nanoparticle exposure: studies of oxidative stress at the ‘nano-bio’ interface. *Toxicol. Res. (Camb)* 6, 580–594. doi:10.1039/c7tx00119c
- Luo, H., Tang, Q., Shang, Y., Liang, S., Yang, M., Robinson, N., et al. (2020). Can Chinese Medicine Be Used for Prevention of Corona Virus Disease 2019 (COVID-19)? A Review of Historical Classics, Research Evidence and Current Prevention Programs. *Chin. J. Integr. Med.* 26, 243–250. doi:10.1007/s11655-020-3192-6
- Mainardes, R. M., and Diedrich, C. (2020). The potential role of nanomedicine on COVID-19 therapeutics. *Ther. Deliv.* 7–9. doi:10.4155/tde-2020-0069
- Manivannan, S., and Ponnuchamy, K. (2020). Quantum dots as a promising agent to combat COVID-19. *Appl. Organomet. Chem.*, 17–22. doi:10.1002/aoc.5887
- Manke, A., Wang, L., and Rojanasakul, Y. (2013). Mechanisms of Nanoparticle-Induced Oxidative Stress and Toxicity. *Biomed. Res. Int.* 2013, 942916. doi:10.1155/2013/942916
- McKay, P. F., Hu, K., Blakney, A. K., Samnuan, K., Brown, J. C., Penn, R., et al. (2020). Self-amplifying RNA SARS-CoV-2 lipid nanoparticle vaccine candidate induces high neutralizing antibody titers in mice. *Nat. Commun.* 11, 3523. doi:10.1038/s41467-020-17409-9
- Miller, M. R., and PolandNanotoxicology, C. A. The Need for a Human Touch? *Small* 2020, 2001516. doi:10.1002/smll.202001516
- Mishra, D. K., Shandilya, R., and Mishra, P. K. (2018). Lipid based nanocarriers: a translational perspective. *Nanomedicine Nanotechnology, Biol. Med.* 14, 2023–2050. doi:10.1016/j.nano.2018.05.021
- Moitra, P., Alafeef, M., Dighe, K., Frieman, M. B., and Pan, D. (2020). Selective Naked-Eye Detection of SARS-CoV-2 Mediated by N Gene Targeted Antisense Oligonucleotide Capped Plasmonic Nanoparticles. *ACS Nano* 14, 7617–7627. doi:10.1021/acsnano.0c03822
- Neogi, U., Hill, K. J., Ambikan, A. T., Heng, X., Quinn, T. P., Byreddy, S. N., et al. (2020). Feasibility of Known RNA Polymerase Inhibitors as Anti-SARS-CoV-2 Drugs. *Pathog* 9. doi:10.3390/pathogens9050320
- Nguyen, T., Bang, D. D., and Wolff, A. (2019). Novel coronavirus disease (COVID-19): Paving the road for rapid detection and point-of-care diagnostics. *Micromachines* 11, 1–7. doi:10.3390/M110303062020
- Orecchioni, M., Bedognetti, D., Newman, L., Fuoco, C., Spada, F., Hendrickx, W., et al. (2017). Single-cell mass cytometry and transcriptome profiling reveal the impact of graphene on human immune cells. *Nat. Commun.*, 1109. doi:10.1038/s41467-017-01015-3
- Palestino, G., Garcia-Silva, I., González-Ortega, O., and Rosales-Mendoza, S. (2020). Can nanotechnology help in the fight against COVID-19? *Expert Rev. Anti. Infect. Ther.* 00, 1–16. doi:10.1080/14787210.2020.1776115
- Phan, T. (2020). Genetic diversity and evolution of SARS-CoV-2. *Infect. Genet. Evol.* 81, 104260. doi:10.1016/j.meegid.2020.104260
- Qiu, G., Gai, Z., Tao, Y., Schmitt, J., Kullak-Ublick, G. A., and Wang, J. (2020). Dual-Functional Plasmonic Photothermal Biosensors for Highly Accurate Severe Acute Respiratory Syndrome Coronavirus 2 Detection. *ACS Nano* 14, 5268–5277. doi:10.1021/acsnano.0c02439
- Rashidzadeh, H., Danafar, H., Rahimi, H., Mozafari, F., Salehiabar, M., Rahmati, M. A., et al. (2021). Nanotechnology against the novel coronavirus (severe acute respiratory syndrome coronavirus 2): diagnosis, treatment, therapy and future perspectives. *Nanomedicine* 16, 497–516. doi:10.2217/nnm-2020-0441
- Ravi, N., Cortade, D. L., Ng, E., and Wang, S. X. (2020). Diagnostics for SARS-CoV-2 detection: A comprehensive review of the FDA-EUA COVID-19 testing landscape. *Biosens. Bioelectron.* 165, 112454. doi:10.1016/j.bios.2020.112454
- Ren, J. ling, Zhang, A. H., and Wang, X. J. (2020). Traditional Chinese medicine for COVID-19 treatment. *Pharmacol. Res.* 155, 104743. doi:10.1016/j.phrs.2020.104743
- Sarkar, S. (2020). Silver nanoparticles with bronchodilators through nebulisation to treat COVID 19 patients. *Curr. Med. Res.* 3, 449–450. doi:10.15520/jcmro.v3i04.276
- Schoeman, D., and Fielding, B. C. (2019). Coronavirus envelope protein: current knowledge. *Virol. J.* 16, 69. doi:10.1186/s12985-019-1182-0
- Scientific Animations (2020). Coronavirus Symptoms and Prevention Explained Through Medical Animation. <https://www.scientificanimations.com/coronavirus-symptoms-and-prevention-explained-through-medical-animation/>.
- Shapiro, R. S. (2021). COVID-19 vaccines and nanomedicine. *Int. J. Dermatol.* doi:10.1111/ijd.15673
- Sharma, A., Kontodimas, K., and Bosmann, M. (2021). Nanomedicine: A Diagnostic and Therapeutic Approach to COVID-19. *Front. Med.*, 8. doi:10.3389/fmed.2021.648005
- Shin, M. D., Shukla, S., Chung, Y. H., Beiss, V., Chan, S. K., Ortega-Rivera, O. A., et al. COVID-19 vaccine development and a potential nanomaterial path forward. *Nat. Nanotechnol.* 2020, 15. 646–655. doi:10.1038/s41565-020-0737-y
- Singh, A. V., Laux, P., Luch, A., Sudrik, C., Wiehr, S., Wild, A.-M., et al. (2019). Review of emerging concepts in nanotoxicology: opportunities and challenges for safer nanomaterial design. *Toxicol. Mech. Methods* 29, 378–387. doi:10.1080/15376516.2019.1566425
- Somvanshi, S. B., Kharat, P. B., Somvanshi, S. B., Shejul, S. B., and Jadhav, K. M. (2020). Multifunctional nano-magnetic particles assisted viral RNA-extraction protocol for potential detection of COVID-19. *Mater. Res. Innov.*, 1–6. doi:10.1080/14328917.2020.1769350
- Vahedifard, F., and Chakravarthy, K. (2021). Nanomedicine for COVID-19: The role of nanotechnology in the treatment and diagnosis of COVID-19. *Emergent Mater.*, 1–25. doi:10.1007/s42247-021-00168-8
- Varahachalam, S. P., Lahooti, B., Chamaneh, M., Bagchi, S., Chhibber, T., Morris, K., et al. (2021). Nanomedicine for the SARS-CoV-2: state-of-the-art and future prospects. *Int. J. Nanomedicine* 16, 539. doi:10.2147/ijn.s283686
- Wang, Q., Zhang, Y., Wu, L., Niu, S., Song, C., Zhang, Z., et al. (2020). Structural and Functional Basis of SARS-CoV-2 Entry by Using Human ACE2. *Cell* 181, 894–904. e9. doi:10.1016/j.cell.2020.03.045
- Weiss, C., Carriere, M., Fusco, L., Capua, I., Regla-Nava, J. A., Pasquali, M., et al. (2020). Toward Nanotechnology-Enabled Approaches against the COVID-19 Pandemic. *ACS Nano* 14, 6383–6406. doi:10.1021/acsnano.0c03697
- Xia, S., Zhu, Y., Liu, M., Lan, Q., Xu, W., Wu, Y., et al. (2020). Fusion mechanism of 2019-nCoV and fusion inhibitors targeting HRI domain in spike protein. *Cell. Mol. Immunol.* 17, 765–767. doi:10.1038/s41423-020-0374-2
- Yan, T., Xiao, R., and Lin, G. (2020). Angiotensin-converting enzyme 2 in severe acute respiratory syndrome coronavirus and SARS-CoV-2: A double-edged sword? *FASEB J.* 34, 6017–6026. doi:10.1096/fj.202000782
- Yang, B., Chen, Y., and Shi, J. (2019). Reactive Oxygen Species (ROS)-Based Nanomedicine. *Chem. Rev.* 119, 4881–4985. doi:10.1021/acs.chemrev.8b00626
- Yang, J., Petitjean, S. J. L., Koehler, M., Zhang, Q., Dumitru, A. C., Chen, W., et al. (2020). Molecular Interaction and Inhibition of SARS-CoV-2 Binding to the ACE2 receptor. *Nat. Commun.* 2020, 11. doi:10.1038/s41467-020-18319-6
- Yang, Y., Islam, M. S., Wang, J., Li, Y., and Chen, X. (2020). Traditional Chinese Medicine in the Treatment of Patients Infected with 2019-New Coronavirus (SARS-CoV-2): A Review and Perspective. *Int. J. Biol. Sci.* 16, 1708–1717. doi:10.7150/ijbs.45538
- Ye, Z., Zhang, Y., Wang, Y., Huang, Z., and Song, B. (2020). Chest CT manifestations of new coronavirus disease 2019 (COVID-19): a pictorial review. *Eur. Radiol.* 30, 4381–4389. doi:10.1007/s00330-020-06801-0

- Yu, Z., Li, Q., Wang, J., Yu, Y., Wang, Y., Zhou, Q., et al. (2020). Reactive Oxygen Species-Related Nanoparticle Toxicity in the Biomedical Field. *Nanoscale Res. Lett.* 15, 1–14. doi:10.1186/s11671-020-03344-7
- Zachar, O. (2020). Formulations for COVID-19 Early Stage Treatment via Silver Nanoparticles Inhalation Delivery at Home and Hospital. *Sci. Prepr.*
- Zaim, S., Chong, J. H., Sankaranarayanan, V., and Harky, A. (2020). COVID-19 and Multiorgan Response. *Curr. Probl. Cardiol.* 45, 100618. doi:10.1016/j.cpcardiol.2020.100618
- Zhao, Z., Cui, H., Song, W., Ru, X., Zhou, W., and Yu, X. (2020). A simple magnetic nanoparticles-based viral RNA extraction method for efficient detection of SARS-CoV-2. *bioRxiv*, 518055. doi:10.1101/2020.02.22.961268
- Zhu, M., Nie, G., Meng, H., Xia, T., Nel, A., and Zhao, Y. (2013). Physicochemical Properties Determine Nanomaterial Cellular Uptake, Transport, and Fate. *Acc. Chem. Res.* 46, 622–631. doi:10.1021/ar300031y
- Łoczechin, A., Séron, K., Barras, A., Giovanelli, E., Belouzard, S., Chen, Y. T., et al. (2019). Functional Carbon Quantum Dots as Medical Countermeasures to Human Coronavirus. *ACS Appl. Mater. Inter.* 11, 42964–42974. doi:10.1021/acsami.9b15032

Conflict of Interest: The authors declare that the research was conducted in the absence of any commercial or financial relationships that could be construed as a potential conflict of interest.

Publisher's Note: All claims expressed in this article are solely those of the authors and do not necessarily represent those of their affiliated organizations, or those of the publisher, the editors and the reviewers. Any product that may be evaluated in this article, or claim that may be made by its manufacturer, is not guaranteed or endorsed by the publisher.

Copyright © 2021 Wang, Hao, Fa, Zheng, Yuan and Wang. This is an open-access article distributed under the terms of the Creative Commons Attribution License (CC BY). The use, distribution or reproduction in other forums is permitted, provided the original author(s) and the copyright owner(s) are credited and that the original publication in this journal is cited, in accordance with accepted academic practice. No use, distribution or reproduction is permitted which does not comply with these terms.



Preparation and Evaluation of Starch Hydrogel/Contact Lens Composites as Epigallocatechin Gallate Delivery Systems for Inhibition of Bacterial Adhesion

Lianghui Zhao^{1,2,3}, Hongwei Wang^{1,2}, Chengcheng Feng^{1,2}, Fangying Song^{1,2*} and Xianli Du^{1,2*}

¹Qingdao Eye Hospital of Shandong First Medical University, Qingdao, China, ²State Key Laboratory Cultivation Base, Shandong Provincial Key Laboratory of Ophthalmology, Shandong Eye Institute, Shandong First Medical University and Shandong Academy of Medical Sciences, Qingdao, China, ³Weifang Medical University, Weifang, China

OPEN ACCESS

Edited by:

Qihui Zhou,
Qingdao University, China

Reviewed by:

Lilong Gao,
Qingdao University, China
Jinpeng Wang,
Jiangnan University, China
Maribel Plascencia-Jatomea,
University of Sonora, Mexico

*Correspondence:

Fangying Song
songfangying_@126.com
Xianli Du
lilibestever@126.com

Specialty section:

This article was submitted to
Biomaterials,
a section of the journal
Frontiers in Bioengineering and
Biotechnology

Received: 16 August 2021

Accepted: 28 October 2021

Published: 16 November 2021

Citation:

Zhao L, Wang H, Feng C, Song F and
Du X (2021) Preparation and
Evaluation of Starch Hydrogel/Contact
Lens Composites as Epigallocatechin
Gallate Delivery Systems for Inhibition
of Bacterial Adhesion.
Front. Bioeng. Biotechnol. 9:759303.
doi: 10.3389/fbioe.2021.759303

Microbial infections caused by wearing contact lenses has become a major health problem, so the design and development of antibacterial contact lenses has attracted widespread attention. To safely and effectively inhibit bacterial adhesion of contact lenses, we have facilely prepared epigallocatechin gallate (EGCG) loaded starch hydrogel/contact lens composites by *in-situ* free radical polymerization of the mixture containing 2-hydroxyethyl methacrylate, methacrylic acid and ethylene glycol dimethacrylate. The adequate transmittance of the resulting contact lenses was characterized by ultraviolet-visible spectrophotometry, and their satisfactory stability was examined using differential scanning calorimetry and thermogravimetric analysis. Whereafter, cytotoxicity and degradation experiments were performed to investigate the biocompatibility and degradability of the contact lenses. The results showed the nontoxicity and good degradability of the composites. Besides, the capacity of the contact lenses for *in vitro* release of EGCG was also evaluated, and the results showed that the EGCG in these contact lenses can be sustainably released for at least 14 days. Further bacterial adhesion assay suggested that the EGCG loaded starch hydrogel/contact lenses could significantly reduce the adhesion of *Pseudomonas aeruginosa* compared to the control. The EGCG loaded starch hydrogel/contact lens composites provide a potential intervention strategy for preventing ocular microbial infections and inhibiting bacterial keratitis.

Keywords: starch hydrogel, composite, contact lens, epigallocatechin gallate, antibacterial activity

INTRODUCTION

There are more than 140 million contact lenses wearers all over the world (Stapleton et al., 2007). The contact lenses have been widely utilized in the vision correction of nearsightedness (myopia), far-sightedness (hyperopia), presbyopia and astigmatism. However, it can also cause several ocular discomforts, such as neovascularization, acute red eye and corneal abrasion (Kates and Tuli, 2021). More seriously, bacterial keratitis was easily induced during wearing or storage of contact lenses, especially in the case of corneal abrasion (Liu et al., 2020) due to the bacterial adhesion and biofilm

formation on their surface. *Pseudomonas aeruginosa* (*P. aeruginosa*), an opportunistic Gram-negative pathogen, is the most common cause for the contact lens-associated bacterial keratitis (Hilliam et al., 2020; Spornovasilis et al., 2020). Biofilm growth of *P. aeruginosa* can enhance the tolerance to antibiotic agents and host immune responses, which involves regulation in its quorum sensing and expression of virulence genes (Liu et al., 2020). The resulting *P. aeruginosa* keratitis can lead to permanent vision loss or even eyeball removal without the prompt treatment (Vazirani et al., 2015; Fernandes et al., 2016). Therefore, it is of significance to develop the highly biocompatible and antimicrobial contact lenses for effective prevention of contact lens-associated bacterial keratitis (Seggio et al., 2019; Fleiszig et al., 2020; Meretoudi et al., 2021).

Due to the complex ocular surface structure and strong resistance to foreign body transport, the drug often stays on the ocular surface for a short time and has low bioavailability, resulting in unsatisfactory therapeutic effects (Gaudana et al., 2010). With the development of material technology, it is possible to drugs deliver to the ocular surface continuously using drug-loaded contact lenses as delivery carriers. With the limited tear exchange rate, the contact lenses can greatly increase the residence time of the drug on the ocular surface and improve the bioavailability (Xu et al., 2018).

Although drug-loaded contact lenses have broad application prospects, the safety and biocompatibility are worrisome. Edible polysaccharide starch has been widely used in the fields of pharmaceutical and biomedical engineering due to its wide sources, low cost, good biocompatibility and degradability (Pandey et al., 2015). It has been reported that the hydrophobic starch can be used as delivery carrier, and the drug can also be chemically bonded to the starch backbone for sustained release, which indicates that starch is an ideal and safe drug delivery system (Pandey et al., 2015; Kou et al., 2020).

EGCG, a member of the polyphenol family, is the main biologically active ingredient in green tea (Ouyang et al., 2020). With a wide range of biological activities including antioxidant, anti-tumor, anti-inflammatory, anti-fibrosis, anti-microbe, antiviral, anti-obesity, EGCG has been used in the prevention and treatment of bacterial infection, cancer and obesity research (Cui et al., 2012; Kwak et al., 2016; Suzuki et al., 2016; Basu et al., 2018; Crous-Masó et al., 2018). In recent years, it has been reported that EGCG can protect lens epithelial cells from UV damage, prevent tryptophan oxidation of γ -crystallin in cataract in the presence of H_2O_2 , slow down retinal degeneration, and relieve dry eye inflammation in rabbits and mice (Heo et al., 2008; Peng et al., 2010; Lee et al., 2011; Chaudhury et al., 2015; Tseng et al., 2016; Perdices et al., 2020) due to its antioxidant, anti-inflammatory and anti-apoptotic activities. However, the antibacterial activity of EGCG has been little studied in ophthalmic drug delivery systems.

In this study, we firstly reported the preparation of EGCG loaded starch hydrogel/contact lens composites by *in-situ* free radical polymerization of the mixture containing 2-hydroxyethyl methacrylate, methacrylic acid, ethylene glycol dimethacrylate, AIBN, starch and EGCG. The resulting composites were assessed

in their physical characterizations, *in vitro* EGCG release, *in vitro* biocompatibility and *in vitro* degradability. Then bacterial adhesion inhibition effects were further evaluated by bacterial adhesion assay (Figure 1).

MATERIALS AND METHODS

Reagents

2-Hydroxyethyl methacrylate (HEMA), *Ipomoea batatas* starch and EGCG were obtained from Macklin (Shanghai, China). Methacrylic acid (MAA) and ethylene glycol dimethacrylate (EGDMA) were obtained from ThermoFisher (United States). 2,2'-azobis (2-methylpropionitrile) (AIBN) was obtained from Sigma-Aldrich (United States) and deionized water was used in the study.

Preparation Methods

Different amounts of starch solution (33.3%, w%), EGCG (0, 0.3, 0.6 and 1%, w%), HEMA/MAA (70:30, 70 wt%), EGDMA (0.45 wt%), and AIBN (0.15 wt%) were mixed into the deionized water. The mixture was sonicated for 5 min, transferred into the contact lens molds, placed in a water-bath at 65°C for 30 h, and then boiled for 5 min to remove the unreacted monomers, affording contact lenses CL-0, CL-1, CL-2, CL-3. Conventional hydrogel contact lenses were prepared according to the same method mentioned above except the absence of starch (CL-1', CL-2', CL-3') or both starch and EGCG (CL).

Physical Characterizations

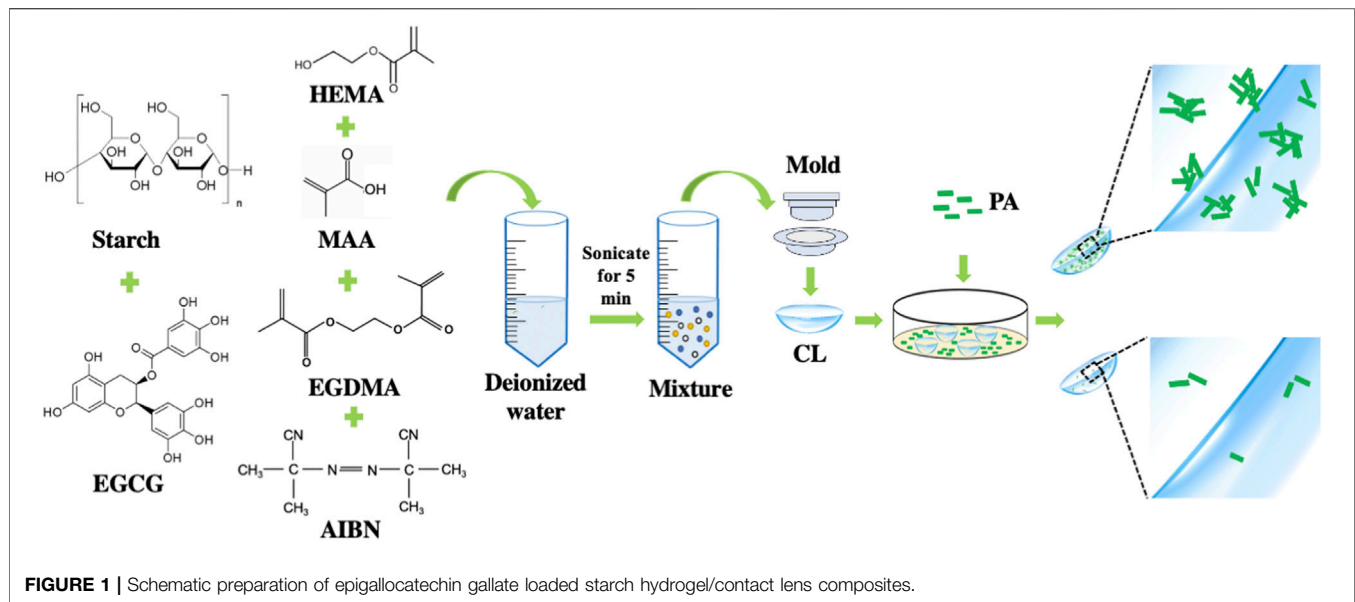
The optical transmittances of the contact lenses were measured with an ultraviolet-visible spectrophotometer (SpectraMax M2, Molecular Devices, MD, United States) at 50 nm intervals in the wavelength range of 250–800 nm. The contact lenses were removed from the molds, dried, and the dry weight (Wd) was recorded. Then immerse the contact lenses in deionized water to assess their expansion performance. Take out the lenses at regular intervals and drain the lenses surface completely with filter paper, and record their wet weight (Wt).

$$\text{Swelling ratio (\%)} = (Wt - Wd)/Wd$$

Differential scanning calorimetry (DSC) detection and thermogravimetric analysis (TGA) were performed through the synchronous thermal analyzer (TA DSC-TGA Q600, United States). The experiment was performed in the following conditions: nitrogen purity, 99.999%; temperature, 20–600°C; sample weight, 5–10 mg. Fourier transform infrared spectrum analysis, X-ray photoelectron spectroscopy, and other characterization tests were carried out for the contact lenses with or without starch.

In vitro Release Study

The contact lenses were immersed into 4 ml of deionized water. At a predetermined time point, 1 ml of the release medium was taken out and replaced with an equal amount of fresh deionized



water. NanoDrop One (Thermo, United States) was used to determine the content of EGCG at the wavelength of 278 nm. Then the cumulative release curve of EGCG with time was plotted by GraphPad Prism 9. The experiment was repeated three times.

Cytotoxicity Test

The cytotoxicity of EGCG loaded starch hydrogel/contact lens composites was evaluated based on the effects of contact lenses extracts on the proliferation of human corneal epithelial cells (HCECs, Seoul, Korea) through cell counting kit-8 (CCK-8) assay. 2.5 and 5 mg of different type contact lenses were respectively dipped in 10 ml DMEM/F12 (Sigma-Aldrich) containing 10% (v/v) fetal bovine serum (Sigma-Aldrich) and 1% (v/v) antibiotic/antimycotics (Sigma-Aldrich) in 37°C, 5% CO₂ incubator for 24 h to obtain contact lenses extracts with concentrations of 1:4 and 1:2 (Li et al., 2020). While the HCECs were plated into a 96-well plate at 2000/well and cultured in standard culture medium (DMEM/F12, 10% FBS, 1% antibiotic/antimycotics) for 24 h in 37°C, 5% CO₂ incubator. Then, the culture medium of all the wells was taken out and different group cells were cultured with the prepared contact lens extracts along with fresh standard culture medium, respectively. After culturing in 37°C, 5% CO₂ incubator for 1, 3, 5 and 7 days, CCK-8 detection reagent (Dojindo Laboratories Kumamoto, Japan) was added to measure the absorbance of the cells at 450 nm wavelength with SpectraMax M2 (Molecular Devices, United States).

In vitro Degradation Assay

The *in vitro* degradation of starch in the EGCG loaded starch hydrogel/contact lens composites was evaluated by *Bacillus* alpha-amylase (Solarbio, Beijing, China, pH 5.5–7.5, T 50–70°C). Briefly, the contact lenses were immersed in iodine solution for 2 min, and the color of contact lenses was observed by slit lamp microscope. The contact lenses were rinsed gently with deionized water to remove residual iodine solution, and then

soaked in active alpha-amylase solution for enzymatic hydrolysis at 50°C for 24 h (0.1 mg/ml and 0.01 mg/ml, 10 ml). At estimated time points, the colorless lenses were taken out and softly rinsed with deionized water to remove residual amylase solution. After addition of iodine solution, the contact lenses were further photographed to detect the color reaction of starch and iodine.

Bacterial Adhesion Assay

P. aeruginosa ATCC 19660 inoculum was cultured on LB agar medium at 37°C, while planktonic culture was grown with an initial optical density (OD) of ~0.02 and shaking in an incubator at 37°C for 24 h (Li et al., 2020). The bacteria were washed with PBS and then serially diluted to 10⁶ CFU/ml. The contact lenses were softly washed with PBS in 24 pore culture plate, and added in 1 ml prepared bacterial suspension, then incubated at 37°C and 120 rpm for 24 h. After incubation, the cocultures of the contact lenses and bacteria were photographed and the number of bacteria left on the lenses was counted. In brief, contact lenses were gently rinsed 3 times with PBS to remove loosely adhered bacteria, then grinded to detect the number of adhered bacteria by plate counting (Salvagni et al., 2020).

Statistical Analysis

Statistical analysis was performed using Kruskal–Wallis test with Statistical Package for Social Sciences software (version 24.0). All the data were obtained from at least three independent experiments. The descriptive statistics were presented as the mean ± SD. *p* < 0.05 was considered a statistically significant difference.

RESULTS AND DISCUSSION

Microbial infection is a common problem associated with contact lenses, and poor sanitary conditions and overnight wearing

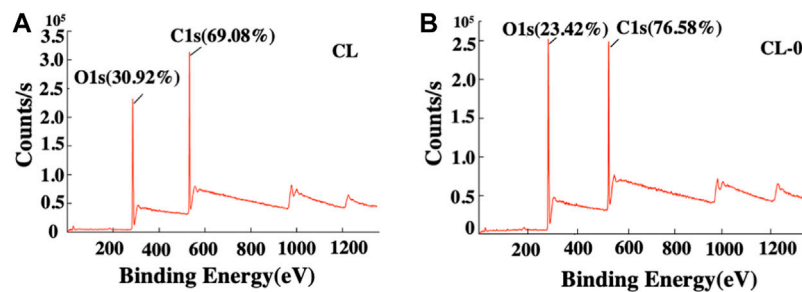


FIGURE 2 | Elemental analysis of the contact lenses CL (A) and CL-0 (B).

contact lenses are the main risk factors for microbial keratitis (Cope et al., 2015; Cope et al., 2017). Long-term contact between cornea and contact lenses will affect the nutrient exchange of normal corneal epithelial cells, causing ocular discomfort or serious complications (Forte et al., 2010; Lim et al., 2018). Hypoxia environment of ocular surface can destruct the integrity of extracellular matrix proteins, promote bacterial adhesion, and provide a good condition for opportunistic pathogens to invade the cornea (Forte et al., 2010). In recent years, with the development of drug delivery, the design and exploitation of antimicrobial contact lenses had attracted extensive attention.

In-situ free radical polymerization is a common method for preparation of therapeutic contact lenses by addition of bioactive ingredients. In this study, antibacterial contact lenses were facily prepared by thermally initiated polymerization of the mixture containing starch, EGCG and conventional hydrogel components. Starch significantly improves the sustained release performance of conventional hydrogel contact lenses without changing the basic physical properties.

Synthesis and Characterizations of the Contact Lenses

The contact lenses were prepared according to specific ratio of different ingredients as reported previously (Dursch et al., 2014). In short, different amounts of EGCG (0, 0.3, 0.6 and 1%, w/w), hydrogel solution and AIBN were added to the starch solution and prepared into CL-0, CL-1, CL-2, CL-3 using specific contact lenses models, while CL was prepared as negative control.

The addition of starch was confirmed through element analysis as shown in **Figure 2**. The initial carbon and oxygen content in CL was 69.08 and 30.92%, respectively. After adding starch, the carbon content increased to 76.58% and the oxygen content reduced to 23.42%, indicating the successful preparation of starch hydrogel/contact lenses. Studies have confirmed that the natural polymers are non-toxic and biodegradable and can bind non-specifically or specifically to proteins and cells, which are the ideal materials for hydrogel-based sustained-release systems or cellular carriers (Kirchhof et al., 2015). As a kind of natural polysaccharide with wide sources and good biocompatibility, starch is widely used in pharmaceutical and biomedical

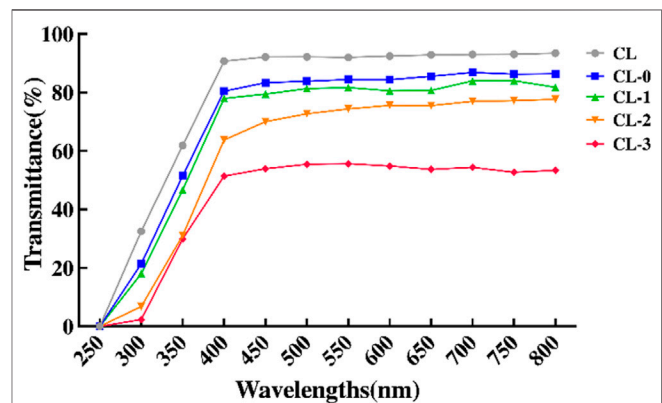


FIGURE 3 | Optical transmittance of the contact lenses.

engineering fields, which was selected as the component of the contact lenses in present study (Pandey et al., 2015; Hadisi et al., 2018; Kou et al., 2020). Based on our data, the addition of starch to the hydrogel material does not affect the basic properties of contact lenses such as transparency, optical transmittance, swelling, thermal stability and thermoplasticity.

The optical transmittance data of contact lenses with different treatments are shown in **Figure 3**. Compared with the negative control CL, there was no significant difference in transmittance between CL-0 and CL group, while the optical transmittance of starch hydrogel/contact lenses (CL-0) decreased slightly (**Figure 3**), indicating that the addition of starch had little effect on transmittance. In EGCG group, with the addition of EGCG, the color of contact lenses became yellowish and the optical transmittance gradually decreased (CL-1, $84.00 \pm 0.72\%$; CL-2, $77.70 \pm 0.90\%$; CL-3, $54.37 \pm 0.53\%$; **Supplementary Figure S1, Figure 3**). Furthermore, swelling test results confirmed that the swelling rate of CL-0 group ($21.92 \pm 1.30\%$) was higher than that of CL group ($18.88 \pm 2.10\%$) after immersion in deionized water for 24 h, (**Figure 4A**). It was indicated that starch improved the swelling ratio of contact lenses to a certain extent.

Fourier transform infrared spectroscopy analysis showed that the corresponding functional groups of starch hydrogel contact lens did not change significantly. In addition, the characteristic peak of starch infrared absorption spectrum didn't appear due to

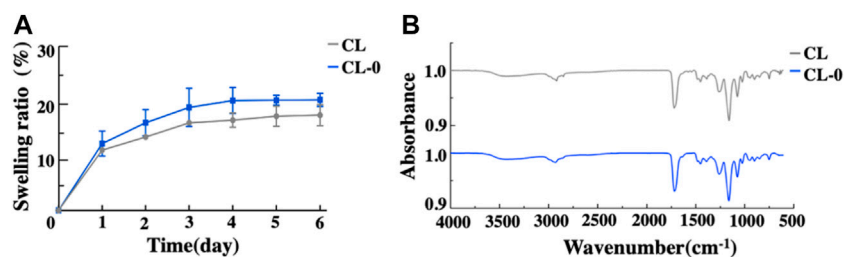


FIGURE 4 | Swelling ratio (A) and Fourier transform infrared spectroscopy analysis of the contact lenses (B).

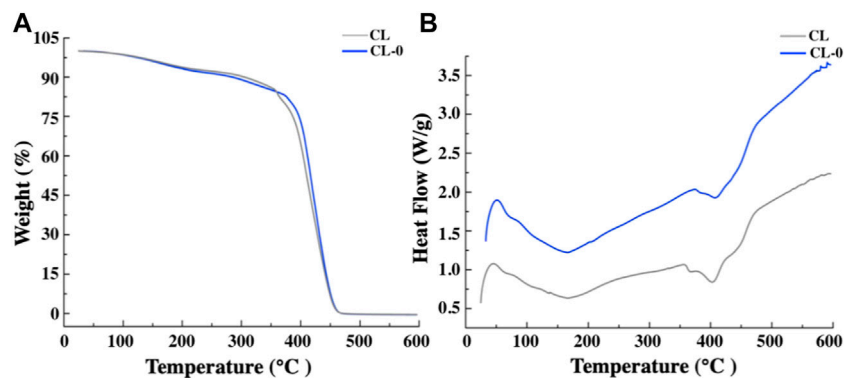


FIGURE 5 | Thermogravimetric analysis (A) and Differential scanning calorimetry test of the contact lenses (B).

TABLE 1 | Representatives of antimicrobial contact lenses in recent years.

Substrates	Antimicrobial agents	Release time(d)	Biological activity	References
<i>In-situ</i> synthesis				
Starch/poly (HEMA-co-MAA-co-EGDMA)	EGCG	14	Antibacterial	In this study
Poly (HTCC-co-HEMA)	HTCC, Vor, Ag	5	Antifungal	Huang et al. (2016)
Silicone/poly (TRIS-co-HEMA-co-NVP-EGDMA)	ALG, CHI, HA, PLL	2–5	Antibacterial	Silva et al. (2018)
Poly (HEMA-co-MAA-co-EGDMA)	Silver NPs	—	Antibacterial	Shayani Rad et al. (2016)
Commercial CL				
Hioxifilcon A	AMPs	7	Antibacterial	Salvagni et al. (2020)
Narafilcon A	Ofloxacin, vitamin E	4.28	Antibacterial	Ubani-Ukoma et al. (2019)
Acuvue	Phomopsidione NPs	4	Antibacterial	Bin Sahadan et al. (2019)
Silicone hydrogel	Vancomycin	0.33	Antibacterial	Guo et al. (2020)
Comfilcon A	ZnO, chitosan, gallic acid	—	Antibacterial	Hoyo et al. (2019)
Narafilcon A	Esculentin-1a (1-21)NH ₂	—	Antibacterial	Casciaro et al. (2017)

EGCG, epigallocatechin gallate; HTCC, N-[(2-Hydroxy-3-trimethylammonium) Propyl] Chitosan Chloride; Vor, voriconazole; TRIS, 3-tris (trimethylsilyloxy)silylpropyl 2-methylprop-2-enoate; NVP, N-vinyl pyrrolidone; ALG, sodium alginate; CHI, chitosan; HA, sodium hyaluronate; PLL, polylysine hydrobromide; NPs, nanoparticles; CL, contact lens; AMPs, antimicrobial peptides.

the low starch content (Figure 4B). Figure 5A showed the similar TGA curves of CL and CL-0 groups. It was clearly found that both samples could maintain 90% of weight even the temperature rose to 300°C. Furthermore, the DSC melting curve of CL group was similar as that of CL-0. The addition of starch has no significant effect on the material fusibility (Figure 5B). These results confirmed the good thermal stability and thermoplasticity of EGCG loaded starch hydrogel/contact lens composites.

Biocompatibility

Biosafety is a great challenge in the development of functional contact lenses. Table 1 lists the research representatives on antimicrobial contact lenses recently, showing that a variety of antimicrobial components are loaded on different types of contact lenses. These contact lenses mainly bind variable antibacterial materials to carriers such as hydrogels through *in-situ* synthesis, coating or covalently attachment. Although

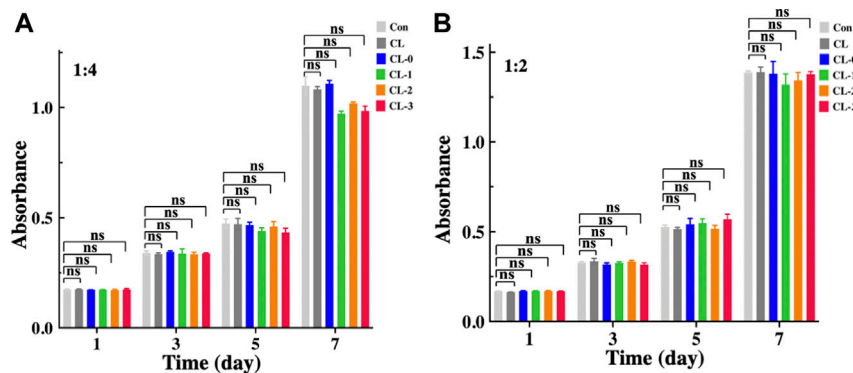


FIGURE 6 | Cytotoxicity and proliferation activities of the contact lenses on human corneal epithelial cells (HCECs). Cell counting kit-8 analysis of HCECs seeded in the contact lenses extracts with a concentration of 1:4 **(A)** and 1:2 **(B)**, $n = 3$.

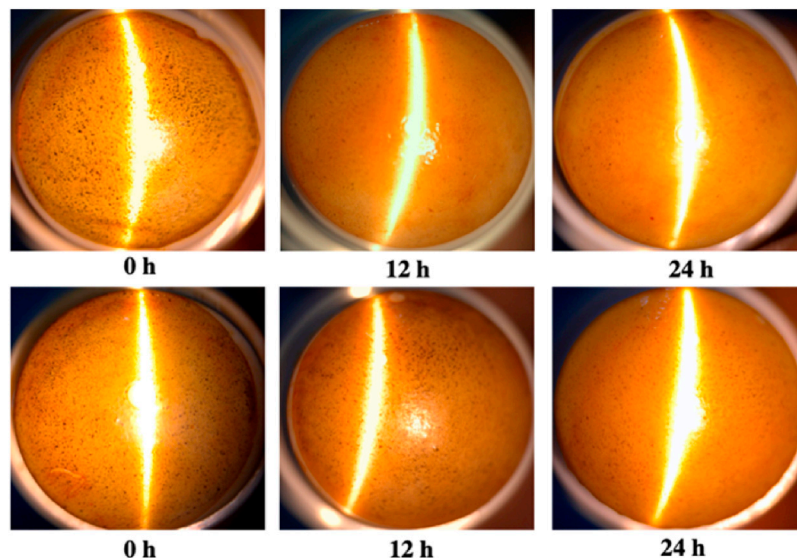


FIGURE 7 | *In vitro* degradation of epigallocatechin gallate loaded starch hydrogel/contact lens composites by alpha-amylase. The concentration of active alpha-amylase was 0.1 mg/ml **(A)** and 0.01 mg/ml **(B)**.

functional contact lenses containing antibiotics, non-steroidal anti-inflammatory drugs or silver ions have significant antibacterial properties, they could cause certain adverse reactions, such as the emergence of drug-resistant strains, eye irritation, and biocompatibility problems of metal ions (Silva et al., 2018; Xiao et al., 2018; Hoyo et al., 2019; Nahum et al., 2019; Khan and Lee, 2020; Salvagni et al., 2020). In this study, cytotoxicity test was investigated to evaluate the cytocompatibility of EGCG-loaded starch hydrogel/contact lenses. After different types of contact lenses were immersed in standard medium for 24 h, the cytotoxicity of contact lenses extracts against HCECs were detected. Based on absorbance data of the solution at 450 nm wavelength, it was showed that contact lens CL-0, CL-1, CL-2 and CL-3 extracts had no inhibitory effect on the proliferation of HCECs compared with untreated HCECs and CL group (**Figure 6**). There was no significant difference in

the absorbance between EGCG groups. Those results demonstrated that EGCG loaded starch hydrogel/contact lens composite exhibited no obvious cytotoxicity, which makes it possible to be applied in the medical field in the future.

***In vitro* Degradation by Alpha-Amylase**

In order to evaluate the degradability of materials, an *in vitro* alpha-amylase degradability detection of the composites was performed. The EGCG starch hydrogel/contact lens composite (CL-1) was stained with iodine solution and showed dark blue spots on the surface. After incubation with active alpha-amylase solution, the amounts of blue spots on the surface decreased with the increase of enzymatic hydrolysis time. The blue spots on the lenses disappeared after 12 h of enzymatic hydrolysis using the 0.1 mg/ml alpha-amylase solution, while there were still a few blue spots on the lenses after 24 h of enzymatic hydrolysis using the 0.01 mg/ml alpha-

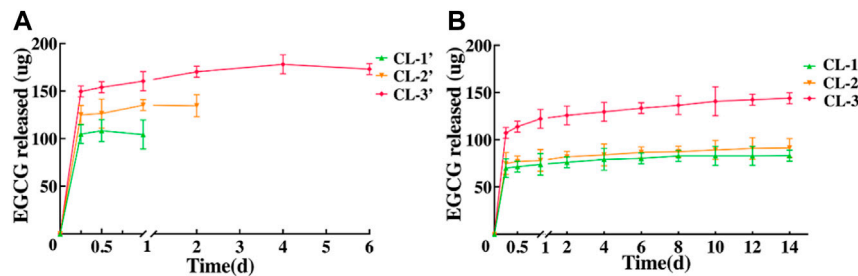


FIGURE 8 | *In vitro* EGCG release from conventional hydrogel contact lenses (A) and starch hydrogel/contact lenses (B).

amylase solution (Figure 7). Above all, it was suggested that the EGCG starch hydrogel/contact lens composites had good degradability.

In vitro EGCG Release

EGCG is the main biologically active ingredient in tea, which has a wide range of antioxidant, anti-tumor, anti-inflammatory, anti-fibrosis, anti-microbe, antiviral, anti-obesity and other activities (Cui et al., 2012; Kwak et al., 2016; Suzuki et al., 2016; Basu et al., 2018; Crous-Masó et al., 2018; Ouyang et al., 2020). In view of the safety and eligible biocompatibility of contact lens extracts against HCECs, we further tested the EGCG release of those contact lenses. After being immersed in deionized water, the cumulative release amount of EGCG from the EGCG loaded starch hydrogel/contact lenses was detected at different time points (Figure 8). The results exhibited that the EGCG in these contact lenses (CL-1, CL-2, CL-3) can be sustainably released for at least 14 days. The durations are obviously longer than those (less than 4 days) in conventional hydrogel contact lenses (Figure 8A). With the increase of EGCG amount in contact lenses, the cumulative release of EGCG continuously increased from 82.79 ± 5.77 to 143.97 ± 5.77 µg (Figure 8B).

It has been reported that drug delivery systems with good sustained release properties, such as peptide-functionalized contact lenses, have a sustained-release time of approximately 7 days (Salvagni et al., 2020). In this study, the sustained-release capacity of EGCG loaded starch hydrogel/contact lens composites were greatly improved. It was indicated that the properties of drug delivery of the contact lenses in this study were effectively improved compared with the commercial CL (Table 1). Extending the drug release time of lenses plays an important role in the long-term inhibition of bacterial adhesion, which is beneficial for prolonging the safe wearing time of contact lenses in the future.

Antimicrobial Activity

Many *in vitro* studies have shown that *P. aeruginosa* had the strongest adhesion to silicone hydrogel and hydrogel contact lenses, reaching the maximum adhesion of bacteria within 1 h, and forming biofilm within 24 h (Dutta et al., 2012). The formation of biofilms relies on the bacterial quorum sensing system to sense and regulate the diffusion signal molecules related to the bacterial population density and the expression of virulence factors, thus providing an ecosystem for bacteria to enhance their virulence and drug resistance (Jimenez et al., 2012).

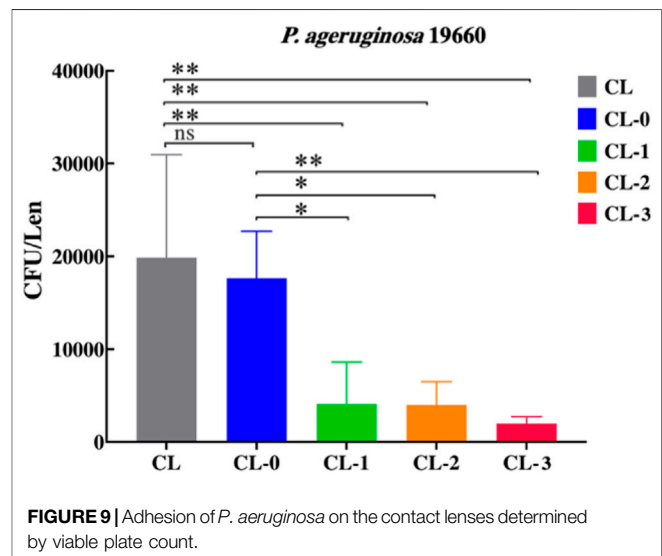


FIGURE 9 | Adhesion of *P. aeruginosa* on the contact lenses determined by viable plate count.

To examine the antimicrobial activity of those contact lenses, bacterial adhesion assay against *P. aeruginosa* ATCC 19660 was performed. After 24 h of incubation with *P. aeruginosa*, the amounts of bacteria adhered onto lenses were quantified. Compared with CL and CL-0, the coculture liquid of CL-1, CL-2 and CL-3 was more clearly and the amount of bacterial adhesion was significantly reduced ($p < 0.05$) (Supplementary Figure S2). Compared with CL and CL-0, the amounts of bacterial adhesion on CL-1, CL-2, CL-3 are significantly reduced ($p < 0.05$). With the increase of EGCG content, the amount of bacterial adhesion on contact lenses decreased gradually (CL-1, 4531 ± 4100 ; CL-2, 3967 ± 2517 ; CL-3, 1967 ± 751) (Figure 9). These results indicated that the composites could effectively inhibit the adhesion of *P. aeruginosa*, which provides the possibility to reduce the incidence of contact lens induced *P. aeruginosa* keratitis in the future.

CONCLUSION

In summary, the EGCG loaded starch hydrogel/contact lens composites have been successfully prepared by *in-situ* free

radical polymerization of the mixture containing HEMA, MAA, EGDMA, starch and EGCG. The resulting composites exhibited favorable biocompatibility and superior drug release ability for EGCG at least 14 days, which processed enhanced sustained release capacity of EGCG than conventional hydrogel contact lens (4 days). Hence, they can effectively inhibit the adhesion of *P. aeruginosa* on the lenses, which is beneficial for prolonging the safe wearing of contact lenses and provides the potential for the clinical therapy of bacterial keratitis in the future. Furthermore, the study enriches the research scope of functional contact lenses, and various natural products with specific activities can be introduced in the preparation of therapeutic contact lenses for treatment of other ophthalmological diseases.

DATA AVAILABILITY STATEMENT

The original contributions presented in the study are included in the article/**Supplementary Material**, further inquiries can be directed to the corresponding authors.

REFERENCES

- Basu, A., Masek, E., and Ebersole, J. (2018). Dietary Polyphenols and Periodontitis—A Mini-Review of Literature. *Molecules* 23, 1786. doi:10.3390/molecules23071786
- Bin Sahadan, M. Y., Tong, W. Y., Tan, W. N., Leong, C. R., Bin Misri, M. N., Chan, M., et al. (2019). Phomopsidione Nanoparticles Coated Contact Lenses Reduce Microbial Keratitis Causing Pathogens. *Exp. Eye Res.* 178, 10–14. doi:10.1016/j.exer.2018.09.011
- Casciaro, B., Dutta, D., Loffredo, M. R., Marcheggiani, S., McDermott, A. M., Willcox, M. D., et al. (2018). Esculentin-1a Derived Peptides kill *Pseudomonas aeruginosa* biofilm on Soft Contact Lenses and Retain Antibacterial Activity upon Immobilization to the Lens Surface. *Pept. Sci.* 110, e23074. doi:10.1002/bip.23074
- Chaudhury, S., Ghosh, I., Saha, G., and Dasgupta, S. (2015). EGCG Prevents Tryptophan Oxidation of Cataractous Ocular Lens Human γ -crystallin in Presence of H₂O₂. *Int. J. Biol. Macromolecules* 77, 287–292. doi:10.1016/j.jbiomac.2015.03.040
- Cope, J. R., Collier, S. A., Nethercut, H., Jones, J. M., Yates, K., and Yoder, J. S. (2017). Risk Behaviors for Contact Lens-Related Eye Infections Among Adults and Adolescents - United States, 2016. *MMWR Morb. Mortal. Wkly. Rep.* 66, 841–845. doi:10.15585/mmwr.mm6632a2
- Cope, J. R., Collier, S. A., Rao, M. M., Chalmers, R., Mitchell, G. L., Richdale, K., et al. (2015). Contact Lens Wearer Demographics and Risk Behaviors for Contact Lens-Related Eye Infections - United States, 2014. *MMWR Morb. Mortal. Wkly. Rep.* 64, 865–870. doi:10.15585/mmwr.mm6432a2
- Crous-Masó, J., Palomeras, S., Relat, J., Camó, C., Martínez-Garza, Ú., Planas, M., et al. (2018). (–)-Epigallocatechin 3-Gallate Synthetic Analogues Inhibit Fatty Acid Synthase and Show Anticancer Activity in Triple Negative Breast Cancer. *Epigallocatechin 3-gallate Synthetic Analogues Inhibit Fatty Acid Synthase and Show Anticancer Activity in Triple Negative Breast Cancer. Molecules* 23, 1160. doi:10.3390/molecules23051160
- Cui, Y., Oh, Y. J., Lim, J., Youn, M., Lee, I., Pak, H. K., et al. (2012). AFM Study of the Differential Inhibitory Effects of the green tea Polyphenol (–)-Epigallocatechin-3-Gallate (EGCG) against Gram-Positive and Gram-Negative Bacteria. *Food Microbiol.* 29, 80–87. doi:10.1016/j.fm.2011.08.019
- Dursch, T. J., Taylor, N. O., Liu, D. E., Wu, R. Y., Prausnitz, J. M., and Radke, C. J. (2014). Water-soluble Drug Partitioning and Adsorption in HEMA/MAA Hydrogels. *Biomaterials* 35, 620–629. doi:10.1016/j.biomaterials.2013.09.109
- Dutta, D., Cole, N., and Willcox, M. (2012). Factors Influencing Bacterial Adhesion to Contact Lenses. *Mol. Vis.* 18, 14–21.

AUTHOR CONTRIBUTIONS

LZ: write manuscript and do the experiment; HW: do statistical analysis and material synthesis; CF: consult literature and do cell experiment; FS: design the experiments, review and edit the manuscript; XD: design and fund experiment.

FUNDING

This work was supported by the Academic Promotion Program of Shandong First Medical University (2019ZL001); Qingdao Science and Technology Project (19-6-1-24-nsh); National Natural Science Foundation of China (82000852).

SUPPLEMENTARY MATERIAL

The Supplementary Material for this article can be found online at: <https://www.frontiersin.org/articles/10.3389/fbioe.2021.759303/full#supplementary-material>

- Fernandes, M., Vira, D., Medikonda, R., and Kumar, N. (2016). Extensively and Pan-Drug Resistant *Pseudomonas aeruginosa* Keratitis: Clinical Features, Risk Factors, and Outcome. *Graefes Arch. Clin. Exp. Ophthalmol.* 254, 315–322. doi:10.1007/s00417-015-3208-7
- Fleisz, S. M. J., Kroken, A. R., Nieto, V., Grosser, M. R., Wan, S. J., Metruccio, M. M. E., et al. (2020). Contact Lens-Related Corneal Infection: Intrinsic Resistance and its Compromise. *Prog. Retin. Eye Res.* 76, 100804. doi:10.1016/j.preteyeres.2019.100804
- Forte, R., Cennamo, G., Del Prete, S., Cesarano, I., and Del Prete, A. (2010). Scanning Electron Microscopy of Corneal Epithelium in Soft Contact Lens Wearers. *Cornea* 29, 732–736. doi:10.1097/ico.0b013e3181c32f1a
- Gaudana, R., Ananthula, H. K., Parenky, A., and Mitra, A. K. (2010). Ocular Drug Delivery. *AAPS J.* 12, 348–360. doi:10.1208/s12248-010-9183-3
- Guo, Y., Qian, S., Wang, L., Zeng, J., Miao, R., Meng, Y., et al. (2020). Reversible Antibiotic Loading and pH-Responsive Release from Polymer Brushes on Contact Lenses for Therapy and Prevention of Corneal Infections. *J. Mater. Chem. B* 8, 10087–10092. doi:10.1039/d0tb01508c
- Hadisi, Z., Nourmohammadi, J., and Nassiri, S. M. (2018). The Antibacterial and Anti-inflammatory Investigation of Lawsonia Inermis-Gelatin-Starch Nano-Fibrous Dressing in Burn Wound. *Int. J. Biol. Macromol.* 107, 2008–2019. doi:10.1016/j.jbiomac.2017.10.061
- Heo, J., Lee, B. R., and Koh, J.-W. (2008). Protective Effects of Epigallocatechin Gallate after UV Irradiation of Cultured Human Lens Epithelial Cells. *Korean J. Ophthalmol.* 22, 183–186. doi:10.3341/kjo.2008.22.3.183
- Hilliam, Y., Kaye, S., and Winstanley, C. (2020). *Pseudomonas aeruginosa* and Microbial Keratitis. *J. Med. Microbiol.* 69, 3–13. doi:10.1099/jmm.0.001110
- Hoyo, J., Ivanova, K., Guaus, E., and Tzanov, T. (2019). Multifunctional ZnO NPs-Chitosan-Gallic Acid Hybrid Nanocoating to Overcome Contact Lenses Associated Conditions and Discomfort. *J. Colloid Interf. Sci.* 543, 114–121. doi:10.1016/j.jcis.2019.02.043
- Huang, J.-F., Zhong, J., Chen, G.-P., Lin, Z.-T., Deng, Y., Liu, Y.-L., et al. (2016). A Hydrogel-Based Hybrid Theranostic Contact Lens for Fungal Keratitis. *ACS Nano* 10, 6464–6473. doi:10.1021/acsnano.6b00601
- Kates, M. M., and Tuli, S. (2021). Complications of Contact Lenses. *JAMA* 325 (18), 1912. doi:10.1001/jama.2020.20328
- Khan, S. A., and Lee, C.-S. (2020). Recent Progress and Strategies to Develop Antimicrobial Contact Lenses and Lens Cases for Different Types of Microbial Keratitis. *Acta Biomater.* 113, 101–118. doi:10.1016/j.actbio.2020.06.039
- Kirchhof, S., Goepferich, A. M., and Brandl, F. P. (2015). Hydrogels in Ophthalmic Applications. *Eur. J. Pharmaceutics Biopharmaceutics* 95 (Pt B), 227–238. doi:10.1016/j.ejpb.2015.05.016

- Kou, Z., Dou, D., Lan, L., Zhang, J., Lan, P., Yu, Q., et al. (2020). Preparation, Characterization, and Performance Analysis of Starch-Based Nanomicelles. *Int. J. Biol. Macromolecules* 145, 655–662. doi:10.1016/j.ijbiomac.2019.12.220
- Kwak, T. W., Park, S.-B., Kim, H.-J., Jeong, Y.-I., and Kang, D. H. (2016). Anticancer Activities of Epigallocatechin-3-Gallate against Cholangiocarcinoma Cells. *Ott* 10, 137–144. doi:10.2147/ott.s112364
- Lee, H. S., Chauhan, S. K., Okanobo, A., Nallasamy, N., and Dana, R. (2011). Therapeutic Efficacy of Topical Epigallocatechin Gallate in Murine Dry Eye. *Cornea* 30, 1465–1472. doi:10.1097/ico.0b013e31821c9b5a
- Li, H., Zhao, L., Wang, F., Wang, H., Dong, M., Liu, T., et al. (2020). Natural Cross-Linker-Stabilized Acellular Porcine Corneal Stroma for Lamellar Keratoplasty. *Acta Biomater.* 114, 270–284. doi:10.1016/j.actbio.2020.07.035
- Li, J., Ma, X., Zhao, L., Li, Y., Zhou, Q., and Du, X. (2020). Extended Contact Lens Wear Promotes Corneal Norepinephrine Secretion and *Pseudomonas aeruginosa* Infection in Mice. *Invest. Ophthalmol. Vis. Sci.* 61, 17. doi:10.1167/iov.61.4.17
- Lim, C. H. L., Stapleton, F., and Mehta, J. S. (2018). Review of Contact Lens-Related Complications. *Eye Contact Lens* 44 (Suppl. 2), S1–S10. doi:10.1097/ICL.0000000000000481
- Liu, G., Li, K., Wang, H., Ma, L., Yu, L., and Nie, Y. (2020). Stable Fabrication of Zwitterionic Coating Based on Copper-Phenolic Networks on Contact Lens with Improved Surface Wettability and Broad-Spectrum Antimicrobial Activity. *ACS Appl. Mater. Inter.* 12 (14), 16125–16136. doi:10.1021/acsami.0c02143
- Meretoudi, A., Banti, C. N., Raptis, P. K., Papachristodoulou, C., Kourkoumelis, N., Ikiades, A. A., et al. (2021). Silver Nanoparticles from Oregano Leaves' Extracts as Antimicrobial Components for Non-infected Hydrogel Contact Lenses. *Ijms* 22, 3539. doi:10.3390/ijms22073539
- Nadal Jimenez, P., Koch, G., Thompson, J. A., Xavier, K. B., Cool, R. H., and Quax, W. J. (2012). The Multiple Signaling Systems Regulating Virulence in *Pseudomonas aeruginosa*. *Microbiol. Mol. Biol. Rev.* 76, 46–65. doi:10.1128/mmb.05007-11
- Nahum, Y., Israeli, R., Mircus, G., Perelshtein, I., Ehrenberg, M., Gutfreund, S., et al. (2019). Antibacterial and Physical Properties of a Novel Sonochemical-Assisted Zn-CuO Contact Lens Nanocoating. *Graefes Arch. Clin. Exp. Ophthalmol.* 257, 95–100. doi:10.1007/s00417-018-4172-9
- Ouyang, J., Zhu, K., Liu, Z., and Huang, J. (2020). Prooxidant Effects of Epigallocatechin-3-Gallate in Health Benefits and Potential Adverse Effect. *Oxid Med. Cel Longev* 2020, 9723686. doi:10.1155/2020/9723686
- Pandey, S., Malviya, R., and Sharma, P. K. (2015). Applicability, Commercial Utility and Recent Patents on Starch and Starch Derivative as Pharmaceutical Drug Delivery Carrier. *Recent Pat Drug Deliv. Formul* 9, 249–256. doi:10.2174/1872211309666150724101454
- Peng, P.-H., Chiou, L.-F., Chao, H.-M., Lin, S., Chen, C.-F., Liu, J.-H., et al. (2010). Effects of Epigallocatechin-3-Gallate on Rat Retinal Ganglion Cells after Optic Nerve Axotomy. *Exp. Eye Res.* 90, 528–534. doi:10.1016/j.exer.2010.01.007
- Perdices, L., Fuentes-Broto, L., Segura, F., Cuenca, N., Orduna-Hospital, E., and Pinilla, I. (2020). Epigallocatechin Gallate Slows Retinal Degeneration, Reduces Oxidative Damage, and Modifies Circadian Rhythms in P23H Rats. *Antioxidants* 9, 718. doi:10.3390/antiox9080718
- Salvagni, E., García, C., Manresa, À., Müller-Sánchez, C., Reina, M., Rodríguez-Abreu, C., et al. (2020). Short and Ultrashort Antimicrobial Peptides Anchored onto Soft Commercial Contact Lenses Inhibit Bacterial Adhesion. *Colloids Surf. B: Biointerfaces* 196, 111283. doi:10.1016/j.colsurfb.2020.111283
- Seggio, M., Nostro, A., Ginestra, G., Quaglia, F., and Sortino, S. (2019). Contact Lenses Delivering Nitric Oxide under Daylight for Reduction of Bacterial Contamination. *Ijms* 20, 3735. doi:10.3390/ijms20153735
- Shayani Rad, M., Khameneh, B., Sabeti, Z., Mohajeri, S. A., and Fazly Bazzaz, B. S. (2016). Antibacterial Activity of Silver Nanoparticle-Loaded Soft Contact Lens Materials: The Effect of Monomer Composition. *Curr. Eye Res.* 41, 1286–1293. doi:10.3109/02713683.2015.1123726
- Silva, D., Sousa, H. C. d., Gil, M. H., Santos, L. F., Moutinho, G. M., Serro, A. P., et al. (2018). Antibacterial Layer-By-Layer Coatings to Control Drug Release from Soft Contact Lenses Material. *Int. J. Pharmaceutics* 553, 186–200. doi:10.1016/j.ijpharm.2018.10.041
- Spernovasilis, N., Maraki, S., Kokorakis, E., Kofteridis, D., Tsilimbaris, M., Siganos, C., et al. (2020). Antimicrobial Susceptibility of Isolated Pathogens from Patients with Contact Lens-Related Bacterial Keratitis in crete, greece: a Ten-Year Analysis. *Cont Lens Anterior Eye* S1367-0484 (20), 30139–9. doi:10.1016/j.clae.2020.07.006
- Stapleton, F., Keay, L., Jalbert, I., and Cole, N. (2007). The Epidemiology of Contact Lens Related Infiltrates. *Optom. Vis. Sci.* 84, 257–272. doi:10.1097/OPX0b013e3180485d5f
- Suzuki, T., Pervin, M., Goto, S., Isemura, M., and Nakamura, Y. (2016). Beneficial Effects of tea and the green tea Catechin Epigallocatechin-3-Gallate on Obesity. *Molecules* 21, 1305. doi:10.3390/molecules21101305
- Tseng, C.-L., Hung, Y.-J., Chen, Z.-Y., Fang, H.-W., and Chen, K.-H. (2016). Synergistic Effect of Artificial Tears Containing Epigallocatechin Gallate and Hyaluronic Acid for the Treatment of Rabbits with Dry Eye Syndrome. *PloS one* 11, e0157982. doi:10.1371/journal.pone.0157982
- Ubani-Ukoma, U., Gibson, D., Schultz, G., Silva, B. O., and Chauhan, A. (2019). Evaluating the Potential of Drug Eluting Contact Lenses for Treatment of Bacterial Keratitis Using an *Ex Vivo* Corneal Model. *Int. J. Pharmaceutics* 565, 499–508. doi:10.1016/j.ijpharm.2019.05.031
- Vazirani, J., Wurity, S., and Ali, M. H. (2015). Multidrug-Resistant *Pseudomonas aeruginosa* Keratitis. *Ophthalmology* 122, 2110–2114. doi:10.1016/j.opht.2015.06.007
- Xiao, A., Dhand, C., Leung, C. M., Beuerman, R. W., Ramakrishna, S., and Lakshminarayanan, R. (2018). Strategies to Design Antimicrobial Contact Lenses and Contact Lens Cases. *J. Mater. Chem. B* 6, 2171–2186. doi:10.1039/c7tb03136j
- Xu, J., Xue, Y., Hu, G., Lin, T., Gou, J., Yin, T., et al. (2018). A Comprehensive Review on Contact Lens for Ophthalmic Drug Delivery. *J. Controlled Release* 281, 97–118. doi:10.1016/j.jconrel.2018.05.020

Conflict of Interest: The authors declare that the research was conducted in the absence of any commercial or financial relationships that could be construed as a potential conflict of interest.

Publisher's Note: All claims expressed in this article are solely those of the authors and do not necessarily represent those of their affiliated organizations, or those of the publisher, the editors and the reviewers. Any product that may be evaluated in this article, or claim that may be made by its manufacturer, is not guaranteed or endorsed by the publisher.

Copyright © 2021 Zhao, Wang, Feng, Song and Du. This is an open-access article distributed under the terms of the Creative Commons Attribution License (CC BY). The use, distribution or reproduction in other forums is permitted, provided the original author(s) and the copyright owner(s) are credited and that the original publication in this journal is cited, in accordance with accepted academic practice. No use, distribution or reproduction is permitted which does not comply with these terms.



Reactive Oxygen Species in Anticancer Immunity: A Double-Edged Sword

Jie Wang^{1,2}, Ning Liu², Hongfei Jiang^{1,2}, Qian Li^{2*} and Dongming Xing^{1,2,3*}

¹The Affiliated Hospital of Qingdao University, Qingdao University, Qingdao, China, ²Qingdao Cancer Institute, Qingdao University, Qingdao, China, ³School of Life Sciences, Tsinghua University, Beijing, China

OPEN ACCESS

Edited by:

Yong Liu,
University of Chinese Academy of
Sciences, China

Reviewed by:

Yuce Li,
Sungkyunkwan University, South
Korea
Wancun Zhang,
Zhengzhou University, China

*Correspondence:

Qian Li
liqian123@qdu.edu.cn
Dongming Xing
xdm@qdu.edu.cn

Specialty section:

This article was submitted to
Biomaterials,
a section of the journal
Frontiers in Bioengineering and
Biotechnology

Received: 28 September 2021

Accepted: 29 October 2021

Published: 17 November 2021

Citation:

Wang J, Liu N, Jiang H, Li Q and Xing D
(2021) Reactive Oxygen Species in
Anticancer Immunity: A Double-
Edged Sword.
Front. Bioeng. Biotechnol. 9:784612.
doi: 10.3389/fbioe.2021.784612

Reactive oxygen species (ROS) are critical mediators in many physiological processes including innate and adaptive immunity, making the modulation of ROS level a powerful strategy to augment anticancer immunity. However, current evidences suggest the necessity of a deeper understanding of their multiple roles, which may vary with their concentration, location and the immune microenvironment they are in. Here, we have reviewed the reported effects of ROS on macrophage polarization, immune checkpoint blocking (ICB) therapy, T cell activation and expansion, as well as the induction of immunogenic cell death. A majority of reports are indicating detrimental effects of ROS, but it is unadvisable to simply scavenge them because of their pleiotropic effects in most occasions (except in T cell activation and expansion where ROS are generally undesirable). Therefore, clinical success will need a clearer illustration of their multi-faced functions, as well as more advanced technologies to tune ROS level with high spatiotemporal control and species-specificity. With such progresses, the efficacy of current immunotherapies will be greatly improved by combining with ROS-targeted therapies.

Keywords: ROS, immunotherapy, macrophage polarization, T cell activation, immunogenic cell death

INTRODUCTION

Reactive oxygen species (ROS) are a class of highly reactive oxygen-derived chemicals, including hydroxyl radical ($\cdot\text{OH}$), singlet oxygen ($^1\text{O}_2$), superoxide anion ($\text{O}_2^{\cdot-}$), and peroxides. A group of biological reactions, with the oxidative metabolisms within mitochondria being a major source, can generate ROS in human body. Despite being byproducts in many occasions, ROS at suitable concentrations and locations are vital messengers in cellular signaling and can trigger important biosynthetic processes such as the crosslinking of extracellular matrix (Schieber and Chandel, 2014; Zhou et al., 2020). On the other hand, given the high reactivity of ROS that can be harmful to protein, DNA, and lipids, an antioxidant system has been built to maintain the homeostasis of ROS generation and elimination (Yu et al., 2020). Under pathological conditions, the delicate balance will be disturbed and usually lead to ROS accumulation and oxidative stress (Aggarwal et al., 2019). In oncology, evidence has linked the increased ROS level with cancer initiation, progression, angiogenesis, and metastasis (Moldogazieva et al., 2018), making ROS elimination a promising strategy for controlling the disease (Zheng et al., 2021). Paradoxically, ROS can also be beneficial for tumor suppression. For example, the expression of many tumor suppressor genes (e.g., *p53*) is controlled by ROS (Liu et al., 2008; Perillo et al., 2020); many drugs including chemotherapeutic and radiotherapeutic agents kill cancer cells by elevating ROS level; (Ji et al., 2021; Perillo et al., 2020) etc.

TABLE 1 | Representative studies reporting the ROS-promoted M2 polarization of macrophages.

Model	Tested markers	ROS modulation	Mechanisms of M2 polarization	References
Mouse bone marrow-derived macrophages	M1: CD86, TNF- α , IL-12; M2: IL-10, CCL17/18/24	O ₂ ^{•-} increment by NOX; elimination by BHA	ROS induce late-phase activation of ERK signaling	Zhang, et al. (2013)
Mouse RAW 264.7 macrophages	M1: CD11b; M2: CD206, Arg-1	mtROS; reduction by antioxidant	Antioxidant reduce M2 type via ROS/ERK and mTOR pathway	Shan, et al. (2017)
Primary human macrophages	M1: TNF- α , IL12b; M2: CD163, CD206	Increased via H ₂ O ₂ addition; reduced using MnTe	Presumably induce Stat3 activation for M2 polarization	Griess, et al. (2020)
Monocytes in human peripheral blood mononuclear cells	M1: not tested; M2: CD163, CD206	Increment via CAF stimulation; reduction by BHA	Not directly tested	Zhang, et al. (2017)
Mouse bone marrow-derived macrophages	M1: IL-6; M2: Arg-1, Mrc1, IL-10, Ym2, Fizz1	mtROS increment via GMFG knockdown; reduction by antioxidant	Increased mtROS presumably alters iron metabolism-related protein expression	Aerbajinai, et al. (2019)
Murine peritoneal macrophage	M1: IL-6, TNF- α , IL-1 β ; M2: Arg-1, Ym1, Fizz1-Relm- α	MCPIP-stimulated ROS production	ROS induced ER stress and autophagy to increase M2 markers	Kapoor, et al. (2015)

NOX: NADPH, oxidase; Arg-1: arginase-1; mtROS: mitochondria ROS; mTOR: mammalian target of rapamycin; MnTe: MnTE-2-PyP⁵⁺; Stat3: signal transducer and activator of transcription 3; CAF: cancer-associated fibroblasts; GMFG: glia maturation factor- λ ; MCPIP: MCP-1-induced protein.

Cancer immunotherapy strengthens one's own immune system to recognize and attack tumor cells. The last decade has witnessed the rapid development of immunotherapy with tens of different therapeutics at various treatment modalities been approved by regulatory administrations for clinical use (Smyth et al., 2016; Waldman et al., 2020; Yang et al., 2021). Interestingly, ROS play multiple roles in immunity and can be explored as potent targets to augment the magnitude and specificity of antitumor response (Kotsafti et al., 2020). A large number of studies have reported the benefits of ROS in anticancer immunity; however, the paradox still exists. The often-encountered immunosuppression, such as the attenuated T cell activation and activity (Qu et al., 2013), raises a necessity for researchers to build a clearer illustration about which role will ROS play under a given condition. This review summarizes recent studies reporting ROS-mediated enhancement or attenuation of antitumor immunity, with an expectation of providing basic rationales for improved immunotherapy.

INTERLACING ROLES OF ROS IN IMMUNOTHERAPY

Among the multiple fields ROS are functioning, the following four are of particular significance.

Macrophage Polarization

Macrophages play critical roles in tissue homeostasis by regulating tissue development, mediating inflammatory responses and clearing pathogens and cell debris (DeNardo and Ruffell, 2019; Zheng et al., 2021). They are inducible in function, with the classically activated M1 type exerting pro-inflammatory and antitumor activities while the M2 type functioning basically the opposite (Mills et al., 2016). Local ROS concentration has an obvious influence on the polarization of macrophages, and based on current evidences ROS may induce pro-inflammatory macrophages more dominantly than doing the opposite. They can activate

nuclear factor κ B (NF κ B) and p38 mitogen-activated protein kinase (MAPK) signaling pathways and promote the expression of M1-associated pro-inflammatory cytokines and chemokines (Rendra, et al., 2019). This mechanism is widely accepted in innate immunity and has also been reported to augment the antitumor immunity. For example, iron overload, which rapidly induced ROS production, polarized macrophages to pro-inflammatory phenotype, enhanced the activity of p300/CBP acetyltransferase and improved p53 acetylation (Zhou et al., 2018). However, other studies indicated the M2-promoting function of ROS. Typical studies involving diverse M2-promoting mechanisms have been summarized in Table 1.

Therefore, ROS can induce the differentiation of macrophages to both M1 and M2 types, raising uncertainty for the direction of ROS modulation (Rendra et al., 2019; Zhou et al., 2020). What further complicates the situation is that factors inducing M1 polarization may not provide benefits for cancer suppression. For example, it was shown that black raspberries, which served as an antioxidant, reduced the incidence of esophageal cancer by suppressing oxidative stress and NF κ B/MAPK signaling (Shi, et al., 2017). Given the presence of pathways that lead to contrary results, it can be envisioned that ROS may simultaneously exert opposite influences on macrophages, and the ultimate impact may depend on ROS concentration (including the relative concentration of different species), location and their interaction with therapeutic agents. It is noteworthy that besides M1/M2 polarization, ROS influence macrophages in many other aspects. Roux et al. showed that ROS mediated the immunosuppression effect of macrophages by up-regulating the expression of programmed death ligand-1 (PD-L1) (Roux et al., 2019). When treated with ROS inducers such as paclitaxel, PD-L1 expression was up-regulated on the surface of tumor-associated (TAMs) in a mouse model of triple negative breast cancer, via the activation of NF κ B signaling. Note that both M1 and M2 signatures positively correlated with the expression of PD-L1.

Efficacy of Immune Checkpoint Blockades

Using monoclonal antibodies to block the immune checkpoint-mediated immune escape has been one of the most promising strategy for tumor control (Havel et al., 2019). The immune microenvironment exerts a great influence on the treatment efficacy, while ROS serve as critical mediators. A large number of studies have shown that ROS generation would lead to augmented expression of the programmed death-ligand 1 (PD-L1) on cancer cells. A straight forward mechanism is that ROS elevation leads to the upregulation or stabilization of multiple transcription factors such as NF κ B and HIF-1 α , while NF κ B initiates PD-L1 expression by binding to the PD-L1 promoter (Guo et al., 2019), and HIF-1 α directly binds to a transcriptionally active hypoxia-response element in the PD-L1 proximal promoter (Noman et al., 2014). Note that hypoxia-induced HIF-1 α activation can either elevate ROS level *via* NOX or reduce ROS by inhibiting the tricarboxylic acid cycle (Chen et al., 2018). There are also studies reporting enhanced ROS generation with reduced PD-L1 expression or vice versa, as summarized in a review article (Bailly, 2020). Nevertheless, in most occasions the PD-L1 expression is positively correlated with ROS level, as demonstrated by using a large variety of ROS-modulating small molecules and human oncoviruses (Montani, et al., 2018). Meanwhile, the role macrophage plays in the connection between ROS and PD-L1 expression is worth noting. ROS is a critical mediator of macrophage polarization, while PD-L1 high expression has been found to be correlated with M2-polarization of macrophages (Zhu, et al., 2020). Therefore, skewing the M1/M2 balance of macrophages may be a potential route by which ROS modulate PD-L1 expression.

ROS also have an impact on programmed death-1 (PD-1) blocking therapy at least due to the ligand/receptor relationship of PD-L1/PD-1. Chamoto et al. reported that tumor-reactive T cells boosted by PD-L1 blockade possessed activated mitochondria with augmented ROS production, and improving ROS generation using ROS precursors or mitochondrial uncouplers synergized the antitumor activity of PD-1 blockade by expansion of effector/memory cytotoxic T cells in draining lymph nodes (Chamoto et al., 2017). A more recent study reported similar results, that in a “bilateral tumor model”, ROS increment in CD8⁺ T cells was observed only in tumors that were responsive to PD-1 blockade therapy (Kumar et al., 2020). Therefore, ROS level in tumoral and lymphatic cells might be a potential indicator of the responsiveness to PD-1/PD-L1 blockade therapy, especially considering that the expression of immune checkpoints has been accepted as a tumor-intrinsic sign of the vulnerability of tumors to ICB therapy (Zappasodi et al., 2018).

Cytotoxic T lymphocyte-associated antigen-4 (CTLA-4) is a vital regulator of T cell function. Studies directly exploring the effect of ROS on CTLA-4 therapy are rare to the best of our knowledge, but ROS have an obvious influence on the development of T regulatory cells (Tregs), on which CTLA-4 is constitutively expressed (Walker 2013). The effects are still multi-faced. For example, macrophage-generated ROS were functional for the induction of Tregs (Kraaij et al., 2010), while neutrophil cytosolic factor 1-deficient mice with a lower level of ROS also carried Tregs more reactive than those from wild

mice (Kim et al., 2014). Obviously, the expansion of CTLA-4 blocking therapy warrants further studies on the effects of ROS.

T Cell Activation and Expansion

Activation of T cells, as the pivotal step in cellular immunity, relies on the binding with main histocompatibility complex, the stimulation by co-stimulatory molecules on antigen-presenting cells, and a suitable biochemical environment that allows these processes to happen. ROS have a great influence on T cell activation. An example is that the local number and phenotype of macrophages, which often function as antigen presenting cells, can be re-/programmed by ROS as described above. Another aspect is the ROS-tuned expression of immune checkpoint molecules on immune cells and cancer cells. More directly, ROS can create an oxidative environment to inactivate T cells. It was reported that the redox level on cell surface physically determines the reactivity of T cells (Sahaf et al., 2003). Researchers found that mice were more susceptible to develop severe arthritis if ROS production was diminished, and then revealed that lower ROS level would increase the number of reduced thiol groups on T cell membrane surface and make T cells more prone to be activated (Gelderman et al., 2006). This is a necessary mechanism to prevent the over-activation of T cells in inflammatory sites, while for cancer treatment this is commonly undesirable (Moro-Garcia et al., 2018; Yin et al., 2021). Artificially increasing cell surface thiol by adding antioxidants (e.g., glutathione, GSH) or reducing ROS generation has been employed to increase the sensitivity of T cells to stimulatory signals (Kesarwani, et al., 2013).

Efficient expansion of tumor-specific T cells upon activation is necessary in cell therapy, and the failure to do so has been a major limitation for adoptive cell therapy to achieve broader application. It was shown that the persistence of effector CD8⁺ T cells and CD62L^{hi} central memory T cells were obviously longer if the cytosolic GSH and surface thiol were higher (Kesarwani et al., 2015), while GSH depletion prevented T cell proliferation despite the stimulation using antigens (Mak et al., 2017). Pretreatment with antioxidant N-acetyl cysteine (NAC) during *ex vivo* T cell expansion process significantly improved the persistence of adoptively transferred cells and led to more effective tumor control in a mouse model of melanoma (Scheffel et al., 2016). The underlying mechanism was revealed to be reduction in DNA damage by reducing ROS and the resultant reduced activation-induced cell death (an immunosuppressive process known to be induced by repeated stimulation of T cell receptor) of T cells in the presence of NAC (Scheffel et al., 2016). All these evidence suggests the necessity of adding antioxidants to the culture media of therapeutic T cell survival and expansion. Note that both GSH and NAC contain thiol groups as potent reducing moiety to scavenge electrons from highly reactive molecules, e.g., to consume ROS.

Immunogenic Cell Death

Cancer develops with mutations, resulting in the emergence of abundant neoepitopes (sequence-altered nucleic acids and proteins) that are foreign to host's immune system. Immune responses induced by a specific neoepitope may fail to damage

tumor cells that do not contain this neoepitope, while immunogenic cell death (ICD), which is featured by the release of tumor-associated antigens and danger-associated molecular patterns, will provide a full spectrum of neoepitopes to eliminate immune escape caused by tumor heterogeneity. ROS generally have an inducing effect to ICD occurrence. The induction of endoplasmic reticulum (ER) stress, surface exposure of calreticulin, and secretion of adenosine triphosphate (ATP), high-mobility group box 1 (HMGB1) and heat shock protein 70 (HSP70) are requisites for ICD (Bugaut et al., 2013; Van Loenhout et al., 2020), while many of these processes can be triggered by ROS. An example is that bleomycin (an anticancer drug relying on its ability to generate ROS) induced ER stress and autophagy, which then led to calreticulin exposure and release of HMGB1 and ATP to trigger ICD (Bugaut et al., 2013). Actually, many chemotherapeutic small molecules known to kill cancer cells *via* ROS generation are undergoing clinical trials as ICD inducers beyond chemo drugs, such as doxorubicin, bortezomib, and epirubicin (Vanmeerbeek et al., 2020). Other kinds of agents are also under exploration. For example, a fluorinated mitochondria-disrupting helical polypeptides, which could destabilize mitochondrial outer membrane, was developed to over-produce intracellular ROS (iROS), induce ICD and enhance PD-L1 blockade therapy (Jeong et al., 2021).

Particularly, a number of treatment modalities have intrinsic capability to induce ICD by producing ROS or other critical stimulators. 1) Photodynamic therapy (PDT), which kills cancer cells by generating abundant ROS with the assistance of photosensitizers and light irradiation, can induce ICD and antitumor immunity (Panzarini et al., 2013). Cellular internalization of photosensitizers causes high iROS level and ER stress especially when photosensitizers localizes near the ER. Using a ER-associated photosensitizer, hypericin, Garg et al. found that PDT generated obvious ER stress, and caused cancer cells to secrete ATP, display damage-associated molecular patterns on cell surface and undergo immunogenic apoptosis (Garg et al., 2012; Garg et al., 2012). The display of calreticulin was crucial by providing the motifs needed for the engulfment of PDT-treated cells by dendritic cells (Garg et al., 2012). Using other photosensitizers other than hypericin failed to induce the exposure of calreticulin on cell surface (Garg et al., 2012), suggesting the necessity of choosing suitable photosensitizers or choosing suitable drug carriers to afford enhanced affinity to ER. 2) Sonodynamic therapy is similar with PDT but employs ultrasound as the energy source (Li et al., 2021), and has been reported to elicit ICD. For instance, a nanocomposite loaded with chlorin e6 (as a sonosensitizer) induced ICD *via* receptor-interacting protein kinase 3-dependent cell necroptosis (Um et al., 2020). 3) Radiotherapy produces ROS *via* radiolysis and induce ICD, although the break of double-strand DNA was previously considered as the primary mechanism of tumor suppression in radiotherapy. Actually, ICD-mediated antitumor immunity has been recognized as the origin of abscopal effect in radiotherapy.

There are also studies reporting obvious inhibition of ICD-induced immune response by elevated ROS. Kazama et al.

reported that ROS would neutralize the stimulatory capacity of dying cells (Kazama et al., 2008). The results showed that caspase activation against mitochondria promoted immune tolerance of apoptotic cells by generating ROS to oxidize the HMGB1 (Kazama et al., 2008). HMGB1 potentially act on dendritic cells to stimulate immunity (Dumitriu et al., 2005), so its inactivation promotes immune tolerance. Using a ROS scavenger to consume extracellular ROS (eROS) enhanced the stimulatory effect of dying cells by avoiding the oxidation of HMGB1 (Deng et al., 2020). Therefore, as depicted in **Figure 1**, there might be a need to induce ER stress *via* iROS and simultaneously eliminate eROS to avoid the oxidation of the exposed calreticulin and the released stimulatory molecules.

CONCLUSIONS AND PERSPECTIVES

ROS are continuously generated in a large variety of biochemical reactions. Although a majority of studies are linking them to disease states such as insulin resistance, inflammation, and cancer, ROS play important roles in immune responses. This warrants a very clear understanding of the multi-faced but tunable roles of ROS. There may be more studies reporting detrimental effects of ROS on antitumor immunity than those indicating beneficial effects, since they can drive macrophages to polarize to immunosuppressive types, promote the expression of PD-L1, attenuate the efficacy of ICB therapy, deactivate T cells and inhibit the occurrence of ICD. However, it is not wise to simply scavenge ROS because they have pleiotropic effects in most cases, and also because the detrimental/beneficial switch can be easily shifted by modulating ROS concentration, location, species, and the scenarios they are in. For example, ROS can increase the expression of PD-L1, but it is unachievable to eliminate PD-L1 by scavenging ROS and doing so will greatly attenuate the immuno-stimulatory effects of ROS and cause redox imbalance-related adverse effects. Therefore, clinical application of directly tuning ROS level still has a long way to go.

Meanwhile, most of the reported works have studied ROS as a whole without distinguishing their species, possibly due to the limited specificity of detection probes (e.g., 2',7'-dichlorodihydrofluorescein) to ROS species (which include $\cdot\text{OH}$, $\text{O}_2^{\cdot-}$ and H_2O_2). Free radicals ($\cdot\text{OH}$ and $\text{O}_2^{\cdot-}$) can readily trigger chain reactions and produce various carbon-centered radicals, while H_2O_2 are relatively long-lived and inactive compared with free radicals and commonly exert oxidative capability with the assistance of metal ions such as iron and copper. Such a chemical basis provides a good reason to consider that different species will cause varied magnitude of oxidative stress and mediate distinct signaling pathways (Collin, 2019). The location of the studied ROS is another parameter being important but easily ignored. For example, ROS-producing nanomaterials are widely employed to treat cancer, while the main location (e.g., intracellular or extracellular; intra-lysosomal or intracytoplasmic) is hard to determine since the cellular internalization rate and lysosomal escape efficiency of nanomaterials are difficult to quantify. In this context, choosing biomaterials as ROS inducers with well-defined pharmacokinetics will help. With

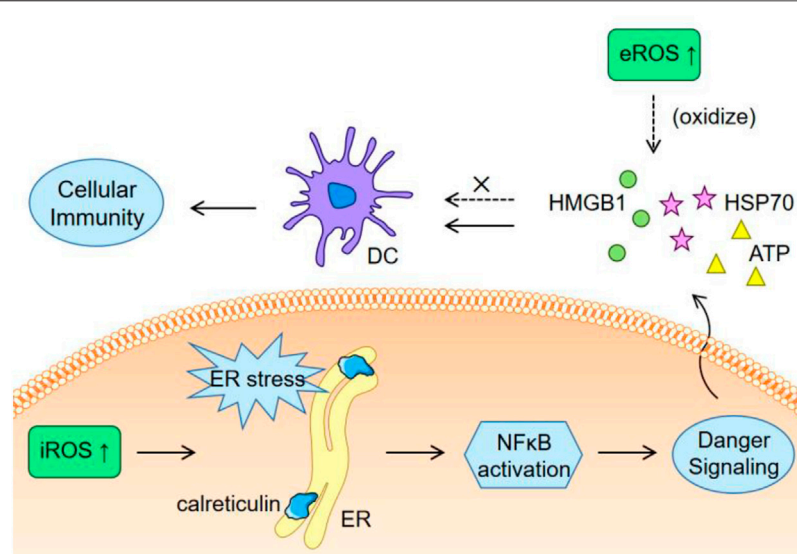


FIGURE 1 | Schematic illustration of the different effects of iROS and eROS on ICD.

the building of such theoretical rationales and technical capabilities, ROS-targeted therapy will eventually synergize with current immunotherapies.

AUTHOR CONTRIBUTIONS

JW and NL: conceptualization. JW and HJ: drafting. QL and DX: editing and revision. All authors contributed to the article and approved the submitted version.

REFERENCES

- Aerbajinai, W., Ghosh, M. C., Liu, J., Kumkhaek, C., Zhu, J., Chin, K., et al. (2019). Glia Maturation Factor- γ Regulates Murine Macrophage Iron Metabolism and M2 Polarization through Mitochondrial ROS. *Blood Adv.* 3, 1211–1225. doi:10.1182/bloodadvances.2018026070
- Aggarwal, V., Tuli, H., Varol, A., Thakral, F., Yerer, M., Sak, K., et al. (2019). Role of Reactive Oxygen Species in Cancer Progression: Molecular Mechanisms and Recent Advancements. *Biomolecules* 9, 735. doi:10.3390/biom9110735
- Bailly, C. (2020). Regulation of PD-L1 Expression on Cancer Cells with ROS-Modulating Drugs. *Life Sci.* 246, 117403. doi:10.1016/j.lfs.2020.117403
- Bugaut, H., Bruchard, M., Berger, H., Derangère, V., Odoul, L., Euvrard, R., et al. (2013). Bleomycin Exerts Ambivalent Antitumor Immune Effect by Triggering Both Immunogenic Cell Death and Proliferation of Regulatory T Cells. *PLoS One* 8, e65181. doi:10.1371/journal.pone.0065181
- Chamoto, K., Chowdhury, P. S., Kumar, A., Sonomura, K., Matsuda, F., Fagarasan, S., et al. (2017). Mitochondrial Activation Chemicals Synergize with Surface Receptor PD-1 Blockade for T Cell-dependent Antitumor Activity. *Proc. Natl. Acad. Sci. USA* 114, E761–E770. doi:10.1073/pnas.1620433114
- Chen, R., Lai, U. H., Zhu, L., Singh, A., Ahmed, M., and Forsyth, N. R. (2018). Reactive Oxygen Species Formation in the Brain at Different Oxygen Levels: The Role of Hypoxia Inducible Factors. *Front. Cell Dev. Biol.* 6, 132. doi:10.3389/fcell.2018.00132
- Collin, F. (2019). Chemical Basis of Reactive Oxygen Species Reactivity and Involvement in Neurodegenerative Diseases. *Int. J. Mol. Sci.* 20, 2407. doi:10.3390/ijms20102407

FUNDING

This work was financially supported by China Postdoctoral Science Foundation (2021T140355), Postdoctoral Innovation Project of Shandong Province (202002025), the Youth Innovation Team Talent Introduction Program of Shandong Province (20190164), the Qingdao Major Scientific and Technological Project for Distinguished Scholars (20170103).

- DeNardo, D. G., and Ruffell, B. (2019). Macrophages as Regulators of Tumour Immunity and Immunotherapy. *Nat. Rev. Immunol.* 19, 369–382. doi:10.1038/s41577-019-0127-6
- Deng, H., Yang, W., Zhou, Z., Tian, R., Lin, L., Ma, Y., et al. (2020). Targeted Scavenging of Extracellular ROS Relieves Suppressive Immunogenic Cell Death. *Nat. Commun.* 11, 4951. doi:10.1038/s41467-020-18745-6
- Dumitriu, I. E., Baruah, P., Valentinis, B., Voll, R. E., Herrmann, M., Nawroth, P. P., et al. (2005). Release of High Mobility Group Box 1 by Dendritic Cells Controls T Cell Activation via the Receptor for Advanced Glycation End Products. *J. Immunol.* 174, 7506–7515. doi:10.4049/jimmunol.174.12.7506
- Garg, A. D., Krysko, D. V., Vandenabeele, P., and Agostinis, P. (2012). Hypericin-based Photodynamic Therapy Induces Surface Exposure of Damage-Associated Molecular Patterns like HSP70 and Calreticulin. *Cancer Immunol. Immunother.* 61, 215–221. doi:10.1007/s00262-011-1184-2
- Garg, A. D., Krysko, D. V., Verfaillie, T., Kaczmarek, A., Ferreira, G. B., Marysael, T., et al. (2012). A Novel Pathway Combining Calreticulin Exposure and ATP Secretion in Immunogenic Cancer Cell Death. *EMBO J.* 31, 1062–1079. doi:10.1038/emboj.2011.497
- Gelderman, K. A., Hultqvist, M., Holmberg, J., Olofsson, P., and Holmdahl, R. (2006). T Cell Surface Redox Levels Determine T Cell Reactivity and Arthritis Susceptibility. *Proc. Natl. Acad. Sci.* 103, 12831–12836. doi:10.1073/pnas.0604571103
- Gilardini Montani, M. S., Santarelli, R., Falcinelli, L., Gonnella, R., Granato, M., Di Renzo, L., et al. (2018). EBV Up-regulates PD-L1 on the Surface of Primary Monocytes by Increasing ROS and Activating TLR Signaling and STAT3. *J. Leukoc. Biol.* 104, 821–832. doi:10.1002/JLB.2A0118-029RR
- Griess, B., Mir, S., Datta, K., and Teoh-Fitzgerald, M. (2020). Scavenging Reactive Oxygen Species Selectively Inhibits M2 Macrophage Polarization and Their

- Pro-tumorigenic Function in Part, via Stat3 Suppression. *Free Radic. Biol. Med.* 147, 48–60. doi:10.1016/j.freeradbiomed.2019.12.018
- Guo, R., Li, Y., Wang, Z., Bai, H., Duan, J., Wang, S., et al. (2019). Hypoxia-inducible Factor-1 α and Nuclear factor- κ B Play Important Roles in Regulating Programmed Cell Death Ligand 1 Expression by Epidermal Growth Factor Receptor Mutants in Non-small-cell Lung Cancer Cells. *Cancer Sci.* 110, 1665–1675. doi:10.1111/cas.13989
- Havel, J. J., Chowell, D., and Chan, T. A. (2019). The Evolving Landscape of Biomarkers for Checkpoint Inhibitor Immunotherapy. *Nat. Rev. Cancer* 19, 133–150. doi:10.1038/s41568-019-0116-x
- Jeong, S. D., Jung, B. K., Ahn, H. M., Lee, D., Ha, J., Noh, I., et al. (2021). Immunogenic Cell Death Inducing Fluorinated Mitochondria-Disrupting Helical Polypeptide Synergizes with PD-L1 Immune Checkpoint Blockade. *Adv. Sci.* 8, 2001308. doi:10.1002/advs.202001308
- Ji, Y., Han, Z., Ding, H., Xu, X., Wang, D., Zhu, Y., et al. (2021). Enhanced Eradication of Bacterial/Fungi Biofilms by Glucose Oxidase-Modified Magnetic Nanoparticles as a Potential Treatment for Persistent Endodontic Infections. *ACS Appl. Mater. Inter.* 13, 17289–17299. doi:10.1021/acsami.1c01748
- Kapoor, N., Niu, J., Saad, Y., Kumar, S., Sirakova, T., Becerra, E., et al. (2015). Transcription Factors STAT6 and KLF4 Implement Macrophage Polarization via the Dual Catalytic powers of MCP1. *J. Immunol.* 194, 6011–6023. doi:10.4049/jimmunol.1402797
- Kazama, H., Ricci, J.-E., Herndon, J. M., Hoppe, G., Green, D. R., and Ferguson, T. A. (2008). Induction of Immunological Tolerance by Apoptotic Cells Requires Caspase-dependent Oxidation of High-Mobility Group Box-1 Protein. *Immunity* 29, 21–32. doi:10.1016/j.immuni.2008.05.013
- Kesarwani, P., Murali, A. K., Al-Khami, A. A., and Mehrotra, S. (2013). Redox Regulation of T-Cell Function: From Molecular Mechanisms to Significance in Human Health and Disease. *Antioxid. Redox Signaling* 18, 1497–1534. doi:10.1089/ars.2011.4073
- Kesarwani, P., Thyagarajan, K., Chatterjee, S., Palanisamy, V., and Mehrotra, S. (2015). Anti-oxidant Capacity and Anti-tumor T Cell Function: A Direct Correlation. *Oncoimmunology* 4, e985942. doi:10.4161/2162402X.2014.985942
- Kim, H.-R., Lee, A., Choi, E.-J., Hong, M.-P., Kie, J.-H., Lim, W., et al. (2014). Reactive Oxygen Species Prevent Imiquimod-Induced Psoriatic Dermatitis through Enhancing Regulatory T Cell Function. *PLoS One* 9, e91146. doi:10.1371/journal.pone.0091146
- Kotsafti, A., Scarpa, M., Castagliuolo, I., and Scarpa, M. (2020). Reactive Oxygen Species and Antitumor Immunity-From Surveillance to Evasion. *Cancers* 12, 1748. doi:10.3390/cancers12071748
- Kraaij, M. D., Savage, N. D. L., van der Kooy, S. W., Koekkoek, K., Wang, J., van den Berg, J. M., et al. (2010). Induction of Regulatory T Cells by Macrophages Is Dependent on Production of Reactive Oxygen Species. *Proc. Natl. Acad. Sci. USA* 107, 17686–17691. doi:10.1073/pnas.1012016107
- Kumar, A., Chamoto, K., Chowdhury, P. S., and Honjo, T. (2020). Tumors Attenuating the Mitochondrial Activity in T Cells Escape from PD-1 Blockade Therapy. *eLife* 9, e52330. doi:10.7554/eLife.52330
- Li, Y., Xie, J., Um, W., You, D. G., Kwon, S., Zhang, L., et al. (2021). Sono/Photodynamic Nanomedicine-Elicited Cancer Immunotherapy. *Adv. Funct. Mater.* 31, 2008061. doi:10.1002/adfm.202008061
- Liu, B., Chen, Y., and St. Clair, D. K. (2008). ROS and P53: a Versatile Partnership. *Free Radic. Biol. Med.* 44, 1529–1535. doi:10.1016/j.freeradbiomed.2008.01.011
- Mak, T. W., Grusdat, M., Duncan, G. S., Dostert, C., Nonnenmacher, Y., Cox, M., et al. (2017). Glutathione Primes T Cell Metabolism for Inflammation. *Immunity* 46, 675–689. doi:10.1016/j.immuni.2017.03.019
- Mills, C. D., Lenz, L. L., and Harris, R. A. (2016). A Breakthrough: Macrophage-Directed Cancer Immunotherapy. *Cancer Res.* 76, 513–516. doi:10.1158/0008-5472.CAN-15-1737
- Moldogazieva, N. T., Lutsenko, S. V., and Terentiev, A. A. (2018). Reactive Oxygen and Nitrogen Species-Induced Protein Modifications: Implication in Carcinogenesis and Anticancer Therapy. *Cancer Res.* 78, 6040–6047. doi:10.1158/0008-5472.CAN-18-0980
- Moro-García, M. A., Mayo, J. C., Sainz, R. M., and Alonso-Arias, R. (2018). Influence of Inflammation in the Process of T Lymphocyte Differentiation: Proliferative, Metabolic, and Oxidative Changes. *Front. Immunol.* 9, 339. doi:10.3389/fimmu.2018.00339
- Noman, M. Z., Desantis, G., Janji, B., Hasmim, M., Karray, S., Dessen, P., et al. (2014). PD-L1 Is a Novel Direct Target of HIF-1 α , and its Blockade under Hypoxia Enhanced MDSC-Mediated T Cell Activation. *J. Exp. Med.* 211, 781–790. doi:10.1084/jem.20131916
- Panzarini, E., Inguscio, V., and Dini, L. (2013). Immunogenic Cell Death: Can it Be Exploited in PhotoDynamic Therapy for Cancer? *Biomed. Res. Int.* 2013, 1–18. doi:10.1155/2013/482160
- Perillo, B., Di Donato, M., Pezone, A., Di Zazzo, E., Giovannelli, P., Galasso, G., et al. (2020). ROS in Cancer Therapy: the Bright Side of the Moon. *Exp. Mol. Med.* 52, 192–203. doi:10.1038/s12276-020-0384-2
- Qu, K., Shen, N.-y., Xu, X.-s., Su, H.-b., Wei, J.-c., Tai, M.-h., et al. (2013). Emodin Induces Human T Cell Apoptosis *In Vitro* by ROS-Mediated Endoplasmic Reticulum Stress and Mitochondrial Dysfunction. *Acta Pharmacol. Sin.* 34, 1217–1228. doi:10.1038/aps.2013.58
- Rendra, E., Riabov, V., Mossel, D. M., Sevastyanova, T., Harmsen, M. C., and Kzyshkowska, J. (2019). Reactive Oxygen Species (ROS) in Macrophage Activation and Function in Diabetes. *Immunobiology* 224, 242–253. doi:10.1016/j.imbio.2018.11.010
- Roux, C., Jafari, S. M., Shinde, R., Duncan, G., Cescon, D. W., Silvester, J., et al. (2019). Reactive Oxygen Species Modulate Macrophage Immunosuppressive Phenotype through the Up-Regulation of PD-L1. *Proc. Natl. Acad. Sci. USA* 116, 4326–4335. doi:10.1073/pnas.1819473116
- Sahaf, B., Heydari, K., Herzenberg, L. A., and Herzenberg, L. A. (2003). Lymphocyte Surface Thiol Levels. *Proc. Natl. Acad. Sci.* 100, 4001–4005. doi:10.1073/pnas.2628032100
- Scheffel, M. J., Scurti, G., Simms, P., Garrett-Mayer, E., Mehrotra, S., Nishimura, M. I., et al. (2016). Efficacy of Adoptive T-Cell Therapy Is Improved by Treatment with the Antioxidant N-Acetyl Cysteine, Which Limits Activation-Induced T-Cell Death. *Cancer Res.* 76, 6006–6016. doi:10.1158/0008-5472.CAN-16-0587
- Schieber, M., and Chandel, N. S. (2014). ROS Function in Redox Signaling and Oxidative Stress. *Curr. Biol.* 24, R453–R462. doi:10.1016/j.cub.2014.03.034
- Shan, M., Qin, J., Jin, F., Han, X., Guan, H., Li, X., et al. (2017). Autophagy Suppresses Isoprenaline-Induced M2 Macrophage Polarization via the ROS/ERK and mTOR Signaling Pathway. *Free Radic. Biol. Med.* 110, 432–443. doi:10.1016/j.freeradbiomed.2017.05.021
- Shi, N., Chen, F., Zhang, X., Clinton, S., Tang, X., Sun, Z., et al. (2017). Suppression of Oxidative Stress and NF κ B/MAPK Signaling by Lyophilized Black Raspberries for Esophageal Cancer Prevention in Rats. *Nutrients* 9, 413. doi:10.3390/nu9040413
- Smyth, M. J., Ngiow, S. F., Ribas, A., and Teng, M. W. L. (2016). Combination Cancer Immunotherapies Tailored to the Tumour Microenvironment. *Nat. Rev. Clin. Oncol.* 13, 143–158. doi:10.1038/nrclinonc.2015.209
- Um, W., Ko, H., You, D. G., Lim, S., Kwak, G., Shim, M. K., et al. (2020). Necroptosis-Inducible Polymeric Nanobubbles for Enhanced Cancer Sonoimmunotherapy. *Adv. Mater.* 32, 1907953. doi:10.1002/adma.201907953
- Van Loenhout, J., Peeters, M., Bogaerts, A., Smits, E., and Deben, C. (2020). Oxidative Stress-Inducing Anticancer Therapies: Taking a Closer Look at Their Immunomodulating Effects. *Antioxidants* 9, 1188. doi:10.3390/antiox9121188
- Vanmeerbeek, I., Sprooten, J., De Ruyscher, D., Tejpar, S., Vandenberghe, P., Fucikova, J., et al. (2020). Trial Watch: Chemotherapy-Induced Immunogenic Cell Death in Immuno-Oncology. *Oncoimmunology* 9, 1703449. doi:10.1080/2162402X.2019.1703449
- Waldman, A. D., Fritz, J. M., and Lenardo, M. J. (2020). A Guide to Cancer Immunotherapy: from T Cell Basic Science to Clinical Practice. *Nat. Rev. Immunol.* 20, 651–668. doi:10.1038/s41577-020-0306-5
- Walker, L. S. K. (2013). Treg and CTLA-4: Two Intertwining Pathways to Immune Tolerance. *J. Autoimmun.* 45, 49–57. doi:10.1016/j.jaut.2013.06.006
- Yang, L., Pijuan-Galito, S., Rho, H. S., Vasilevich, A. S., Eren, A. D., Ge, L., et al. (2021). High-Throughput Methods in the Discovery and Study of Biomaterials and Materiobiology. *Chem. Rev.* 121, 4561–4677. doi:10.1021/acs.chemrev.0c00752
- Yin, X., Hao, Y., Lu, Y., Zhang, D., Zhao, Y., Mei, L., et al. (2021). Bio-Multifunctional Hydrogel Patches for Repairing Full-Thickness Abdominal Wall Defects. *Adv. Funct. Mater.* 31, 2105614. doi:10.1002/adfm.202105614
- Yu, Z., Li, Q., Wang, J., Yu, Y., Wang, Y., Zhou, Q., et al. (2020). Reactive Oxygen Species-Related Nanoparticle Toxicity in the Biomedical Field. *Nanoscale Res. Lett.* 15, 115. doi:10.1186/s11671-020-03344-7

- Zappasodi, R., Wolchok, J. D., and Merghoub, T. (2018). Strategies for Predicting Response to Checkpoint Inhibitors. *Curr. Hematol. Malign. Rep.* 13, 383–395. doi:10.1007/s11899-018-0471-9
- Zhang, A., Qian, Y., Ye, Z., Chen, H., Xie, H., Zhou, L., et al. (2017). Cancer-associated Fibroblasts Promote M2 Polarization of Macrophages in Pancreatic Ductal Adenocarcinoma. *Cancer Med.* 6, 463–470. doi:10.1002/cam4.993
- Zhang, Y., Choksi, S., Chen, K., Pobezińska, Y., Linnoila, I., and Liu, Z.-G. (2013). ROS Play a Critical Role in the Differentiation of Alternatively Activated Macrophages and the Occurrence of Tumor-Associated Macrophages. *Cell Res* 23, 898–914. doi:10.1038/cr.2013.75
- Zheng, W., Hao, Y., Wang, D., Huang, H., Guo, F., Sun, Z., et al. (2021). Preparation of Triamcinolone Acetonide-Loaded Chitosan/fucoidan Hydrogel and its Potential Application as an Oral Mucosa Patch. *Carbohydr. Polym.* 272, 118493. doi:10.1016/j.carbpol.2021.118493
- Zheng, W., Zhou, Q., and Yuan, C. (2021). Nanoparticles for Oral Cancer Diagnosis and Therapy. *Bioinorganic Chem. Appl.* 2021, 1–14. doi:10.1155/2021/9977131
- Zhou, Q., Chen, J., Luan, Y., Vainikka, P. A., Thallmair, S., Marrink, S. J., et al. (2020). Unidirectional Rotating Molecular Motors Dynamically Interact with Adsorbed Proteins to Direct the Fate of Mesenchymal Stem Cells. *Sci. Adv.* 6, eaay2756. doi:10.1126/sciadv.aay2756
- Zhou, Y., Que, K.-T., Zhang, Z., Yi, Z. J., Zhao, P. X., You, Y., et al. (2018). Iron Overloaded Polarizes Macrophage to Proinflammation Phenotype through ROS/acetyl-p53 Pathway. *Cancer Med.* 7, 4012–4022. doi:10.1002/cam4.1670
- Zhou, Z., Ni, K., Deng, H., and Chen, X. (2020). Dancing with Reactive Oxygen Species Generation and Elimination in Nanotheranostics for Disease Treatment. *Adv. Drug Deliv. Rev.* 158, 73–90. doi:10.1016/j.addr.2020.06.006
- Zhu, Z., Zhang, H., Chen, B., Liu, X., Zhang, S., Zong, Z., et al. (2020). PD-L1-Mediated Immunosuppression in Glioblastoma Is Associated with the Infiltration and M2-Polarization of Tumor-Associated Macrophages. *Front. Immunol.* 11, 588552. doi:10.3389/fimmu.2020.588552

Conflict of Interest: The authors declare that the research was conducted in the absence of any commercial or financial relationships that could be construed as a potential conflict of interest.

Publisher's Note: All claims expressed in this article are solely those of the authors and do not necessarily represent those of their affiliated organizations, or those of the publisher, the editors and the reviewers. Any product that may be evaluated in this article, or claim that may be made by its manufacturer, is not guaranteed or endorsed by the publisher.

Copyright © 2021 Wang, Liu, Jiang, Li and Xing. This is an open-access article distributed under the terms of the Creative Commons Attribution License (CC BY). The use, distribution or reproduction in other forums is permitted, provided the original author(s) and the copyright owner(s) are credited and that the original publication in this journal is cited, in accordance with accepted academic practice. No use, distribution or reproduction is permitted which does not comply with these terms.



An Antioxidant Enzyme Therapeutic for Sepsis

Feifei Li^{1,2}, Ran Yan³, Jun Wu², Zeren Han¹, Meng Qin^{1,2*}, Chaoyong Liu^{1,2*} and Yunfeng Lu³

¹Beijing Advanced Innovation Center for Soft Matter Science and Engineering, Beijing University of Chemical Technology, Beijing, China, ²College of Life Science and Technology, Beijing University of Chemical Technology, Beijing, China, ³Department of Chemical and Biomolecular Engineering, The University of California, Los Angeles, CA, United States

OPEN ACCESS

Edited by:

Qihui Zhou,
Qingdao University,
China

Reviewed by:

Cuihong Yang,
Chinese Academy of Medical
Sciences and Peking
Union Medical College, China
Zhuo Ao,
National Center for Nanoscience and
Technology (CAS), China

*Correspondence:

Meng Qin
qinmeng212@mail.buct.edu.cn
Chaoyong Liu
chaoyongliu@mail.buct.edu.cn

Specialty section:

This article was submitted to
Biomaterials,
a section of the journal
Frontiers in Bioengineering and
Biotechnology

Received: 23 October 2021

Accepted: 08 November 2021

Published: 23 November 2021

Citation:

Li F, Yan R, Wu J, Han Z, Qin M, Liu C
and Lu Y (2021) An Antioxidant
Enzyme Therapeutic for Sepsis.
Front. Bioeng. Biotechnol. 9:800684.
doi: 10.3389/fbioe.2021.800684

Sepsis is a systemic inflammatory response syndrome caused by infections that may lead to organ dysfunction with high mortality. With the rapid increase in the aging population and antimicrobial resistance, developing therapeutics for the treatment of sepsis has been an unmet medical need. Excessive production of reactive oxygen species (ROS) during inflammation is associated with the occurrence of sepsis. We report herein a treatment for sepsis based on PEGylated catalase, which can effectively break down hydrogen peroxide, a key component of ROS that is chemically stable and able to diffuse around the tissues and form downstream ROS. PEGylated catalase can effectively regulate the cytokine production by activated leukocytes, suppress the elevated level of AST, ALT, TNF- α , and IL-6 in mice with induced sepsis, and significantly improve the survival rate.

Keywords: sepsis, reactive oxygen species, cytokines, enzyme therapeutic, catalase

INTRODUCTION

Sepsis is a life-threatening organ dysfunction caused by the host's unbalanced response to infection. Septic shock is a type of sepsis in which the changes in metabolism, cells, and hemodynamics significantly increase the likelihood of fatality (Singer et al., 2016; Rhodes et al., 2017; Korneev, 2019). Relevant studies have shown that there are more than 19 million sepsis patients worldwide each year, of which 6 million patients die, and the case fatality rate is greater than 25%. About 3 millions of those who survived had cognitive impairments that severely affected their quality of life (Reinhart et al., 2017; Aziz and Wang, 2019). Septic shock is also one of the common clinical manifestations of severe patients with COVID-19 (Huang et al., 2020). People over 65 years of age, infants, immunocompromised patients, and patients with autoimmune diseases, tumors, kidney diseases, and lung diseases are the most susceptible to sepsis (Gotts and Matthay, 2016). At present, treatments for sepsis mainly include fluid therapy (crystal fluid and albumin), antibacterial drugs, vasoactive drugs (norepinephrine), glucocorticoids, injection immunoglobulin, etc (Rhodes et al., 2017). Due to factors such as individual difference, aging, and antimicrobial resistance, the morbidity and mortality of sepsis remain high.

It has been documented that cytokines (Rittirsch et al., 2008) and reactive oxygen species (ROS) (Mittal et al., 2014) play essential roles in sepsis. Reactive oxygen species (ROS) mainly come from cell respiration, protein folding, or various by-products of metabolism (Reczek and Chandel, 2015). In another source, it is mainly produced by NADPH oxidase, which mainly exists in phagocytes and vascular endothelial cells (Lambeth, 2004; Mittal et al., 2014). ROS mainly include superoxide anion (O_2^-), hydroxyl radical (OH^\cdot), hydrogen peroxide (H_2O_2), and hypochlorous acid (HOCl), etc (Thannickal and Fanburg, 2000; Mittal et al., 2014; Reczek and Chandel, 2015). Partial reduction of O_2 and electron-transfer reactions in the mitochondria generate O_2^- , which is converted to hydrogen

peroxide (H_2O_2) mediated by superoxide dismutase (SOD) (Lambeth, 2004; Phaniendra et al., 2015). H_2O_2 may be subsequently reacted generating OH through the Fenton's reaction (Reyhani et al., 2019), HOCl through myeloperoxidase (MPO), H_2O through glutathione/glutathione peroxidase (GSH/GPX), and $\text{H}_2\text{O}/\text{O}_2$ through catalase (CAT) (Patlevič et al., 2016). Under pathological conditions, an unbalance of the generation and elimination of ROS results in oxidative stress with excess ROS. Since H_2O_2 is chemically stable and able to diffuse through cells and tissues, it may accumulate locally or systematically (Majewska et al., 2004) and activate the inflammatory response (Naik and Dixit, 2011).

Upon the occurrence of infection, leukocytes are attracted to affected sites and release cytokines and ROS (Qin et al., 2020). An excessive level of ROS may damage the biological macromolecules such as DNA, proteins, and lipids, which may cause dysfunction of cells and tissues (Yang et al., 2019) and further exacerbate the immune response. Uncontrolled production of ROS and cytokines may eventually lead to excessive inflammatory response and cytokine storm. Therefore, eliminating the excessively produced H_2O_2 helps to reduce the oxidative stress and to regulate the expression of pro-inflammatory cytokines, which is beneficial for the treatment of sepsis.

Organisms can effectively regulate their H_2O_2 levels through efficient enzymatic reactions. Catalase is the most abundant antioxidant enzyme commonly found in the liver, erythrocytes, and alveolar epithelial cells, and is the most effective catalyst for the decomposition of H_2O_2 (Nishikawa et al., 2009). Catalase has attracted much attention in maintaining normal physiological functions and relieving pathological processes. However, exogenous catalase generally exhibits poor *in vivo* stability and short plasma half-life (only 6–10 min) (Qi et al., 2021), which preclude its broad use as therapeutics. Conjugation therapeutic proteins with poly (ethylene glycol) (PEG) is the golden standard to improve their pharmacokinetics and immunogenicity, which has been approved by the Food and Drug Administration (Abuchowski et al., 1977; Kinstler et al., 2002; Basu et al., 2006). Herein, we explore the use of PEG-conjugated catalase as a therapeutic treatment for sepsis. Our results suggest that PEGylated catalase can effectively regulate cytokine production by activated leukocytes, suppress the elevated level of AST, ALT, TNF- α , and IL-6 in mice with induced sepsis, and significantly improve the survival rate of the mice.

MATERIALS AND METHODS

Materials

All reagents were used as received unless otherwise specified. Catalase (CAT) from *Aspergillus niger* was purchased from Sunson Industry Group (Beijing, China). Methoxy polyethylene glycol acetic acid N-succinimidyl ester, Mw 20,000 (mPEG-NHS 20000) was purchased from JenKem Technology (Beijing, China). Trypsin and the 2,7-Dichlorodihydrofluorescein diacetate (DCFH-DA) were

purchased from Sigma Aldrich (St. Louis, MO). Sulfo-Cyanine7 NHS ester was purchased from Beijing Okeanos Technology Co., Ltd. (Beijing, China). Lipopolysaccharides (LPS) (*Escherichia coli* 055: B5), Cell Counting Kit-8 (CCK-8), Bicinchoninic Acid (BCA) Protein Assay Kit, Catalase Activity Assay Kit, Endotoxin Erasol and Hoechst were purchased from Beijing Solarbio Science and Technology Co., Ltd. (Beijing, China). Tachypiens Amebocyte Lysate was purchased Zhanjiang Bokang Marine Biology Co., Ltd. (Zhanjiang, China). D-galactosamine (D-GalN) was purchased from J&K Scientific (Beijing, China). Human pulmonary alveolar epithelial (HPAEpi) cells were purchased from BeNa Culture Collection (Beijing, China). Alanine Aminotransferase Kit (ALT) and Aspartate Aminotransferase Kit (AST) were purchased from Abcam (Cambridge, United Kingdom). Mouse TNF- α enzyme-linked immunosorbent assay (ELISA) kit and mouse IL-6 ELISA kit were purchased from PeptoTech (Suzhou, China). TUNEL Apoptosis Detection Kit was purchased Boster Biological Technology Co., Ltd. (Wuhan, China). Zeba Spin 7 K MWCO Desalting Columns was purchased from Thermo Fisher Scientific, Inc. (Waltham, MA). Amicon ultra centrifugal filter was purchased from Merck Millipore (Burlington, MA). Roswell Park Memorial Institute 1,640 Medium (RPMI), fetal bovine serum (FBS), penicillin/streptomycin (P/S, 1%), trypsin-EDTA (0.25%) were purchased from Corning (Corning, NY).

Instruments

The purity of catalase was examined by a size-exclusion column with a separation range of 10,000 Da–10,000,000 Da BioCore SEC-300) using a high-performance liquid chromatography (HPLC, 1,260 Infinity II system, Agilent) system. Transmission electron microscope (TEM, HT7700, Hitachi Ltd.) was employed to characterize the morphologies of CAT-PEG. Dynamic light scattering (DLS) measurements were performed on a Zetasizer Nano instrument (Malvern Instruments Ltd., United Kingdom) with a 10-mW helium–neon laser and thermoelectric temperature controller. Fluorescent intensity was measured with a Spectra Max M2 plate reader (Molecular Devices). The bioluminescent imaging of the mice was imaged with the IVIS Imaging System (IVIS Spectrum, PerkinElmer). H and E images were taken using inverted fluorescence microscope fluorescence microscope (BK-FL4, ChongQing Optec Instrument Co., Ltd.). TUNEL images were taken using a confocal laser scanning microscopy (Leica TCS SP8). The complete blood count and blood biochemical examination were performed using auto biochemistry analyzer (BS-420, Mindray) and auto hematology analyzer (RJ-0C107223, Mindray), respectively.

Animals

Balb/c mice (6 weeks old; weight range, 18–22 g) were purchased from Beijing Huafukang Biotechnology Co., Ltd. All mice received human care in accordance with the guidelines of the local Institute of Health on the care and use of laboratory animals. The mice were socially housed under standardized conditions of light (12 h day/night rhythm), temperature (22°C) and humidity (55%), environmental enrichment, and had access to food and water ad libitum.

Synthesis of Catalase-PEG

Catalase (CAT) was conjugated with methoxy polyethylene glycol acetic acid N-succinimidyl ester (mPEG-NHS) through the reaction of NHS ester with primary amine. Briefly, CAT was dialyzed against phosphate buffer (200 mM, pH 8.0) to remove any amine-reactive salt. After dialysis, the CAT solution was diluted to 0.5 mg/ml with phosphate buffer (200 mM, pH 8.0), followed by addition of mPEG-NHS solution (100 mg/ml in anhydrous DMSO) at a molar ratio of 500:1 (mPEG-NHS to CAT). The reaction was kept at room temperature for 2 h to achieve the conjugation. The unreacted mPEG-NHS was removed by an ultracentrifugal filter with a molecular weight cutoff of 100 kDa using 1× Phosphate-Buffered Saline (PBS, pH 7.4) as the washing buffer. The resulting PEGylated CAT (CAT-PEG) was then placed at 4°C for further use.

Fluorescence Labeling of Catalase and Catalase-PEG

For the imaging purposes, CAT and CAT-PEG were fluorescently labeled with sulfo-Cyanine7 NHS ester (sulfo-Cy7-NHS), respectively. Briefly, 1 mg sulfo-Cy7-NHS was first dissolved in 200 µl anhydrous DMSO to make a stock solution (5 mg/ml). To achieve the labeling, sulfo-Cy7-NHS was added to CAT or CAT-PEG at a molar ratio of 5:1 (sulfo-Cy7-NHS to CAT), and the reaction was kept at room temperature for 2 h under dark. Finally, excess sulfo-Cy7-NHS was removed using a desalting column equilibrated with 1× PBS (pH = 7.4). The resulting sample was then placed at 4°C for further use.

Preparation of Endotoxin-free Catalase and Catalase-PEG

The endotoxins in the CAT or CAT-PEG sample were removed using Endotoxin Erasol according to the manufacture's protocol. Briefly, endotoxin erasol and the samples were mixed at a volume ratio of 10:1. The mixture was then placed on ice for 5 min and incubated at 37°C for 5 min. Afterwards, the mixture was centrifuged at 12,000 rpm for 10 min at room temperature to collect the upper supernatant. This process was repeated for at least three times until the endotoxin level in the sample was below 5 EU/ml. The endotoxin level was determined using the tachypleus amebocyte lysate method according to the manufacture's protocol. All the reagents and vials used during the preparation and detection process should be endotoxin-free.

Characterization of Catalase and Catalase-PEG

Sodium dodecyl sulfate polyacrylamide gel electrophoresis (SDS-PAGE). SDS-PAGE was carried out in a 10% (w/v) polyacrylamide resolving gel. Briefly, 15 µl of CAT (0.5 mg/ml) or CAT-PEG (0.5 mg/ml) solution was mixed with 5× loading buffer (Solarbio) and incubated at 70°C for 15 min. Then, the samples were applied to 10% (w/v) sodium dodecyl sulfate polyacrylamide gel for electrophoresis at 120 V for 60 min. The gel was stained with Coomassie Brilliant Blue R-250 staining solution (Solarbio) for 1 h at room temperature, and

then de-stained in the solution of 10% glacial acetic acid and 30% methanol overnight.

Transmission electron microscopy (TEM). TEM sample was prepared by dropping 10 µl of CAT-PEG (0.5 mg/ml) on a copper grid, followed by staining using 1% phosphotungstic acid solution for 2 min. The grid was then rinsed three times with deionized water and dried for further observation with an HT7700 field emission electron microscope operated at 100 kV.

Dynamic light scattering (DLS) measurement. DLS experiments were performed with a Zetasizer Nano instrument equipped with a 10-mW helium-neon laser and thermoelectric temperature controller. The measurements were taken at 25°C with a 90° scattering angle. The sizes and the standard derivations of CAT and CAT-PEG were obtained by averaging the values of at least three measurements. Zeta potentials of CAT and CAT-PEG were determined by photon correlation spectroscopy using a Zetasizer Nano instrument. The measurements were performed at 25°C with a detection angle of 90°, and the raw data were subsequently correlated to Z average mean size using a cumulative analysis by the Zetasizer software package.

High pressure liquid chromatography (HPLC) measurement. HPLC measurement was conducted using an Agilent 1,260 Infinity II high-performance liquid chromatography packed with a BioCore™ SEC column (NanoChrom Analytical Technology Co., Ltd.). The flow rate of the mobile phase (phosphate buffer, 10 mM, pH 8.0) was set at 1 ml/min to establish a baseline, after which 50 µl of CAT (1 mg/ml) or CAT-PEG (1 mg/ml) was injected under a flow rate of mobile phase at 0.5 ml/min. The signals of CAT and CAT-PEG were monitored by a UV detector at the wavelength of 405 nm.

Determination of the Catalase and Catalase-PEG Concentrations

The concentrations of CAT and CAT-PEG were determined by optical absorption measurements using an extinction coefficient of $\epsilon = 324,000 \text{ M}^{-1} \text{ cm}^{-1}$ at 405 nm (Samejima and Yang, 1963). The concentration of Cy7-labeled CAT or CAT-PEG was determined with the BCA protein assay. Briefly, the BCA working reagent were prepared by mixing 50 volumes of BCA reagent with 1 volume of Cu reagent (50:1) together. Standard curves of CAT were established using CAT with a series of concentrations (0.03125, 0.0625, 0.125, 0.25, 0.5, 1 mg/ml). This was achieved by repeating 2-fold dilutions of 1 mg/ml CAT solution with PBS. Then the standard sample and Cy7-labeled CAT were mixed with the BCA working reagent in a volume ratio of 1:10, respectively, and incubated at 37°C for 30 min. The absorbance at 562 nm was determined with a UV/Vis spectrophotometer (NanoDrop, Thermo Fisher Scientific). Concentration of the Cy7-labeled CAT or CAT-PEG was calculated by using its absorbance at 562 nm and the standard curve established at the same condition.

Determination of the Catalase and Catalase-PEG Activities

The activities of CAT and CAT-PEG were tested using a catalase activity assay kit according to the manufacture's protocol. Briefly,

1 ml of H_2O_2 solution (pH = 7.4, 0.1 M HEPES buffer, H_2O_2 concentration 0.03% w/v) and 35 μl of sample were added to a 1 ml quartz cuvette and mixed for 5 s. Then, the absorbance at 240 nm was measured immediately (A1) and after 1 min (A2), respectively. The activity of catalase was calculated by the following equation: catalase activity (U/mL) = $[\Delta A \times V_{\text{total}} \div (\epsilon \times d) \times 10^6] \div V_{\text{sample}} \div T = 678 \times \Delta A$. Where $\Delta A = A1 - A2$; V_{total} stands for the total volume of the reaction system, 1.035 ml; ϵ stands for the molar absorptivity of H_2O_2 , 43.6 L/mol/cm; d stands for the optical path of cuvette, 1 cm; V_{sample} stands for the volume of the sample added, 0.035 ml; T stands for the reaction time, 1 min.

Determination of the Catalase and Catalase-PEG Stabilities

To measure the proteolytic stability of CAT or CAT-PEG, trypsin was mixed with CAT or CAT-PEG at a final trypsin concentration of 50 $\mu\text{g}/\text{ml}$ and a final CAT concentration of 0.1 mg/ml. The mixture was incubated at 37°C for 4 h, followed by the enzyme activity test using a similar method as abovementioned. To measure the psychological stability of CAT-PEG, CAT-PEG was diluted with 1× PBS to a final concentration of 0.1 mg/ml, and further incubated at 37°C for 24, 48, 72, 96 and 120 h, respectively. The enzyme activity was then tested using a catalase activity assay kit as abovementioned.

Cytotoxicity of Catalase-PEG

The cytotoxicity of CAT-PEG was evaluated by measuring the cell viability after the incubation of human pulmonary alveolar epithelial (HPAEpi) cells with different amount of CAT-PEG. Briefly, HPAEpi cells were seeded into a 96-well plate (1×10^4 cells/well, 100 $\mu\text{l}/\text{well}$) and cultured in RPMI1640 supplemented with 10% FBS and 1% P/S for 24 h. The cells were then incubated with 20, 100, 500, or 1,000 $\mu\text{g}/\text{ml}$ of CAT-PEG for 24 h, respectively. The cell viability was then assessed using CCK-8 Kit (Hao et al., 2021; Zheng et al., 2021), and measured the absorbance at 450 nm by a plate reader. The viability of untreated cells was used as 100% during the data analysis.

The Ability of Catalase-PEG to Eliminate the Intracellular Reactive Oxygen Species

The ability of CAT-PEG to regulate the intracellular ROS level was investigated in the HPAEpi cells with a fluorescent probe for ROS (DCFH-DA). Briefly, HPAEpi cells were seeded in a glass-bottomed cell culture dish (1×10^5 cells/dish) and cultured in RPMI1640 for 24 h. Then, HPAEpi cells were incubated with 8, 16, and 40 $\mu\text{g}/\text{ml}$ of CAT-PEG for 12 h, respectively, followed by incubation with 10 μM DCFH-DA in the dark for 30 min at 37°C. Then the intracellular ROS of the HPAEpi cells was induced by incubating 1 mM H_2O_2 with the cells for 30 min at 37°C. The cell nuclei were stained with Hoechst and washed extensively with a fresh RPMI1640 medium for further observation using a confocal laser scanning microscopy (Leica TCS SP8).

To quantify the intracellular level of ROS, HPAEpi cells were seeded in 96-well plate (1×10^4 cells/well, 100 $\mu\text{l}/\text{well}$) and cultured in RPMI1640 for 24 h. Then cells were incubated with 8, 16, and 40 $\mu\text{g}/\text{ml}$ of CAT-PEG for 12 h, respectively, followed by

incubation with 10 μM DCFH-DA in the dark for 30 min at 37°C. Then the intracellular ROS of the HPAEpi cells was induced by incubating 1 mM H_2O_2 with the cells for 30 min at 37°C. After being rinsed with cold PBS three times, the DCFH-DA fluorescence was measured using a plate reader (Ex. = 488 nm, Em. = 525 nm).

The Ability of Catalase-PEG to Prevent Cell Injury

The ability of CAT-PEG to prevent cell injury was evaluated in a H_2O_2 -induced cell injury model (Qin et al., 2020). Briefly, HPAEpi cells were seeded into a 96-well plate (1×10^4 cells/well, 100 $\mu\text{l}/\text{well}$) and cultured in RPMI1640 for 24 h. Then, HPAEpi cells were incubated with 8, 16, and 40 $\mu\text{g}/\text{ml}$ of CAT-PEG for 12 h, respectively, followed by addition of H_2O_2 at a final concentration of 500 μM . The cells were cultured for another 24 h for cell viability test. The cell viability was measured and analyzed as abovementioned.

The Ability of Catalase-PEG to Regulate the Production of Inflammatory Factors

An *in-vitro* model by co-culture of leukocytes and HPAEpi cells was used to confirm the ability of CAT-PEG to regulate cytokine production as previously reported (Qin et al., 2020). Leukocytes were separated from whole blood from a donor according to the protocol provided by Thermo Fisher Scientific. The model was induced by addition of lipopolysaccharides (LPS) at a final concentration of 1 $\mu\text{g}/\text{ml}$ to the co-cultured leukocytes and HPAEpi cells to activate the leukocytes. CAT-PEG was then added at a final concentration of 8, 16, and 40 $\mu\text{g}/\text{ml}$, respectively, and further incubated with the cells for 12 h. The concentrations of TNF- α and IL-6 in the media were measured with an enzyme-linked immunosorbent assay kit following the protocols provided. HPAEpi cells without any treatment, HPAEpi cells treated with 1 $\mu\text{g}/\text{ml}$ LPS, and co-cultured leukocytes and HPAEpi cells without any treatment were used as controls.

Pharmacokinetics of Catalase and Catalase-PEG

To evaluate the pharmacokinetics, BALB/c mice (8 w, 22 ± 2 g, $n = 3$) received 5 mg/kg CAT or CAT-PEG through tail-vein injection, and blood samples were collected at 0.1, 1, 2, 4, 6, 12, 24, 36 and 48 h post-injection. The serum was separated from the whole blood by centrifugation at 4,000 g for 10 min, and the serum catalase activity was assessed by the catalase activity assay kit as abovementioned. To plot the pharmacokinetics curve, the activity of each serum sample was normalized to the activity of the serum collected from the mice treated with CAT-PEG at 0.1 h, which was recorded as 100%.

Biodistribution of Catalase and Catalase-PEG

To assess the biodistribution of CAT-PEG, CAT and CAT-PEG labeled with sulfo-Cy7-NHS were used for intravenous injection,

respectively. BALB/c mice (8 w, 22 ± 2 g) received 5 mg/kg of sulfo-Cy7-labeled CAT or sulfo-Cy7-labeled CAT-PEG through tail-vein injection and were euthanized 6, 12, 24, and 48 h post-injection. The organs of these animals (heart, liver, spleen, lung, and kidney) were collected and imaged with an *in vivo* imaging system (IVIS spectrum). The fluorescence intensity of region-of-interests (ROI) was inspected by Living Image software. Each sample has triplicates to generate statistical significance.

***In vivo* Therapeutic Efficacy of Catalase-PEG in the Sepsis Model**

The sepsis model was established as previously reported (Lehmann et al., 1987; Silverstein, 2004; Poli-de-Figueiredo et al., 2008; Maes et al., 2016). Briefly, 20 healthy mice were evenly divided into two groups. Each mouse was intravenously injected with LPS (100 µg/kg) and D-GalN (800 mg/kg) through the tail vein to induce the model. One hour after the injection of LPS/D-GalN, the model animals were injected with either 5 mg/kg CAT-PEG or equal volume of 1× PBS through the tail-vein. Healthy mice without any treatment were used as control. The survival rates of the mice were monitored for 12 h after CAT-PEG injection.

Blood Routine and Blood Chemistry Tests

For the blood routine and blood chemistry tests, the blood samples were collected 6 h after the injection of CAT-PEG or PBS to the model mice. For the blood routine examination, 100 µl of blood samples were taken from the orbital venous plexus of the anesthetized mice and placed in an anticoagulant tube. Blood routine examination was then performed using the whole blood by a routine blood test instrument. For the blood chemistry assay, 300–500 µl of blood was collected from the orbital venous cluster of the anesthetized mice and placed in a centrifuge tube at room temperature for 1 h for a clot to form. The serum was separated from the whole blood by centrifugation at 4,000 g for 10 min. ALT and AST activities were measured using ALT Activity Assay Kit and AST Activity Assay Kit, respectively, according to the manufacturer's instructions. TNF-α and IL-6 levels were profiled in the blood of treated animals using murine TNF-α and IL-6-specific ELISA assays according to the manufacturer's instructions.

Histologic Analysis

Six hours after the injection of CAT-PEG or PBS to the model mice, the mice were anesthetized by isoflurane and perfused with 50 ml of cold 1×PBS through the vascular system. Afterwards, the heart, liver, spleen, lung, and kidney tissues were dissected and fixed in 4% paraformaldehyde; and subsequently embedded in paraffin for histologic analysis. Sections (5 µm) were cut and dried, deparaffinized, and rehydrated. Then, the sections were stained with hematoxylin-eosin (H and E) using a standard protocol and analyzed by light microscopy. Terminal deoxynucleotidyl transferase dUTP nick-end labeling (TUNEL) assay was performed using a TUNEL Apoptosis Detection Kit according to the manufacturer's protocol. The nuclei were stained with DAPI and further imaged by a Confocal Laser Scanning Microscope.

Statistical Analysis

All results are presented as the mean \pm standard error of the mean (s.e.m.) as indicated. Paired t-tests and one-way ANOVA were used for multiple comparisons (when more than two groups were compared). All statistical analyses were conducted with Prism Software (Prism 8.0).

RESULT

Characterization of Catalase and Catalase-PEG

Figure 1A shows high pressure liquid chromatography (HPLC) of CAT and CAT-PEG, denoted respectively as CAT and CAT-PEG hereinafter. Compared with CAT, CAT-PEG shows a shorter retention time indicating successful conjugation of CAT with PEG (**Figure 1A**). Sodium dodecyl sulphate-polyacrylamide gel electrophoresis (SDS-PAGE) revealed CAT-PEG mainly remained in the upper end due to the conjugation with PEG (**Supplementary Figure S1**). Transmission electron microscopic (TEM) image confirmed CAT-PEG has an average size of 15 nm (**Figure 1B**). Consistently, dynamic light scattering (DSL) suggests CAT-PEG displays a size distribution centered at 17 nm and zeta potential near neutral, in comparison with CAT with a size centered at 10 nm and a negative zeta potential of 6.5 mV (**Figures 1C,D**). The changes of CAT in size and zeta potential after PEG conjugation are consistent with previous studies, which can be attributed to the formation of the PEG layer around the CAT and the shielding effect by such a PEG layer (Harris and Chess, 2003). Compared with CAT, CAT-PEG exhibited a similar enzymatic activity (**Figure 1E**) and a significantly enhanced enzyme stability (**Figure 1F**). After incubation in PBS with 1 mg/ml trypsin at 37°C for 4 h, CAT-PEG and CAT retained 79 and 40% of the activity, respectively. This is mainly due to the hydration layer formed by the combination of PEG and the hydrogen bond of water molecules in the solution, which protects the active center of the protein and makes it difficult to be hydrolyzed by protease (Harris and Chess, 2003). Furthermore, after incubation with PBS at 37°C for 120 h, CAT-PEG still retained 90% of its activity (**Supplementary Figure S2**), which will be beneficial for its *in vivo* use.

The Ability of Catalase-PEG to Eliminate the Intracellular Reactive Oxygen Species and Prevent Cell Injury

We first investigated the cytotoxicity of CAT-PEG by culturing HPAEpi cells with different concentrations of CAT-PEG (**Supplementary Figure S3**). The cells with CAT-PEG exhibited similar or higher cell viability than the control cells, indicating that CAT-PEG did not show any noticeable cytotoxicity to HPAEpi cells. To investigate the ability of CAT-PEG to eliminate the intracellular ROS, the HPAEpi cells were first incubated with different concentrations of CAT-PEG, followed by exposing the cells to H₂O₂, a commonly used intracellular ROS inducer, to induce a cell injury model. The intracellular ROS was subsequently detected with DCFH-DA, a fluorescent probe for ROS. **Figure 2A** shows the fluorescence images of the HPAEpi cells after different treatments. The cells

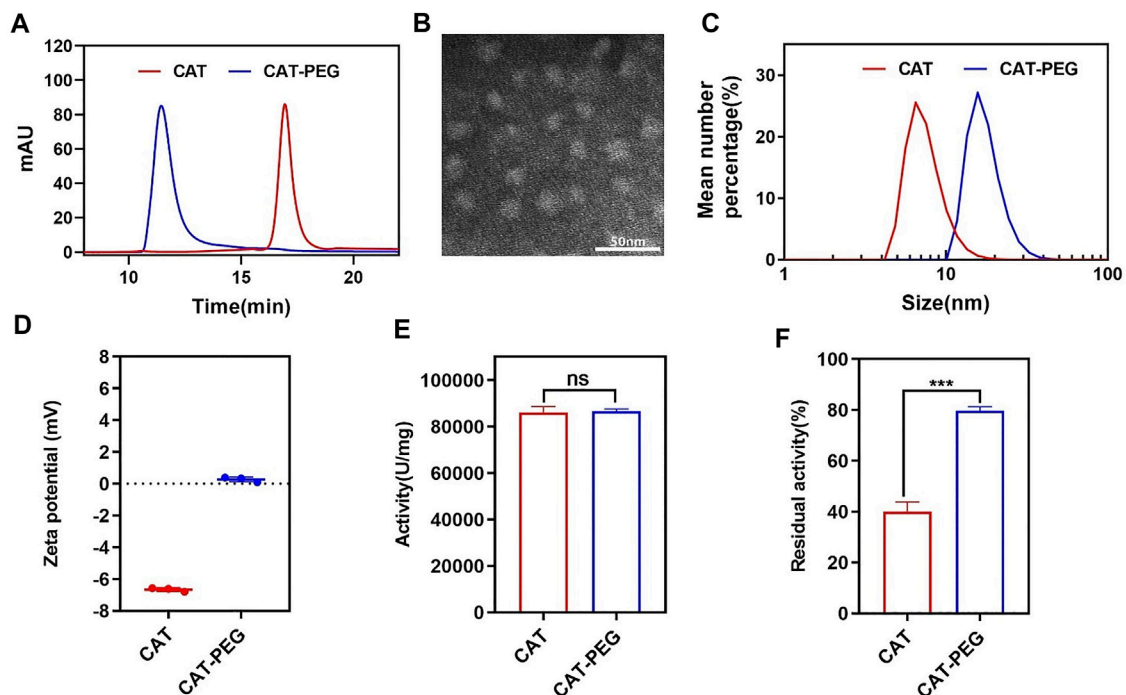


FIGURE 1 | Characteristics of CAT and CAT-PEG. **(A)** HPLC of CAT and CAT-PEG; **(B)** TEM image of CAT-PEG; **(C)** DLS and **(D)** zeta potential of CAT and CAT-PEG; **(E)** The enzyme activity and **(F)** proteolytic stability of CAT and CAT-PEG. $n = 3$. Data represent means \pm s.e.m. *** $p < 0.001$. ns means not significant.

with H_2O_2 show highly intense fluorescence (high level of intracellular ROS), whereas the cells with CAT-PEG show decreased fluorescence signal as the CAT-PEG concentration increased from 8 $\mu\text{g/ml}$ to 40 $\mu\text{g/ml}$, confirming CAT-PEG can effectively eliminate the intracellular ROS. Further quantitative results showed that the H_2O_2 -treated cells exhibit 2.5-folds higher fluorescence intensity than those cells with 40 $\mu\text{g/ml}$ of CAT-PEG treatment (Figure 2B). Such an eliminated ROS ability by CAT-PEG can prevent the cells from oxidative injury. As shown in Figure 2C, the cells without CAT-PEG treatment show only a viability of 25%, while the cells with the treatment of 8 $\mu\text{g/ml}$, 16 $\mu\text{g/ml}$ and 40 $\mu\text{g/ml}$ of CAT-PEG retain 43, 89 and 100% of the cell viability, respectively. These results suggest that CAT-PEG can reduce the intracellular ROS level of the HPAEpi cells and prevent the cells from oxidative injury.

The Ability of Catalase-PEG to Regulate the Production of Inflammatory Factors

Sepsis is a systemic inflammatory response syndrome caused by infection and mediated by immune cells (Matsuda et al., 2012). In the early stage of inflammation, release of pro-inflammatory factors such as TNF- α and IL-6 stimulates the endogenous immune response. However, in patients with sepsis, the uncontrolled release of such cytokines may cause a series of pathological damages (Cai et al., 2010). In addition, such pro-inflammatory cytokines may also activate the blood coagulation system and upregulate the expression of inflammatory mediators, leading to the occurrence of life-threatening syndrome (Kast,

2000). In this context, regulating the production of cytokines is essential to restore a homeostasis, and TNF- α antagonist has been suggested for the alleviation of hyperinflammation in severe cases (Marchesoni et al., 2009).

The ability of CAT-PEG to regulate the production of cytokines was studied using human leukocytes (white blood cells, WBC) and HPAEpi cells. To test the ability of CAT-PEG to regulate the production of cytokines, leukocytes and HPAEpi cells were cultured with lipopolysaccharides (LPS, a bacterial endotoxin that activates leukocytes) with and without CAT-PEG. The cells without CAT-PEG treatment showed significantly increased secretion of both TNF- α and IL-6. The cells with CAT-PEG showed dramatically reduced levels of TNF- α and IL-6 when the leukocytes were pre-cultured with CAT-PEG followed by adding LPS (Pre-addition) or pre-cultured with LPS followed by addition of CAT-PEG (Post-addition) (Figures 2D,E). This study suggests that CAT-PEG can downregulate the production of TNF- α and IL-6 by the activated leukocytes.

For therapeutic use, we first investigated the pharmacokinetics and biodistribution of CAT-PEG in mice using near-infrared fluorescence imaging. Two groups of healthy BALB/c mice were intravenously injected with the same amount of CAT or CAT-PEG. Figure 3A shows the plasma concentrations of CAT and CAT-PEG, where CAT-PEG exhibits a much longer half-life (5.30 h) than CAT (0.36 h), an approximate improvement of 15 folds (Supplementary Table S1). To further investigate the biodistribution of CAT-PEG, same amount of CAT and CAT-PEG was fluorescently labeled with sulfo-Cy7 and intravenously injected to two groups of healthy BALB/c mice respectively. Figure 3B shows the fluorescence imaging of the

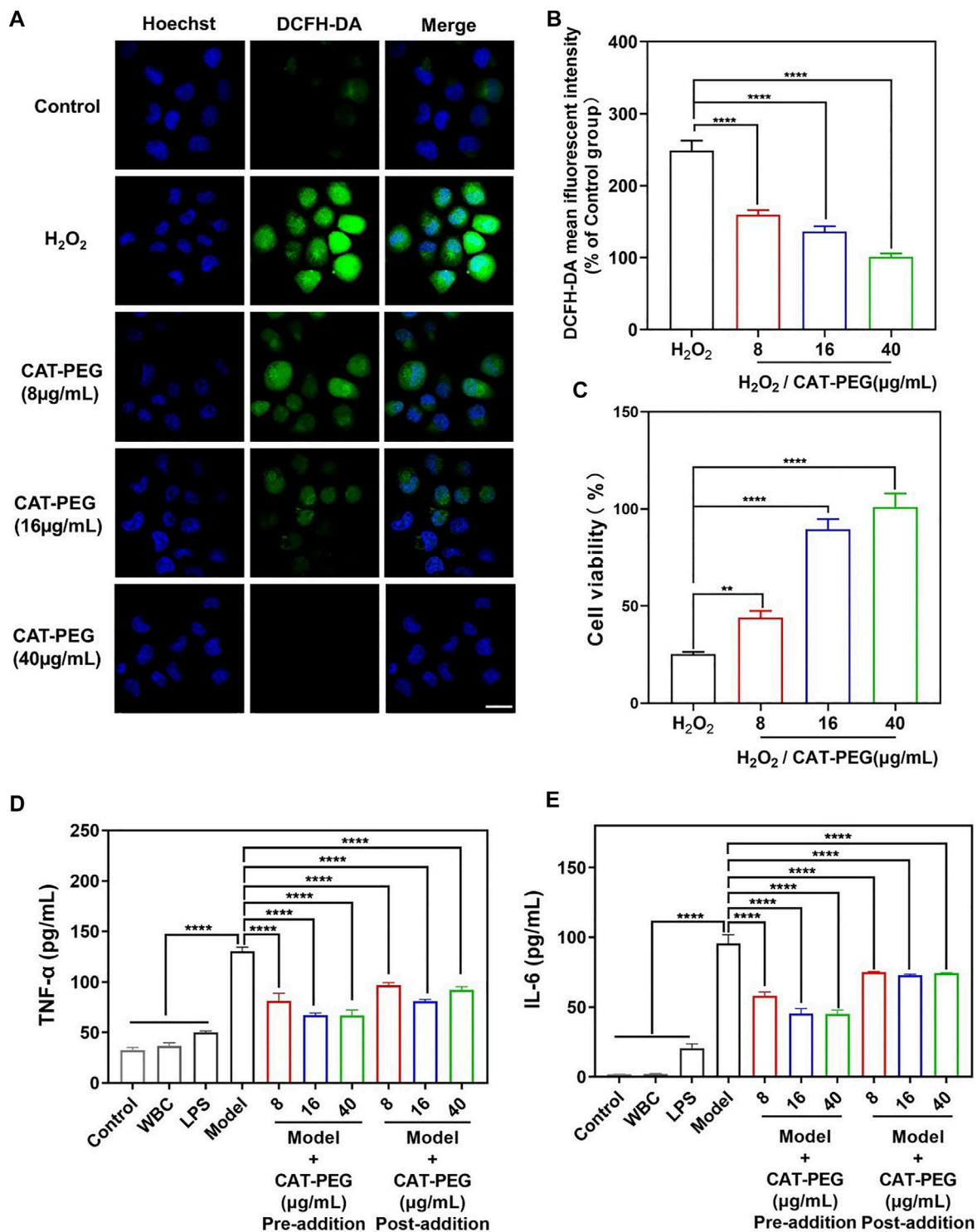


FIGURE 2 | The ability of CAT-PEG to reduce ROS level, prevent cell injury and to regulate the production of inflammatory factors. **(A)** Fluorescence images of HPAEpi cells after incubation with CAT-PEG for 12 h followed by adding 1 mM H_2O_2 and 10 μ M DCFH-DA and incubating for 30 min (green: ROS, blue: nuclei). Scale bar: 50 μ m. **(B)** Relative fluorescent intensity of DCFH-DA in the HPAEpi cells after incubation with CAT-PEG for 12 h followed by adding 1 mM H_2O_2 and 10 μ M DCFH-DA and incubating for 30 min (% of Control group). **(C)** Cell viability of the HPAEpi cells with 8 μ g/mL, 16 μ g/mL, 40 μ g/mL of CAT-PEG for 12 h, followed by addition of H_2O_2 (1 mM) and culturing for 24 h. **(D, E)** The concentration of TNF- α (D) and IL-6 (E) in the media of HPAEpi cells cultured with WBC, LPS, and different concentrations of CAT-PEG. In the Pre-addition study, HPAEpi cells were first cultured with different concentrations of CAT-PEG for 12 h, followed by adding LPS (1 μ g/mL) and culturing for 24 h. In the Post-addition study, HPAEpi cells were cultured with 1 μ g/mL LPS for 24 h, followed by culturing in fresh media containing different concentrations of CAT-PEG for 12 h $n = 3$. Data represent means \pm s.e.m., p value: * $p < 0.05$, ** $p < 0.01$, *** $p < 0.001$ and **** $p < 0.0001$. ns means not significant.

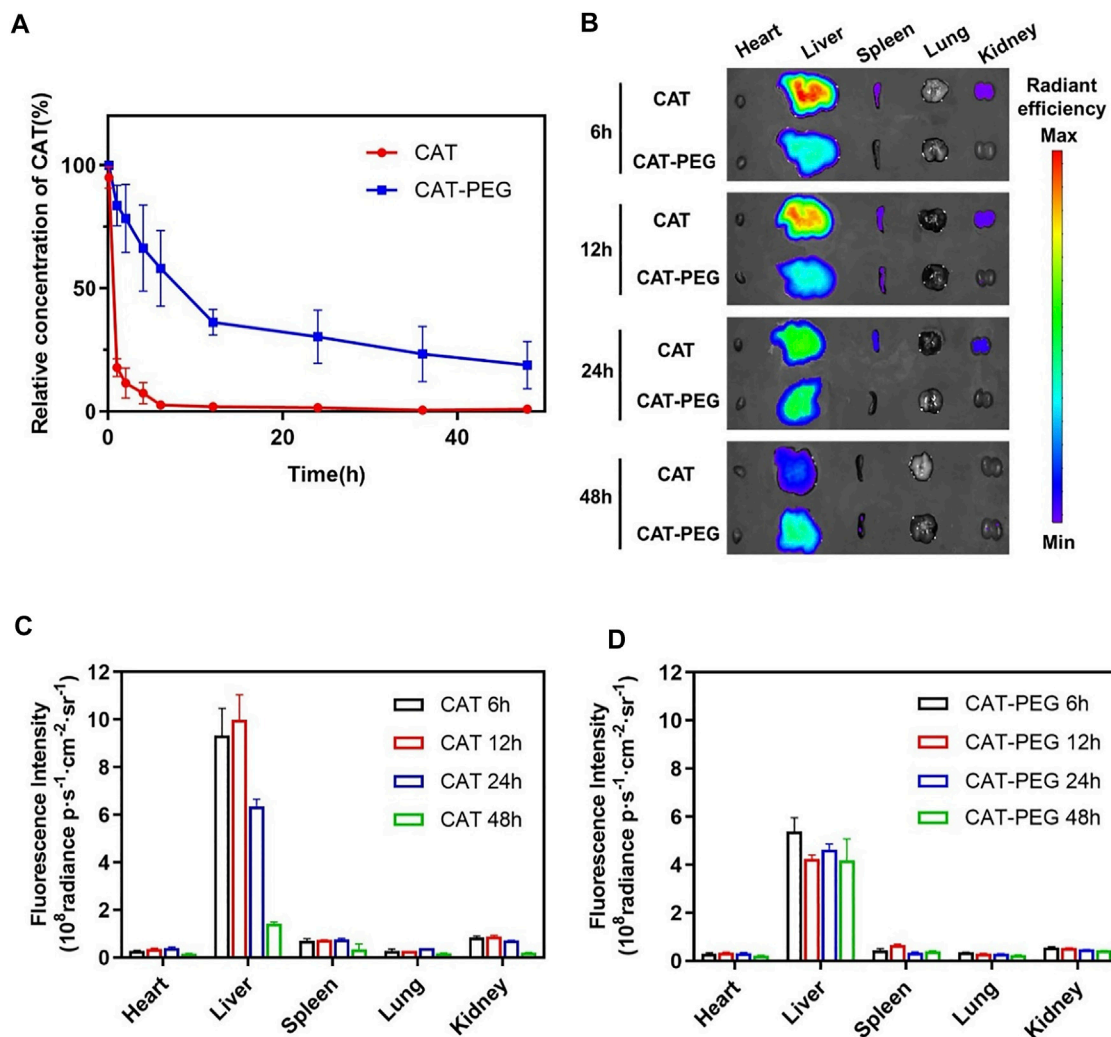


FIGURE 3 | Pharmacokinetics and biodistribution of CAT and CAT-PEG. **(A)** Pharmacokinetics of CAT and CAT-PEG after intravenous administration of 5 mg/kg^{-1} CAT or CAT-PEG. **(B)** Fluorescence imaging of the major organs after intravenous administration of 5 mg/kg^{-1} sulfo-Cy7-labeled CAT or CAT-PEG. **(C, D)** Quantitative analysis of the accumulation of CAT (C) and CAT-PEG (D) in the organs. $n = 3$. Data represent means \pm s.e.m. Pharmacokinetics and biodistribution of CAT-PEG in mice.

major organs, including heart, liver, spleen, lung, and kidney, of which the average radiation intensity is shown in **Figures 3C,D**. Both CAT and CAT-PEG were mainly accumulated in the reticuloendothelial system organs (liver and spleen), of which fluorescence intensity decreased with time. Compared with CAT, CAT-PEG showed significantly lower accumulation in the liver, spleen, and kidney, which is consistent with the ability of PEGylation to prolong the circulation time of a conjugated protein.

Therapeutic Effect of Catalase-PEG in Mice With Sepsis

The sepsis model was established by tail-vein injection of LPS ($100 \mu\text{g/kg}$) and D-galactosamine (D-GalN, 800 mg/kg) to the mice. To evaluate the therapeutic effect of CAT-PEG in mice with sepsis, the model animals were injected with either 5 mg/kg CAT-PEG or equal volume of $1\times$ PBS through the tail-vein 1 h after the

injection of LPS/D-GalN. Healthy mice without any treatment were used as control. As shown in **Figure 4A**, 60% of the mice died within 6 h in the model group, with a survival rate of 20% after 12 h. In the CAT-PEG treatment group, death of the mice occurred after 8 h, with a significantly higher survival rate of 60% after 12 h. **Figures 4B–E** further compares the counts of the inflammatory cells in the blood samples of the mice from the model group and the CAT-PEG treatment group. Compared with the control group, the model group showed significantly increased counts of the white blood cells (WBC), lymphocytes, monocytes, and neutrophils. In contrast, the model mice showed significantly lowered counts of these inflammatory cells after CAT-PEG treatment, which are similar to those of the control group. These results suggest that CAT-PEG treatment significantly reduced the inflammation syndrome of the model animals. In addition, the liver is one of the organs most affected by sepsis (Yan et al., 2014). The model group showed significantly elevated levels of serum aspartate aminotransferase

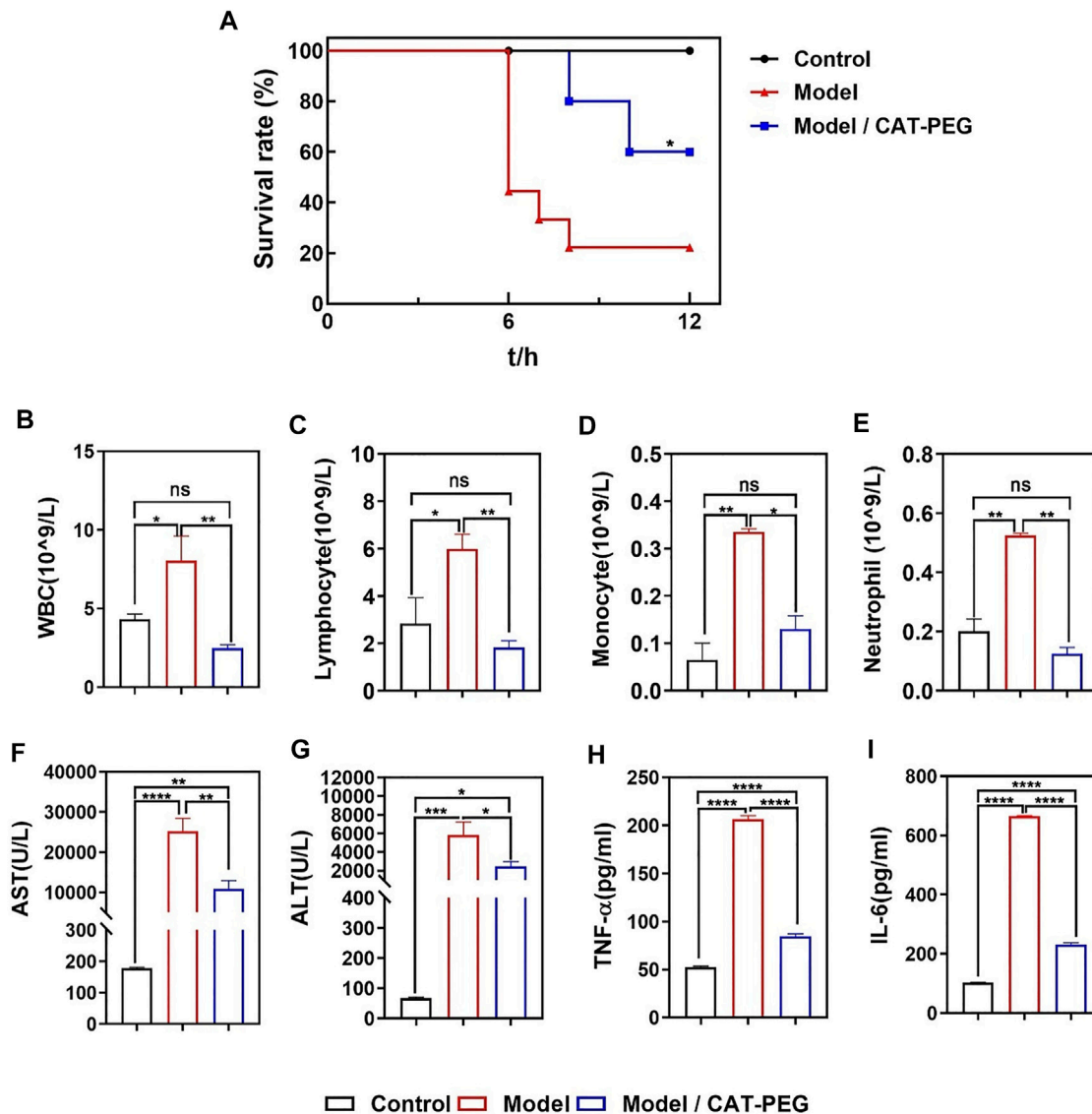


FIGURE 4 | Effectiveness of CAT-PEG treatment in mice with induced sepsis. **(A)** Survival curve of the healthy mice (Control group), the mice with induced sepsis (Model group) and the model mice with CAT-PEG treatment (Model + CAT-PEG group). The survival of mice was monitored for 12 h $n = 9$. * $p < 0.05$ (Log-rank (Mantel-Cox) test). **(B–E)** counts of white blood cells (WBC), lymphocytes, monocytes, and neutrophils, **(F)** aspartate aminotransferase (AST), **(G)** alanine aminotransferase (ALT), **(H)** TNF- α , **(I)** IL-6 levels of the control group, model group, and treatment group. $n = 3$. Data represent means \pm s.e.m. p value: * $p < 0.05$, ** $p < 0.01$, *** $p < 0.001$ and **** $p < 0.0001$. ns means not significant.

(AST) and alanine aminotransferase (ALT), which were also reduced significantly in the treatment group (Figures 4F,G). Similarly, compared with the control group, the model group also showed significantly elevated levels of TNF- α and IL-6, which were significantly reduced after the CAT-PEG treatment (Figures 4H,I).

Histologic Analysis

Figure 5A shows the hematoxylin-eosin (H and E) staining of the liver, lung and kidney in the model and treatment groups. In the model group, the liver cells were swollen and deformed, the liver cords were not arranged neatly, and liver sinusoid congestion and necrosis were serious. For lung tissue, the wall thickness of the alveoli was

significantly thicker than that of the control group, and the alveoli were partially congested, accompanied by a large amount of inflammatory cell infiltration. For the kidney, the structure of the kidney tissue was disorderly arranged, the extracellular matrix increased more than normal, a large number of inflammatory cells infiltrated, and the necrosis of renal tubular epithelial cells was serious. On the contrary, the above-mentioned pathological changes were significantly reduced in the treatment group. Similarly, the treatment group also showed reduced damage in the heart and spleen (Supplementary Figure S4). Specifically, compared with the control group, the arrangement of myocardial fibers was disordered, myocardial cells were swollen, and the interstitium of

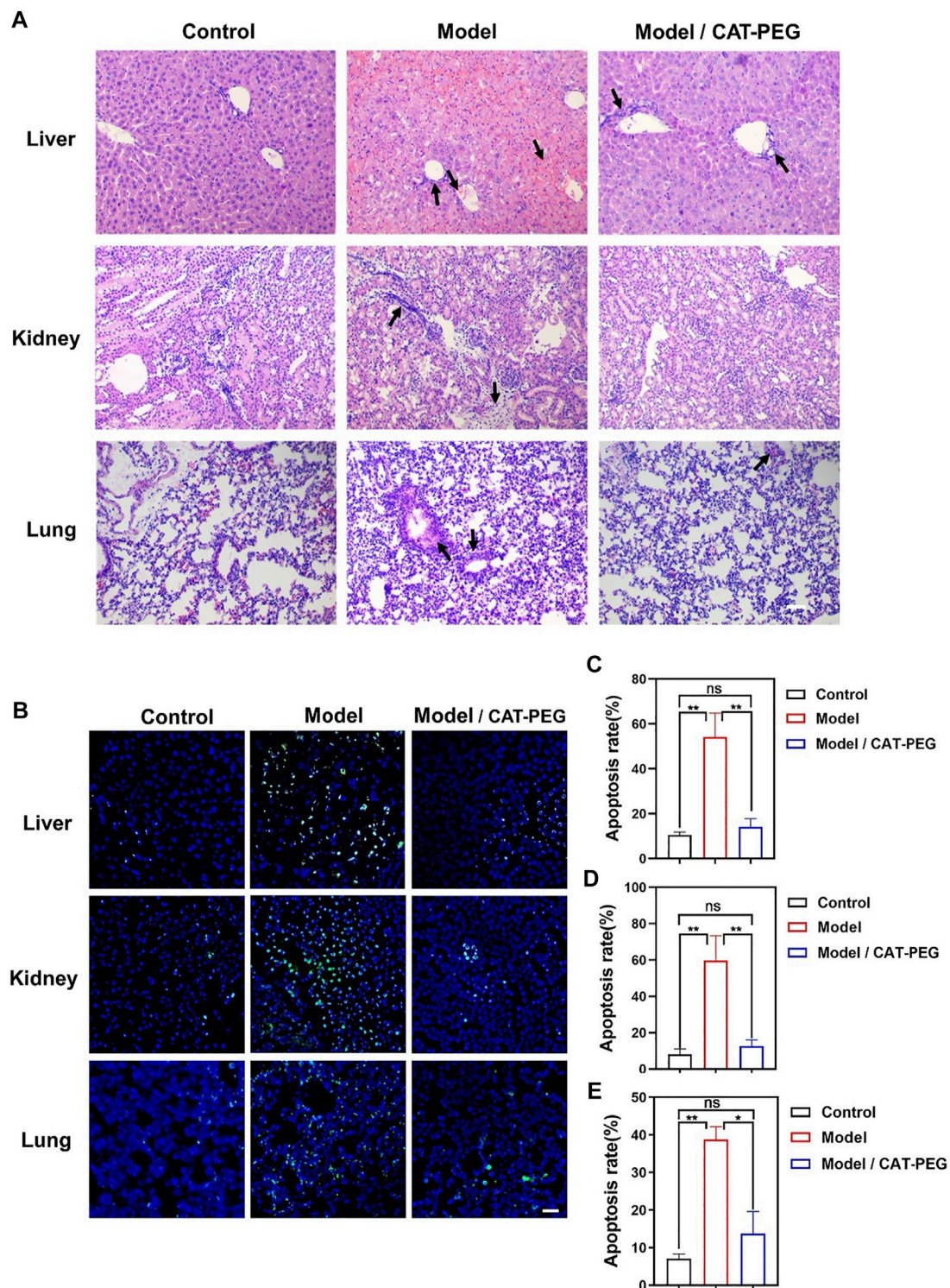


FIGURE 5 | Histologic analysis of the control, model, and treatment group. **(A)** Representative H and E staining sections of the major organs (Original Magnification $\times 200$). **(B)** Terminal deoxynucleotidyl transferase dUTP nick-end labeling (TUNEL) staining of the liver, kidney, and lung sections. Scale bar: 50 μ m. The nucleus was stained with DAPI (blue). Apoptotic cells were stained showing green color. **(C–E)** The percentage of TUNEL positive cells, which was counted by Leica TCS SP8 Confocal laser scanning microscope for each section and counted at least three viewing fields in each experiment. The tissue from top to bottom: liver, kidney, and lung. $n = 3$. Data represent means \pm s.e.m. * $p < 0.05$ and ** $p < 0.01$. ns means not significant.

the myocardial cells widened, accompanied by inflammatory cytokine infiltration in the model group. For the spleen, the proportion of red and white pulp was imbalanced with irregular distribution, the spleen was severely congested, and the cell density of the lymphatic sheath around the arteries was significantly reduced. **Figure 5B** shows the terminal deoxynucleotidyl transferase dUTP nick-end labeling (TUNEL) staining of the liver, kidney, and lung sections. Compared with the control group, the apoptotic cells in the liver, kidney, and lung of the model groups increase significantly. In contrast, the apoptotic cells are significantly reduced in after the CAT-PEG treatment. Further quantitative analysis results show that the CAT-PEG treatment resulted in 4-fold, 6-fold and 3-fold lowered apoptosis rate in the liver, kidney, and lung than the model group, respectively (**Figures 5C–E**).

DISCUSSION

Sepsis involves complex network effects of multiple systems, including inflammation, immune dysfunction, coagulation dysfunction, endothelial injury, multiple organ injury, and shock, etc. We have shown that CAT-PEG can effectively downregulate the production of TNF- α and IL-6 by activated leukocytes, suppress the level of AST, ALT, TNF- α , and IL-6 in the mice with induced sepsis, leading to significantly reduced mortality rate. TNF- α is a pleiotropic cytokine that mediates the inflammatory cascade though inducing cytokines such as IL-6 (Zhang et al., 2010), as well as cell apoptosis in the early stage through a series of signal transmissions (Kaplowitz, 2000). Therefore, TNF- α and IL-6 are related to a wide range of inflammatory or autoimmune diseases. In this study, administration of LPS/D-GalN significantly increased the levels of plasma TNF- α and IL-6, which was restored after CAT-PEG treatment, leading to reduced apoptosis of the liver, lung, kidney and other organs.

In addition to being a weapon against pathogens, ROS is also involved in many physiological processes, serving as both an inflammatory signaling molecule and an inflammatory mediator (Mittal et al., 2014). Long-term or chronic ROS molecules are considered to be the core of the development of inflammatory diseases (Pendyala and Natarajan, 2010). As a representative of ROS, increasing number of studies have shown that H₂O₂ plays an important role in the physiology of cells and organs (Rhee, 2006; Sies, 2014). For example, H₂O₂ plays an irreplaceable role as a “messenger” and “guide” during an inflammatory response (Wittmann et al., 2012). The presence of H₂O₂ is necessary for the release of pro-inflammatory cytokines and regulate an appropriate immune response (Nathan and Cunningham-Bussel, 2013), whereas excessive production of ROS including H₂O₂ could cause immunopathogenesis. We speculate that CAT-PEG can also

regulate the production of cytokines, restoring immune balance by removing excess ROS produced.

In summary, we have demonstrated the PEGylated catalase can effectively regulate the production of cytokines by leukocytes, suppress the elevated level of AST, ALT, TNF- α , and IL-6 and mitigate the damage to the liver, kidney, lung function and other organs in mice with induced sepsis. These factors collectively contributed to a dramatic increase of survival rate. These findings suggest that CAT-PEG may provide an efficient therapeutic solution to sepsis, as well as other hyperinflammation-related diseases.

DATA AVAILABILITY STATEMENT

The original contributions presented in the study are included in the article/**Supplementary Material**, further inquiries can be directed to the corresponding authors.

ETHICS STATEMENT

The animal study was reviewed and approved by Institutional Animal Care and Use Committee of the Chinese Academy of Medical Sciences & Peking Union Medical College.

AUTHOR CONTRIBUTIONS

MQ and CL conceived or designed this study. FL, RY, JW, and ZH performed the experiment. FL analyzed the data and performed the statistical analysis. FL, CL and YL co-wrote the manuscript. All authors discussed the results and commented on the manuscript.

FUNDING

This work was supported by the National Key Research and Development Program of China (No. 2019YFA0903801), the National Natural Science Foundation of China (Nos. 52073015 and 52003021), and Fundamental Research Funds for the Central Universities (No. ZY 2006).

SUPPLEMENTARY MATERIAL

The Supplementary Material for this article can be found online at: <https://www.frontiersin.org/articles/10.3389/fbioe.2021.800684/full#supplementary-material>

REFERENCES

- Abuchowski, A., van Es, T., Palczuk, N. C., and Davis, F. F. (1977). Alteration of Immunological Properties of Bovine Serum Albumin by Covalent Attachment of Polyethylene Glycol. *J. Biol. Chem.* 252, 3578–3581. doi:10.1016/S0021-9258(17)40291-2
- Aziz, M., and Wang, P. (2019). DAMPs and NETs in Sepsis. *Front. Immunol.* 10, 15. doi:10.3389/fimmu.2019.02536
- Basu, A., Yang, K., Wang, M., Liu, S., Chintala, R., Palm, T., et al. (2006). Structure–Function Engineering of Interferon- β -1b for Improving Stability, Solubility, Potency, Immunogenicity, and Pharmacokinetic Properties by Site-Selective Mono-PEGylation. *Bioconjug. Chem.* 17, 618–630. doi:10.1021/bc050322y

- Cai, B., Deitch, E. A., and Ulloa, L. (2010). Novel Insights for Systemic Inflammation in Sepsis and Hemorrhage. *Mediators Inflamm.* 2010, 1–10. doi:10.1155/2010/642462
- Gotts, J. E., and Matthay, M. A. (2016). Sepsis: Pathophysiology and Clinical Management. *BMJ*, i1585. doi:10.1136/bmj.i1585
- Hao, Y., Zheng, W., Sun, Z., Zhang, D., Sui, K., Shen, P., et al. (2021). Marine Polysaccharide-Based Composite Hydrogels Containing Fucoidan: Preparation, Physicochemical Characterization, and Biocompatible Evaluation. *Int. J. Biol. Macromolecules* 183, 1978–1986. doi:10.1016/j.ijbiomac.2021.05.190
- Harris, J. M., and Chess, R. B. (2003). Effect of Pegylation on Pharmaceuticals. *Nat. Rev. Drug Discov.* 2, 214–221. doi:10.1038/nrd1033
- Huang, C., Wang, Y., Li, X., Ren, L., Zhao, J., Hu, Y., et al. (2020). Clinical Features of Patients Infected with 2019 Novel Coronavirus in Wuhan, China. *The Lancet* 395, 497–506. doi:10.1016/S0140-6736(20)30183-5
- Kaplowitz, N. (2000). Mechanisms of Liver Cell Injury. *J. Hepatol.* 32, 39–47. doi:10.1016/S0168-8278(00)80414-6
- Kast, R. E. (2000). Tumor Necrosis Factor Has Positive and Negative Self Regulatory Feed Back Cycles Centered Around cAMP. *Int. J. Immunopharmacology* 22, 1001–1006. doi:10.1016/S0192-0561(00)00046-1
- Kinstler, O., Molineux, G., Treuheit, M., Ladd, D., and Gegg, C. (2002). Mono-N-terminal Poly(ethylene Glycol)-Protein Conjugates. *Adv. Drug Deliv. Rev.* 54, 477–485. doi:10.1016/S0169-409X(02)00023-6
- Korneev, K. V. (2019). Mouse Models of Sepsis and Septic Shock. *Mol. Biol.* 53, 704–717. doi:10.1134/S0026893319050108
- Lambeth, J. D. (2004). NOX Enzymes and the Biology of Reactive Oxygen. *Nat. Rev. Immunol.* 4, 181–189. doi:10.1038/nri1312
- Lehmann, V., Freudenberg, M. A., and Galanos, C. (1987). Lethal Toxicity of Lipopolysaccharide and Tumor Necrosis Factor in normal and D-Galactosamine-Treated Mice. *J. Exp. Med.* 165, 657–663. doi:10.1084/jem.165.3.657
- Maes, M., Vinken, M., and Jaeschke, H. (2016). Experimental Models of Hepatotoxicity Related to Acute Liver Failure. *Toxicol. Appl. Pharmacol.* 290, 86–97. doi:10.1016/j.taap.2015.11.016
- Majewska, E., Kasiński, M., Luczynski, R., Bartosz, G., Białasiewicz, P., and Nowak, D. (2004). Elevated Exhalation of Hydrogen Peroxide and Thiobarbituric Acid Reactive Substances in Patients with Community Acquired Pneumonia. *Respir. Med.* 98, 669–676. doi:10.1016/j.rmed.2003.08.015
- Marchesoni, A., Zaccara, E., Gorla, R., Bazzani, C., Sarzi-Puttini, P., Atzeni, F., et al. (2009). TNF- α Antagonist Survival Rate in a Cohort of Rheumatoid Arthritis Patients Observed under Conditions of Standard Clinical Practice. *Ann. N. Y. Acad. Sci.* 1173, 837–846. doi:10.1111/j.1749-6632.2009.04621.x
- Matsuda, A., Jacob, A., Wu, R., Aziz, M., Yang, W.-L., Matsutani, T., et al. (2012). Novel Therapeutic Targets for Sepsis: Regulation of Exaggerated Inflammatory Responses. *J. Nippon Med. Sch.* 79, 4–18. doi:10.1272/jnms.79.4
- Mittal, M., Siddiqui, M. R., Tran, K., Reddy, S. P., and Malik, A. B. (2014). Reactive Oxygen Species in Inflammation and Tissue Injury. *Antioxid. Redox Signaling* 20, 1126–1167. doi:10.1089/ars.2012.5149
- Naik, E., and Dixit, V. M. (2011). Mitochondrial Reactive Oxygen Species Drive Proinflammatory Cytokine Production. *J. Exp. Med.* 208, 417–420. doi:10.1084/jem.20110367
- Nathan, C., and Cunningham-Bussell, A. (2013). Beyond Oxidative Stress: an Immunologist's Guide to Reactive Oxygen Species. *Nat. Rev. Immunol.* 13, 349–361. doi:10.1038/nri3423
- Nishikawa, M., Hashida, M., and Takakura, Y. (2009). Catalase Delivery for Inhibiting ROS-Mediated Tissue Injury and Tumor Metastasis. *Adv. Drug Deliv. Rev.* 61, 319–326. doi:10.1016/j.addr.2009.01.001
- Patlevič, P., Vašková, J., Švorc, P., Vaško, L., and Švorc, P. (2016). Reactive Oxygen Species and Antioxidant Defense in Human Gastrointestinal Diseases. *Integr. Med. Res.* 5, 250–258. doi:10.1016/j.imr.2016.07.004
- Pendyala, S., and Natarajan, V. (2010). Redox Regulation of Nox Proteins. *Respir. Physiol. Neurobiol.* 174, 265–271. doi:10.1016/j.resp.2010.09.016
- Phaniendra, A., Jestadi, D. B., and Periyasamy, L. (2015). Free Radicals: Properties, Sources, Targets, and Their Implication in Various Diseases. *Ind. J. Clin. Biochem.* 30, 11–26. doi:10.1007/s12291-014-0446-0
- Poli-de-Figueiredo, L. F., Garrido, A. G., Nakagawa, N., and Sannomiya, P. (2008). Experimental Models of Sepsis and Their Clinical Relevance. *Shock* 30, 53–59. doi:10.1097/SHK.0b013e318181a343
- Qi, H., Shan, P., Wang, Y., Li, P., Wang, K., and Yang, L. (2021). Nanomedicines for the Efficient Treatment of Intracellular Bacteria: The “ART” Principle. *Front. Chem.* 9, 7. doi:10.3389/fchem.2021.775682
- Qin, M., Cao, Z., Wen, J., Yu, Q., Liu, C., Wang, F., et al. (2020). An Antioxidant Enzyme Therapeutic for COVID-19. *Adv. Mater.* 32, 2004901. doi:10.1002/adma.202004901
- Reczek, C. R., and Chandel, N. S. (2015). ROS-dependent Signal Transduction. *Curr. Opin. Cell Biol.* 33, 8–13. doi:10.1016/j.ceb.2014.09.010
- Reinhart, K., Daniels, R., Kissoon, N., Machado, F. R., Schachter, R. D., and Finfer, S. (2017). Recognizing Sepsis as a Global Health Priority - A WHO Resolution. *N. Engl. J. Med.* 377, 414–417. doi:10.1056/NEJMp1707170
- Reyhani, A., McKenzie, T. G., Fu, Q., and Qiao, G. G. (2019). Fenton-Chemistry-Mediated Radical Polymerization. *Macromol. Rapid Commun.* 40, 1900220. doi:10.1002/marc.201900220
- Rhee, S. G. (2006). H₂O₂, a Necessary Evil for Cell Signaling. *Science* 312, 1882–1883. doi:10.1126/science.1130481
- Rhodes, A., Evans, L. E., Alhazzani, W., Levy, M. M., Antonelli, M., Ferrer, R., et al. (2017). Surviving Sepsis Campaign: International Guidelines for Management of Sepsis and Septic Shock: 2016. *Intensive Care Med.* 43, 304–377. 2016. doi:10.1007/s00134-017-4683-6
- Rittirsch, D., Flierl, M. A., and Ward, P. A. (2008). Harmful Molecular Mechanisms in Sepsis. *Nat. Rev. Immunol.* 8, 776–787. doi:10.1038/nri2402
- Samejima, T., and Yang, J. T. (1963). Reconstitution of Acid-Denatured Catalase. *J. Biol. Chem.* 238, 3256–3261. doi:10.1016/S0021-9258(18)48655-3
- Sies, H. (2014). Role of Metabolic H₂O₂ Generation. *J. Biol. Chem.* 289, 8735–8741. doi:10.1074/jbc.R113.544635
- Silverstein, R. (2004). D-galactosamine Lethality Model: Scope and Limitations. *J. Endotoxin Res.* 10, 147–162. doi:10.1179/096805104225004879
- Singer, M., Deutschman, C. S., Seymour, C. W., Shankar-Hari, M., Annane, D., Bauer, M., et al. (2016). The Third International Consensus Definitions for Sepsis and Septic Shock (Sepsis-3). *JAMA* 315, 801. doi:10.1001/jama.2016.0287
- Thannickal, V. J., and Fanburg, B. L. (2000). Reactive Oxygen Species in Cell Signaling. *Am. J. Physiology-Lung Cell Mol. Physiol.* 279, L1005–L1028. doi:10.1152/ajplung.2000.279.6.L1005
- Wittmann, C., Chockley, P., Singh, S. K., Pase, L., Lieschke, G. J., and Grabher, C. (2012). Hydrogen Peroxide in Inflammation: Messenger, Guide, and Assassin. *Adv. Hematol.* 2012, 1–6. doi:10.1155/2012/541471
- Yan, J., Li, S., and Li, S. (2014). The Role of the Liver in Sepsis. *Int. Rev. Immunol.* 33, 498–510. doi:10.3109/08830185.2014.889129
- Yang, L., Han, D., Zhan, Q., Li, X., Shan, P., Hu, Y., et al. (2019). Blood TfR+ Exosomes Separated by a pH-Responsive Method Deliver Chemotherapeutics for Tumor Therapy. *Theranostics* 9, 7680–7696. doi:10.7150/thno.37220
- Zhang, L., Li, H.-z., Gong, X., Luo, F.-l., Wang, B., Hu, N., et al. (2010). Protective Effects of Asiaticoside on Acute Liver Injury Induced by lipopolysaccharide/D-Galactosamine in Mice. *Phytomedicine* 17, 811–819. doi:10.1016/j.phymed.2010.01.008
- Zheng, W., Hao, Y., Wang, D., Huang, H., Guo, F., Sun, Z., et al. (2021). Preparation of Triamcinolone Acetonide-Loaded Chitosan/fucoidan Hydrogel and its Potential Application as an Oral Mucosa Patch. *Carbohydr. Polym.* 272, 118493. doi:10.1016/j.carbpol.2021.118493

Conflict of Interest: The authors declare that the research was conducted in the absence of any commercial or financial relationships that could be construed as a potential conflict of interest.

Publisher's Note: All claims expressed in this article are solely those of the authors and do not necessarily represent those of their affiliated organizations, or those of the publisher, the editors and the reviewers. Any product that may be evaluated in this article, or claim that may be made by its manufacturer, is not guaranteed or endorsed by the publisher.

Copyright © 2021 Li, Yan, Wu, Han, Qin, Liu and Lu. This is an open-access article distributed under the terms of the Creative Commons Attribution License (CC BY). The use, distribution or reproduction in other forums is permitted, provided the original author(s) and the copyright owner(s) are credited and that the original publication in this journal is cited, in accordance with accepted academic practice. No use, distribution or reproduction is permitted which does not comply with these terms.



Reactive Oxygen Species-Based Biomaterials for Regenerative Medicine and Tissue Engineering Applications

Muhammad Shafiq^{1,2}, Yujie Chen¹, Rashida Hashim³, Chuanglong He¹, Xiumei Mo¹ and Xiaojun Zhou^{1*}

¹Shanghai Engineering Research Center of Nano-Biomaterials and Regenerative Medicine, College of Chemistry, Chemical Engineering and Biotechnology, Donghua University, Shanghai, China, ²Department of Biotechnology, Faculty of Life Science, University of Central Punjab (UCP), Lahore, Pakistan, ³Department of Chemistry, Faculty of Science, Quaid-i-Azam University (QAU), Islamabad, Pakistan

OPEN ACCESS

Edited by:

Qihui Zhou,
Qingdao University, China

Reviewed by:

Jiajia Xue,
Beijing University of Chemical
Technology, China
Hongshi Ma,
Shanghai Institute of Ceramics (CAS),
China

*Correspondence:

Xiaojun Zhou
zxj@dhru.edu.cn

Specialty section:

This article was submitted to
Biomaterials,
a section of the journal
Frontiers in Bioengineering and
Biotechnology

Received: 24 November 2021

Accepted: 10 December 2021

Published: 23 December 2021

Citation:

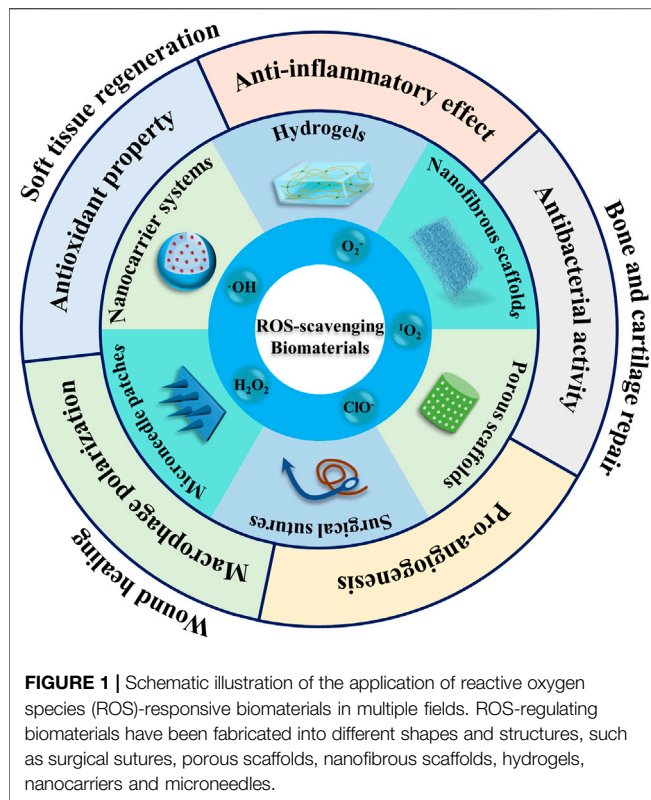
Shafiq M, Chen Y, Hashim R, He C,
Mo X and Zhou X (2021) Reactive
Oxygen Species-Based Biomaterials
for Regenerative Medicine and Tissue
Engineering Applications.
Front. Bioeng. Biotechnol. 9:821288.
doi: 10.3389/fbioe.2021.821288

Reactive oxygen species (ROS), acting as essential mediators in biological system, play important roles in the physiologic and pathologic processes, including cellular signal transductions and cell homeostasis interference. Aberrant expression of ROS in tissue microenvironment can be caused by the internal/external stimuli and tissue injury, which may leads to an elevated level of oxidative stress, inflammatory response, and cellular damage as well as disruption in the tissue repair process. To prevent the formation of excess ROS around the injury site, advanced biomaterials can be remodeled or instructed to release their payloads in an injury microenvironment-responsive fashion to regulate the elevated levels of the ROS, which may also help downregulate the oxidative stress and promote tissue regeneration. A multitude of scaffolds and bioactive cues have been reported to promote the regeneration of damaged tissues based on the scavenging of free radicals and reactive species that confer high protection to the cellular activity and tissue function. In this review, we outline the underlying mechanism of ROS generation in the tissue microenvironment and present a comprehensive review of ROS-scavenging biomaterials for regenerative medicine and tissue engineering applications, including soft tissues regeneration, bone and cartilage repair as well as wound healing. Additionally, we highlight the strategies for the regulation of ROS by scaffold design and processing technology. Taken together, developing ROS-based biomaterials may not only help develop advanced platforms for improving injury microenvironment but also accelerate tissue regeneration.

Keywords: reactive oxygen species, oxidative stress, inflammatory response, regenerative medicine, tissue engineering

INTRODUCTION

Reactive oxygen species (ROS) are highly reactive ions or free radicals, such as superoxide (O_2^-), hydrogen peroxide (H_2O_2), hydroxyl radicals ($\cdot OH$), hypochlorite ion (ClO^-), singlet oxygen (1O_2) and so on. The ROS play a significant role in homeostasis and physiological functions, which are precisely modulated by their amount, duration, and localization. Both, a lack or an excess of ROS



may cause different types of diseases, including autoimmune disease, cardiovascular disease, and neurodegenerative disease (Saravanakumar et al., 2017; Hameister et al., 2020). While the wound healing and tissue repair processes are governed by the different phases of inflammation, the excessive inflammation may exacerbate oxidative stress and ROS. Most of the tissues, including skin, bone, soft tissues (muscle, ligament, fascia nerves, fibrous tissues, fat, blood vessels, synovial tissues and so on) are susceptible to oxidative stress. For instance, ROS act as signaling molecules in managing multiple endothelial cells (ECs) and smooth muscle cells pathways, including their proliferation, migration, and apoptosis. However, the excessive ROS accumulated at the injury site can induce strong inflammatory response to interfere with the tissue repair process. The ROS level under pathological conditions can exceed 500 μm in inflammatory tissues, which is much higher than that in the normal tissues (1–15 μm). While on the one hand, excessive ROS at the injury site can perturb tissue repair through overlying signaling pathway and oxidative stress, on the other hand, the excessive ROS can lead to the damage of the biological molecules and disturbance of the immune system. The ROS-mediated altered cellular behaviour may lead to inflammatory signaling resulting into leukocytes and platelets activation as well as their recruitment. Moreover, the implantation of biomaterials has been found to elevate oxidative stress as well as recruit polymorphonuclear cells and monocytes, which may further increase inflammatory response. Therefore, a thorough understanding of ROS and oxidative stress will help understand biomaterials-host interactions and interrogate the injury microenvironment.

Since systematic ROS scavengers can interfere with the several physiological processes, it is imperative to develop localized ROS scavengers. While substantial research has been carried out on the use of ROS-sensitive materials for drug delivery applications and cancer therapy, ROS-responsive biomaterials which can simultaneously release their payloads and regulate ROS level in the injured tissues, while simultaneously impact tissue repair process have received only a little attention (Lee et al., 2013; Saravanakumar et al., 2017). Nonetheless, these instructive biomaterials may possess several functions, such as the regulation of the injury microenvironment by the alleviation of the oxidative stress or ROS, which may help modulate inflammatory response and inflammatory signaling mediated cellular processes, harness oxidative stress and/or ROS as microenvironmental cues to afford drug/growth factor release, and induce the degradation of implanted scaffolds. We have discussed the role of ROS-sensitive biomaterials for the regeneration of soft tissues (nerves, heart, and muscles), osteochondral tissues (bone and cartilage) and wound healing (Figure 1). As oxidative stress and ROS are central to almost all types of tissues, these can be an important design criterion in biomaterials engineering and worthy of further investigations.

Regulation of ROS for Soft Tissues Regeneration

ROS pose debilitating threats for various types of diseases of soft tissues, such as atherosclerosis, ischemia, diabetes, and myocardial infarction/reperfusion injuries. Excessive ROS species also impair tissue regeneration. Particularly, excessive ROS can cause inflammation and fibrosis, which can further mount injury burden. Consequently, timely resolution of ROS holds great promise. Wagner et al., designed polymers with an inherent ability to scavenge ROS by conjugating 4-Amino-2,2,6,6-tetramethylpiperidine-1-oxyl (TEMPO) to the thermo-responsive hydrogels (Zhu et al., 2018). In a myocardial reperfusion/injury model, these hydrogels reduced apoptosis and preserved left ventricular (LV) function. Similarly, Bai et al., have designed ROS-degradable hydrogels to lower the degeneration of the intervertebral disk. It was delineated that the scaffolds-mediated ROS suppression led to the controlled release of rapamycin, which also resulted into macrophages polarization by increasing the number of M2 macrophages while depleting the number of M1 macrophages (Bai et al., 2020). Liu et al., leveraged hyper-branched poly (β -amino esters) to scavenge ROS, which ameliorated infarcted heart conditions (Wang et al., 2019).

To scavenge ROS, a myriad of strategies have been used, including the use of radical scavenging polymers, ROS-responsive crosslinkers, biologics, or therapeutics (Zhao et al., 2020; Chen Z. et al., 2021). Gu et al., exploited poly (ester amide) (PEA) as an antioxidant and blended it with poly (acrylic acid) (PAA), which not only scavenged free radicals but also promoted cell growth and viability as well as angiogenesis (Zhang J. et al., 2021). The ROS scavenging ability of these hydrogels emanated from the arginine release. Likewise, Duvall et al. have exploited poly (propylene sulphide) (PPS) to scavenge ROS and release

anti-oxidative and anti-inflammatory curcumin (Poole et al., 2015). Since PPS is a hydrophobic polymer, it can efficiently improve drug efficiency and can trigger the drug release in a ROS-responsive manner by transforming into more hydrophilic poly (propylene sulfoxide) and poly (propylene sulfone) polymers. Consequently, curcumin-encapsulating PPS microparticles considerably decreased the ROS level in activated macrophages and oxidative stress induced cell death *in vitro*. Besides, these biomaterials increased angiogenesis in a hind-limb ischemia model. While the incorporation of antioxidants and radical scavengers can afford the reduction of the oxidative stress and ROS-related cell dysfunction, the immobilization or encapsulation of these moieties into scaffolds provides only a marginal benefit. To circumvent this limitation, inherently anti-oxidative polymers have been synthesized (Van Lith et al., 2014; Shiekh et al., 2018). Kumar et al. synthesized ascorbic acid incorporated polyurethane (Shiekh et al., 2018). Since ascorbic acid was incorporated into the main chain of the polymer, the localized and sustained presence of the antioxidant successfully reduced the oxidative stress in H9C2 cardiomyocytes and ROS-induced cell death, which may have great promise for the treatment of diseased conditions with increased oxidative stress, such as cardiovascular diseases, chronic wounds, and myocardial infarction. Liu et al. have designed poly (vinyl alcohol) (PVA) based hydrogels crosslinked via ROS-responsive linkers and systematically studied their ROS scavenging ability *in vitro* in human umbilical vein endothelial cells (HUVECs) and *in vivo* in lipopolysaccharide (LPS)-induced infection model and diabetes/infection model (Zhao et al., 2020). Importantly, these hydrogels, not only scavenged ROS as indicated by the lower expression of the H_2O_2 and OH but also induced the release of mupirocin and granulocyte-macrophage colony-stimulating factor (GM-CSF), which increased antibacterial effect and macrophages polarization toward M2 phenotypes, respectively. By using a similar approach, Shan et al. designed ROS-responsive PVA based hydrogels, which not only modulated inflammation in injured skeletal muscles but also promoted the survival of mesenchymal stem cells (MSCs) under oxidative environment as well as induced myogenesis and macrophages polarization toward M2 phenotypes (Shan et al., 2021). Cheng et al. further exploited these ROS-responsive PVA polymers to afford an epicardial patch, which sustainably and controllably released fibroblast growth factor-2 (FGF-2) *in vitro* in response to the H_2O_2 as well as improved its retention in the pericardial cavity *in vivo* via overproduced ROS following ischemia-reperfusion injury in mice. More importantly, these scaffolds also reduced cardiac fibrosis and promoted neo-myogenesis (Li Z. et al., 2021). Likewise, Martin et al. synthesized ROS-sensitive poly (thioketal)urethane (PTK-UR), which degraded in a cell-mediated manner upon an increase in the ROS and induced tissue regeneration after subcutaneous implantation (Martin et al., 2021). Gao et al. designed ROS cleavable hyperbranched polymers and leveraged them along with methacrylated hyaluronic acid (HAMA) to afford ultraviolet (UV)-crosslinkable hydrogels (Ding et al., 2020). Importantly, while ROS-cleavable linker can scavenge ROS, catalase could generate

oxygen from the decomposition of H_2O_2 , making this combinatorial strategy capable of alleviating hypoxia and rejuvenating oxygen, and enhancing their suitability for the treatment of various pathological hallmarks, including myocardial infarction (MI). Consequently, these hydrogels promoted cell viability under oxidative stress as well as reduced infarct size and promoted angiogenesis in an MI model.

Nitric oxide (NO) has several implications for maintaining vascular hemostasis, which can be activated by cells expressing endothelial NO synthase, inducible NO synthase, and neuronal NO synthase. The NO has been delivered to promote neo-vessel formation in blood vessels. However, given to the short half-life of NO, the therapeutic level cannot be maintained. Besides, elevated levels of ROS rapidly react with the NO to reduce its bioavailability. Nagasaki et al. designed poly (arginine) based NO-releasing and ROS-responsive hydrogels, which not only afforded the NO release by the degradation of arginine moieties but also suppressed ROS in a redox-sensitive manner (Vong et al., 2018). Hydrogels simultaneously eluting NO and scavenging ROS significantly reduced infarct size as well as improved blood vessel formation than that of their counterparts which only released NO or scavenged ROS in MI model in mice.

To date, different types of strategies have been adopted to scavenge ROS and alleviate free radicals, such as the application of oxidant scavengers and engineered enzymes. However, the low bioavailability of therapeutic compounds and their tendency to become oxidants at high doses limit their applications (Table 1). Consequently, a sustained and localized delivery of antioxidants may improve the clinical benefits of lowering the oxidative stress. Jain et al. leveraged cerium oxide nanoparticles (nCe) to alleviate oxidative stress and scavenge ROS (Jain et al., 2021). Nanofibrous poly (caprolactone)/gelatin (PCL/Gel) scaffolds containing nCe reduced ROS level in H_2O_2 -induced cardiomyocytes as well as suppressed agonist-induced cardiac hypertrophy. Therefore, further research is warranted to afford nanomaterials-based ROS scavengers, which may have broad applications. Similarly, other members of the antioxidants, such as fullereneol have been leveraged to improve stem cell function, especially in the ROS microenvironment. The ROS can be adhered to the electron deficient positions of fullereneol nanoparticles; alleviating the oxidative stress. Once delivered along with extracellular matrix (ECM)-mimetic alginate hydrogels, fullereneol nanoparticles were reported to scavenge ROS, alleviate oxidative stress, and improve stem cell function, such as survival, retention, and engraftment by activating mitogen-activated protein kinase (MAPK) signaling pathways (i.e. ERK, p38, and JNK, etc), which collectively translated into enhanced clinical outcome, including angiogenesis and cardiac functional recovery (Hao et al., 2017). Wang et al. leveraged hydrogen sulphide (H_2S)-releasing electrospun PCL fibers by encapsulating N-(benzoylthio)benzamides derivatives (NSHD), which can induce H_2S release triggered by biological thiols such as cysteine and glutathione (GSH), which prevail in the

TABLE 1 | Reactive oxygen species-regulating biomaterials for tissue regeneration applications.

Bioactive cue/scaffold	Animal model	Key findings	References
Rapamycin-loaded scaffolds	Intervertebral disk	Macrophages polarization toward M2 phenotypes increased while ROS level decreased	Bai et al. (2020)
ROS-cleavable polymers, catalase, 4-amino-TEMPO based HA hydrogels	Myocardial infarction	ROS level and infarct size decreased while cell viability, cardiac function and angiogenesis increased	Ding et al. (2020), Wang et al. (2019), Zhu et al. (2018)
Nitric oxide releasing poly (arginine) hydrogels		Nitric oxide release and angiogenesis increased while ROS level and infarct size decreased	Vong et al. (2018)
Curcumin-loaded poly (propylene sulphide) nanoparticles	Hind-limb ischemia or reperfusion	ROS level, oxidative stress, and cell apoptosis decreased while limb regeneration increased	Poole et al. (2015)
Ascorbic acid loaded polyurethane		Oxidative stress and cell apoptosis decreased	Shiekh et al. (2018)
FGF-2-loaded cardiac patch		FGF-2 release and neo-myogenesis increased while cardiac fibrosis decreased	Li Z. et al. (2021)
ROS-scavenging PLGA hydrogels	Bone/cartilage	Inflammation decreased while glycosaminoglycans and collagen increased	Wu et al. (2021)
BMP-2-loaded PTK-based coatings		BMP-2 delivery and bone regeneration increased	Martin et al. (2021)
PEA-PAA hydrogels	Skin injury	Cell growth, cell viability, wound healing, and arginine release increased	Zhang J. et al. (2021)
Mupirocin and GM-CSF-loaded PVA scaffolds		ROS level decreased while M2 macrophages and wound healing increased	Zhao et al. (2020)
Tannic acid, curcumin or <i>Spirulina</i> extract loaded chitin hydrogels or PCL nanofibers		Antibacterial activity, wound healing, angiogenesis, and anti-inflammatory activity increased while oxidative stress decreased	Jung et al. (2016), He et al. (2020), Ma et al. (2020), Yang et al. (2021)
Gallic acid loaded hydrogels or sutures		Oxidative damage decreased while cell viability, neovascularization, and wound repair increased	Le Thi et al. (2020), Zhu et al. (2021)
EGF-loaded PEG hydrogels		ROS level and scar formation decreased while EGF release and skin repair increased	An et al. (2022)
MnO ₂ -loaded HA hydrogels		ROS level decreased while oxygen release and angiogenesis increased	Xiong et al. (2021)
Curcumin and Zn ²⁺ -loaded PLLA scaffolds		ROS level and inflammatory response decreased while Zn ²⁺ and epithelialization increased	Wang Y. et al. (2020)
PNA nanogel-loaded PLLA nanofibers		Cell adhesion and proliferation increased while ROS level decreased	Zhang J. et al. (2021)
Ce6, Mg ²⁺ , and EGCG loaded chitosan NPs		Mg ²⁺ release, skin repair, and antibacterial activity increased while ROS level decreased	Hu et al. (2019)
SDF-1 α -loaded PPADT		SDF-1 α release, skin repair, and BMSCs homing increased	Tang et al. (2015)
Clindamycin-loaded PVA microneedle patch		Bacterial growth decreased while drug penetration increased	Zhang et al. (2018)
Ceria-loaded PCL scaffold	<i>In vitro</i> studies	ROS level and cardiac hypertrophy decreased	Jain et al. (2021)
H ₂ S-releasing scaffolds		H ₂ S, cell survival and proliferation increased	Feng et al. (2015)

EGF, epidermal growth factor; PLLA, poly(L-lactic acid); EGCG, epigallocatechin-3-gallate.

biological system (Feng et al., 2015). The H₂S releasing nanofibrous scaffolds promoted the survival and proliferation of myoblasts and fibroblasts by reducing the oxidative stress.

Regulation of ROS for Bone and Cartilage Tissue Repair

ROS signaling is also enhanced during bone and cartilage degeneration, which is considerably exacerbated with an increase in inflammation, such as in osteoarthritis (OA). The chondrocytes are quiescent under normal conditions, and they reside in a hypoxic environment due to the lack of blood vessels in cartilaginous tissues. Upon the disruption of the mitochondrial function, chondrocytes become activated, which upregulates the expression of the intracellular ROS, further disrupting homeostasis and increasing OA (Blanco et al., 2011). Furthermore, a myriad of literatures have established age-mediated exacerbation of the oxidative stress causing an

imbalance in ROS production and antioxidant capacities (Carlo and Loeser, 2003).

A multitude of antioxidants and free radical scavengers, such as phenols (e.g., vitamin E), ubiquitin (e.g., vitamin Q), flavonoids (e.g., curcumin, quercetin), thiols (e.g., glutathione, thioredoxin) (Grover and Samson, 2016; Chin and Ima-Nirwana, 2018), xanthan gum and alginate (Chen et al., 2017), dopamine melanin (Zhong et al., 2019), fullerene and fullerol (Pei et al., 2019), chondroitin sulfate (CS) and hyaluronic acid (Chen et al., 2017; Chen Y. et al., 2021) have been demonstrated to reduce the oxidative stress, thus delaying cartilage degeneration. These supplements upregulate the expression of antioxidants (e.g., superoxide dismutase, glutathione, catalase and nuclear factor erythroid 2-related factor 2 and lead to the downregulation of ROS (Li et al., 2016; Marchev et al., 2017). For example, theaflavins (TFs), the primary active polyphenols in black tea, have been extensively investigated for their antioxidative abilities as well as antiviral and anticancer activities (Maron et al., 2003). Li et al. explored the protective effect of TFs on chondrocytes and

reported a decrease in the ROS level and cell apoptosis (Li and Zheng, 2019). In addition, CS, a naturally occurring glycosaminoglycans (GAGs) which constitutes soft tissues has been widely explored for its anti-inflammatory properties (Abe et al., 2016). Woo et al. reported a reduction in the secretion of inflammatory cytokines and ROS in LPS-treated murine RAW 264.7 macrophages after treatment with skate cartilage CS (Woo et al., 2020).

However, systematically or orally administered antioxidants exhibit poor retention at the injury site, which necessitates their spatiotemporal presentation. Liang et al. explored the antioxidative potential of PCL-grafted lignin in H_2O_2 -stimulated human chondrocytes and rabbit OA model, which was plausibly mediated by an autophagic mechanism (Liang et al., 2020). Pei et al. leveraged water-soluble polyhydroxylated fullerene C60 (fullerol) nanoparticles to scavenge ROS, which significantly reduced LPS-induced NO production and pro-inflammatory gene expression *in vitro* as well as lowered inflammation in an OA model (Pei et al., 2019). Yet another study explored the antioxidative potential of alpha-tocopheryl succinate (α -TOS) and tumor necrosis factor alpha (TNF- α) siRNA co-loaded poly (amidoamine) dendrimer-entrapped gold nanoparticles (Au DENPs) (Li et al., 2020). The α -TOS enhanced the antioxidant capacity of macrophages. The *in vivo* studies further established the downregulation of the inflammatory cytokines in OA. Li et al. developed tannic acid/strontium (TA/Sr²⁺) coated silk/graphene oxide-based meniscal scaffolds to modulate inflammatory response and reduce ROS in the OA model, which displayed anti-inflammatory and ROS scavenging abilities as well as downregulated the expression of inflammatory factors, including interleukin-6 (IL-6), interleukin-8 (IL-8), and matrix metalloproteinases (MMPs) in rat knee tissues (Li Y. et al., 2021). Similarly, ionic liquids (ILs) have been incorporated into bacterial nanocellulose (BC) based membranes, which exhibited anti-inflammatory and antioxidant properties (Sintra et al., 2015). We have recently developed metal organic frameworks (MOFs) decorated mesoporous polydopamine nanoparticles and conjugated collagen-II-targeting peptide for OA therapy (Xue et al., 2021). Rapamycin and bilirubin were loaded into the MOFs and polydopamine shells to modulate inflammatory response and activate autophagic mechanism, respectively. These nanoparticles delayed cartilage degeneration as well as modulated the inflammatory response and protected chondrocytes. The inflammatory factors, such as interleukin-1 (IL-1), IL-6, Interleukin-1 β (IL-1 β), and TNF- α as well as ROS species are widely expressed after cartilage degeneration, which provoke the inflammatory reaction. Consequently, Gao et al. designed hybrid scaffolds consisting of poly (L-lactide-co-glycolide) (PLGA) and ROS-scavenging HAMA hydrogels containing ROS-sensitive hyperbranched polymers with thioether linkages, which not only modulated ROS but also regulated inflammation and promoted hyaline cartilage regeneration (Wu et al., 2021).

Similarly, different types of biomaterials have been designed to regulate ROS level for bone tissue regeneration. Huang et al. designed aniline tetramer (AT) and glycine ethyl ester co-substituted polyorganophosphazene (PATGP) based scaffolds

(Huang et al., 2020). The AT moieties possessed antioxidative properties and phosphazene induced bone regeneration, which exhibited ROS-scavenging effect in a cranial defect model. Lee et al. fabricated bone morphogenetic protein-2 (BMP-2) loaded PCL/TA scaffolds, which displayed antioxidative and anti-inflammatory properties by scavenging ROS in H_2O_2 -pretreated MC3T3-E1 cells (Lee et al., 2018). Similarly, Zhou et al. exploited polypyrrole-polydopamine (PPy-PDA) coating on hydroxyapatite scaffolds, which exhibited ROS scavenging ability both *in vivo* and *in vitro* (Zhou et al., 2019). The composite porous scaffold provided excellent bone regeneration through the synergistic effects of electroactivity, cellular affinity, and antioxidant activity of PPy-PDA nanoparticles and osteogenic induction of hydroxyapatite NPs. Wang et al. prepared a series of novel chemically modified N-polyphenol substituted chitosan derivatives, which displayed antioxidative activity as well as promoted the differentiation of MSCs (Wang J. et al., 2020). Hammond et al. further exploited poly (thioethers) (PTK) to afford layer-by-layer coatings to deliver BMP-2 for calvarial defect regeneration in a ROS mediated manner (Martin et al., 2021). Cell-mediated increase in the ROS can cleave the PTK-based LBL coatings, which can then release BMP-2 to promote bone repair and may have broad applications to leverage therapeutics delivery in a stimuli-responsive manner. Similarly, Chen et al. synthesized chitosan nitrogen-doped carbon dots (N-CDs) to scavenge ROS (Chen et al., 2020). The N-CDs effectively inhibited osteoclast formation and bone resorption *in vitro*. In addition, the *in vivo* administration of N-CDs protected mice from LPS-induced cranial bone destruction and breast cancer cell-induced tibial bone loss.

REGULATION OF ROS FOR WOUND HEALING

Wound healing is a complex biological process that occurs in various tissues/organs of human body, consisting of multiple phases including hemostasis, inflammation, proliferation and remodeling (Wu et al., 2019). It has been well-established that wounds express high ROS level as compared to normal tissues. The excessive amount of ROS generated at the wound sites aggravate oxidative stress, which eventually leads to dysfunction in the cellular machinery, including DNA/RNA damage, protein dysfunction and apoptosis. As a result, the elevated production of ROS can perturb the wound healing. Therefore, different types of ROS-responsive biomaterials have been developed and implemented for wound repair, including hydrogels, nanofibrous materials, nanoparticulate drug delivery systems, surgical sutures and microneedle patches by the direct or indirect management of local ROS production to regulate wound healing process (Figure 1 and Table 1).

Hydrogel dressings, a kind of biomaterials that can provide a moist environment due to their three-dimensional (3D) porous network with high water content, are considered as ideal candidates for promoting wound healing (Yin et al., 2021; Zheng et al., 2021). However, the excessive amount of ROS accumulated at the injury site hampers the wound healing process. Consequently, to decrease the ROS level in the

wounds, many ROS-scavenging materials have been incorporated into hydrogel dressings, such as antioxidants, enzymes and nanomaterials (Cheng et al., 2021). Antioxidants can be either directly loaded into hydrogels or conjugated with the polymer chains to achieve their localized and sustained release (Ren et al., 2021). These types of hydrogels were able to eliminate excess ROS production. For example, TA, a natural plant-derived polyphenol, has attracted widespread interest because of its outstanding biological functions such as antioxidative, antibacterial and anti-inflammatory properties. Inspired by these characteristics, TA was introduced into multifunctional hydrogels for infected wound healing application (He et al., 2020; Ma et al., 2020). Similarly, the antioxidant gallic acid was conjugated onto gelatin chains and blended with gelatin-hydroxyphenyl propionic (GH) hydrogels to fabricate an injectable hydrogel (Le Thi et al., 2020). Because of their ROS-scavenging potential, these hydrogels effectively reduced intracellular ROS production and accelerated wound closure. Interestingly, the ROS-scavenging hydrogels can also be developed by using a ROS-responsive linker. In the presence of ROS-sensitive linkers, such hydrogels were able to consume excessive ROS and induce drug release to inhibit bacterial infection, modulate inflammatory response, and promote angiogenesis and wound healing (Zhao et al., 2020; Yang et al., 2021; An et al., 2022). Since the oxygen acts as a key factor in maintaining normal cellular metabolism and promoting cell proliferation, to improve the healing process, a feasible strategy involves the simultaneous elimination of ROS and concomitant supply of oxygen at the wound site. Liu et al. designed an injectable hyaluronic acid (HA)-based hydrogels consisting of manganese dioxide (MnO_2) nanosheets, M2 macrophages-derived exosomes and FGF-2 (Xiong et al., 2021). The MnO_2 nanosheets can efficiently catalyze the decomposition of the excess ROS (H_2O_2) into oxygen (O_2), thus reducing the ROS levels and increasing O_2 production to provide cellular protective action against oxidative microenvironment. The *in vivo* results manifested that these hydrogels can create a favorable microenvironment to accelerate healing of diabetic wounds by alleviating oxidative stress and inducing angiogenesis.

The topography of biomaterials is an important biophysical cue which affects cellular behavior, such as adhesion, proliferation and differentiation (Chaudhuri et al., 2020). Nanofibrous materials which exhibit similar microstructure to the ECM, are considered to be ideal candidates for wound dressing (Chen et al., 2019). Electrospinning technology has been widely used for fabricating nanofibrous wound dressings. The Spirulina extract was loaded into electrospun PCL nanofibers to reduce ROS production and restore cellular activities in a cutaneous wound healing model (Jung et al., 2016). The Spirulina extract-loaded PCL scaffolds exerted significant antioxidant and anti-inflammatory activities to induce wound repair. Similarly, diabetic patients, the excessive ROS and inflammatory factors delay wound healing. To address this issue, Lin et al. fabricated hierarchical micro/nanofibrous scaffolds by using electrospinning and crystal engineering methods to achieve the sustained release of curcumin and Zn^{2+} , which acted synergistically and not only reduced ROS level but also impeded the secretion of inflammatory factors (Wang

Y. et al., 2020). The *in vivo* experiments further demonstrated a reduction in the oxidative stress and anti-inflammatory response, whereas an enhancement in ECs proliferation and neo-angiogenesis, ultimately translating into enhanced diabetic wound healing. Li and co-workers developed redox-sensitive poly (N-isopropylacrylamide-acrylic acid) (PNA) nanogels-incorporated nanofibrous poly (L-lactic acid) membranes (Zhang S. et al., 2021). The disulfide-containing PNA nanogels can balance the ROS level to create favorable microenvironment for tissue repair. Consequently, the PNA-containing nanofibrous membranes accelerated wound healing process via adjusting the ROS level.

Bacterial-infected wounds could not heal quickly (Ji et al., 2021; Wang et al., 2021). Nanomaterials exhibiting light-responsive multifunctional properties were designed as an enticing platform for the management of bacterial-infected wounds. To leverage synergistic chemical and photodynamic therapy for bacteria-contaminated skin wounds, Wang et al. developed photosensitizer chlorin e6 (Ce6) and magnesium (Mg)-contained nanocomplexes (Hu et al., 2019). The multifunctional nanoparticles could efficiently produce ROS under laser irradiation to kill the bacteria. Additionally, ROS-responsive release of Mg^{2+} from the nanoparticles could promote cell proliferation and migration and significantly accelerate wound healing. Xia et al. synthesized ROS-responsive poly-(1,4-phenyleneacetone dimethylene thioketal) (PPADT) nanoparticles loaded with stromal cell-derived factor-1 α (SDF-1 α), which can achieve targeted delivery of SDF-1 α to wound sites with high concentrations of ROS (Tang et al., 2015). The thioketal bonds in the PPADT can be cleaved in the presence of ROS, which then lead to the local release of SDF-1 α to induce bone marrow mesenchymal stem cells (BMSCs) homing and wound healing. Since surgical sutures are often used for wound closure, ROS-scavenging gallic acid-based nanoparticles (GANPs) coated collagen sutures were fabricated (Zhu et al., 2021). These sutures with GANPs coating can effectively scavenge ROS, promote macrophages polarization toward M2 phenotype, upregulate the expression level of anti-inflammatory factors, and accelerate wound healing process.

Microneedle patches are novel therapeutic systems in the field of wound healing. They have minimal invasion towards the skin and imperceptible pain after treatment. To achieve ROS-responsive on-demand drug delivery in the inflammatory tissues, a drug-loaded ROS-responsive poly (vinyl alcohol) (RR-PVA) microneedle patch was prepared (Zhang et al., 2018). A dual phenylboronic acid contained linker was introduced into PVA matrix, which can be cleaved by the ROS. With the ROS-dependent degradation of RR-PVA, sustained release of antibiotic clindamycin (CDM) was achieved. Thus, the CDM-loaded microneedle patch can deliver drugs into the dermis for acne vulgaris treatment. Therefore, it is a feasible and efficient strategy to develop ROS-responsive biomaterials to manipulate the balance of ROS levels for wound healing applications.

CONCLUSIONS AND OUTLOOK

ROS play a significant role in numerous biological functions. A lack or an excess of oxidative stress and ROS may cause different

types of diseases, including auto-immune diseases, cardiovascular diseases, and neurodegenerative diseases and so on. The excessive ROS and oxidative stress can induce strong inflammatory response to interfere tissue repair as well as perturb tissue repair and disturb immune system. The implantation of biomaterials also elevates oxidative stress as well as recruit inflammatory cell types. Overall, this necessitates a thorough understanding of ROS-mediated cellular/tissues injury and devise strategies to manage ROS level. A further insight on ROS signaling in injury and tissue microenvironment is warranted.

So far, a myriad of ROS scavengers, including systematically delivered nanoparticles, therapeutics, and biomaterials have been put forwarded. It is however only the latter which can help realize ROS regulation, as well as ROS-responsive payload release for inflammation regulation and tissue repair. Biomaterial with the inherent ability to regulate ROS by scavenging ROS have been designed, including those containing ROS-responsive linkers, radical scavenging polymers, controlled release of biologics or therapeutics, antioxidants, enzymes, and nanomaterials and have been used for the regeneration of infarcted heart, injured intervertebral disk, defected bone/cartilage tissues and skeletal muscles, chronic diabetic wounds, and cell therapy. ROS-responsive biomaterials which can help release biological signaling molecules, growth factors, and therapeutics in injury microenvironment and cell-mediated manner could help regulate ROS as well as alleviate oxidative stress and modulate tissue repair. These ROS-regulating biomaterials need further attention of the scientific community. Since elevated oxidative stress can perturb tissue repair and cellular functions, biomaterials with the ability to concurrently regulate ROS, alleviate oxidative stress, induce tissue regeneration, and enhance stem cell function,

including survival, retention, and engraftment hold great promise for regenerative medicine and tissue regeneration and need further attention.

Tissue regeneration involves multiple steps manifesting the key role of inflammatory and fibrotic responses, intelligent biomaterials with multiple functionalities and with the capabilities to regulate ROS, and modulate macrophages polarization towards M2 phenotypes and induce tissue repair are warranted. The ROS-responsive biomaterials can be processed into different shapes and structures, such as nanoparticles, nanofibers, microneedles, hydrogels, and so on to further enhance their applicability and harness ROS for tissue regeneration.

AUTHOR CONTRIBUTIONS

MS, YC, RH, and XZ wrote the original manuscript; MS, CH, XM, and XZ reviewed and edited the manuscript. All authors read and approved the final manuscript.

FUNDING

This study was supported by the Fundamental Research Funds for the Central Universities (2232021D-10), National Natural Science Foundation of China (32171404, 32071350, 32050410286), Natural Science Foundation of Shanghai (21ZR1403100) and Shanghai Committee of Science and Technology (19441902600, 20DZ2254900, 20S31900900).

REFERENCES

- Abe, S., Obata, Y., Oka, S., Koji, T., Nishino, T., and Izumikawa, K. (2016). Chondroitin Sulfate Prevents Peritoneal Fibrosis in Mice by Suppressing NF- κ B Activation. *Med. Mol. Morphol.* 49, 144–153. doi:10.1007/s00795-016-0133-8
- An, Z., Zhang, L., Liu, Y., Zhao, H., Zhang, Y., Cao, Y., et al. (2022). Injectable Thioketal-Containing Hydrogel Dressing Accelerates Skin Wound Healing with the Incorporation of Reactive Oxygen Species Scavenging and Growth Factor Release. *Biomater. Sci.* doi:10.1039/D1BM01179K
- Bai, J., Zhang, Y., Fan, Q., Xu, J., Shan, H., Gao, X., et al. (2020). Reactive Oxygen Species-Scavenging Scaffold with Rapamycin for Treatment of Intervertebral Disk Degeneration. *Adv. Healthc. Mater.* 9, 1901186. doi:10.1002/adhm.201901186
- Blanco, F. J., Rego, I., and Ruiz-Romero, C. (2011). The Role of Mitochondria in Osteoarthritis. *Nat. Rev. Rheumatol.* 7, 161–169. doi:10.1038/nrrheum.2010.213
- Carlo, M. D., Jr, and Loeser, R. F. (2003). Increased Oxidative Stress with Aging Reduces Chondrocyte Survival: Correlation with Intracellular Glutathione Levels. *Arthritis Rheum.* 48, 3419–3430. doi:10.1002/art.11338
- Chaudhuri, O., Cooper-White, J., Janmey, P. A., Mooney, D. J., and Shenoy, V. B. (2020). Effects of Extracellular Matrix Viscoelasticity on Cellular Behaviour. *Nature* 584, 535–546. doi:10.1038/s41586-020-2612-2
- Chen, Q., Shao, X., Ling, P., Liu, F., Han, G., and Wang, F. (2017). Recent Advances in Polysaccharides for Osteoarthritis Therapy. *Eur. J. Med. Chem.* 139, 926–935. doi:10.1016/j.ejmech.2017.08.048
- Chen, Q., Wu, J., Liu, Y., Li, Y., Zhang, C., Qi, W., et al. (2019). Electrospun chitosan/PVA/bioglass Nanofibrous Membrane with Spatially Designed Structure for Accelerating Chronic Wound Healing. *Mater. Sci. Eng. C* 105, 110083. doi:10.1016/j.msec.2019.110083
- Chen, R., Liu, G., Sun, X., Cao, X., He, W., Lin, X., et al. (2020). Chitosan Derived Nitrogen-Doped Carbon Dots Suppress Osteoclastic Osteolysis via Downregulating ROS. *Nanoscale* 12, 16229–16244. doi:10.1039/d0nr02848g
- Chen, Y., Xu, W., Shafiq, M., Tang, J., Hao, J., Xie, X., et al. (2021). Three-dimensional Porous Gas-Foamed Electrospun Nanofiber Scaffold for Cartilage Regeneration. *J. Colloid Interf. Sci.* 603, 94–109. doi:10.1016/j.jcis.2021.06.067
- Chen, Z., Duan, J., Diao, Y., Chen, Y., Liang, X., Li, H., et al. (2021). ROS-responsive Capsules Engineered from EGCG-Zinc Networks Improve Therapeutic Angiogenesis in Mouse Limb Ischemia. *Bioactive Mater.* 6, 1–11. doi:10.1016/j.bioactmat.2020.07.013
- Cheng, H., Shi, Z., Yue, K., Huang, X., Xu, Y., Gao, C., et al. (2021). Sprayable Hydrogel Dressing Accelerates Wound Healing with Combined Reactive Oxygen Species-Scavenging and Antibacterial Abilities. *Acta Biomater.* 124, 219–232. doi:10.1016/j.actbio.2021.02.002
- Chin, K.-Y., and Ima-Nirwana, S. (2018). The Role of Vitamin E in Preventing and Treating Osteoarthritis - A Review of the Current Evidence. *Front. Pharmacol.* 9, 946. doi:10.3389/fphar.2018.00946
- Ding, J., Yao, Y., Li, J., Duan, Y., Nakkala, J. R., Feng, X., et al. (2020). A Reactive Oxygen Species Scavenging and O₂ Generating Injectable Hydrogel for Myocardial Infarction Treatment *In Vivo*. *Small* 16, 2005038. doi:10.1002/smll.202005038
- Feng, S., Zhao, Y., Xian, M., and Wang, Q. (2015). Biological Thiols-Triggered Hydrogen Sulfide Releasing Microfibers for Tissue Engineering Applications. *Acta Biomater.* 27, 205–213. doi:10.1016/j.actbio.2015.09.010
- Grover, A. K., and Samson, S. E. (2016). Benefits of Antioxidant Supplements for Knee Osteoarthritis: Rationale and Reality. *Nutr. J.* 15, 1–13. doi:10.1186/s12937-015-0115-z

- Hameister, R., Kaur, C., Dheen, S. T., Lohmann, C. H., and Singh, G. (2020). Reactive Oxygen/nitrogen Species (ROS/RNS) and Oxidative Stress in Arthroplasty. *J. Biomed. Mater. Res.* 108, 2073–2087. doi:10.1002/jbm.b.34546
- Hao, T., Li, J., Yao, F., Dong, D., Wang, Y., Yang, B., et al. (2017). Injectable Fullerene/alginic Acid Hydrogel for Suppression of Oxidative Stress Damage in Brown Adipose-Derived Stem Cells and Cardiac Repair. *ACS Nano* 11, 5474–5488. doi:10.1021/acsnano.7b00221
- He, X., Liu, X., Yang, J., Du, H., Chai, N., Sha, Z., et al. (2020). Tannic Acid-Reinforced Methacrylated Chitosan/methacrylated Silk Fibroin Hydrogels with Multifunctionality for Accelerating Wound Healing. *Carbohydr. Polym.* 247, 116689. doi:10.1016/j.carbpol.2020.116689
- Hu, C., Zhang, F., Kong, Q., Lu, Y., Zhang, B., Wu, C., et al. (2019). Synergistic Chemical and Photodynamic Antimicrobial Therapy for Enhanced Wound Healing Mediated by Multifunctional Light-Responsive Nanoparticles. *Biomacromolecules* 20, 4581–4592. doi:10.1021/acs.biomac.9b01401
- Huang, Y., Du, Z., Wei, P., Chen, F., Guan, B., Zhao, Z., et al. (2020). Biodegradable Microspheres Made of Conductive Polyorganophosphazene Showing Antioxidant Capacity for Improved Bone Regeneration. *Chem. Eng. J.* 397, 125352. doi:10.1016/j.cej.2020.125352
- Jain, A., Behera, M., Mahapatra, C., Sundaresan, N. R., and Chatterjee, K. (2021). Nanostructured Polymer Scaffold Decorated with Cerium Oxide Nanoparticles toward Engineering an Antioxidant and Anti-hypertrophic Cardiac Patch. *Mater. Sci. Eng. C* 118, 111416. doi:10.1016/j.msec.2020.111416
- Ji, Y., Han, Z., Ding, H., Xu, X., Wang, D., Zhu, Y., et al. (2021). Enhanced Eradication of Bacterial/fungi Biofilms by Glucose Oxidase-Modified Magnetic Nanoparticles as a Potential Treatment for Persistent Endodontic Infections. *ACS Appl. Mater. Inter.* 13, 17289–17299. doi:10.1021/acsami.1c01748
- Jung, S.-M., Min, S. K., Lee, H. C., Kwon, Y. S., Jung, M. H., and Shin, H. S. (2016). Spirulina-PCL Nanofiber Wound Dressing to Improve Cutaneous Wound Healing by Enhancing Antioxidative Mechanism. *J. Nanomater.* 2016, 6135727. doi:10.1155/2016/6135727
- Lee, J., Lim, H., Ahn, J., Jang, D., Lee, S., Park, K., et al. (2018). Design of a 3D BMP-2-Delivering Tannylated PCL Scaffold and its Anti-oxidant, Anti-inflammatory, and Osteogenic Effects *In Vitro*. *Int. J. Mol. Sci.* 19, 3602. doi:10.3390/ijms19113602
- Lee, S. H., Gupta, M. K., Bang, J. B., Bae, H., and Sung, H.-J. (2013). Current Progress in Reactive Oxygen Species (ROS)-Responsive Materials for Biomedical Applications. *Adv. Healthc. Mater.* 2, 908–915. doi:10.1002/adhm.201200423
- Li, J., and Zheng, J. (2019). Theaflavins Prevent Cartilage Degeneration via AKT/FOXO3 Signaling *In Vitro*. *Mol. Med. Rep.* 19, 821–830. doi:10.3892/mmr.2018.9745
- Li, J., Chen, L., Xu, X., Fan, Y., Xue, X., Shen, M., et al. (2020). Targeted Combination of Antioxidative and anti-Inflammatory Therapy of Rheumatoid Arthritis Using Multifunctional Dendrimer-entrapped Gold Nanoparticles as a Platform. *Small* 16, e2005661. doi:10.1002/smll.202005661
- Li, Y.-S., Zhang, F.-J., Zeng, C., Luo, W., Xiao, W.-F., Gao, S.-G., et al. (2016). Autophagy in Osteoarthritis. *Jt. Bone Spine* 83, 143–148. doi:10.1016/j.jbspin.2015.06.009
- Li, Y., Chen, M., Yan, J., Zhou, W., Gao, S., Liu, S., et al. (2021). Tannic acid/Sr2+-Coated Silk/graphene Oxide-Based Meniscus Scaffold with Anti-inflammatory and Anti-ROS Functions for Cartilage protection and Delaying Osteoarthritis. *Acta Biomater.* 126, 119–131. doi:10.1016/j.actbio.2021.02.046
- Li, Z., Zhu, D., Hui, Q., Bi, J., Yu, B., Huang, Z., et al. (2021). Injection of ROS-Responsive Hydrogel Loaded with Basic Fibroblast Growth Factor into the Pericardial Cavity for Heart Repair. *Adv. Funct. Mater.* 31, 2004377. doi:10.1002/adfm.202004377
- Liang, R., Zhao, J., Li, B., Cai, P., Loh, X. J., Xu, C., et al. (2020). Implantable and Degradable Antioxidant Poly(ϵ -Caprolactone)-Lignin Nanofiber Membrane for Effective Osteoarthritis Treatment. *Biomaterials* 230, 119601. doi:10.1016/j.biomaterials.2019.119601
- Ma, M., Zhong, Y., and Jiang, X. (2020). Thermosensitive and pH-Responsive Tannin-Containing Hydroxypropyl Chitin Hydrogel with Long-Lasting Antibacterial Activity for Wound Healing. *Carbohydr. Polym.* 236, 116096. doi:10.1016/j.carbpol.2020.116096
- Marchev, A. S., Dimitrova, P. A., Burns, A. J., Kostov, R. V., Dinkova-Kostova, A. T., and Georgiev, M. I. (2017). Oxidative Stress and Chronic Inflammation in Osteoarthritis: Can NRF2 Counteract These Partners in Crime? *Ann. N.Y. Acad. Sci.* 1401, 114–135. doi:10.1111/nyas.13407
- Maron, D. J., Lu, G. P., Cai, N. S., Wu, Z. G., Li, Y. H., Chen, H., et al. (2003). Cholesterol-Lowering Effect of a Theaflavin-Enriched Green Tea Extract. *Arch. Intern. Med.* 163, 1448–1453. doi:10.1001/archinte.163.12.1448
- Martin, J. R., Howard, M. T., Wang, S., Berger, A. G., and Hammond, P. T. (2021). Oxidation-Responsive, Tunable Growth Factor Delivery from Polyelectrolyte-Coated Implants. *Adv. Healthc. Mater.* 10, 2001941. doi:10.1002/adhm.202001941
- Pei, Y., Cui, F., Du, X., Shang, G., Xiao, W., Yang, X., et al. (2019). Antioxidative Nanofullerene Inhibits Macrophage Activation and Development of Osteoarthritis in Rats. *Int. J. Nanomedicine* 14, 4145–4155. doi:10.2147/ijn.s202466
- Poole, K. M., Nelson, C. E., Joshi, R. V., Martin, J. R., Gupta, M. K., Haws, S. C., et al. (2015). ROS-responsive Microspheres for on Demand Antioxidant Therapy in a Model of Diabetic Peripheral Arterial Disease. *Biomaterials* 41, 166–175. doi:10.1016/j.biomaterials.2014.11.016
- Ren, Y., Zhang, D., He, Y., Chang, R., Guo, S., Ma, S., et al. (2021). Injectable and Antioxidative HT/QGA Hydrogel for Potential Application in Wound Healing. *Gels* 7, 204. doi:10.3390/gels7040204
- Saravanakumar, G., Kim, J., and Kim, W. J. (2017). Reactive-Oxygen-Species-Responsive Drug Delivery Systems: Promises and Challenges. *Adv. Sci.* 4, 1600124. doi:10.1002/advs.201600124
- Shan, H., Gao, X., Zhang, M., Huang, M., Fang, X., Chen, H., et al. (2021). Injectable ROS-Scavenging Hydrogel With MSCs Promoted the Regeneration of Damaged Skeletal Muscle. *J. Tissue Eng.* 12, 1–15. doi:10.1177/20417314211031378
- Shiekh, P. A., Singh, A., and Kumar, A. (2018). Engineering Bioinspired Antioxidant Materials Promoting Cardiomyocyte Functionality and Maturation for Tissue Engineering Application. *ACS Appl. Mater. Inter.* 10, 3260–3273. doi:10.1021/acsami.7b14777
- Sintra, T. E., Luís, A., Rocha, S. N., Lobo Ferreira, A. I. M. C., Gonçalves, F., Santos, L. M. N. B. F., et al. (2015). Enhancing the Antioxidant Characteristics of Phenolic Acids by Their Conversion into Cholinium Salts. *ACS Sustainable Chem. Eng.* 3, 2558–2565. doi:10.1021/acssuschemeng.5b00751
- Tang, T., Jiang, H., Yu, Y., He, F., Ji, S. Z., Liu, Y. Y., et al. (2015). A New Method of Wound Treatment: Targeted Therapy of Skin Wounds with Reactive Oxygen Species-Responsive Nanoparticles Containing SDF-1 α . *Int. J. Nanomedicine* 10, 6571–6585. doi:10.2147/IJN.S88384
- Thi, P. L., Lee, Y., Tran, D. L., Thi, T. T. H., Kang, J. I., Park, K. M., et al. (2020). *In Situ* forming and Reactive Oxygen Species-Scavenging Gelatin Hydrogels for Enhancing Wound Healing Efficacy. *Acta Biomater.* 103, 142–152. doi:10.1016/j.actbio.2019.12.009
- Van Lith, R., Gregory, E. K., Yang, J., Kibbe, M. R., and Ameer, G. A. (2014). Engineering Biodegradable Polyester Elastomers with Antioxidant Properties to Attenuate Oxidative Stress in Tissues. *Biomaterials* 35, 8113–8122. doi:10.1016/j.biomaterials.2014.06.004
- Vong, L. B., Bui, T. Q., Tomita, T., Sakamoto, H., Hiramatsu, Y., and Nagasaki, Y. (2018). Novel Angiogenesis Therapeutics by Redox Injectable Hydrogel - Regulation of Local Nitric Oxide Generation for Effective Cardiovascular Therapy. *Biomaterials* 167, 143–152. doi:10.1016/j.biomaterials.2018.03.023
- Wang, J., Zhou, L., Sun, Q., Cai, H., and Tan, W.-S. (2020). Porous Chitosan Derivative Scaffolds Affect Proliferation and Osteogenesis of Mesenchymal Stem Cell via Reducing Intracellular ROS. *Carbohydr. Polym.* 237, 116108. doi:10.1016/j.carbpol.2020.116108
- Wang, W., Chen, J., Li, M., Jia, H., Han, X., Zhang, J., et al. (2019). Rebuilding Postinfarcted Cardiac Functions by Injecting TIIA@PDA Nanoparticle-Cross-Linked ROS-Sensitive Hydrogels. *ACS Appl. Mater. Inter.* 11, 2880–2890. doi:10.1021/acsami.8b20158
- Wang, Y., Ying, T., Li, J., Xu, Y., Wang, R., Ke, Q., et al. (2020). Hierarchical Micro/nanofibrous Scaffolds Incorporated with Curcumin and Zinc Ion Eutectic Metal Organic Frameworks for Enhanced Diabetic Wound Healing via Anti-oxidant and Anti-inflammatory Activities. *Chem. Eng. J.* 402, 126273. doi:10.1016/j.cej.2020.126273
- Wang, Z., Mei, L., Liu, X., and Zhou, Q. (2021). Hierarchically Hybrid Biocoatings on Ti Implants for Enhanced Antibacterial Activity and Osteogenesis. *Colloids Surf. B: Biointerfaces* 204, 111802. doi:10.1016/j.colsurfb.2021.111802

- Woo, M., Kwon, D. H., Choi, Y. H., and Noh, J. S. (2020). Inhibitory Effects of Skate Cartilage Chondroitin Sulfate-Rich Extract on the Production of Inflammatory Mediators and ROS in Lipopolysaccharide-Treated Murine Macrophages: a Comparison with Shark Cartilage Chondroitin Sulfate. *In Vitro Cell.Dev.Biol.-Animal* 56, 271–276. doi:10.1007/s11626-020-00443-8
- Wu, J., Chen, A., Zhou, Y., Zheng, S., Yang, Y., An, Y., et al. (2019). Novel H2S-Releasing Hydrogel for Wound Repair via *In Situ* Polarization of M2 Macrophages. *Biomaterials* 222, 119398. doi:10.1016/j.biomaterials.2019.119398
- Wu, X., Ding, J., Xu, P., Feng, X., Wang, Z., Zhou, T., et al. (2021). A Cell-free ROS-Responsive Hydrogel/oriented Poly(lactide-Co-Glycolide) Hybrid Scaffold for Reducing Inflammation and Restoring Full-Thickness Cartilage Defects *In Vivo*. *Biomed. Mater.* 16, 064101. doi:10.1088/1748-605x/ac21dd
- Xiong, Y., Chen, L., Liu, P., Yu, T., Lin, C., Yan, C., et al. (2021). All-in-One: Multifunctional Hydrogel Accelerates Oxidative Diabetic Wound Healing through Timed-Release of Exosome and Fibroblast Growth Factor. *Small*, 2104229. doi:10.1002/sml.202104229
- Xue, S., Zhou, X., Sang, W., Wang, C., Lu, H., Xu, Y., et al. (2021). Cartilage-targeting Peptide-Modified Dual-Drug Delivery Nanoplatfrom with NIR Laser Response for Osteoarthritis Therapy. *Bioactive Mater.* 6, 2372–2389. doi:10.1016/j.bioactmat.2021.01.017
- Yang, C., Chen, Y., Huang, H., Fan, S., Yang, C., Wang, L., et al. (2021). ROS-eliminating Carboxymethyl Chitosan Hydrogel to Enhance Burn Wound-Healing Efficacy. *Front. Pharmacol.* 12, 679580. doi:10.3389/fphar.2021.679580
- Yin, X., Hao, Y., Lu, Y., Zhang, D., Zhao, Y., Mei, L., et al. (2021). Bio-Multifunctional Hydrogel Patches for Repairing Full-Thickness Abdominal Wall Defects. *Adv. Funct. Mater.* 31, 2105614. doi:10.1002/adfm.202105614
- Zhang, J., Hu, J., Chen, B., Zhao, T., and Gu, Z. (2021). Superabsorbent Poly(acrylic Acid) and Antioxidant Poly(ester Amide) Hybrid Hydrogel for Enhanced Wound Healing. *Regener. Biomater.* 8, rbaa059. doi:10.1093/rb/rbaa059
- Zhang, S., Li, Y., Qiu, X., Jiao, A., Luo, W., Lin, X., et al. (2021). Incorporating Redox-Sensitive Nanogels into Bioabsorbable Nanofibrous Membrane to Acquire ROS-Balance Capacity for Skin Regeneration. *Bioactive Mater.* 6, 3461–3472. doi:10.1016/j.bioactmat.2021.03.009
- Zhang, Y., Feng, P., Yu, J., Yang, J., Zhao, J., Wang, J., et al. (2018). ROS-responsive Microneedle Patch for Acne Vulgaris Treatment. *Adv. Therap.* 1, 1800035. doi:10.1002/adtp.201800035
- Zhao, H., Huang, J., Li, Y., Lv, X., Zhou, H., Wang, H., et al. (2020). ROS-scavenging Hydrogel to Promote Healing of Bacteria Infected Diabetic Wounds. *Biomaterials* 258, 120286. doi:10.1016/j.biomaterials.2020.120286
- Zheng, W., Hao, Y., Wang, D., Huang, H., Guo, F., Sun, Z., et al. (2021). Preparation of Triamcinolone Acetonide-Loaded Chitosan/fucoidan Hydrogel and its Potential Application as an Oral Mucosa Patch. *Carbohydr. Polym.* 272, 118493. doi:10.1016/j.carbpol.2021.118493
- Zhong, G., Yang, X., Jiang, X., Kumar, A., Long, H., Xie, J., et al. (2019). Dopamine-melanin Nanoparticles Scavenge Reactive Oxygen and Nitrogen Species and Activate Autophagy for Osteoarthritis Therapy. *Nanoscale* 11, 11605–11616. doi:10.1039/c9nr03060c
- Zhou, T., Yan, L., Xie, C., Li, P., Jiang, L., Fang, J., et al. (2019). A Mussel-Inspired Persistent ROS-Scavenging, Electroactive, and Osteoinductive Scaffold Based on Electrochemical-Driven *In Situ* Nanoassembly. *Small* 15, 1805440. doi:10.1002/sml.201805440
- Zhu, J., Jin, Q., Zhao, H., Zhu, W., Liu, Z., and Chen, Q. (2021). Reactive Oxygen Species Scavenging Sutures for Enhanced Wound Sealing and Repair. *Small Structures* 2, 2100002. doi:10.1002/sstr.202100002
- Zhu, Y., Matsumura, Y., Velayutham, M., Foley, L. M., Hitchens, T. K., and Wagner, W. R. (2018). Reactive Oxygen Species Scavenging with a Biodegradable, Thermally Responsive Hydrogel Compatible with Soft Tissue Injection. *Biomaterials* 177, 98–112. doi:10.1016/j.biomaterials.2018.05.044

Conflict of Interest: The authors declare that the research was conducted in the absence of any commercial or financial relationships that could be construed as a potential conflict of interest.

Publisher's Note: All claims expressed in this article are solely those of the authors and do not necessarily represent those of their affiliated organizations, or those of the publisher, the editors and the reviewers. Any product that may be evaluated in this article, or claim that may be made by its manufacturer, is not guaranteed or endorsed by the publisher.

Copyright © 2021 Shafiq, Chen, Hashim, He, Mo and Zhou. This is an open-access article distributed under the terms of the Creative Commons Attribution License (CC BY). The use, distribution or reproduction in other forums is permitted, provided the original author(s) and the copyright owner(s) are credited and that the original publication in this journal is cited, in accordance with accepted academic practice. No use, distribution or reproduction is permitted which does not comply with these terms.



Hybrid Hydrogel Composed of Hyaluronic Acid, Gelatin, and Extracellular Cartilage Matrix for Perforated TM Repair

Yili Wang^{1,2}, Feng Wen^{1,2}, Xueting Yao³, Lulu Zeng³, Jiaming Wu³, Qinhong He³, Huaqiong Li^{1,2,3,4*} and Lian Fang^{1*}

¹ENT Department, Joint Centre of Translational Medicine, The First Affiliated Hospital of Wenzhou Medical University, Wenzhou, China, ²Joint Centre of Translational Medicine, Zhejiang Engineering Research Center for Tissue Repair Materials, Wenzhou Institute, University of Chinese Academy of Sciences, Wenzhou, China, ³School of Biomedical Engineering, School of Ophthalmology and Optometry and Eye Hospital, Wenzhou Medical University, Wenzhou, China, ⁴Oujiang Laboratory (Zhejiang Lab for Regenerative Medicine, Vision and Brain Health), Wenzhou, China

OPEN ACCESS

Edited by:

Qihui Zhou,
Qingdao University, China

Reviewed by:

Zuyong Wang,
Hunan University, China
Huan Zhou,
Hebei University of Technology, China

*Correspondence:

Huaqiong Li
lihq@ucas.ac.cn
Lian Fang
fanglian@wzhospital.cn

Specialty section:

This article was submitted to
Biomaterials,
a section of the journal
Frontiers in Bioengineering and
Biotechnology

Received: 09 November 2021

Accepted: 02 December 2021

Published: 24 December 2021

Citation:

Wang Y, Wen F, Yao X, Zeng L, Wu J, He Q, Li H and Fang L (2021) Hybrid Hydrogel Composed of Hyaluronic Acid, Gelatin, and Extracellular Cartilage Matrix for Perforated TM Repair. *Front. Bioeng. Biotechnol.* 9:811652. doi: 10.3389/fbioe.2021.811652

A novel series of composite hydrogels, built from the three components 1), hyaluronic acid methacryloyl (HAMA); 2), gelatin methacryloyl (GelMA), and 3), extracellular cartilage matrix (ECM), was prepared and studied regarding the possible utility in the surgical repair of damaged (perforated) tympanic membrane (TM). Noteworthy is component 3), which was harvested from the ribs of α -1,3-galactosidyltransferase-knockout (α -1,3 GalT-KO) pigs. The absence of α -1,3-galactosyl glycoprotein is hypothesized to prevent rejection due to foreign-body immunogenicity. The composite hydrogels were characterized by various aspects, using a variety of physicochemical techniques: aqueous swelling, structural degradation, behavior under compression, and morphology, e.g., *in vitro* biocompatibility was assessed by the CCK-8 and live-dead assays and through cytoskeleton staining/microscopy. Alcian blue staining and real-time PCR (RT-PCR) were performed to examine the chondrogenic induction potential of the hydrogels. Moreover, a rat TM defect model was used to evaluate the *in vivo* performance of the hydrogels in this particular application. Taken together, the results from this study are surprising and promising. Much further development work will be required to make the material ready for surgical use.

Keywords: tissue engineering, tympanic membrane perforation, extracellular cartilage matrix, hyaluronic acid, gelatin

1 INTRODUCTION

The evidence of the role of trauma, otitis media, and iatrogenic injuries in the origin of TM perforation was increasing in recent years. Concurrently, the TM perforation therapy can be approximately segmented into two categories: surgery (autografts, allografts, and xenografts) and non-surgery (filling materials such as cotton sheet, silk, gelatin sponge) (Azimi et al., 2021; Immich et al., 2017). However, autologous graft is a conventional treatment of perforated TM. The shortage of available tissues and multiple postoperative complications limit the widespread clinical application (Seonwoo et al., 2019).

In order to overcome the limitation of tissue transplantation, various artificial materials have been tried in the field of tissue engineering. For instance, calcium alginate, silk fibroin, and chitosan extract

matrix have been used for TM regeneration, but they generally have limited material properties and poor acoustic performance (Wang et al., 2021c). In recent years, 3D printing technology, melt molding technology, and other technologies have also been introduced into TM engineering, but its degradation rate, acoustic performance, anti-fouling performance of bacterial biofilm, and other aspects need more detailed clinical application research. Hence, developing an ideal artificial TM with better acoustic performance and mechanical strength, stronger adhesion, and biocompatibility is a significant challenge (Wang et al., 2021).

Recent advances in the development of biomaterials and tissue engineering have spurred the extended use of hydrogel in tissue engineering (Pan et al., 2020; Zhu et al., 2021). Compared with traditional treatments, synthetic materials afford some unique advantages including rich source and minimization of the problem of immunogenicity. In biomaterial and tissue engineering, hydrogel aroused interest for the biomimetic scaffolds, due to its structural similarity to the extracellular matrix and with high water content (Gao et al., 2021; Zheng et al., 2021). Synthetic hydrogels have good mechanical property; however, their absence of bioactivity limits their practical applications. The biological characterization of hydrogel-based biomaterials can satisfy the requirements above. Therefore, hydrogels combined to biomaterials could be an ideal scaffold material for regenerating TM.

GelMA and HAMA are often used as naturally derived biomaterials in tissue engineering and regenerative medicine, which has many advantages, such as biocompatibility, degradability, non-toxicity, large processing capacity, and photo-polymerization (Fan et al., 2020). The cellular actions of gelatin (Gel) include the promotion of cellular proliferation, differentiation, and migration, as well as adhesion, spreading, and activation (Aguilar et al., 2019). Hyaluronic acid (HA) is a ubiquitous structural component of the extracellular matrix and is abundant in the chondral and vitreous tissues. Moreover, HA has favorable hyperelasticity, strength, and biocompatibility for biomaterial applications (Xiao et al., 2019).

Animal-derived biomaterials have been a subject of growing interest in recent years. In this article, the extracellular cartilage matrix (ECM) scaffold not only has a similar biochemical composition to the natural articular cartilage ECM but also is fabricated to mimic cartilage physiological morphology with its well-oriented structure (Assuncao et al., 2020; Sekijima et al., 2014). The α -1,3 GalT-KO pigs are expected to be an excellent biomedical research model contributing to clinical medicine and reducing the widening gap between the demand and supply of human donor organs (Gasek et al., 2021; Liguori et al., 2020).

2 MATERIALS AND METHODS

2.1 Preparation of HAMA

A volume of 1.00 g of sodium hyaluronate (Bloomage Biotechnology Co., Ltd., Shandong, China) was completely dissolved in 100 ml of distilled water, and then methacrylate anhydride (1.00 ml) was added to reach a final concentration of 1% (v/v) and reacted for 24 h (4°C), while 5 M sodium hydroxide was added to maintain the pH of the

reaction solution between 8 and 10. After the reaction, the solution was transferred into a 12–14-kDa dialysis bag for dialysis for 3 days (4°C). Finally, the solution in the dialysis bag was frozen at –80°C for 3 h and then dried in the freeze dryer for 2 days to obtain the final product of HAMA.

2.2 Preparation of ECM

Fresh cartilage tissue (300 g) was collected from the ribs of a α -1, 3-Gal gene knockout pig (Yifan Dai's lab from Nanjing Medical University, Nanjing, China), blood was removed, and then the tissue was cut into small pieces. The following steps were performed subsequently: 1) soak in 10 mM Tris-HCl solution (500 ml), stir for 24 h (45°C), and discard the supernatant; 2) soak in 0.25% (m/v) trypsin (500 ml) and stir for 24 h (37°C), then discard the supernatant (Wang et al., 2021); 3) soak in 0.1% (m/v) SDS (500 ml) for 24 h (45°C) and discard the supernatant; 4) soak in solution (PBS, 500 ml) with a protease inhibitor (Aprotinin 10 KIU/ml; Leupeptin 1 g/ml; PMSF 1 mM; 1% w/t EDTA) for 1 h (at room temperature), then discard the supernatant; 5) repeat step (3); 6) repeat step (4); and 7) after PBS washing for a few times (500 ml, 3×), freeze dry the tissue (Wang et al., 2020). After drying, the cartilage tissue was ground into powder by using the Automatic Freezing Grinding Machine and then lyophilized, and powder with particle size less than 40 μ m was sieved and screened for use.

2.3 Preparation of Composite Hydrogel

The composite hydrogel material was prepared by mixing three types of materials, in which the HAMA content was 1% (m/v), and the contents of GelMA (Cure Gel Co., Ltd., Wenzhou, China) were 10% (m/v) and 15% (m/v), respectively, and the contents of ECM were 0% (m/v), 6% (m/v), 12% (m/v), and 24% (m/v), respectively. After the three materials were mixed evenly, 0.5% (m/v) Irgacur 2959 was added as that photoinitiated and mixed well.

The preparation of the polyvinyl alcohol (PVA)-coated cover plate was as follows: 30 mg PVA was dispersed in 1 ml water and stirred to dissolve completely. The cover plate was soaked in PVA solution, then taken out and placed in an oven at 60°C for drying. The prepared composite hydrogel material was dropped onto a cover plate with PVA coating (45 μ l) without air bubble formation, and another cover plate with PVA coating was lightly covered immediately. The two cover plates were adhered together evenly without external force and then cross-linked under UV (365 nm, 18 mW/cm²) for 2 min. Subsequently, they were immersed in water until PVA was dissolved, and the cover plates fell off. The composite hydrogel scaffold (approximately 0.2 mm) was naturally separated from the cover plates (Figure 1).

The characterization analysis of the composite hydrogel includes the contents of DNA, H&E, and Masson staining; spectroscopic and internal structure are provided in the supplementary materials.

2.4 Characterization of Composite Hydrogel Materials

1) Swelling test

The swelling property of a hydrogel is evaluated by a weighing method. Firstly, the prepared hydrogel was weighed and recorded

as M_0 . Then, the hydrogel was soaked in PBS solution (37°C, 24 h). After swelling equilibrium, the hydrogel was removed and water on the surface was wiped with a filter paper, and then mass was recorded as M_t . The swelling rate is calculated as follows: $S = (M_t - M_0)/M_0 \times 100\%$, where S : swelling rate; M_t : mass after swelling balance; and M_0 : mass before soaked in PBS (Hao et al., 2021). Experiments were done thrice per composition.

2) Degradability test

The hydrogel (5.0 mm diameter, 5.0 mm depth) was prepared by a PTFE mold. The prepared hydrogel was soaked in PBS solution to reach swelling equilibrium (24 h), weighed as W_0 , followed by soaking in 0.5 mg/ml collagenase solution (37°C), and taken out at 4, 8, 12, 24, 48, and 72 h, respectively; a filter paper was used to absorb the excess liquid on the surface and weighed as W_n . Samples in each group were triplicate. The calculation formula of the degradation rate is as follows: $D = (W_0 - W_n)/W_0 \times 100\%$, where D is the degradation rate, W_0 is the initial weight, and W_n is the weight at the predetermined time points.

3) Storage modulus

The hydrogel (8.0 mm diameter, 1.0 mm depth) was prepared, and the rheological mechanics of the hydrogel was accessed using a rheometer (DHR-2, USA). The constant strain was 1%, the angular frequency range was 0.1–100 rad/s, and the temperature was maintained at 37°C during the measurement. Samples in each group were triplicate.

2.5 Biocompatibility

2.5.1 Cell Culture

Human bone marrow mesenchymal stem cells (BMSCs, Stem Cell Bank, Chinese Academy of Sciences, Beijing, China) were thawed and seeded into a 25-cm² culture flask, then 5 ml of DMEM medium (containing 10% fetal bovine serum and 1% penicillin–streptomycin mixture) was added and cultured in a 37°C incubator with 5% CO₂ (Xu et al., 2021). After 24 h, cells were examined (light microscopy); morphology and growth were assessed. When the cells covered 90% of the culture flask, the cells were passaged.

2.5.2 Cytotoxicity

The hydrogel materials (50 µl) were firstly added to the 48-well plate and cross-linked by UV (samples in each group were triplicate). Then, the hydrogel materials were soaked with 200 µl of 75% ethanol for 2 h followed by PBS washing three times (30 min each) in a biological safety cabin. After PBS washing, 200 µl DMEM containing 5×10^3 BMSCs was seeded into each well and cultured in an incubator (5% CO₂, 37°C). The culture medium was changed every 3 days. Cell Counting Kit-8 (CCK-8, Beijing Solarbio Science and Technology Co., Ltd., Beijing, China) was used to detect material cytotoxicity on days 7 and 14 (Zheng et al., 2021). The absorbance value of the reactant was measured at 450-nm wavelength using a microplate reader. The cell survival rate was calculated by the following: cell survival rate $= [(A_s - A_b)/(A_c - A_b)] \times 100\%$; A_s :

absorbance of experimental well (including cells, medium, CCK-8 solution and materials); A_c : absorbance of control well (including cells, medium, CCK-8 solution, but not materials); A_b : absorbance of blank well (including medium, CCK-8 solution, excluding cells and materials).

2.5.3 Cellular Morphology

The morphology of the cells was evaluated by live–dead and cytoskeleton staining on the 7th and 14th days after cell seeding. Acridine orange (AO) and ethidium bromide (EB) solution (1:1) were mixed in the dark according to supplier instructions. After washing with 200 µl PBS for three times, AO/EB mixture solution was added in each well and incubated for 5 min, then the solution was removed and each well was rinsed with PBS for three times (Yin et al., 2021). Cells were observed and recorded with a fluorescence microscope. For cell cytoskeleton staining, 4% paraformaldehyde was firstly used to fix the cells for 2 h followed by PBS washing, and then 200 µl of 0.1% Triton X-100 was added (10 min) to permeabilize cell membranes, and then 200 µl of Rhodamine Phalloidin was added in dark conditions for staining cell cytoskeleton (10 min). The cell cytoskeleton was stained red. After washing with PBS, DAPI was added to stain the cell nuclei for 8 min. The nuclei were stained blue. After washing with PBS, cells were observed and recorded with a fluorescence microscope.

2.5.4 Cell Differentiation—Chondrogenesis-Related Gene Expression

On the 7th and 14th days post cell seeding, the total RNA of cells was extracted and reverse transcribed into cDNA as template. The relative expression levels of ACAN (forward primer: ACTCTGGGTTTTTCGTGACTCT, reverse primer: ACACTCAGC GAGTTGTCATGG), Sox9 (forward primer: AGCGAACGC ACATCAAGAC, reverse primer: CTGTAGGCGATCTGTTGG GG), and Coll2 (forward primer: CCAGATGACCTTCCTACG CC, reverse primer: TTCAGGGCAGTGTACGTGAAC), the markers of chondrogenic differentiation, were examined by a fluorescence quantitative PCR (RT-PCR), with GAPDH (forward primer: GGCACAGTCAAGGCTGAGAAT, reverse primer: ATGGTGGTGAAGACGCCAGT) as a housekeeping gene (Lu et al., 2018). In addition, the ability of the material to induce stem cell chondrogenic differentiation was further verified by Alcian blue staining, as presented in the supplementary materials.

2.6 In vivo Study

The animal experiment procedure in this study was approved by the Ethics Committee of Wenzhou Institute of University of Chinese Academy of Sciences (WIUCAS 20033115, 20200331). Eight healthy rats with a body weight of 400–500 g with sensitive auricle reflex, intact TM, and clear structure were purchased for the construction of a chronic TM perforation injury model. Before operation, 10% chloral hydrate (4 µl/g) was injected intraperitoneally for anesthesia, and the external auditory canal was cleaned. After 75% ethanol disinfection, the anterior part of the TM of the bilateral TM was excised using an iris incision knife under a microscope, and the perforation area accounted for 40%–50% of the TM.

The part of mucosa at the tympanic side of the perforation edge was scraped 1–2 mm using an ear micro curette, and the edge of the perforation was inverted after the four corners of the perforation were cut 1 mm. Intramuscular injection of sulfadiazine sodium (0.125 ml/kg) was used 1 day before surgery and continuously for 5 days after surgery. After the operation, the healing of the TM was observed daily after anesthesia, and the exudate was cleaned. If the perforation healed, the healed TM was opened with a microscopic ear probe, and the wound margin was inverted again. After 2 months of postoperative follow-up, the unhealed TM perforation was considered as chronic perforation, which could be used as an animal experimental model.

Composite hydrogel material 1% HAMA/15% GelMA/24% ECM was implanted into the inner TM of the TM chronic-perforated rats in our experimental group. Rats with perforated TM without implantation were set as blank control. Eight weeks post implantation, after rats were euthanatized using barbiturates, the TM repaired and the surrounding tissue were harvested immediately, observing inflammation or infection, fixed in methyl methacrylate resin after gradient ethanol dehydration, and sliced to an 8- μ m-thick tissue section using a microtome for follow-up H&E staining and morphological analysis.

2.7 Statistical Analysis

GraphPad Prism 5 software was used for statistical analysis. Data were expressed as mean \pm standard deviation, and the t test was used to compare the data of different groups. The level of statistical significance was expressed as * and **: $p < 0.05$; **: $p < 0.01$; and ***: $p < 0.001$.

3 RESULTS

3.1 Characterization of Composite Hydrogel Materials

3.1.1 Swelling

The swelling of composite hydrogels used for TM repair in PBS solution is shown in **Figure 2A**. The capacity of water absorption of the material has an effect on the adhesion and growth of the cells. With the increase in GelMA and ECM contents, the water absorption capacity of the material gradually decreased, and the swelling rate reduced continuously.

3.1.2 Degradability

The degradability of composite hydrogels will affect the growth of new tissues *in vivo*. If the degradation is too fast, the new tissue has not been grown, which is not conducive to the repair of damage. A too slow degradation will hinder the growth of new tissue. The degradation results showed that the degradability of the composite hydrogel was tunable (**Figure 2B**). With the increase in the concentration of GelMA, the degradation rate would decline, and the degradation would be further slowed down after the addition of ECM.

3.1.3 Storage Modulus

The behavior of cells can be guided by the hardness and softness of hydrogels where they were cultured, such as the regulation of cell phenotypes. The results of the rheometer test showed that without decellularized ECM, the maximum storage moduli of hydrogels of 1% HAMA/5% GelMA, 1% HAMA/10% GelMA, and 1% HAMA/15% GelMA were about 4.5, 5, and 6 kPa, respectively (**Figure 2C**). After addition of ECM, the storage modulus of the composite hydrogel gradually increased with the increase in ECM content, and the maximum storage modulus of the 1% HAMA/15% GelMA/24% ECM group was about 24 kPa. From another point of view, these data also confirmed that the composite hydrogels have adjustable mechanical properties.

3.2 Biocompatibility

According to our results of physical properties of the composite hydrogel, the swelling rate of 1% HAMA/5% GelMA was high, the degradation rate was too fast, and the mechanical properties were slightly inadequate. Therefore, only 1% HAMA/10% GelMA and 1% HAMA/15% GelMA were selected in the following experiments.

The CCK-8 kit was used to assess the cell proliferation of the material. As shown in **Figure 3A**, 14 days post cell seeding on the material, the survival rate of cells showed an upward trend with the increase in GelMA and ECM contents. The reason may be that the hard matrix is in favor of cell growth, while the hardness of the hydrogel will increase with the increase in GelMA and ECM contents. In addition, some bioactive factors and components in ECM can further promote cell proliferation and adhesion. The good biocompatibility of the material was further confirmed by cell viability and cytoskeleton staining. After live–dead staining, living cells were green and dead cells were red under a fluorescence microscope. Results showed that there were many living cells on the material on the 7th and 14th days, and no dead cells were found (**Figure 3B**). A few dead cells may have been removed during PBS cleaning. On the seventh day, the cell proliferation on the material surface was not obvious, which may be due to the effect of glycosaminoglycan in ECM on cell adhesion. However, on the 14th day, the cells proliferated and adhered well. The cytoskeleton was stained red, the nucleus was stained blue, and the cell morphology was clearly visible by fluorescence microscopy (**Figure 3C**). With the further proliferation of cells, the cells interwove with each other to form a network. In terms of proliferation and spreading, cells in the ECM-containing group were better than the control.

3.3 Chondrogenic Differentiation

Fluorescence quantitative PCR was used to quantitatively characterize chondrogenic differentiation at the gene level. The relative expression levels of Sox9, ACAN, and Coll2, the key genes of chondrogenic differentiation, were quantitatively measured by RT-PCR on the 14th and 21st days after cell seeding, to characterize the induction of material on cell chondrogenic differentiation (**Figure 3D**). The expression of Sox9 was significantly upregulated at the 14th day and was most obvious in the material group with 24% ECM content. ACAN

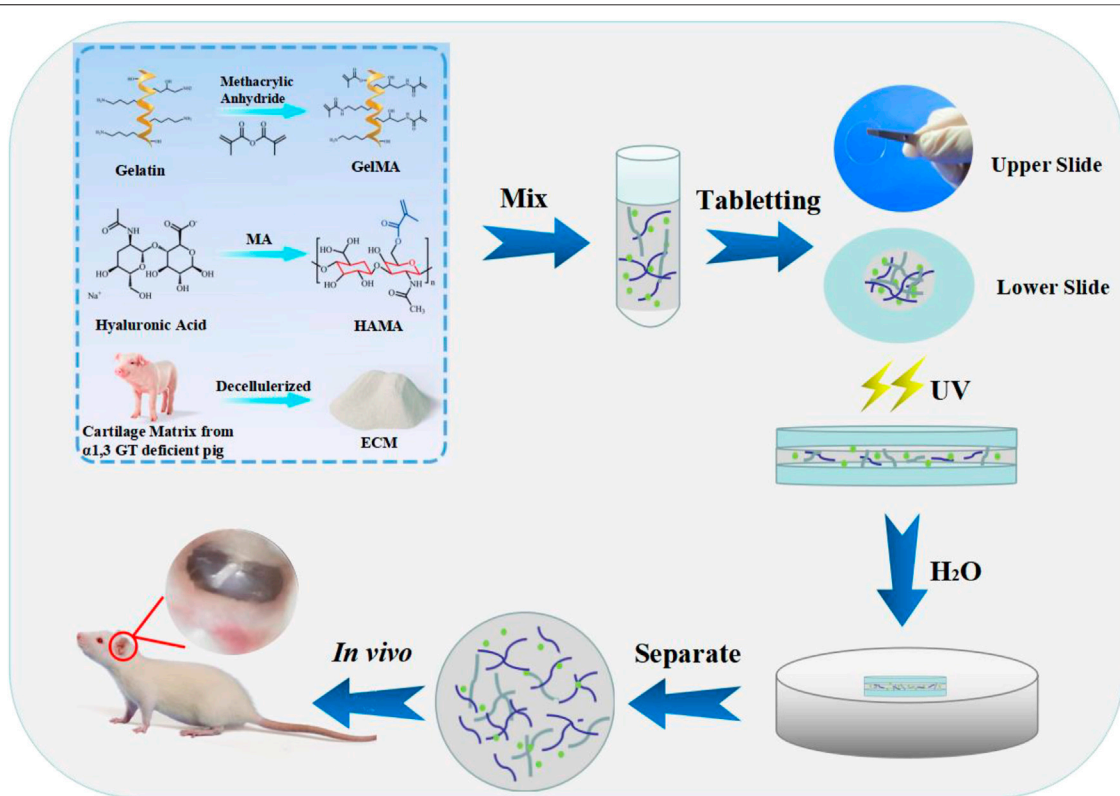


FIGURE 1 | Illustration of the fabrication of the composite hydrogels. The sheet hydrogel was fabricated by photopolymerization of methacrylate gelatin, hyaluronic acid, and extracellular cartilage matrix via tablet.

and Coll2 are the main organic components in the extracellular matrix of chondrogenic tissue and the middle and late stages of chondrogenic differentiation markers. With the increase of culture time, the secretion of ACNA and Coll2 gradually increased, and the gene expression increased significantly with the increase in the proportion of ECM content and reached the highest expression by the induction of 24% ECM. Alcian blue staining further confirmed that the material binding ECM ability had a good ability to induce stem cell differentiation *in vitro* (Supplementary Figure S4).

3.4 In vivo Study

Figure 4A shows a natural transparent eardrum with a thickness of about 0.2 mm. A model of 60%–70% TM area perforated was constructed by piercing the TM tension part of rats with a microscopic ear probe (Figure 4B). The perforated site was observed weekly after surgery, and it was found that about 60% of the perforated TM injury could heal by itself within a week, but 40% of the perforated TM healing process was delayed or non-healing, and the healed TM was no more transparent under ear endoscope (Figure 4C), the tissue proliferation and adhesion in the tympanic cavity were obvious, and the healed TM was thin (Figure 4E). The TM perforation could heal within a week after implantation of the composite hydrogel scaffold (1% HAMA/15% GelMA/24% ECM) in the injured site of TM (Figure 4D). Moreover, the repair site was well recognized.

There is less tissue over proliferation and adhesion in the tympanic cavity, and the TM repaired was significantly thickened, which implied a significant effect on improvement of healing (Figure 4A) (Abaci et al., 2020).

4 DISCUSSION

In recent years, TM perforation has become a common disease in the department of otolaryngology; if the treatment of TM injury is not timely, it may lead to a series of diseases, which often need some medical means to assist the treatment (Gur et al., 2016). The self-healing ability of the TM exists but slowly. At present, there are various drawbacks in the treatment of TM repair (Lee et al., 2018). To overcome the problem of clinical TM perforation repair, we developed a new TM repair scaffold by combining GelMA and HAMA with a decellularized cartilage tissue matrix.

The main objective of this project is to use a new extrusion method, combining hydrogel material with acellular cartilage matrix, to create a bionic eardrum for the treatment of perforated TM. First, an innovative extrusion technique allows the material to be fabricated into a lamellar scaffold without the need for special instrumentations. In recent years, bio-printing technology has been widely used in the study of tissue engineering. For example, Kuo et al. (2018) used bio-printing GelMA to prepare a butterfly-shaped scaffold for TM defect.

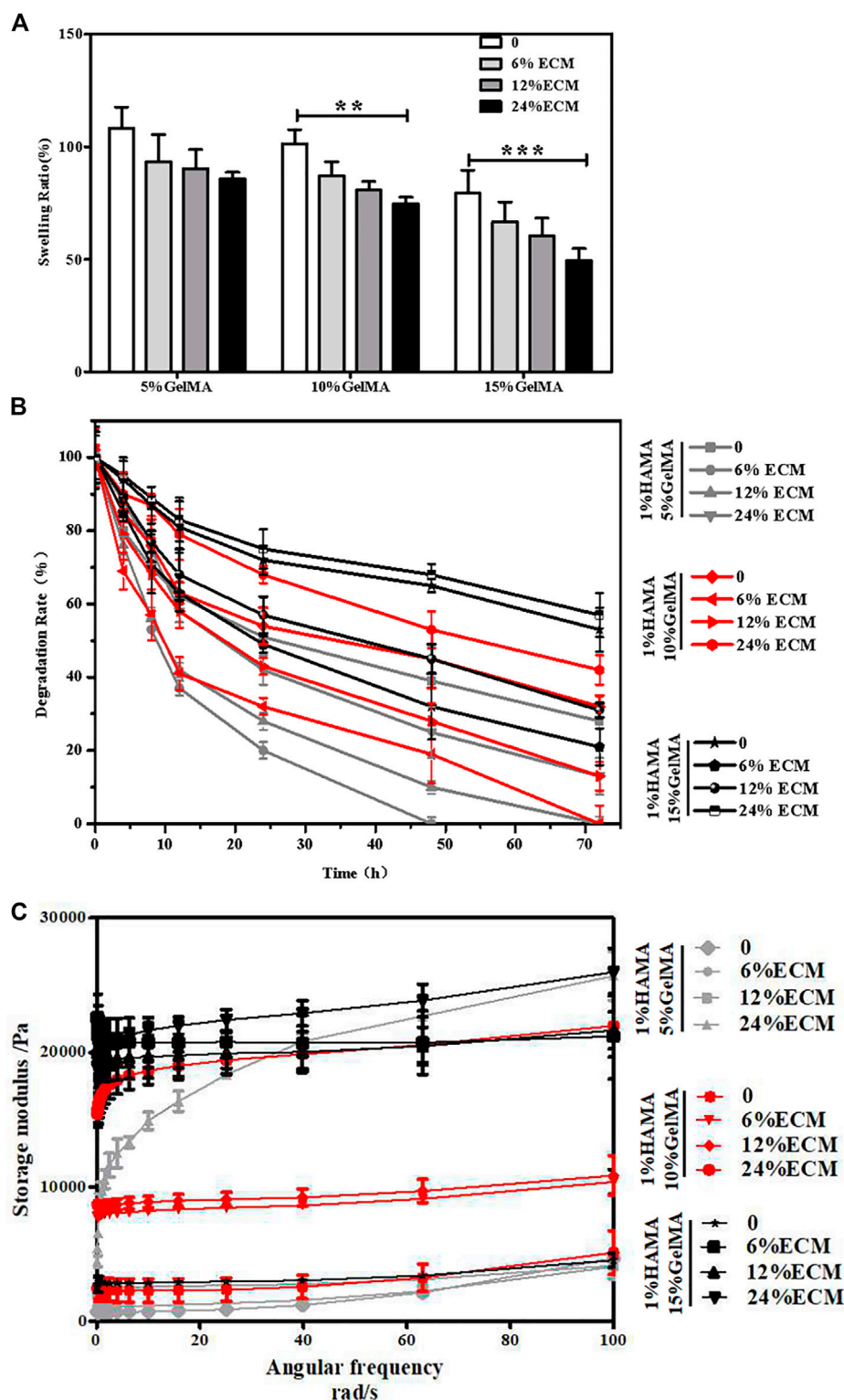


FIGURE 2 | Characterization of the materials. **(A)** Swelling rate of the materials. **(B)** Degradation rate of the materials. **(C)** Storage modulus of the materials. Error bars: \pm SD, * $p < 0.05$, ** $p < 0.01$, *** $p < 0.001$.

Although the butterfly structure is convenient to fix on the damaged site and reduces the operation of suture, it is unable to match actual defect very well. The lamellar hydrogel scaffold

obtained by the innovative extrusion technology is simple and easy to operate, and the maximum storage modulus of the scaffold obtained is 24 kPa (Figure 2C), with excellent

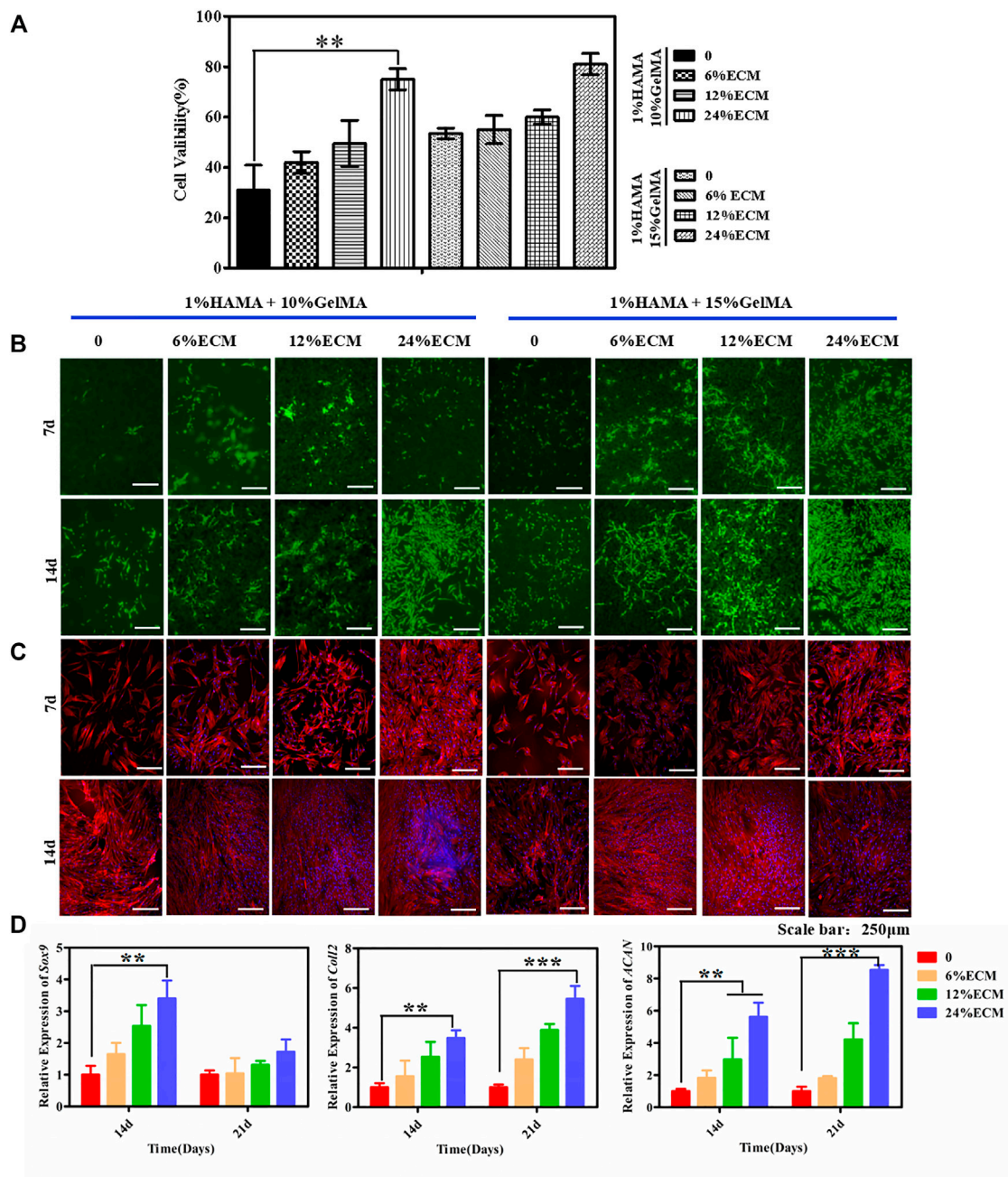
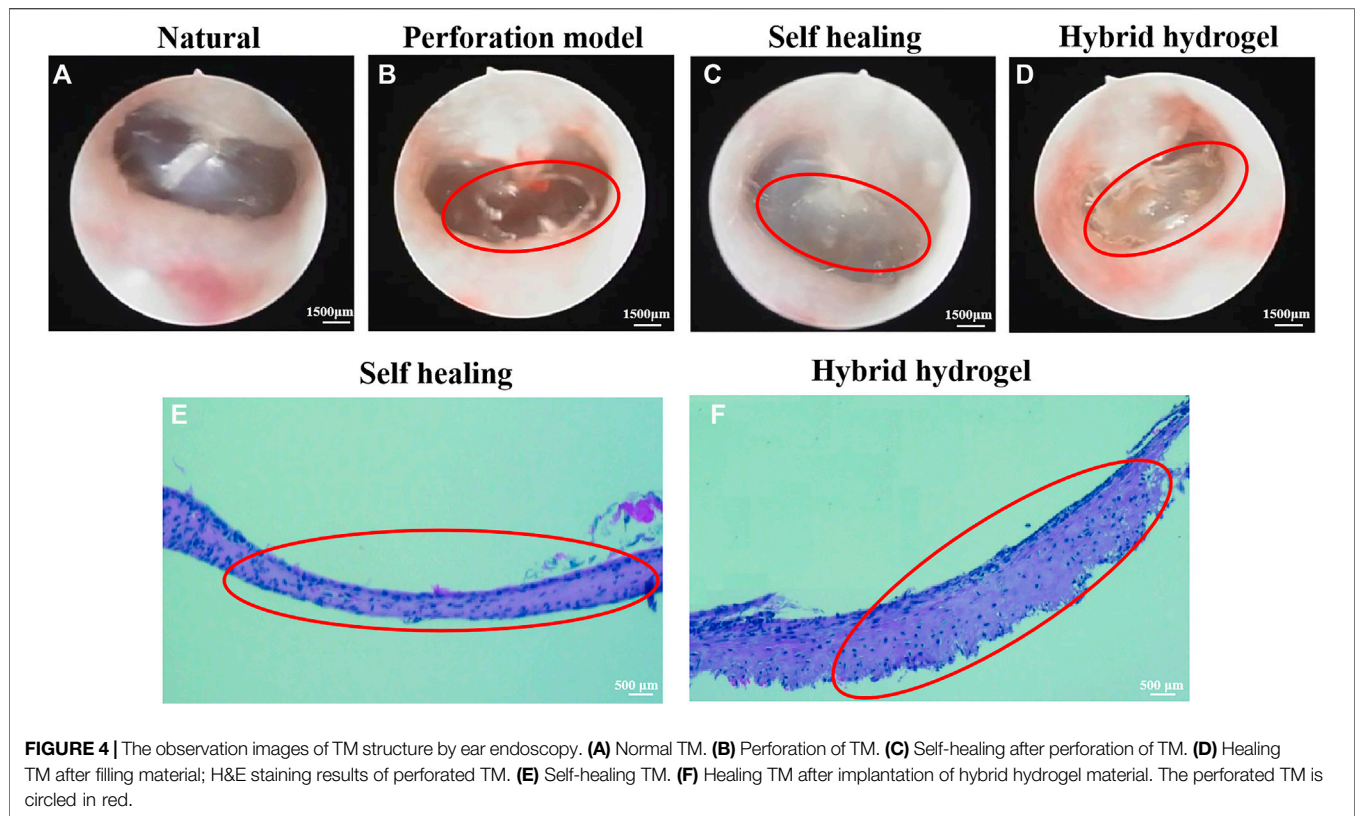


FIGURE 3 | Biocompatibility of the hybrid hydrogel materials. **(A)** The CCK-8 kit was used to detect cytotoxicity. **(B)** Live/dead staining. **(C)** Cytoskeleton staining. **(D)** The chondrogenic differentiation ability of the cells was detected. The relative expression levels of Sox9, Col2, and ACAN were detected by RT-PCR. Error bars: \pm SD, * $p < 0.05$, ** $p < 0.01$, *** $p < 0.001$. Scale bar = 250 μ m.

mechanical properties and certain elasticity, and therefore increase the success rate of tympanoplasty.

Hydrogels have good biocompatibility but lack biological activity and the ability to induce tissue regeneration. In this study, the incorporation of the acellular cartilage matrix mitigated this deficiency. Decellularization removed immunogenic substances from porcine cartilage, leaving mostly extracellular matrix components and some active

factors, which provided a great impetus for improvement of tissue regeneration. Park et al. (Park et al., 2006) have examined the use of various hydrogels for eardrum repair, such as Carbylan (a semisynthetic glycosaminoglycan prepared by introducing an additional carboxyl group into HA), GelMA, HA, Gelfoam, Epifilm, and chondroitin sulfate. Although simple hydrogel scaffold can promote the repair of the injured site to a certain extent, the mechanical properties of the scaffold are weak,



and it is easy to rupture when the pressure changes too fast or the amplitude is too large. Our composite materials enhance the mechanical properties of the scaffolds to a certain extent (**Figure 2**), and *in vitro* cell experiments further confirmed that ECM could promote cell adhesion and proliferation on the surface of the scaffolds (**Figure 3**), making composite hydrogels scaffold become a potential alternative for clinical tympanoplasty.

Compared with the self-healing group, applying a composite hydrogel scaffold in the perforated TM of rats showed that it can achieve an ideal effect, and the new tissue was well connected with the surrounding natural tissue; on the contrary, the self-healing group did not achieve complete repair and the new tissue was sticky and cloudy. Peter Luke Santa Maria et al. (Maria et al., 2016) combined heparin with a growth factor to repair TM defect. Although the repair effect was achieved after 2 months, the recovery of function still needed 1–4 months, and the whole tissue regeneration and function improvement had taken for half year, which was too long. In this regard, our scaffold was superior, and the recovery of the eardrum can be completed within 2 months without affecting the function.

5 CONCLUSION

In this study, in order to better repair the perforated TM, the widely used GelMA/HAMA hydrogel material and acellular cartilage

matrix with non-immunogenicity and good biocompatibility were selected, and the mixed hydrogel material was constructed by UV cross-linking. GelMA and HAMA have been widely used in regenerative tissue engineering and clinical medicine due to their high water content and high elasticity. As a relatively new material, ECM has been decellularized to eliminate the risk of immune rejection and retain most of the extracellular matrix and collagen fibers. The addition of ECM can further induce the chondrogenic differentiation of BMSCs. The experiment of TM perforation repair further confirmed that ECM hydrogel scaffold could promote cartilage regeneration. In conclusion, our results suggest that a combination of three materials that mimic the composition of natural tissues may be a promising candidate functional material.

DATA AVAILABILITY STATEMENT

The original contributions presented in the study are included in the article/**Supplementary Material**; further inquiries can be directed to the corresponding authors.

ETHICS STATEMENT

The animal study was reviewed and approved by the Ethics Committee of Wenzhou Institute of University of Chinese Academy of Sciences (WIUCAS 20033115, 20200331).

AUTHOR CONTRIBUTIONS

HL and YW designed the experiments; YW, XY, and LZ performed the physicochemical characterization of materials. YW, JW, and QH did the *in vitro* assessment of materials. FL created the *in vivo* animal models. FW and LW wrote the manuscript and analyzed the data. HL provided funding for this project. HL and LF supervised the experiments. All authors edited and approved the final manuscript.

ACKNOWLEDGMENTS

The authors acknowledged the financial support from the Zhejiang Provincial Natural Science of Foundation of China (Y20C070010), the ninth Session of the Croatia-China

Scientific and Technological Cooperation Committee Researchers Exchange Program and start-up funding from Wenzhou Institute, University of Chinese Academy of Sciences (WIUCASQD2019002), and The First Affiliated Hospital of Wenzhou Medical University. The authors would also like to acknowledge the Yifan Dai's lab for providing cartilage tissue from α -1,3-galactose-deficient pigs. We are also grateful to LH Koole for his valuable suggestions on the manuscript.

SUPPLEMENTARY MATERIAL

The Supplementary Material for this article can be found online at <https://www.frontiersin.org/articles/10.3389/fbioe.2021.811652/full#supplementary-material>

REFERENCES

- Abaci, A., and Guvendiren, M. (2020). Designing Decellularized Extracellular Matrix-Based Bioinks for 3D Bioprinting. *Adv. Healthc. Mater.* 9, e2000734. doi:10.1002/adhm.202000734
- Assunção, M., Dehghan-Baniani, D., Yiu, C. H. K., Später, T., Beyer, S., and Blocki, A. (2020). Cell-Derived Extracellular Matrix for Tissue Engineering and Regenerative Medicine. *Front. Bioeng. Biotechnol.* 8, 602009. doi:10.3389/fbioe.2020.602009
- Azimi, B., Milazzo, M., and Danti, S. (2021). Cellulose-Based Fibrous Materials from Bacteria to Repair Tympanic Membrane Perforations. *Front. Bioeng. Biotechnol.* 9, 669863. doi:10.3389/fbioe.2021.669863
- Caballero Aguilar, L. M., Kapsa, R. M., O'Connell, C. D., McArthur, S. L., Stoddart, P. R., and Moulton, S. E. (2019). Controlled Release from PCL-Alginate Microspheres via Secondary Encapsulation Using GelMA/HAMA Hydrogel Scaffolds. *Soft Matter* 15, 3779–3787. doi:10.1039/c8sm02575d
- Fan, Y., Yue, Z., Lucarelli, E., and Wallace, G. G. (2020). Hybrid Printing Using Cellulose Nanocrystals Reinforced GelMA/HAMA Hydrogels for Improved Structural Integration. *Adv. Healthc. Mater.* 9, 2001410. doi:10.1002/adhm.202001410
- Gao, C., Sow, W. T., Wang, Y., Wang, Y., Yang, D., Lee, B. H., et al. (2021). Hydrogel Composite Scaffolds with an Attenuated Immunogenicity Component for Bone Tissue Engineering Applications. *J. Mater. Chem. B* 9, 2033–2041. doi:10.1039/d0tb02588g
- Gasek, N., Dearborn, J., Enes, S. R., Pouliot, R., Louie, J., Phillips, Z., et al. (2021). Comparative Immunogenicity of Decellularized Wild Type and Alpha 1,3 Galactosyltransferase Knockout Pig Lungs. *Biomaterials* 276, 121029. doi:10.1016/j.biomaterials.2021.121029
- Gür, Ö. E., Ensari, N., Öztürk, M. T., Boztepe, O. F., Gün, T., Selçuk, Ö. T., et al. (2016). Use of a Platelet-Rich Fibrin Membrane to Repair Traumatic Tympanic Membrane Perforations: a Comparative Study. *Acta Oto-Laryngologica* 136, 1017–1023. doi:10.1080/00016489.2016.1183042
- Hao, Y., Zheng, W., Sun, Z., Zhang, D., Sui, K., Shen, P., et al. (2021). Marine Polysaccharide-Based Composite Hydrogels Containing Fucoidan: Preparation, Physicochemical Characterization, and Biocompatible Evaluation. *Int. J. Biol. Macromolecules* 183, 1978–1986. doi:10.1016/j.jbiomac.2021.05.190
- Immich, A. P. S., Pennacchi, P. C., Naves, A. F., Felisbino, S. L., Boemo, R. L., Maria-Engler, S. S., et al. (2017). Improved Tympanic Membrane Regeneration after Myringoplasty Surgery Using an Artificial Biograft. *Mater. Sci. Eng. C* 73, 48–58. doi:10.1016/j.msec.2016.12.007
- Kuo, C.-Y., Wilson, E., Fuson, A., Gandhi, N., Monfaredi, R., Jenkins, A., et al. (2018). Repair of Tympanic Membrane Perforations with Customized Bioprinted Ear Grafts Using Chinchilla Models. *Tissue Eng. A* 24, 527–535. doi:10.1089/ten.tea.2017.0246
- Lee, M. C., Seonwoo, H., Garg, P., Jang, K. J., Pandey, S., Park, S. B., et al. (2018). Chitosan/PEI Patch Releasing EGF and the EGFR Gene for the Regeneration of the Tympanic Membrane after Perforation. *Biomater. Sci.* 6, 364–371. doi:10.1039/c7bm01061c
- Liguori, G. R., Liguori, T. T. A., de Moraes, S. R., Sinkunas, V., Terlizzi, V., van Dongen, J. A., et al. (2020). Molecular and Biomechanical Clues from Cardiac Tissue Decellularized Extracellular Matrix Drive Stromal Cell Plasticity. *Front. Bioeng. Biotechnol.* 8, 520. doi:10.3389/fbioe.2020.00520
- Lu, J., Shen, X., Sun, X., Yin, H., Yang, S., Lu, C., et al. (2018). Increased Recruitment of Endogenous Stem Cells and Chondrogenic Differentiation by a Composite Scaffold Containing Bone Marrow Homing Peptide for Cartilage Regeneration. *Theranostics* 8, 5039–5058. doi:10.7150/thno.26981
- Pan, Q., Gao, C., Wang, Y., Wang, Y., Mao, C., Wang, Q., et al. (2020). Investigation of Bone Reconstruction Using an Attenuated Immunogenicity Xenogenic Composite Scaffold Fabricated by 3D Printing. *Bio-des. Manuf.* 3, 396–409. doi:10.1007/s42242-020-00086-4
- Park, A. H., Hughes, C. W., Jackson, A., Hunter, L., McGill, L., Simonsen, S. E., et al. (2006). Crosslinked Hydrogels for Tympanic Membrane Repair. *Otolaryngol. Head Neck Surg.* 135, 877–883. doi:10.1016/j.otohns.2006.02.040
- Santa Maria, P. L., Kim, S., and Yang, Y. P. (2016). No Systemic Exposure of Transtympanic Heparin-Binding Epidermal Growth Factor like Growth Factor. *Drug Chem. Toxicol.* 39, 451–454. doi:10.3109/01480545.2016.1143482
- Sekijima, M., Waki, S., Sahara, H., Tasaki, M., Wilkinson, R. A., Villani, V., et al. (2014). Results of Life-Supporting Galactosyltransferase Knockout Kidneys in Cynomolgus Monkeys Using Two Different Sources of Galactosyltransferase Knockout Swine. *Transplantation* 98, 419–426. doi:10.1097/tp.0000000000000314
- Seonwoo, H., Shin, B., Jang, K. J., Lee, M., Choo, O. S., Park, S. B., et al. (2019). Epidermal Growth Factor-Releasing Radially Aligned Electrospun Nanofibrous Patches for the Regeneration of Chronic Tympanic Membrane Perforations. *Adv. Healthc. Mater.* 8, 1801160. doi:10.1002/adhm.201801160
- Wang, B., Xin, T., Shen, L., Zhang, K., Zhang, D., Zhang, H., et al. (2021c). Acoustic Transmitted Electrospun Fibrous Membranes for Tympanic Membrane Regeneration. *Chem. Eng. J.* 419, 129536. doi:10.1016/j.cej.2021.129536
- Wang, Y., Koole, L. H., Gao, C., Yang, D., Yang, L., Zhang, C., et al. (2021a). The Potential Utility of Hybrid Photo-Crosslinked Hydrogels with Non-immunogenic Component for Cartilage Repair. *NPJ Regen. Med.* 6, 54. doi:10.1038/s41536-021-00166-8
- Wang, Y., Xu, Y., Zhou, G., Liu, Y., and Cao, Y. (2020). Biological Evaluation of Acellular Cartilaginous and Dermal Matrixes as Tissue Engineering Scaffolds for Cartilage Regeneration. *Front. Cell Dev. Biol.* 8, 624337. doi:10.3389/fcell.2020.624337
- Wang, Z., Mei, L., Liu, X., and Zhou, Q. (2021b). Hierarchically Hybrid Biocoatings on Ti Implants for Enhanced Antibacterial Activity and Osteogenesis. *Colloids Surf. B: Biointerfaces* 204, 111802. doi:10.1016/j.colsurfb.2021.111802
- Xiao, S., Zhao, T., Wang, J., Wang, C., Du, J., Ying, L., et al. (2019). Gelatin Methacrylate (GelMA)-Based Hydrogels for Cell Transplantation: an Effective Strategy for Tissue Engineering. *Stem Cell Rev Rep* 15, 664–679. doi:10.1007/s12015-019-09893-4

- Xu, Y., Wang, Z., Hua, Y., Zhu, X., Wang, Y., Duan, L., et al. (2021). Photocrosslinked Natural Hydrogel Composed of Hyaluronic Acid and Gelatin Enhances Cartilage Regeneration of Decellularized Trachea Matrix. *Mater. Sci. Eng. C* 120, 111628. doi:10.1016/j.msec.2020.111628
- Yin, X., Hao, Y., Lu, Y., Zhang, D., Zhao, Y., Mei, L., et al. (2021). Bio-Multifunctional Hydrogel Patches for Repairing Full-Thickness Abdominal Wall Defects. *Adv. Funct. Mater.* 31, 2105614. doi:10.1002/adfm.202105614
- Zheng, W., Hao, Y., Wang, D., Huang, H., Guo, F., Sun, Z., et al. (2021). Preparation of Triamcinolone Acetonide-Loaded Chitosan/fucoidan Hydrogels and its Potential Application as an Oral Mucosa Patch. *Carbohydr. Polym.* doi:10.1016/j.carbpol.2021.118493
- Zhu, Y., Liu, L., Sun, Z., Ji, Y., Wang, D., Mei, L., et al. (2021). Fucoidan as a marine-origin Prebiotic Modulates the Growth and Antibacterial Ability of Lactobacillus Rhamnosus. *Int. J. Biol. Macromolecules* 180, 599–607. doi:10.1016/j.ijbiomac.2021.03.065

Conflict of Interest: The authors declare that the research was conducted in the absence of any commercial or financial relationships that could be construed as a potential conflict of interest.

Publisher's Note: All claims expressed in this article are solely those of the authors and do not necessarily represent those of their affiliated organizations, or those of the publisher, the editors, and the reviewers. Any product that may be evaluated in this article, or claim that may be made by its manufacturer, is not guaranteed or endorsed by the publisher.

Copyright © 2021 Wang, Wen, Yao, Zeng, Wu, He, Li and Fang. This is an open-access article distributed under the terms of the Creative Commons Attribution License (CC BY). The use, distribution or reproduction in other forums is permitted, provided the original author(s) and the copyright owner(s) are credited and that the original publication in this journal is cited, in accordance with accepted academic practice. No use, distribution or reproduction is permitted which does not comply with these terms.



Reactive Oxygen Species (ROS)-Responsive Biomaterials for the Treatment of Bone-Related Diseases

Xiaoxiang Ren^{1†}, Han Liu^{1†}, Xianmin Wu^{2†}, Weizong Weng^{1*}, Xiuhui Wang^{1*} and Jiacan Su^{1,3*}

¹Institute of Translational Medicine, Shanghai University, Shanghai, China, ²Department of Orthopedics, Zhongye Hospital of Shanghai, Shanghai, China, ³Department of Orthopedics Trauma, Shanghai Changhai Hospital, Naval Military Medical University, Shanghai, China

OPEN ACCESS

Edited by:

Huihua Yuan,
Nantong University, China

Reviewed by:

Jingyao Li,
University of Wisconsin-Madison,
United States
Yu Tian,
Renji Hospital, China

*Correspondence:

Weizong Weng
drwengweizong@163.com
Xiuhui Wang
blackrabbit@shu.edu.cn
Jiacan Su
drsujiacan@163.com

[†]These authors have contributed
equally to this work

Specialty section:

This article was submitted to
Biomaterials,
a section of the journal
Frontiers in Bioengineering and
Biotechnology

Received: 23 November 2021

Accepted: 10 December 2021

Published: 11 January 2022

Citation:

Ren X, Liu H, Wu X, Weng W, Wang X
and Su J (2022) Reactive Oxygen
Species (ROS)-Responsive
Biomaterials for the Treatment of
Bone-Related Diseases.
Front. Bioeng. Biotechnol. 9:820468.
doi: 10.3389/fbioe.2021.820468

Reactive oxygen species (ROS) are the key signaling molecules in many physiological signs of progress and are associated with almost all diseases, such as atherosclerosis, aging, and cancer. Bone is a specific connective tissue consisting of cells, fibers, and mineralized extracellular components, and its quality changes with aging and disease. Growing evidence indicated that overproduced ROS accumulation may disrupt cellular homeostasis in the progress of bone modeling and remodeling, leading to bone metabolic disease. Thus, ROS-responsive biomaterials have attracted great interest from many researchers as promising strategies to realize drug release or targeted therapy for bone-related diseases. Herein, we endeavor to introduce the role of ROS in the bone microenvironment, summarize the mechanism and development of ROS-responsive biomaterials, and their completion and potential for future therapy of bone-related diseases.

Keywords: bone remodeling, ROS-responsive biomaterials, bone-related diseases, bone regeneration, photodynamic therapy

INTRODUCTION

As an internal support system, bone is a dynamic connective tissue with highly mineralized architecture giving it substantial strength, providing a structural foundation for the human body and muscle (McEnery et al., 2016). Bone is in the dynamic modeling and remodeling processes by developing the activities of bone formation and resorption, for the healthy development of the skeleton (Flores-Silva et al., 2015). With the increased longevity of human life and the aging of population, bone-related diseases, such as osteoporosis, osteosarcoma, bone metastasis, osteoarthritis, and osteomyelitis, cause significant pain and amplify the economic burden for millions of people worldwide. Growing evidence indicates that bone homeostasis is adversely affected by oxidative stress induced by reactive oxygen species (ROS), thus targeting ROS might be a vital approach for the treatment of bone metabolic disorders (Agidigbi and Kim, 2019). In the meantime, ROS are necessary for bone remodeling machinery as they can enhance the degradation of the mineralized matrix and affect the behaviors of all the cells involved in bone remodeling. ROS is normally divided into two categories: non-radical derivatives of oxygen and free chemically reactive oxygen radicals (Phaniendra et al., 2015). ROS production could lead to an increased level of oxidative stress, which increases the risk of mutations in mitochondrial and nuclear DNA (Russo et al., 2012). Besides, oxidative stress has been known as a major donor to the immune response and linked with the pathophysiology of almost all organs (Mittal et al., 2014). It has also been proved that

oxidative stress play role in aging and lead to degenerative diseases with increasing age (Sharifi-Rad et al., 2020). Therefore, it is important to understand how ROS modulate bone biology and pathology.

In addition, for the therapy of bone-related diseases, researchers are developing various scaffolds, hydrogels, nanocarriers, and drugs (Yao et al., 2019; Yin et al., 2021; Zheng et al., 2021). Synthetic or natural biomaterials can enhance the restoration of bone structure and function. Implant materials make contact with the patient's tissue, permitting interactions with endogenous bone. Among all kinds of treatments, developing novel biomaterials and drugs which targeted the high-level ROS should be promising solutions for bone-related diseases. The antioxidants or selected therapeutic compounds can be loaded with biomaterials and will be stimuli-responsive released with the presence of oxidation. Hubbel's team was the first to use ROS-responsive biomaterials for drug delivery in 2001 (Napoli et al., 2001), and then this new strategy quickly spreads for different biomedical applications. However, the summary of the recently developed strategies about ROS-responsive biomaterial for bone-related diseases is still lacking. In this review, we will introduce the major findings of the regulatory role of ROS in osteoclast biology, including the influence of ROS on signaling, proliferation, and differentiation of bone cells. The review will also mention the ROS-responsive biomaterials which could be excellent options sense and respond ROS microenvironment. How targeting ROS may be a solution for the therapy of bone-related diseases, such as osteoarthritis, will be discussed. Finally, we propose a prospect for the trends and future development of ROS-responsive biomaterials for the application in bone tissue.

REACTIVE OXYGEN SPECIES IN BONE REMODELING

Bone is a dynamic organ to achieve the functions such as growth, movement, organ protection, or calcium/phosphate equilibrium (Hardy and Fernandez-Patron, 2020). Bone remodeling is mediated by the progress of formation and resorption led by the activities of osteoblast and osteoclast, allowing bone growth and tissue regeneration (Callaway and Jiang, 2015). In bone tissues, ROS generation is an essential signal in living organisms which could regulate cell functions, mediate inflammation, and affect the pathophysiology of tissues (Wauquier et al., 2009). Among all forms of ROS, the majority of forms related to the osteoclastogenesis are superoxide (O_2^-) and hydrogen peroxide (H_2O_2). Early research in the 1990s was about the first connecting ROS and osteoclast function by assessing the osteoclast activity after adding oxidants or antioxidant enzymes, indicating that the superoxide radical could enhance bone resorption (Garrett et al., 1990). ROS originated from nicotinamide adenine dinucleotide phosphate (NADPH) oxidase (Nox) were localized to the interface of bone-osteoclast, resulting in the production of superoxide within the osteoclast (Key et al., 1990). At the same time, other studies indicated that H_2O_2 was the main ROS to promote the formation

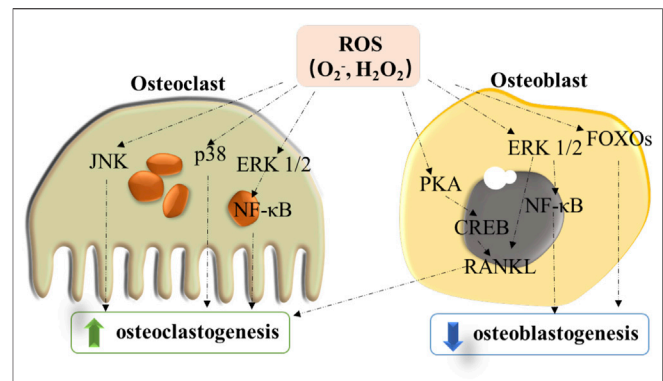


FIGURE 1 | Modulation role of ROS for signaling pathways in inhibiting osteoblast differentiation and enhancing osteoclastogenesis.

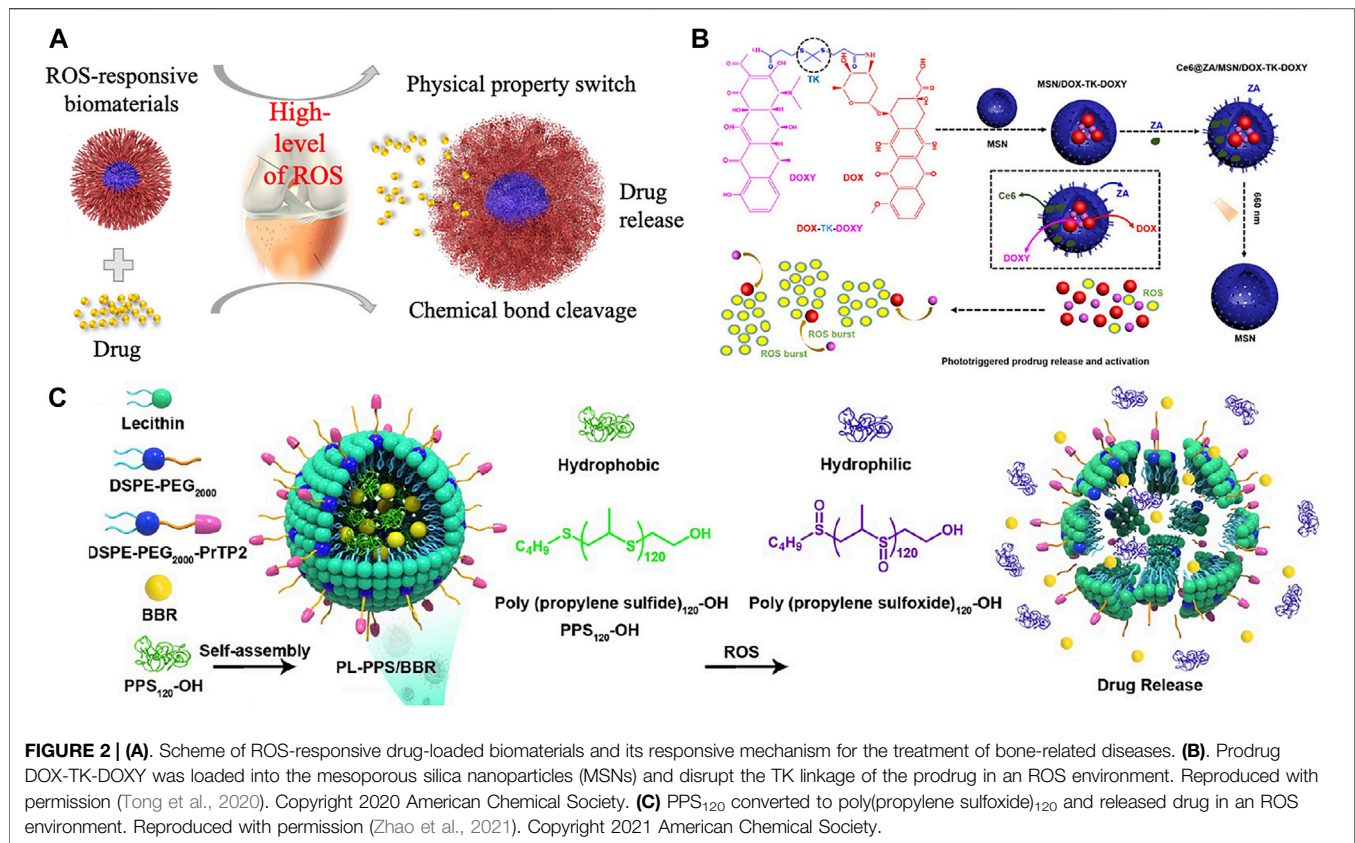
and activity of osteoclast (Kim et al., 2006). However, different from these studies describing a direct role of ROS in bone resorption, subsequent studies suggested that ROS could promote osteoclast formation and activity *via* an indirect mechanism in activating signaling pathways (Hall et al., 1995). Specifically, ROS could influence several signaling pathways such as nuclear factor κ B (NF- κ B) and produce the following receptor activator of NF- κ B ligand (RANKL).

Upon to the enhanced activity of osteoclast by ROS, H_2O_2 has shown an inhibition effect on the cell differentiation of osteoblast activities. Oxidative stress originated from H_2O_2 restrained the process of osteoblastic differentiation in the bone marrow stromal cells (BMSCs) of mouse and rabbit (Bai et al., 2004), showing a reduction in the alkaline phosphatase (ALP) activity. In addition to influencing the differentiation process, ROS also affects the lifespan of osteoblast (Linares et al., 2009). Thus, as shown in **Figure 1**, ROS not only directly promotes osteoclastogenesis but also inhibits the differentiation and growth of osteoblasts by stimulating RANKL-induced formation of osteoclast. ROS seems to perform an important role in bone by affecting both cell types. These findings also indicate that the treatment strategies for bone diseases by targeting ROS should be promising.

THE MECHANISM OF REACTIVE OXYGEN SPECIES-RESPONSIVE BIOMATERIALS

ROS are overproduced in diseased cells, and this property has been employed to develop ROS-responsive biomaterials as an intelligent drug delivery system. In response to ROS, ROS-responsive biomaterials can release drugs, used as targeting delivery agents, imaging agents, and therapeutic agents for regulating the tissue microenvironments and tissue regeneration. As described in **Figure 2**, mechanisms of the responsive function for ROS-responsive biomaterials can be classified into two types: ROS affect the physical properties of biomaterials especially affect their solubility, or ROS mediate the chemical properties which will lead to the bond cleavage reaction.

ROS can affect the physical property, especially the solubility of poly(propylene sulfide) (PPS), thioether-



containing polymers, tellurium-, and selenium-containing polymers, favoring the drug release property (Gao and Xiong, 2021). In the presence of an oxidative environment, the hydrophobic sulfides can convert into hydrophilic sulfoxides and sulfones, contributing to their increased water solubility and potential application for drug delivery (Napoli et al., 2004). Poly(ethylene glycol) (PEG)-b-PPS and PPS-b-pyromellitic dianhydride (PMDA) copolymers are sensitized to H_2O_2 , but shows no response against superoxide. While the PPS-PEG-superoxide dismutase (SOD) micelles are capable to turn into hydrophilic under both superoxide and hydrogen peroxide. In addition, thioether-based biomaterials also will be oxidized under the ROS environment. When susceptible to ROS (100 mM H_2O_2), the hydrophobic backbone of thioether containing biomaterials will be transformed to hydrophilic (Mahmoud et al., 2011). When simulated the ROS environment with 1 mM H_2O_2 , a fast release of berberine (BBR) was observed from PL-PPS/BBR at 48 h (Figure 2C). During this progress, PPS₁₂₀ scavenged ROS and converted to poly(propylene sulfoxide)₁₂₀ when reacted with ROS to obtain the rapid release of BBR (Zhao et al., 2021). Thioether-containing polymers contribute an effective method for loading and delivering hydrophobic drugs especially for the application of cancer therapy. Selenium-containing copolymers show a similar solubility change under ROS as PPS, but more sensitive to ROS due to the bigger lower bond energy and

larger radius of the selenium atom, making selenium-containing polymers a promising material for drug delivery. It was reported that the diselenide-containing micelles could react with ROS at a low concentration of H_2O_2 (0.01% v/v) and release drug in a short time (Xu et al., 2013).

In addition to the oxidant-induced solubility conversion, ROS can cleave the chemical bonds linkage of poly(thioether) (TK), poly(proline), phenylboronic acid, and ester-containing polymers, giving rise to their degradation under the ROS environment. TK-containing polymers can be prepared by directly condensing polymerization using thiols for cancer therapy. With the degradation of thioether linkages after exposure to 0.2 mM KO_2 , poly(1,4-phenylene-acetone dimethylenethioether) (PPADT) has been used for the oral delivery of TNF- α -siRNA to the intestine of mice to treat ulcerative colitis (Wilson et al., 2010). Another ROS and pH dual-responsive PPADT-based biomaterial was developed for antiinflammatory therapy, showing 50% drug releasing in response to 1 mM H_2O_2 within 4 h (Pu et al., 2014). The poly(thioether urethane) (PTK-URs) scaffolds are degraded in contact with the ROS released by cells, showing promising applications for wound repair (Martin et al., 2014) and bone regeneration (McEnery et al., 2016).

Among the various functional groups, phenylboronic acid and ester are unique because they are highly selectively and rapidly

oxidized in response to H_2O_2 and generate phenol and boronic acid (Li et al., 2017). Being a polymer backbone or connected through an ether linkage were two strategies to include the groups in ROS sensitivity polymers which can be degraded in H_2O_2 (50–100 mM). An ROS-responsive nanocarrier (3I-NM@siRNA), which achieve the ROS-responsive property by adding the arylboronic ester group, was designed to carry small interfering RNA (siRNA) to improve long circulation stability of siRNA and increase their delivery efficiency (Zheng et al., 2019). Proline, as one of the amino acids, could also be cleaved by oxidation because of the metal-catalyzed oxidation of the proline segments, which make them a good candidate for ROS-responsive biomaterials (Amici et al., 1989).

REACTIVE OXYGEN SPECIES-RESPONSIVE BIOMATERIALS FOR TREATING BONE-RELATED DISEASES

Osteoarthritis (OA) is the most common form of arthritis, occurring most frequently in the population aged over 60 years (Shane Anderson and Loeser, 2010). OA was a degenerative joint disease and referred as an imbalance between the decay and formation of chondrocytes, extracellular matrix (ECM), and subchondral bone with a main feature of the destruction of cartilage (Sharma et al., 2013). Many factors could increase the risk of OA, including biomechanical forces, ROS, and autoimmunity (Corti, 2003). ROS is suspected in the pathological variation of microenvironments. The excessive ROS in OA will induce the damage of DNA and chondrocytes, and affect the production and turnover of ECM by stimulating matrix metalloproteinases (MMPs). In addition, the excess ECM production will stimulate immune cells to generate more ROS (Khan et al., 2017).

Since there is a positive relation between the high-level ROS and OA, many antioxidants which could scavenge the ROS are used to suppress inflammatory response in OA, including vitamin C, polysaccharides, or polymers without drugs. Polyphenols are derived from plants such as tea or grape, and have high antioxidant property, which have been extensively applied in bone regeneration and encapsulated in a layer-by-layer coated gelatin nanoparticle (Shutava et al., 2009). To obtain a longer site-specific retention time, the ROS scavenger such as nitroxide radical compounds were loaded into triblock copolymers. Sponge polymeric microsphere (PPS-MS) was prepared to treat post-traumatic osteoarthritis (PTOA) by inhibiting the MMP activity and the destruction of articular cartilage (O'Grady et al., 2018).

Traditional therapy for OA requires frequent drug administration due to the quick removal speed. The drug delivery systems maintain the concentration of drugs and achieve specific release at the desirable site. The high concentration of ROS in OA can play as a trigger for the drug release from ROS-responsive biomaterials. For example, hollow poly(lactide-co-glycolide) (PLGA) microspheres were designed to treat OA for the delivery of antiinflammatory drug

dexamethasone, $FeCl_2$, sodium bicarbonate, and ethanol. PLGA shells allow the penetration of H_2O_2 and excessive H_2O_2 will active Fenton's reaction, leading ethanol transform into acetic acid, thus making the sodium bicarbonate generate CO_2 gas to breaks the PLGA shells and release dexamethasone. Compared to free dexamethasone, the responsive drug-loaded biomaterials show significant therapeutic effects (Chung et al., 2015).

Though the presence of ROS would worsen the condition in OA, ROS is required during the early phase of the antimicrobial (Ren et al., 2020a; Ji et al., 2021; Wang et al., 2021; Zhu et al., 2021) and anticancer (Ren et al., 2020b) progress for osteomyelitis and osteosarcomas. Particular emphasis is placed on the ROS-mediated photochemical and molecular mechanisms that give rise to the establishment of photothermal therapy as a treatment of highly resistant diseases, especially invasive and metastatic tumors. The inadequate ROS suppression could hinder the healing but the redox balance needs to be carefully maintained during the tissue regeneration phase.

The photodynamic therapy is a recently developed treatment that produces ROS from photosensitizers or photosensitizing agents by light activation to kill cancer cells or bacteria (Shi et al., 2019). Hu et al. (2019) reported a lipid-polymer hybrid nanocarrier with an ROS-responsive core consisted of homopolymer poly(thioketal phosphoester) (TK-PPE) to encapsulate chlorin e6 (Ce6) and DOX for the treatment of cancer. With the irradiation of 660 nm laser, the encapsulated Ce6 will generate ROS, inducing PDT for cancer treatment and rapidly degrades TK-PPE to burst release the loaded DOX, leading to an efficient combinational therapy of chemo-PDT to inhibit the growth of tumor *in vitro* and *in vivo* (Hu et al., 2019). Similarly, a size changeable HPBTK-Ce6 was designed by conjugating Ce6 onto the micelles containing thioketal units and loaded the anticancer drug camptothecin (CPT). The irradiation of 660 nm laser lead to the size reducing of HPBTK-Ce6@CPT and boost CPT release, which contribute a much deeper penetration in tumor to kill inner tumor cells compared with the original large-size micelles (Jin et al., 2019). More recently, bone-targeting prodrug mesoporous silica-based nanoreactor was developed to treat osteosarcoma. Upon laser irradiation, the loaded Ce6 produces *in situ* ROS and disrupt the TK linkage to release DOX and doxycycline (DOXY) from the prodrugs (Figure 2B) (Tong et al., 2020).

PROSPECT AND CONCLUSION

Many bone-related diseases such as osteoporosis, rheumatoid arthritis, and bone metastases have been linked to the states of higher ROS, thus understanding how ROS interacts with osteoclasts and other cells in the bone could enhance the development of novel therapeutic biomaterials to target ROS in the bone tissue. Antioxidant compounds may be beneficial to bone health, such as dried plum polyphenols (Bu et al., 2008) or simvastatin (Moon et al., 2011). Although it seems promising to use antioxidant agents to target ROS and treat bone diseases, ROS is present over the whole body. Therefore, the non-specificity ROS

targeted compounds may affect other tissues, which are not limited to bone. To specifically treat the bone-related disease, biomaterials which could specifically target bone with ROS responsible property should be focused in the future. The combination with bone targeted drug such as bisphosphonates, oligopeptides, or tetracycline could be a prospective solution. In addition, adapter with ligand-receptor binding with the bone site could be decorated with the surface of ROS-responsive biomaterials. Moreover, multiple responsive carriers can be developed by the combination of ROS-responsive system with functional groups to achieve more accurate controlled release of drugs.

To sum up, ROS-responsive biomaterials have advantages when mediating oxidative stress-related diseases as drug delivery carriers or therapeutic agents, and thus should be a promising strategy for regulating bone microenvironments and bone regeneration.

REFERENCES

- Agidigbi, T. S., and Kim, C. (2019). Reactive Oxygen Species in Osteoclast Differentiation and Possible Pharmaceutical Targets of ROS-Mediated Osteoclast Diseases. *Ijms* 20, 3576–3616. doi:10.3390/ijms20143576
- Amici, A., Levine, R. L., Tsai, L., and Stadtman, E. R. (1989). Conversion of Amino Acid Residues in Proteins and Amino Acid Homopolymers to Carbonyl Derivatives by Metal-Catalyzed Oxidation Reactions. *J. Biol. Chem.* 264, 3341–3346. doi:10.1016/s0021-9258(18)94071-8
- Bai, X.-c., Lu, D., Bai, J., Zheng, H., Ke, Z.-y., Li, X.-m., et al. (2004). Oxidative Stress Inhibits Osteoblastic Differentiation of Bone Cells by ERK and NF-Kb. *Biochem. Biophysical Res. Commun.* 314, 197–207. doi:10.1016/j.bbrc.2003.12.073
- Bu, S. Y., Lerner, M., Stoeker, B. J., Boldrin, E., Brackett, D. J., Lucas, E. A., et al. (2008). Dried Plum Polyphenols Inhibit Osteoclastogenesis by Downregulating NFATc1 and Inflammatory Mediators. *Calcif. Tissue Int.* 82, 475–488. doi:10.1007/s00223-008-9139-0
- Callaway, D. A., and Jiang, J. X. (2015). Reactive Oxygen Species and Oxidative Stress in Osteoclastogenesis, Skeletal Aging and Bone Diseases. *J. Bone Miner. Metab.* 33, 359–370. doi:10.1007/s00774-015-0656-4
- Chung, M.-F., Chia, W.-T., Wan, W.-L., Lin, Y.-J., and Sung, H.-W. (2015). Controlled Release of an Anti-inflammatory Drug Using an Ultrasensitive ROS-Responsive Gas-Generating Carrier for Localized Inflammation Inhibition. *J. Am. Chem. Soc.* 137, 12462–12465. doi:10.1021/jacs.5b08057
- Corti, M. C., and Rigon, C. (2003). Epidemiology of Osteoarthritis: Prevalence, Risk Factors and Functional Impact. *Aging Clin. Exp. Res.* 15, 359–363. doi:10.1007/BF03327356
- Florencio-Silva, R., Sasso, G. R. D. S., Sasso-Cerri, E., Simões, M. J., and Cerri, P. S. (20152015). Biology of Bone Tissue: Structure, Function, and Factors that Influence Bone Cells. *Biomed. Res. Int.* 2015, 1–17. doi:10.1155/2015/421746
- Gao, F., and Xiong, Z. (2021). Reactive Oxygen Species Responsive Polymers for Drug Delivery Systems. *Front. Chem.* 9, 1–17. doi:10.3389/fchem.2021.649048
- Garrett, I. R., Boyce, B. F., Oreffo, R. O., Bonewald, L., Poser, J., and Mundy, G. R. (1990). Oxygen-derived Free Radicals Stimulate Osteoclastic Bone Resorption in Rodent Bone *In Vitro* and *In Vivo*. *J. Clin. Invest.* 85, 632–639. doi:10.1172/JCI114485
- Hall, T. J., Schaeublin, M., Jeker, H., Fuller, K., and Chambers, T. J. (1995). The Role of Reactive Oxygen Intermediates in Osteoclastic Bone Resorption. *Biochem. Biophysical Res. Commun.* 207, 280–287. doi:10.1006/bbrc.1995.1184
- Hardy, E., and Fernandez-Patron, C. (2020). Destroy to Rebuild: The Connection between Bone Tissue Remodeling and Matrix Metalloproteinases. *Front. Physiol.* 11, 1–24. doi:10.3389/fphys.2020.00047
- Hu, L., Cao, Z., Ma, L., Liu, Z., Liao, G., Wang, J., et al. (2019). The Potentiated Checkpoint Blockade Immunotherapy by ROS-Responsive Nanocarrier-Mediated cascade Chemo-Photodynamic Therapy. *Biomaterials* 223, 119469. doi:10.1016/j.biomaterials.2019.119469
- Ji, Y., Han, Z., Ding, H., Xu, X., Wang, D., Zhu, Y., et al. (2021). Enhanced Eradication of Bacterial/Fungi Biofilms by Glucose Oxidase-Modified Magnetic

AUTHOR CONTRIBUTIONS

XR, HL, and XW contributed equally. XW contributed to the conception. XR and HL drew the figures and wrote the article. WW, XW, and JS revised the manuscript. All authors read and approved the submitted version.

ACKNOWLEDGMENTS

The authors acknowledge the financial support from National Key R&D Program of China (2018YFC2001500); National Natural Science Foundation of China (91749204, 82172098, 81771491); Shanghai Municipal Health Commission General Program (201740237).

- Nanoparticles as a Potential Treatment for Persistent Endodontic Infections. *ACS Appl. Mater. Inter.* 13, 17289–17299. doi:10.1021/acsami.1c01748
- Jin, H., Zhu, T., Huang, X., Sun, M., Li, H., Zhu, X., et al. (2019). ROS-responsive Nanoparticles Based on Amphiphilic Hyperbranched Polyphosphoester for Drug Delivery: Light-Triggered Size-Reducing and Enhanced Tumor Penetration. *Biomaterials* 211, 68–80. doi:10.1016/j.biomaterials.2019.04.029
- Key, L. L., Ries, W. L., Taylor, R. G., Hays, B. D., and Pitzer, B. L. (1990). Oxygen Derived Free Radicals in Osteoclasts: The Specificity and Location of the Nitroblue Tetrazolium Reaction. *Bone* 11, 115–119. doi:10.1016/8756-3282(90)90058-7
- Khan, N. M., Haseeb, A., Ansari, M. Y., Devarapalli, P., Haynie, S., and Haqqi, T. M. (2017). Wogonin, a Plant Derived Small Molecule, Exerts Potent Anti-inflammatory and Chondroprotective Effects through the Activation of ROS/ERK/Nrf2 Signaling Pathways in Human Osteoarthritis Chondrocytes. *Free Radic. Biol. Med.* 106, 288–301. doi:10.1016/j.freeradbiomed.2017.02.041
- Kim, H., Kim, I. Y., Lee, S. Y., and Jeong, D. (2006). Bimodal Actions of Reactive Oxygen Species in the Differentiation and Bone-Resorbing Functions of Osteoclasts. *FEBS Lett.* 580, 5661–5665. doi:10.1016/j.febslet.2006.09.015
- Li, C., Pan, R., Li, P., Guan, Q., Ao, J., Wang, K., et al. (2017). Hydrogen Peroxide-Responsive Nanoprobe Assists Circulating Tumor Cell Identification and Colorectal Cancer Diagnosis. *Anal. Chem.* 89, 5966–5975. doi:10.1021/acs.analchem.7b00497
- Linares, G. R., Xing, W., Govoni, K. E., Chen, S.-T., and Mohan, S. (2009). Glutaredoxin 5 Regulates Osteoblast Apoptosis by Protecting against Oxidative Stress. *Bone* 44, 795–804. doi:10.1016/j.bone.2009.01.003
- Mahmoud, E. A., Sankaranarayanan, J., Morachis, J. M., Kim, G., and Almutairi, A. (2011). Inflammation Responsive Logic Gate Nanoparticles for the Delivery of Proteins. *Bioconjug. Chem.* 22, 1416–1421. doi:10.1021/bc200141h
- Martin, J. R., Gupta, M. K., Page, J. M., Yu, F., Davidson, J. M., Guelcher, S. A., et al. (2014). A Porous Tissue Engineering Scaffold Selectively Degraded by Cell-Generated Reactive Oxygen Species. *Biomaterials* 35, 3766–3776. doi:10.1016/j.biomaterials.2014.01.026
- McEnery, M. A. P., Lu, S., Gupta, M. K., Zienkiewicz, K. J., Wenke, J. C., Kalpakci, K. N., et al. (2016). Oxidatively Degradable Poly(thioketal Urethane)/ceramic Composite Bone Cements with Bone-like Strength. *RSC Adv.* 6, 109414–109424. doi:10.1039/c6ra24642g
- Mittal, M., Siddiqui, M. R., Tran, K., Reddy, S. P., and Malik, A. B. (2014). Reactive Oxygen Species in Inflammation and Tissue Injury. *Antioxid. Redox Signaling* 20, 1126–1167. doi:10.1089/ars.2012.5149
- Moon, H.-J., Kim, S. E., Yun, Y. P., Hwang, Y.-S., Bang, J. B., Park, J.-H., et al. (2011). Simvastatin Inhibits Osteoclast Differentiation by Scavenging Reactive Oxygen Species. *Exp. Mol. Med.* 43, 605–612. doi:10.3858/emmm.2011.43.11.067
- Napoli, A., Tirelli, N., Kilcher, G., and Hubbell, A. (2001). New Synthetic Methodologies for Amphiphilic Multiblock Copolymers of Ethylene Glycol and Propylene Sulfide. *Macromolecules* 34, 8913–8917. doi:10.1021/ma0108057
- Napoli, A., Valentini, M., Tirelli, N., Müller, M., and Hubbell, J. A. (2004). Oxidation-responsive Polymeric Vesicles. *Nat. Mater.* 3, 183–189. doi:10.1038/nmat1081

- O'Grady, K. P., Kavanaugh, T. E., Cho, H., Ye, H., Gupta, M. K., Madonna, M. C., et al. (2018). Drug-Free ROS Sponge Polymeric Microspheres Reduce Tissue Damage from Ischemic and Mechanical Injury. *ACS Biomater. Sci. Eng.* 4, 1251–1264. doi:10.1021/acsbomaterials.6b00804
- Phaniendra, A., Jestadi, D. B., and Periyasamy, L. (2015). Free Radicals: Properties, Sources, Targets, and Their Implication in Various Diseases. *Ind. J. Clin. Biochem.* 30, 11–26. doi:10.1007/s12291-014-0446-0
- Pu, H.-L., Chiang, W.-L., Maiti, B., Liao, Z.-X., Ho, Y.-C., Shim, M. S., et al. (2014). Nanoparticles with Dual Responses to Oxidative Stress and Reduced pH for Drug Release and Anti-inflammatory Applications. *ACS Nano* 8, 1213–1221. doi:10.1021/nn4058787
- Ren, X., Gao, R., Van Der Mei, H. C., Ren, Y., Peterson, B. W., and Busscher, H. J. (2020a). Eradicating Infecting Bacteria while Maintaining Tissue Integration on Photothermal Nanoparticle-Coated Titanium Surfaces. *ACS Appl. Mater. Inter.* 12, 34610–34619. doi:10.1021/acsmi.0c08592
- Ren, X., Yi, Z., Sun, Z., Ma, X., Chen, G., Chen, Z., et al. (2020b). Natural Polysaccharide-Incorporated Hydroxyapatite as Size-Changeable, Nuclear-Targeted Nanocarrier for Efficient Cancer Therapy. *Biomater. Sci.* 8, 5390–5401. doi:10.1039/d0bm01320j
- Russo, G., Curcio, F., Bulli, G., Aran, L., Della-morte, D., Testa, G., et al. (2012). *Oxidative Stress and Diseases*. *Oxidative Stress Dis.* 757–772. doi:10.5772/2535
- Shane Anderson, A., and Loeser, R. F. (2010). Why Is Osteoarthritis an Age-Related Disease? *Best Pract. Res. Clin. Rheumatol.* 24, 15–26. doi:10.1016/j.berh.2009.08.006
- Sharifi-Rad, M., Anil Kumar, N. V., Zucca, P., Varoni, E. M., Dini, L., Panzarini, E., et al. (2020). Lifestyle, Oxidative Stress, and Antioxidants: Back and Forth in the Pathophysiology of Chronic Diseases. *Front. Physiol.* 11, 1–21. doi:10.3389/fphys.2020.00694
- Sharma, A., Jagga, S., Lee, S.-S., and Nam, J.-S. (2013). Interplay between Cartilage and Subchondral Bone Contributing to Pathogenesis of Osteoarthritis. *Ijms* 14, 19805–19830. doi:10.3390/ijms141019805
- Shi, X., Zhang, C. Y., Gao, J., and Wang, Z. (2019). Recent Advances in Photodynamic Therapy for Cancer and Infectious Diseases. *WIREs Nanomed Nanobiotechnol* 11, e1560. doi:10.1002/wnan.1560
- Shutava, T. G., Balkundi, S. S., Vangala, P., Steffan, J. J., Bigelow, R. L., Cardelli, J. A., et al. (2009). Layer-by-layer-coated Gelatin Nanoparticles as a Vehicle for Delivery of Natural Polyphenols. *ACS Nano* 3, 1877–1885. doi:10.1021/nn900451a
- Tong, F., Ye, Y., Chen, B., Gao, J., Liu, L., Ou, J., et al. (2020). Bone-Targeting Prodrug Mesoporous Silica-Based Nanoreactor with Reactive Oxygen Species Burst for Enhanced Chemotherapy. *ACS Appl. Mater. Inter.* 12, 34630–34642. doi:10.1021/acsmi.0c08992
- Wang, Z., Mei, L., Liu, X., and Zhou, Q. (2021). Hierarchically Hybrid Biocoatings on Ti Implants for Enhanced Antibacterial Activity and Osteogenesis. *Colloids Surf. B: Biointerfaces* 204, 111802. doi:10.1016/j.colsurfb.2021.111802
- Wauquier, F., Leotoing, L., Coxam, V., Guicheux, J., and Wittrant, Y. (2009). Oxidative Stress in Bone Remodelling and Disease. *Trends Mol. Med.* 15, 468–477. doi:10.1016/j.molmed.2009.08.004
- Wilson, D. S., Dalmasso, G., Wang, L., Sitaraman, S. V., Merlin, D., and Murthy, N. (2010). Orally Delivered Thioketal Nanoparticles Loaded with TNF- α -siRNA Target Inflammation and Inhibit Gene Expression in the Intestines. *Nat. Mater.* 9, 923–928. doi:10.1038/nmat2859
- Xu, H., Cao, W., and Zhang, X. (2013). Selenium-containing Polymers: Promising Biomaterials for Controlled Release and Enzyme Mimics. *Acc. Chem. Res.* 46, 1647–1658. doi:10.1021/ar4000339
- Yao, Y., Zhang, H., Wang, Z., Ding, J., Wang, S., Huang, B., et al. (2019). Reactive Oxygen Species (ROS)-responsive Biomaterials Mediate Tissue Microenvironments and Tissue Regeneration. *J. Mater. Chem. B* 7, 5019–5037. doi:10.1039/c9tb00847k
- Yin, X., Hao, Y., Lu, Y., Zhang, D., Zhao, Y., Mei, L., et al. (2021). Bio-Multifunctional Hydrogel Patches for Repairing Full-Thickness Abdominal Wall Defects. *Adv. Funct. Mater.* 31, 2105614. doi:10.1002/adfm.202105614
- Zhao, Z., Han, Z., Naveena, K., Lei, G., Qiu, S., Li, X., et al. (2021). ROS-responsive Nanoparticle as a Berberine Carrier for OHC-Targeted Therapy of Noise-Induced Hearing Loss. *ACS Appl. Mater. Inter.* 13, 7102–7114. doi:10.1021/acsmi.0c21151
- Zheng, M., Liu, Y., Wang, Y., Zhang, D., Zou, Y., Ruan, W., et al. (2019). ROS-Responsive Polymeric siRNA Nanomedicine Stabilized by Triple Interactions for the Robust Glioblastoma Combinational RNAi Therapy. *Adv. Mater.* 31, 1903277–1903279. doi:10.1002/adma.201903277
- Zheng, W., Hao, Y., Wang, D., Huang, H., Guo, F., Sun, Z., et al. (2021). Preparation of Triamcinolone Acetonide-Loaded Chitosan/fucoidan Hydrogel and its Potential Application as an Oral Mucosa Patch. *Carbohydr. Polym.* 272, 118493. doi:10.1016/j.carbpol.2021.118493
- Zhu, Y., Liu, L., Sun, Z., Ji, Y., Wang, D., Mei, L., et al. (2021). Fucoidan as a marine-origin Prebiotic Modulates the Growth and Antibacterial Ability of Lactobacillus Rhamnosus. *Int. J. Biol. Macromolecules* 180, 599–607. doi:10.1016/j.ijbiomac.2021.03.065

Conflict of Interest: The authors declare that the research was conducted in the absence of any commercial or financial relationships that could be construed as a potential conflict of interest.

Publisher's Note: All claims expressed in this article are solely those of the authors and do not necessarily represent those of their affiliated organizations, or those of the publisher, the editors, and the reviewers. Any product that may be evaluated in this article, or claim that may be made by its manufacturer, is not guaranteed or endorsed by the publisher.

Copyright © 2022 Ren, Liu, Wu, Weng, Wang and Su. This is an open-access article distributed under the terms of the Creative Commons Attribution License (CC BY). The use, distribution or reproduction in other forums is permitted, provided the original author(s) and the copyright owner(s) are credited and that the original publication in this journal is cited, in accordance with accepted academic practice. No use, distribution or reproduction is permitted which does not comply with these terms.



Light-Triggered Adhesive Silk-Based Film for Effective Photodynamic Antibacterial Therapy and Rapid Hemostasis

Tingting Huang¹, Zhihao Zhou¹, Qiaoyuan Li¹, Xiaoxuan Tang^{1,2}, Xiaoli Chen¹, Yifan Ge^{1*} and Jue Ling^{1*}

¹Key Laboratory of Neuroregeneration, Ministry of Education and Jiangsu Province, Co-innovation Center of Neuroregeneration, Jiangsu Clinical Medicine Center of Tissue Engineering and Nerve Injury Repair, Nantong University, Nantong, China, ²Medical School of Nantong University, Nantong University, Nantong, China

OPEN ACCESS

Edited by:

Qihui Zhou,
Qingdao University, China

Reviewed by:

Yikai Xu,
Queen's University Belfast,
United Kingdom
Sainan Li,
Massachusetts General Hospital and
Harvard Medical School, United States

*Correspondence:

Yifan Ge
yifange@ntu.edu.cn
Jue Ling
jl2016@ntu.edu.cn

Specialty section:

This article was submitted to
Biomaterials,
a section of the journal
Frontiers in Bioengineering and
Biotechnology

Received: 23 November 2021

Accepted: 06 December 2021

Published: 11 January 2022

Citation:

Huang T, Zhou Z, Li Q, Tang X, Chen X,
Ge Y and Ling J (2022) Light-Triggered
Adhesive Silk-Based Film for Effective
Photodynamic Antibacterial Therapy
and Rapid Hemostasis.
Front. Bioeng. Biotechnol. 9:820434.
doi: 10.3389/fbioe.2021.820434

Successful control of massive hemorrhage in deep wounds with irregular shape and low elasticity still remains great challenges in the clinic. As the wound sites are usually at risk of bacterial infection, it is necessary to design an ideal hemostatic agent with rapid hemostasis and excellent antibacterial activity. In this study, we developed a light responsive hemostatic film for effective handling of liver bleeding with promising photodynamic therapy against *S. aureus* on near infrared (NIR) irradiation. Based on silk fibroin, the film exhibited desirable biocompatibility and mechanical property as a hemostat tape. Significantly, the film tape achieved excellent tissue adhesion and hemostasis *in vivo* within 2 min of UV exposure, which would have a great potential as a multifunctional biomedical material in the field of tissue repair such as wound healing, bone repair, and nerve regeneration.

Keywords: hemostasis, antibacterial activity, reactive oxygen species, silk fibroin, photodynamic therapy

INTRODUCTION

Massive hemorrhage caused by trauma, traffic accidents, and surgery can lead to excessive blood loss and even death if the effective control of bleeding is not in time (Han et al., 2020; Qiao et al., 2021; Roy et al., 2021). Commercial hemostats, such as gauze, gelatin sponge, and bandages, have been considered to be highly effective in handling bleeding by sealing the wound surface of the bleeding site (Arnaud et al., 2008; Lan et al., 2015; Vilaro et al., 2017). However, they are often invalid for deep wounds with irregular shape and low elasticity, such as the liver, brittle tissue, and abundant capillaries, which are inconvenient to press. Meanwhile, the injury sites are usually at high risk of bacterial infection, which can result in serious symptoms (Deng et al., 2021; Zheng et al., 2021; Zhu et al., 2021). Therefore, it is necessary to develop multifunctional nonpressing hemostatic agents that can perform rapid hemostasis with effective antibacterial activity for minimizing blood loss and improving survival in the clinic.

Silk fibroin (SF) is a natural protein from the silk cocoon with tunable mechanical strength and low immunogenicity (Kim et al., 2021). It is considered as a bioactive and biocompatible protein biomaterial that is suitable for various biomedical applications, such as wound healing, bone repair, and nerve regeneration (Tang et al., 2021a; Bigham et al., 2021; Tang et al., 2021b; Gu et al., 2021; Li et al., 2021). Especially for hemostasis, it has been reported that SF can bind with fibrinogen and blood platelets to facilitate the clotting cascade (Chouhan and Mandal,

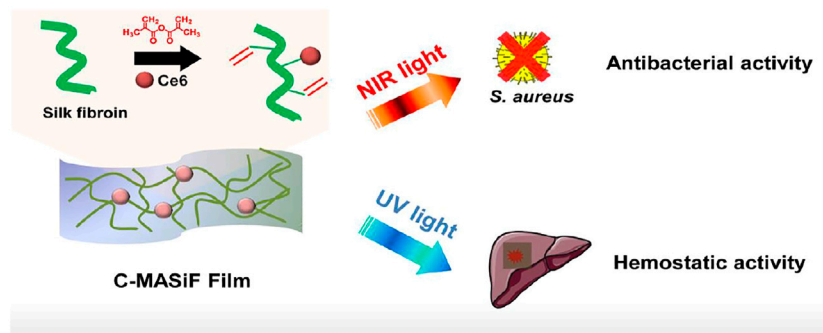


FIGURE 1 | Schematic illustration of silk-based film with effective photodynamic antibacterial therapy and rapid hemostatic activity for handling liver bleeding.

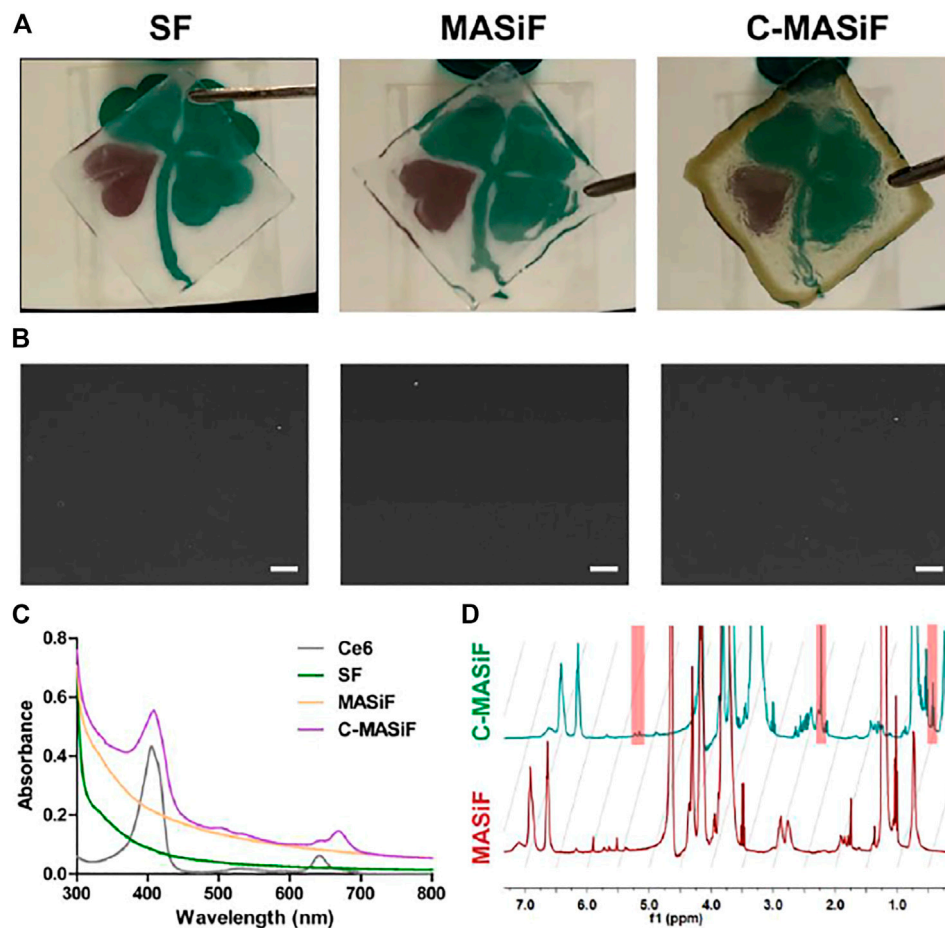


FIGURE 2 | Characterization of MASiF and C-MASiF film. (A) Photographs of SF, MASiF, and C-MASiF film. (B) SEM images of SF, MASiF, and C-MASiF film. Scale bar: 20 μ m. (C) UV-vis spectra of Ce6, SF, MASiF, and C-MASiF. (D) ¹H NMR spectra of MASiF and C-MASiF.

2020). Importantly, the hemostatic activity of SF can further act as a cargo to release inflammatory factors to lead hemostasis to the next phase of the healing process (Santin et al., 1999). However, lack of antibacterial activity limits the further application of SF on handling bleeding and dressing the wounds (Xuan et al., 2020).

Recently, as the extensive use of antibiotics causes the emergence of antibiotic-resistant bacteria, photodynamic therapy (PDT) has been regarded as an effective method to kill multidrug-resistant bacteria, such as *Staphylococcus aureus* (*S. aureus*) (Mao et al., 2020). By generating reactive oxygen species (ROS) under light exposure, PDT

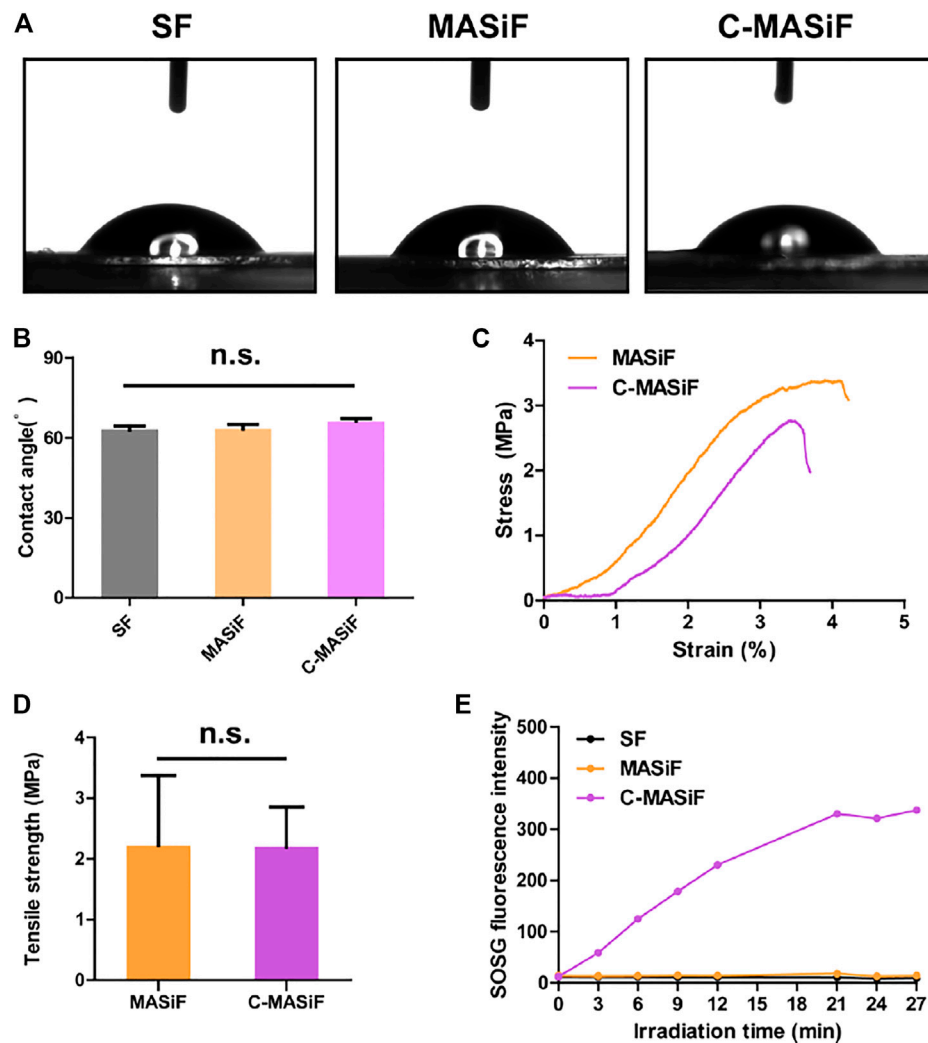


FIGURE 3 | Hydrophilicity and mechanical property of MASiF and C-MASiF film and ROS production by PDT. **(A)** and **(B)** Contact angle of MASiF and C-MASiF film. **(C)** and **(D)** Mechanical property of MASiF and C-MASiF film. **(E)** Fluorescence intensity of SOSG as the functional of irradiation time.

can kill *S. aureus* in a highly spatiotemporal manner, which prevents abscess recurrence with minimal invasion (Zhou et al., 2020). However, rapid clearance and poor biocompatibility of photodynamic agents limits the efficacy of PDT on treating bacterial infection. Currently, conjugation of photodynamic agents with biocompatible polymers has been considered as a promising strategy to improve efficacy of PDT (Kim et al., 2019; Wang et al., 2020).

In this study, we developed a silk fibroin based antibacterial film as a rapid hemostatic agent for treating hemorrhage in deep wounds. By conjugating photodynamic agent (Chlorin e6) on methacrylated silk fibroin, C-MASiF film exhibited high toxicity against *S. aureus* under near infrared (NIR) irradiation for treating infection. Importantly, this film achieved excellent *in vivo* hemostasis for handling liver bleeding within 2 min by UV exposure as a desirable hemostatic agent (Figure 1).

MATERIALS AND METHODS

Preparation of MASiF Film

There was 50 g of natural silk (Nantong xianjida cocoon and Silk Fabric Co., Ltd., China) boiled in 2 L of 0.2% w/v sodium carbonate (Xilong Chemical Co., Ltd., China) solution for 30 min at 100°C and dried in the air at room temperature. Then, silk was dissolved in 9.3 M LiBr (Shanghai meiruier Chemical Technology Co., Ltd., China) solution to 20% w/v silk fibroin solution and stirred at 60°C for 3 h and then dialyzed in ultrapure water for 3 days. Then, after concentrated to 10% w/v, 400 μ L of silk fibroin solution was added dropwise onto a 2.2 cm \times 2.2 cm square glass slide and dried in air to obtain MASiF film. After dried in the air, the film was soaked in absolute ethanol for enhancing β -folding of silk fibroin protein.

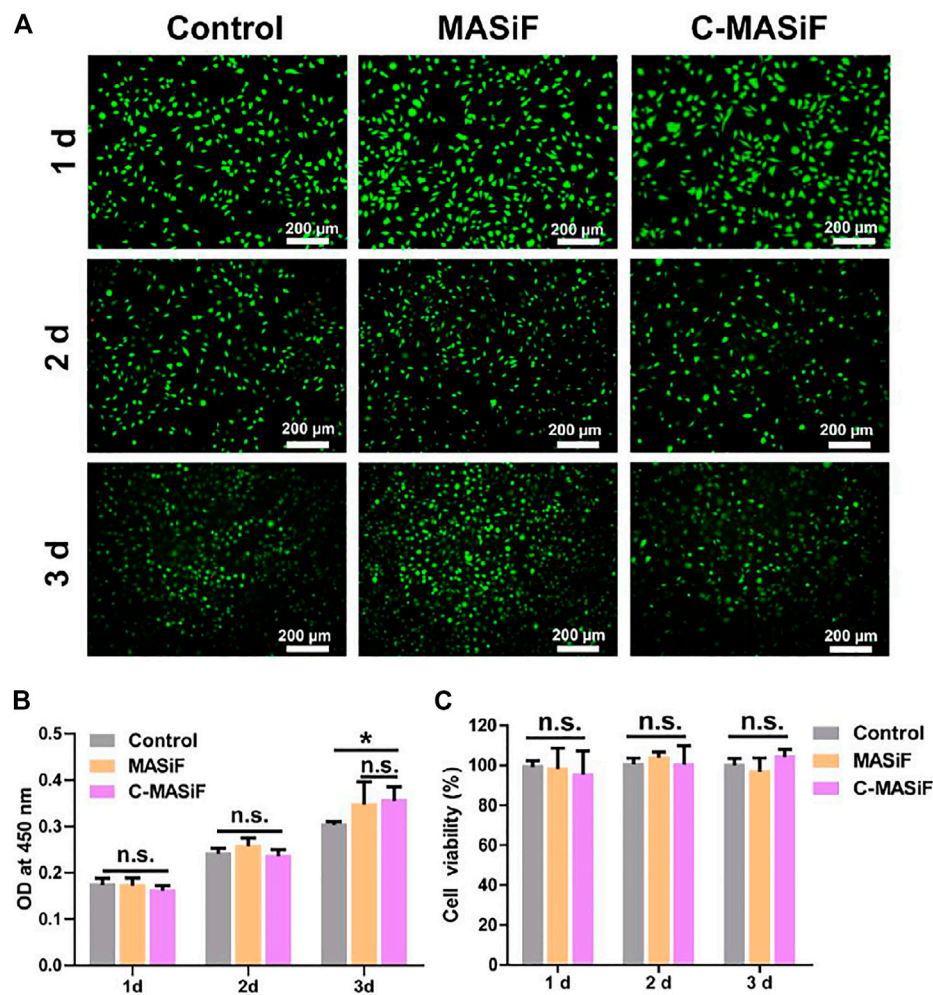


FIGURE 4 | Cytocompatibility of MASiF and C-MASiF film. **(A)** Live/dead assay of L929 cells. **(B)** and **(C)** CCK8 assays of L929 cells. Values represent means \pm S.D. ($n = 3$). * $p < 0.05$.

Preparation of C-MASiF Film

Chlorin e6 (Ce6, APExBIO, United States) was activated in a solution containing N-Hydroxysuccinimide (NHS, 98%, Sigma-Aldrich) and 1-(3-Dimethylaminopropyl)-3-ethylcarbodiimide hydrochloride (EDC, Ailan, China) for 2 h. The ratio of Ce6/NHS/EDC was 1:6:6. Then the activated Ce6 solution was slowly added dropwise to the above-mentioned methacrylic acid silk fibroin at a ratio of 1:100 and reacted for 8 h in the dark. The mixture was then dialyzed in the dark for 2 days and concentrated to 15% solution and added onto a 2.2 cm \times 2.2 cm square glass slide to obtain MASiF film. After dried in the air, the film was soaked in absolute ethanol for enhancing β -folding of silk fibroin protein.

Mechanical Performance Test

The stress and strain data were recorded for testing tensile strength of dry films with a constant crosshead separation velocity at 50 mm/min at room temperature.

Contact Angle

The angle between water droplets and the surface of the film was measured using a contact angle meter (JYPHa, Chengde, China).

Measurement of Singlet Oxygen Generation

SF film, MASiF film, and C-MASiF film were placed in Singlet Oxygen Sensor Green Reagent (SOSG Meilunbio, Dalian, China) solutions, respectively, and irradiated under NIR laser (20 mW cm^{-2}). The fluorescence intensity of the solutions was measured.

Cytocompatibility

The films were placed in a 24-well plate and then L929 cells were seeded onto the films at a density of 3×10^4 cells/mL in DMEM (Gibco, United States), and incubated at 37°C for 3 days. A live/dead cytotoxicity kit (Molecular Probes, United States) was utilized to visualize the cell behavior. The cytotoxicity of the films was assessed by the cell counting kit-8 (CCK-8) (Beyotime Biotechnology, China).

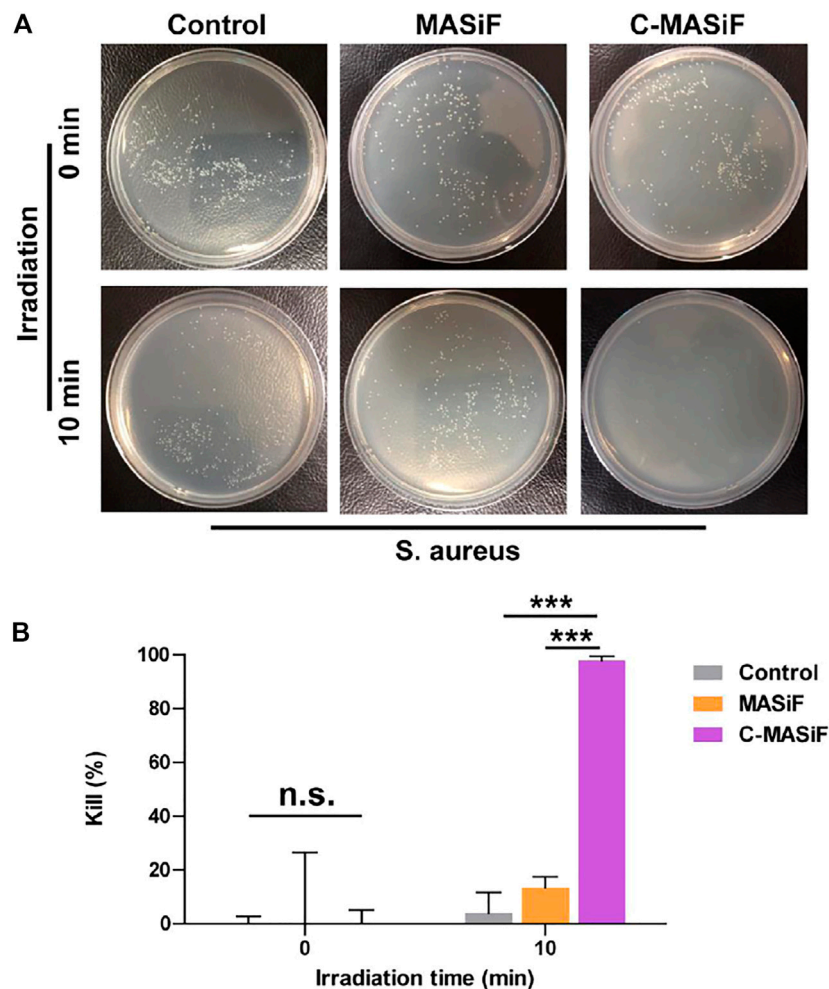


FIGURE 5 | *In vitro* photodynamic antibacterial property of MASiF and C-MASiF films. **(A)** Photographs of *S. aureus* formed on LB-agar plates after PDT. **(B)** Antibacterial efficiency of MASiF and C-MASiF films with NIR irradiation. Values represent means \pm S.D. ($n = 3$). *** $p < 0.001$.

***In vitro* Antibacterial Activity**

A total of 100 μ L of *S. aureus* (10^4 CFU ml^{-1}) were incubated with films at 37°C for 20 min and then irradiated under NIR light (20 mW cm^{-2}) for 10 min. *S. aureus* on films was resuspended using 900 μ L of phosphate-buffered saline (PBS). Then, 100 μ L of the resuspended *S. aureus* solution was spread on solid LB agar plate for 24 h of incubation. Bacterial kill rate: Kill% = $C_0 - C/C_0 \times 100\%$ (where C is the CFU of the experimental group and C_0 is the CFU of the control group inoculated on a blank plate and without irradiation.)

Hemolysis Test

A total of 0.005 g/ml of the film's pieces were dispersed in saline at 37°C for 30 min, respectively. Then fresh anticoagulant rabbit blood was diluted with dispersion liquids at 37°C and the mixture was incubated for 1 h. After centrifugation, the absorbance of the supernatant was measured at 545 nm with a spectrophotometer. Pure saline was used as a negative control, and ultrapure water was used as a positive control. The calculation formula of the

hemolysis rate is as follows: $\text{HR}\% = (A - A_{\text{negative}}) / (A_{\text{positive}} - A_{\text{negative}}) \times 100\%$.

***In vivo* Hemostatic Performance**

ICR mice (18–20 g) were first anesthetized and the liver was exposed. Then the liver trauma model was established by puncturing the liver with a syringe. Then, the wound site was covered by MASiF or C-MASiF films with photoinitiator solution (0.5% w/v) and irradiated under UV light for 2 min. The pre-weighed filter paper was placed on the wound for recording the amount of bleeding.

RESULTS AND DISCUSSION

Fabrication and Characterization of Films

The MASiF and C-MASiF films were successfully fabricated and **Figure 2A** displays that both films were transparent and C-MASiF film possessed dark color, due to Ce6 moiety on silk fibroin

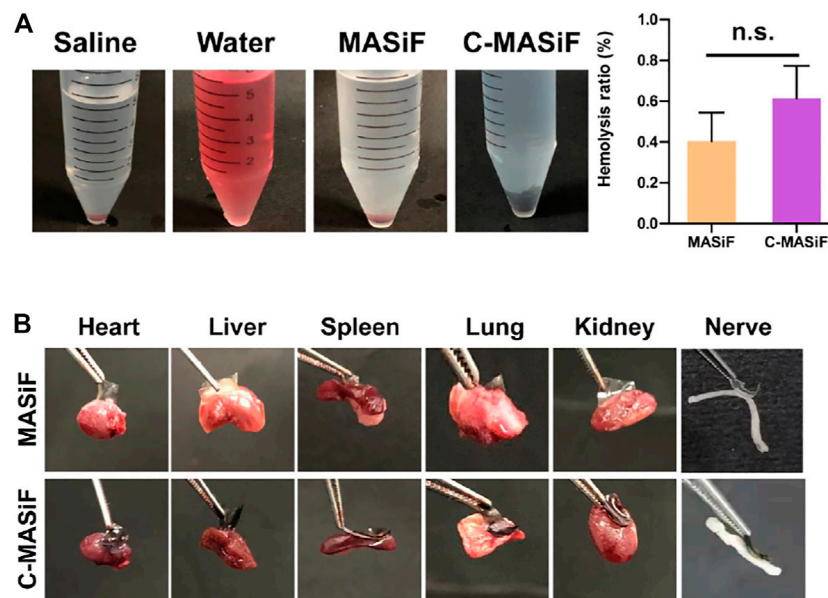


FIGURE 6 | Hemocompatibility and tissue adhesion property of MASiF and C-MASiF films. **(A)** Photographs of MASiF and C-MASiF films incubated with the erythrocytes and hemolysis ratio. Values represent means \pm S.D. ($n = 3$). **(B)** Photographs of MASiF and C-MASiF films adhering to various tissues.

chains. The images of scanning electron microscopy (SEM) in **Figure 2B** show that all the films have uniformly dense and smooth surfaces. As shown in **Figure 2C**, the UV-vis spectrum of C-MASiF demonstrated that the characteristic peaks of Ce6 moiety appeared at 400 and at 640 nm. Furthermore, ^1H NMR spectra of MASiF and C-MASiF shows that the characteristic peaks of methacrylate vinyl group were at $\delta \approx 6.2$ and 5.8 , and Ce6 moiety was at $\delta \approx 2.8$ and 1.1 ppm. These results indicate the successful modification of Ce6 on silk fibroin.

Hydrophilicity, Mechanical Property, and ROS Production

Next, as surface wettability reveals the hydrophilicity and biocompatibility of biomedical materials (Tang et al., 2020), the wettability of the films was evaluated by measuring the contact angle (θ) of water droplets on films. As shown in **Figures 3A,B**, the contact angles of both MASiF and C-MASiF films were less than 90° , indicating the good hydrophilicity of the films. Then, the mechanical property of the films was evaluated using a tensile test. The results show that the average tensile strength of the MASiF and C-MASiF films are more than 2 MPa and there was no statistical difference in the tensile strength of the film (**Figures 3C,D**), demonstrating that the addition of Ce6 moiety has very limited effect on film tensile strength. In order to exam the efficiency of light-triggered ROS production, the amount of singlet oxygen produced by the films under NIR irradiation (20 mW cm^{-2}) was measured by singlet oxygen sensor reagent (SOSG). Upon irradiation of 660 nm light (20 mW cm^{-2}), the fluorescence intensity in C-MASiF group enhanced gradually within 20 min, whereas no fluorescence enhancement was obtained for SF or

MASiF group, showing that C-MASiF film can effectively produce ROS under NIR light (**Figure 3E**).

Cytocompatibility

Fine cytocompatibility is essential for a well-designed biomaterial (Chen et al., 2021; Hao et al., 2021; Ji et al., 2021). Therefore, to evaluate the biocompatibility of films *in vitro*, L929 cells were cultured on the films for 3 days and assessed via live/dead staining and CCK-8 assay. As shown in **Figure 4A**, by staining with a live/dead cytotoxicity kit, there were very few dead cells found on both MASiF and C-MASiF films after 3 days of incubation, indicating the good biocompatibility of these films. Meanwhile, the L929 cells cultured on the films exhibited normal cell proliferation during 3 days of incubation and cell viability were more than 95% on both films (**Figures 4B,C**).

Photodynamic Antibacterial Activity of Films

Ideal wound dressings should possess promising antibacterial activity to prevent infection on the wound site (Li et al., 2020; Wang et al., 2021). Therefore, the photodynamic antibacterial activity of the films against *S. aureus* was evaluated. As shown in **Figures 5A,B**, more than 90% of *S. aureus* was killed on C-MASiF film within 10 min of NIR irradiation (20 mW cm^{-2}), due to the effective production of ROS by Ce6 moiety. However, MASiF had poor antibacterial effect on *S. aureus*. Meanwhile, very limited antibacterial effect against *S. aureus* was obtained for the blank plate (the control group) even after 10 min of NIR irradiation (20 mW cm^{-2}), illustrating poor antibacterial property of weak NIR laser. These results demonstrated that the C-MASiF film possesses broader potential applications in fields of tissue engineering.

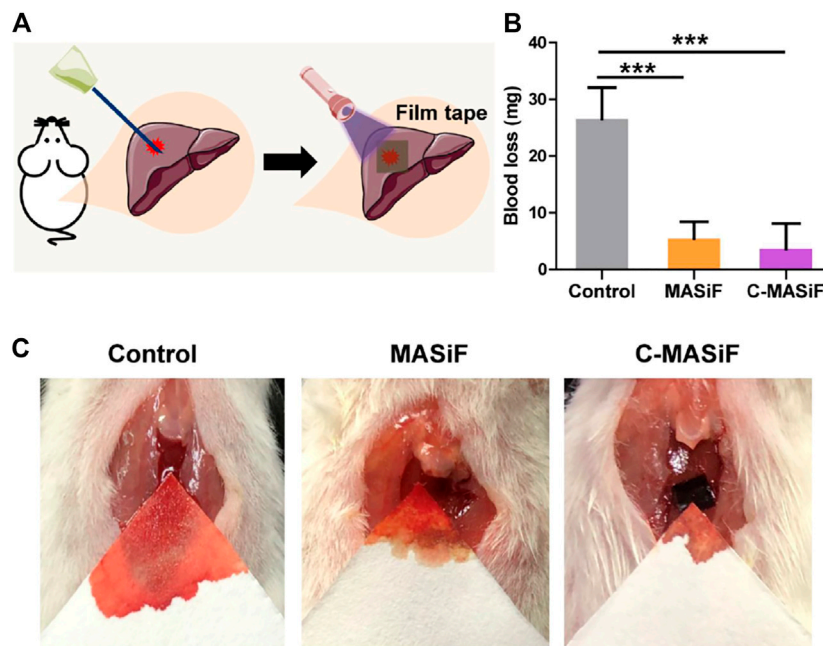


FIGURE 7 | Liver hemostasis *in vivo*. **(A)** Schematic diagram of liver hemostasis process. **(B)** Blood loss of MASiF and C-MASiF films. Values represent means \pm S.D. ($n = 5$). *** $p < 0.001$. **(C)** Photographs of liver hemostasis.

Hemocompatibility and Tissue Adhesion

Good hemocompatibility is essential for hemostatic agents or wound dressings (He et al., 2020; Yin et al., 2021). The hemocompatibility of the films was evaluated by *in vitro* hemolytic activity assay. The images of solution in **Figure 6A** showed that liquids in both MASiF and C-MASiF groups had similar color to the saline group. All MASiF and C-MASiF films showed a hemolysis ratio of less than 1%, suggesting that the MASiF and C-MASiF films possess good blood compatibility. Then, the tissue adhesion property of the films to various tissues was evaluated, as it is important for wound dressings and hemostats. As shown in **Figure 6B**, MASiF and C-MASiF films containing 0.5% of photoinitiator exhibited strong adhesive ability to various tissues, including the heart, liver, spleen, lung, kidney, and nerve tissue, irradiated under UV light (30 mW cm^{-2}) for 5 min, due to the photo-chemistry reaction of sulfhydryl groups on tissue with double bonds on films.

Liver Hemostasis *in vivo*

To further evaluate the hemostatic capacity of the films *in vivo*, a mouse liver trauma model was established. ICR mice were anesthetized, and the liver was punctured with a syringe. All the films were soaked in absolute ethanol to obtain β -folding of silk fibroin protein for enhancing their stability for *in vivo* applications in hemostasis. Then MASiF and C-MASiF films containing 0.5% of photoinitiator were applied to the bleeding site with UV irradiation (**Figure 7A**). The blood loss of the mice in the control group (without any treatment) was 26.5 mg. In contrast, the mice in the MASiF and C-MASiF

group showed significantly less blood loss after 2 min of UV irradiation on films, which were 5.5 and 3.7 mg, respectively. The representative photographs in **Figure 7C** shows the bleeding volume in MASiF and C-MASiF groups was much lower than that in the control group. These results indicate that MASiF and C-MASiF film had a desirable hemostatic effect, due to excellent binding property of SF with fibrinogen and blood platelets to facilitate the clotting and the rapid photo-chemistry reaction of sulfhydryl groups on tissue with double bonds on films.

CONCLUSION

In summary, we designed a multifunctional silk fibroin film with rapid light-triggered hemostatic effect and excellent antibacterial performance against *S. aureus* for sealing the wound bleeding and preventing infection. The hemostatic film held good mechanical and biocompatibility. Moreover, the film also exhibited strong tissue adhesion to various biological tissues upon UV light and achieved successful liver hemostasis *in vivo*. Thereby, we believe that this silk-based hemostatic film would have great potential for applications in hemostasis, wound dressings, and tissue repair.

DATA AVAILABILITY STATEMENT

The raw data supporting the conclusion of this article will be made available by the authors, without undue reservation.

ETHICS STATEMENT

The animal study was reviewed and approved by The Animal Ethics Committee of Nantong University.

AUTHOR CONTRIBUTIONS

JL and YG contributed to the conception and design of the study. TH, ZZ, QL, XT, and XC performed the experiment. TH and ZZ

analyzed the data and performed the statistical analysis. TH wrote the first draft of the manuscript.

FUNDING

This research was financially supported by Postgraduate Research & Practice Innovation Program of Jiangsu Province (Project No: KYCX21-3074), National Science Foundation of China (Project No: 21702112), and Jiangsu Provincial Key Medical Center.

REFERENCES

- Arnaud, F., Tomori, T., Carr, W., McKeague, A., Teranishi, K., Prusaczyk, K., et al. (2008). Exothermic Reaction in Zeolite Hemostatic Dressings: QuikClot ACS and ACS+. *Ann. Biomed. Eng.* 36, 1708–1713. doi:10.1007/s10439-008-9543-7
- Bigham, A., Salehi, A. O. M., Rafienia, M., Salamat, M. R., Rahmati, S., Raucchi, M. G., et al. (2021). Zn-substituted Mg₂SiO₄ Nanoparticles-Incorporated PCL-Silk Fibroin Composite Scaffold: A Multifunctional Platform towards Bone Tissue Regeneration. *Mater. Sci. Eng. C* 127, 112242. doi:10.1016/j.msec.2021.112242
- Chen, Y., Zhu, H., Hao, Y., Sun, Z., Shen, P., and Zhou, Q. (2021). Preparation of Fucoidan-Based Electrospun Nanofibers and Their Interaction with Endothelial Cells. *Front. Bioeng. Biotechnol.* 9, 739209. doi:10.3389/fbioe.2021.739209
- Chouhan, D., and Mandal, B. B. (2020). Silk Biomaterials in Wound Healing and Skin Regeneration Therapeutics: From Bench to Bedside. *Acta Biomater.* 103, 24–51. doi:10.1016/j.actbio.2019.11.050
- Deng, P., Chen, F., Zhang, H., Chen, Y., and Zhou, J. (2021). Conductive, Self-Healing, Adhesive, and Antibacterial Hydrogels Based on Lignin/Cellulose for Rapid MRSA-Infected Wound Repairing. *ACS Appl. Mater. Inter.* 13, 52333–52345. doi:10.1021/acsami.1c14608
- Gu, X., Chen, X., Tang, X., Zhou, Z., Huang, T., Yang, Y., et al. (2021). Pure-silk Fibroin Hydrogel with Stable Aligned Micropattern toward Peripheral Nerve Regeneration. *Nanotechnology Rev.* 10, 10–19. doi:10.1515/ntrev-2021-0002
- Han, W., Zhou, B., Yang, K., Xiong, X., Luan, S., Wang, Y., et al. (2020). Biofilm-inspired Adhesive and Antibacterial Hydrogel with Tough Tissue Integration Performance for Sealing Hemostasis and Wound Healing. *Bioactive Mater.* 5, 768–778. doi:10.1016/j.bioactmat.2020.05.008
- Hao, Y., Zheng, W., Sun, Z., Zhang, D., Sui, K., Shen, P., et al. (2021). Marine Polysaccharide-Based Composite Hydrogels Containing Fucoidan: Preparation, Physicochemical Characterization, and Biocompatible Evaluation. *Int. J. Biol. Macromolecules* 183, 1978–1986. doi:10.1016/j.jbiomac.2021.05.190
- He, Y., Shi, M., Liang, Y., and Guo, B. (2020). Conductive Adhesive Self-Healing Nanocomposite Hydrogel Wound Dressing for Photothermal Therapy of Infected Full-Thickness Skin Wounds. *Chem. Eng. J.* 394, 124888. doi:10.1016/j.cej.2020.124888
- Ji, Y., Han, Z., Ding, H., Xu, X., Wang, D., Zhu, Y., et al. (2021). Enhanced Eradication of Bacterial/Fungi Biofilms by Glucose Oxidase-Modified Magnetic Nanoparticles as a Potential Treatment for Persistent Endodontic Infections. *ACS Appl. Mater. Inter.* 13, 17289–17299. doi:10.1021/acsami.1c01748
- Kim, K., Lee, S., Jin, E., Palanikumar, L., Lee, J. H., Kim, J. C., et al. (2019). MOF × Biopolymer: Collaborative Combination of Metal-Organic Framework and Biopolymer for Advanced Anticancer Therapy. *ACS Appl. Mater. Inter.* 11, 27512–27520. doi:10.1021/acsami.9b05736
- Kim, S. H., Hong, H., Ajitru, O., Sultan, M. T., Lee, Y. J., Lee, J. S., et al. (2021). 3D Bioprinted Silk Fibroin Hydrogels for Tissue Engineering. *Nat. Protoc.* 16, 5484–5532. doi:10.1038/s41596-021-00622-1
- Lan, G., Lu, B., Wang, T., Wang, L., Chen, J., Yu, K., et al. (2015). Chitosan/gelatin Composite Sponge Is an Absorbable Surgical Hemostatic Agent. *Colloids Surf. B: Biointerfaces* 136, 1026–1034. doi:10.1016/j.colsurfb.2015.10.039
- Li, J., Ding, Z., Zheng, X., Lu, G., Lu, Q., and Kaplan, D. L. (2021). Injectable Silk Nanofiber Hydrogels as Stem Cell Carriers to Accelerate Wound Healing. *J. Mater. Chem. B* 9, 7771–7781. doi:10.1039/d1tb01320c
- Li, M., Zhang, Z., Liang, Y., He, J., and Guo, B. (2020). Multifunctional Tissue-Adhesive Cryogel Wound Dressing for Rapid Nonpressing Surface Hemorrhage and Wound Repair. *ACS Appl. Mater. Inter.* 12, 35856–35872. doi:10.1021/acsami.0c08285
- Mao, D., Hu, F., Yi, Z., KenryXu, K., Xu, S., Yan, S., et al. (2020). AIEgen-Coupled Upconversion Nanoparticles Eradicate Solid Tumors through Dual-Mode ROS Activation. *Sci. Adv.* 6, eabb2712. doi:10.1126/sciadv.abb2712
- Qiao, Z., Lv, X., He, S., Bai, S., Liu, X., Hou, L., et al. (2021). A Mussel-Inspired Supramolecular Hydrogel with Robust Tissue Anchor for Rapid Hemostasis of Arterial and Visceral Bleedings. *Bioactive Mater.* 6, 2829–2840. doi:10.1016/j.bioactmat.2021.01.039
- Roy, A., Guha Ray, P., Manna, K., Banerjee, C., Dhara, S., and Pal, S. (2021). Poly(N-vinyl Imidazole) Cross-Linked Beta-Cyclodextrin Hydrogel for Rapid Hemostasis in Severe Renal Arterial Hemorrhagic Model. *Biomacromolecules*. doi:10.1021/acs.biomac.1c01174
- Santin, M., Motta, A., Freddi, G., and Cannas, M. (1999). *In Vitro* evaluation of the Inflammatory Potential of the Silk Fibroin. *J. Biomed. Mater. Res.* 46, 382–389. doi:10.1002/(sici)1097-4636(19990905)46:3<382:aid-jbm11>3.0.co;2-r
- Tang, X., Chen, X., Zhang, S., Gu, X., Wu, R., Huang, T., et al. (2021a). Silk-Inspired *In Situ* Hydrogel with Anti-tumor Immunity Enhanced Photodynamic Therapy for Melanoma and Infected Wound Healing. *Adv. Funct. Mater.* 31, 2101320. doi:10.1002/adfm.202101320
- Tang, X., Gu, X., Huang, T., Chen, X., Zhou, Z., Yang, Y., et al. (2021b). Anisotropic Silk-Inspired Nerve Conduit with Peptides Improved the Microenvironment for Long-Distance Peripheral Nerve Regeneration. *ACS Macro Lett.* 10, 1501–1509. doi:10.1021/acsmacrolett.1c00533
- Tang, X., Gu, X., Wang, Y., Chen, X., Ling, J., and Yang, Y. (2020). Stable Antibacterial Polysaccharide-Based Hydrogels as Tissue Adhesives for Wound Healing. *RSC Adv.* 10, 17280–17287. doi:10.1039/d0ra02017f
- Vilardo, N., Feinberg, J., Black, J., and Ratner, E. (2017). The Use of QuikClot Combat Gauze in Cervical and Vaginal Hemorrhage. *Gynecol. Oncol. Rep.* 21, 114–116. doi:10.1016/j.gore.2017.07.012
- Wang, X., Li, M., Hou, Y., Li, Y., Yao, X., Xue, C., et al. (2020). Tumor-Microenvironment-Activated *In Situ* Self-Assembly of Sequentially Responsive Biopolymer for Targeted Photodynamic Therapy. *Adv. Funct. Mater.* 30, 2000229. doi:10.1002/adfm.202000229
- Wang, Z., Mei, L., Liu, X., and Zhou, Q. (2021). Hierarchically Hybrid Biocoatings on Ti Implants for Enhanced Antibacterial Activity and Osteogenesis. *Colloids Surf. B: Biointerfaces* 204, 111802. doi:10.1016/j.colsurfb.2021.111802
- Xuan, H., Tang, X., Zhu, Y., Ling, J., and Yang, Y. (2020). Freestanding Hyaluronic Acid/Silk-Based Self-Healing Coating toward Tissue Repair with Antibacterial Surface. *ACS Appl. Bio Mater.* 3, 1628–1635. doi:10.1021/acsabm.9b01196
- Yin, X., Hao, Y., Lu, Y., Zhang, D., Zhao, Y., Mei, L., et al. (2021). Bio-Multifunctional Hydrogel Patches for Repairing Full-Thickness Abdominal Wall Defects. *Adv. Funct. Mater.* 31, 105614. doi:10.1002/adfm.202105614
- Zheng, W., Hao, Y., Wang, D., Huang, H., Guo, F., Sun, Z., et al. (2021). Preparation of Triamcinolone Acetonide-Loaded Chitosan/fucoidan Hydrogel and its Potential Application as an Oral Mucosa Patch. *Carbohydr. Polym.* 272, 118493. doi:10.1016/j.carbpol.2021.118493
- Zhou, T., Hu, R., Wang, L., Qiu, Y., Zhang, G., Deng, Q., et al. (2020). An AIE-Active Conjugated Polymer with High ROS-Generation Ability and Biocompatibility for Efficient Photodynamic Therapy of Bacterial Infections. *Angew. Chem. Int. Ed.* 59, 9952–9956. doi:10.1002/anie.201916704

Zhu, Y., Liu, L., Sun, Z., Ji, Y., Wang, D., Mei, L., et al. (2021). Fucoidan as a marine-origin Prebiotic Modulates the Growth and Antibacterial Ability of *Lactobacillus Rhamnosus*. *Int. J. Biol. Macromolecules* 180, 599–607. doi:10.1016/j.ijbiomac.2021.03.065

Conflict of Interest: The authors declare that the research was conducted in the absence of any commercial or financial relationships that could be construed as a potential conflict of interest.

Publisher's Note: All claims expressed in this article are solely those of the authors and do not necessarily represent those of their affiliated organizations, or those of

the publisher, the editors, and the reviewers. Any product that may be evaluated in this article, or claim that may be made by its manufacturer, is not guaranteed or endorsed by the publisher.

Copyright © 2022 Huang, Zhou, Li, Tang, Chen, Ge and Ling. This is an open-access article distributed under the terms of the Creative Commons Attribution License (CC BY). The use, distribution or reproduction in other forums is permitted, provided the original author(s) and the copyright owner(s) are credited and that the original publication in this journal is cited, in accordance with accepted academic practice. No use, distribution or reproduction is permitted which does not comply with these terms.



Bioengineered Zinc Oxide Nanoparticle-Loaded Hydrogel for Combinative Treatment of Spinal Cord Transection

Sen Lin^{1†}, Hao-sen Zhao^{1†}, Chang Xu^{1†}, Zi-peng Zhou¹, Da-hao Wang¹, Shu-rui Chen^{2*} and Xi-fan Mei^{1*}

¹Department of Orthopedic, First Affiliated Hospital of Jinzhou Medical University, Jinzhou, China, ²Department of Endocrinology, First Affiliated Hospital of Jinzhou Medical University, Jinzhou, China

OPEN ACCESS

Edited by:

Qihui Zhou,
Qingdao University, China

Reviewed by:

Paolo Bigini,
Mario Negri Pharmacological
Research Institute, Italy
Xianwen Wang,
Anhui Medical University, China

*Correspondence:

Shu-rui Chen
272146792@qq.com
Xi-fan Mei
meixifan@jzmu.edu.cn

[†]These authors have contributed
equally to this work

Specialty section:

This article was submitted to
Biomaterials,
a section of the journal
Frontiers in Bioengineering and
Biotechnology

Received: 16 October 2021

Accepted: 01 December 2021

Published: 13 January 2022

Citation:

Lin S, Zhao H-s, Xu C, Zhou Z-p,
Wang D-h, Chen S-r and Mei X-f
(2022) Bioengineered Zinc Oxide
Nanoparticle-Loaded Hydrogel for
Combinative Treatment of Spinal
Cord Transection.
Front. Bioeng. Biotechnol. 9:796361.
doi: 10.3389/fbioe.2021.796361

Spinal cord injury (SCI) is one of the most destructive diseases. The neuroinflammation microenvironment needs comprehensive mitigation of damages. Thus, regulation of local, microenvironment drugs could be a potential effective treatment. However, clinical studies on SCI with common treatment have reported it to cause systemic toxicity and side effects. Zinc oxide nanoparticles (ZnONPs) have been widely reported to have satisfying anti-inflammation function. Furthermore, green synthesis procedures can improve the capability and possible utilization of ZnONPs. However, the efficient administration and underlying mechanism of ZnONPs in SCI treatment remain unclear. Herein, an innovative approach was built by utilizing ZnONPs loaded in a skeletal muscle-derived adhesive hydrogel (ZnONPs-Gel). Different from the systemic application of ZnONPs, the local administration of ZnONPs-Gel offered the ZnONPs-loaded extracellular matrix with beneficial biocompatibility to the injured spinal cord, thereby promoting effective function recovery. Mechanistically, the ZnONPs-Gel treatment not only markedly reduced ROS production but also decreased apoptosis in the injured spinal cord. Therefore, the strategy based on local administration of the ZnONPs-Gel in the early stage of SCI may be an effective therapeutic treatment.

Keywords: zinc oxide nanoparticles, hydrogel, spinal cord injury, immunomodulation, neuroinflammation

INTRODUCTION

Spinal cord injury (SCI) is a destructive disease of the central nervous system (CNS) (McDonald and Sadowsky, 2002), accompanied by motor and/or sensory dysfunctions. Secondary injury followed by primary trauma in the development of SCI includes impairment of the extracellular matrix (ECM), the activation of reactive oxidative stress (ROS), and neuroinflammation (Fawcett, 2015; Ahuja et al., 2017). Several methods have been used clinically such as spinal canal decompression intervention and high-dose corticosteroid (McDonald and Sadowsky, 2002). However, these approaches cause severe side effects, which is a clinically serious problem in patients with SCI that has not yet been resolved (McDonald and Sadowsky, 2002). Therefore, comprehensive strategies of the injured spinal cord are critical to SCI treatment.

Nanoparticles (NPs) are characterized as substances with a size of 1–100 nm (Boraschi et al., 2017). It has been indicated that the application of NPs have anti-inflammation and anticancer function (Baetke et al., 2015; Dadfar et al., 2019). Zinc, as an essential element, is involved in various

metabolic processes *in vivo* (Frederickson et al., 2005). The pathological imbalance of the zinc level causes various disorders of the CNS, such as epilepsy and dementia (Pochwat et al., 2015). Zinc plays an important role in the formation and maturation of fetal CNS (Frederickson et al., 2005). As a common zinc-contained nanomaterial, zinc oxide nanoparticles (ZnONPs) have been reported to be applied in biological research because of their low toxicity, biocompatibility, and bioactivity (Basnet et al., 2018). Therefore, local application of ZnONPs will ameliorate the inflammatory microenvironments and therefore attenuate injured spinal cord dysfunction.

Hydrogel has been suggested as a promising therapy for trauma-related diseases such as SCI and wound healing (Zhao et al., 2017; Koffler et al., 2019). Previous studies have demonstrated that skeletal muscle-derived hydrogel has sufficient adhesion and histocompatibility (Ungerleider et al., 2015; Hernandez et al., 2020). We presented a novel promising treatment for the local delivery of ZnONPs in injured spinal cord based on skeletal muscle-derived hyaluronic acid (HA) hydrogel (ZnONPs-Gel). In this study, the implantation of ZnONPs-Gel effectively recovered the hindlimb motor function in SCI mice *via* regulating the focus microenvironment and suppressing inflammation and ROS. This study developed an innovative strategy for the local delivery of ZnONPs for SCI treatment.

MATERIALS AND METHODS

Culture of Primary Bone Marrow Mesenchymal Stem Cells

According to a previous study (Li et al., 2016), BALB/C mice (4–5 weeks) were killed after being anesthetized and soaked in 75% ethanol for 5 min. Bilateral femurs were separated on a sterile operation platform. The femurs with the muscle tissues around being removed were soaked in the dish containing saline. The syringe took an appropriate amount of culture medium containing 10% FBS to flush the bone marrow into the culture bottle. The bone marrow cell suspension was blown repeatedly to make a single-cell suspension. The cell suspension was centrifuged at 1,000 rpm for 5 min, and then the cells were collected. The cells were cultured at 37°C under 5% CO₂.

Isolation and Characterization of Biosynthetic ZnONPs *In Vitro*

According to previous studies (Ogunyemi et al., 2019), the produced ZnONPs were isolated from the culture supernatant of BMSCs. The medium was centrifuged for 5 min at 900 × g followed by centrifuging for 1 h at 10,000 × g to remove cell debris, and the supernatant was filtered with a 0.2-μm pore filter. After that, the samples were centrifuged 30 min at 4°C and 400 × g, followed by passing through a CL-2B column. Then, the filtrate was used with a freeze-dryer. The characterizations of ZnONPs were performed by transmission electron microscopy (TEM), energy-dispersive X-ray spectroscopy (EDS), and X-ray diffraction (XRD).

TABLE 1 | Primer sequences used for quantitative real-time PCR.

Gene	Forward primer (5' to 3')	Reverse primer (5' to 3')
iNOS	TTTGCCAATTCATTACTTCCA	ATCACACCGCCTCCTGATTCC
Arg-1	CTCCAAGCCAAAGTCCTTAGAG	AGGAGCTGTCATTAGGGACATC
RPS18	GCAATTATTCCCATGAAG	GGCCTCACTAAACCATCCAA

Fabrication of ZnONPs-Loaded Hydrogels

For a typical fabrication of tissue-specific hydrogels (Ungerleider et al., 2015), 20–35 mg of skeletal muscle was added into 800 ml of 1% wt/vol sodium dodecyl sulfate (SDS) solution and stirred at 125 rpm for 2 h. After being rinsed with ultrapure water, tissue was added to a certain volume of fresh 1% SDS solution and spun at 125 rpm for 24 h. An aqueous solution of isopropyl alcohol (400 ml) was added slowly to the mixture, and the stirring was continued for 12 h. Afterward, ZnONPs were added to the samples, and ECM was used with a freeze-dryer. Frozen ECM is lyophilized and ground to generate particles for subsequent protease digestion. Fresh pepsin was dissolved in 0.1 M HCl at a rate of 1 mg/ml by shaking for 5–10 min. While the pepsin is shaking, approximately 20–30 mg of ground ECM was added to a 20-ml scintillation vial with a small stir bar. The closed vial was then placed on a stirring plate (60–120 rpm) at room temperature for 48 h. To ensure that the entire material is digested in the pepsin solution, a spatula was used to gently scrape off the material on the side of the vial once or twice during the 48-h digestion process. After 48 h, the liquid ECM was titrated to pH 7.4 PBS, and the final concentration was 6 mg ECM/ml.

SCI Model and Treatments

Male BALB/C mice (weighing 22–28 g) were used for this study. Rats were fed in a controlled place with standard rodents. Animals were stayed at 22 ± 1°C with a half-day light, half-day cycle. The study complied with the Animal Research: Reporting of *In Vivo* Experiments (ARRIVE) guidelines and obtained permission by the Jinzhou Medical University Review Board for the care of animals. Complete contusion SCI mice were prepared as previously described. An impounder (2 mm diameter, 10 g) was fallen on the T9–T10 spinal cord from a 2.5-cm height to form a spinal cord moderate contusion. The bladder was massaged twice a day until bladder function recovered normally. The blank group was transplanted with hydrogel. The ZnONPs-Gel group was transplanted with hydrogel-loaded ZnONPs.

Behavioral Assessment

The behavioral assessment was tested by behavioral analysis using the Basso Mouse Scale (BMS) open-field locomotor test (Basso et al., 1995). Double-blind assessment was used at 0, 1, 3, 7, 14, 21, and 28 days post-injury. BMS scores range from 0 to 9 points. The 0 point indicates complete paralysis, and 9 points indicates normal function. The average scores were calculated in accordance with the grading standard in locomotion recovery after SCI.

RT-qPCR

The injured spinal cord tissue was collected from the time point for the experiment of RT-qPCR. The relative expression levels of the target genes were normalized to those of the housekeeping gene ribosomal protein S18 (RPS18), and the target genes from the experimental group were compared with the corresponding target genes from the control group using the $(1 + e)^{-\Delta\Delta CT}$ method. The following oligonucleotide primers are listed in Table 1.

Western Blot

At 7 days post-operation, the injured spinal cord (1 cm from the center of the injury point) was removed. Tissues were chopped and then dissolved in RIPA lysis buffer. The same amount of protein samples was added into polyacrylamide gels. The samples were added to SDS-PAGE and transferred to a membrane, then blocked with 1% BSA in TBST at room temperature for 2 h. Then, the membranes were immersed with the primary antibodies at 4°C overnight. On the second day, membranes were incubated with the secondary antibodies at room temperature for 2 h. The membranes were imaged by using the ChemiDoc-It™ TS2 Imager, and relative optical density was analyzed by ImageJ2x software.

Histological Staining and Immunofluorescence Staining

Mice were anesthetized with urethane (20%, 5 ml/kg) after operation. A 5-mm segment of the spinal cord including the injury lesion was taken. The segments were soaked in 4% paraformaldehyde for 3 days and added to 30% sucrose in 4% paraformaldehyde for 3 days. For HE staining, frozen sections were dried at room temperature for 30 min and immersed into hematoxylin for 6 min, the slides were sluiced in running water for 10 s. The sections were differentiated in HCl/95% alcohol (1:50) solution for 5 s. After washing with running water for 25 min, the slides were re-stained with eosin and then fixed with neutral balsam after dehydration *via* 75% alcohol, 95% alcohol, and 100% alcohol and transparency with xylene. For immunofluorescent analysis, sections were blocked 5% normal goat serum for 1 h and incubated overnight at 4°C with primary antibodies. Next day, the tissues were rewashed with PBS and incubated with Alexa Fluor-488 or Alexa Fluor-568 at room temperature for 2 h. The nucleus was dyed with DAPI solution (1:1,000).

ROS Activity Assay

Superoxide dismutase (SOD) and glutathione (GSH) activity in the spinal cord tissue were measured using assay kits (Jiancheng, Nanjing, China) according to the manufacturer's instructions (Qin et al., 2019).

Statistical Analysis

Data represented as mean \pm SD and analyzed by SPSS 23.0. Student's t-test and one-way ANOVA were detected the data of two groups and more groups. In addition, the BMS score was analyzed using the Mann-Whitney U-test. Differences were considered statistically significant with a value of $p < 0.05$.

RESULTS AND DISCUSSION

Characterization of ZnONPs and ZnONPs-Gel

In the synthesis of nanomaterials, the use of biological components has always been the better choice of environmentally friendly methods known as green synthesis. In addition to environmental and ecological benefits, green synthesis has proven to be very useful in controlling the required size and shape. Various studies have shown that the synthesis of animal extracts is more compatible than that of other organisms, so it is more suitable for large-scale synthesis of green NPs (Hussain et al., 2016).

Flow analysis showed that BMSCs had high expression levels of CD44 and low expression of CD45 (Figure 1A) (Soleimani and Nadri, 2009). The cultured BMSCs were fibroblast-like cells, and the BMSCs formed homogenous colonies. Most of the BMSCs had clear cellular boundaries and administration of zinc chloride ($ZnCl_2$) did not disturb the cells' form (Figure 1B). ZnONPs were isolated from BMSC culture supernatant and purified by chromatography and ultracentrifugation. The purified ZnONPs showed spherical morphology. The result of TEM indicated that the sizes of the purified ZnONPs ranged from 10 to 50 nm (Figure 1D). The viability of BMSCs was investigated in the absence and presence of ZnONPs based on the MTT experiments (Supplementary Figure S1). After BMSCs were treated 24 h, the cell viabilities were near 100% with ZnONPs, at various concentrations from 0 to 30 μg (exceeded the maximum load of ZnONPs-Gel). Moreover, ZnONPs decreased the ROS expression after being treated with H_2O_2 (Supplementary Figure S2). The result showed that green production of ZnONPs significantly reduced cell toxicity. ZnONPs were released continuously from gel for about 14 days, and more than 92% of ZnONPs was finally released (Figures 1E,F). Furthermore, we measured characterizations of ZnONPs and ZnONPs-Gel (Supplementary Figures S3, S4). Therefore, the retention and slow release of ZnONPs from skeletal muscle-derived hydrogel were demonstrated *in vitro*. These data suggested that the adhesion and retention of ZnONPs in gels (ZnONPs-Gel) had possible application prospects in effective delivery.

Neuroprotective Effect of ZnONPs-Gel *In Vivo*

Gel treatment (blank group) and ZnONPs-Gel treatment (ZnONPs-Gel group) were performed to evaluate the effect of implanted ZnONPs in a severe long-span spinal cord transection model in mice (Figures 2A,B). Mice received only PBS after transection serving as the control group (SCI group). The animals from the SCI group were almost completely paralyzed lasting 28 days after SCI, while the implantation of ZnONPs-Gel significantly recovered motor function (Figures 2C,D). The findings demonstrated that ZnONPs-Gel administration had a significant effectiveness on nerve recovery.

Moreover, to investigate the tissue recovery of implanted ZnONPs-Gel, assessment was performed on day 28 after injury *via* immunofluorescence double staining (Figure 3A and Supplementary Figure S5) and HE staining (Figure 4). The distributions of Tuj1 and glial fibrillary acidic protein (GFAP)

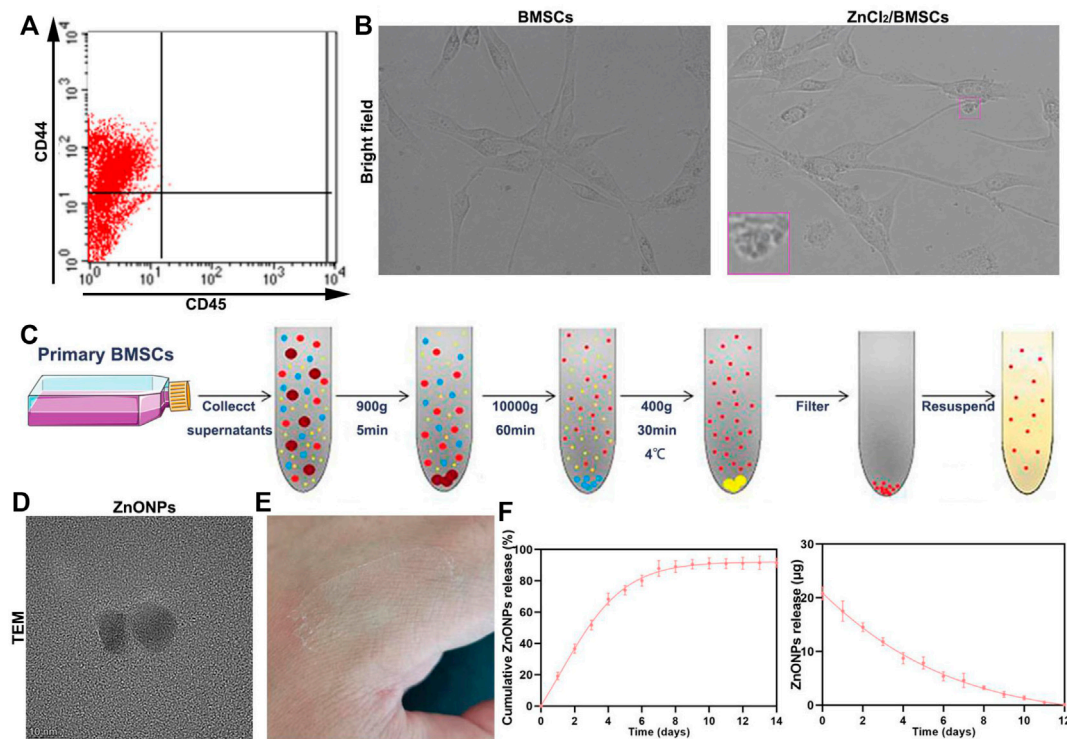


FIGURE 1 | Fabrication characterization of ZnONP-loaded hydrogels. Flow cytometry of primary BMSCs (A). Representative images of BMSCs (B). Scheme of steps for extracting BMSCs (C). Representative image of ZnONPs (D). Representative image of ZnONP-loaded hydrogel solidification (E). Representative quantifications of ZnONP release (F–G) in ZnONPs-Gel. Data are mean \pm SD ($n = 3$).

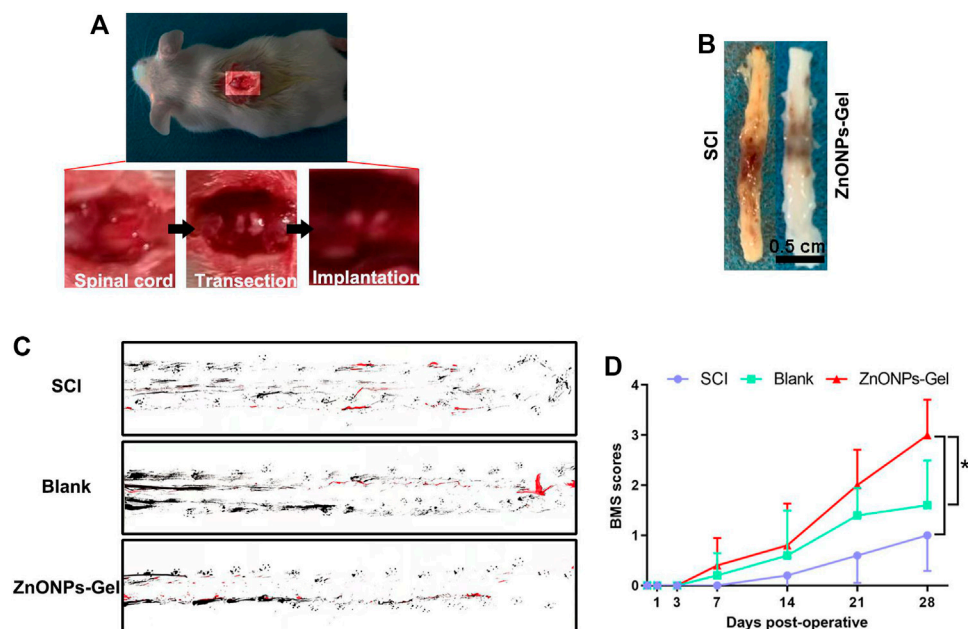


FIGURE 2 | ZnONPs-Gel recovered motor function on days 28 after SCI. Model of injured spinal cord (A). Representative images of the injured spinal cord in SCI and ZnONPs-Gel groups (B). Representative images of footprint analysis in the SCI, blank, and ZnONPs-Gel groups (C). Representative quantification of BMS scores in SCI, blank, and ZnONPs-Gel groups (D). Data are mean \pm SD ($n = 3$).

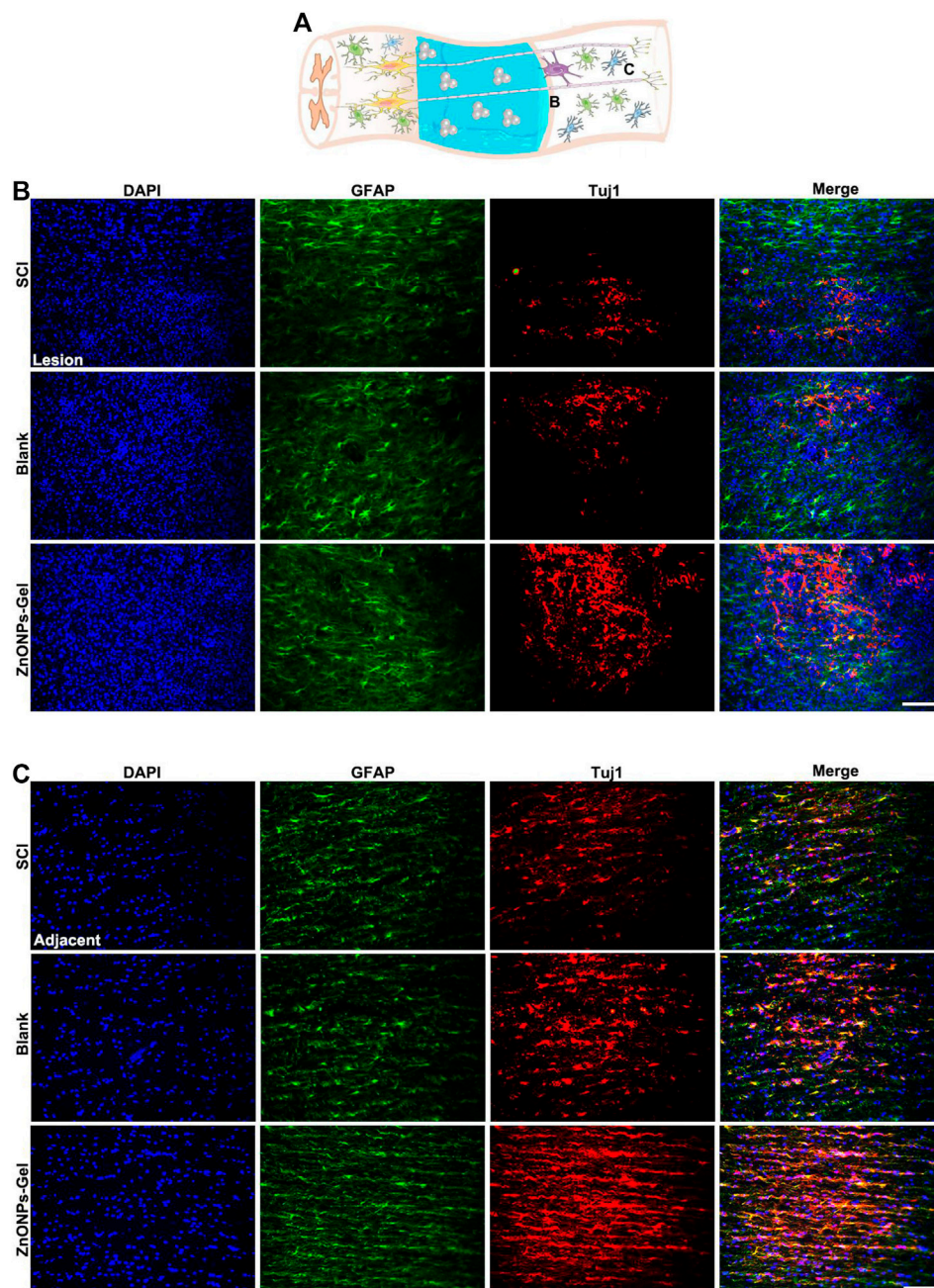


FIGURE 3 | ZnONPs-Gel improved injured the spinal cord on days 28 after SCI. Model of injured spinal cord (A). Representative images showing Tuj1 (red) and glial fibrillary acidic protein (GFAP, green) staining in the lesion (B) and the adjacent (C) of SCI, blank, and ZnONPs-Gel groups. Scale bar = 100 μm . Data are mean \pm SD ($n = 3$).

astrocytes have been reported to represent the degree of nerve tissue recovery. We found that in the blank group, GFAP-positive cells gathered in the margin of the cavity, with few Tuj1 (Figure 3B). Compared with the blank group and SCI group, the double-positive stainings of Tuj1 and GFAP cells in the ZnONPs-Gel group were significantly increased (Figure 3B). As shown in Figure 3C, the double-positive stainings of Tuj1 and GFAP cells in the ZnONPs-Gel group were not different as compared to the blank and SCI groups.

The results indicated that the injured spinal cord tissue repaired by ZnONPs-Gel exhibited a higher expression of Tuj1 in different segments, accompanied by fewer astrocytes. On day 28 after implanting ZnONPs-Gel, the cavity was less than that in the SCI and blank groups. Four weeks after injury, a dramatic tissue loss on the injured spinal cord was observed, reflecting that ZnONPs-Gel significantly decreased the lesion volume (Figure 4 and Supplementary Figure S5). Besides the long-term effect of

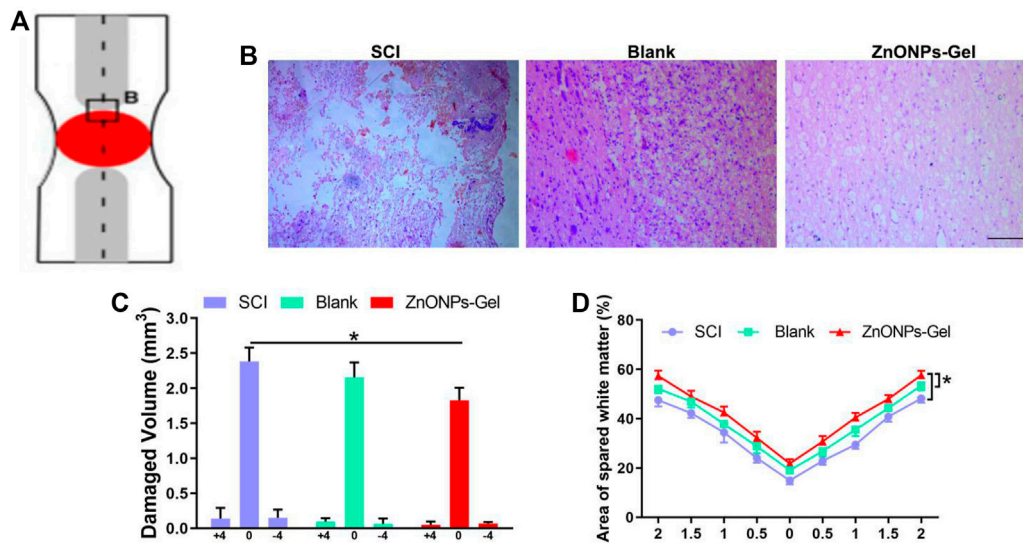


FIGURE 4 | ZnONPs-Gel promoted injured spinal cord tissue repair after SCI. Model of injured spinal cord (A). HE staining (B) and quantification of damaged volume (C) and area of spared white matter (D). Scale bar = 100 μ m. Data are mean \pm SD ($n = 3$); *significant difference compared to the SCI group.

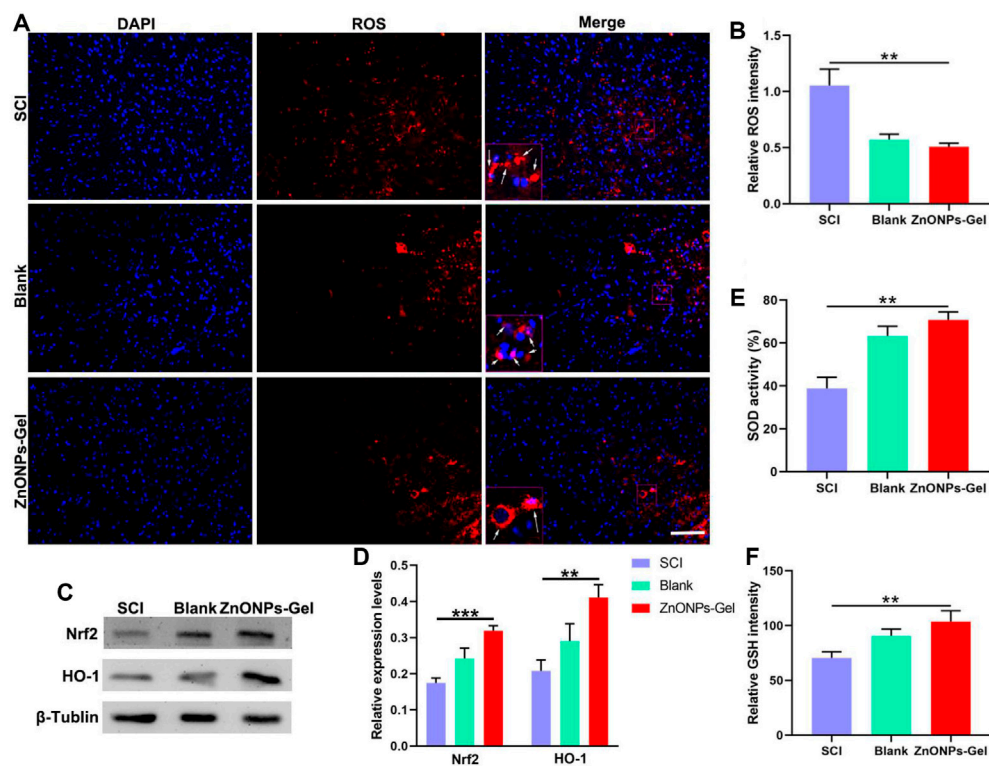


FIGURE 5 | ZnONPs-Gel inhibited injured spinal cord oxidation on days 28 after SCI. Representative images (A) and quantification (B) showing DAPI (blue) and ROS (red) staining in the lesion of SCI, blank, and ZnONPs-Gel groups. Representative images (C) and quantification (D) of the expression of Nrf2 and HO-1 in the spinal cord of Sham, SCI, blank, and ZnONPs-Gel groups. Representative quantification showing SOD activity (E) and GSH (F) assays in the injured spinal cord of SCI, blank, and ZnONPs-Gel groups. Scale bar = 100 μ m. Data are mean \pm SD ($n = 3$).

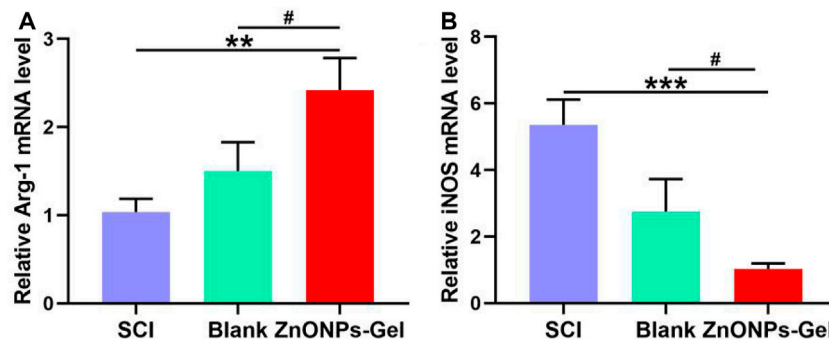


FIGURE 6 | ZnONPs-Gel-polarized M2 markers after SCI. Quantification of expression of M1: iNOS (A) or M2 markers: Arg-1 (B) in the injured spinal cord of SCI group, blank group, or ZnONPs-Gel group at 7 days during the acute course of SCI. Data are mean \pm SD ($n = 3$); *significant difference compared to SCI group (* $p < 0.05$; ** $p < 0.01$; *** $p < 0.001$); #, compared to the blank group (# $p < 0.05$).

ZnONPs-Gel on SCI which was investigated by a survival curve (Supplementary Figure S6), we found that ZnONPs-Gel promoted long-term SCI recovery and mouse survival. Consistent with Figure 2, these data suggested the important role of ZnONPs in the implantation of nerve repair with hydrogel and supported the effective delivery of ZnONPs with the implantation of ZnONPs-Gel.

Anti-ROS Effect of ZnONPs-Gel *In Vivo*

SCI resulted in the increase in ROS expression; the activation of ROS caused secondary injury in the acute development of SCI (Shadel and Horvath, 2015). After being treated with ZnONPs-Gel on day 28, the antioxidant markers of SOD, GSH, Nrf2, and HO-1 were detected by ELISA and Western blot. According to Figures 5A,B, ZnONPs-Gel effectively downregulated ROS intensity as compared to the SCI and blank groups. Moreover, implantation of ZnONPs-Gel extended the production of SOD, GSH, Nrf2, and HO-1 in the injured spinal cord tissue (Figures 5C–E). The quantitative analysis of the results showed a significant difference between the ZnONPs-Gel group and SCI group. These findings demonstrated the antioxidant role of ZnONPs-Gel in the treatment of nerve repair after SCI.

Anti-Inflammation Effect of ZnONPs-Gel *In Vivo*

Inducible nitric oxide synthase (iNOS), as a proinflammatory messenger molecule, aggravates the progress of neuroinflammation.

Arginase-1 (Arg-1) has been indicated to promote nerve recovery (Hickman et al., 2018). To further extend the neuroprotective effects of ZnONPs-Gel on the hyperinflammation microenvironment after SCI, we detected the mRNA levels of iNOS and Arg-1 by quantitative real-time PCR (RT-qPCR). At 7 days after implantation of ZnONPs-Gel, the expression of iNOS decreased significantly, accompanied by the expression of Arg-1 which increased significantly (Figure 6). These results indicated that ZnONPs-Gel implantation has anti-inflammatory effects in the acute phase of SCI. In addition, the data of TUNEL staining revealed a decrease in nerve death after therapy of ZnONPs-Gel (Figure 7). These findings offered evidence for the underlying mechanism of spinal cord repair by ZnONPs-Gel.

Immune Response of the Administration of ZnONPs-Gel *In Vivo*

After 28 days of treatment, the toxicity of ZnONPs-Gel to the organs was investigated by histopathological analysis (Figure 8). No obvious change was observed from the H&E-stained major organs of the heart, liver, spleen, lung, and kidney. Moreover, no apparent histopathological abnormalities or lesions were observed in each organ (Figure 8A). The serum biochemistry analysis results (Figures 8B,C) showed that serum concentrations of liver function indicators [aspartate transaminase (AST) and alanine transaminase (ALT)] and kidney function indicators (BUN and

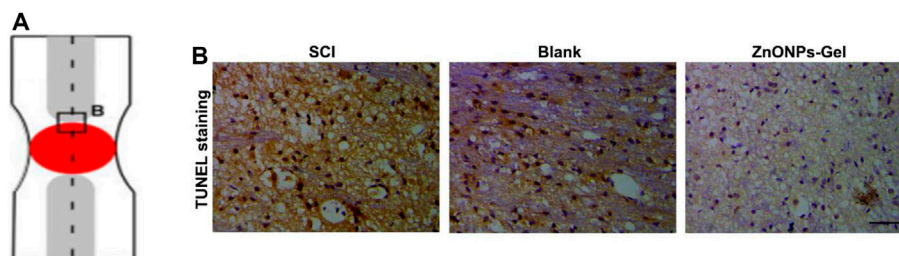


FIGURE 7 | ZnONPs-Gel decreased injured spinal cord tissue apoptosis after SCI. Model of injured spinal cord (A). TUNEL staining (B) in the injured spinal cord of SCI group, blank group, or ZnONPs-Gel group at 7 days during the acute course of SCI. Scale bar = 100 μ m.

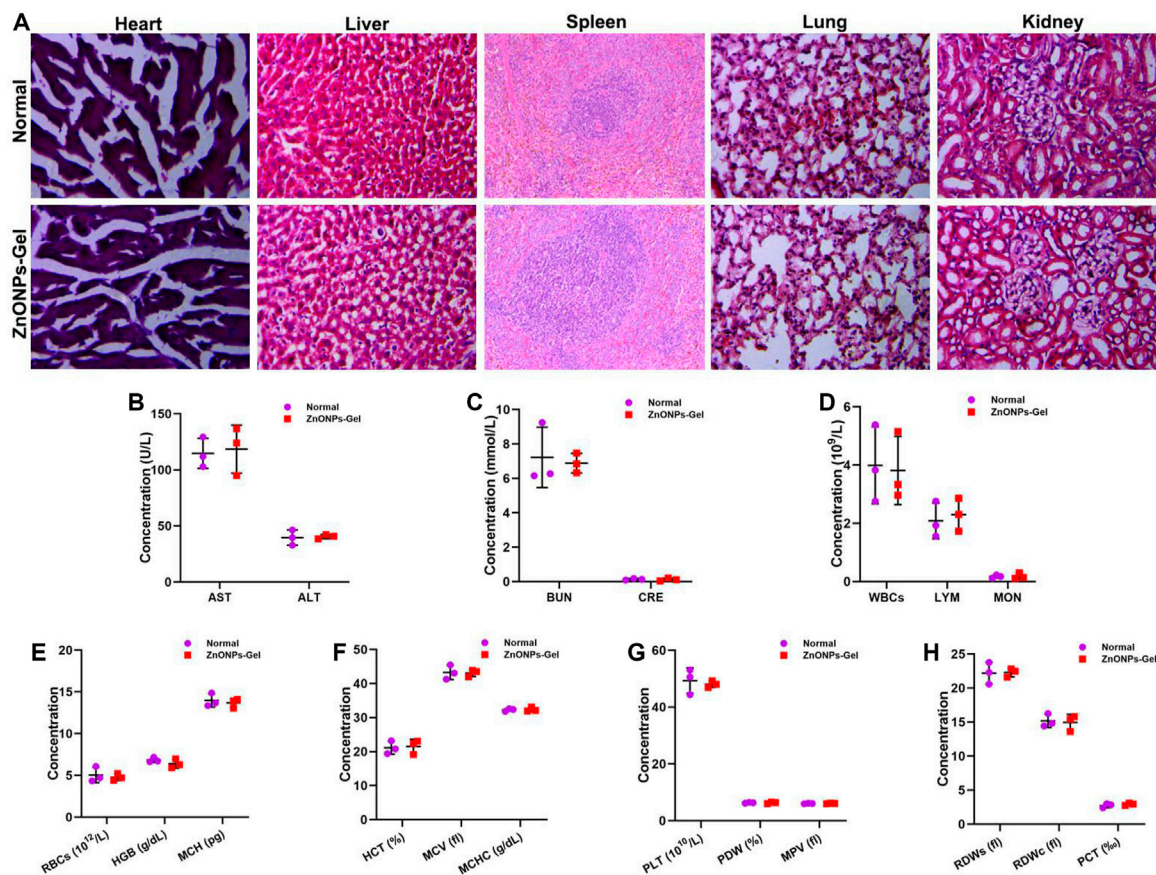


FIGURE 8 | Implantation of ZnONPs-Gel had biological safety in SCI mice. HE staining of heart, liver, spleen, lung, and kidney in normal mice and ZnONPs-Gel-implanted mice (A). Representative quantification of the AST (B), ALT (B), BUN (C), CRE (C), WBCs (D), LYM (D), MON (D), RBCs (E), HGB (E), MCH (E), HCT (F), MCV (F), MCHC (F), PLT (G), PDW (G), MPV (G), RDWs (H), RDWc (H), and PCT (H) content in normal mice and ZnONPs-Gel implanted mice at 28 days after SCI. Data are mean ± SD ($n = 3$).

CRE) in the ZnONPs-Gel-treated group were similar to those in the normal group ($p > 0.05$), revealing good biocompatibility in the liver and kidney. Moreover, the results of complete blood panel analysis (Figures 8D–H) showed no obvious differences in the hematology of the ZnONPs-Gel USNP-treated group when compared to that of the control group ($p > 0.05$).

CONCLUSION

In our study, we conducted a promising therapy for microenvironment regulation based on BMSC-derived ZnONPs adherent on a hydrogel that originated from skeletal muscle. The implantation treatment of ZnONPs-Gel presented high capability in nerve recovery *via* inflammation and ROS inhibition. Taken together, we reported that ZnONPs-Gel application posed a promising ZnONP-loaded implantation approach for an effective and biocompatible treatment of SCI.

DATA AVAILABILITY STATEMENT

The original contributions presented in the study are included in the article/Supplementary Material, further inquiries can be directed to the corresponding authors.

ETHICS STATEMENT

The animal study was reviewed and approved by the Institutional Animal Care and Use Committee of Jinzhou Medical University. Written informed consent was obtained from the owners for the participation of their animals in this study.

AUTHOR CONTRIBUTIONS

X-fM and S-rC designed and supervised this study. SL, H-sZ, and CX conducted the majority of the experiments and completed the

manuscript. Z-pZ participated in the experiments and manuscript writing. D-hW participated in editing the manuscript. All authors read and approved the final manuscript.

FUNDING

This work was supported by the National Natural Science Foundation of China (NSFC) (Nos. 81871556 and 82072165), Liaoning Revitalization Talents Program (No. XLYC1902108)

REFERENCES

- Ahuja, C. S., Nori, S., Tetreault, L., Wilson, J., Kwon, B., Harrop, J., et al. (2017). Traumatic Spinal Cord Injury-Repair and Regeneration. *Neurosurgery* 80, S9–S22. doi:10.1093/neuros/nyw080
- Baetke, S. C., Lammers, T., and Kiessling, F. (2015). Applications of Nanoparticles for Diagnosis and Therapy of Cancer. *Bjr* 88, 20150207. doi:10.1259/bjr.20150207
- Basnet, P., Inakhunbi Chanu, T., Samanta, D., and Chatterjee, S. (2018). A Review on Bio-Synthesized Zinc Oxide Nanoparticles Using Plant Extracts as Reductants and Stabilizing Agents. *J. Photochem. Photobiol. B: Biol.* 183, 201–221. doi:10.1016/j.jphotobiol.2018.04.036
- Basso, D. M., Beattie, M. S., and Bresnahan, J. C. (1995). A Sensitive and Reliable Locomotor Rating Scale for Open Field Testing in Rats. *J. Neurotrauma* 12, 1–21. doi:10.1089/neu.1995.12.1
- Boraschi, D., Italiani, P., Palomba, R., Decuzzi, P., Duschl, A., Fadeel, B., et al. (2017). Nanoparticles and Innate Immunity: New Perspectives on Host Defence. *Semin. Immunol.* 34, 33–51. doi:10.1016/j.smim.2017.08.013
- Dadfar, S. M., Roemhild, K., Drude, N. I., von Stillfried, S., Knüchel, R., Kiessling, F., et al. (2019). Iron Oxide Nanoparticles: Diagnostic, Therapeutic and Theranostic Applications. *Adv. Drug Deliv. Rev.* 138, 302–325. doi:10.1016/j.addr.2019.01.005
- Fawcett, J. W. (2015). The Extracellular Matrix in Plasticity and Regeneration after CNS Injury and Neurodegenerative Disease. *Prog. Brain Res.* 218, 213–226. doi:10.1016/bs.pbr.2015.02.001
- Frederickson, C. J., Koh, J.-Y., and Bush, A. I. (2005). The Neurobiology of Zinc in Health and Disease. *Nat. Rev. Neurosci.* 6, 449–462. doi:10.1038/nrn1671
- Hernandez, M. J., Yakutis, G. E., Zelus, E. I., Hill, R. C., Dzieciatkowska, M., Hansen, K. C., et al. (2020). Manufacturing Considerations for Producing and Assessing Decellularized Extracellular Matrix Hydrogels. *Methods* 171, 20–27. doi:10.1016/j.ymeth.2019.09.015
- Hickman, S., Izzy, S., Sen, P., Morsett, L., and El Khoury, J. (2018). Microglia in Neurodegeneration. *Nat. Neurosci.* 21, 1359–1369. doi:10.1038/s41593-018-0242-x
- Hussain, I., Singh, N. B., Singh, A., Singh, H., and Singh, S. C. (2016). Green Synthesis of Nanoparticles and its Potential Application. *Biotechnol. Lett.* 38, 545–560. doi:10.1038/s41593-018-0242-x
- Koffler, J., Zhu, W., Qu, X., Platoshyn, O., Dulin, J. N., Brock, J., et al. (2019). Biomimetic 3D-Printed Scaffolds for Spinal Cord Injury Repair. *Nat. Med.* 25, 263–269. doi:10.1038/s41591-018-0296-z
- Li, H., Ghazanfari, R., Zacharaki, D., Lim, H. C., and Scheduling, S. (2016). Isolation and Characterization of Primary Bone Marrow Mesenchymal Stromal Cells. *Ann. N.Y. Acad. Sci.* 1370, 109–118. doi:10.1111/nyas.13102

and 2021 Youth Science and Technology Talents Support Plan from Boze Project of Jinzhou Medical University (No. JYBZQT2108).

SUPPLEMENTARY MATERIAL

The Supplementary Material for this article can be found online at: <https://www.frontiersin.org/articles/10.3389/fbioe.2021.796361/full#supplementary-material>

- McDonald, J. W., and Sadowsky, C. (2002). Spinal-cord Injury. *The Lancet* 359, 417–425. doi:10.1016/s0140-6736(02)07603-1
- Ogunyemi, S. O., Abdallah, Y., Zhang, M., Fouad, H., Hong, X., Ibrahim, E., et al. (2019). Green Synthesis of Zinc Oxide Nanoparticles Using Different Plant Extracts and Their Antibacterial Activity against *Xanthomonas Oryzae* P. *Oryzae. Artif. Cell Nanomedicine, Biotechnol.* 47, 341–352. doi:10.1080/21691401.2018.1557671
- Pochwat, B., Nowak, G., and Szewczyk, B. (2015). Relationship between Zinc (Zn (2+)) and Glutamate Receptors in the Processes Underlying Neurodegeneration. *Neural Plast.* 2015, 591563. doi:10.1155/2015/591563
- Qin, T., Ma, R., Yin, Y., Miao, X., Chen, S., Fan, K., et al. (2019). Catalytic Inactivation of Influenza Virus by Iron Oxide nanozymeMitochondrial ROS Signaling in Organismal Homeostasis. *TheranosticsCell* 9163, 6920560–6935569. doi:10.7150/thno.35826
- Soleimani, M., and Nadri, S. (2009). A Protocol for Isolation and Culture of Mesenchymal Stem Cells from Mouse Bone Marrow. *Nat. Protoc.* 4, 102–106. doi:10.1038/nprot.2008.221
- Ungerleider, J. L., Johnson, T. D., Rao, N., and Christman, K. L. (2015). Fabrication and Characterization of Injectable Hydrogels Derived from Decellularized Skeletal and Cardiac Muscle. *Methods* 84, 53–59. doi:10.1016/j.jymeth.2015.03.024
- Zhao, X., Wu, H., Guo, B., Dong, R., Qiu, Y., and Ma, P. X. (2017). Antibacterial Anti-oxidant Electroactive Injectable Hydrogel as Self-Healing Wound Dressing with Hemostasis and Adhesiveness for Cutaneous Wound Healing. *Biomaterials* 122, 34–47. doi:10.1016/j.biomaterials.2017.01.011

Conflict of Interest: The authors declare that the research was conducted in the absence of any commercial or financial relationships that could be construed as a potential conflict of interest.

Publisher's Note: All claims expressed in this article are solely those of the authors and do not necessarily represent those of their affiliated organizations, or those of the publisher, the editors, and the reviewers. Any product that may be evaluated in this article, or claim that may be made by its manufacturer, is not guaranteed or endorsed by the publisher.

Copyright © 2022 Lin, Zhao, Xu, Zhou, Wang, Chen and Mei. This is an open-access article distributed under the terms of the Creative Commons Attribution License (CC BY). The use, distribution or reproduction in other forums is permitted, provided the original author(s) and the copyright owner(s) are credited and that the original publication in this journal is cited, in accordance with accepted academic practice. No use, distribution or reproduction is permitted which does not comply with these terms.



Osseointegration Effect of Micro-Nano Implants Loaded With Kaempferol in Osteoporotic Rats

Anyue Wang¹, Wenhong Yuan², Yu Song³, Yanjun Zang³ and Yanling Yu^{3*}

¹Department of Stomatology, School of Stomatology of Qingdao University, Qingdao, China, ²Qingdao Municipal Hospital, Qingdao, China, ³Qingdao Stomatological Hospital Affiliated to Qingdao University, Qingdao, China

Objective: To investigate the effect of osseointegration of kaempferol loaded on the surface of micro-nanomorph implants in ovariectomized rats.

Methods: Titanium flakes were polished to obtain the PT group, anodized and acid-etched to obtain the NT and WNT groups, loaded with kaempferol to obtain the KNT and KWNT groups, and spin-coated on chitosan-gelatin composite film to obtain the KNT-CG and KWNT-CG groups. *In vitro* experiments were performed to observe the physicochemical properties of the titanium tablets in each group through scanning electron microscopy and contact angle experiments. The cytotoxicity and drug release pattern were observed using CCK-8 and drug release assays. An osteoporosis rat model was established. Pure titanium implants were divided into PT, NT, WNT, KNT-CG, and KWNT-CG groups after the same treatment and used in the *in vivo* experiments and then implanted in the femur of mice in each group. After 4 weeks, all samples were collected for toluidine blue staining, micro-computed tomography scanning, and bone morphometry analysis to evaluate their osteogenic properties.

Results: According to scanning electron microscopy, the surface of the titanium flakes had a micro-nano morphology in the WNT group and the KNT and KWNT groups were functionally loaded with kaempferol. In CCK-8 and drug release experiments, the loaded kaempferol and gelatin composite membranes showed no significant toxic effects on cells. The drug release time in the KNT-CG and KWNT-CG groups was significantly longer than that in the KNT and KWNT groups, with the release time in the KWNT-CG group reaching 15 days. *In vivo* experiments micro-computed tomography and bone morphometry analysis showed that the osteoporosis model had been successfully constructed. The bone volume fraction around the implant increased. Toluidine blue staining showed new bone formation and a significantly increased number of bone trabeculae.

Conclusion: Kaempferol micro-nanocomposite coating improved the osseointegration ability of implants in osteoporotic rats.

Keywords: Osteoporosis, implants, micro-nano, Kaempferol, Osseointegration, chitosan, gelatin

OPEN ACCESS

Edited by:

Huihua Yuan,
Nantong University, China

Reviewed by:

Bingcheng Yi,
Shanghai Jiao Tong University, China
Kao Li,
China University of Petroleum
(Huadong), China

*Correspondence:

Yanling Yu
yqdkqyyl@126.com

Specialty section:

This article was submitted to
Biomaterials,
a section of the journal
Frontiers in Bioengineering and
Biotechnology

Received: 23 December 2021

Accepted: 21 January 2022

Published: 23 February 2022

Citation:

Wang A, Yuan W, Song Y, Zang Y and
Yu Y (2022) Osseointegration Effect of
Micro-Nano Implants Loaded With
Kaempferol in Osteoporotic Rats.
Front. Bioeng. Biotechnol. 10:842014.
doi: 10.3389/fbioe.2022.842014

INTRODUCTION

Osteoporosis (OP) is divided into two major categories: primary and secondary. Postmenopausal OP in women is the most common form of primary OP. As the world population increases, OP has become an important medical issue (Teitelbaum, 2010; Rachner et al., 2011).

Additionally, the rate of missing teeth in middle-aged and elderly people is gradually increasing. Currently, titanium dental implants are widely used because they can achieve osseointegration by crossing the area of cancellous bone, inducing the cytotomes and bone trabeculae of fibroblasts and osteoblasts to reach the titanium surface and form a biomechanical bond with the interfacial interface of the body's fine weave via a chemical reaction (Noguerol et al., 2006; Turkyilmaz et al., 2008). However, in the case of OP, the clinical presentation is often characterized by alveolar ridge resorption and reduced alveolar bone density due to lower local and overall bone density. This results in a prolonged bone healing time after implant placement as well as a decreased osseointegration rate and a lower initial stability of the implant. Thus OP patients have a poor osseointegration profile (Merheb et al., 2016). In order to improve the success rate of implant surgery in patients with osteoporosis, the following methods are currently used for treatment: bone extrusion technique, systemic drug treatment and implant surface treatment. Since the bone extrusion technique is not easy to master, excessive extrusion can easily cause implant failure. The systemic drug treatment will bring inevitable side effects, so the main focus of this group is on implant surface treatment. Numerous studies have shown that micro-nano treatment of the implant surface can improve the osseointegration effect. Numerous studies have shown that micro-nano treatment of the implant surface can be performed to improve the osseointegration effect, but the results remain unsatisfactory (Milinkovic et al., 2012; Sulka et al., 2013; Zhao et al., 2020; Yang et al., 2021). Micro-nanostructures have the effect of promoting osteoblast adhesion, while drug can be loaded on their surface as drug delivery carriers. However, the drug release time of micro-nanostructures alone is short for long-term osteogenesis, so membranous materials that can prolong the drug release time are considered to cover the surface. Both chitosan and gelatin have good biocompatibility and biodegradability. Wang et al. found that chitosan exhibited higher drug loading and better sustained release performance after forming composites with nanostructures (Wang et al., 2008). Javanbakht et al. demonstrated the sustained release function of gelatin and its high stability for long-term drug delivery through *in vivo* drug tests, meanwhile the results of cytotoxicity experiments showed that it has low toxicity to cells. Therefore, this experiment proposes to load both on the material surface (Javanbakht et al., 2019).

Chinese herbal medicine has been used in China for more than 2000 years to treat OP and in recent years has gradually attracted worldwide attention because of its low side effects (Yza et al., 2021). Modern pharmacological studies have shown that kaempferol, an extract of many herbal medicines, can promote osteoblast differentiation (Trivedi et al., 2008; Kumar et al., 2010; Guo et al., 2012) and inhibit osteoclast activity (Wattel et al., 2003;

Kim et al., 2018). Therefore, it may be possible to form a composite structure by loading kaempferol on the surface of micro-nanomorph materials to exert joint effects. In this study, by simulating bilateral ovariectomy in rats, a postmenopausal female OP model was established to investigate the effects of combining micro-nanoformations with kaempferol on bone metabolism neonatal bone tissue, bone density, and bone trabecular microstructure in de-ovary rats.

MATERIALS AND METHODS

Experimental Animals

Thirty-six 3-month-old specific pathogen-free-grade female Sprague-Dawley rats were purchased from Jinan Pengyue Experimental Animal Breeding Company (Shandong, China). All animal-related experiments were performed using the protocols approved by our institute (The Ethics Committee of Qingdao Stomatological Hospital Affiliated to Qingdao University, 2019KQYX025). The body weight of the rats was 240 ± 20 g. Two rats were housed in each metabolic cage under standard conditions and used in the experiment after 1 week of acclimatization feeding.

Experimental Methods

Functionalized Morphology Construction and Material Characterization

We sanded 14×1 -mm pure titanium flakes samples (Dongguan Shengyue Precision Hardware Products Co., Guangdong, China) with 600-, 1,000-, 3,000-, 5,000- and 7000-mesh sandpaper until their surfaces were smooth and mirror-like. The samples were ultrasonically cleaned with acetone, anhydrous ethanol, and deionized water for 15 min each in turn to remove surface impurities and then dried naturally to obtain the smooth (PT) group samples. PT samples were placed in 1.25 wt% hydrofluoric acid (HF) solution for acid etching to form a micron-level morphology. Further experiments were conducted to reduce the surface diameter, and the specimens with a micron-level morphology were placed in 1.5 wt% HF to prepare the nanoscale morphology by anodic oxidation. The specimens were cleaned by ultrasonic cleaning with deionized water for 15 min and dried under natural air. The micro-nano group (WNT) with micron-nano coexistence morphology and nano group (NT) with pure nanoscale morphology were obtained.

Loading of Kaempferol on the Material Surface

The randomly selected NT and WNT group were placed in $10 \mu\text{M}$ (Kim et al., 2016) kaempferol (Beijing Solebro Technology Co., Beijing, China, purity 99.62%, molecular weight 286.24 Da) in anhydrous ethanol, and then placed in a vacuum drying oven and evacuated. The vacuum pump was turned off after 15 min, and the samples were left under vacuum for 3 days, followed by natural air-drying for 1 day. Residual drug on the surface was removed by washing with phosphate-buffered saline (PBS) to obtain the kaempferol nano-group (KNT) and kaempferol micro-nano-group (KWNT).

Sample Surface Covered With Chitosan/Gelatin Composite Film

First, a mixture of 1% formic acid solution and 2 g of chitosan was added to the formic acid solution to prepare a 2% chitosan formic acid solution by stirring with a magnetic rotor for 2 h at a speed of 1,000 r/min at 37°C. Next, 10 mg of gelatin was dissolved in deionized water and incubated at room temperature until the gelatin was completely dissolved. A homogeneous 1% gelatin solution was prepared by stirring in a water bath at 60°C for 2 h (Hao et al., 2021; Zheng et al., 2021). The KNT and KWNT samples were placed in a vacuum rotary coater set to a speed of 4,000 r/min. Chitosan solution was added slowly with a dropper onto the sample surface and rotated to coat the sample for 40 s. The configured gelatin solution was sucked again in the same manner, and two layers of each solution were applied alternately. Dried and ready for use (Wang et al., 2021). Finally, kaempferol nano plus film set (KNT-CG) and kaempferol micro nano plus film set (KWNT-CG) were produced.

Scanning Electron Microscopy Observation of Sample Surface Morphology

The surface morphology and characteristics of the samples were observed using scanning electron microscopy (SEM; Thermo Fisher Scientific, Waltham, MA, United States) of the PT, NT, WNT, KNT, KWNT, KNT-CG, KWNT-CG groups. Samples from each group were fixed with conductive adhesive, observed, and photographed.

Contact Angle Detection

Five samples were randomly selected from each group, and the contact angle of each sample was tested with a static contact angle tester (DSA25E, Kruss, Germany). Deionized water (10 µL) was added dropwise to the sample surface at room temperature and left for 40 s. After the water droplets were stabilized, images of the water droplet spreading on the sample surface were obtained with a camera. Each sample was evaluated three times and the average value was taken. Software was used for detection and analysis. The results were 90° < contact angle < 180° for hydrophobic and 0° < contact angle < 90° for hydrophilic.

Detection of Early Release Pattern of Kaempferol

A solution of kaempferol at 28.6 mg/L in ethanol was prepared as the master solution and diluted into a series of solutions with concentrations of 1.43, 2.86, 4.29, 5.57, 8.58, and 11.44 mg/L. Anhydrous ethanol was used as a control, and kaempferol was detected at a wavelength of 366 nm. The samples were sequentially injected into a UV spectrophotometer (UV, Shanghai Metash Instruments Co., China) to evaluate the peak areas.

The samples were injected into the UV spectrophotometer, and the peak areas were recorded. Samples from the KNT, KWNT, KNT-CG, and KWNT-CG groups were added to a 24-well plate, soaked dropwise with 3 ml of PBS, pH 7.4, and heated in a water bath and set at 100 r/min and 37°C. Every second day, 500 µL of soaking solution was collected by aspiration, and 500 µL of fresh PBS was added to continue soaking. The concentration of kaempferol in the aspirated solution was detected by UV detection until the concentration

was no longer detectable, i.e., all kaempferol had been released into the PBS. The average release dose and load of all samples was calculated at the same time point. A cumulative release curve was drawn (He et al., 2021).

CCK-8 Assay for Cytotoxicity

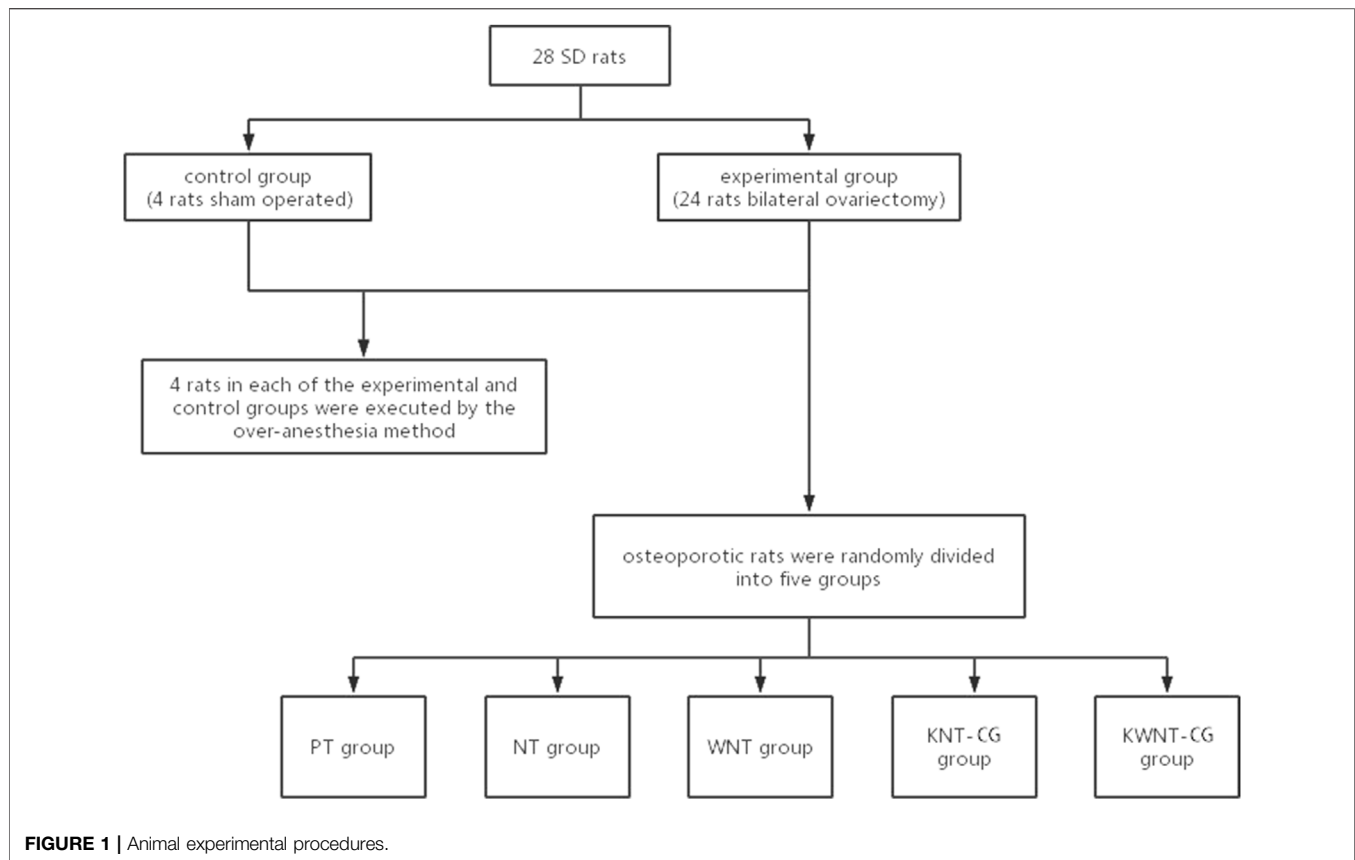
A 10 µM kaempferol solution was prepared and CCK-8 was used to detect the cytotoxicity of kaempferol towards MC3T3-E1 cells after binding to the micro-nanomorphs. Samples from each group were disinfection and placed at the bottom of 24-well plates, the cells were inoculated at a density of 5×10^4 cells/mL, and the plates were incubated for 1, 3, 5, and 7 days at 37°C and 5% CO₂ in an incubator. The samples were then washed with PBS, and 0.25% trypsin was added for digestion. Then transferred to 96-well plate and incubated in an incubator. After 24 h, 10 µL CCK-8 was added to each well, and the plate was incubated at 37°C for 4 h to induce nasal production. The optical density of each well at 450 nm was measured using an enzyme immunoassay analyzer (BioTek Instruments, Winooski, VT, United States), and cytotoxicity was considered to exist when the relative cell viability was below 70% (ISO, 2009).

Both the drug release and cytotoxicity assays demonstrated that the KNT-CG and KWNT-CG groups had better performance than the KNT and KWNT groups. Therefore, the latter two groups were excluded from subsequent animal experiments.

Animal Experiments

Twenty-eight Sprague-Dawley rats were randomly divided into two groups: 24 rats in the experimental group underwent bilateral ovariectomy (OVX); in the control group of four rats, only a small portion of adipose tissue around the ovaries was removed (sham operated). Sprague-Dawley rats were acclimatized for 1 week and anesthetized by intraperitoneal injection. The skin, fascia, and muscles were separated bluntly layer-by-layer, and the ovaries were removed from the experimental group after ligating the fallopian tubes and adjacent vascular tissues around the ovaries with a No.0 surgical wire; a small amount of adipose tissue around the ovaries was removed from the control group. After the operation, the rats moved normally and had free access to food. Penicillin was injected intramuscularly at 250,000 IU/kg for three consecutive days to prevent infection. Four weeks later, four rats in each from the experimental and control groups were sacrificed using an overdose of anesthesia. Both femurs from each rat were separated, and the surrounding attached soft tissues were removed to preserve the integrity of the femur as much as possible. The femurs were completely soaked in 4% paraformaldehyde for micro-CT (µCT-100, Hangzhou Yuebo Biotechnology Co., China) scanning to confirm the generation of the OP model.

After successful modeling, the osteoporotic rats were randomly divided into five groups of four rats each, and the skin was cut at the distal femur bilaterally. The subcutaneous tissue was bluntly separated to reach the femoral epiphysis, and pre-prepared titanium nails from the PT, NT, WNT, KNT-CG, and KWNT-CG groups were implanted (titanium nails were treated in the same manner as titanium pieces). Postoperatively, penicillin was injected intramuscularly for three consecutive days at 250,000 IU/kg to prevent infection. At 4 weeks after nail implantation, the rats were



sacrificed through anesthesia overdose to extract the material, and the same method was used as above for subsequent testing. The specific process is shown in **Figure 1**.

Micro-CT Scanning

After 24 h of fixation, the samples were removed, scanning and 3D reconstruction were performed by micro-CT with the implant as the axis and bone spread at around 2 mm to the surrounding bone. The scanning parameters were as follows: voltage 70 kV, current 200 μ A, resolution 14.8 μ m, and exposure time 300 ms. Bone volume (BV), tissue volume (TV), object surface/volume ratio (BV/TV), trabecular number (Tb.N), trabecular thickness (Tb.Th), trabecular spacing (Tb.Sp) and degree of anisotropy (DA) were measured separately.

Toluidine Blue Staining

The grinding slides were prepared using an EXAKT hard tissue cutting and grinding system (300 CP/400CS/AW, EXAKT, Germany) as follows. Fresh tissue specimens were fixed in 40 g/L paraformaldehyde fixative at 4°C for 24–48 h. After fixation, the specimens were dehydrated in ethanol solution and then immersed in anhydrous ethanol and light-curing resin for infiltration. The fully infiltrated tissues were placed in a light-curing embedding machine for polymerization. The tissue blocks were cut to obtain the target sections and polished step-by-step to prepare approximately 50- μ m-thick tissue abrasives. Finally, the slices were sealed with neutral resin after toluidine blue staining.

Statistical Analysis

Paired *t*-tests were performed using SPSS 12.0 software (SPSS, Inc., Chicago, IL, United States), and differences were considered as statistically significant when $p < 0.05$.

RESULTS

SEM Observation Results

The surface morphology of titanium flakes in the PT group was smooth with only a few polishing marks (**Figure 2A**). The surface morphology formed by acid etching was micron-sized and stepped (**Figure 2B**). The KNT and KWNT groups had a nanoscale and micro-nanoscale morphology surface loaded with kaempferol, most nanotubes orifices were not visible because of drug blockage, and kaempferol was successfully loaded into the nanotubes (**Figures 2E,F**). The KNT-CG and KWNT-CG groups formed nanotubes with a micro-nanoscale structure after the surface was coated with chitosan and a gelatin film bilayer (**Figure 2E**). The microstructure was covered, appearing to have a patchy surface (**Figures 2G,H**).

Contact Angle Analysis

The contact angles of the seven groups of samples were determined, as shown in **Figure 3**. The relationship between the surface contact angle of the experimental materials in each group is PT group > KNT-CG group > KWNT-CG group > KNT group >

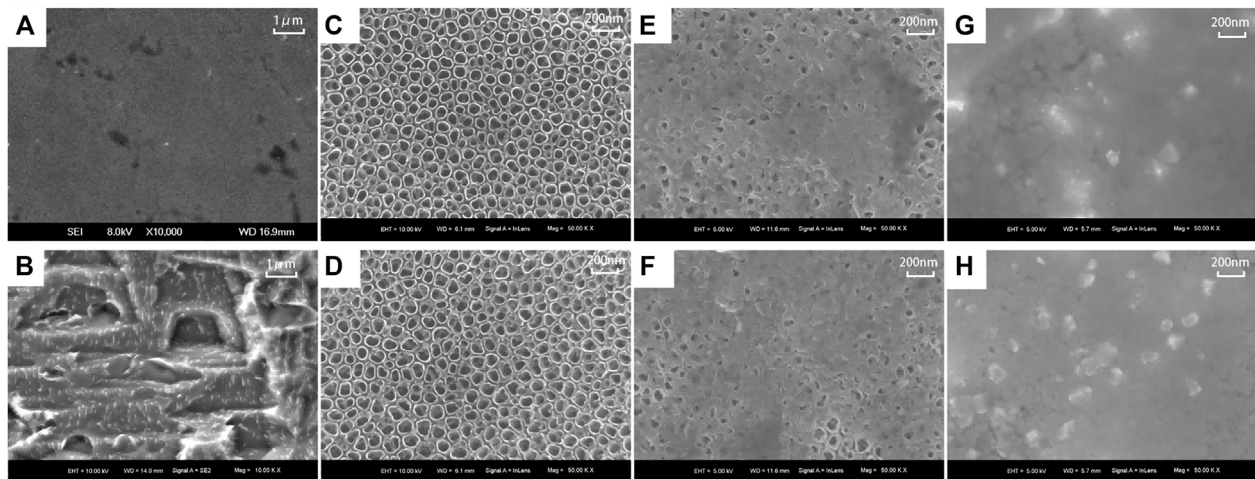


FIGURE 2 | Surface morphology of each titanium sheet under SEM. (A): PT group; (B): Micron structure; (C): NT group; (D): WNT group; (E): KNT group; (F): KWNT group; (G): KNT-CG group; (H): KWNT-CG group.

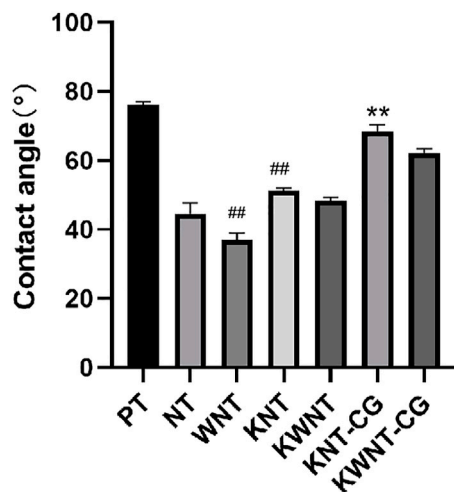


FIGURE 3 | Analysis of the results of contact angle comparison between groups. Bar graphs: Data are presented as mean \pm SD. # represents comparison with NT group, ## $p < 0.01$; * represents comparison with PT group, ** $p < 0.01$.

KWNT group > NT group > WNT group. Due to the formation of micron structure and binding to nanotubes enhanced hydrophilicity, the contact angle of the NT group > WNT group ($p < 0.01$). The KNT group showed lower hydrophilicity compared to the NT group because of drug loading ($p < 0.01$). However, since titanium metal was relatively hydrophobic, the KWNT-CG group < PT group ($p < 0.01$).

CCK-8 Assay Results

The results of the CCK-8 assay are shown in Figure 4; the PT group was used as the control. The cytotoxicity of the KNT and KWNT groups increased from 1 to 3 days because of rapid drug release; the

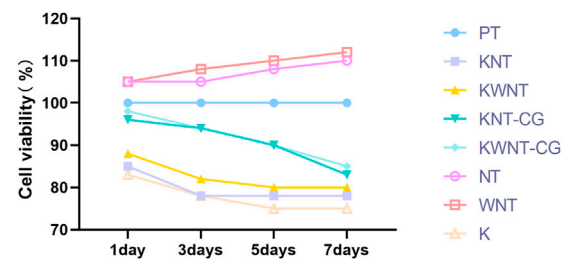


FIGURE 4 | Analysis of CCK-8 results.

KNT-CG and KWNT-CG groups were coated with chitosan and gelatin membranes, which slowed drug release and reduced cytotoxicity. However, the relative cell viability was greater than 70%, demonstrating that the micro-nanostructures loaded with kaempferol and coated with membranes were less toxic towards cells (Zhou et al., 2020).

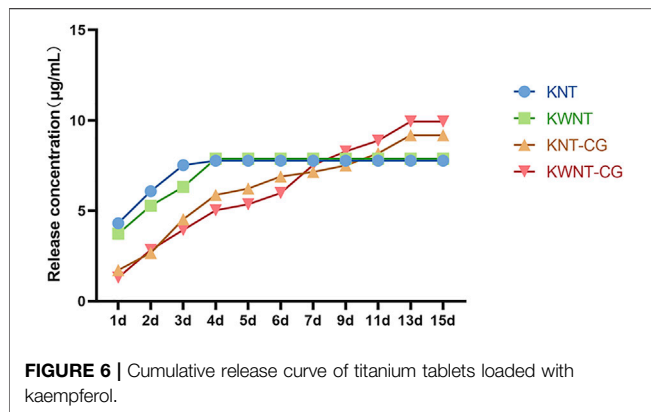
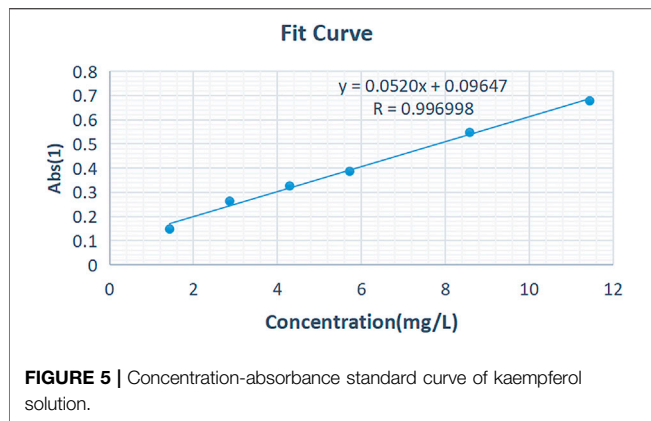
Analysis of Kaempferol Release

Establishment of the Standard Curve

The standard curve was drawn using linear regression with the concentration C (mg/L) as the horizontal coordinate and absorbance Abs of the solution as the vertical coordinate. The linear equation was as follows: $Y = 0.0520X + 0.0947$ ($R = 0.996998$). A linear relationship was observed between the kaempferol concentration and absorbance in the range of 0.1–15 mg/L, as shown in Figure 5.

Determination of Drug Release

Figure 6 shows the cumulative release curves of kaempferol from the four groups of samples within 15 days. The KNT group showed complete drug release in the first 3 days, with the KWNT group exhibiting drug release within 4 days because of its micron



structure. After coating with the chitosan and gelatin composite film, the loaded kaempferol in the KNT-CG and KWNT-CG groups showed a longer slow release, and the total amount of drug released exceeded that in the KNT and KWNT groups. The KWNT-CG group showed the highest total drug release.

Results of Micro-CT Scans

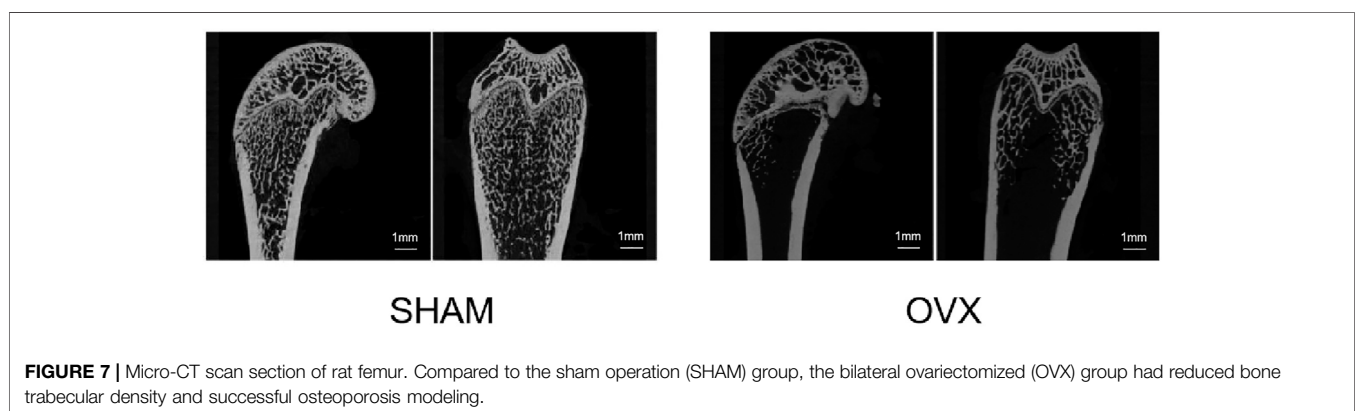
Scanning Results of OP Mouse Model

Figure 7 shows the micro-CT images of the femur in the sham and OVX groups. Bone density was significantly lower in the

OVX group than in the sham group, indicating that the animal model of OP was successfully constructed.

Micro-CT Bone Volume and Bone Microstructure Parameters

As shown in Figure 8A, the bone trabecular spaces around the femoral implants of rats in the PT group were larger, with sparser and more slender bone trabecular structures formed locally. As shown in Figure 8B–E, the number of bone trabeculae was significantly increased, continuity was higher, and separation was reduced, indicating that kaempferol release promoted osseointegration. The best improvement was observed in the KWNT-CG group, where the bone trabeculae were tightly interwoven to form an irregular three-dimensional meshwork resembling a sponge. Bone morphometric analysis was performed (Figure 9). The BV/TV value is the most important parameter reflecting bone remodeling. BV/TV values increased in the KNT-CG group compared with the NT group ($p < 0.01$) and in the KWNT-CG group compared with the PT group ($p < 0.05$). These results indicate the osteogenic effect of micro-nanoconjugated loaded drugs and chitosan-gelatin bilayer. Tb.N, Tb.Th and Tb.Sp are the main indicators for evaluating the spatial morphological structure of bone trabeculae, and each of these values was higher in the WNT group than in the PT group ($p < 0.01$), indicating that the micro-nano structure did promote an increase in the number of bone trabeculae and led to a decrease in their separation. Owing to the loading of the drug and covered with chitosan-gelatin bilayer, the Tb.N and Tb.sp values were higher in the KNT-CG group than in the NT group ($p < 0.01$). The Tb.Sp values were also higher than in the NT group, but there was no statistical difference in Tb.Sp ($p > 0.05$). The DA values in the KWNT-CG group were higher than those in the PT group ($p < 0.05$), indicating better orientation and symmetry of the bone trabeculae. The titanium implants in each experimental group increased the number, thickness, and volume fraction of the bone trabeculae, improving local femoral OP and contributing to osseointegration of the implants.



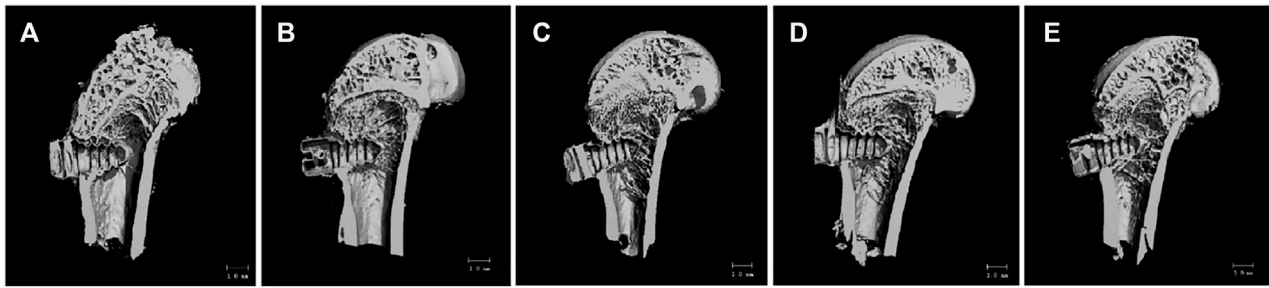


FIGURE 8 | 3D Micro-CT scan of rat femur. (A):PT group; (B):NT group; (C): WNT group; (D):KNT-CG group; (E):KWNT-CG group.

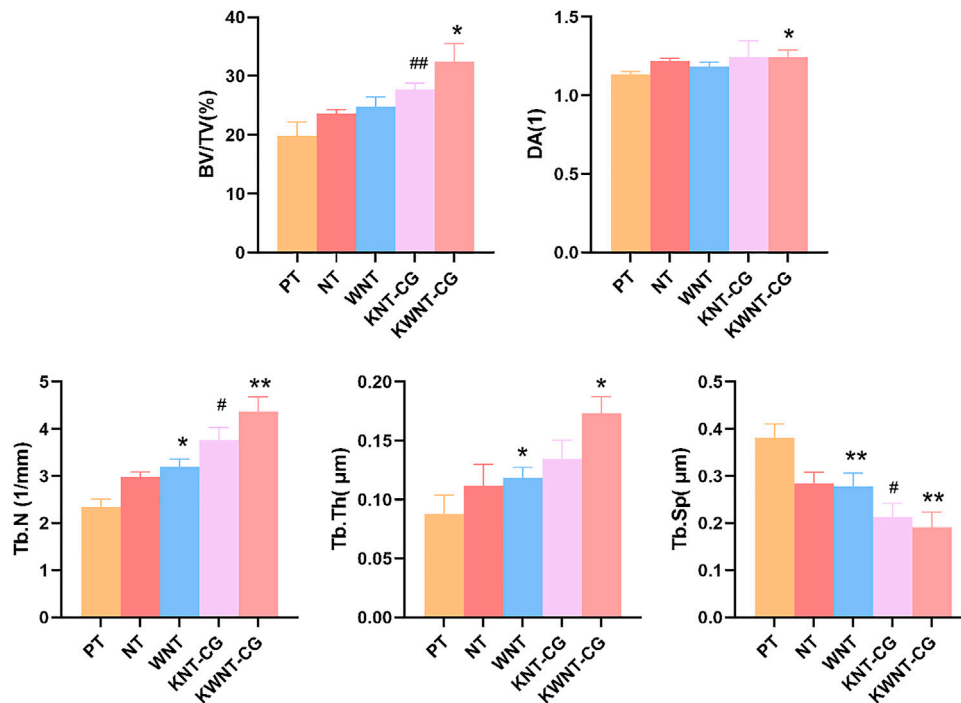


FIGURE 9 | Morphometric analysis of rat femur. BV/TV, bone volume per tissue volume; DA, degree of anisotropy; Tb.N, trabecular number; Tb.Th, trabecular thickness; Tb. Sp, trabecular spacing. Bar graphs: Data are presented as mean \pm SD. # represents comparison with NT group, ## $p < 0.01$, * $p < 0.05$; * represents comparison with PT group, ** $p < 0.01$; * $p < 0.05$.

Analysis of Toluidine Blue Staining Results

Toluidine blue tissue staining of the samples from each group after 4 weeks is shown in **Figure 10**, in which the black area is the implant thread, white area on the left is the peri-implant bone tissue, and dark blue area is the new bone tissue. Compared to the PT group, the NT, WNT, KNT-CG, and KWNT-CG groups showed significantly more new bone tissue and increased continuity. The PT group had less new bone tissue production, which only existed locally in the implant thread, with discontinuous bone trabeculae and more faults. Compared to the PT group, the NT and WNT groups showed a significant improvement, with an increased amount of continuous new bone. The KNT-CG group showed a further increase in new bone, with

only a small number of discontinuities, although the bone trabeculae was not dense. The KWNT-CG group showed dense bone trabeculae at the implant threads, with uniform continuity, full contact between the implant and new bone, and optimal new bone formation on the surface.

DISCUSSION

The basic building blocks of natural bone are mineralized collagen fibers with a diameter of about 80 nm, while the collagen fibers spiral forward around a Haver's tube with a thickness of 3 μ m. (Gittens et al., 2011; Jeon et al., 2015).

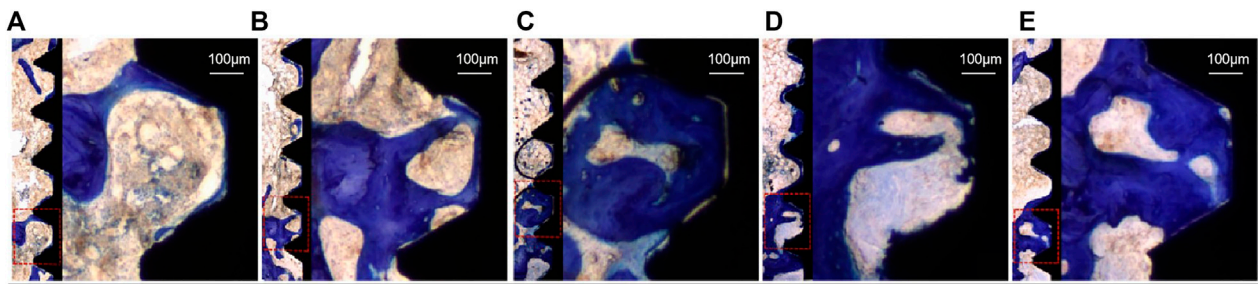


FIGURE 10 | Rat femur toluidine blue staining, dark blue part represents new bone tissue. (A): PT group; (B): NT group; (C): WNT group; (D): KNT-CG group; (E): KWNT-CG group.

Therefore, from a bionic perspective, the surface treatment of implants into micro- and nano-structures more closely resembles the natural bone morphology compared to micron or nano single-level structures. Li et al. (2010) found that the increase in the surface roughness and change in oxygen and fluorine content of titanium implants after HF treatment improved their biocompatibility and thus enhanced the osseointegration ability of implants. Different concentrations of HF solution were used for acid etching to form micron structure and anodic oxidation to form nanotubes with a diameter of around 80 ± 10 nm. The hollow structure facilitates the differentiation of osteoblasts and can be used to accommodate adsorbed drugs and enhance the mechanical embedding ability between the implant surface and bone. Treatment of the implant to form a micron surface also increases its surface area and alters the force on the bone tissue.

Anodization of the implant surface not only changes the surface microstructure, but also affects its hydrophilicity. Hydrophilicity facilitates cell adhesion, proliferation, osteogenesis, and differentiation on the surface by inhibiting immune inflammatory cells and releasing more bioactive factors, further promoting osseointegration (Elias et al., 2008; Günay-Bulutsuz et al., 2018). The use of a combination of nanotubes and micron step structures led to a decrease in the contact angle of the samples, likely because of the greater surface roughness obtained by micro- and nano-binding, thus presenting better hydrophilicity. After loading the surface with drugs, the contact angle did not greatly change, whereas after coating with chitosan and gelatin, the contact angle tended to increase because kaempferol contained fewer hydroxyl groups that could not fully react with the groups in chitosan and gelatin to form hydrogen bonds. However, the hydrophilicity of the experimental group remained higher than that of the control group. Thus, this micro-nano treatment of the implant surface increases hydrophilicity, which is favorable for osteogenesis.

In addition, Filová found (Elena et al., 2014) that the micro-nanocomposite structure promoted cellular ground attachment growth, proliferation, and differentiation. In our study, the cell survival rate of the NT and WNT groups increased over 7 days, which is consistent with the results of Filová showing that the micro-nanostructures promoted cell proliferation. In contrast, the cell survival rate in the KNT and KWNT groups decreased significantly with increasing kaempferol release in the first 3 days.

This may be because of the rapid drug release; the cell survival rate gradually stabilized after 3 days with complete release of the drug. Both chitosan and gelatin show good biocompatibility and can be degraded and absorbed by organisms, and chitosan exhibits slow and controlled release (Bastami et al., 2017; Wu et al., 2020). To alleviate reduced cell proliferation caused by rapid drug release, we uniformly coated the surface of titanium sheets loaded with kaempferol in micro-nanomorphic form and constructed KNT-CG and KWNT-CG groups, which did not significantly inhibit cell growth, slowed the drug release rate, increased the release time, increased drug release, and facilitated osseointegration, with the KWNT-CG group showing more obvious advantages. The vacuum method was used to load kaempferol into the nanotubes, eliminating the influence of other gases in the air. This approach also avoids the toxic side effects of systemic administration and increases local drug action.

Nowak et al. (2017) Suggested that oral kaempferol prevents OVX-induced bone loss by inhibiting bone resorption, and Kumar et al. (2012) found that oral kaempferol increases the stimulatory effect on osteoblasts, thereby increasing the bone anabolic effect. To verify the osteogenic effect of kaempferol, we established a rat OP model for *in vivo* experiments. Analysis of the femurs showed that new bone was generated at the implant threads in all experimental groups. The number and thickness of bone trabeculae increased and microstructure of the bone trabeculae was significantly improved. Bone trabeculae at the implant threads in the KWNT-CG group were dense, uniform, and continuous, and the implant was in full contact with new bone, showing optimal new bone formation on the surface. The number and thickness of bone trabeculae increased in the experimental group and the microstructure of bone trabeculae was significantly improved. These results suggest that the combination of micro-nano structures and kaempferol had an anti-osteoporotic effect. The Tb.N, Tb.Th, and BV/TV values increased and Tb. Sp value decreased in all experimental groups, indicating that bone anabolism was greater than bone catabolism, and the combination of the micro-nano structures and kaempferol had anti-OP effect. This is consistent with the results of drastic injury experiments on restoring trabecular structures in rats, confirming the role of kaempferol (Adhikary et al., 2018).

Therefore, the micro- and nano-structures on the implant surface may have promoted osteogenesis and increased the loadable drug volume, but increased drug release increased cytotoxicity and decreased cell proliferation. The surface membrane coverage enabled slow and long-term drug release, mitigating the cytotoxic effects. However, kaempferol loaded on the implant surface has an osteogenic effect, and long-term slow release is beneficial for reducing local OP. The dual effect of the implant micro-nanostructure and kaempferol promoted early osseointegration of the implant. The osteogenic effect of kaempferol may also be related to the induction of osteogenesis by effectors downstream of the mTOR signaling pathway (Zhao et al., 2019). In addition, Trivedi found (Trivedi et al., 2008) that OVX rats given oral kaempferol showed significantly higher bone mineral density and lower serum ALP in the treated trabeculae. Meanwhile, in line with Trivedi's study, both Ashish (Sharma and Nam, 2019) and (Xie et al., 2021) found in cellular experiments that kaempferol promotes osteogenesis by increasing the activity of ALP and the expression of osteogenic factors Runx2 and osterix.

In conclusion, kaempferol combined with micro-nano-implants promoted the osseointegration of implants and surrounding bone tissue to some extent by constructing TiO₂ nanotubes and micron structures on the surface of pure titanium flakes loaded with kaempferol under vacuum conditions and coated with a chitosan-gelatin composite film. However, the long-term stability of the micro-nanomorphs loaded with kaempferol is unclear, as we only investigated the early osseointegration for 4 weeks. Long-term properties should be further evaluated.

REFERENCES

- Adhikary, S., Choudhary, D., Ahmad, N., Karvande, A., Kumar, A., Banala, V. T., et al. (2018). Dietary Flavonoid Kaempferol Inhibits Glucocorticoid Induced Bone Loss by Promoting Osteoblast Survival. *Nutrition* 53, 64–76. doi:10.1016/j.nut.2017.12.003
- Bastami, F., Paknejad, Z., Jafari, M., Salehi, M., Rezai Rad, M., and Khojasteh, A. (2017). Fabrication of a Three-Dimensional β -tricalcium-phosphate/gelatin Containing Chitosan-Based Nanoparticles for Sustained Release of Bone Morphogenetic Protein-2: Implication for Bone Tissue Engineering. *Mater. Sci. Eng. C* 72, 481–491. doi:10.1016/j.msec.2016.10.084
- Elena, F., Tomas, S., Zbynek, S., Monika, S., Margit, Z., Karel, B., et al. (2014). Support for the Initial Attachment, Growth and Differentiation of MG-63 Cells: a comparison between Nano-Size Hydroxyapatite and Micro-size Hydroxyapatite in Composites. *Int. J. Nanomedicine* 9, 3687–3706. doi:10.2147/IJN.S56661
- Elias, C. N., Oshida, Y., Lima, J., and Muller, C. A. (2008). Relationship between Surface Properties (Roughness, Wettability and Morphology) of Titanium and Dental Implant Removal Torque. *J. Mech. Behav. Biomed. Mater.* 1 (3), 234–242. doi:10.1016/j.jmbbm.2007.12.002
- Gittens, R. A., Mclachlan, T., Olivares-Navarrete, R., Ye, C., Berner, S., Tannenbaum, R., et al. (2011). The Effects of Combined Micron-/submicron-Scale Surface Roughness and Nanoscale Features on Cell Proliferation and Differentiation. *Biomaterials* 32 (13), 3395–3403. doi:10.1016/j.biomaterials.2011.01.029
- Günay-Bulutuz, A., Berrak, Ö., Yeprem, H. A., Arisan, E. D., and Yurci, M. E. (2018). Biological Responses of Ultrafine Grained Pure Titanium and Their Sand Blasted Surfaces. *Mater. Sci. Eng. C Mater. Biol. Appl.* 91, 382–388. doi:10.1016/j.msec.2018.05.056

DATA AVAILABILITY STATEMENT

The original contributions presented in the study are included in the article/Supplementary Material, further inquiries can be directed to the corresponding author.

ETHICS STATEMENT

All animal-related experiments were performed using the protocols approved by our institute (The Ethics Committee of Qingdao Stomatological Hospital Affiliated to Qingdao University, 2019KQYX025).

AUTHOR CONTRIBUTIONS

AW conceived and designed the study. AW, YY, YS, and YZ performed the experiments. AW wrote the paper. All authors read and approved the manuscript.

FUNDING

This work was supported by the Qingdao Public Sector Science and Technology Support Project (No.19-6-1-48-nsh) and Qingdao Key Health Discipline Development Fund (No. 2020-2022).

- Guo, A., Choi, R., Zheng, K., Chen, V., Dong, T., Wang, Z., et al. (2012). Kaempferol as a Flavonoid Induces Osteoblastic Differentiation via Estrogen Receptor Signaling. *Chin. Med.* 7, 10. doi:10.1186/1749-8546-7-10
- Hao, Y., Zheng, W., Sun, Z., Zhang, D., Sui, K., Shen, P., et al. (2021). Marine Polysaccharide-Based Composite Hydrogels Containing Fucoidan: Preparation, Physicochemical Characterization, and Biocompatible Evaluation. *Int. J. Biol. Macromol.* 183, 1978–1986. doi:10.1016/j.jbiomac.2021.05.190
- He, Y., Zhao, W., Dong, Z., Ji, Y., Li, M., Hao, Y., et al. (2021). A Biodegradable Antibacterial Alginate/carboxymethyl chitosan/Kangfuxin Sponges for Promoting Blood Coagulation and Full-Thickness Wound Healing. *Int. J. Biol. Macromol.* 167, 182–192. doi:10.1016/j.jbiomac.2020.11.168
- ISO (2009). *Biological Evaluation of Medical Devices – Part 5: Tests for in Vitro Cytotoxicity*. Beijing: Standards Press of China.
- Javanbakht, S., Nezhad-Mokhtari, P., Shaabani, A., Arsalani, N., and Ghorbani, M. (2019). Incorporating Cu-Based Metal-Organic Framework/drug Nanohybrids into Gelatin Microsphere for Ibuprofen Oral Delivery. *Mater. Sci. Eng. C Mater. Biol. Appl.* 96, 302–309. doi:10.1016/j.msec.2018.11.028
- Jeon, H. J., Simon, C. G., and Kim, G. H. (2015). A Mini-Review: Cell Response to Microscale, Nanoscale, and Hierarchical Patterning of Surface Structure. *J. Biomed. Mater. Res. B Appl. Biomater.* 102 (7), 1580–1594. doi:10.1002/jbm.b.33158
- Kim, C., Shin, S., Kim, B., Kim, C., Kim, J., Kang, H., et al. (2018). The Effects of Kaempferol-Inhibited Autophagy on Osteoclast Formation. *Int. J. Mol. Sci.* 19 (1), 125. doi:10.3390/ijms19010125
- Kim, I., Kim, S., Baek, H., Kim, B., Kim, C., Chung, I., et al. (2016). The Role of Kaempferol-Induced Autophagy on Differentiation and Mineralization of Osteoblastic MC3T3-E1 Cells. *BMC Complement. Altern. Med.* 16 (1), 333. doi:10.1186/s12906-016-1320-9
- Kumar, A., Gupta, G. K., Khedgikar, V., Gautam, J., and Trivedi, R. (2012). *In Vivo* efficacy Studies of Layer-By-Layer Nano-Matrix Bearing Kaempferol for the

- Conditions of Osteoporosis: A Study in Ovariectomized Rat Model. *Eur. J. Pharm. Biopharm.* 82 (3), 508–517. doi:10.1016/j.ejpb.2012.08.001
- Kumar, A., Singh, A., Gautam, A., Chandra, D., Singh, D., Changkija, B., et al. (2010). Identification of Kaempferol-Regulated Proteins in Rat Calvarial Osteoblasts during Mineralization by Proteomics. *Proteomics* 10 (9), 1730–1739. doi:10.1002/pmic.200900666
- Li, Y., Zou, S., Wang, D., Ge, F., Bao, C., and Hu, J. (2010). The Effect of Hydrofluoric Acid Treatment on Titanium Implant Osseointegration in Ovariectomized Rats. *Biomaterials* 31 (12), 3266–3273. doi:10.1016/j.biomaterials.2010.01.028
- Merheb, J., Temmerman, A., Rasmusson, L., Kübler, A., Thor, A., and Quirynen, M. (2016). Influence of Skeletal and Local Bone Density on Dental Implant Stability in Patients with Osteoporosis. *Clin. Implant dentistry Relat. Res.* 18 (2), 253–260. doi:10.1111/cid.12290
- Milinkovic, I., Rudolf, R., Rai, K. T., Aleksic, Z., and Dr, A. S. (2012). Aspects of Titanium-Implant Surface Modification at the Micro and Nano Levels. *Materiali in Tehnologije* 46 (3), 251–256.
- Noguerol, B., Muñoz, R., Mesa, F., de Dios Luna, J., and O'Valle, F. (2006). Early Implant Failure. Prognostic Capacity of Periotest: Retrospective Study of a Large Sample. *Clin. Oral Implants Res.* 17 (4), 459–464. doi:10.1111/j.1600-0501.2006.01250.x
- Nowak, B., Matuszewska, A., Nikodem, A., Filipiak, J., Landwójtowicz, M., Sadanowicz, E., et al. (2017). Oral Administration of Kaempferol Inhibits Bone Loss in Rat Model of Ovariectomy-Induced Osteopenia. *Pharmacol. Rep.* 69 (5), 1113–1119. doi:10.1016/j.pharep.2017.05.002
- Rachner, T. D., Khosla, S., and Hofbauer, L. C. (2011). Osteoporosis: Now and the Future. *The Lancet* 377 (9773), 1276–1287. doi:10.1016/s0140-6736(10)62349-5
- Sharma, A., and Nam, J. (2019). Kaempferol Stimulates WNT/ β -catenin Signaling Pathway to Induce Differentiation of Osteoblasts. *J. Nutr. Biochem.* 74, 108228. doi:10.1016/j.jnutbio.2019.108228
- Sulka, G. D., Kapusta-Koodziej, J., Brzózka, A., and Jaskua, M. (2013). Anodic Growth of TiO₂ Nanopore Arrays at Various Temperatures. *Electrochimica Acta* 104 (8), 526–535. doi:10.1016/j.electacta.2012.12.121
- Teitelbaum, S. (2010). Stem Cells and Osteoporosis Therapy. *Cell stem cell* 7 (5), 553–554. doi:10.1016/j.stem.2010.10.004
- Trivedi, R., Kumar, S., Kumar, A., Siddiqui, J., Swarnkar, G., Gupta, V., et al. (2008). Kaempferol Has Osteogenic Effect in Ovariectomized Adult Sprague-Dawley Rats. *Mol. Cel Endocrinol* 289, 85–93. doi:10.1016/j.mce.2008.02.027
- Turkylmaz, I., Aksoy, U., and McGlumphy, E. (2008). Two Alternative Surgical Techniques for Enhancing Primary Implant Stability in the Posterior Maxilla: a Clinical Study Including Bone Density, Insertion Torque, and Resonance Frequency Analysis Data. *Clin. Implant dentistry Relat. Res.* 10 (4), 231–237. doi:10.1111/j.1708-8208.2008.00084.x
- Wang, X., Du, Y., and Luo, J. (2008). Biopolymer/montmorillonite Nanocomposite: Preparation, Drug-Controlled Release Property and Cytotoxicity. *Nanotechnology* 19 (6), 065707. doi:10.1088/0957-4484/19/6/065707
- Wang, Z., Mei, L., Liu, X., and Zhou, Q. (2021). Hierarchically Hybrid Coatings on Ti Implants for Enhanced Antibacterial Activity and Osteogenesis. *Colloids Surf. B: Biointerfaces* 204, 111802. doi:10.1016/j.colsurfb.2021.111802
- Wattel, A., Kamel, S., Mentaverri, R., Lorget, F., Prouillet, C., Petit, J., et al. (2003). Potent Inhibitory Effect of Naturally Occurring Flavonoids Quercetin and Kaempferol on *In Vitro* Osteoclastic Bone Resorption. *Biochem. Pharmacol.* 65 (1), 35–42. doi:10.1016/s0006-2952(02)01445-4
- Wu, D., Zhu, L., Li, Y., Zhang, X., and Delair, T. (2020). Chitosan-based Colloidal Polyelectrolyte Complexes for Drug Delivery: A Review. *Carbohydr. Polym.* 238, 116126. doi:10.1016/j.carbpol.2020.116126
- Xie, B., Zeng, Z., Liao, S., Zhou, C., Wu, L., and Xu, D. (2021). Kaempferol Ameliorates the Inhibitory Activity of Dexamethasone in the Osteogenesis of MC3T3-E1 Cells by JNK and P38-MAPK Pathways. *Front. Pharmacol.* 12, 739326. doi:10.3389/fphar.2021.739326
- Yang, L., Pijuan-Galito, S., Rho, H. S., Vasilevich, A. S., and Eren, A. D. (2021). High-Throughput Methods in the Discovery and Study of. *Biomater. Microbiology* 121 (8), 4561–4677. doi:10.1021/acs.chemrev.0c00752
- Yza, B., Li, B., Zs, D., Yja, B., Dwab, C., Li, M., et al. (2021). Fucoidan as a marine-origin Prebiotic Modulates the Growth and Antibacterial Ability of *Lactobacillus Rhamnosus*. *Int. J. Biol. Macromolecules* 180, 599–607. doi:10.1016/j.ijbiomac.2021.03.065
- Zhao, J., Wu, J., Xu, B., Yuan, Z., Leng, Y., Min, J., et al. (2019). Kaempferol Promotes Bone Formation in Part via the mTOR Signaling Pathway. *Mol. Med. Rep.* 20 (6), 5197–5207. doi:10.3892/mmr.2019.10747
- Zhao, X., You, L., Wang, T., Zhang, X., Li, Z., Ding, L., et al. (2020). Enhanced Osseointegration of Titanium Implants by Surface Modification with Silicon-Doped Titania Nanotubes. *Int. J. nanomedicine* 15, 8583–8594. doi:10.2147/ijn.s270311
- Zheng, W., Hao, Y., Wang, D., Huang, H., Guo, F., Sun, Z., et al. (2021). Preparation of Triamcinolone Acetonide-Loaded Chitosan/fucoidan Hydrogel and its Potential Application as an Oral Mucosa Patch. *Carbohydr. Polym.* 272, 118493. doi:10.1016/j.carbpol.2021.118493
- Zhou, Q., Chen, J., Luan, Y., Vainikka, P. A., and Thallmair, S. (2020). Unidirectional Rotating Molecular Motors Dynamically Interact with Adsorbed Proteins to Direct the Fate of Mesenchymal Stem Cells. *Sci. Adv.* 6 (5), eaay2756. doi:10.1126/sciadv.aay2756

Conflict of Interest: The authors declare that the research was conducted in the absence of any commercial or financial relationships that could be construed as a potential conflict of interest.

Publisher's Note: All claims expressed in this article are solely those of the authors and do not necessarily represent those of their affiliated organizations, or those of the publisher, the editors and the reviewers. Any product that may be evaluated in this article, or claim that may be made by its manufacturer, is not guaranteed or endorsed by the publisher.

Copyright © 2022 Wang, Yuan, Song, Zang and Yu. This is an open-access article distributed under the terms of the Creative Commons Attribution License (CC BY). The use, distribution or reproduction in other forums is permitted, provided the original author(s) and the copyright owner(s) are credited and that the original publication in this journal is cited, in accordance with accepted academic practice. No use, distribution or reproduction is permitted which does not comply with these terms.



A Transcriptome Sequencing Study on Genome-Wide Gene Expression Differences of Lung Cancer Cells Modulated by Fucoidan

Yanjie Zhao^{1,2}, Xinmei Li², Heng Zhang², Mingzhe Yan¹, Mengmeng Jia^{1,2} and Qihui Zhou^{1*}

¹Institute for Translational Medicine, The Affiliated Hospital of Qingdao University, Qingdao University, Qingdao, China, ²School of Public Health, Qingdao University, Qingdao, China

OPEN ACCESS

Edited by:

Jianxun Ding,
Changchun Institute of Applied
Chemistry (CAS), China

Reviewed by:

Dan Shao,
South China University of Technology,
China

Nemany A. N. Hanafy,
Nano Science and Technology
Institute, Kafrelsheikh University, Egypt

*Correspondence:

Qihui Zhou
qihuizhou@qdu.edu.cn

Specialty section:

This article was submitted to
Biomaterials,
a section of the journal
Frontiers in Bioengineering and
Biotechnology

Received: 29 December 2021

Accepted: 27 January 2022

Published: 01 March 2022

Citation:

Zhao Y, Li X, Zhang H, Yan M, Jia M
and Zhou Q (2022) A Transcriptome
Sequencing Study on Genome-Wide
Gene Expression Differences of Lung
Cancer Cells Modulated by Fucoidan.
Front. Bioeng. Biotechnol. 10:844924.
doi: 10.3389/fbioe.2022.844924

Fucoidan has received increasing attention in anti-(lung) tumors. However, the effect of fucoidan on the gene changes of lung cancer cells (LCCs) has not been examined systematically. Herein, we investigate the effect of fucoidan on the phenotypes of LCCs and their gene expression by transcriptome sequencing analysis. The phenotypes of LCCs are significantly inhibited by fucoidan. Importantly, compared to LCCs, 1 mg/ml fucoidan has no effect on the phenotypes of normal cells. Further, 6,930 differentially expressed genes (DEGs) in the transcriptome of LCCs (3,501 up-regulated and 3,429 down-regulated genes) are detected *via* RNA-sequencing between the fucoidan and control groups. Gene Ontology analysis confirms that DEGs are reflected in DNA replication, cell-substrate junction, regulation of cell cycle phase transition, apoptosis, focal adhesion, cadherin binding, and cell adhesion molecule binding. Thus, our findings on the transcriptomic level highlight the therapeutic potential of fucoidan for lung cancer treatment.

Keywords: marine biopolysaccharide, fucoidan, cancer, lung tumor, transcriptome sequencing

INTRODUCTION

In the last few decades, marine polysaccharides from algae have gained considerable attention from the fundamental research and practical biomedical applications owing to their inherent (bio)physicochemical characteristics, such as favorable biocompatibility and biodegradability, remarkable bioactivity, as well as outstanding structural functionalities (Bilal and Iqbal, 2020; Zheng et al., 2020; He et al., 2021; Jing et al., 2021; Yang et al., 2021). In particular, fucoidan is a water-soluble fucose-based sulfated polysaccharide, which has remarkable multiple bioactivities, including antioxidant, antimicrobial, antithrombotic, anticoagulant, anti-inflammatory, antifibrotic, immunomodulatory, and antitumor functions (Lin et al., 2020a; Apostolova et al., 2020; Etman et al., 2020; Hao et al., 2020; Zhu et al., 2021a; Hao et al., 2021; Zheng et al., 2021). Among them, its characteristic of anti-cancer cells makes it a promising candidate in the therapy of tumors, which has recently attracted increasing attention in healthy food and biomedicine (Chung et al., 2020; Etman et al., 2020; Oliveira et al., 2020). The antitumor feature of fucoidan has been reported for various cancers *in vitro* and *in vivo* (Lin et al., 2020b).

Among them, lung cancer is the second most diagnosed tumor and one of the deadliest cancers around the world, resulting in long-standing cough, chest infections, persistent and breathlessness (Minna et al., 2002; Herbst et al., 2018; Howlader et al., 2020). Conventional chemotherapy has serious side effects, such as lowered white blood cell counts, increased risk of infection, and issues with heart function (Chen et al., 2006; Lee et al., 2014). Therefore, it is vital to find naturally derived

anti-cancer agents with no or minimal side effects. As reported, fucoidan has the ability to effectively destroy lung cancer cells without significant side effects (Oliveira et al., 2020; Qiu et al., 2020). For instance, Lee *et al.* reported that fucoidan had the anti-metastatic ability on lung cancer cells (A549 cell line) through affecting ERK1/2, Akt-mTOR, and NF- κ B signaling pathways, inhibiting the migration and invasion of A549 cells (Lee et al., 2012). Boo et al. found that fucoidan caused apoptosis of A549 cells *via* hindering p38 and PI3K/Akt as well as inducing the ERK1/2 MAPK pathway (Boo et al., 2011). However, the effect of fucoidan on the gene changes of lung cancer cells has not been examined systematically in a high-throughput manner. Elucidating how fucoidan modulates the responses of lung cancer cells plays a critical role in treating lung tumors efficiently.

Inspired by the observations above, in this work, fucoidan was used to investigate its effect on the phenotypes of lung cancer cells and their gene expression by transcriptome sequencing analysis. The effects of fucoidan on the adhesion, morphology, proliferation, and migration of normal and lung cancer cells were detected. Particularly, the transcriptomics analysis of lung cancer cells was performed.

MATERIALS AND METHODS

Materials

Fucoidan derived from *Undaria pinnatifida* [Molecular weight (Mw) = 276 kDa, purity $\geq 95\%$, sulfate: 29.65% (Table 1)] was provided by Qingdao Bright Moon Seaweed Group Co., Ltd. (China). Dextran sulfate and monosaccharide standards, including rhamnose, galactose, glucose, arabinose, xylose, mannose, and fucose, were supplied by Sigma Chemical Co., Ltd. (United States). Human lung squamous cell line (H226) and bronchial epithelial cells (16HBE) were obtained from the American Type Culture Collection (ATCC, Manassas, United States). All chemicals were used as received without further purification.

Cell Culture

16HBE, a commonly used lung bronchial epithelial cell, was represented as normal lung cell in this study. H226, a commonly used lung squamous cell carcinoma cell, was represented cancer cells in this study. These cells were incubated in MEM/EBSS or RPMI-1640 Medium (Hyclone) containing 10% fetal bovine serum (FBS, Gibco, Amarillo, TX), 0.1 mg/ml streptomycin (ThermoFisher, United States), and 100 U/mL penicillin (ThermoFisher, United States) at 37°C in a humidified 5% CO₂ atmosphere. Fucoidan was dissolved in a serum-free medium and then sterilized by a 0.45 μ m filter. The cells were co-cultured with the above fucoidan solution with various concentrations (i.e., 0, 1, 10, and 100 mg/ml).

Cell Adhesion Assay

Cells were seeded in 96-well plates with a density of 2×10^4 cells/well and incubated with fucoidan/medium solutions for 1 day. Cells were fixated with 4% paraformaldehyde for 10 min and then rinsed three times with PBS. Afterward, cells were permeabilized with Triton X-100 (Solarbio, Beijing, China) at 0.5% (v/v) for

5 min, and then rinsed three times with PBS. Finally, the cells were stained with FITC-Phalloidin and DAPI (Solarbio, Beijing, China) and imaged by the High Content Analysis System-Operetta CLS™ (PerkinElmer, Waltham Mass, United States). The expression of the actin cytoskeleton, cell density and elongation were analyzed by ImageJ software. Firstly, open the figure in the software and set it to 8-bit format. Then select the parameters such as area, integrated density to be measured, and analyze to obtain quantitative data.

Cell Proliferation Assay

Cells were seeded in 96-well plates with a density of 3,000 cells/well and incubated with fucoidan/medium solutions for 1, 3, and 5 days. Afterward, the medium was exchanged with a fresh medium containing cell counting kit 8 (Dojindo labs, Kumamoto, Japan). The ratio of serum-free medium to CCK8 was 10:1 and then incubated for 2 h at 37°C. The optical density (OD) values were measured using a microplate reader (SynergyH1/H1M, Bio-Tek, China) at 450 nm.

Cell Migration Assay

H226 cells were seeded in 12-well plates with 2.5×10^4 cells/well and cultured for 1 day to reach confluence. Afterward, a 200 μ L pipette tip was used to make a straight scratch. Images at 0, 12, 24, and 48 h after scratches were collected using the Olympus inverted fluorescence microscope (Olympus, Tokyo, Japan), and the results were calculated with ImageJ software.

Transcriptome Analysis

Illumina transcriptome sequencing (Novogene, Beijing, China) was performed on abundant H226 cells co-cultured with different concentrations (0 and 1 mg/ml) of fucoidan. Next, differentially expressed genes (DEGs) were analyzed using DESeq2 1.16.1 software. We used $|\log_2(\text{Fold Change})| > 0$ & $p < 0.05$ as the screening criteria. Results of DEGs were presented as a volcano plot and a heatmap. Moreover, to analyze the DEGs at the functional level, Genetic Ontology (GO) and Kyoto Encyclopedia of Genes and Genomics (KEGG) analyses were performed using the DAVID database as previously described (Ju et al., 2019). There were three biological replicates in each group.

Statistical Analysis

All data were shown as mean \pm standard deviation (SD). Statistical analyses were evaluated using Graphpad Prism 8. The student's *t*-tests were used to determine the difference between the two groups. A value of $p < 0.05$ was considered to be statistically significant.

RESULTS AND DISCUSSION

Effect of Fucoidan on the Adhesion of H226 and 16HBE Cells

Cellular adhesion has been considered as the initial and critical response of the cell with its surrounding microenvironment, which determines the subsequent behaviors of the cell, such as morphology change, migration, proliferation, and

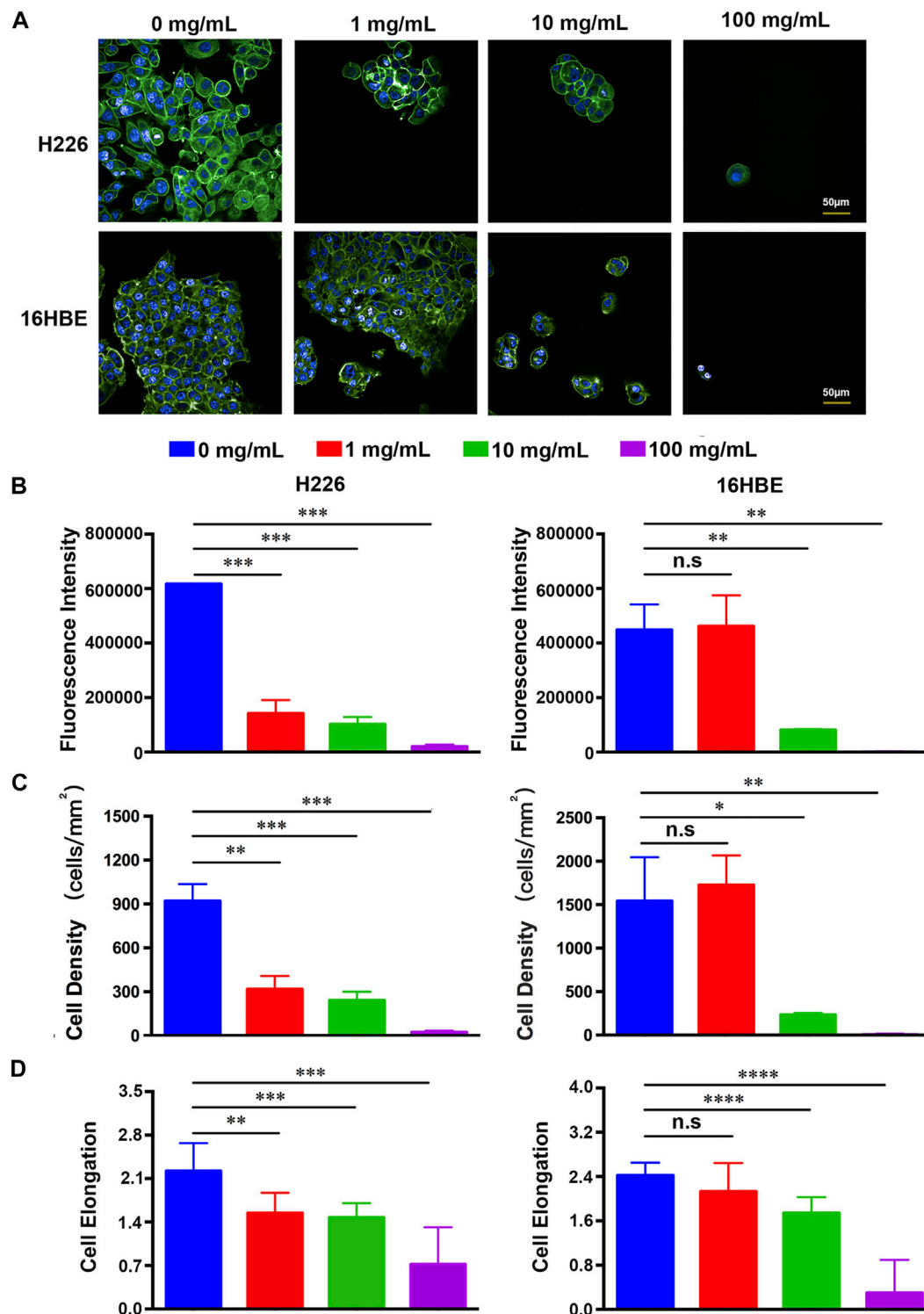


FIGURE 1 | (A) Fluorescence images of H226 and 16HBE cells treated with different concentrations of fucoidan. **(B–D)** Quantitative results of the expression of the actin cytoskeleton, cell density and elongation in H226 and 16HBE.

functionalization (Zhou et al., 2018; Li et al., 2019; Mierke, 2020; Zhou et al., 2020). The adhesion of H226 and 16HBE cells in different concentrations of fucoidan solutions after 1 day of cell

culture was investigated with a double-label fluorescence staining of the actin cytoskeleton (green) and nucleus (blue). As shown in **Figure 1A**, compared to the control group, the number of

TABLE 1 | The Mw and chemical composition of fucoidan.

Samples	Mw (kDa)	Total sugar	Sulfate (%)	Uronic acid (%)	Monosaccharide ^a (%)				
					L-fucose	Galactose	Mannose	Rhamnose	D-glucose
Fucoidan	276	78.61	29.65	2.01	54.26	42.19	1.6	1.1	0.85

^aTaking total monosaccharide as 100%.

attached H226 cells significantly reduced and cell spreading also decreased in 1 mg/ml fucoidan, while the morphology and adhesion of 16HBE cells were not affected in 1 mg/ml fucoidan. It indicates that the effect of 1 mg/ml fucoidan on H226 cells may specifically be modulated by attenuating the attachment of cancer cells but not by cytotoxicity. With increasing the fucoidan concentration from 1 to 100 mg/ml, for both types of cells, the expression of the actin cytoskeleton, cell density and elongation greatly decreased.

To better understand the effect of fucoidan on cell adhesion, the expression of the actin cytoskeleton, cell density and elongation were quantified by the analysis of the positively stained cells using ImageJ software as indicated in **Figures 1B–D**. For H226 cells, the expression of the actin cytoskeleton, cell density and elongation greatly decreased with an increased concentration of fucoidan, suggesting that fucoidan remarkably inhibited cancer cell adhesion. For 16HBE cells, the expression of the actin cytoskeleton, cell density and elongation in 1 mg/ml fucoidan had no significant difference with the blank control. However, with increasing the fucoidan concentration from 1 to 100 mg/ml, the cell parameters greatly reduced, which reveals that high fucoidan concentration suppressed 16HBE cells adhesion. This phenomenon may be due to the down-regulation of adhesion signal by 1 mg/ml fucoidan in cancer cells. These results are consistent with previous reports. Zhang reported that fucoidan inhibited osteosarcoma cell adhesion by suppression of the phosphorylation of FAK and paxillin (Zhang et al., 2020). In addition, fucoidan suppressed mouse hepatocarcinoma Hca-F cells adhesion *via* downregulating L-selectin and upregulating protein levels of tissue inhibitor of metalloproteinases (TIMPs) (Wang et al., 2014). Taken together, these results indicate that 1 mg/ml fucoidan could significantly suppress cancer cell adhesion but had no effect on normal cells.

Effect of Fucoidan on the Proliferation of H226 and 16HBE Cells

Unregulated proliferation is considered a key hallmark of cancer development and progression (Hanahan and Weinberg, 2011). Inhibiting cancer cell proliferation is fundamental to cancer therapy (Chen et al., 2021). To detect the effect of fucoidan on the proliferation of H226 and 16HBE cells, a CCK-8 viability assay was performed on 1, 3, and 5 days as shown in **Figure 2**. It was found that the viability of H226 greatly reduced with the increment of fucoidan concentration, indicating that fucoidan could significantly inhibit the proliferation of cancer cells (**Figure 2A**). Particularly, when the fucoidan concentration increased from 1 to 10 mg/ml, the viability of H226 decreased abruptly. However, there was no significant difference between 10 and 100 mg/ml.

Although inhibition of cancer cell proliferation is crucial, we expect it would not affect the proliferation and activity of normal cells. We tested the effect of the fucoidan on the proliferation of 16HBE. Interestingly, compared to the blank control, 1 mg/ml fucoidan had no effect on the viability of 16HBE. When the fucoidan concentration increased from 1 to 10 mg/ml, the viability of 16HBE reduced abruptly. However, there was no significant difference between 10 mg/ml and 100 mg/ml, which is a similar trend to the result of H226 (**Figure 2B**). These may be due to the effect of 10 mg/ml and 100 mg/ml fucoidan on cells is caused by its own toxicity. Taken together, 1 mg/ml fucoidan could be a suitable concentration that significantly inhibited the proliferation of H226, and had no effect on the proliferation of 16HBE. These results suggest that 1 mg/ml fucoidan may specifically interact with the proliferation-related genes in H226 cells, but not cytotoxicity.

Effects of Fucoidan on the Migration of H226 Cells

The invasion and metastasis of cancer cells is another major feature of cancer development and progression (Hanahan and Weinberg, 2011). Previous studies have reported that fucoidan could suppress the migration of cancer cells, such as gastric cancer (Xu et al., 2020), pancreatic cancer (Etman et al., 2021), and triple-negative breast cancer (Hsu et al., 2020). However, the effect of fucoidan in lung cancer is still unknown. A wound-healing assay was carried out to test the influence of 1 mg/ml fucoidan on the metastasis of lung cancer cells. It was found that the migration of H226 greatly reduced with the increment of the fucoidan concentration from 0 to 1 mg/ml (**Figure 3A**). Quantitative results showed 1 mg/ml fucoidan group significantly inhibited wound closure ratio compared with the blank control (**Figure 3B**). These results indicate that 1 mg/ml fucoidan could inhibit the migration of lung cancer cells.

Effect of Fucoidan on the Gene Expression of H226 Cells

To investigate the impact of fucoidan on genome-wide gene expression of lung cancer cells, RNA transcriptome sequencing was carried out on the H226 cells treated with 1 mg/ml fucoidan. To ensure the sequencing data reliable, we conducted quality control on the biological repetition of samples. The results show that there was no significant difference in the distribution of gene expression levels between the exposed 1 mg/ml fucoidan group and the blank control (**Figure 4A**). Moreover, analysis of inter-group sample difference and intra-group sample repetition showed that the correlation coefficient is close to 1

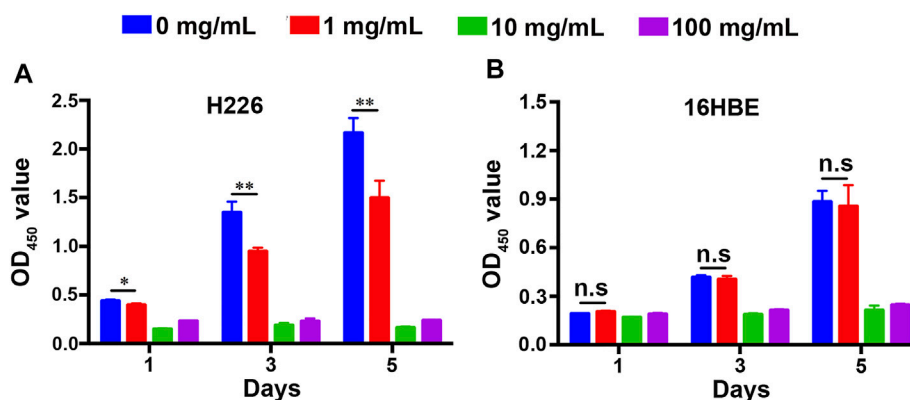


FIGURE 2 | Cell proliferation of (A) 16HBE and (B) H226 cells after being treated with different concentrations of fucoidan in 1, 3, and 5 days.

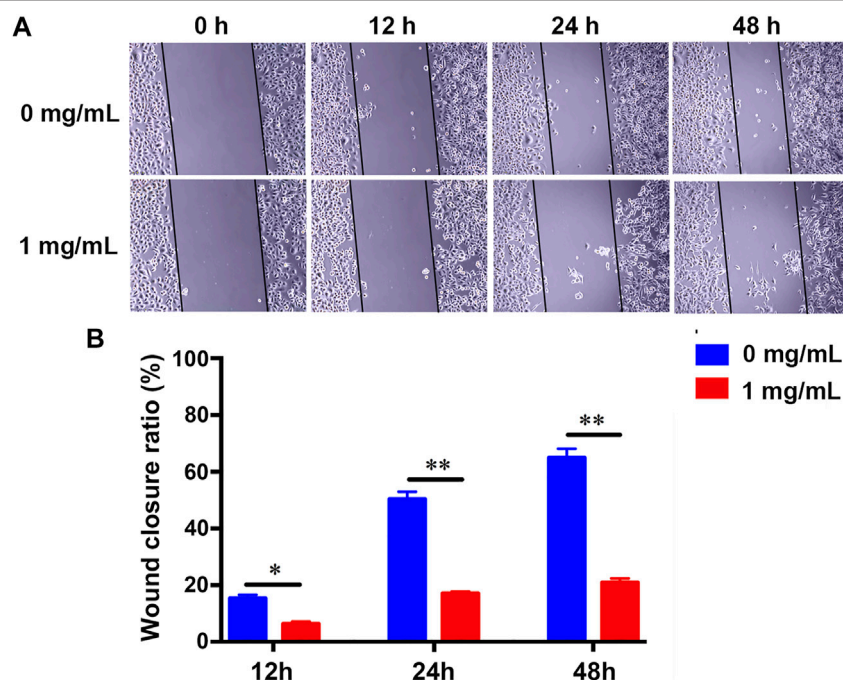


FIGURE 3 | (A) The migration changes of H226 with the treatment of 1 mg/ml fucoidan by wound-healing assay. (B) Wound closure ratio of H226 after treated with 1 mg/ml fucoidan in 12, 24, and 48 h.

(Figure 4B). This indicates that the repeatability of the sample is good and the sequencing data is reliable.

Furthermore, DEGs were analyzed using DESeq2 software. Compared to the blank control, the volcano plot showed that 6,930 DEGs (3,501 up-regulated and 3,429 down-regulated genes) were identified (Figure 4C). Among these DEGs, some genes which with cell cycle (PRKDC, CDC20, CCNB1), cell apoptosis (CTSB, CTSD) and focal adhesion (COL4A2, COL1A1, ACTN1) were identified. Moreover, the DEGs were combined and analyzed by clustering. The heat map demonstrated that the DEGs were mainly protein-coding

genes (Figure 4D). These results indicate that 1 mg/ml fucoidan may play anti-tumor roles by significantly modulating some protein-coding genes.

Pathway Analysis of Fucoidan-Induced DEGs

To better understand the function of those DEGs regulated by fucoidan, GO and KEGG analysis was performed *via* DAVID. GO analysis indicated these DEGs were significantly enriched in many biological processes (BP), cellular component (CC),

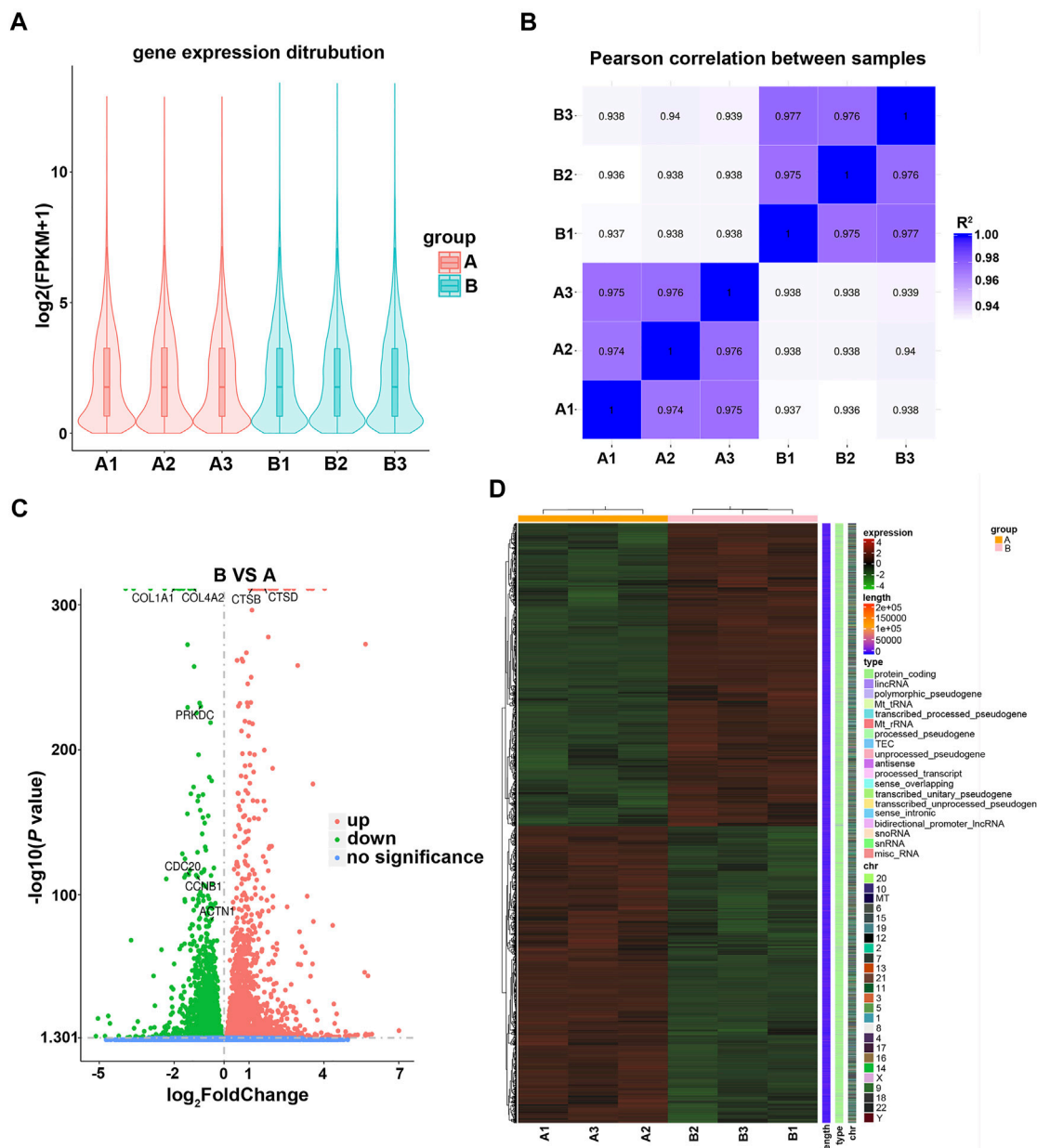
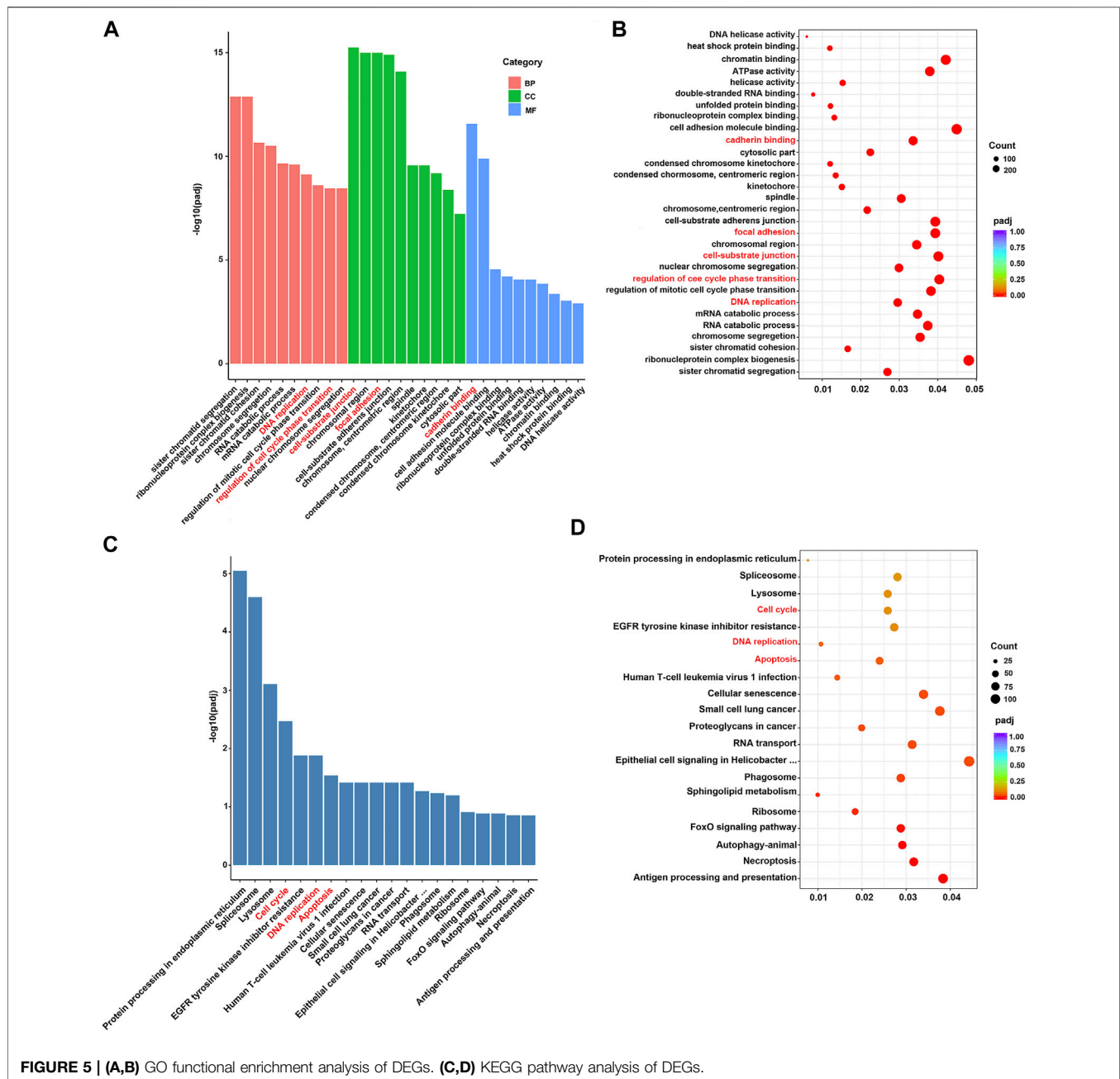


FIGURE 4 | (A) Violin plot of the gene expression distribution between control and 1 mg/ml fucoidan exposed group. A1, A2, A3 indicate 0 mg/ml fucoidan exposed group; B1, B2, B3 indicate 1 mg/ml fucoidan exposed group. **(B)** The heat map of Pearson correlation between samples. **(C)** The volcano plots of DEGs. The red dots indicate upregulated genes, green dots indicate downregulated genes, and blue dots indicate non-differentially expressed genes. **(D)** The heat map of DEGs between the 0 mg/ml fucoidan exposed group and 1 mg/ml fucoidan exposed group.

molecular function (MF), including DNA replication, cell-substrate junction, regulation of cell cycle phase transition, focal adhesion, cadherin binding, and cell adhesion molecule binding (Figures 5A,B). It has been well-demonstrated that DNA replication is one of the fundamental biological processes in which dysregulation can cause genome instability (Ubhi and Brown, 2019). DNA replication stress should drive cancer development and be considered a hallmark of cancer (Macheret and Halazonetis, 2015). Cell-substrate junction is

associated with the EMT process and then affects cancer cells migration (Baronsky et al., 2017); (Paddillaya et al., 2019). Cell cycle phase transition is very finely regulated. The abnormal cell cycle, especially uncontrolled G1/S phase transition, is a key step in carcinogenesis (Rubin et al., 2020). Focal adhesion is a protein complex containing integrins that are regulated by a network of interactions between hundreds of proteins (Zhu et al., 2021b). The focal adhesion signal hub is composed of a variety of pro-survival signal molecules, including integrins and growth factor



receptors, which strictly regulate cellular behavior, affect the survival of tumor cells (Eke and Cordes, 2015). Cadherin is a class of Ca^{2+} dependent transmembrane glycoproteins that mediate intercellular adhesion and play an important role in maintaining cellular polarity and maintaining the stability of intercellular adhesion (Nose and Takeichi, 1986). In tumor cells, the loss of this connective complex leads to the decrease of cell-cell adhesion, promotes the detachment of tumor cells from the primary lesion and the ability to cross the basal membrane, which is conducive to tumor metastasis (Kaszak et al., 2020). Adhesion-mediated cell adhesion is a key step in cancer invasion and metastasis, including integrins, selectin,

cadherin, immunoglobulin superfamily, and CD44 (Mousa, 2010). Moreover, KEGG analysis showed the top 20 pathways, including “cell cycle”, “DNA replication”, and “apoptosis” (Figures 5C, D). Apoptosis is an active programmed cell death, which ensures a homeostatic balance between the rate of cell formation and cell death (Obeng, 2021). Once this balance is broken, it will lead to cancer. Recent studies showed apoptosis is the main way of cell death induced by various anticancer drugs (Ball and Borthakur, 2020; Tanaka et al., 2021). All these suggest fucoidan may induce dysregulation of DNA replication and cell cycle, reduce cell adhesion, cause cell death in the form of apoptosis, to achieve the effect of anti-cancer (Figure 6).

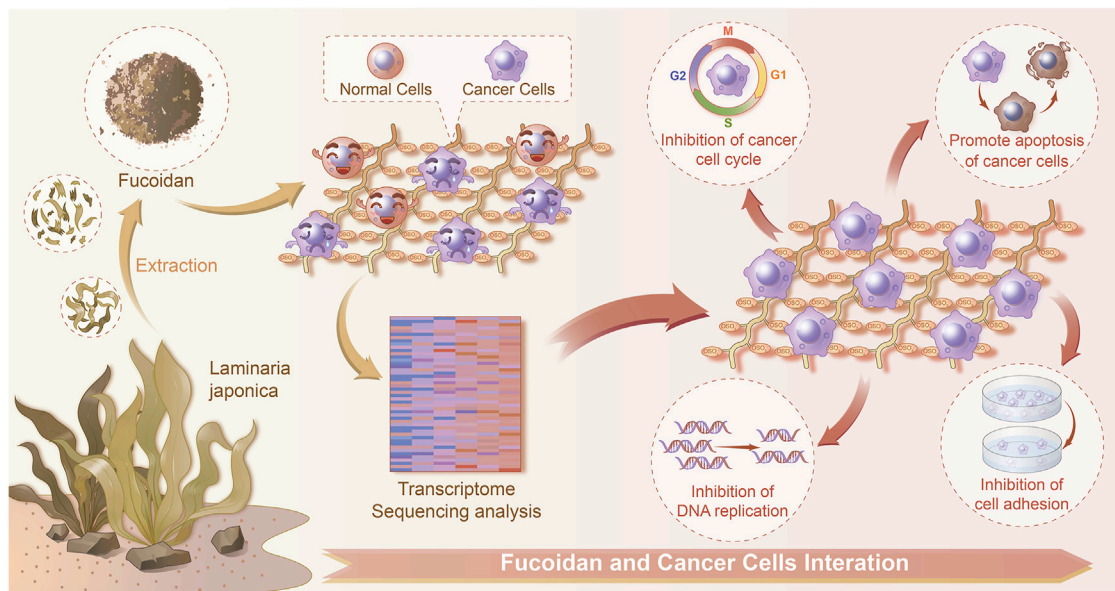


FIGURE 6 | Schematic diagram of the interactions between normal/cancer cell and fucoidan detected by a transcriptome sequencing study.

CONCLUSION

In summary, the adhesion, proliferation, and migration of H226 cells as well as their gene expression were greatly modulated by fucoidan. Moreover, the H226 cell responses were significantly dependent on the concentration of fucoidan. Importantly, 1 mg/ml fucoidan suppressed lung cancer cell adhesion and proliferation but had no effect on normal cells. A transcriptome sequencing study demonstrated that DEGs were reflected in DNA replication, cell-substrate junction, regulation of cell cycle phase transition, focal adhesion, cadherin binding, and cell adhesion molecule binding. It was found that apoptosis and cell cycle-related DEGs were up-regulated in 1 mg/ml fucoidan. Thus, our work demonstrated on the transcriptomic level that fucoidan modulates the phenotype and gene expression of LCCs, displaying great potential for the treatment of lung tumors.

DATA AVAILABILITY STATEMENT

The data presented in the study are deposited in the NCBI Sequence Read Archive (SRA) Database repository, accession number PRJNA801098.

AUTHOR CONTRIBUTIONS

Conceptualization, YZ and QZ; validation, XL, HZ, MY, and MJ; writing—original draft preparation, XL; writing—review

and editing, YZ, and QZ; project administration, QZ; All authors have read and agreed to the published version of the manuscript.

FUNDING

This research was funded by the National Natural Science Foundation of China (Grant No. 31900957), Shandong Provincial Natural Science Foundation (Grant No. ZR2019QC007), Innovation and technology program for the excellent youth scholars of higher education of Shandong province (Grant No. 2019KJE015), China Postdoctoral Science Foundation (Grant No. 2019M652326), and the National Natural Science Foundation of China (Grant No. 8217121619 to YZ).

ACKNOWLEDGMENTS

The authors sincerely thank all participants involved in this study.

SUPPLEMENTARY MATERIAL

The Supplementary Material for this article can be found online at: <https://www.frontiersin.org/articles/10.3389/fbioe.2022.844924/full#supplementary-material>

REFERENCES

- Apostolova, E., Lukova, P., Baldzhieva, A., Katsarov, P., Nikolova, M., Iliev, I., et al. (2020). Immunomodulatory and Anti-inflammatory Effects of Fucoidan: a Review. *Polymers* 12, 2338. doi:10.3390/polym12102338
- Ball, S., and Borthakur, G. (2020). Apoptosis Targeted Therapies in Acute Myeloid Leukemia: an Update. *Expert Rev. Hematol.* 13, 1373–1386. doi:10.1080/17474086.2020.1852923
- Baronsky, T., Ruhlandt, D., Brückner, B. R., Schäfer, J., Karedla, N., Isbaner, S., et al. (2017). Cell-Substrate Dynamics of the Epithelial-To-Mesenchymal Transition. *Nano Lett.* 17, 3320–3326. doi:10.1021/acs.nanolett.7b01558
- Bilal, M., and Iqbal, H. (2020). Marine Seaweed Polysaccharides-Based Engineered Cues for the Modern Biomedical Sector. *Mar. Drugs* 18, 7. doi:10.3390/md18010007
- Boo, H.-J., Hyun, J.-H., Kim, S.-C., Kang, J.-I., Kim, M.-K., Kim, S.-Y., et al. (2011). Fucoidan from Undaria Pinnatifida Induces Apoptosis in A549 Human Lung Carcinoma Cells. *Phytother. Res.* 25, 1082–1086. doi:10.1002/ptr.3489
- Chen, X., Zeh, H. J., Kang, R., Kroemer, G., and Tang, D. (2021). Cell Death in Pancreatic Cancer: from Pathogenesis to Therapy. *Nat. Rev. Gastroenterol. Hepatol.* 18, 804–823. doi:10.1038/s41575-021-00486-6
- Chen, Y.-M., Shih, J.-F., Perng, R.-P., Tsai, C.-M., and Whang-Peng, J. (2006). A Randomized Trial of Different Docetaxel Schedules in Non-small Cell Lung Cancer Patients Who Failed Previous Platinum-Based Chemotherapy. *Chest* 129, 1031–1038. doi:10.1378/chest.129.4.1031
- Chung, C.-H., Lu, K.-Y., Lee, W.-C., Hsu, W.-J., Lee, W.-F., Dai, J.-Z., et al. (2020). Fucoidan-based, Tumor-Activated Nanoplatform for Overcoming Hypoxia and Enhancing Photodynamic Therapy and Antitumor Immunity. *Biomaterials* 257, 120227. doi:10.1016/j.biomaterials.2020.120227
- Eke, I., and Cordes, N. (2015). Focal Adhesion Signaling and Therapy Resistance in Cancer. *Semin. Cancer Biol.* 31, 65–75. doi:10.1016/j.semcancer.2014.07.009
- Etmann, S. M., Elnaggar, Y. S. R., and Abdallah, O. Y. (2020). "Fucoidan, a Natural Biopolymer in Cancer Combating: From Edible Algae to Nanocarrier Tailoring". *Int. J. Biol. Macromolecules* 147, 799–808. doi:10.1016/j.ijbiomac.2019.11.191
- Etmann, S. M., Mehanna, R. A., Bary, A. A., Elnaggar, Y. S. R., and Abdallah, O. Y. (2021). Undaria Pinnatifida Fucoidan Nanoparticles Loaded with Quinacrine Attenuate Growth and Metastasis of Pancreatic Cancer. *Int. J. Biol. Macromolecules* 170, 284–297. doi:10.1016/j.ijbiomac.2020.12.109
- Hanahan, D., and Weinberg, R. A. (2011). Hallmarks of Cancer: The Next Generation. *Cell* 144, 646–674. doi:10.1016/j.cell.2011.02.013
- Hao, Y., Zhao, W., Zhang, L., Zeng, X., Sun, Z., Zhang, D., et al. (2020). Bio-multifunctional Alginate/chitosan/fucoidan Sponges with Enhanced Angiogenesis and Hair Follicle Regeneration for Promoting Full-Thickness Wound Healing. *Mater. Des.* 193, 108863–108875. doi:10.1016/j.matdes.2020.108863
- Hao, Y., Zheng, W., Sun, Z., Zhang, D., Sui, K., Shen, P., et al. (2021). Marine Polysaccharide-Based Composite Hydrogels Containing Fucoidan: Preparation, Physicochemical Characterization, and Biocompatible Evaluation. *Int. J. Biol. Macromolecules* 183, 1978–1986. doi:10.1016/j.ijbiomac.2021.05.190
- He, Y., Zhao, W., Dong, Z., Ji, Y., Li, M., Hao, Y., et al. (2021). A Biodegradable Antibacterial Alginate/carboxymethyl chitosan/Kangfuxin Sponges for Promoting Blood Coagulation and Full-Thickness Wound Healing. *Int. J. Biol. Macromolecules* 167, 182–192. doi:10.1016/j.ijbiomac.2020.11.168
- Herbst, R. S., Morgensztern, D., and Boshoff, C. (2018). The Biology and Management of Non-small Cell Lung Cancer. *Nature* 553, 446–454. doi:10.1038/nature25183
- Howlader, N., Forjaz, G., Mooradian, M. J., Meza, R., Kong, C. Y., Cronin, K. A., et al. (2020). The Effect of Advances in Lung-Cancer Treatment on Population Mortality. *N. Engl. J. Med.* 383, 640–649. doi:10.1056/nejmoa1916623
- Hsu, W.-J., Lin, M.-H., Kuo, T.-C., Chou, C.-M., Mi, F.-L., Cheng, C.-H., et al. (2020). Fucoidan from Laminaria Japonica Exerts Antitumor Effects on Angiogenesis and Micrometastasis in Triple-Negative Breast Cancer Cells. *Int. J. Biol. Macromolecules* 149, 600–608. doi:10.1016/j.ijbiomac.2020.01.256
- Jing, X., Sun, Y., Ma, X., and Hu, H. (2021). Marine Polysaccharides: Green and Recyclable Resources as Wound Dressings. *Mater. Chem. Front* 5, 5595–5616. doi:10.1039/d1qm00561h
- Ju, Q., Zhao, Y. J., Dong, Y., Cheng, C., Zhang, S., Yang, Y., et al. (2019). Identification of a miRNA-mRNA Network Associated with Lymph Node Metastasis in Colorectal Cancer. *Oncol. Lett.* 18, 1179–1188. doi:10.3892/ol.2019.10460
- Kaszak, I., Witkowska-Piłaszewicz, O., Niewiadomska, Z., Dworecka-Kaszak, B., Ngosa Toka, F., and Jurka, P. (2020). Role of Cadherins in Cancer-A Review. *Ijms* 21, 7624. doi:10.3390/ijms21207624
- Lee, H., Kim, J.-S., and Kim, E. (2012). Fucoidan from Seaweed Fucus Vesiculosus Inhibits Migration and Invasion of Human Lung Cancer Cell via PI3K-Akt-mTOR Pathways. *PLoS One* 7, e50624. doi:10.1371/journal.pone.0050624
- Lee, J.-K., Hahn, S., Kim, D.-W., Suh, K. J., Keam, B., Kim, T. M., et al. (2014). Epidermal Growth Factor Receptor Tyrosine Kinase Inhibitors vs Conventional Chemotherapy in Non-small Cell Lung Cancer Harboring Wild-type Epidermal Growth Factor Receptor. *Jama* 311, 1430–1437. doi:10.1001/jama.2014.3314
- Li, W., Mao, S., Khan, M., Zhang, Q., Huang, Q., Feng, S., et al. (2019). Responses of Cellular Adhesion Strength and Stiffness to Fluid Shear Stress during Tumor Cell Rolling Motion. *ACS Sens.* 4, 1710–1715. doi:10.1021/acssensors.9b00678
- Lin, Y., Qi, X., Liu, H., Xue, K., Xu, S., and Tian, Z. (2020). The Anti-cancer Effects of Fucoidan: A Review of Both *In Vivo* and *In Vitro* Investigations. *Cancer Cell Int* 20, 154–214. doi:10.1186/s12935-020-01233-8
- Lin, Z., Tan, X., Zhang, Y., Li, F., Luo, P., and Liu, H. (2020). Molecular Targets and Related Biologic Activities of Fucoidan: A Review. *Mar. Drugs* 18, 376. doi:10.3390/md18080376
- Macheret, M., and Halazonetis, T. D. (2015). DNA Replication Stress as a Hallmark of Cancer. *Annu. Rev. Pathol. Mech. Dis.* 10, 425–448. doi:10.1146/annurev-pathol-012414-040424
- Mierke, C. T. (2020). Editorial: Biomechanical Properties of Cells and Tissues and Their Impact on Cellular Adhesion and Motility. *Front. Cell Dev. Biol.* 8, 1–2. doi:10.3389/fcell.2020.00475
- Minna, J. D., Roth, J. A., and Gazdar, A. F. (2002). Focus on Lung Cancer. *Cancer Cell* 1, 49–52. doi:10.1016/s1535-6108(02)00027-2
- Mousa, S. A. (2010). Adhesion Molecules: Potential Therapeutic and Diagnostic Implications. *Methods Mol. Biol. (Clifton, N.J.)* 663, 261–276. doi:10.1007/978-1-60761-803-4_11
- Nose, A., and Takeichi, M. (1986). A Novel Cadherin Cell Adhesion Molecule: its Expression Patterns Associated with Implantation and Organogenesis of Mouse Embryos. *J. Cell Biol.* 103, 2649–2658. doi:10.1083/jcb.103.6.2649
- Obeng, E. (2021). Apoptosis (Programmed Cell Death) and its Signals - A Review. *Braz. J. Biol.* 81, 1133–1143. doi:10.1590/1519-6984.228437
- Oliveira, C., Neves, N. M., Reis, R. L., Martins, A., and Silva, T. H. (2020). A Review on Fucoidan Antitumor Strategies: From a Biological Active Agent to a Structural Component of Fucoidan-Based Systems. *Carbohydr. Polym.* 239, 116131. doi:10.1016/j.carbpol.2020.116131
- Paddillaya, N., Mishra, A., Kondaiah, P., Pullarkat, P., Menon, G. I., and Gundiah, N. (2019). Biophysics of Cell-Substrate Interactions under Shear. *Front. Cell Dev. Biol.* 7, 1–16. doi:10.3389/fcell.2019.00251
- Qiu, W.-L., Tseng, A.-J., Hsu, H.-Y., Hsu, W.-H., Lin, Z.-H., Hua, W.-J., et al. (2020). Fucoidan Increased the Sensitivity to Gefitinib in Lung Cancer Cells Correlates with Reduction of TGFβ-Mediated Slug Expression. *Int. J. Biol. Macromolecules* 153, 796–805. doi:10.1016/j.ijbiomac.2020.03.066
- Rubin, S. M., Sage, J., and Skotheim, J. M. (2020). Integrating Old and New Paradigms of G1/S Control. *Mol. Cell* 80, 183–192. doi:10.1016/j.molcel.2020.08.020
- Tanaka, K., Yu, H. A., Yang, S., Han, S., Selcuklu, S. D., Kim, K., et al. (2021). Targeting Aurora B Kinase Prevents and Overcomes Resistance to EGFR Inhibitors in Lung Cancer by Enhancing BIM- and PUMA-Mediated Apoptosis. *Cancer Cell* 39, 1245–1261. doi:10.1016/j.ccell.2021.07.006
- Ubhi, T., and Brown, G. W. (2019). Exploiting DNA Replication Stress for Cancer Treatment. *Cancer Res.* 79, 1730–1739. doi:10.1158/0008-5472.CAN-18-3631
- Wang, P., Liu, Z., Liu, X., Teng, H., Zhang, C., Hou, L., et al. (2014). Anti-metastasis Effect of Fucoidan from Undaria Pinnatifida Sporophylls in Mouse Hepatocarcinoma Hca-F Cells. *PLoS One* 9, e106071. doi:10.1371/journal.pone.0106071
- Xu, L., Liu, F., Li, C., Li, S., Wu, H., Guo, B., et al. (2020). Fucoidan Suppresses the Gastric Cancer Cell Malignant Phenotype and Production of TGF-β1 via CLEC-2. *Glycobiology* 30, 301–311. doi:10.1093/glycob/cwz097

- Yang, L., Pijuan-Galito, S., Rho, H. S., Vasilevich, A. S., Eren, A. D., Ge, L., et al. (2021). High-Throughput Methods in the Discovery and Study of Biomaterials and Materiobiology. *Chem. Rev.* 121, 4561–4677. doi:10.1021/acs.chemrev.0c00752
- Zhang, M., Chen, L., Liu, Y., Chen, M., Zhang, S., and Kong, D. (2020). Sea Cucumber *Cucumaria Frondosa* Fucoidan Inhibits Osteosarcoma Adhesion and Migration by Regulating Cytoskeleton Remodeling. *Oncol. Rep.* 44, 469–476. doi:10.3892/or.2020.7614
- Zheng, L.-X., Chen, X.-Q., and Cheong, K.-L. (2020). Current Trends in marine Algae Polysaccharides: The Digestive Tract, Microbial Catabolism, and Prebiotic Potential. *Int. J. Biol. Macromolecules* 151, 344–354. doi:10.1016/j.ijbiomac.2020.02.168
- Zheng, W., Hao, Y., Wang, D., Huang, H., Guo, F., Sun, Z., et al. (2021). Preparation of Triamcinolone Acetonide-Loaded Chitosan/fucoidan Hydrogel and its Potential Application as an Oral Mucosa Patch. *Carbohydr. Polym.* 272, 118493. doi:10.1016/j.carbpol.2021.118493
- Zhou, Q., Chen, J., Luan, Y., Vainikka, P. A., Thallmair, S., Marrink, S. J., et al. (2020). Unidirectional Rotating Molecular Motors Dynamically Interact with Adsorbed Proteins to Direct the Fate of Mesenchymal Stem Cells. *Sci. Adv.* 6, 1–14. doi:10.1126/sciadv.aay2756
- Zhou, Q., Zhao, Z., Zhou, Z., Zhang, G., Chiechi, R. C., and van Rijn, P. (2018). Directing Mesenchymal Stem Cells with Gold Nanowire Arrays. *Adv. Mater. Inter.* 5, 1800334–1800338. doi:10.1002/admi.201800334
- Zhu, L., Plow, E. F., and Qin, J. (2021). Initiation of Focal Adhesion Assembly by Talin and Kindlin: A Dynamic View. *Protein Sci.* 30, 531–542. doi:10.1002/pro.4014
- Zhu, Y., Liu, L., Sun, Z., Ji, Y., Wang, D., Mei, L., et al. (2021). Fucoidan as a marine-origin Prebiotic Modulates the Growth and Antibacterial Ability of *Lactobacillus Rhamnosus*. *Int. J. Biol. Macromolecules* 180, 599–607. doi:10.1016/j.ijbiomac.2021.03.065

Conflict of Interest: The authors declare that the research was conducted in the absence of any commercial or financial relationships that could be construed as a potential conflict of interest.

Publisher's Note: All claims expressed in this article are solely those of the authors and do not necessarily represent those of their affiliated organizations, or those of the publisher, the editors and the reviewers. Any product that may be evaluated in this article, or claim that may be made by its manufacturer, is not guaranteed or endorsed by the publisher.

Copyright © 2022 Zhao, Li, Zhang, Yan, Jia and Zhou. This is an open-access article distributed under the terms of the Creative Commons Attribution License (CC BY). The use, distribution or reproduction in other forums is permitted, provided the original author(s) and the copyright owner(s) are credited and that the original publication in this journal is cited, in accordance with accepted academic practice. No use, distribution or reproduction is permitted which does not comply with these terms.



Comparative Study of Traditional Single-Needle Electrospinning and Novel Spiral-Vane Electrospinning: Influence on the Properties of Poly(caprolactone)/Gelatin Nanofiber Membranes

OPEN ACCESS

Edited by:

Yong Liu,
Wenzhou Institute (CAS), China

Reviewed by:

Afeesh Rajan Unnithan,
University of Birmingham,
United Kingdom
Farnaz Ghorbani,
University of Erlangen Nuremberg,
Germany

*Correspondence:

Bingcheng Yi
bingchengyi@163.com
Wei Liu
liuwei_2000@yahoo.com

Specialty section:

This article was submitted to
Biomaterials,
a section of the journal
Frontiers in Bioengineering and
Biotechnology

Received: 03 January 2022

Accepted: 18 February 2022

Published: 18 March 2022

Citation:

Xu Q, Liu W and Yi B (2022)
Comparative Study of Traditional
Single-Needle Electrospinning and
Novel Spiral-Vane Electrospinning:
Influence on the Properties of
Poly(caprolactone)/Gelatin
Nanofiber Membranes.
Front. Bioeng. Biotechnol. 10:847800.
doi: 10.3389/fbioe.2022.847800

Qi Xu¹, Wei Liu^{1,2*} and Bingcheng Yi^{1,2*}

¹Plastic Surgery Research Institute, Weifang Medical University, Weifang, China, ²Department of Plastic and Reconstructive Surgery, Shanghai Key Laboratory of Tissue Engineering, Shanghai Ninth People's Hospital, Shanghai Jiao Tong University School of Medicine, Shanghai, China

Spiral-vane electrospinning (SVE), a novel needleless electrospinning, was proven effective in obtaining high-throughput production of nanofibers. However, the properties of the electrospun nanofibers produced by SVE remain relatively underexplored, especially in comparison with those made by traditional single-needle electrospinning (SNE). Hence, for the comparative study of SNE and SVE in this study, the difference in the preparation mechanism was first analyzed using numerical simulation, followed by the experimental analysis of the effects of spinneret types on the quality and biocompatibility of electrospun poly(caprolactone)/gelatin (PCL/Gel) nanofibers. The values predicted by the electric field results were consistent with the experimental data, showing that the PCL/Gel nanofibers prepared by SVE have higher yields than SNE. Although the different spinnerets (i.e., needle and spiral vane) had little effect on the surface chemistry, thermal stability, and composition of the PCL/Gel nanofibers, they had great effects on the fiber diameter distribution and mechanical properties in which SVE-electrospun nanofibers have the wider diameter distribution and higher softness. Furthermore, the SVE-electrospun nanofibers were also proven to exhibit good biocompatibility for cell growth of human adipose-derived stem cells (hADSCs) and cell-fiber interactions. Summarily, compared to the traditional SNE, SVE-electrospun nanofibers exhibited many merits including high-throughput yield, good air permeability, and compliance, which provide a facile and effective platform for the improvement of nanofiber applications in biomedical fields (e.g., tissue engineering, cosmetic, and medical textiles).

Keywords: single-needle electrospinning, spiral-vane electrospinning, poly(caprolactone), gelatin, high-throughput production

INTRODUCTION

Owing to the characteristics of high specific surface area for biomolecule binding and biomimetic extracellular matrix (ECM)-like fibrous structure for cell growth, nanofibers are developed and widely used in the various biomedical fields, such as skin-beauty, wound dressings, and tissue engineering (Xue et al., 2019; Xie et al., 2020; Yi et al., 2021a; Wang et al., 2021). Among the current developed technologies for preparing nanofibers (e.g., phase separation (Kang et al., 2020), self-assembly (Wu et al., 2020), and electrospinning (Xue et al., 2019)), electrospinning is regarded as a viable and highly versatile method to massively prepare continuous ultrafine fibers from various polymers and composites. However, traditional electrospinning using a single needle to supply spinning solution lacks efficiency, resulting in the low productivity of the electrospun nanofibers for commercial application (Zhang et al., 2020). To meet the increased demand for nanofibers, remarkable progress has been made concerning the increase of the jet number for high-throughput production of nanofibers. For example, multi-needle electrospinning is developed as a straightforward and effective way to increase the electrospinning throughput (Zhu et al., 2021). Nevertheless, it has exhibited obvious shortcomings including complicated design and potential clogging of the spinneret that may lead to reduced fiber production rate and poor fiber quality (Liu and Guo, 2013), which seriously limits the wide application of this technique in the industry.

In this context, needleless electrospinning that initiates the charged jets from the open free-liquid surface is exploited and demonstrated to present some unique advantages compared to multi-needle electrospinning, especially in the achievement of nanofibers with high throughput (Yin et al., 2021). It has been confirmed that the free surface of the spinning solution is subjected to unsteadiness and begins to produce tiny fluctuations under the action of a high enough electric field during the needleless electrospinning process. Once the surface tension of each peak position of the tiny fluctuations is overcome, numerous jets are formed and stretched into nanofibers (Jiang et al., 2019). Thus, the jet initiation and resulting fiber morphology rely heavily on the electric field intensity profile around the spinneret and in the electrospinning zone that is governed by the applied voltage and the shape of the needleless spinneret (Niu et al., 2009). Recently, needleless electrospinning setups have been developed, in which spinnerets with various geometries, such as cylinder, disk, ball, and coil, were used to produce nanofibers (Jirsak and Petrik, 2012; Wang et al., 2012; Yu et al., 2017; Ranjbari et al., 2020). Under the same applied voltage, these spinnerets present fairly different electric field profiles. To reveal the influence of spinneret shape on the electric field, efforts have been made and demonstrated that spiral vane would be the most prominent spinneret of needleless electrospinning that concentrates the strongest electric field in the largest areas of itself (Wang et al., 2012).

Hence, as a newly exploited strategy of needleless electrospinning, spiral-vane electrospinning (SVE) was regarded as a very efficient device for preparing nanofibers with high quality and yield (Gao et al., 2016; Liu and Zuo,

2018; Liu and Zuo, 2020), and the yield of nanofibers is usually positively correlated with the size of the spiral vane. As reported by Gao et al. (2016), SVE was performed to fabricate nanomembranes with a certain thickness, aiming to improve their sound absorption properties. Later, Liu and Zuo (2018) and Liu and Zuo (2020) used SVE to attain nanofiber membranes with better sound absorption property by modifying polyvinyl alcohol nanofiber membranes. These findings establish significant supremacy for the aggressive promotion of nanofibers to be applied in the market. Nevertheless, in addition to the yield of nanofibers, little has been reported in the literature on how the nozzle structure influences the needleless electrospinning process and resulting fiber morphology in comparison to traditional single-needle electrospinning, which serves as an important indicator for the reference of SVE performances. Therefore, to benefit the development and application of needleless electrospinning in the industry, it is worthwhile to perform a comparative study of the novel spiral-vane electrospinning and the traditional single-needle electrospinning.

In tissue engineering, polymer blending for electrospinning is one of the most effective methods to provide desirable biocomposite nanofibers for the guidance of tissue remodeling (Ghasemi-Mobarakeh et al., 2008). For example, a synthetic polymer can be blended with a natural polymer to obtain a fibrous scaffold with good biocompatibility and improved mechanical or other physical/chemical properties. A typical example is the blending of poly(3-caprolactone) (PCL) lacking surface cell-recognition sites and gelatin (Gel) suffering from poor mechanical properties. Such composite fibers can overcome their shortcomings and produce a new biomaterial with desired cell adhesion and degradation rate (Zhang et al., 2005; Ghasemi-Mobarakeh et al., 2008). Thus, PCL/Gel nanofibrous scaffolds were used in this study for the comparative study of SNE and SVE. In brief, the electrospinning processes and mechanisms were first observed and analyzed between SNE and SVE. Then, the material properties of SVE-generated PCL/Gel nanofibers were compared to those of SNE-generated PCL/Gel nanofibers. Furthermore, the cellular responses of human adipose-derived stem cells (hADSCs) to two PCL/Gel nanofibers were studied to understand the difference in their biofunctions between SNE and SVE.

MATERIALS AND METHODS

Fabrication of PCL/Gel Nanofibers

Using 1,1,1,3,3,3-hexafluoro-2-propanol (HFIP) as the dissolving solvent, the mixed polymer solution of PCL (M_w 550,000, Jinan Daigang Biomaterials) and Gel (type A, Shanghai Yeasen Biotechnology) with the weight ratio of 70:30 was prepared at the total concentration of 10% w/v and stirred for 12 h at room temperature. After the dissolved solution was transferred into a syringe with a 19 G blunt-tip needle, SNE was performed to generate PCL/Gel nanofibers using the following parameters: applied voltage 13 kV, flow rate 1 ml/h, needle tip to collector gap distance 15 cm, and ambient conditions (20–25°C, 25–30%

humidity). According to the resulting fiber morphology relying heavily on the applied voltage and the shape of the needleless spinneret in needleless electrospinning (Jirsak and Petrik, 2012; Yu et al., 2017), the applied voltage was mainly regulated during the SVE process to form the nanofibrous scaffolds with a similar diameter to those formed by SNE. Thus, SVE was performed as follows: applied voltage 60 kV, spiral vane to collector gap distance 15 cm, and spiral vane speed (6 cm in diameter, 10 cm in length) 5 rpm. During SNE and SVE, the emitted jets were monitored by using a digital camera. After manufacturing, all the electrospun nanofibrous membranes were dried for a week under vacuum to remove residual solvent.

Simulation of Electric Field Distribution

The two-dimensional (2D) electric fields of the single-needle system (i.e., SNE) and spiral-vane system (i.e., SVE) were simulated by the COMSOL Multiphysics software (COMSOL Inc., Sweden). The physical geometries of these electrospinning setups (e.g., electrode, collector) were established according to their practical dimensions and locations. Then, all the electric field strengths and distributions were visualized using the software.

Characterization of PCL/Gel Nanofibrous Membranes

Fiber morphology: surface morphologies of electrospun PCL/Gel nanofibers were observed by using a scanning electron microscope (SEM, ZEISS Gemini 300, Germany) at an acceleration voltage of 0.02–30 kV. Before SEM imaging, all the fibrous mats were sputter-coated for 30 s with gold to increase conductivity. The distribution of fiber diameter ($n > 100$) was further analyzed directly from the obtained SEM images using the ImageJ software (NIH, Bethesda, Maryland, United States).

Surface chemistry and crystallinity structure: Fourier transform infrared (FTIR) spectroscopy of the electrospun PCL/Gel nanofibers was qualitatively analyzed by using an FTIR spectrometer (Thermo Fisher IN10, United States) over the wavenumber range of 4,000–600 cm^{-1} at a scanning resolution of 2 cm^{-1} . The crystalline structure of the PCL/Gel nanofibers was determined by using an X-ray diffractometer (XRD, Rigaku, Japan) at the operating voltage of 40 kV and current of 200 mA, respectively. After background subtraction, the crystallinity was calculated from the fractional area of the crystalline peaks to the total area.

Thermal stability: thermogravimetric analysis (TG) of the electrospun PCL/Gel nanofibers was carried out using thermal analyzer apparatus (NETZSCH STA 449F5, Germany). The 3–7 mg samples were heated in a nitrogen atmosphere in the temperature range from 30 to 800°C at the heating rate of 20°C min^{-1} . Derivative thermogravimetry (DTG) was calculated from the derivative of the TG curve, which represents the difference in the thermogravimetry ratio of weight loss measurement at heating.

Tensile properties: tensile properties of the electrospun PCL/Gel nanofibers were determined using a tabletop tensile tester

(5542-C8609, INSTRON Instrument, United States) equipped with a 50 N load cell at ambient conditions. All samples were cut into a rectangle with 3 cm length and 1 cm width and fixed on the fixture of the biomechanics analyzer. Then, the stress–strain curves of the samples ($n > 8$) were recorded under stretching at a cross-head speed of 10 mm/min until fracture. The fibers' mechanical parameters such as Young's modulus, tensile strength, strain at break, and maximum load were further obtained from the stress–strain curve.

Cellular Responses of hADSCs to the PCL/Gel Nanofibers

Isolation of the primary hADSCs and cell culture: human adipose-derived stem cells (hADSCs) were extracted from adipose tissue according to the Animal Care and Experiment Committee of Shanghai Ninth People's Hospital, Shanghai Jiao Tong University School of Medicine. In brief, adipose tissue was immersed in 0.25% chloramphenicol solution for 15 min; after thoroughly rinsing in PBS solution three times, the tissue was cut into pieces and then shaken for digestion in type IV collagenase at 37°C for 1 h. The obtained cell suspension was finally centrifuged at 1,500 rpm for 5 min and then resuspended and cultured with mesenchymal stem cell medium (Shanghai Zhongqiao Xinzhou Biotechnology Co., Ltd, ScienCell, United States) containing 5% fetal calf serum, 1% growth supplement, and 1% penicillin/streptomycin solution.

Cell morphology: hADSCs were seeded onto the fibrous membranes in 24-well plates at a density of 5×10^4 cells/well. After 3 days of culture, the cell morphology was stained with TRITC-labeled phalloidin (1:200 dilution in PBS, Yeasen Biotech Co., Ltd., Shanghai), and the cell nuclei were stained with 0.8 mg/ml 4',6-diamidino-2-phenylindole (DAPI, SouthernBiotech, United States) for 10 min at room temperature in the dark. Morphology of the hADSCs was observed using a laser confocal scanning microscope (Carl Zeiss, Germany). ImageJ further analyzed cell numbers based on the obtained microscope images.

Cell proliferation: hADSCs were seeded onto the PCL/Gel nanofibers at a density of 1×10^4 cells/well in 24-well plates. According to the manufacturer's instruction, after 1, 3, 5, and 7 days of culture after seeding, cell proliferation was monitored by using the Cell Counting Kit-8 (CCK-8, Dojindo, Japan). In brief, the cellularized fibrous mats were incubated with a 300 μL culture medium containing 15 μL of CCK-8 at 37°C for 3.5 h. Then, 100 μL of the solution was transferred to a 96-well plate for absorbance measurements at 450 nm using a microplate reader (ARIOSKAN, Thermo Scientific, Germany) to analyze cell numbers.

Cell spreading: cells were seeded onto the PCL/Gel nanofibers at a density of 5×10^4 cells/well in 24-well plates. After culturing the cell–fiber constructs for 2 days, cell spreading was observed by scanning electron microscopy (SEM, ZEISS Gemini 300, Germany). In brief, the samples were washed with PBS three times and fixed overnight at 4°C in 2.5% glutaraldehyde and then dehydrated through a graded series of ethanol (30–100%, v/v) at 4°C for 15 min at each step. Once

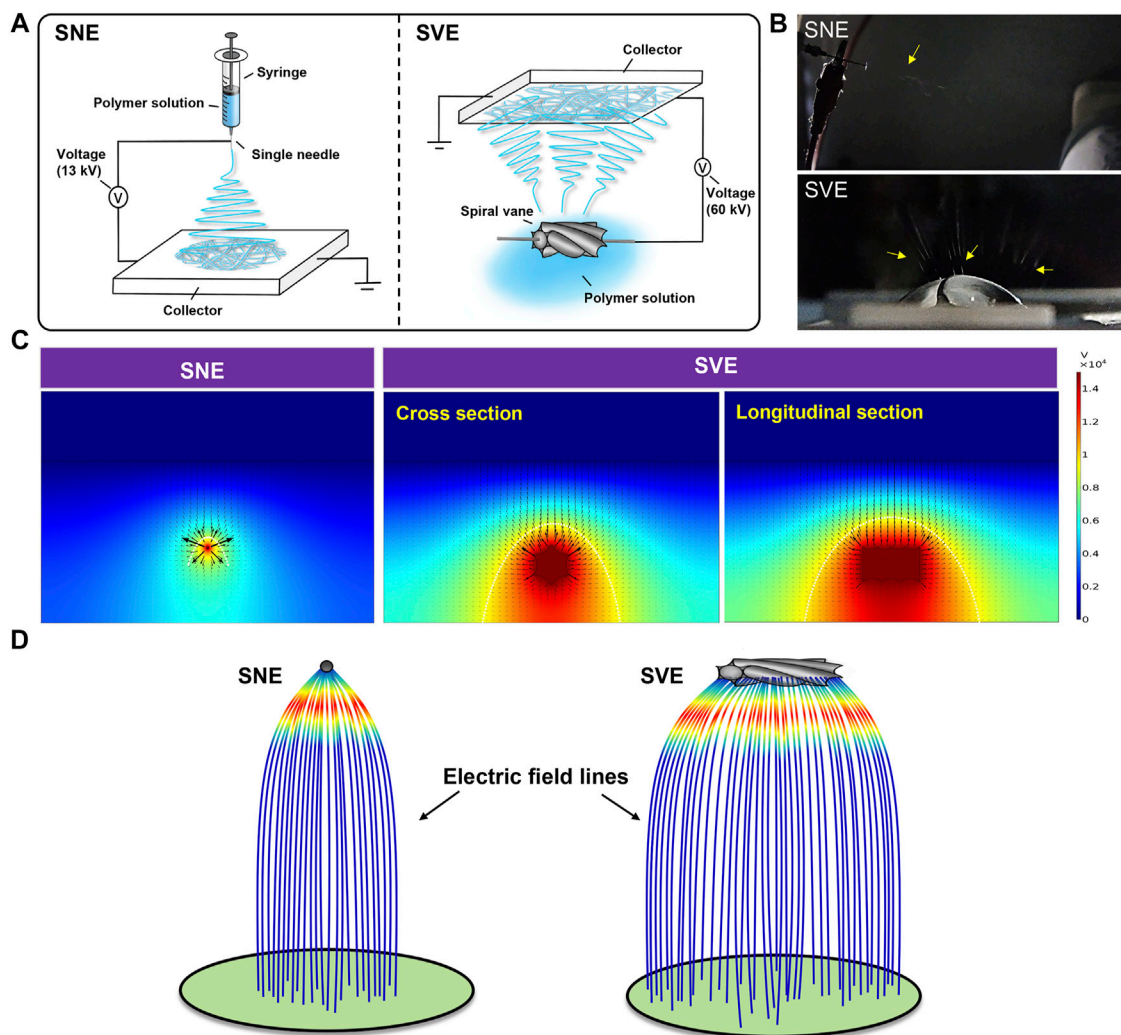


FIGURE 1 | Mechanism analysis of SNE and SVE processes: **(A)** schematic diagrams; **(B)** pictures of electrospinning processes. The yellow arrows represent the generated jets. **(C)** Electric field distributions of single-needle and spiral-vane systems; **(D)** simulative electric field lines produced by the single-needle and spiral-vane spinnerets.

dried, the samples were examined by SEM at an acceleration voltage of 0.02–30 kV.

Live/dead staining: cells were seeded onto the PCL/Gel nanofibers at a density of 5×10^4 cells/well in 24-well plates. After culturing the cell–fiber constructs for 3 days, live/dead assays (Dojindo, Shanghai) were used to evaluate the viability of hADSCs. In brief, 0.2% (v/v) calcein-AM and 0.3% (v/v) propidium iodide were mixed into PBS to make a working solution. After 30 min of incubation with the working solution at 37°C, cell viability was observed under a fluorescence microscope (Axiocam 503 color, Carl Zeiss, Germany).

Cell–fiber interaction: hADSCs were seeded onto the PCL/Gel nanofibers in 24-well plates at a density of 5×10^4 cells/well. After 3 days of culture, immunofluorescence staining was performed to examine the expression of integrin in cells to analyze the cell–fiber interaction. In brief, the cellularized fibrous mats were fixed using 4% paraformaldehyde for

30 min, permeabilized using 0.2% Triton X-100 for 5 min, and blocked using 10% goat serum for 30 min. After that, the rabbit anti-human integrin- $\beta 1$ antibody (1:200 dilution, Proteintech, United States) was incubated overnight at 4°C, followed by the incubation of goat anti-rabbit IgG (H + L) secondary antibody (1:100 dilution, Proteintech, United States) for 90 min in the dark at room temperature. The cell nuclei were counter-stained with DAPI for 10 min at room temperature. Finally, the samples were observed using a laser confocal scanning microscope.

Statistical Analysis

Data are presented as means \pm standard deviation. Statistical analysis was carried out using the Origin 8.0 software, and Tukey's HSD post hoc tests were used to make pair-wise comparisons between groups. The obtained p values ($p < 0.05$, $**p < 0.01$, and $***p < 0.001$) were considered statistically

significant. All of the experiments were repeated at least three times.

RESULTS AND DISCUSSION

Wide Distribution of Electric Field in the SVE Process Brings in Nanofibers' High-Throughput Production

Spiral-vane electrostatic machine, using spiral vane as a free surface spinneret, is a current exploited strategy to achieve the high-throughput production of nanofibers among needleless electrospinning. Similar to the traditional SNE, SVE involves an electrohydrodynamic process. Each peak position of the tiny fluctuations was electrified to generate a jet under the action of a high enough electric field, followed by stretching and elongation into nanofibers (**Figure 1A**) (Xue et al., 2017). However, the charged precursor liquid was extruded from the needle spinneret to produce only one jet during traditional electrospinning resulting in the low yield of nanofibers (**Figure 1B**) (Yin et al., 2021). Moreover, to break the steady state of the solution surface for fluctuations and overcome the surface tension of the charged precursor solution for jet formation, higher voltage is usually required to be applied between the spiral vane spinneret end and the collector in SVE, whereas in the needle spinneret-based electrospinning, the applied electric voltage just needs to overcome the solution surface tension. For example, if the spiral vane spinneret was performed at a low applied voltage, the jets were only generated from two end areas, without any jets/filaments produced from the middle spiral vane surface. Further increasing the applied voltage can generate a high-intensity electric field and then lead to the generation of jets from the entire spiral vane surface, which is consistent with a previous study (Niu et al., 2009). Thus, to fabricate the PCL/Gel nanofibers with similar diameter in this study, the applied electric voltage of SVE was set as 60 kV, while that of SNE was 13 kV (**Figure 1A**).

Considering the critical role of the electric field in the electrospinning process, numerical simulation was further performed to visualize the electric field intensity and distribution. As illustrated in **Figure 1C**, the direction of arrows indicates the direction of the electric field, and the length of the arrows is proportional to the strength of the electric field at the corresponding position. The maximum E_z (z-directional electric field strength) at the needle spinneret and the spiral vane spinneret is different, in which the weak electric field is formed at the central position, while the strong electric field is at the outside position. Under this circumstance, the central jets suffer from a lower electrostatic force than the jets formed on the sides (Xie and Zeng, 2012). Furthermore, the bigger size of the spiral vane expands the electric field distribution in the region near the spinneret than that near the needle, creating more electrospinning area. As shown in **Figure 1D**, the electric field lines generated in the spiral vane spinneret are more likely scattered outward at the edge of the spinneret leading to scattered fiber mats, while those in the needle spinneret concentrated and intensified at the central position.

SVE-Electrospun Nanofibers Exhibit Lower Crystallinity and Higher Compliance Than SNE-Electrospun Nanofibers

Based on the PCL/Gel 70:30 formulation, the physical properties of electrospun nanofibers including fiber morphology, surface chemistry, thermostability, and mechanical properties were analyzed to perform the comparative study of SNE and SVE. SEM examination revealed the nonsignificant difference of average fiber diameter between SNE- and SVE-electrospun nanofibers (**Figure 2A, left**). However, the fiber diameter of SVE-electrospun nanofibers was observed to be distributed more widely than that of SNE-electrospun ones (0.69 ± 0.70 vs. 0.72 ± 0.15 μm , **Figure 2A, right**), which was also observed in other needleless electrospinnings (Yu et al., 2017). This mainly attributes to the larger and more nonuniform electric field generated near the spiral vane than near the needle, resulting in the significant difference of drawing force that existed in the jets for the production of nanofibers. Interestingly, the wide fiber diameter distribution in nanofibrous membranes is always accompanied by high porosity for excellent air permeability (Wanasekara et al., 2015).

FTIR analysis was carried out for the surface chemistry characterization of PCL/Gel nanofibers produced by SNE and SVE (**Figure 2B**). It can be seen that the FTIR spectra of SVE-electrospun nanofibers were nearly the same as those of SNE-electrospun nanofibers, in which infrared spectra for PCL-related stretching modes were observed at $2,941\text{ cm}^{-1}$ (asymmetric CH_2 stretching) and $2,863\text{ cm}^{-1}$ (symmetric CH_2 stretching) and those for Gel-related stretching modes appeared at approximately $1,535\text{ cm}^{-1}$ (a coupling of bending of the N-H bond and stretching of C-N bonds in amide II) (Ghasemi-Mobarakeh et al., 2008). **Figures 2C,D** show the thermal stability of SVE- and SNE-electrospun nanofibers. The obtained nearly similar TG and DTG curves further indicated that there was a nonsignificant difference in the thermal stability and composition of these electrospun PCL/Gel nanofibers. However, the crystallinity of SVE-electrospun PCL/Gel nanofibers was lower compared to that of SNE-electrospun nanofibers (**Figure 2E**, 74.09 vs. 84.24%). As the mechanical performance of nanofibers is well known to be closely connected with the molecular crystallinity, the mechanical properties of the electrospun PCL/Gel nanofibers were further examined. The stress-strain curve is shown in **Figure 2F**. It was found that the nanofibers from traditional SNE had Young's modulus of 38.75 MPa, close to that reported by Zhang et al. (2005). In contrast, the mechanical properties of the SVE-electrospun nanofibers were significantly decreased with Young's modulus of 25.86 MPa. The tendency is quite similar to that of molecular crystallinity. Nevertheless, the type of spinneret appeared to not significantly affect the ultimate tensile strength, the strain at break, and the maximum load of the PCL/Gel nanofibers (**Figure 2F**).

For the underlying mechanisms, it is well known that there are several forces (i.e., electrical forces, surface tension, inner viscoelastic force, and gravity force) exerting an influence on the fluid jets (Yu et al., 2011). Usually, surface tension and inner viscoelastic force are the inherent performances of the spinning

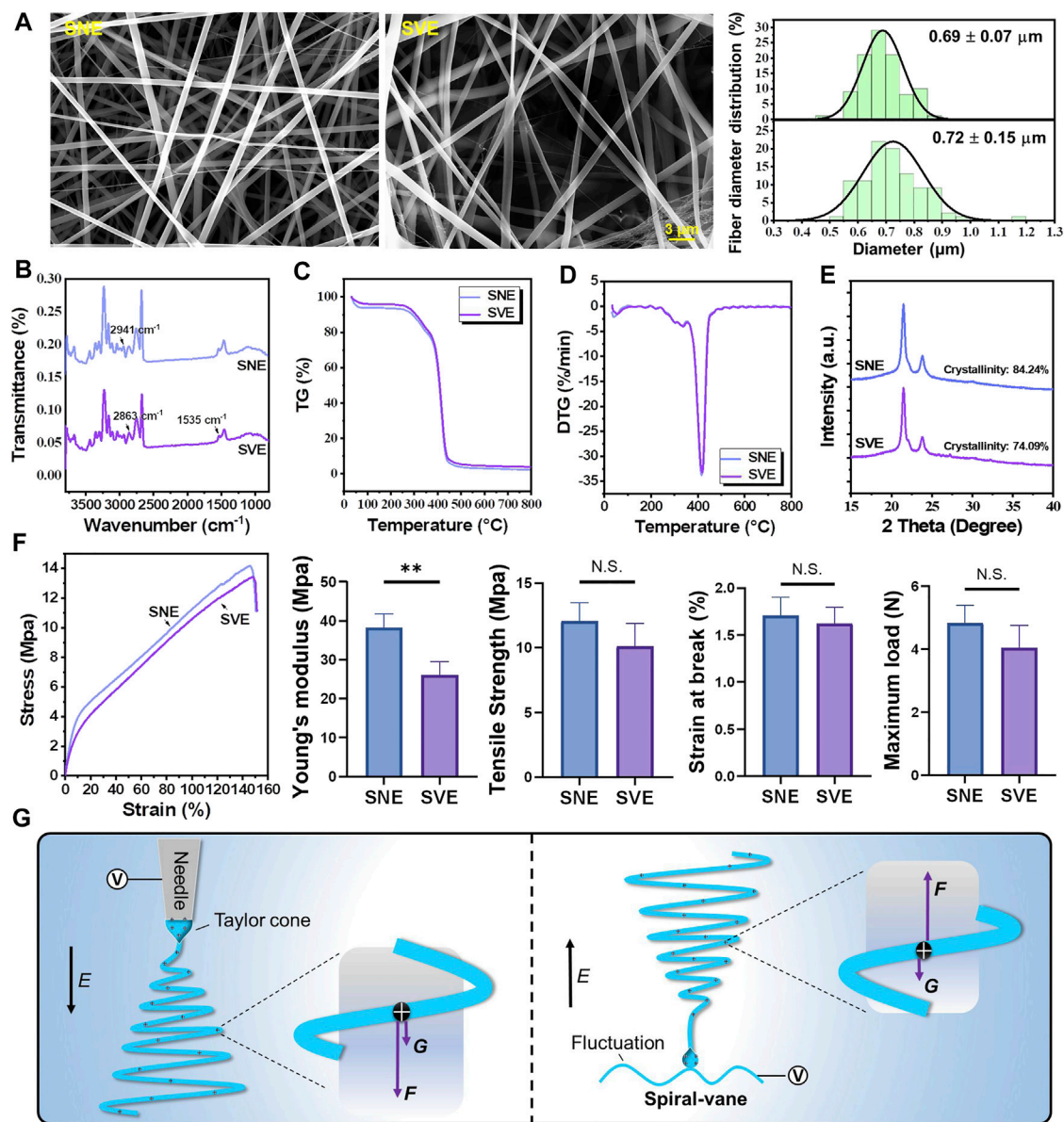


FIGURE 2 | Characterization of the PCL/Gel nanofibers produced by SNE and SVE: **(A)** SEM and the distribution of fiber diameter; **(B)** FTIR; **(C,D)** thermogravimetry and derivative thermogravimetry; **(E)** XRD and crystallinity; **(F)** stress-strain curves, Young's modulus, tensile strength, strain at break, and maximum load; and **(G)** the proposed mechanisms for molecule elongation and crystallinity. *E* indicates the direction of the electric field. *F* and *G* represent the electric force and gravity force actioned on jets, respectively.

solution which are not affected by the type of spinneret. This implies that the electrical and gravitational forces are mainly responsible for drawing and downsizing the fluid jets. As illustrated in **Figure 2G**, the action of the gravity force can be deduced to enhance the influence of electrical force on the stretching and elongation of polymer molecules during SNE, while that in the SVE process, in contrast, can weaken the stretched effect of the electrical force on the jets. The higher extensional forces stretching the polymer chains may consequently increase the molecular chain orientation by preventing the occurrence of molecule relaxation, in favor of

enhancing crystallization in SNE-electrospun nanofibers (Yi et al., 2018).

SVE-Electrospun PCL/Gel Nanofibers Exhibit Good Biocompatibility for Cell-Fiber Interaction

hADSCs were demonstrated to possess many of the same regenerative properties as mesenchymal stem cells (MSCs): the potential of multidirectional differentiation and the excellent ability to proliferate *in vitro* (Miana and Prieto González,

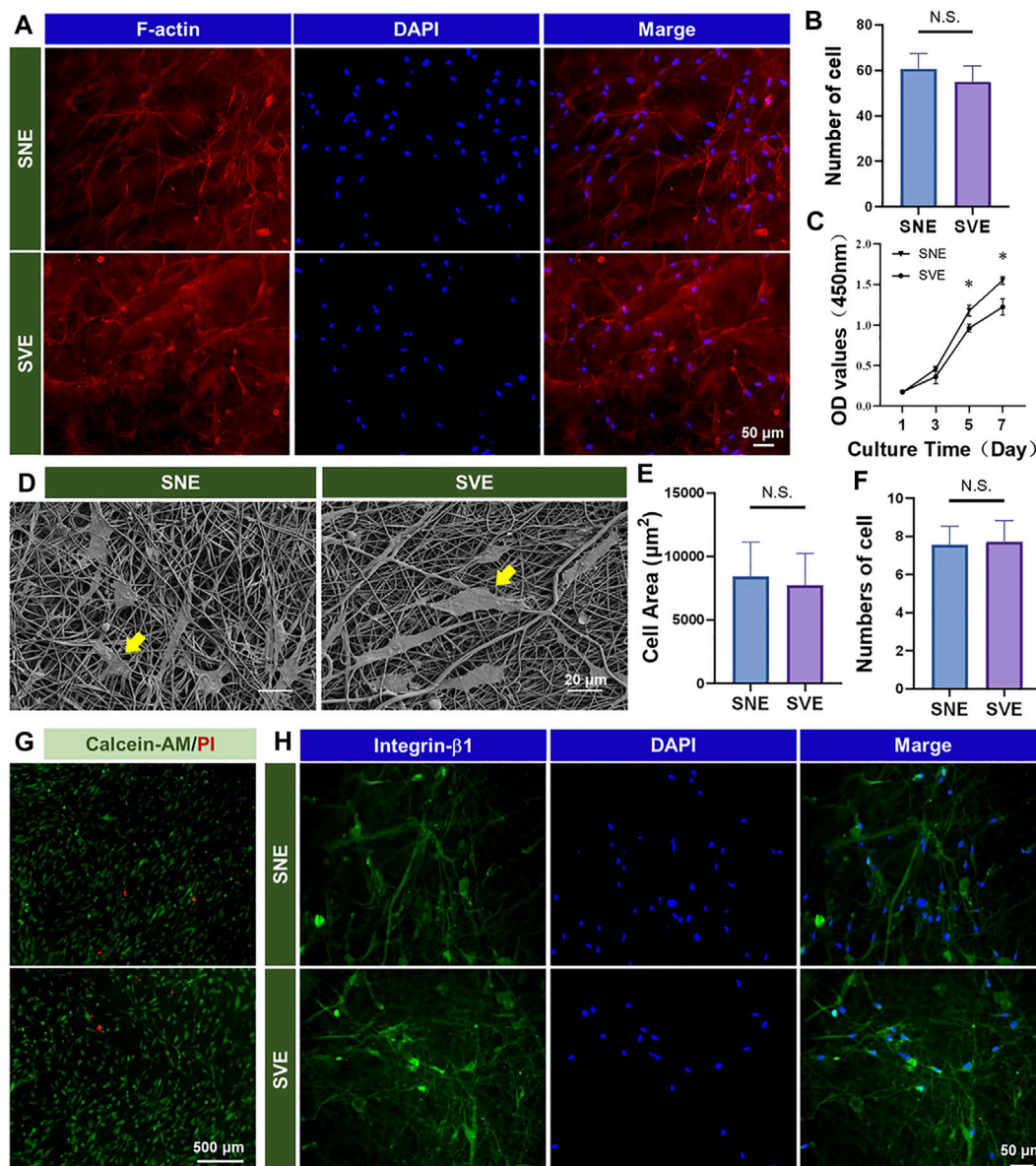


FIGURE 3 | Biocompatibility of the PCL/Gel nanofibers produced by SNE and SVE: **(A,B)** morphology and quantified cell number of hADSCs on different samples; **(C)** cell proliferation; **(D–F)** cell spreading and quantified spreading area and adhered cell number on different samples; **(G)** cell viability; and **(H)** expression of integrin- β 1 for cell-fiber interactions.

2018; Si et al., 2019). Hence, hADSCs were selected and chosen as the model cells to analyze the difference in the biocompatibility of the different PCL/Gel nanofibers. Cell morphology was first analyzed using a fluorescence microscope after 3 days of culture (Figure 3A). The results showed that both nanofibers appeared to support good cell growth and elongation. The quantified results on cell number indicated the subtle higher cell growth on SNE-electrospun nanofibers than SVE-electrospun nanofibers (Figure 3B). It is well known that when placed into scaffolds, cells can sense the physicochemical and biochemical properties (e.g., fiber stiffness, surface pattern, and surface chemistry) of the underlying substrates through cell

membrane-bound receptors and then initiate the intracellular signaling cascades for the cellular responses including migration, proliferation, and differentiation (Fernandez-Yague et al., 2015). Due to no significant difference in the fiber diameter and surface chemistry of SNE- and SVE-electrospun PCL/Gel nanofibers, the increased modulus of nanofibers was deduced to play a key role in promoting cell growth (Yi et al., 2019). Likewise, a softer surface enhances cell secretory activity, while a stiffer substrate increases cell proliferation (Yi et al., 2019; Yi et al., 2021b). Therefore, cell proliferation was quantified at 1, 3, 5, and 7 days. As proven by the previous studies, the enhanced cell proliferation of hADSCs was observed for the cells cultured on stiff nanofibers (SNE) after

5 days of culture (**Figure 3C**). Nevertheless, the cell spreading observed by SEM at 2 days exhibited no significant difference concerning the cell spreading area and adhered cell number (**Figure 3D–F**). This indicates that a short culture time was not sufficient to allow the different nanofibers to cause the obvious variation of cell behaviors. Moreover, live/dead assay was carried out to evaluate the cell viability of hADSCs on these PCL/Gel nanofibers. As shown in **Figure 3G**, a lot of live cells and a few dead cells were observed on both PCL/Gel nanofibers, revealing the good biocompatibility of the SVE-electrospun nanofibers.

The results, as mentioned above, revealed that the PCL/Gel nanofibers electrospun by SVE had weaker mechanical properties than those electrospun by SNE (**Figure 2F**). Usually, when cells contact the fiber surface, large protein complexes called focal adhesions (FAs) are formed to tether the cell cytoskeleton (e.g., integrins) to nanofibers. Then, the formed FAs repetitively tug onto the nanofibers to gauge their stiffness and remodel their structure by matrix assembling and matrix metalloproteinase secretion (Kennedy et al., 2017). Thus, a sufficient softness of scaffolds benefits cells to interact with the underlying matrix for remodeling (Meshel et al., 2005; Yi et al., 2019; Tang et al., 2021). To verify this, the expression of integrin- $\beta 1$ in hADSCs was detected to observe the cell–fiber interactions after 3 days of cell culture. As shown in **Figure 3H**, both the PCL/Gel nanofibers were found to support cell growth and spreading along the direction of fiber orientation after the period of incubation. These observations indicate a good integration of hADSCs with PCL/Gel nanofibers.

CONCLUSION

In this study, biocomposite PCL/Gel nanofibers were used for the comparative study of SNE and SVE. The numerical simulation revealed the expanded electric field distribution for high-throughput production of nanofibers in SVE. The results reported in physical properties demonstrated that although the type of spinneret (i.e., needle and spiral vane) has no significant impact on the surface chemistry, thermal stability, and composition of the obtained electrospun nanofibers, the PCL/Gel nanofibrous membranes produced by SVE exhibited higher air permeability (more wide distribution of fiber diameter) and better compliance (lower mechanical properties). Furthermore, the SVE-electrospun PCL/Gel nanofibers exhibited good biocompatibility for cell growth and cell–fiber interactions. This study provides a better understanding of the comparative study of SNE and SVE, offering essential knowledge in assisting the applications of SVE devices for the production of nanofibers to gain a larger market share, including tissue engineering,

cosmetic product, and textile. In addition, although the results presented in this article were focused on PCL/Gel nanofibers, the observed performance variations of nanofibers can be speculated on other SVE-electrospun fibers, and the performed experimental scheme can also be a reference to the further comparative studies of other electrospinning setups.

DATA AVAILABILITY STATEMENT

The original contributions presented in this study are included in the article/Supplementary Material, further inquiries can be directed to the corresponding authors.

ETHICS STATEMENT

The studies involving human participants were reviewed and approved by the Scientific Research Projects Approval Determination of the Independent Ethics Committee of Shanghai Ninth People's Hospital Affiliated to Shanghai Jiao Tong University School of Medicine. The patients/participants provided their written informed consent to participate in this study.

AUTHOR CONTRIBUTIONS

QX: experiment, data collection and analysis, and writing—original draft; WL: funding acquisition, project administration, and writing—review and editing; BY: experimental design, data analysis, supervision, funding acquisition, and writing—review and editing.

FUNDING

This work was supported by the Fundamental Research Funds for China Postdoctoral Science Foundation (2020M681322), National Key Research and Development Program of China (2018YFC1105800), and National Natural Science Foundation of China (31870967 and 81671921).

ACKNOWLEDGMENTS

The authors are grateful to Shiyanjia Lab (www.shiyanjia.com) for the kind help in the numerical simulation of electric field distribution.

REFERENCES

- Fernandez-Yague, M. A., Abbah, S. A., McNamara, L., Zeugolis, D. I., Pandit, A., and Biggs, M. J. (2015). Biomimetic Approaches in Bone Tissue Engineering: Integrating Biological and Physicomechanical Strategies. *Adv. Drug Deliv. Rev.* 84, 1–29. doi:10.1016/j.addr.2014.09.005
- Gao, B., Zuo, L., and Zuo, B. (2016). Sound Absorption Properties of Spiral Vane Electrospun PVA/nano Particle Nanofiber Membrane and Non-woven Composite Material. *Fibers Polym.* 17, 1090–1096. doi:10.1007/s12221-016-6324-z
- Ghasemi-Mobarakeh, L., Prabhakaran, M. P., Morshed, M., Nasr-Esfahani, M.-H., and Ramakrishna, S. (2008). Electrospun Poly(ϵ -Caprolactone)/gelatin Nanofibrous Scaffolds for Nerve Tissue Engineering. *Biomaterials* 29, 4532–4539. doi:10.1016/j.biomaterials.2008.08.007

- Jiang, G., Johnson, L., and Xie, S. (2019). Investigations into the Mechanisms of Electrohydrodynamic Instability in Free Surface Electrospinning. *Open Phys.* 17, 313–319. doi:10.1515/phys-2019-0033
- Jirsak, O., and Petrik, S. (2012). Recent Advances in Nanofibre Technology: Needleless Electrospinning. *Ijnt* 9, 836–845. doi:10.1504/ijnt.2012.046756
- Kang, J., Hwang, J.-Y., Huh, M., and Yun, S. I. (2020). Porous Poly(3-Hydroxybutyrate) Scaffolds Prepared by Non-solvent-induced Phase Separation for Tissue Engineering. *Macromol. Res.* 28, 835–843. doi:10.1007/s13233-020-8109-x
- Kennedy, K. M., Bhaw-Luximon, A., and Jhurry, D. (2017). Cell-matrix Mechanical Interaction in Electrospun Polymeric Scaffolds for Tissue Engineering: Implications for Scaffold Design and Performance. *Acta Biomater.* 50, 41–55. doi:10.1016/j.actbio.2016.12.034
- Liu, H., and Zuo, B. (2018). Structure and Sound Absorption Properties of Spiral Vane Electrospun PVA/PEO Nanofiber Membranes. *Appl. Sciences-Basel* 8, 296. doi:10.3390/app8020296
- Liu, H., and Zuo, B. (2020). Sound Absorption Property of PVA/PEO/GO Nanofiber Membrane and Non-woven Composite Material. *J. Ind. Textiles* 50, 512–525. doi:10.1177/1528083719832857
- Liu, Y., and Guo, L. (2013). Homogeneous Field Intensity Control during Multi-Needle Electrospinning via Finite Element Analysis and Simulation. *J. Nanosci. Nanotech.* 13, 843–847. doi:10.1166/jnn.2013.6017
- Meshel, A. S., Wei, Q., Adelstein, R. S., and Sheetz, M. P. (2005). Basic Mechanism of Three-Dimensional Collagen Fibre Transport by Fibroblasts. *Nat. Cell Biol* 7, 157–164. doi:10.1038/ncb1216
- Miana, V. V., and Prieto González, E. A. (2018). Adipose Tissue Stem Cells in Regenerative Medicine. *ecancer* 12, 822. doi:10.3332/ecancer.2018.822
- Niu, H., Lin, T., and Wang, X. (2009). Needleless Electrospinning. I. A Comparison of Cylinder and Disk Nozzles. *J. Appl. Polym. Sci.* 114, 3524–3530. doi:10.1002/app.30891
- Ranjbari, E., Bazgir, S., and Shirazi, M. M. A. (2020). Needleless Electrospinning of Poly(acrylic Acid) Superabsorbent: Fabrication, Characterization and Swelling Behavior. *Polym. Test.* 84, 106403. doi:10.1016/j.polymertesting.2020.106403
- Si, Z., Wang, X., Sun, C., Kang, Y., Xu, J., Wang, X., et al. (2019). Adipose-derived Stem Cells: Sources, Potency, and Implications for Regenerative Therapies. *Biomed. Pharmacother.* 114, 108765. doi:10.1016/j.biopha.2019.108765
- Tang, H., Yi, B., Wang, X., Shen, Y., and Zhang, Y. (2021). Understanding the Cellular Responses Based on Low-Density Electrospun Fiber Networks. *Mater. Sci. Eng. C* 119, 111470. doi:10.1016/j.msec.2020.111470
- Wanasekara, N. D., Ghosh, S., Chen, M., Chalivendra, V. B., and Bhowmick, S. (2015). Effect of Stiffness of Micron/sub-Micron Electrospun Fibers in Cell Seeding. *J. Biomed. Mater. Res.* 103, 2289–2299. doi:10.1002/jbm.a.35362
- Wang, X.-X., Yu, G.-F., Zhang, J., Yu, M., Ramakrishna, S., and Long, Y.-Z. (2021). Conductive Polymer Ultrafine Fibers via Electrospinning: Preparation, Physical Properties and Applications. *Prog. Mater. Sci.* 115, 100704. doi:10.1016/j.pmatsci.2020.100704
- Wang, X., Wang, X., and Lin, T. (2012). Electric Field Analysis of Spinneret Design for Needleless Electrospinning of Nanofibers. *J. Mater. Res.* 27, 3013–3019. doi:10.1557/jmr.2012.346
- Wu, Y., Kelly, S. H., Sanchez-Perez, L., Sampson, J. H., and Collier, J. H. (2020). Comparative Study of α -helical and β -sheet Self-Assembled Peptide Nanofiber Vaccine Platforms: Influence of Integrated T-Cell Epitopes. *Biomater. Sci.* 8, 3522–3535. doi:10.1039/d0bm00521e
- Xie, S., and Zeng, Y. (2012). Effects of Electric Field on Multineedle Electrospinning: Experiment and Simulation Study. *Ind. Eng. Chem. Res.* 51, 5336–5345. doi:10.1021/ie2020763
- Xie, X., Chen, Y., Wang, X., Xu, X., Shen, Y., Khan, A. u. R., et al. (2020). Electrospinning Nanofiber Scaffolds for Soft and Hard Tissue Regeneration. *J. Mater. Sci. Tech.* 59, 243–261. doi:10.1016/j.jmst.2020.04.037
- Xue, J., Wu, T., Dai, Y., and Xia, Y. (2019). Electrospinning and Electrospun Nanofibers: Methods, Materials, and Applications. *Chem. Rev.* 119, 5298–5415. doi:10.1021/acs.chemrev.8b00593
- Xue, J., Xie, J., Liu, W., and Xia, Y. (2017). Electrospun Nanofibers: New Concepts, Materials, and Applications. *Acc. Chem. Res.* 50, 1976–1987. doi:10.1021/acs.accounts.7b00218
- Yi, B., Xu, Q., and Liu, W. (2021). An Overview of Substrate Stiffness Guided Cellular Response and its Applications in Tissue Regeneration. *Bioactive Mater.* doi:10.1016/j.bioactmat.2021.12.005
- Yi, B., Shen, Y., Tang, H., Wang, X., Li, B., and Zhang, Y. (2019). Stiffness of Aligned Fibers Regulates the Phenotypic Expression of Vascular Smooth Muscle Cells. *ACS Appl. Mater. Inter.* 11, 6867–6880. doi:10.1021/acsami.9b00293
- Yi, B., Yu, L., Tang, H., Wang, W., Liu, W., and Zhang, Y. (2021). Lysine-doped Polydopamine Coating Enhances Antithrombogenicity and Endothelialization of an Electrospun Aligned Fibrous Vascular Graft. *Appl. Mater. Today* 25, 101198. doi:10.1016/j.apmt.2021.101198
- Yi, B., Zhang, H., Yu, Z., Yuan, H., Wang, X., and Zhang, Y. (2018). Fabrication of High Performance Silk Fibroin Fibers via Stable Jet Electrospinning for Potential Use in Anisotropic Tissue Regeneration. *J. Mater. Chem. B* 6, 3934–3945. doi:10.1039/c8tb00535d
- Yin, J., Ahmed, A., and Xu, L. (2021). High-Throughput Free Surface Electrospinning Using Solution Reservoirs with Different Depths and its Preparation Mechanism Study. *Adv. Fiber Mater.* 3, 251–264. doi:10.1007/s42765-021-00078-8
- Yu, D. G., Lu, P., Branford-White, C., Yang, J. H., and Wang, X. (2011). Polyacrylonitrile Nanofibers Prepared Using Coaxial Electrospinning with LiCl Solution as Sheath Fluid. *Nanotechnology* 22, 435301. doi:10.1088/0957-4484/22/43/435301
- Yu, M., Dong, R.-H., Yan, X., Yu, G.-F., You, M.-H., Ning, X., et al. (2017). Recent Advances in Needleless Electrospinning of Ultrathin Fibers: From Academia to Industrial Production. *Macromolecular Mater. Eng.* 302, 1700002. doi:10.1002/mame.201700002
- Zhang, C., Li, Y., Wang, P., and Zhang, H. (2020). Electrospinning of Nanofibers: Potentials and Perspectives for Active Food Packaging. *Compr. Rev. Food Sci. Food Saf.* 19, 479–502. doi:10.1111/1541-4337.12536
- Zhang, Y., Ouyang, H., Lim, C. T., Ramakrishna, S., and Huang, Z.-M. (2005). Electrospinning of Gelatin Fibers and Gelatin/PCL Composite Fibrous Scaffolds. *J. Biomed. Mater. Res.* 72B, 156–165. doi:10.1002/jbm.b.30128
- Zhu, Z., Zheng, G., Zhang, R., Xu, G., Zeng, J., Guo, R., et al. (2021). Nanofibrous Membrane through Multi-Needle Electrospinning with Multi-Physical Field Coupling. *Mater. Res. Express* 8, 075012. doi:10.1088/2053-1591/ac1510

Conflict of Interest: The authors declare that the research was conducted in the absence of any commercial or financial relationships that could be construed as a potential conflict of interest.

Publisher's Note: All claims expressed in this article are solely those of the authors and do not necessarily represent those of their affiliated organizations, or those of the publisher, the editors, and the reviewers. Any product that may be evaluated in this article, or claim that may be made by its manufacturer, is not guaranteed or endorsed by the publisher.

Copyright © 2022 Xu, Liu and Yi. This is an open-access article distributed under the terms of the Creative Commons Attribution License (CC BY). The use, distribution or reproduction in other forums is permitted, provided the original author(s) and the copyright owner(s) are credited and that the original publication in this journal is cited, in accordance with accepted academic practice. No use, distribution or reproduction is permitted which does not comply with these terms.



Preparation of Novel ICT-CMC-CD59sp Drug-Loaded Microspheres and Targeting Anti-Tumor Effect on Oral Squamous Cell Carcinoma

Xiang Gao¹, Wanchun Wang^{2*} and Meihua Gao²

¹Department of Stomatology, School of Stomatology of Weifang Medical University, Weifang, China, ²Qingdao Stomatological Hospital, Qingdao, China

OPEN ACCESS

Edited by:

Yong Liu,
Wenzhou Institute (CAS), China

Reviewed by:

Xixi Zhu,
Shandong University of Science and
Technology, China
Xuemei Hu,
Binzhou Medical University, China

*Correspondence:

Wanchun Wang
kqwwch@126.com

Specialty section:

This article was submitted to
Biomaterials,
a section of the journal
Frontiers in Bioengineering and
Biotechnology

Received: 18 February 2022

Accepted: 28 February 2022

Published: 21 March 2022

Citation:

Gao X, Wang W and Gao M (2022)
Preparation of Novel ICT-CMC-
CD59sp Drug-Loaded Microspheres
and Targeting Anti-Tumor Effect on
Oral Squamous Cell Carcinoma.
Front. Bioeng. Biotechnol. 10:878456.
doi: 10.3389/fbioe.2022.878456

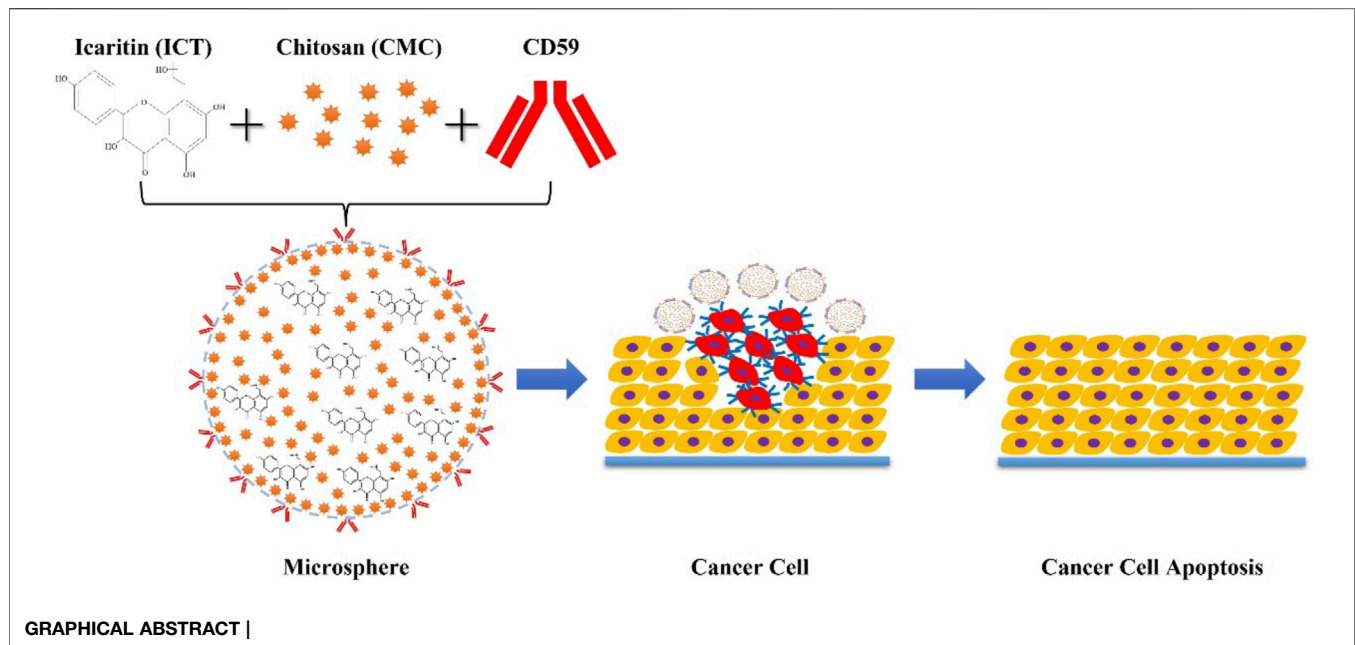
The treatment of oral squamous cell carcinoma (OSCC) remains a great clinical challenge, and the malignant proliferation of OSCC cells can lead to the overexpression of CD59. In this study, a novel microsphere (ICT-CMC-CD59sp) composed of icariin (ICT), carboxymethyl chitosan (CMC), and cell differentiation antigen 59-specific ligand peptide (CD59sp) was successfully prepared by using the emulsion cross-linking method. Through the guidance of CD59sp, the microspheres can target OSCC cells and play a therapeutic role ($p < 0.01$). The MTT test and trypan blue staining showed that the microspheres could promote the apoptosis of oral squamous cell carcinoma and had a significant difference ($p < 0.01$). In this study, the regulatory effect of the microspheres on OSCC cells was investigated at the cellular level, and its therapeutic effect on OSCC was discussed, which provided a new perspective for the targeted therapy of OSCC.

Keywords: ICT-CMC-CD59sp microspheres, oral squamous cell carcinoma, CD59-specific ligand peptide, targeted antitumor effect, drug-loaded

INTRODUCTION

Oral cancer is the sixth most common malignant tumor in the world, with more than 350,000 cases every year, of which nearly 90% of oral mucosa and lip malignant tumors are diagnosed as oral squamous cell carcinoma (OSCC) (Bray et al., 2018; Panarese et al., 2019). Common sites of OSCC are the tongue and floor of the mouth (Duray et al., 2012; Kouketsu et al., 2016). OSCC results in ulcerative lesions in the lesion area, with central necrosis and surrounding bulges (Pires et al., 2013). It mainly affects men aged 50–60 years, but the incidence rate of young patients has increased in recent decades (Tsimplaki et al., 2014; Kouketsu et al., 2016). The occurrence of OSCC may be caused by pre-existing oral lesions, and smoking and drinking are also important risk factors for OSCC (Dotto and Rustgi, 2016; Cramer et al., 2019). At present, the World Health Organization believes that oral leukoplakia, erythroplakia, oral submucosal fibrosis, reverse smoking palatal lesions, and oral lichen planus will increase the risk of cancer progression (Vitorio et al., 2020).

The treatment of OSCC has always been a difficult problem in clinics. At present, radiotherapy, chemotherapy, surgery, and anticancer drugs are still the main methods for the treatment of oral cancer, but these methods still have serious side effects (Sivanantham et al., 2016). Therefore, it is urgent to adopt new methods to change the treatment of oral cancer. In



recent years, the rapid development of biomedical materials has shown a great progress in cancer treatment. At present, due to the enhancement of targeting and specificity of biomaterials, many drug-loaded biomaterials have shown great tumor cell killing ability. Among them, tumor targeted therapy has high specificity, which can accurately deliver drugs to tumor cells, reduce the toxic and side effects of drugs, prolong the half-life of drugs *in vivo* and enhance the curative effect (Masood, 2016). Therefore, it is imperative to explore new targeted therapies.

In recent years, many studies have been carried out on the anticancer effect of icaritin (ICT) (Zhang et al., 2018; Zhou et al., 2018; Wu et al., 2020; Tao et al., 2021), the main active component of *Epimedium*. For example, studies have shown that ICT can inhibit cell viability, migration, and invasion and induce apoptosis by downregulating miR-625-3p and inactive PI3K/AKT and MEK/ERK signaling pathways in thyroid cancer cells (Fang et al., 2019). Another study showed that ICT can delay tumor progression, reduce the percentage of myelogenous suppressor cells (MDSCs) and have immunosuppressive function (Gabrilovich and Nagaraj, 2009). Previous studies by our research group also found that ICT could induce tumor cell apoptosis and inhibit tumor cell invasion (Wang et al., 2021). However, if ICT is used as a single component in cancer treatment, its bioavailability will be very low (2%), so it is necessary to organically combine ICT with a drug carrier capable of drug delivery for cancer treatment. Carboxymethyl chitosan is a good marine drug carrier, which can wrap a variety of antitumor drugs, prolong the drug action time, reduce side effects, and improve the drug efficacy. CD59 is a membrane complement regulatory protein, which is highly expressed in many reproductive system tumors and is related to tumor immune deficiency (Sivasankar et al., 2009). Therefore, in this study, triad-targeted drug delivery microspheres (ICT-CMC-

CD59sp) were prepared with ICT as the antitumor model drug, CMC as the carrier, and CD59sp as the targeting molecule to explore its antitumor effect, which opened up a new way for targeted treatment of OSCC, which has important clinical value.

MATERIALS AND METHODS

Materials

Icaritin (ICT) was purchased from Tauto Biotech (Shanghai, China); carboxymethyl chitosan (CMC, CAS 83512-85-0), MTT cell proliferation and cytotoxicity assay kits, and trypan blue staining cell viability assay kits were purchased from Solarbio (Beijing, China); CD59 peptide ligands were purchased from Chinese Peptide (Hangzhou, China); Human TNF- α ELISA kits were purchased from JiuBang Biotech (Quanzhou, China); N-(3-dimethylaminopropyl)-N'-ethylcarbodiimide hydrochloride (EDC) was purchased from Sigma-Aldrich (Shanghai, China); and oral squamous cell carcinoma (OSCC-9) was purchased from Procell (Wuhan, China).

Detection of CD59 on Cell Surface of Oral Squamous Cell Carcinoma

Paraffin sections were placed in fresh xylene, soaked for 10 min, and repeated once. After removing the excess liquid, the sections were placed in absolute ethanol, soaked it for 3 min, and repeated it once. After removing the excess liquid, the sections were soaked in 95% ethanol for 3 min and repeated once. After removing the excess liquid, the sections were soaked in 75% ethanol for 3 min and repeated it once. The sections were washed with distilled water for 1 min (wash away the alcohol) and were placed in PBS buffer for 1–3 min.

Then microwave antigen repair was carried out for 2 min and cooled to room temperature. After that, an appropriate amount of endogenous peroxidase blocker was added to the sections, washed with PBS buffer for 2 min, and repeated 3 times. Primary antibody was added, incubated overnight at 4°C, washed in PBS buffer for 2 min, and repeated twice; 100 µl reaction enhancer was then added, incubated at room temperature for 20 min, washed with PBS for 2 min and repeated twice; goat anti-mouse/rabbit IgG polymer with enhanced enzyme labeling was added; followed by DAB chromogenic solution, incubated at room temperature for 5 min, and rinsed with tap water. Hematoxylin counterstaining was performed, incubated with staining solution for 12 s, washed with tap water for 5 min, followed by differentiation washing and anti-blue, gradient dehydration, transparent, drip neutral gum seal, and finally the film was read.

Preparation of Microspheres

In total, 120 mg of carboxymethyl chitosan powder was added to 7.5 ml of aqueous solution and stirred evenly to form the aqueous phase. Then 37.5 ml of liquid paraffin and 3 ml of EL35 was added to a 50-ml beaker and stirred evenly to form the oil phase. After mixing the aqueous and oil phases, the mixture was stirred at room temperature at 1,000 r/min, allowing it to emulsify for 70 min. After that, 0.25 ml of 50% glutaraldehyde was added to the emulsion, which was left for 150 min for cross-linking and curing, static, and abandoning the upper emulsion. The mixture was then washed with dioxane, acetone, and anhydrous ethanol, followed by drying by filtration. A brown powder was obtained as CMC microspheres, was stored at 4°C for standby.

In total, 6 mg ICT was taken and dissolved in 3 ml anhydrous ethanol, and then ultrasound was carried out for 30 min to fully dissolve it. Centrifugation was performed at 8,000 r/min. After that, the solution was discarded, the supernatant was taken to dissolve it, making 2 mg/ml of ICT ethanol solution, and 3 ml of the solution was taken and added to 7 ml of chitosan aqueous solution. Then 37.5 ml liquid paraffin and 3 ml EL35 were added to a 50-ml beaker and stirred evenly at a speed of 1,000 r/min to form an oil phase. The prepared ICT solution was added to the oil phase, stirred at room temperature, left to emulsify for 70 min, and then 0.25 ml 50% glutaraldehyde was added to the emulsion and left 150 min to cross-link. After that, the upper emulsion was discarded and cleaned with dioxane, acetone, and anhydrous ethanol. After suction filtration and drying, the final brown powder was an ICT-CMC microsphere, which was stored at 4°C for standby.

In total, 5 mg of ICT-CMC microspheres were taken, resuspended in PBS, and thoroughly mixed. To the mixture, 2 mg of EDC was added, the pH of which was adjusted to 5.6, stirred at room temperature for 1 h, and centrifuged at 8,500 rpm for 10 min, and the unreacted EDC was then removed. Then the mixture was resuspended in 1 ml PBS, 1 mg/ml FITC-labeled CD59sp was added to it, stirred overnight, centrifuged to remove unbound CD59sp, resuspended in 1 ml PBS, and lyophilized into powder, namely, ICT-CMC-CD59sp microsphere, which was stored at 4°C for standby.

Characterization

The microstructure of the microsphere was imaged using a scanning electron microscope (SEM, JSM-5600, Japan). An appropriate number of microspheres were taken and directly stuck to the conductive adhesive surface. After spraying gold, it was observed and photos were taken under a scanning electron microscope. Fourier Transform Infrared Spectroscopy (FTIR) characterization and detection were carried out as follows: an appropriate number of ICT-CMC-CD59sp microspheres were taken, ground into powder, and then were detected with an infrared spectrometer with a scanning range of 500–4,000 cm⁻¹.

In Vitro Anticancer Assay

Cell Experiment

Cell experiments were divided into three groups: the CMC microsphere group, the ICT-CMC microsphere group, and the ICT-CMC-CD59sp microsphere group. The microsphere concentrations of each group in this part were 2 mg/ml, 1 mg/ml, and 0.5 mg/ml, respectively.

MTT Assay for Cytotoxicity

The effect of microspheres on the proliferation of OSCC cells is as follows:

- 1) Logarithmic growth stage cells were collected, and cell suspension concentrations were adjusted to 4×10^4 ml, 100 µl of which were added to each well.
- 2) The cells were cultured at 37°C and 5% CO₂ environment for 24 h to adhere to the wall.
- 3) Different concentrations of 100 µl of different types of microspheres were added and cultured for 24 h.
- 4) The supernatant was removed, which was added to 90 µl fresh culture solution, and 10 µl MTT solution, and then cultured for 4 h.
- 5) The supernatant was removed. Then 110 µl Formazan solution was added to each well and shaken on a shaking table at low speed for 10 min to fully dissolve the crystals. The absorption value of each was measured at 490 nm by using an enzyme immunoassay apparatus.

Trypan Blue Staining

The process of trypan blue staining is as follows: 4 g of trypan blue was taken and a small amount of distilled water was added for grinding. Double distilled water was added to 100 ml to prepare 4% trypan blue liquor, filtered, and stored at 4°C, which was diluted to 0.4% with PBS. Adherent OSCC cells were digested with trypsin to prepare a single cell suspension and diluted appropriately. The cell suspension and 0.4% trypan blue solution were mixed evenly at 9:1 (final concentration 0.04%). For the stained cell materials, a drop of cell suspension was taken on a glass slide, then the glass slide was covered, and observed under a high-power microscope. The number of living cells and dead cells were counted within 3 min. The dead cells were light blue, swollen, and dull. The living cells do not stain and maintain their normal shape and luster. Statistical staining cells and cell mortality were calculated (Cell mortality = number of stained cells/total number of observed cells×100%).

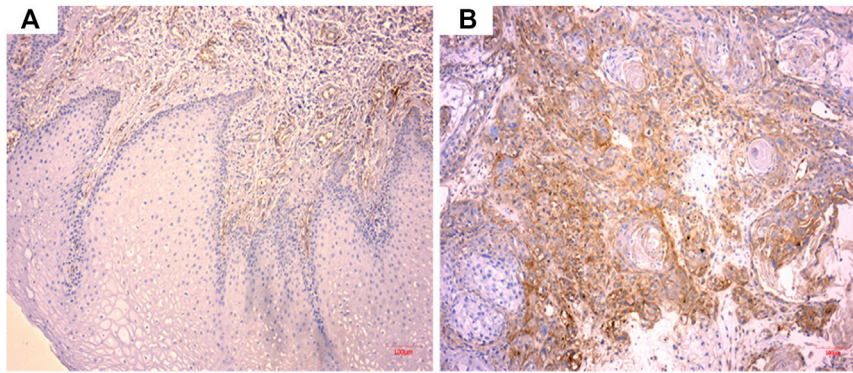


FIGURE 1 | CD59 expression in oral squamous cancer cells. **(A)** Low expression of CD59 in normal oral keratinocytes. **(B)** High expression of CD59 in oral squamous carcinoma cells.

TABLE 1 | Comparison of synergistic antitumor effects of ICT/CMC/CD59sp.

Group	OD ($\bar{x} \pm s$)	<i>p</i>
ICT	0.371 \pm 0.047	-
ICT + CMC	0.269 \pm 0.025*	<0.05
ICT + CMC + CD59sp	0.228 \pm 0.026**	<0.01

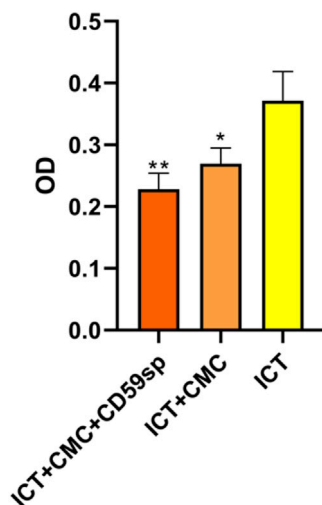


FIGURE 2 | Comparison of the synergistic antitumor effects of ICT/CMC/CD59sp (**p* < 0.05, ***p* < 0.01).

Enzyme-Linked Immunosorbent Assay Test: Detect TNF- α in Cell Supernatant Level

The cell supernatant of different groups of microspheres were taken after 24 h and centrifuged at 1,000 \times g for 20 min. The required strips were taken out from the aluminum foil bag after 20 mins of room temperature balance, and the remaining strips were sealed with natural sealing bags and put back at 4°C. The standard hole and sample hole were set, then 50 μ l of each of the 80, 40, 20, 10, 5 and 2.5 pg/ml standard samples were added to

the standard hole. Then 50 μ l samples were added to the hole to be tested, and the blank was not added. In addition to the blank, 100 μ l of horseradish peroxidase (HRP)-labeled detection antibody was added to each standard hole. The reaction hole was sealed and incubated in the incubator for 60 min. After washing the plate for 5 times, 50 μ l substrates A and B were added to each well and incubated in the dark at 37°C for 15 mins. Then 50 μ l termination solution was added to each well. The OD value of each hole was measured at a wavelength of 450 nm within 15 min.

Statistical Analysis

We used OriginPro 8 and GraphPad Prism8 to process the image analysis data, and the values were expressed as mean \pm standard deviation. In the analysis of variance between groups, *p* < 0.05 was considered statistically significant.

RESULTS

CD59 Expression in Oral Squamous Carcinoma Tissue Cells

As shown in **Figure 1**, CD59 was overexpressed in oral squamous carcinoma cells compared with normal keratinocytes.

Comparison of Synergistic Antitumor Effects of ICT/CMC/CD59sp

As shown in **Table 1** and **Figure 2**, the ICT-CMC-CD59sp group (*p* < 0.01) and ICT-CMC group (*p* < 0.01) have significant differences compared with the ICT group, indicating that ICT-CMC-CD59sp and ICT-CMC have better synergistic effects and antitumor effects than ICT.

Scanning Electron Microscope Observation Results

Figure 3 shows the SEM images of CMC microspheres, ICT-CMC microspheres, and ICT-CMC-CD59sp microspheres,

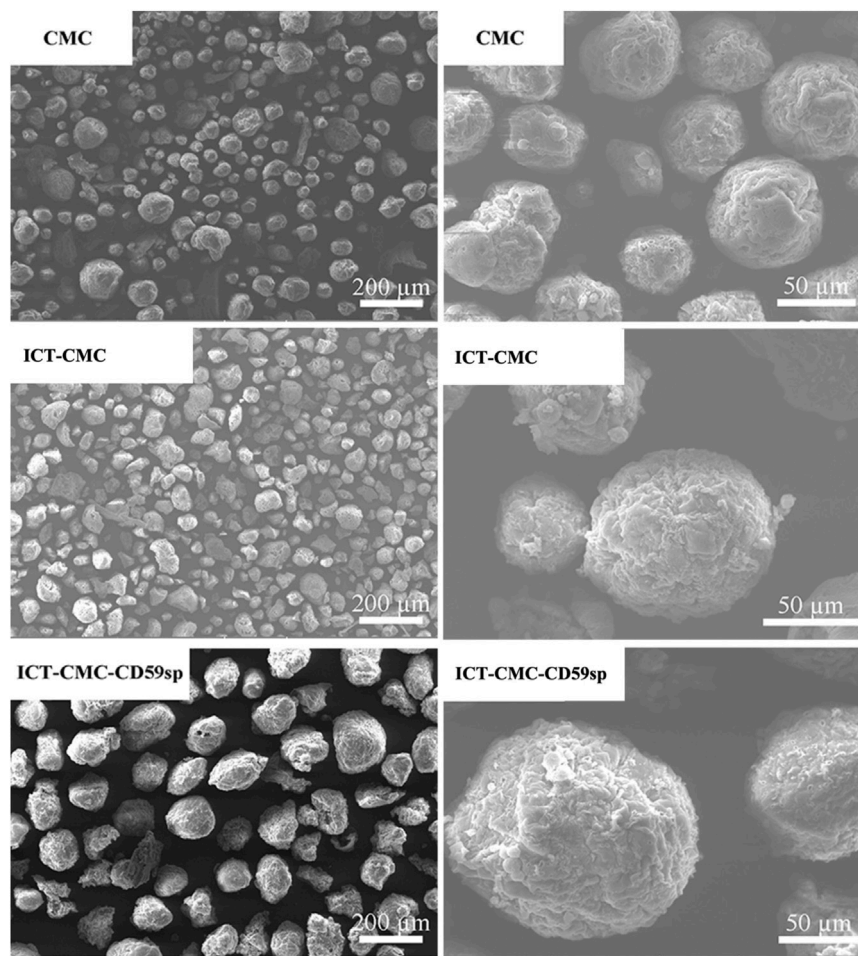


FIGURE 3 | Images of CMC, ICT-CMC, and ICT-CMC-CD59sp microspheres.

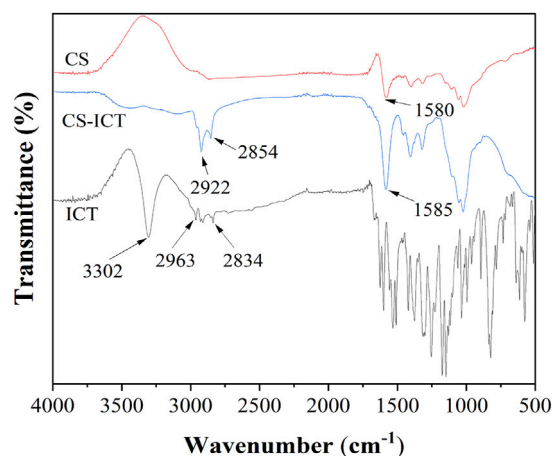


FIGURE 4 | Infrared spectrum images of ICT, CMC, and ICT-CMC microspheres.

respectively. It can be seen from the figure that the microspheres show regular spheres, evenly dispersed and with clear pores.

FTIR Characterization

Figure 4 shows the infrared analysis of ICT, CMC, and ICT-CMC microspheres; $3,302\text{ cm}^{-1}$ is the stretching vibration peak of O–H in ICT, $2,963\text{ cm}^{-1}$ and $2,834\text{ cm}^{-1}$ are the stretching vibration peaks of C–H in CH₂ and CH₃, and the corresponding is the characteristic peak of ICT. The corresponding peaks of $1,580\text{ cm}^{-1}$ and $1,585\text{ cm}^{-1}$ were characteristic peaks of amide in chitosan. After drug loading, characteristic peaks of ICT and CMC were found in ICT-CMC microspheres at the same time, indicating that ICT was successfully loaded into CMC microspheres.

Drug-Loaded Microspheres Targeting Combining With Cell Surface

OSCC cell surface fluorescence intensity (Figures 5A, B) shows that OSCC cells wrinkled into bar cord by using a fluorescence microscope 24 h after ICT-CMC-CD59sp targeting microspheres. Thus, it can be seen that CD59sp can specifically bind OSCC-9 cell CD59 molecules and deliver ICT to OSCC-9 cells with high penetration of CMC, jointly killing oral squamous cancer cells, thus exerting a good synergistic antitumor effect.

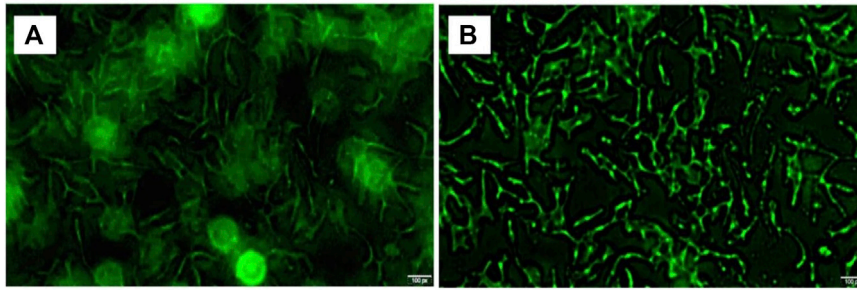


FIGURE 5 | Image of high expression of CD59 on oral squamous cell carcinoma cells **(A)** and ICT-CMC-CD59sp targeting microspheres' killing effect **(B)**.

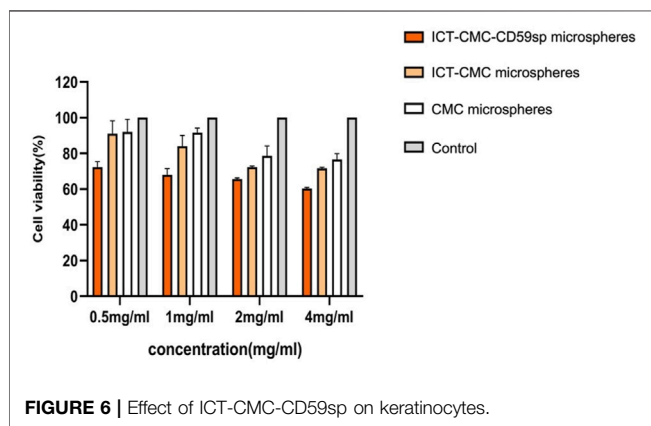


FIGURE 6 | Effect of ICT-CMC-CD59sp on keratinocytes.

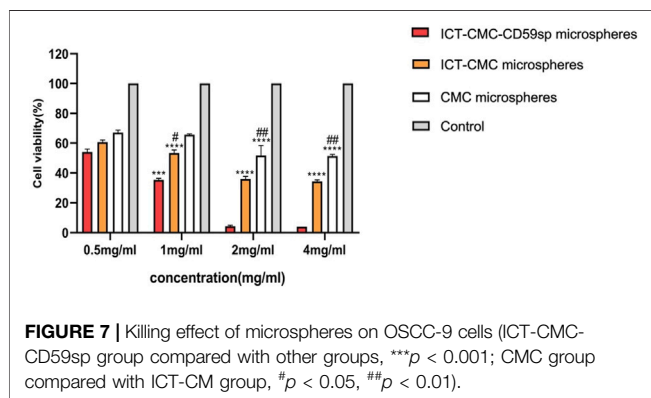


FIGURE 7 | Killing effect of microspheres on OSCC-9 cells (ICT-CMC-CD59sp group compared with other groups, *** $p < 0.001$; CMC group compared with ICT-CM group, # $p < 0.05$, ## $p < 0.01$).

TABLE 2 | Comparison of trypan blue staining results in living cells.

Group	Cell mortality (%) ($\bar{x} \pm s$)	p
CMC	10 \pm 7.65***	<0.01
ICT-CMC	54.18 \pm 4.1**	<0.01
ICT-CMC-CD59sp	71.5 \pm 6.64	-

Inhibition Effect of Microspheres on Keratinocytes and OSCC-9 Cells at Different Concentrations

As shown in **Figures 6, 7**, microspheres containing different components and concentrations of 0.5 mg/ml, 1 mg/ml, 2 mg/

ml, and 4 mg/ml were used to detect the effects on keratinocytes and OSCC-9 cells. As shown in **Figure 6**, different microspheres had little effect on the keratinocytes. However, ICT-CMC-CD59sp microspheres had a great inhibitory effect on the growth of tumor cells. Among them, 4 mg/ml and 2 mg/ml ICT-CMC-CD59sp microsphere groups had the best effects. Since there is no significant difference between the two groups, 2 mg/ml is selected for subsequent experiments. There was a significant difference between the ICT-CMC-CD59sp microsphere group and the ICT-CMC microsphere group and the CMC microsphere group ($p < 0.01$). The aforementioned results showed that the ICT-CMC-CD59sp group had a good antitumor effect in a concentration-dependent manner.

Oral Squamous Cell Carcinoma Trypan Blue Staining Detects Cell Mortality of OSCC-9 Cells

According to the analysis of **Table 2**, the ICT-CMC-CD59sp microsphere group had the best effect compared with the ICT-CMC microsphere group and the CMC empty microsphere group ($p < 0.01$).

Effects of Different Microspheres on Tumor Necrosis Factor in SCC-9 Cells

The results of ELISA showed that each microsphere group could promote the secretion of tumor necrosis factor α (**Figures 8, 9**). Compared with the ICT-CMC microsphere group and the CMC microsphere group, the ICT-CMC-CD59sp microsphere group with 2 mg/ml had the best effect ($p < 0.01$).

DISCUSSION

In recent years, research into targeting drug delivery systems has become a focus in the oncology field. Targeted drugs can deliver drugs to the targeted sites, reduce drug toxicity, prolong circulation half-lives, increase bioavailability, and enhance tumor disposition (Arranja et al., 2017).

Carboxymethyl chitosan is a water-soluble polysaccharide with higher solubility, moisture retention, and adsorption

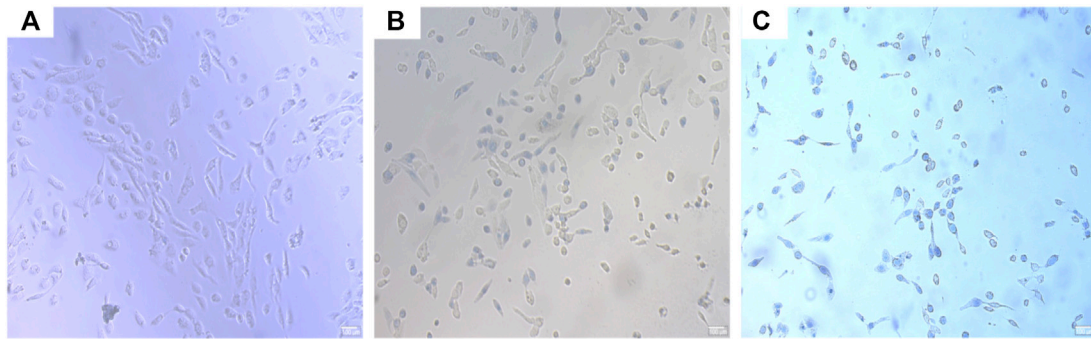


FIGURE 8 | OSCC trypan blue staining. **(A)** CMC microsphere group, **(B)** ICT-CMC microsphere group, and **(C)** ICT-CMC-CD59sp microsphere group.

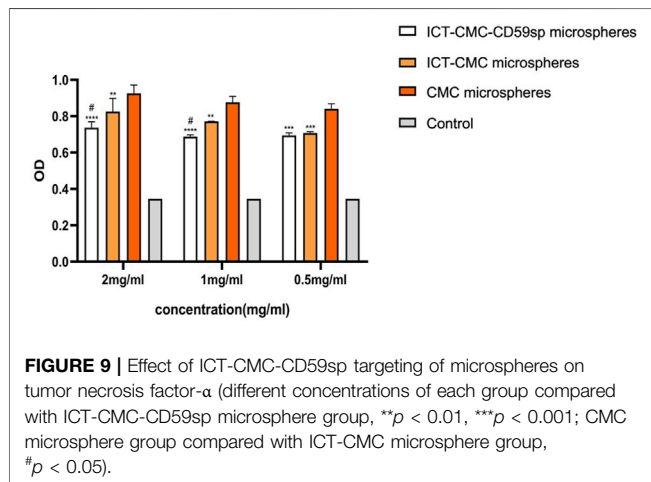


FIGURE 9 | Effect of ICT-CMC-CD59sp targeting of microspheres on tumor necrosis factor- α (different concentrations of each group compared with ICT-CMC-CD59sp microsphere group, ** $p < 0.01$, *** $p < 0.001$; CMC microsphere group compared with ICT-CMC microsphere group, # $p < 0.05$).

(Qing Chen et al., 2006; Shariatnia, 2018; Xu et al., 2018). It has stronger antibacterial properties, biocompatibility, and safety for the human body (Liu et al., 2005; Liyun et al., 2009; Jayakumar et al., 2010). It has been gradually used as a controlled release carrier of drugs in the biomedical field in recent years (Zhou et al., 2004; Ray-Neng Chen et al., 2006; Wang et al., 2010). Yang et al. (2017) prepared carboxymethyl chitosan nanoparticles (CMCNPs) coated with phycocyanin (C-PC) in an ion cross-linking method, and their cell experiments confirmed the obvious inhibitory effect of their microspheres on Hela cells. Hefnawy et al. (2020) target ASGP receptors highly expressed on the tumor cell surface and deliver DOX complexed with carboxymethyl chitosan-g-poly (acrylate) to achieve the targeted killing of HCC cells.

As the active ingredient of *Epimedium*, ICT has a good curative effect. It can not only promote blood circulation and enhance immunity and cardiac function but also induce apoptosis, downregulate tumor angiogenesis, and inhibit human cancer cell invasion of prostate cancer cells and endometrial cancer cells. In addition, ICT can promote tumor necrosis factor- α so as to promote the apoptosis of cancer cells (Li et al., 2013; Zhu et al., 2015; Wu et al., 2020). However, its stability is poor and is easily degraded, and its bioavailability is low.

The previous study found that CD59 molecules are overexpressed in various reproductive system tumors (cervical cancer, prostate cancer, breast cancer, etc.) (Zhang et al., 2018; Wang and Liang, 2020), but the correlation between CD59 and oral squamous cancer has not been reported. In this study, we targeted squamous carcinoma of the oral cavity using CMC as the vector to prepare an ICT-containing microsphere and connected CD59sp to the microsphere by EDC activation to obtain the targeted drug-carrying microsphere, CD59 ligand peptide, and CD59 protein on the tumor cell surface to achieve drug targeting.

The results showed that the microspheres had good dispersibility. By Scanning electron microscopy, the particle size of the microspheres was about 100 μm , and the microspheres were spherical by electron microscopy. The results of the MTT assay and trypan blue dyeing showed that microspheres inhibited the proliferation of OSCC cells, and there were significant differences between groups at different concentrations ($p < 0.01$), among which the ICT-CMC-CD59sp group had the best inhibition effect.

Mechanism of the anti-tumor effect of ICT-CMC-CD59sp microspheres: The overexpression of CD59 suppresses the formation of the membrane attack complex (MAC), by which tumor cells can avoid recognition by the complement pathway (Huang et al., 2002). Our microspheres can bind specifically to the CD59 receptor of tumor cell CD59 led by CD59sp, guide drugs to reach the cell surface, activate complement to form MAC, and dissolve OSCC tumor cells, and then, through receptor-mediated endocytosis, the drug were taken to the cells' interior. The ICT-CMC-CD59sp microspheres constructed in this experiment can bind CD59sp specifically to the tumor cell CD59 to guide the drug to the surface of oral squamous cancer cells, intake Epanin inside the cells, activate the complement to form MAC and lyse OSCC tumor cells. TNF- α can also bind to TNF-receptors and then activate the caspase protease family, promote caspase-3 activation, and induce death of oral squamous cancer cells.

CONCLUSION

In conclusion, this study optimized the preparation conditions of ICT-CMC-CD59sp and successfully made the ICT-CMC-CD59sp triad of targeted drug delivery microspheres with high efficiency and

sustained-release performance. It was confirmed that the microspheres could inhibit the proliferation of OSCC cells, providing a new perspective and approach for the application of ICT-CMC-CD59sp in the field of oral tumors, which has important theoretical significance and clinical application value.

DATA AVAILABILITY STATEMENT

The raw data supporting the conclusion of this article will be made available by the authors, without undue reservation.

REFERENCES

- Arranja, A. G., Pathak, V., Lammers, T., and Shi, Y. (2017). Tumor-targeted Nanomedicines for Cancer Theranostics. *Pharmacol. Res.* 115, 87–95. doi:10.1016/j.phrs.2016.11.014
- Bray, F., Ferlay, J., Soerjomataram, I., Siegel, R. L., Torre, L. A., and Jemal, A. (2018). Global Cancer Statistics 2018: GLOBOCAN Estimates of Incidence and Mortality Worldwide for 36 Cancers in 185 Countries. *CA: A Cancer J. Clinicians* 68, 394–424. doi:10.3322/caac.21492
- Cramer, J. D., Burtneiss, B., Le, Q. T., and Ferris, R. L. (2019). The Changing Therapeutic Landscape of Head and Neck Cancer. *Nat. Rev. Clin. Oncol.* 16, 669–683. doi:10.1038/s41571-019-0227-z
- Dotto, G. P., and Rustgi, A. K. (2016). Squamous Cell Cancers: A Unified Perspective on Biology and Genetics. *Cancer Cell* 29, 622–637. doi:10.1016/j.ccell.2016.04.004
- Duray, A., Descamps, G., Decaestecker, C., Remmelink, M., Sirtaine, N., Lechien, J., et al. (2012). Human Papillomavirus DNA Strongly Correlates with a Poorer Prognosis in Oral Cavity Carcinoma. *The Laryngoscope* 122, 1558–1565. doi:10.1002/lary.23298
- Fang, L., Xu, W., and Kong, D. (2019). RETRACTED: Icaritin Inhibits Cell Proliferation, Migration and Invasion by Down-Regulation of microRNA-625-3p in Thyroid Cancer Cells. *Biomed. Pharmacother.* 109, 2456–2463. doi:10.1016/j.biopha.2018.04.012
- Gabrivovich, D. I., and Nagaraj, S. (2009). Myeloid-derived Suppressor Cells as Regulators of the Immune System. *Nat. Rev. Immunol.* 9, 162–174. doi:10.1038/nri2506
- Hefnawy, A., Khalil, I. H., Arafa, K., Emara, M., and El-Sherbiny, I. M. (2020). Dual-Ligand Functionalized Core-Shell Chitosan-Based Nanocarrier for Hepatocellular Carcinoma-Targeted Drug Delivery. *Int. J. Nanomedicine* 15, 821–837. doi:10.2147/ijn.s240359
- Huang, L., Cheng, Y. Y., Chow, L. T., Zheng, M. H., and Kumta, S. M. (2002). Tumour Cells Produce Receptor Activator of NF-kappaB Ligand (RANKL) in Skeletal Metastases. *J. Clin. Pathol.* 55, 877–878. doi:10.1136/jcp.55.11.877
- Jayakumar, R., Prabakaran, M., Nair, S. V., Tokura, S., Tamura, H., and Selvamurugan, N. (2010). Novel Carboxymethyl Derivatives of Chitin and Chitosan Materials and Their Biomedical Applications. *Prog. Mater. Sci.* 55, 675–709. doi:10.1016/j.pmatsci.2010.03.001
- Kouketsu, A., Sato, I., Abe, S., Oikawa, M., Shimizu, Y., Takahashi, T., et al. (2016). Detection of Human Papillomavirus Infection in Oral Squamous Cell Carcinoma: a Cohort Study of Japanese Patients. *J. Oral Pathol. Med.* 45, 565–572. doi:10.1111/jop.12416
- Li, Q., Huai, L., Zhang, C., Wang, C., Jia, Y., Chen, Y., et al. (2013). Icaritin Induces AML Cell Apoptosis via the MAPK/ERK and PI3K/AKT Signal Pathways. *Int. J. Hematol.* 97, 617–623. doi:10.1007/s12185-013-1317-9
- Liu, S.-Q., Qiu, B., Chen, L.-y., Peng, H., and Du, Y.-M. (2005). The Effects of Carboxymethylated Chitosan on Metalloproteinase-1, -3 and Tissue Inhibitor of Metalloproteinase-1 Gene Expression in Cartilage of Experimental Osteoarthritis. *Rheumatol. Int.* 26, 52–57. doi:10.1007/s00296-004-0569-3
- Liuyun, J., Yubao, L., and Chengdong, X. (2009). Preparation and Biological Properties of a Novel Composite Scaffold of Nano-Hydroxyapatite/chitosan/carboxymethyl Cellulose for Bone Tissue Engineering. *J. Biomed. Sci.* 16, 65. doi:10.1186/1423-0127-16-65
- Masood, F. (2016). Polymeric Nanoparticles for Targeted Drug Delivery System for Cancer Therapy. *Mater. Sci. Eng. C* 60, 569–578. doi:10.1016/j.msec.2015.11.067
- Panarese, I., Aquino, G., Ronchi, A., Longo, F., Montella, M., Cozzolino, I., et al. (2019). Oral and Oropharyngeal Squamous Cell Carcinoma: Prognostic and Predictive Parameters in the Etiopathogenetic Route. *Expert Rev. Anticancer Ther.* 19, 105–119. doi:10.1080/14737140.2019.1561288
- Pires, F. R., Ramos, A. B., Oliveira, J. B. C. d., Tavares, A. S., Luz, P. S. R. d., and Santos, T. C. R. B. d. (2013). Oral Squamous Cell Carcinoma: Clinicopathological Features from 346 Cases from a Single Oral Pathology Service during an 8-year Period. *J. Appl. Oral Sci.* 21, 460–467. doi:10.1590/1679-775720130317
- Qing Chen, Q., Liu, S.-Q., Du, Y.-M., Peng, H., and Sun, L.-P. (2006). Carboxymethyl-chitosan Protects Rabbit Chondrocytes from Interleukin-1 β -Induced Apoptosis. *Eur. J. Pharmacol.* 541, 1–8. doi:10.1016/j.ejphar.2006.03.044
- Ray-Neng Chen, R.-N., Wang, G.-M., Chen, C.-H., Ho, H.-O., and Sheu, M.-T. (2006). Development of N,O-(carboxymethyl)chitosan/collagen Matrixes as a Wound Dressing. *Biomacromolecules* 7, 1058–1064. doi:10.1021/bm050754b
- Shariatnia, Z. (2018). Carboxymethyl Chitosan: Properties and Biomedical Applications. *Int. J. Biol. Macromolecules* 120, 1406–1419. doi:10.1016/j.ijbiomac.2018.09.131
- Sivanantham, B., Sethuraman, S., and Krishnan, U. M. (2016). Combinatorial Effects of Curcumin with an Anti-neoplastic Agent on Head and Neck Squamous Cell Carcinoma through the Regulation of EGFR-Erk1/2 and Apoptotic Signaling Pathways. *ACS Comb. Sci.* 18, 22–35. doi:10.1021/acscmbsci.5b00043
- Sivasankar, B., Longhi, M. P., Gallagher, K. M. E., Betts, G. J., Morgan, B. P., Godkin, A. J., et al. (2009). CD59 Blockade Enhances Antigen-specific CD4+ T Cell Responses in Humans: a New Target for Cancer Immunotherapy? *J. Immunol.* 182, 5203–5207. doi:10.4049/jimmunol.0804243
- Tao, C.-C., Wu, Y., Gao, X., Qiao, L., Yang, Y., Li, F., et al. (2021). The Antitumor Effects of Icaritin against Breast Cancer Is Related to Estrogen Receptors. *Curr. Mol. Med.* 21, 73–85. doi:10.2174/1566524020666200530212440
- Tsimplaki, E., Argyri, E., Xesfyngi, D., Daskalopoulou, D., Stravopodis, D. J., and Panotopoulou, E. (2014). Prevalence and Expression of Human Papillomavirus in 53 Patients with Oral Tongue Squamous Cell Carcinoma. *Anticancer Res.* 34, 1021–1025. doi:10.1093/annonc/mdt567
- Vitório, J. G., Duarte-Andrade, F. F., Dos Santos Fontes Pereira, T., Fonseca, F. P., Amorim, L. S. D., Martins-Chaves, R. R., et al. (2020). Metabolic Landscape of Oral Squamous Cell Carcinoma. *Metabolomics* 16, 105. doi:10.1007/s11306-020-01727-6
- Wang, L., and Liang, T.-T. (2020). CD59 Receptor Targeted Delivery of miRNA-1284 and Cisplatin-Loaded Liposomes for Effective Therapeutic Efficacy against Cervical Cancer Cells. *AMB Expr.* 10, 54. doi:10.1186/s13568-020-00990-z
- Wang, G., Lu, G., Ao, Q., Gong, Y., and Zhang, X. (2010). Preparation of Cross-Linked Carboxymethyl Chitosan for Repairing Sciatic Nerve Injury in Rats. *Biotechnol. Lett.* 32, 59–66. doi:10.1007/s10529-009-0123-1
- Wang, Y., Xu, Y., Cong, B., and Wei, X. (2021). Apoptosis Promoting Effect of Icaritin on Human Oral Squamous Cell Carcinoma Cells by Regulating Ki-67 and Notch-1 Gene Expression. *J. Oral Sci. Res.* 37, 505–508.
- Wu, X., Long, X., Yang, C., Chen, H., Sharkey, C., Rashid, K., et al. (2020). Icaritin Reduces Prostate Cancer Progression via Inhibiting High-Fat Diet-Induced

AUTHOR CONTRIBUTIONS

WW and MG conceived and designed the study. XG performed the experiments and wrote the manuscript. All authors read and approved the manuscript.

FUNDING

This work was supported by the Qingdao Key Health Discipline Development Fund.

- Serum Adipokine in TRAMP Mice Model. *J. Cancer* 11, 6556–6564. doi:10.7150/jca.48413
- Xu, C., Zhan, W., Tang, X., Mo, F., Fu, L., and Lin, B. (2018). Self-healing Chitosan/vanillin Hydrogels Based on Schiff-Base Bond/hydrogen Bond Hybrid Linkages. *Polym. Test.* 66, 155–163. doi:10.1016/j.polymertesting.2018.01.016
- Yang, P., Li, B., Yin, Q. F., and Wang, Y. J. (2017). Carboxymethyl Chitosan Nanoparticles Coupled with CD59-specific Ligand Peptide for Targeted Delivery of C-Phycocyanin to HeLa Cells. *Tumour Biol.* 39, 1010428317692267. doi:10.1177/1010428317692267
- Zhang, R., Liu, Q., Liao, Q., and Zhao, Y. (2018). CD59: a Promising Target for Tumor Immunotherapy. *Future Oncol.* 14, 781–791. doi:10.2217/fon-2017-0498
- Zhou, J., Elson, C., and Lee, T. D. (2004). Reduction in Postoperative Adhesion Formation and Re-formation after an Abdominal Operation with the Use of N, O - Carboxymethyl Chitosan. *Surgery* 135, 307–312. doi:10.1016/j.surg.2003.07.005
- Zhou, Y., Chu, L., Wang, Q., Dai, W., Zhang, X., Chen, J., et al. (2018). CD59 Is a Potential Biomarker of Esophageal Squamous Cell Carcinoma Radioresistance by Affecting DNA Repair. *Cell Death Dis* 9, 887. doi:10.1038/s41419-018-0895-0
- Zhu, S., Wang, Z., Li, Z., Peng, H., Luo, Y., Deng, M., et al. (2015). Icaritin Suppresses Multiple Myeloma, by Inhibiting IL-6/JAK2/STAT3. *Oncotarget* 6, 10460–10472. doi:10.18632/oncotarget.3399
- Conflict of Interest:** The authors declare that the research was conducted in the absence of any commercial or financial relationships that could be construed as a potential conflict of interest.
- Publisher's Note:** All claims expressed in this article are solely those of the authors and do not necessarily represent those of their affiliated organizations, or those of the publisher, the editors, and the reviewers. Any product that may be evaluated in this article, or claim that may be made by its manufacturer, is not guaranteed or endorsed by the publisher.
- Copyright © 2022 Gao, Wang and Gao. This is an open-access article distributed under the terms of the Creative Commons Attribution License (CC BY). The use, distribution or reproduction in other forums is permitted, provided the original author(s) and the copyright owner(s) are credited and that the original publication in this journal is cited, in accordance with accepted academic practice. No use, distribution or reproduction is permitted which does not comply with these terms.



Porous Se@SiO₂ Nanoparticles Enhance Wound Healing by ROS-PI3K/Akt Pathway in Dermal Fibroblasts and Reduce Scar Formation

Bo-Yu Yang^{1†}, Zhi-Yuan Zhou^{2†}, Shi-Yun Liu^{3†}, Ming-Jun Shi¹, Xi-Jian Liu⁴, Tian-Ming Cheng³, Guo-Ying Deng⁵, Ye Tian^{1*}, Jian Song^{1*} and Xuan-Hao Li^{1*}

OPEN ACCESS

Edited by:

Qihui Zhou,
Qingdao University, China

Reviewed by:

Bo Li,
Shanghai Jiao Tong University, China
Qiwei Tian,
Shanghai University of Medicine and
Health Sciences, China
Jingchao Li,
Donghua University, China

*Correspondence:

Ye Tian
tianye166@126.com
Jian Song
songjian1974@yahoo.com
Xuan-Hao Li
xuanhaoli@ccmu.edu.cn

[†]These authors have contributed
equally to this work.

Specialty section:

This article was submitted to
Biomaterials,
a section of the journal
Frontiers in Bioengineering and
Biotechnology

Received: 11 January 2022

Accepted: 18 February 2022

Published: 21 March 2022

Citation:

Yang B-Y, Zhou Z-Y, Liu S-Y, Shi M-J,
Liu X-J, Cheng T-M, Deng G-Y,
Tian Y, Song J and Li X-H (2022)
Porous Se@SiO₂ Nanoparticles
Enhance Wound Healing by ROS-
PI3K/Akt Pathway in Dermal
Fibroblasts and Reduce
Scar Formation.
Front. Bioeng. Biotechnol. 10:852482.
doi: 10.3389/fbioe.2022.852482

¹Department of Urology, Beijing Friendship Hospital, Capital Medical University, Beijing, China, ²Shanghai Pudong New Area Gongli Hospital, Shanghai, China, ³Department of Urology, Shanghai General Hospital, Shanghai Jiao Tong University School of Medicine, Shanghai, China, ⁴College of Chemistry and Chemical Engineering, Shanghai University of Engineering Science, Shanghai, China, ⁵Trauma Center, Shanghai General Hospital, Shanghai Jiaotong University School of Medicine, Shanghai, China

Hypertrophic scarring, which is characterized by excessive extracellular matrix deposition and abnormal fibroblast homeostasis, is an undesirable outcome of dermal wound healing. Once formed, the scar will replace the normal function of local skin, and there are few noninvasive clinical treatments that can cure it. Se@SiO₂ nanoparticles were synthesized to suppress oxidative stress, which induced the presence and activation of myofibroblasts during wound recovery. The characterization, antioxidant capacity and biological safety of Se@SiO₂ NPs were evaluated. A full-thickness excisional wound model was established, and the wounds were divided into three groups. The re-epithelization and distribution of collagen fibers were assessed using hematoxylin and eosin staining and Masson's trichrome staining after specific treatments. Our results revealed that the Se@SiO₂ NPs accelerated dermal wound healing and suppressed the formation of hypertrophic scars, accompanied by oxidative stress inhibition. Moreover, we found that Se@SiO₂ NPs worked by activating the PI3K/Akt pathway and upregulating the phosphorylation of Akt. The findings of our study provide a new method to promote dermal scar-free wound healing by suppressing excessive oxidative stress and through PI3K/Akt pathway activation.

Keywords: porous se@SiO₂ nanoparticles, wound healing, fibrosis, oxidative stress, PI3K/akt pathway

1 INTRODUCTION

Skin is the largest immune organ in the human body and plays a vital role in resisting external pathogen stimulation (Chambers and Vukmanovic-Stejić 2020). When traumatized or burned, the skin initiates a series of coordinated and orderly cellular biological responses to restore primary normal status, which is called wound healing. Wound healing is well described as a physiological process composed of three consecutive and overlapping stages, including the inflammatory response, granulation formation and tissue remodeling (Gurtner et al., 2008). There are many factors that can affect dermal wound repair, such as wound size, infection and immune function (Tatara et al., 2018). In terms of structure, the skin can be divided into three layers from outside to inside, namely, the

epidermis, dermis and hypodermis. When skin damage reaches the dermis, fibrotic repair involves the participation of multiple cell types, such as fibroblasts, keratinocytes and macrophages, and excessive extracellular matrix (ECM) deposition occurs (Driskell et al., 2013; Ogawa 2017). The occurrence of excessive fibrosis is a key issue that affects the quality of skin wound repair (Finnerty et al., 2016). In addition, studies have shown that the downregulation of fibrosis-related genes can directly alleviate scar formation but delay wound healing (Chogan et al., 2020). Therefore, seeking strategies that act on these dual roles to solve the problem of fibrosis is the focus of promoting wound repair and an urgent need.

Fibrosis, which results in hypertrophic scarring, refers to the pathological process of parenchymal cell necrosis and excessive ECM deposition in tissues. It has been demonstrated that myofibroblasts have a strong ECM secretory function and are the activated form of resident wound tissue fibroblasts (Zhang et al., 2020). As the most important effector cell associated with scar formation, myofibroblasts are usually activated during the inflammatory response (Woodcock et al., 2019; Wu et al., 2019). Multiple factors in the wound microenvironment can initiate fibroblast differentiation into myofibroblasts (Wang et al., 2020). Reactive oxygen species (ROS) generation is another major event associated with tissue fibrosis (Park et al., 2015). ROS such as hydrogen peroxide (H₂O₂), which is known to be an essential part of the early stage of wound healing, play pivotal roles in fibroblast activation and fibrosis (Akasaka et al., 2021). Moreover, high levels of ROS, which induce oxidative stress *in situ*, could hinder wound healing (Cheng et al., 2021). There is also evidence that low levels of ROS have positive effects on cell proliferation rather than promoting apoptosis (Dunnill et al., 2017; Schmidt et al., 2021). Therefore, topical administration of a drug with a sustained-release effect to maintain ROS at beneficial levels is particularly needed.

As one of the main ingredients in common antioxidant drugs, selenium (Se) is an essential trace element in the human body and a powerful antioxidant that works through glutathione peroxidase (GSH-Px) to scavenge free radicals and repair cell damage (Schrauzer 2009; Hariharan and Dharmaraj 2020). Se is seldom applied in the clinic because of its narrow therapeutic window (Clark et al., 1996; Alkie et al., 2020). In recent years, due to the development of nanomedical technology and drug delivery systems, Se particles have been modified for several generations, and finally porous Se@SiO₂ nanoparticles (Se@SiO₂ NPs) with excellent slow release capacity and biosafety were synthesized (Liu et al., 2016; Wang et al., 2018; Yang et al., 2019). Our previous study showed that porous Se@SiO₂ nanosphere-coated catheters could promote prostatic urethral wound healing (Yang et al., 2019). Thus, we hypothesized that Se@SiO₂ NPs could both promote dermal wound recovery and reduce scarring. In our study, we successfully synthesized Se@SiO₂ NPs and dissolved them in a chitosan (CS)/acetic acid solution. A full-thickness excision wound model on the backs of rats was established. The properties and biosafety of this nanocomposite were characterized, and the re-epithelization of wound tissues and degree of fibrosis were investigated. In addition, we explored the specific molecular mechanism by which Se@SiO₂ NPs promote

scar-free wound repair. The results of this study suggested that the application of Se@SiO₂ NPs effectively enhanced dermal scar-free wound healing.

2 MATERIALS AND METHODS

2.1 Reagents and Antibodies

H₂O₂ (30%) was obtained from Sigma (St Louis, MO, United States). Antibodies targeting α -SMA (ab5694), fibronectin (ab2413) and Col1A (ab96723) were purchased from Abcam (Cambridge, United Kingdom). Akt (sc-8312) and PARP/c-PARP (sc-7150) antibodies were purchased from Santa Cruz Biotechnology (Santa Cruz, CA, United States). GAPDH (#2118), phospho-Akt (#4060), and caspase-3/c-caspase-3 (#9665T) antibodies, horseradish peroxidase (HRP)-linked anti-rabbit IgG (#7074) and HRP-linked anti-mouse IgG (#7076) were purchased from Cell Signaling Technology (Danvers, MA, United States).

2.2 Synthesis of Se@SiO₂ Nanoparticles

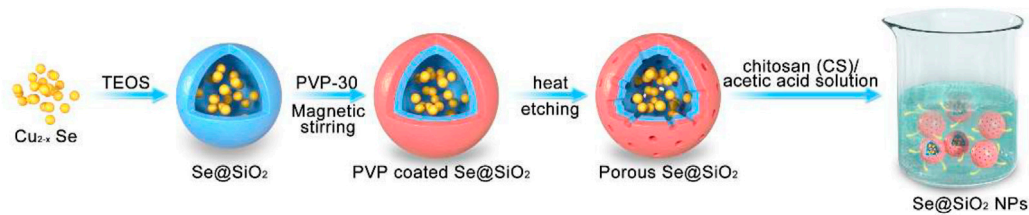
Porous Se@SiO₂ nanospheres were synthesized according to a previously reported process (Liu et al., 2016; Wang et al., 2018). Cu₂-xSe nanocrystals were first prepared by the thermal injection method. Then, n-hexanol, Triton X-100, n-hexane, deionized water, TEOS and ammonia were added individually to the solution dropwise while stirring, according to the one-pot method. After being kept at room temperature for 24 h, Se@SiO₂ core-shell nanospheres were collected by the addition of ethanol and were dispersed in deionized water. PVP-K30 was added and incubated for 1 h with magnetic stirring. The reaction mixture was heated to 95°C for 2 h and then rapidly cooled to 60°C. Porous Se@SiO₂ nanospheres were collected by centrifugation and washed twice with ethanol. First, 0.1 g of CS was dissolved in 20 ml of 1% acetic acid solution with stirring. Then, the porous Se@SiO₂ nanospheres were mixed with the solution after being dried, and we finally obtained Se@SiO₂ NPs (Scheme 1). The mixture was evenly stirred and sealed for later use.

2.3 X-Ray Diffraction and Transmission Electron Microscopy

X-ray diffraction (XRD) analysis of the Se and m Se@SiO₂ NPs was performed using an X-ray diffractometer (D/max-2550, Rigaku, Japan) in the range of 10°–80° (2 θ) to detect phase consistency. The mean diameter, structure and morphology of the Se@SiO₂ NPs were examined by transmission electron microscopy (TEM, JEM-2100F, JOEL, Japan). ImageJ was used to determine the size of the dried Se@SiO₂ NPs.

2.4 Establishment of a Dermal Full-Thickness Excisional Wound Model

Twelve 1-year-old Sprague-Dawley rats weighing 250–300 g were obtained from Shanghai General Hospital. After a few days of adaptation to the laboratory environment, the backs of the rats



SCHEME 1 | Schematic diagram of Se@SiO₂ NPs synthesis.

were shaved to expose the area to be wounded and cleaned with phosphate-buffered saline (PBS). To establish a dermal full-thickness excisional wound model, we anaesthetized the animals with pentobarbital sodium and utilized a 1 cm sterile drill to remove skin tissues to the depth that adipose tissues were exposed. The four wounds were divided into three experimental groups: a “(-) group” (the wound in the top left corner was treated with PBS), a “SiO₂ group” (the wound in the bottom left corner was treated with SiO₂ nanospheres only), and a “Se@SiO₂ group” (the two wounds on the right were treated with 1 mg/ml Se@SiO₂ NPs). The wounds were covered with gauze bandages after the specific treatments, and each rat was tagged with ear studs. The rats were housed in groups and allowed food and water normally after the surgery. The rats were sacrificed at 1, 3, 7, 14, 21, and 28 days. The wound tissues were excised using surgical scissors and dissected into two equal parts. Venous blood (10 ml) was collected and centrifuged at 3,000 rpm for 20 min. The serum was stored at -80°C for further use. In addition, control groups were established by treatment of PBS to all four wounds on the back of rats. Animal experiments were authorized by the Medical Science Ethics Committee of Shanghai General Hospital and performed according to the principles of the Chinese Council on Animal Care. All procedures were in accordance with the ethical standards of The Medical Ethics Committee of Beijing Friendship Hospital Affiliated to Capital Medical University. All institutional and national guidelines and rules for the care and use of laboratory animals were followed.

2.5 Flow Cytometry

Cell apoptosis was examined using a FITC-Annexin V Apoptosis Detection Kit (BD Biosciences, CA, United States). Flow cytometry was used to assess the proportion of apoptotic cells after the different treatments according to the manufacturer's instructions. Briefly, after being cultured with 300 μM H₂O₂ or 30 μg/ml Se@SiO₂ NPs for 24 h, the cells were harvested with scrapers. After being washed twice with cold PBS (HyClone), the cells were resuspended in binding buffer and stained with Annexin V-FITC and PI solutions in the dark. Then, the cell suspensions were analyzed using a BD Accuri C6 flow cytometer (BD Biosciences, CA, United States).

2.6 Quantitative Real-Time Polymerase Chain Reaction

Total RNA was extracted from human skin fibroblasts (HSFs) using TRIzol reagent (Invitrogen, United States). Complementary

DNA was synthesized using SuperScript III Reverse Transcriptase (Invitrogen, United States) according to the manufacturer's guidelines. qRT-PCR was conducted using PowerUp™ SYBR® Green Master Mix (Thermo Scientific, Waltham, MA, United States). Relative mRNA expression was quantified using the 2-ΔΔCt method and normalized to GAPDH as an internal control. The primers used in this study are listed in **Supplementary Table S1**.

2.7 Western Blotting

Cells were lysed with RIPA buffer (Beyotime, Suzhou, China) containing a phosphatase inhibitor cocktail (Yeasen, Shanghai, China) on ice for 30 min after the treatments and then vibrated by ultrasound. Protein levels were quantified using a Pierce BCA protein assay kit (Thermo Scientific, Waltham, MA, United States). Duplicate quantities of protein were loaded and separated on 10–15% SDS-polyacrylamide gels. Then, the proteins were transferred onto polyvinylidene fluoride (PVDF) membranes (Millipore, Bedford, MA, United States). After being blocked with skimmed milk for 1.5 h at room temperature, the membranes were incubated with specific primary antibodies overnight and HRP-conjugated secondary antibodies for 1.5 h after being washed with Tris-buffered saline plus Tween-20 (TBST). The immunoreactive bands were visualized using ChemiLucent ECL reagent (Millipore) and ImageJ software (National Institutes of Health).

2.8 Cell Viability Assay

The viability of HSFs was detected using Cell Counting Kit-8 (CCK-8, Dojindo, Japan). Cells were plated in 96-well plates at a density of 1×10^4 /well. After being treated with different concentrations of Se@SiO₂ NPs for 24 h, HSFs were incubated with 10 μl of CCK-8 reagent for an additional 2 h. Then, the absorption at 450 nm was measured using a microplate reader.

2.9 Liver and Kidney Function Analysis

Serum was collected from rats at each time point to analyze liver and kidney functions, including ALB, ALP, ALT, AST, BUN, Cre, γ-GT, UA and TBIL, using a Chemray 240 automatic biochemical analyzer (Rayto Life and Analytical Sciences, Shenzhen, China).

2.10 Histology and Immunofluorescence

The wound tissues were fixed in 10% formalin for 12 h, embedded in paraffin and cut into 5 μm-thick sections. Hematoxylin and eosin (H&E) staining and Masson's trichrome staining were

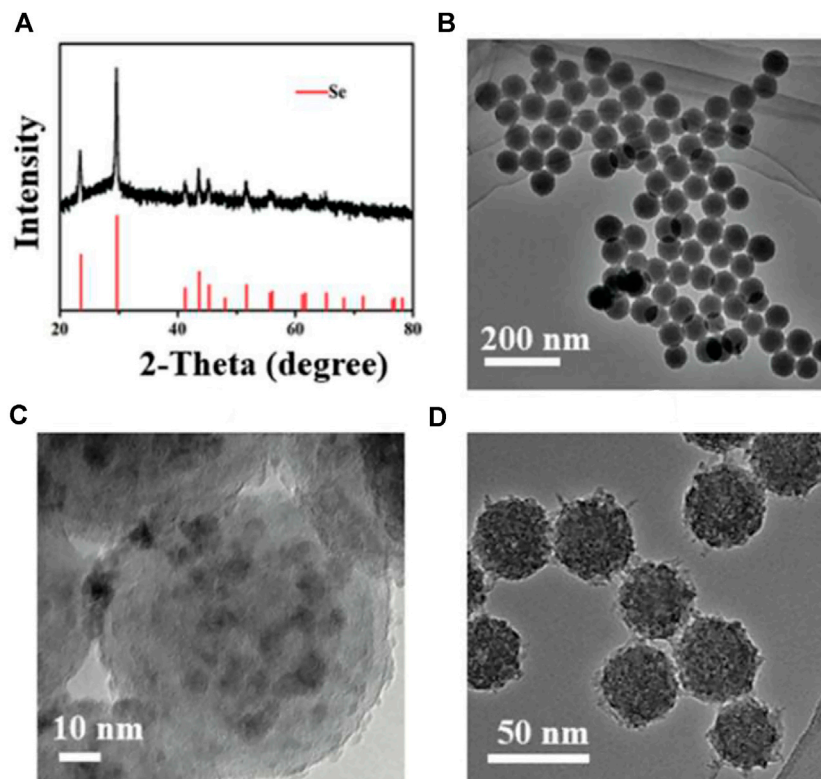


FIGURE 1 | Characterization of the Se@SiO₂ NPs. **(A)** The XRD spectra of the Se@SiO₂ NPs and the standard Se hexagonal phase (JCPDS card number: 65–1876). **(B)** Low- and **(C)** high-magnification images of Se@SiO₂ nanoparticles. **(D)** TEM characterization of the synthetic Se@SiO₂ NPs. TEM microphotographs indicated the structure of Se@SiO₂ NPs which consist of a porous silicon shell and encapsulated Se. Abbreviations: Se@SiO₂ NPs, porous Se@SiO₂ nanoparticles; XRD, X-ray diffraction; TEM, transmission electron microscopy; Se, selenium.

performed. To determine the expression of α -SMA, immunofluorescence assays were also performed. The sections were treated with blocking buffer and then incubated with primary antibodies targeting α -SMA overnight at 4°C and secondary antibodies with fluorescent conjugates for 1.5 h at room temperature. Finally, the sections were washed with PBS plus Tween-20 (PBST) three times and incubated with DAPI for nuclear staining before being observed using a Leica DMi8 fluorescence microscope or a Leica TCS SP8 confocal microscope (Wetzlar, Germany).

2.11 DCFH-DA Assay

HSFs were seeded in a 35 mm confocal dish (Coverglass Bottom Dish; 5 × 10⁵ cells/well) and pretreated with 30 μ g/ml Se@SiO₂ NPs for 24 h, followed by stimulation with 300 μ M H₂O₂ or ddH₂O for 30 min. Next, the HSFs were washed three times with cold PBS and incubated with DCFH-DA (Beyotime) for 15 min at 37°C. The dishes were screened using a Leica TCS SP8 confocal microscope (Wetzlar, Germany).

2.12 Wound Healing Assay

HSFs were seeded evenly in 6-well plates. We made an artificial wound in the cells using a plastic pipette tip when the HSFs had formed a monolayer. Then, the HSFs were cultured in the same culture medium and specific treatments until they reached

90–100% confluence relative to the primary wound. Cell migration at each time point was recorded by photography.

2.13 EdU Assay

Cell proliferation was analyzed using a Cell-Light™ EdU DNA Cell Proliferation Kit (RiboBio, Guangzhou, China) according to the manufacturer's instructions. The results were observed using a fluorescence microscope, and the ratio of positive cells was calculated.

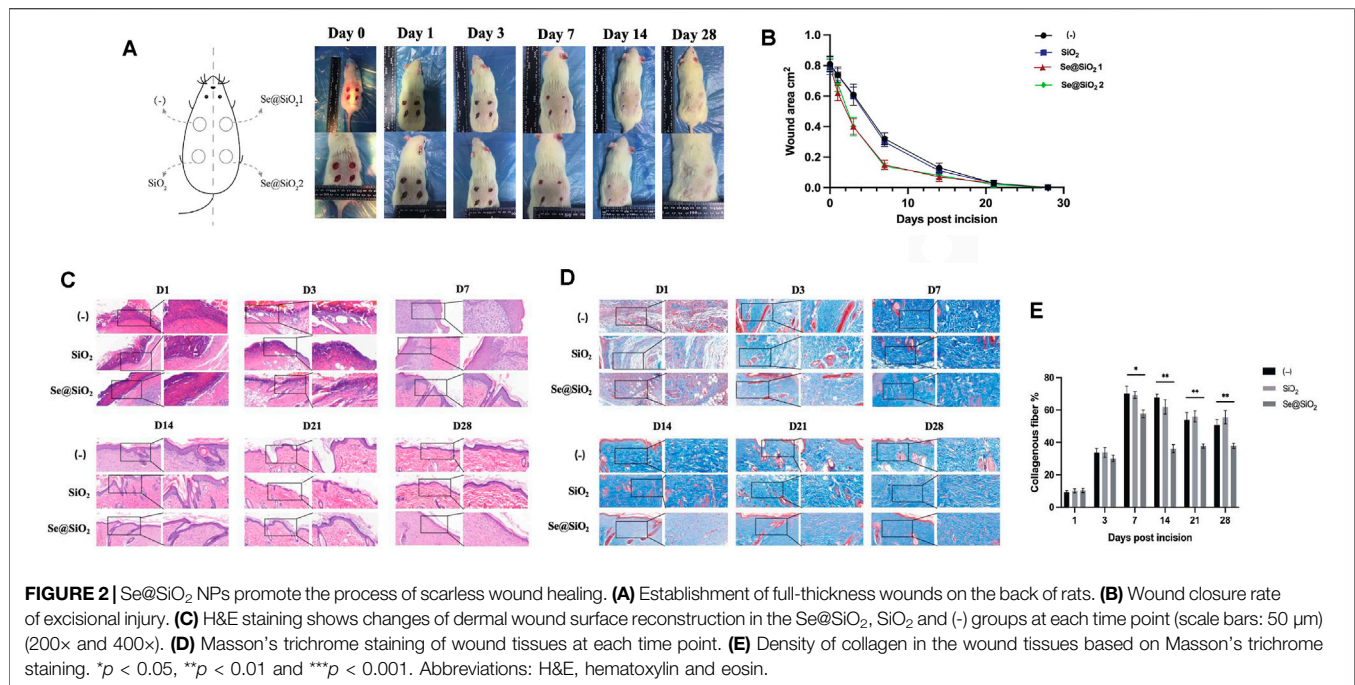
2.14 Statistical Analysis

Statistical analysis was performed using SPSS 19.0.0 software (SPSS Inc., Chicago, IL, United States). All data are expressed as the means \pm standard deviation (SD) and were analyzed using a two-tailed Student's *t*-test or one-way ANOVA. A *p*-value < 0.05 was considered statistically significant. All experiments were performed in triplicate.

3 RESULTS

3.1 Production, Particle Size and Patterns of Se@SiO₂ Nanoparticles

The XRD pattern of Se@SiO₂ NPs is shown in **Figure 1A**. The characteristic (1 0 0), (0 1 1), (1 1 0) and (0 1 2) peaks



demonstrated that the Se@SiO₂ NPs matched the standard hexagonal phase of Se (JCPDS card number 65–1876). The XRD analysis indicated that the presence of the amorphous silica coating showed a steady increase in the baseline of the low-angle region. The average diameter of the Se@SiO₂ nanoparticles as detected by TEM was approximately 55 nm. The Se@SiO₂ nanoparticles were monodispersed in a uniform spherical structure with Se quantum dots distributed from the center of the nanosphere to the surface (Figures 1B,C). After they were immersed in the PVP solution and heat-treated to form a porous silicon shell, Se@SiO₂ NPs were synthesized (Figure 1D). Finally, Se@SiO₂ NPs were dissolved in the carrier CS solution for practical use to ensure sustained release.

3.2 Promotion of Excisional Wound Closure With Wound Contracture and Dermal Morphology Optimization in Rats

Since the dermal full-thickness wound model was established with a drill, excisional wounds on the backs of the rats were divided into three groups. The progression of wound repair was recorded according to the scheduled observation times (Figure 2A). During the first 3 days, there was no difference in the groups. On day 3, the Se@SiO₂ group exhibited an accelerated repair process in terms of the wound area, and the wounds in the (-) group and SiO₂ group were moist with fresh granulation tissue. On day 7, the wound healing speed of Se@SiO₂ group achieved almost 80%, which was pivotally faster than that of (-) group and SiO₂ group ($p < 0.01$). Eventually, the wound in the Se@SiO₂ group healed thoroughly by day 21. The Se@SiO₂ NPs promoted flat closure that was fully filled in the cavity and almost the same as the adjacent normal skin. In contrast, wounds in the (-) group closed on day 28, but the palpable hypertrophic

scar was reddish and obviously raised, which was similar to that in the SiO₂ nanosphere-treated group. Measurement of the wound area confirmed that Se@SiO₂ NPs could accelerate wound healing (Figure 2B). To demonstrate the effect of Se@SiO₂ NPs histologically, we performed H&E staining at each time point (Figure 2C). One week after the dermal full-thickness wound model was established, we observed a more actively proliferating epithelium consisting of one or two layers of cells in both Se@SiO₂ groups. By week 4, histological analysis indicated that both Se@SiO₂ groups developed a continuous regenerative epithelium; moreover, well-formed basal lamina layers arranged in distinct levels were observed compared to those in the (-) group and SiO₂ group. Masson's trichrome staining was used to assess the degree of wound fibrosis (Figure 2D). Consistently, we found that the density of collagen deposition in both Se@SiO₂ groups was markedly reduced compared to that in the (-) and SiO₂ groups at the fourth week (Figure 2E). Thus, our results confirmed that Se@SiO₂ NPs promoted dermal wound healing with accelerated wound closure, optimized morphology and reduced hypertrophic scar formation.

3.3 Evaluation of Se@SiO₂ Nanoparticles Release Profiles, Biosafety and Oxidation Resistance

To describe the release spectrum of Se@SiO₂ NPs, ICP-AES was used to evaluate the Se content in the wound area in the groups. The Se concentration in wound tissue in the Se@SiO₂ group reached a maximum in the first week and remained steady thereafter (Figure 3A). As expected, there was no increase in Se in the (-) group or SiO₂ group. Moreover, no significant increase in Se was detected in serum (Supplementary Table S1). Furthermore, abnormal behaviors in the rats, such as spasm,

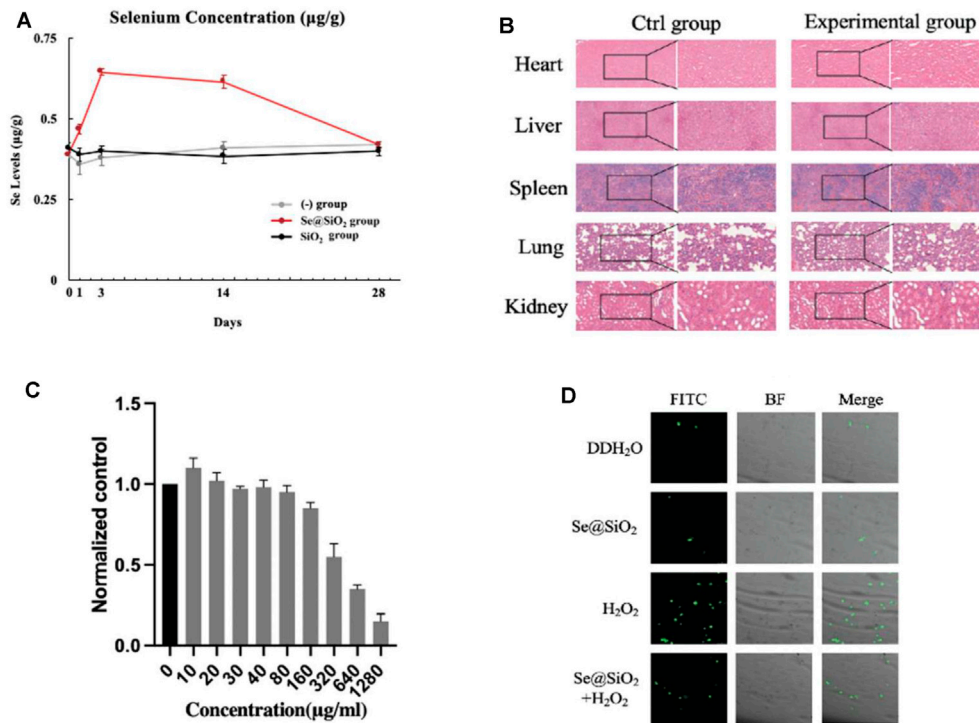


FIGURE 3 | Release profile, biosafety and oxidation resistance of Se@SiO₂ NPs *in vivo* and *in vitro*. **(A)** ICP-AES defined the Se contents in regenerated tissues of dermal wound at each time point. **(B)** Histological analysis of the heart, liver, spleen, lung and kidney tissues of rats at 4 weeks after the *in vivo* models were established (scale bars: 50 µm) (200× and 400×). **(C)** The viability of HSFs was detected after 24 h of coculture with different concentrations of porous Se@SiO₂ nanoparticles using a CCK-8 assay. **(D)** ROS expression was demonstrated by FITC images, BF images and merged views combining BF and FITC images using a DCFH-DA assay observed by confocal microscopy. **p* < 0.05, ***p* < 0.01 and ****p* < 0.001. Abbreviations: ICP-AES, inductively coupled plasma atomic emission spectroscopy; HSFs, human scar fibroblasts cell line; CCK-8, Cell Counting Kit-8; ROS, reactive oxygen species; FITC, fluorescein isothiocyanate; BF, bright field; DCFH-DA, 2',7'-dichlorodihydrofluorescein diacetate.

coma, vomiting, and incontinence, did not occur after full-thickness wound models were established, indicating the high biosafety of Se@SiO₂ NPs. H&E staining of major organs was performed, and there was no histological difference among the groups (Figure 3B). Plasma samples were collected at each time point to examine liver and kidney function. As shown in **Supplementary Table S2**, the serum levels of ALB, ALP, ALT, AST, BUN, Cre, γ-GT, UA and TBIL in the experimental groups were not significantly changed compared to those in the control groups throughout the experiment; the experimental groups did not exhibit metabolic dysfunction. Before subsequent examinations, we also determined the safety of the Se@SiO₂ NPs *in vitro*. The CCK-8 assay results demonstrated that concentrations ranging from 0 to 160 µg/ml were not significantly toxic to HSFs (Figure 3C). We simulated the oxidative stress environment in wound tissue by incubating HSFs with H₂O₂. HSFs were pretreated with Se@SiO₂ NPs and SiO₂ nanospheres, and then, a DCFH-DA assay and confocal microscopy were performed to investigate the ROS levels. Pretreatment with Se@SiO₂ NPs effectively downregulated H₂O₂-induced ROS levels (Figure 3D). Therefore, the Se@SiO₂ NPs decreased oxidative stress, which is crucial during wound healing, at safe concentrations and with a slow release.

3.4 Se@SiO₂ Nanoparticles Suppress Oxidative Stress-Induced Dermal Fibroblast Activation

Considering that better outcomes such as scarless wound healing were observed histologically in the Se@SiO₂ group, we further explored the activation of fibroblasts in this process. Immunofluorescence staining showed that in wound tissues, α-SMA, a biomarker of activated fibroblasts, was highly expressed in the (-) group and SiO₂ group but was decreased in the Se@SiO₂ group (Figure 4A, B). Incubation with H₂O₂ markedly upregulated α-SMA protein expression in HSFs. The expression of type I collagen and fibronectin was also examined to evaluate whether Se@SiO₂ NPs modulated the accumulation of ECM, which was highly enhanced by fibroblast activation (Figure 4C). The results confirmed that Se@SiO₂ NPs could suppress the upregulated expression of α-SMA, fibronectin and Col1A1 proteins caused by H₂O₂, which are essential for scar formation. In addition, Se@SiO₂ NPs also downregulated the mRNA expression of α-SMA, fibronectin and Col1A1 (Figure 4D). Our results showed that Se@SiO₂ NPs reversed the profibrotic effect induced by oxidative stress *in vivo* and *in vitro*.

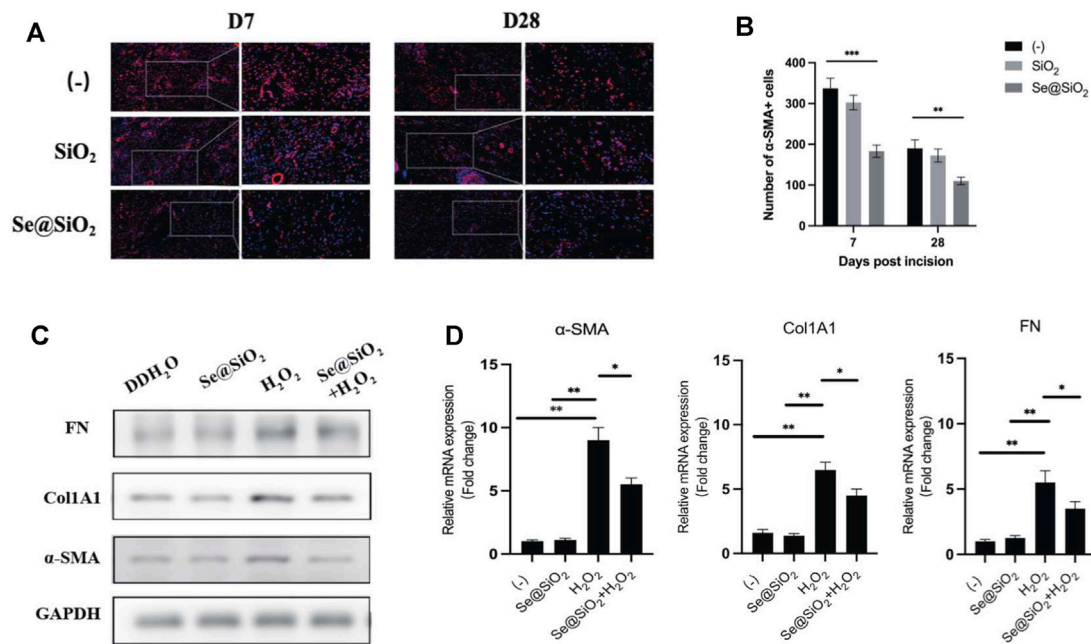


FIGURE 4 | Se@SiO₂ NPs repress collagen deposition of dermal fibroblasts caused by oxidative stress. **(A)** Representative images of immunofluorescence for α-SMA (red) in wound tissues at Day 7 and Day 28 (scale bars: 50 μm) (200× and 400×). Nuclei were stained with DAPI (blue). **(B)** Statistical analysis of α-SMA+ cells in immunofluorescence images. **(C)** Western blot analysis of relative α-SMA, Col1A1 and FN expression levels with Se@SiO₂ NPs and H₂O₂ treatment. **(D)** The mRNA levels of the α-SMA, Col1A1 and FN were further detected using qRT-PCR (*n* = 3). **p* < 0.05, ***p* < 0.01 and ****p* < 0.001. Abbreviations: α-SMA, alpha smooth muscle actin; DAPI, 4',6-diamidino-2-phenylindole; Col1A1, collagen 1A1; FN, fibronectin; qRT-PCR, quantitative real-time polymerase chain reaction.

3.5 Se@SiO₂ Nanoparticles Efficiently Attenuate ROS-Mediated Apoptosis via PI3K/Akt Activation

Next, we examined the mechanism by which Se@SiO₂ NPs promoted wound healing. Flow cytometry showed that Se@SiO₂ NPs abrogated the effect of H₂O₂ on apoptosis (Figures 5A, B). Additionally, TUNEL staining was used, and the results showed that the number of a-TUNEL+ cells decreased in the Se@SiO₂ group, which indicated that Se@SiO₂ NPs suppressed oxidative stress-induced apoptosis in fibroblasts (Figure 5C).

PI3K/Akt has been reported to be a vital factor that regulates apoptosis, and the antiapoptotic effect of Se@SiO₂ NPs on dermal fibroblasts has been verified. Thus, we examined whether Se@SiO₂ NPs could regulate ROS-induced apoptosis by triggering the phosphorylation of Akt. We used Western blotting to measure the expression of total and phosphorylated Akt. As shown in Figure 5D, the expression of cleaved Caspase-3 and cleaved PARP1 decreased, and phospho-Akt was upregulated in the Se@SiO₂+H₂O₂ group compared to the H₂O₂ group. In conclusion, Se@SiO₂ NPs protected against ROS-mediated apoptosis in HSFs via PI3K/Akt activation.

4 DISCUSSION

Wound healing is a continuous process with multiple stages, including the inflammatory response, granulation formation and

tissue remodeling (Gurtner et al., 2008). As the most important part of initial wound formation, the inflammatory response, especially when accompanied by excessive oxidative stress, plays a vital role in wound healing. Our previous study revealed that the polarization of M1 macrophages to M2 macrophages by modulating ROS levels could shorten the proinflammatory stage and accelerate re-epithelialization (Yang et al., 2019). Fibroblasts, one of the main effector cells that facilitate repair, are generally activated during the inflammatory response. Studies have shown that oxidative stress is one of the initiators of fibroblast activation (Akasaka et al., 2021). The number of myofibroblasts is in dynamic balance. The major characteristic of dermal scarring is persistent myofibroblast activation, as well as ECM deposition (Hinz and Lagares 2020). Thus, preventing apoptosis and the differentiation of fibroblasts is a feasible strategy that can not only accelerate wound healing but also reduce scar formation.

In the present study, our team successfully synthesized Se@SiO₂ NPs to promote scar-free dermal wound healing using a thermal injection method and a one-pot method as previously reported (Liu et al., 2016; Wang et al., 2018). Se, which is located in the core of Se@SiO₂ NPs, has been recognized as a therapeutic agent against oxidative stress. Several studies have confirmed Se-mediated promotion of cell growth, but Se is difficult to apply clinically due to its narrow treatment concentration range. In the present study, we dissolved Se@SiO₂ NPs in a solution of CS with good adhesion properties. The solution could prevent the NPs from easily falling off of the wound and prolong the action time.

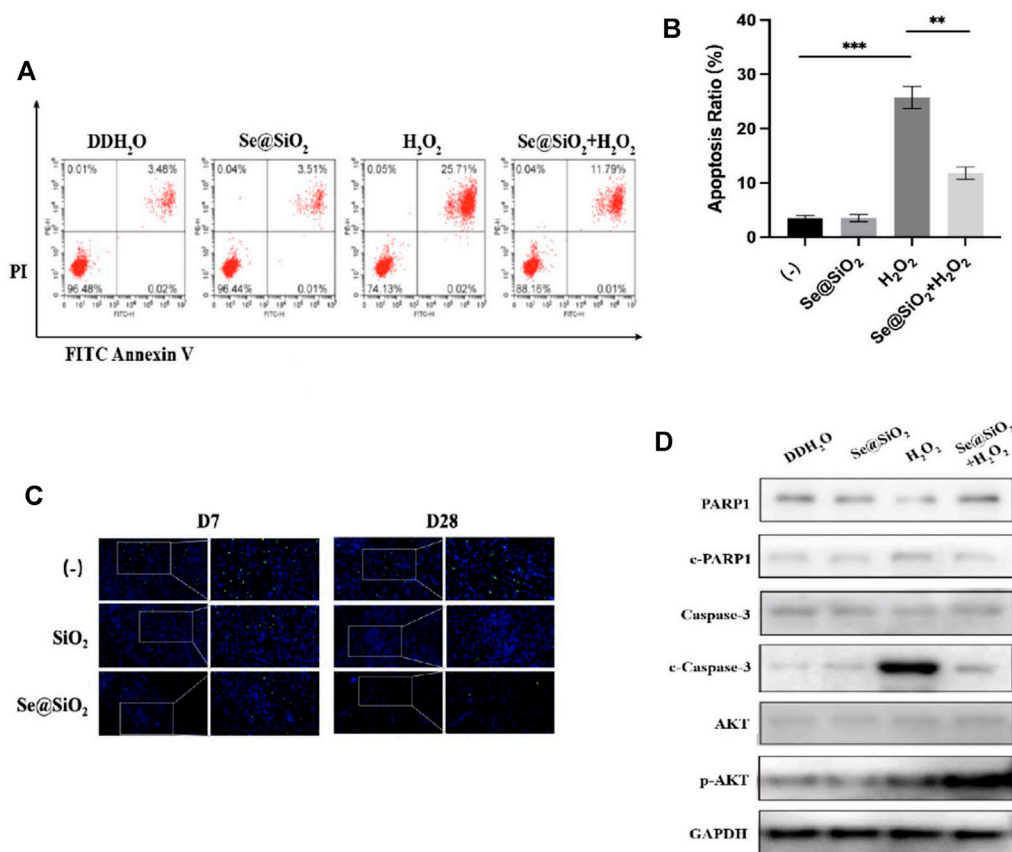


FIGURE 5 | Se@SiO₂ NPs can efficiently attenuate ROS-mediated apoptosis via PI3K/Akt activation. **(A)** Flow cytometry was conducted to detect the HSF apoptosis after pretreatment with 30 μg/ml Se@SiO₂ NPs for 24 h, followed by coculture with 300 μM H₂O₂ or DDH₂O for another 24 h. **(B)** Statistical analysis of the apoptotic cell percentage. **(C)** Immunofluorescence for TUNEL staining (green) was performed to validate the results of flow cytometry analysis. Nuclei were stained with DAPI (blue). **(D)** Relative expression levels of PARP1, c-PARP1, Caspase-3, c-Caspase-3, AKT and p-AKT proteins were detected via western blotting. **p* < 0.05, ***p* < 0.01 and ****p* < 0.001. Abbreviations: PI3K/Akt, Phosphatidylinositol 3-kinase/Akt; DDH₂O, double distilled H₂O; TUNEL, TdT mediated dUTP Nick End Labeling; PARP1, poly ADP-ribose polymerase 1; c-PARP1, cleaved poly ADP-ribose polymerase 1; c-Caspase-3, cleaved Caspase-3; p-AKT, Phosphorylated Akt.

Then, we established a full-thickness incision model on the backs of rats by and coated the solutions directly on the wounds. Compared to systemic administration, directly coating the wound with Se@SiO₂ NPs was faster and is safer since it allowed more flexible dosing control. Additionally, topical application of Se@SiO₂ NPs does not enter the blood circulation, so damage to other major organs was also minimized.

Until now, there has been no definitively effective therapy to promote scar-free wound healing because of its unclear mechanism. Dermal fibroblasts in the early stage after skin injury are responsible for wound closure to some extent. Excessive and uncontrolled oxidative stress could lead to fibroblast apoptosis and delayed healing. As we expected, Se@SiO₂ NPs effectively elevated the levels of endogenous antioxidants in wound tissues. Se@SiO₂ NPs protected HSFs from ROS-induced apoptosis, and TUNEL staining confirmed this effect histologically. Caspase-3, an executioner caspase that functions through the heteroactivation pathway, plays an indispensable role in apoptosis; however, it has no catalytic activity itself. Once cleaved and activated, caspase-3 hydrolyses the target protein and initiates apoptosis (Esteban-Fernández de

Ávila et al., 2017). PARP is considered to be a sensor of DNA damage and a primary cleavage target of Caspase-3. Cleaved PARP is an important indicator of cell apoptosis, and it is also generally regarded as an indicator of Caspase-3 activation (Chang et al., 2011; Bergamaschi et al., 2019). In the current study, we found that the expression of c-caspase-3 and c-PARP was upregulated by H₂O₂ and subsequently downregulated after Se@SiO₂ NP administration.

The fibrosis degree in the recovered tissue is another important index to evaluate wound repair. Serious scarring can damage the normal structure and function of various tissues (Mor et al., 2019). The level of collagen fibers in scar tissue was significantly higher than that in adjacent normal skin tissue. In this study, the tissues treated with Se@SiO₂ NPs exhibited less positive collagen fiber arranged in the dermis than the (-) group, as shown by Masson's staining. As collagen and fibronectin are key components of the ECM, the overexpression of Col1 and fibronectin is one of the typical characteristics of ECM deposition that is distinct from normalized scar-free tissues (Patten and Wang 2021; Russo et al., 2021; Witherel et al., 2021). Furthermore, we explored

the expression of myofibroblast cell marker α -SMA in fibroblasts treated with Se@SiO₂ NPs. The elevated α -SMA expression in fibroblasts induced by H₂O₂ was abolished after the pretreatment of Se@SiO₂ NPs. Therefore, our results demonstrated Se@SiO₂ NPs didn't stimulate the trans-differentiation of fibroblasts into myofibroblasts.

The mechanism by which the inhibition of excessive ROS by Se@SiO₂ NPs reduced HSF apoptosis and differentiation remains unclear. Studies have shown that the PI3K/Akt pathway plays a pivotal role in cell survival (Franke et al., 1997). We found that treatment with Se@SiO₂ NPs increased the expression of p-Akt, which confirmed the activation of the PI3K/Akt pathway. Combined with the ROS scavenging capacity of Se@SiO₂ NPs, our study indicated that Se@SiO₂ NPs could reverse ROS-induced apoptosis through Akt phosphorylation.

Although Se@SiO₂ NPs have been proven to inhibit oxidative stress, which in turn could promote scar-free wound healing, the effect of reduced ROS on other cellular components in the wound microenvironment is unknown. We found that Se@SiO₂ NPs could accelerate the re-epithelialization of wounds histologically, but we did not further explore the role of epithelial cells in this process. In future studies, we would investigate the nanomaterial-epithelial or matrix-epithelial interaction in the process of wound healing. Additionally, we ignored the effect of CS, which has an anti-inflammatory effect. As mentioned previously, inflammatory factors also changed with Se@SiO₂ NP treatment, but we did not consider this change. Other potential effects of Se@SiO₂ NPs that are conducive to wound repair, such as antibacterial effects, should be further explored. Last but not least, the PI3K/Akt pathway was researched in this study, while other signaling pathways involved in the Se@SiO₂ NPs mediated wound repair promotion are still awaited to be explored.

5 CONCLUSION

In the current study, our team demonstrated that the administration of Se@SiO₂ NPs could accelerate the re-epithelialization of wound tissues, thus promoting dermal wound healing in rats. Additionally, the application of these NPs to wounds was effective in decreasing scar formation during recovery. We confirmed that Se@SiO₂ NPs suppressed oxidative stress levels *in vivo* and *in vitro* with biosafety. Se@SiO₂ NPs improved wound repair and optimized fibrotic tissue structure by reducing the high levels of ROS associated with

inflammatory responses. Moreover, we also proved that Se@SiO₂ NPs prevented apoptosis and blocked the differentiation of fibroblasts through PI3K/Akt pathway suppression. In summary, the findings of this study illustrate a new strategy in which treatment with Se@SiO₂ NPs could shorten the healing process and enhance scarless dermal wound healing.

DATA AVAILABILITY STATEMENT

The original contributions presented in the study are included in the article/Supplementary Material, further inquiries can be directed to the corresponding author/s.

ETHICS STATEMENT

The animal study was reviewed and approved by Medical Science Ethics Committee of Shanghai General Hospital.

AUTHOR CONTRIBUTIONS

B-YY, ZZ contributed to the conception and design of the study. ZZ and SL implemented the experiments of the study. ZZ performed the statistical analysis. B-YY, ZZ wrote the first draft of the manuscript. SL, MS, TC, and GD wrote sections of the manuscript. XL synthesized the nanomaterials. YT, JS, and XL provided financial supports, revised the manuscript and supervised the research.

FUNDING

This work was supported by grants from the National Natural Scientific Foundation of China (Grant Nos: 82002711), Beijing Municipal Administration of Hospitals' Youth Programme (Code: QML20200105).

SUPPLEMENTARY MATERIAL

The Supplementary Material for this article can be found online at: <https://www.frontiersin.org/articles/10.3389/fbioe.2022.852482/full#supplementary-material>

REFERENCES

- Akasaka, E., Kleiser, S., Sengle, G., Bruckner-Tuderman, L., and Nyström, A. (2021). Diversity of Mechanisms Underlying Latent TGF- β Activation in Recessive Dystrophic Epidermolysis Bullosa. *J. Invest. Dermatol.* 141, 1450–1460. e9. doi:10.1016/j.jid.2020.10.024
- Alkie, T. N., de Jong, J., Moore, E., and DeWitte-Orr, S. J. (2020). Phytoglycogen Nanoparticle Delivery System for Inorganic Selenium Reduces Cytotoxicity without Impairing Selenium Bioavailability. *Ijn* Vol. 15, 10469–10479. doi:10.2147/ijn.s286948
- Bergamaschi, D., Vossenkamper, A., Lee, W. Y. J., Wang, P., Bochukova, E., and Warnes, G. (2019). Simultaneous Polychromatic Flow Cytometric Detection of Multiple Forms of Regulated Cell Death. *Apoptosis* 24, 453–464. doi:10.1007/s10495-019-01528-w
- Chambers, E. S., and Vukmanovic-Stejić, M. (2020). Skin Barrier Immunity and Ageing. *Immunology* 160, 116–125. doi:10.1111/imm.13152
- Chang, H.-Y., Fan, C.-C., Chu, P.-C., Hong, B.-E., Lee, H. J., and Chang, M.-S. (2011). hPuf-A/KIAA0020 Modulates PARP-1 Cleavage upon Genotoxic Stress. *Cancer Res.* 71, 1126–1134. doi:10.1158/0008-5472.can-10-1831
- Cheng, H., Shi, Z., Yue, K., Huang, X., Xu, Y., Gao, C., et al. (2021). Sprayable Hydrogel Dressing Accelerates Wound Healing with Combined Reactive

- Oxygen Species-Scavenging and Antibacterial Abilities. *Acta Biomater.* 124, 219–232. doi:10.1016/j.actbio.2021.02.002
- Chogan, F., Mirmajidi, T., Rezayan, A. H., Sharifi, A. M., Ghahary, A., Nourmohammadi, J., et al. (2020). Design, Fabrication, and Optimization of a Dual Function Three-Layer Scaffold for Controlled Release of Metformin Hydrochloride to Alleviate Fibrosis and Accelerate Wound Healing. *Acta Biomater.* 113, 144–163. doi:10.1016/j.actbio.2020.06.031
- Clark, R. F., Strukle, E., Williams, S. R., and Manoguerra, A. S. (1996). Selenium Poisoning from a Nutritional Supplement. *Jama* 275, 1087–1088. doi:10.1001/jama.1996.03530380029025
- Driskell, R. R., Lichtenberger, B. M., Hoste, E., Kretschmar, K., Simons, B. D., Charalambous, M., et al. (2013). Distinct Fibroblast Lineages Determine Dermal Architecture in Skin Development and Repair. *Nature* 504, 277–281. doi:10.1038/nature12783
- Dunnill, C., Patton, T., Brennan, J., Barrett, J., Dryden, M., Cooke, J., et al. (2017). Reactive Oxygen Species (ROS) and Wound Healing: the Functional Role of ROS and Emerging ROS-Modulating Technologies for Augmentation of the Healing Process. *Int. Wound J.* 14, 89–96. doi:10.1111/iwj.12557
- Esteban-Fernández de Ávila, B., Ramírez-Herrera, D. E., Campuzano, S., Angsantikul, P., Zhang, L., and Wang, J. (2017). Nanomotor-Enabled pH-Responsive Intracellular Delivery of Caspase-3: Toward Rapid Cell Apoptosis. *ACS nano* 11, 5367–5374. doi:10.1021/acsnano.7b01926
- Finnerty, C. C., Jeschke, M. G., Branski, L. K., Barret, J. P., Dziewulski, P., and Herndon, D. N. (2016). Hypertrophic Scarring: the Greatest Unmet challenge after Burn Injury. *The Lancet* 388, 1427–1436. doi:10.1016/s0140-6736(16)31406-4
- Franke, T. F., Kaplan, D. R., and Cantley, L. C. (1997). PI3K: Downstream AKTion Blocks Apoptosis. *Cell* 88, 435–437. doi:10.1016/s0092-8674(00)81883-8
- Gurtner, G. C., Werner, S., Barrandon, Y., and Longaker, M. T. (2008). Wound Repair and Regeneration. *Nature* 453, 314–321. doi:10.1038/nature07039
- Hariharan, S., and Dharmaraj, S. (2020). Selenium and Selenoproteins: It's Role in Regulation of Inflammation. *Inflammopharmacol* 28, 667–695. doi:10.1007/s10787-020-00690-x
- Hinz, B., and Lagares, D. (2020). Evasion of Apoptosis by Myofibroblasts: a Hallmark of Fibrotic Diseases. *Nat. Rev. Rheumatol.* 16, 11–31. doi:10.1038/s41584-019-0324-5
- Liu, X., Deng, G., Wang, Y., Wang, Q., Gao, Z., Sun, Y., et al. (2016). A Novel and Facile Synthesis of Porous SiO₂-Coated Ultrasmall Se Particles as a Drug Delivery Nanoplatform for Efficient Synergistic Treatment of Cancer Cells. *Nanoscale* 8, 8536–8541. doi:10.1039/c6nr02298g
- Mor, A., Segal Salto, M., Katav, A., Barashi, N., Edelshtein, V., Manetti, M., et al. (2019). Blockade of CCL24 with a Monoclonal Antibody Ameliorates Experimental Dermal and Pulmonary Fibrosis. *Ann. Rheum. Dis.* 78, 1260–1268. doi:10.1136/annrheumdis-2019-215119
- Ogawa, R. (2017). Keloid and Hypertrophic Scars Are the Result of Chronic Inflammation in the Reticular Dermis. *Int. J. Mol. Sci.* 18, 606. doi:10.3390/ijms18030606
- Park, S.-A., Kim, M.-J., Park, S.-Y., Kim, J.-S., Lee, S.-J., Woo, H. A., et al. (2015). EW-7197 Inhibits Hepatic, Renal, and Pulmonary Fibrosis by Blocking TGF- β /Smad and ROS Signaling. *Cell. Mol. Life Sci.* 72 (CMLS 72), 2023–2039. doi:10.1007/s00018-014-1798-6
- Patten, J., and Wang, K. (2021). Fibronectin in Development and Wound Healing. *Adv. Drug Deliv. Rev.* 170, 353–368. doi:10.1016/j.addr.2020.09.005
- Russo, B., Borowczyk, J., Boehncke, W. H., Truchetet, M. E., Modarressi, A., Brembilla, N. C., et al. (2021). Dysfunctional Keratinocytes Increase Dermal Inflammation in Systemic Sclerosis: Results from Studies Using Tissue-Engineered Scleroderma Epidermis. *Arthritis Rheumatol.* 73, 1311–1317. doi:10.1002/art.41659
- Schmidt, A., Liebelt, G., Nießner, F., von Woedtke, T., and Bekeschus, S. (2021). Gas Plasma-Spurred Wound Healing Is Accompanied by Regulation of Focal Adhesion, Matrix Remodeling, and Tissue Oxygenation. *Redox Biol.* 38, 101809. doi:10.1016/j.redox.2020.101809
- Schrauzer, G. N. (2009). Selenium and Selenium-Antagonistic Elements in Nutritional Cancer Prevention. *Crit. Rev. Biotechnol.* 29, 10–17. doi:10.1080/07388550802658048
- Tatara, A. M., Kontoyiannis, D. P., and Mikos, A. G. (2018). Drug Delivery and Tissue Engineering to Promote Wound Healing in the Immunocompromised Host: Current Challenges and Future Directions. *Adv. Drug Deliv. Rev.* 129, 319–329. doi:10.1016/j.addr.2017.12.001
- Wang, Y., Liu, X., Deng, G., Sun, J., Yuan, H., Li, Q., et al. (2018). Se@SiO₂-FA-CuS Nanocomposites for Targeted Delivery of DOX and Nano Selenium in Synergistic Combination of Chemo-Photothermal Therapy. *Nanoscale* 10, 2866–2875. doi:10.1039/c7nr09237g
- Wang, Z.-C., Zhao, W.-Y., Cao, Y., Liu, Y.-Q., Sun, Q., Shi, P., et al. (2020). The Roles of Inflammation in Keloid and Hypertrophic Scars. *Front. Immunol.* 11, 603187. doi:10.3389/fimmu.2020.603187
- Witherell, C. E., Sao, K., Brisson, B. K., Han, B., Volk, S. W., Petrie, R. J., et al. (2021). Regulation of Extracellular Matrix Assembly and Structure by Hybrid M1/M2 Macrophages. *Biomaterials* 269, 120667. doi:10.1016/j.biomaterials.2021.120667
- Woodcock, H. V., Eley, J. D., Guillotin, D., Platé, M., Nanthakumar, C. B., Martufi, M., et al. (2019). The mTORC1/4E-BP1 axis Represents a Critical Signaling Node during Fibrogenesis. *Nat. Commun.* 10, 6. doi:10.1038/s41467-018-07858-8
- Wu, M., Skaug, B., Bi, X., Mills, T., Salazar, G., Zhou, X., et al. (2019). Interferon Regulatory Factor 7 (IRF7) Represents a Link between Inflammation and Fibrosis in the Pathogenesis of Systemic Sclerosis. *Ann. Rheum. Dis.* 78, 1583–1591. doi:10.1136/annrheumdis-2019-215208
- Yang, B.-Y., Deng, G.-Y., Zhao, R.-Z., Dai, C.-Y., Jiang, C.-Y., Wang, X.-J., et al. (2019). Porous Se@SiO₂ Nanosphere-Coated Catheter Accelerates Prostatic Urethra Wound Healing by Modulating Macrophage Polarization through Reactive Oxygen Species-NF-K β Pathway Inhibition. *Acta Biomater.* 88, 392–405. doi:10.1016/j.actbio.2019.02.006
- Zhang, Y., Shen, L., Zhu, H., Dreissigacker, K., Distler, D., Zhou, X., et al. (2020). PGC-1 α Regulates Autophagy to Promote Fibroblast Activation and Tissue Fibrosis. *Ann. Rheum. Dis.* 79, 1227–1233. doi:10.1136/annrheumdis-2020-216963

Conflict of Interest: The authors declare that the research was conducted in the absence of any commercial or financial relationships that could be construed as a potential conflict of interest.

The reviewer BL declared a shared affiliation, with no collaboration, with several of the authors S-YL, T-MC and G-YD to the handling editor at the time of the review.

Publisher's Note: All claims expressed in this article are solely those of the authors and do not necessarily represent those of their affiliated organizations, or those of the publisher, the editors and the reviewers. Any product that may be evaluated in this article, or claim that may be made by its manufacturer, is not guaranteed or endorsed by the publisher.

Copyright © 2022 Yang, Zhou, Liu, Shi, Liu, Cheng, Deng, Tian, Song and Li. This is an open-access article distributed under the terms of the Creative Commons Attribution License (CC BY). The use, distribution or reproduction in other forums is permitted, provided the original author(s) and the copyright owner(s) are credited and that the original publication in this journal is cited, in accordance with accepted academic practice. No use, distribution or reproduction is permitted which does not comply with these terms.



OPEN ACCESS

EDITED BY

Brandon W. Peterson,
University Medical Center Groningen,
Netherlands

REVIEWED BY

Yifan Ge,
Nantong University, China
Hongzhao Qi,
Qingdao University, China

*CORRESPONDENCE

Dorota Bartusik-Aebisher,
dbartusikaebisher@ur.edu.pl
David Aebisher,
daebisher@ur.edu.pl

SPECIALTY SECTION

This article was submitted to
Biomaterials,
a section of the journal
Frontiers in Bioengineering and
Biotechnology

RECEIVED 19 June 2022

ACCEPTED 01 August 2022

PUBLISHED 30 August 2022

CITATION

Sottan M, Bartusik-Aebisher D and
Aebisher D (2022), The potential of
oxygen and nitrogen species-regulating
drug delivery systems in medicine.
Front. Bioeng. Biotechnol. 10:973080.
doi: 10.3389/fbioe.2022.973080

COPYRIGHT

© 2022 Sottan, Bartusik-Aebisher and
Aebisher. This is an open-access article
distributed under the terms of the
[Creative Commons Attribution License](https://creativecommons.org/licenses/by/4.0/)
(CC BY). The use, distribution or
reproduction in other forums is
permitted, provided the original
author(s) and the copyright owner(s) are
credited and that the original
publication in this journal is cited, in
accordance with accepted academic
practice. No use, distribution or
reproduction is permitted which does
not comply with these terms.

The potential of oxygen and nitrogen species-regulating drug delivery systems in medicine

Michał Sottan¹, Dorota Bartusik-Aebisher^{2*} and
David Aebisher^{1,2*}

¹English Division Science Club, Medical College of The University of Rzeszów, Rzeszów, Poland,

²Department of Biochemistry and General Chemistry, Medical College of The University of Rzeszów, Rzeszów, Poland, ³Department of Photomedicine and Physical Chemistry, Medical College of The University of Rzeszów, Rzeszów, Poland

The focus of this review is to present most significant advances in biomaterials used for control of reactive oxygen/nitrogen species (ROS/RNS, RONS) in medicine. A summary of the main pathways of ROS production and the main pathways of RNS production are shown herein. Although the physiological and pathological roles of RONS have been known for at least 2 decades, the potential of their control in management of disease went unappreciated. Recently, advances in the field of biochemical engineering and materials science have allowed for development of RONS-responsive biomaterials for biomedical applications, which aim to control and change levels of reactive species in tissue microenvironments. These materials utilize polymers, inorganic nanoparticles (NPs), or organic-inorganic hybrids. Thus, biomaterials like hydrogels have been developed to promote tissue regeneration by actively scavenging and reducing RONS levels. Their promising utility comes from thermo- and RONS-sensitivity, stability as a delivery-medium, ease for incorporation into other materials and facility for injection. Their particular attractiveness is attributed to drug release realized in targeted tissues and cells with elevated RONS levels, which leads to enhanced treatment outcomes and reduced adverse effects. The mechanism of their action depends on the functional groups employed and their response to oxidation, and may be based on solubility changes or cleavage of chemical bonds. When talking about antioxidants, one should also mention oxidative stress, which we call the imbalance between antioxidants and reactive oxygen species, which occurs due to a deficiency of endogenous antioxidants and a low supply of exogenous antioxidants. This study is a review of articles in English from the databases PubMed and Web of Science retrieved by applying the search terms "Oxygen Species, Nitrogen Species and biomaterials" from 1996 to 2021.

KEYWORDS

oxygen species, nitrogen species, biomaterials, biomedical applications, oxygen

Introduction

Reactive species, also commonly called free radicals, is a term that describes atoms and functional groups with one or more unpaired electrons. Due to this odd number of electrons, free radicals are potent electrophiles, making them unstable and highly reactive. The dire atomic need for obtaining an even number of electrons on the valence shell and the resultant stability, drives these reactive species to react with (“attack”) other molecules to attain the needed electrons. In turn, this process leads to the attacked molecule losing electrons and it becoming a free radical itself. The aforementioned electron-capturing process continues, forming a cascade of reactions that usually leads to a degenerative process, mostly cell death. Along the way, molecules like lipids, proteins and nucleic acids may fall victims to reactive species (Mittal et al., 2014). The sources of free radicals in the human organism can be exogenous (e.g., UV radiation, alcohol, pesticides, heavy metals, some drugs) or endogenous (usually from oxidative processes in mitochondria, peroxisomes, and the endoplasmic reticulum) (Yoboue et al., 2018; Burtenshaw et al., 2019). To counteract free radicals, cells employ many enzymes and other non-enzymes that scavenge these highly reactive molecules and neutralize them; all these enzymes and non-enzymes are collectively referred to as the antioxidant defense system. Under normal conditions, there is a balance between oxidants and antioxidants, meaning the free radicals are neutralized nearly immediately and at a sufficient rate. However, an imbalance between these two components can occur when there is a greater production of free radicals and the antioxidant capacity is exceeded, or when the antioxidant defense system itself is impaired (Birben et al., 2012). This in turn leads to the state of oxidative stress that commonly results in overall aging, but may also result in many diseases (rheumatoid osteoarthritis, atherosclerosis, asthma, cataract, Alzheimer’s disease, Parkinson’s disease, multiple sclerosis and many cancers) (Phaniendra et al., 2015). Due to oxygen and nitrogen being among the primary building elements of human organisms, and because of the many redox reactions in which these two elements are involved, this article will focus on their reactive forms - reactive oxygen/nitrogen species (RONS).

RNS/RNO sensitive biomaterials can be used as a RONS regulating drug delivery systems due to several advantages resulting from their structure. The advantages that make RNS/RNO sensitive biomaterials attractive include biodegradability, biocompatibility, improved circulation and reduced toxicity (Joshi-Barr et al., 2014). Biomaterials often elicit a strong inflammatory response *in vivo* due to an immune response to their presence which is likely to cause higher levels of oxidative stress. Oxidative stress using drug-containing nanoparticles is yet to be explored. Oxidative stress can be

managed during the implantation of biomaterials to promote their integration. Today, the most common approach to dealing with oxidative stress is to use antioxidants. Biomaterials such as collagen and elastin are natural polymers and exhibit improved biological properties such as adhesion and proliferation compared to *in vitro* synthetic materials. Factors influencing this response include manufacturing processes, rate of material degradation, and the presence of antigens (Troy et al., 2021). Extracellular matrix (ECM) degradation may also induce the formation of oxidants indirectly as ECM fragments have been shown to promote immune cell recruitment. However, some natural polymers used in scaffolds can break down into products that act as antioxidants. ECM scaffolds are typically processed by decellularization and chemical cross-linking methods to remove or mask antigenic epitopes, DNA, and Damage Associated Molecular Pattern (DAMP). Inadequate removal of DAMP from biological materials can lead to oxidative stress when released *in vivo* (Aamodt and Grainger, 2016). Moreover, for example, glycosaminoglycans (such as chondroitin sulfate and hyaluronic acid) have been identified as antioxidants capable of reducing free radicals, protecting both cells and materials from ROS damage (Shafiq et al., 2021).

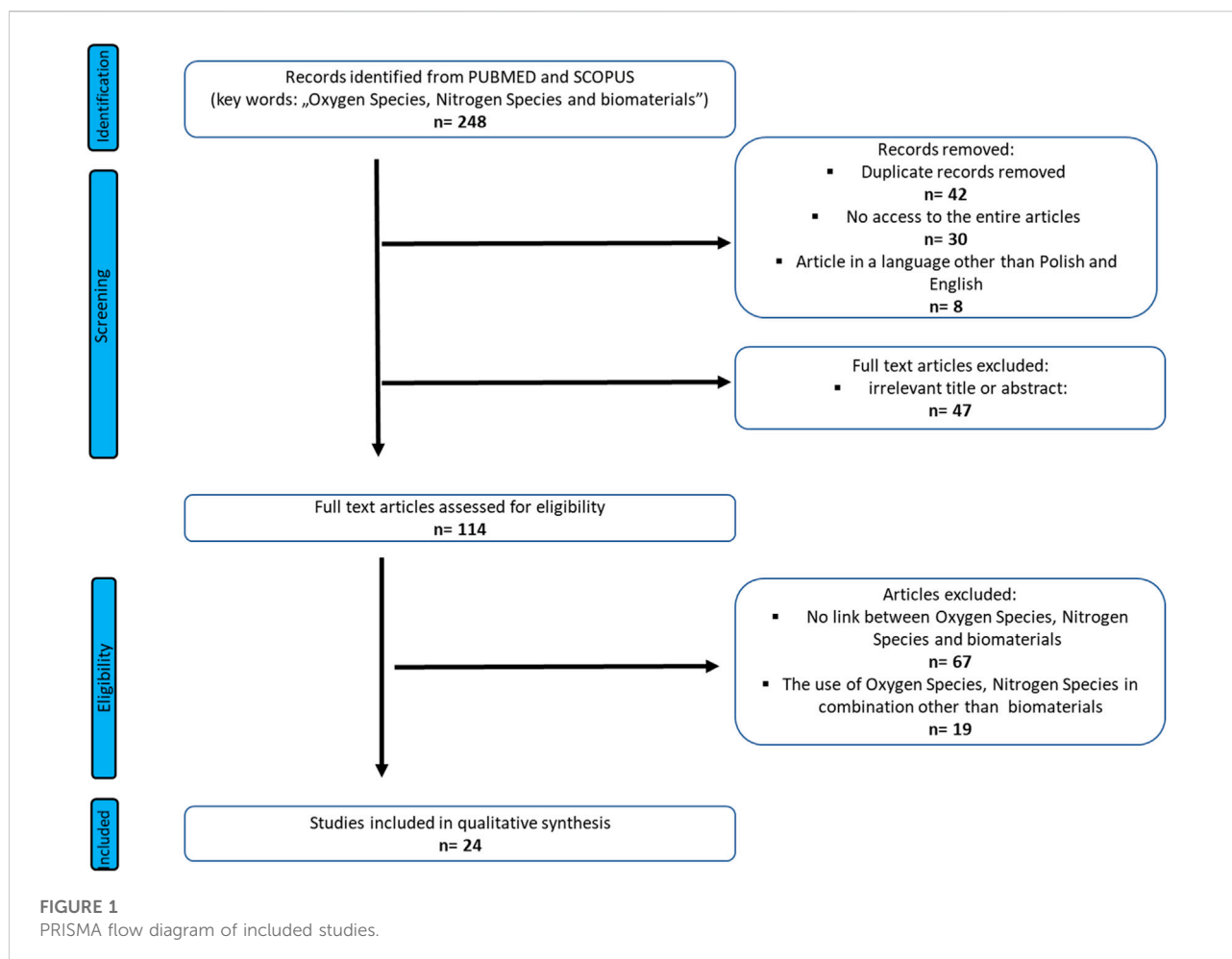
Search strategy and select criteria

A search focused on the Oxygen Species, Nitrogen Species and biomaterials was done on Pub-med, and Scopus from inception (1973) to July 2022. The study was performed based on the Preferred Reporting Items for Systematic Reviews and Meta-Analyses (PRISMA) guidelines (Page et al., 2021). The search term included was as follows: “Oxygen Species, Nitrogen Species and biomaterials”. Three authors undertook the task of identification data. Any discrepancies between the reviewers were resolved by the third author. The authors of the reviews worked on the basis of an agreed scheme, distinguishing: title, language of the work, abstract and access to the entire article. Duplicate records were removed first.

Full-text and accessible articles were further analyzed. In order to minimize the selection bias, the inclusion and exclusion criteria were established as follows (Figure 1):

Inclusion criteria

- Oxygen Species and biomaterials;
- Nitrogen Species and biomaterials;
- Oxygen Species, Nitrogen Species and biomaterials Regulating Drug Delivery Systems in Medicine, have been included in the review;
- both Oxygen Species, Nitrogen Species and biomaterials were included in the review



Exclusion criteria

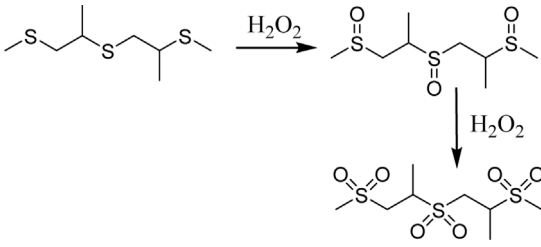
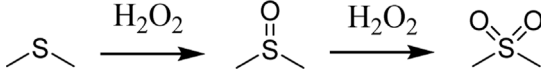
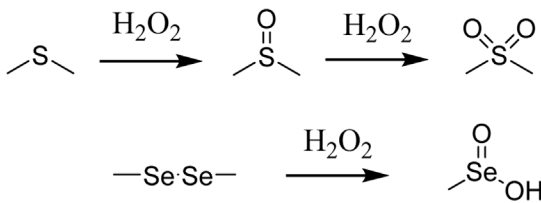
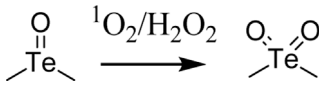
- no analysis of the relationship between Oxygen Species, Nitrogen Species and biomaterials
- no analysis of the relationship between Oxygen Species, Nitrogen Species and biomaterials

Reactive oxygen species

Reactive oxygen species (ROS) are oxygen-containing molecules with one or more unpaired electrons. Due to human organisms respiring aerobically, most of these free radicals are formed in mitochondria, as molecular oxygen is reduced during electron transport in the electron transport chain (ETC). The central ROS is superoxide anion ($O_2^{\bullet-}$); although not strongly reactive, it is a precursor for the formation of other, stronger reactive forms and may propagate other oxidative chain reactions. Due to such dangerous potential, superoxide dismutase (SOD) immediately converts it into hydrogen peroxide (H_2O_2), a less toxic non-radical (Turrens, 2003). It

still may reverse back to superoxide anion and in combination with the fact that hydrogen peroxide is an uncharged molecule and may leak from mitochondria into cytoplasm, it is also crucial to rapidly neutralize it. Thus, enzymes catalase (CAT) and glutathione peroxidase (GSH-Px) further dismutate hydrogen peroxide into water (H_2O) (Bienert et al., 2006). Along the way, superoxide anion may reduce some transition metals, particularly Fe^{3+} into Fe^{2+} , which in turn may react with hydrogen peroxide to form hydroxyl radical (OH^{\bullet}) (Vidrio et al., 2008). Hydroxyl radical is amongst the most reactive and deleterious free radicals, as it causes DNA/RNA damage, protein modification and lipid peroxidation, thus being the main contributor to oxidative stress (Scarcello et al., 2020). Aside from mitochondria, peroxisomes are also associated with substantial ROS production and neutralization, due to the presence of many oxygenases, superoxide dismutases, and catalase (Sandalo et al., 2013). Despite such noxious nature, stable and controlled nanomolecular concentrations of ROS have certain physiologic functions. Although it is not clear to what extent they are useful under normal cellular conditions, cellular stress induces ROS production and their utilization as signaling transducers

TABLE 1 Main ROS-responsive solubility switch DDSs (Yao et al., 2019).

ROS-responsive linker	Chemical structure and oxidation	Material format	Ref
Poly(propylene sulfide)		Polymeric micelles	Gupta et al. (2012)
Thioether		Polymeric NPs	Gong et al. (2019)
Selenium-containing polymers		Polymeric aggregates Polymeric micelles	Ma et al. (2010) Ji et al. (2013)
Tellurium-containing polymers		Spherical aggregates	Wang et al. (2015)

(Schieber and Chandel, 2014). The main physiological functions of ROS include: 1) direct antimicrobial activity against pathogens in macrophages and neutrophils, 2) cytokine-activated signaling in many pro-inflammatory pathways, primarily through induction of MAPK, STAT1, STAT6 and NFκB, 3) post-translational regulation of many proteins and enzymes through thiol group oxidation, 4) p53-controlled apoptosis, 5) transcriptional adaptation to hypoxia, through stabilization of HIFs (Johnson et al., 1996; Movafagh et al., 2015; Rendra et al., 2019; Finelli, 2020; Herb and Schramm, 2021). ROS responsive polymers are ideal candidates for the development of stimuli-responsive biomaterials for target therapies. Among different ROS-responsive polymers, those containing thioether groups are widely investigated in the biomedical field due to their hydrophobic to hydrophilic phase transition under oxidative conditions (Criado-Gonzalez and Mecerreyes, 2022). ROS play important roles in cell signaling pathways, while increased production of ROS may disrupt cellular homeostasis, giving rise to oxidative stress and a series of diseases. Utilizing these cell-generated species as triggers for selective tuning polymer structures and properties represents a promising methodology

for disease diagnosis and treatment (Xu et al., 2016). ROS-responsive polymer carriers allow the targeted delivery of drugs, reduce toxicity and side effects on normal cells, and control the release of drugs, which are all advantages compared with traditional small-molecule chemotherapy agents (Gao and Xiong, 2021). Polyoxalate (POx) and copolyoxalate (CPOx) smart polymers are topics of interest the field of inflammation. This is due to their drug delivery ability and their potential to target reactive ROS and to accommodate small molecules such as curcumin, vanilline, and p-Hydroxybenzyl alcohol (Yao et al., 2019). Recently, ROS-responsive biomaterials have been identified as a type of promising therapeutic substance to alleviate oxidative stress in tissue microenvironments, and for use as a vehicle triggered by inflammatory diseases to realize drug release under physiological oxidative microenvironments. The various applications of ROS-responsive biomaterials in tissue regeneration and disease therapy, such as cardiovascular diseases, osteoarthritis, chronic diabetic wounds, inflammatory bowel disease and other inflammatory diseases, are summarized (Swami Vetha et al., 2021).

TABLE 2 Main ROS-induced degradation DDSs (Yao et al., 2019).

ROS-responsive linker	Chemical structure and oxidation	Material format	Ref
Poly(thioether)		Polymeric NPs Polymeric scaffolds	Wilson et al. (2010) Martin et al. (2014)
Arylboric ester- containing polymers		Polymeric NPs Polymeric NPs	de Gracia Lux et al. (2012)
Poly(proline)		Polymeric scaffolds	Yu et al. (2011)

Reactive nitrogen species

Reactive nitrogen species (RNS) are all derived from nitric oxide ($\bullet\text{NO}$) reacting with superoxide anion ($\text{O}_2^{\bullet-}$) (Ronzio, 2020). Nitric oxide is a free radical itself and is produced through enzymatic activity of three isoforms of NO synthase (NOS), namely endothelial NOS (eNOS), neuronal NOS (nNOS), and inducible NOS (iNOS) (Costa et al., 2016). Although not a potent radical, nitric oxide may combine with superoxide anion to produce peroxynitrite (ONOO^-), which aside to hydroxyl radical, is regarded as the second most reactive radical. Due to its powerful oxidizing and nitrating character, peroxynitrite may attack proteins and DNA/RNA, causing alterations to their functions and subsequent cellular damage (Islam et al., 2015). Additionally, nitric oxide may combine with molecular oxygen to form dinitrogen trioxide (N_2O_3), which in turn may nitrosate thiols of amino acids, also leading to loss of protein functionality (Jour'dheuil et al., 2003). Similarly, to ROS, RNS also display certain physiological functions when kept within safe concentrations. These functions include: 1) vasodilation produced by nitric oxide through activation of soluble

guanylyl cyclase (sGC) and second messenger-mediated decrease of Ca^{2+} release, 2) direct antimicrobial activity against pathogens in macrophages and neutrophils, 3) signaling in many pro-inflammatory pathways, primarily through activation of TLR4 and NF- κB , 4) post-translational regulation of many proteins and enzymes, through thiol group oxidation, nitration and nitrosation, 5) apoptosis by inducing NF- κB , BAX and BAK, as well as activating caspases-3 and -9, 6) additionally, nitric oxide prevents platelet aggregation and leukocyte adhesion to endothelial walls (Ryan et al., 2004; Snyder et al., 2009; Rathnasamy et al., 2014; Gao et al., 2018; Kollau et al., 2018; Fang and Vázquez-Torres, 2019). These materials utilize polymers, nanoparticles (NPs), or gel systems.

Reactive oxygen species-sensitive drug delivery systems

Since ROS and RNS are usually overproduced in inflamed tissues and tumors, researchers have been inspired to harness this potential for designing site- and stimuli-specific drug delivery

systems (DDSs). Thus, two main types of DDSs can be distinguished: (1) DDSs with ROS-mediated solubility switch, and (2) DDSs with ROS-mediated degradation (Tao and He, 2018). Reactive oxygen species-mediated solubility switch DDSs (1) base their mode of action on the change in the solubility of the polymer in oxidative microenvironments. Upon oxidation of functional groups (amphiphilic, typically containing thioether, selenide, or tellurium), side chains transition from hydrophobic to hydrophilic, and the carried drug is released (Gao and Xiong, 2021). The main solubility switch DDSs are presented in Table 1.

The first DDSs of this type was developed by Hubbell *et al.* in 2004. By means of anionic ring opening polymerization, a triblock ABA copolymer was prepared, with hydrophilic poly(ethylene glycol) (PEG) as A block and hydrophobic poly(propylene sulfide) PPS as B block. This PEG-b-PPS copolymer was found to self-assemble into stable U-shaped vesicles in aqueous solution through hydrophilic/hydrophobic interactions. Upon treatment with 10% H₂O₂, hydrophobic sulfide is oxidized to more hydrophilic sulfoxide or sulfone, leading to destabilization of the vesicle and release of the carried agent (Napoli *et al.*, 2004). However, PPS is not responsive to superoxide and thus Tirelli *et al.* have conjugated SOD with PEG-b-PPS copolymer. That way, PPS-PEG-SOD micelles can scavenge and react with both superoxide and hydrogen peroxide (Hu and Tirelli, 2012). For direct measure of applicability in drug delivery, Cheng *et al.* designed free-blockage mesoporous silica nanocarriers with hydrophobic phenyl sulfide groups (MSNs-PhS). As the phenyl sulfide groups oxidized to phenyl sulfoxide or phenyl sulfone, wettability of the nanopores increased and doxorubicin (DOX) was gradually released. This study revealed great potential of MSNs-PhS for selective chemotherapy, as DOX was released human breast adenocarcinoma (MCF-7) cells with high levels of ROS, and not in normal human umbilical vein endothelial cells (HUVECs) with low ROS levels (Cheng *et al.*, 2017). In 2020, Ford *et al.* designed a diblock copolymer for localized release of loaded diflunisal, as therapeutic approach to combating osteomyelitis caused by *Staphylococcus aureus*. Through RAFT polymerization the PPS₁₃₅-b-p(Cy7₁-ran-DMA₁₄₉) nanoparticles were produced, where DMA unit composed the hydrophilic corona and the PPS unit constituted hydrophobic ROS-responsive core in close association with loaded drug. Upon parenteral administration of nanoparticles with diflunisal into mice subjected to osteomyelitis, polymer preferential distributed to infected femurs. There, owing to the inflamed milieu, PPS moiety underwent ROS-mediated oxidation, which resulted in change of core character from hydrophobic to hydrophilic and final release of diflunisal (Ford *et al.*, 2021).

ROS-mediated degradation DDSs (2) base their mode of action on polymer chain breakdown induced by oxidative species and subsequent drug release. Functional groups serving as linkers are characterized by selective oxidation by ROS and rapid

cleavage. Importantly, the generated byproducts are easily metabolized (Wilson *et al.*, 2010). The main degradable DDSs are presented in Table 2.

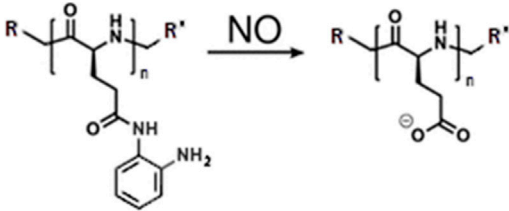
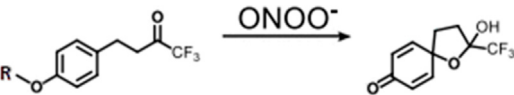
The most notable DDSs of this kind are polymers utilizing thioketal groups as linkers, since they show high sensitivity to different ROS species, including H₂O₂, •OH, and O₂^{•-} (Shim and Xia, 2013). In 2010 Wilson *et al.* developed poly(1,4-phenyleneacetone dimethylene thioketal) (PPADT) through step-growth polymerization, intended for treatment of gastrointestinal inflammatory diseases. Loaded with tumor necrosis factor-α (TNFα)-siRNA, these nanoparticles were administered orally and showed stability in acidic and basic environments, as well as resistance to protease-catalyzed degradation. Those properties in combination with sensitivity to ROS allowed for relatively precise delivery of carried agent into the inflamed intestinal tissue (Wilson *et al.*, 2010). As determined by Pu *et al.* in a different study, a similar PPADT polymer used for anti-inflammatory therapy responded to H₂O₂ in concentration as low as 1 mM, releasing 50% of the drug within 4 h (Pu *et al.*, 2014).

Discussion

Overproduction of RONS in tissue microenvironments is the main factor impeding normal healing and regeneration. Inflammatory responses induce DNA/protein damage and cell apoptosis, as well as hinder endogenous stem cells and macrophages.

Zhao *et al.* (2020) designed a hydrogel with ability to scavenge ROS in difficult-to-heal diabetic wounds with coexisting bacterial infections that further impede regeneration. First, the ROS-responsive linker, N1-(4-boronobenzyl)-N3-(4-boronophenyl)-N1,N1,N3,N3-tetramethylpropane-1,3-diaminium (TPA), was synthesized by quaternization reaction and then mixed with poly(vinyl alcohol) (PVA). The created PVA-TPA hydrogel showed ROS-scavenging ability; testing, where the hydrogel was incubated with H₂O₂ and titanil sulfate as a H₂O₂-responsive probe, showed elimination of 65% of H₂O₂ within 1 h and nearly 100% within 24 h. Similar results were demonstrated *in vitro* testing, where the largest reduction of intracellular ROS levels was observed in hydrogel group combined with human umbilical vein endothelial cells (HUVECs) previously incubated with H₂O₂. For direct measure of healing properties, *in vivo* testing was conducted in mouse animal models. Inflammation was induced by injecting lipopolysaccharide (LPS), a cell wall component of Gram-negative bacteria, into mouse back skin. Photoacoustic (PA) imaging with the H₂O₂-specific Lipo@HRP&ABTS nanoprobe, showed that hydrogel could continuously decrease the ROS levels triggered by LPS. For assessment of wound closure-promoting abilities, dorsal wounds were created in mouse back skin, which were later treated with PVA-TPA hydrogel, and TPA and PVA

TABLE 3 Main RNS-responsive DDSs (Zhao et al., 2021).

RNS-responsive linker	Chemical structure and oxidation	Material format	Ref
o-phenylenediamine		Liposomes Nanofilaments Micelles	Wang et al. (2019) Liu et al. (2020) Lu et al. (2020)
0 trifluoromethyl ketone		Polymersomes	Zhang et al. (2016)

separately. At day 8, 60% wound closure was noted in wounds treated with hydrogel, as opposed to closure of only 28% and 33% in TPA and PVA groups respectively. Additionally, aiding to promotion of wound healing, PVA-TPA hydrogel was found to reduce pro-inflammatory cytokines (interleukin-6 (IL-6), tumor necrosis factor (TNF- α), interleukin-1 β (IL-1 β), interleukin-23 (IL-23) and monocyte chemotactic protein 1 (MCP-1)), increase the percent of M2 phenotype macrophages, and stimulate angiogenesis and collagen synthesis around the wound.

In an even more complex and effective approach to tissue repair, stem cells are delivered to the site of damage. Particularly, undifferentiated mesenchymal stem cells (MSCs) exhibit high potential in cell therapies, as they possess immunomodulatory functions through the secretion of paracrine factors that can positively direct tissue regeneration. Unfortunately, the main limiting factor in utility of this type of therapy is the poor survival of delivered cells due to the host's immune response and production of high levels of RONS. Thus, Dollinger et al. developed an ABC triblock polymeric hydrogel, with poly(propylene sulfide) (PPS) as block A, N,N-dimethyl acrylamide (PDMA) as block B, and N-isopropylacrylamide (PNIPAAm) as block C (PPS-block-PDMA-block-PNIPAAm, PDN). Forming the core of the micelle, PPS enabled drug loading and its controlled ROS-mediated release. PDMA stabilized the hydrophilic side-chains and prevented syneresis of the assembled gels, while PNIPAAm provided for thermal gelation properties. Moreover, because delivered cells often suffer from poor adhesion due to lack of reinforcing structures, type 1 collagen (T1C) was added to provide for cellular adhesion motifs. *In vitro* testing on NIH 3T3 mouse fibroblasts grown in tissue culture plates, showed that PDN hydrogels scavenge H₂O₂. Additionally, fibroblasts suspended within PDN hydrogel + collagen composite were injected onto a heated surface and remained exclusively associated with the gelled hydrogel and viable for at least 24 h. To assess protective abilities against ROS-induced toxicity, hMSCs

were encapsulated in PDN hydrogel, hydrogel without PPS (thus, no ROS-scavenging ability) and collagen gel, all of which were then cultured for 24 h and then treated with H₂O₂. In the PDN group, no significant change in the number of viable cells was noted, as opposed to considerable decrease in two other groups, and the viability was maintained at 80% or higher for at least 6 days in the presence of cytotoxic H₂O₂ concentrations. Such results confirm that PDN hydrogel possesses cyto-protective properties against ROS-induced apoptosis and may be a useful agent in increasing the feasibility of cell therapies (Dollinger et al., 2017). More recently, Yi et al. (2021) synthesized a modified liposome for localized NIR irradiation-triggered DOX release. In this polymer, boronic acid was used as ROS-sensitive moiety and conjugated with DOX and indocyanine green (ICG). Then encapsulated into PEG-modified liposomes, yielding Lipo/pB-DOX/ICG. *In vivo* testing where Lipo/pB-DOX/ICG was injected into mice with MDA-MB-231 tumors showed accumulated of liposomes at the tumor site within 24 h. Under 808 nm laser irradiation, ICG generated ROS which selectively cleaved boronate prodrug, releasing DOX.

Reactive nitrogen species sensitive drug delivery systems

Similarly to ROS-DDS, polymeric systems have been designed, where the mechanism of loaded drug release was driven by NO- or ONOO⁻-mediated oxidation of RNS-sensitive moiety and subsequent solubility change or degradation. Table 3. Shows main RNS-DDS.

In the past 2 decades, o-phenylenediamine has been evidenced as a highly selective and efficient reductor group of NO in the presence of O₂, owing to its electron rich character (Plater et al., 2001). Since then, many fluorescent probes containing this moiety have been in common for *in vitro* and *in vivo* NO detection. A significant development was done in

2014 by Hu et al. who designed a thermoresponsive copolymers which exhibited considerable solubility change, with subsequent self-assembly into spherical micelles and fluorescence upon exposure to mild levels of NO (0–48 μM). Such self-assembly was attributed to NO-triggered formation of amide-substituted benzotriazole intermediates and urea-functionalized benzotriazole derivatives, with concomitant change in lower critical solution temperature (LCST). Later in 2019, Wang et al. produced a liposome with o-phenylenediamine-containing lipid embedded into its phospholipid bilayer, which further encapsulated L-arginine (L-Arg)/DOX-loaded gold-copper sulfide yolk-shell nanoparticles ($_{\text{AD}}\text{Au@CuS}$ YSNPs) to form $_{\text{ADL}}\text{Au@CuS}$ YSNPs (Wang et al., 2019). Using 808 nm NIR laser irradiation, ROS generation was induced, which then drove conversion of L-arginine into NO. Timed release of DOX was achieved by progressive regional destabilization of phospholipid bilayer by NO and molecular scaffold limit, allowing for final DOX release when liposome structure was destabilized severely enough. *In vivo* testing on mice elucidated this programmable liposome as a viable target therapy of DOX-resistant MCF-7/ADR cells and possible treatment option for other multidrug resistance (MDR) cancers. Next, Liu et al. exploited the nature of o-phenylenediamine by developing a block polymer poly(ethylene oxide)-b-poly(o-phenylenediamine L-glutamate) (PEO-b-PEOPA) through ring-opening polymerization (Liu et al., 2020). The obtained polypeptide chains exhibited self-assembly behavior, forming nanofilaments, which could then be cleaved by a biologically relevant level of NO into comparably small disassemblies within 3 h. Measurement of nanocarrier capacity and load release showed most of PEO-b-PEOPA efficiently releasing Rhodamine 6G under 40 μM (2.0 equiv.) of NO stimulus within 30–90 min. Additionally, Lu et al. prepared a system for targeted antibiotic delivery, by conjugating levofloxacin (LF) and hyaluronic acid (HA) via NO-sensitive o-phenylenediamine as linker, yielding HA-NO-LF nanomicelles (Lu et al., 2020). *In vitro* drug release testing demonstrated total drug release efficiency of nearly 70% achieved within 6–15 h in the presence of NO. Evidenced to easily enter macrophages via CD44 mediated endocytosis, therapeutic efficacy of these micelles was then tested *in vivo* in pneumonia-induced mice infected with *Staphylococcus aureus*, which showed greatest bactericidal effect in the group with HA-NO-LF and NO-stimulus present. Growing research into NO as an endogenous biosignal for RNS-DDSs has also brought focus onto ONOO[−] as a possible exploitable trigger and prompted search for a ONOO[−]-selective linker group. However, number of studies reporting development of ONOO[−]-specific nanoparticles seems to be currently limited. So far, the only notable invention in this category has been done by Zhang et al. (2016) in 2016, who utilized ONOO[−]-selective and specific cleavage of trifluoromethyl ketone (TFK) moiety and developed a block polymer poly(ethylene oxide)-b-PMATFK (PEO-b-PMATFK).

In aqueous solution, this copolymer exhibited self-assembly into vesicular polymersomes, which then disassembled when subjected to ONOO[−] (35 μM , 5 equiv). Additionally, this disassembly ability was dose-dependent, allowing for regulation of the vesicle dissociation rates for desirable drug delivery regimens by modifying ONOO[−]-concentration. For drug release capacity testing, PEO-b-PMATFK was loaded with vasodilator hydrochlorothiazide, which then revealed great drug delivery efficiency under ONOO[−]-stimulus and near no release under other radical stimuli. With advances made in the field of sensitive and selective biomimetic nanomaterials for RONS-regulation, more attention has been paid to direct reduction of radicals implicated to cause pathology. As for RNS, newly devised polymers are often designed to directly scavenge and remove nitrogenous radicals in diseases characterized by their overproduction, particularly rheumatoid arthritis (RA). Similarly to ROS-scavenging materials, these RNS-reducing composites are often in the form of hydrogels of homologous nature (Plater et al., 2001). In 2019, Yeo et al. developed a NO-scavenging nanogel (NO-Scv gel) for alternative treatment of RA (Yeo et al., 2019). Aforementioned o-phenylenediamine group was incorporated, forming a NO-cleavable cross-linker (NOCCL) which was polymerized with acrylamide into a hydrogel. Scavenging ability is realized upon NOCCL cleavage and consumption of NO when exposed to this molecule. *In vitro* testing employing concentration range of 0–2 mg/ml evinced NO-Scv gel as having good biocompatibility and NO-scavenging capacity with low cytotoxicity. *In vivo* testing in collagen-induced arthritis (CIA) mouse model mice was performed with intra-articular injections of researched materials after immunization. 25 mg/ml of NO-Scv gel injections presented with better therapeutic outcome than 0.32 mg/ml of dexamethasone (DEXA), more efficiently quenching of NO levels in tissue and resulting in better RA onset suppression. NOCCL functionality was further employed by Kim et al. who synthesized a more sophisticated NO-scavenging and sequential drug-releasing (M-NO) gel system for the combinatorial treatment of RA (Wilson et al., 2010). Providing for rapid gelation *in situ* via a “click” cycloaddition reaction, dialkyne-functionalized-NOCCL (DA-NOCCL, *N,N*-(2-amino-1,4-phenylene)dipentyn-4-amide) linker has been synthesized. Next, DA-NOCCL was incorporated into an azide-functionalized hyaluronic acid backbone (HA-N₃) and then cross-linked with azide-functionalized PEG-PLA block copolymer (PLA-*b*-PEG-N₃). Polymerization with these units endows biocompatibility, lubricating self-healing character and drug loading capacity. Moreover, M-NO gel presented with on-demand dual-stage drug-releasing pattern, allowing for combined release of hydrophilic and hydrophobic together, further tunable by NO concentration. *In vitro* evaluation confirmed M-NO gel as being low cytotoxic and efficient NO-scavenger with resultant decrease in pro-inflammatory cytokine levels in LPS-stimulated macrophages using 50 μl of gel. *In vivo*

investigation done on immunized CIA mice that received intra-articular 20 μ l sample injections revealed that M-NO gel led to no significant inflammation, damage nor toxicity. Finally, as compared to other control groups, M-NO gel loaded with DEXA exhibited greatest slowing of disease progression most efficiently alleviated the arthritis symptoms in animal models (Kim et al., 2021). ROS/RNS responsive materials for implant are often biointerfaces composed of polymer antioxidants eliminate excessive ROS at the interface between living tissues and materials, and do not disturb regulated redox balance inside cells, thus eliminating unexpected cell responses, such as inflammation and dysfunction (Ikeda and Nagasaki, 2018). ROS/RNS play a fundamental role in response after the implant introduction and can influence its success. A new smart biomaterials and molecular medicine for the oxidative stress modulation in a programmable way, by the use of ROS responsive materials or by the targeting of selective molecular pathways involved in ROS generation was presented (Cerqueni et al., 2021). Moreover, neutrophil interaction with rough-hydrophilic surfaces seems to produce less proinflammatory cytokines and ROS when compared to naive smooth and rough titanium surfaces. Neutrophil responses were assessed based on adhesion, cell number, surface coverage, cell structure, cytokine secretion, ROS production, neutrophil activation, receptor expression, and neutrophil extracellular traps (NETs) release (Elangovan et al., 2022). Highly reactive free radicals, mainly ROS and RNS, damage the cell membrane, proteins, and DNA, which triggers a self-propagating inflammatory cascade of degenerative events. Dysfunctional mitochondria under oxidative stress conditions are considered a key mediator in progressive neurodegeneration. Exogenous delivery of antioxidants holds promise to alleviate oxidative stress to regain the redox balance. In this regard, natural and synthetic antioxidants have been evaluated (Ashok et al., 2022). RONS sensitive nanoparticles as a delivery system accomplish the site-specific action at the therapeutically optimal level of drug. A recent example is the development of metal chelators have also been combined with antioxidants in some advanced polymeric RONS sensitive biomaterials (Ashok et al., 2022). Ceramic and bioglasses are the main RONS sensitive biomaterials exploiting metallic elements to lower oxidative stress levels. Zinc for instance, may protect cells from oxidative protein and DNA damage as well as lipid peroxidation and improved the oxidative stress balance (Ashok et al., 2022). The appropriate delivery of the therapeutic agents, in relevant concentrations that respond to oxidative stress variations, will therefore be one the main challenges for the future development of these strategies. L-3,4-dihydroxyphenylalanine (L-dopa) was evaluated using a ROS sensitive dye, 2',7'-dichlorodihydrofluorescein (DCFH) by Luna-Velasco and coworkers (Gulcin and Alwasel, 2022). The same group used CeO₂, Fe₂O₃ and Fe(0) nanoparticles to enhance ROS production during the autoxidation of L-dopa by more than four-fold in reactions that were dependent on O₂ [71]. RONS

sensitive nanoparticles they could indirectly initiate the production of ROS that damage microbial cell components and viruses. Some like silver nanoparticles have broad spectrum antibacterial activity while others like cadmium containing QDs shows both antibacterial as well as antiprotozoal activity (Luna-Velasco et al., 2011). The potential toxicity of inorganic nanoparticles due to their low biodegradability, background signals interference and treatment side effects limit their clinical application. Therefore, developing biodegradable and intelligent nanoparticles are beneficial to avoid excessive metal ions deposition, specific tumor imaging and treatment (Reshma et al., 2017). Controlled RONS production was demonstrated in human mesenchymal stem cells through 1) production of nanoparticles functionalized with varying percentages of Zn(II) porphyrin and 2) modulating the number of doses of excitation light to internalized nanoparticles (Yang et al., 2020).

In this review notable developments in the field of RONS-responsive biomaterials from the past decade have been outlined, with focus on Drug Delivery Systems and radical-scavenging hydrogels. Special attention was paid to providing information on main chemical functionalities in each group of biomaterials and relating it to prominent advancements and discoveries in the field. Rapidly evolving discipline of nanomedicine with growing knowledge about reactive species, accompanied by technological progress with development of novel methods and approaches to researching and designing these molecules, creates an promising outlook for the future of RONS and numerous other materials yet to be devised. Particular potential lies in ROS- and RNS-polymers, owing to the action selectivity and sensitivity of many of those nanostructures. Supplied by wide range and variability in number of different RONS-sensitive linkers for varying molecules, it may seem like the possibilities for harnessing RONS potential for biomedical applications is infinite. However, certain challenges and limitations in the science of RONS nanochemistry can be delineated. Foremost obstacle is still insufficient knowledge about reactive species. Specifically, their exact molecular levels and interactions in different cells and tissue microenvironments remain unclear. Especially in pathological states such reliable determinations are difficult, owing to internal body milieu being a high dynamic system. Another significant issue seems result from the nature of RONS themselves. Being potent electrophiles with short half-life and high reactivity, reactive species are short-lived, minute molecules. It is why sensible generation and manipulation of RONS and their derivatives require proper storage and control of utilized materials. Finally, most pending direct problem in development of quality RONS-biomaterials is the design rationale. Virtually all probes and polymers should be specific and selective, which calls for generation of controlled, standardized and systematized materials. In addition, careful determination of biocompatibility, bioavailability, biodistribution, pharmacodynamics and

pharmacokinetics, as well as toxicity. Presented challenges are significant and have to be addressed as part of individual work of researchers, as well as joint efforts of scientific communities contributing to the field. Despite abovementioned hurdles, work invested into developing RONS-regulating materials for biomedical applications will most likely continue to expand and gain in importance.

Conclusion

Under normal physiological concentrations, reactive oxygen/nitrogen species (RONS) play a significant role in some physiological processes such as signal transduction. However, disturbances in redox balance lead to induction of oxidative stress, which in turn is associated with development of various diseases and injuries. Knowing the link between oxidative species and pathologies prompted research in the direction of developing RONS-responsive biomaterials for biomedical applications. Amongst many, some of these materials include ROS-sensitive polymers for delivery of drugs (Drug Delivery Systems, DDSs), as well as ROS-scavenging hydrogels for promotion of tissue regeneration.

References

- Aamodt, J. M., and Grainger, D. W. (2016). Extracellular matrix-based biomaterial scaffolds and the host response. *Biomaterials* 86, 68–82. doi:10.1016/j.biomaterials.2016.02.003
- Ashok, A., Andrabi, S. S., Mansoor, S., Kuang, Y., Kwon, B. K., and Labhasetwar, V. (2022). Antioxidant therapy in oxidative stress-induced neurodegenerative diseases: Role of nanoparticle-based drug delivery systems in clinical translation. *Antioxidants (Basel)* 11 (2), 408. doi:10.3390/antiox11020408
- Bienert, G. P., Schjoerring, J. K., and Jahn, T. P. (2006). Membrane transport of hydrogen peroxide. *Biochimica Biophysica Acta - Biomembr.* 1758 (8), 994–1003. doi:10.1016/j.bbamem.2006.02.015
- Birben, E., Sahiner, U. M., Sackesen, C., Erzurum, S., and Kalayci, O. (2012). Oxidative stress and antioxidant defense. *World Allergy Organ. J.* 5 (1), 9–19. doi:10.1097/wox.0b013e3182439613
- Burtenshaw, D., Kitching, M., Redmond, E. M., Megson, I. L., and Cahill, P. A. (2019). Reactive oxygen species (ROS), intimal thickening, and subclinical atherosclerotic disease. *Front. Cardiovasc. Med.* 6, 89. doi:10.3389/fcvm.2019.00089
- Cerqueni, G., Scalzone, A., Licini, C., Gentile, P., and Mattioli-Belmonte, M. (2021). Insights into oxidative stress in bone tissue and novel challenges for biomaterials into oxidative stress in bone tissue and novel challenges for biomaterials. *Mater. Sci. Eng. C* 130, 112433. doi:10.1016/j.msec.2021.112433
- Cheng, Y., Jiao, X., Xu, T., Wang, W., Cao, Y., Wen, Y., et al. (2017). Free-blockage mesoporous anticancer nanoparticles based on ROS-responsive wetting behavior of nanopores. *Small* 13 (40), 1701942. doi:10.1002/smll.201701942
- Costa, E. D., Rezende, B. A., Cortes, S. F., and Lemos, V. S. (2016). Neuronal nitric oxide synthase in vascular physiology and diseases. *Front. Physiol.* 7, 206. doi:10.3389/fphys.2016.00206
- Criado-Gonzalez, M., and Mecerreyes, D. (2022). Thioether-based ROS responsive polymers for biomedical applications. *J. Mat. Chem. B* 2022, doi:10.1039/d2tb00615d
- de Gracia Lux, C., Joshi-Barr, S., Nguyen, T., Mahmoud, E., Schopf, E., Fomina, N., et al. (2012). Biocompatible polymeric nanoparticles degrade and release cargo in response to biologically relevant levels of hydrogen peroxide. *J. Am. Chem. Soc.* 134 (38), 15758–15764. doi:10.1021/ja303372u
- Dollinger, B. R., Gupta, M. K., Martin, J. R., and Duvall, C. L. (2017). Reactive oxygen species shielding hydrogel for the delivery of adherent and nonadherent therapeutic cell Types. *Tissue Eng. Part A* 23 (19–20), 1120–1131. doi:10.1089/ten.tea.2016.0495
- Elangovan, G., Mello-Neto, J. M., Tadakamadla, S. K., Reher, P., and Figueredo, C. M. S. (2022). A systematic review on neutrophils interactions with titanium and zirconia surfaces: Evidence from *in vitro* studies. surfaces: Evidence from *in vitro* studies. *Clin. Exp. Dent. Res.* 2022. Epub ahead of print. PMID: 35535662. doi:10.1002/cre2.582
- Fang, F. C., and Vázquez-Torres, A. (2019). Reactive nitrogen species in host-bacterial interactions. *Curr. Opin. Immunol.* 60, 96–102. doi:10.1016/j.coi.2019.05.008
- Finelli, M. J. (2020). Redox post-translational modifications of protein thiols in brain aging and neurodegenerative conditions-focus on S-nitrosation. *Front. Aging Neurosci.* 12, 254. doi:10.3389/fnagi.2020.00254
- Ford, C. A., Spoonmore, T. J., Gupta, M. K., Duvall, C. L., Guelcher, S. A., and Cassat, J. E. (2021). Diflunisal-loaded poly(propylene sulfide) nanoparticles decrease *S. aureus*-mediated bone destruction during osteomyelitis. *J. Orthop. Res.* 39 (2), 426–437. doi:10.1002/jor.24948
- Gao, F., Lucke-Wold, B. P., Li, X., Logsdon, A. F., Xu, L. C., Xu, S., et al. (2018). Reduction of endothelial nitric oxide increases the adhesiveness of constitutive endothelial membrane ICAM-1 through src-mediated phosphorylation. *Front. Physiol.* 8, 1124. doi:10.3389/fphys.2017.01124
- Gao, F., and Xiong, Z. (2021). Reactive oxygen species responsive polymers for drug delivery systems. *Front. Chem.* 9, 649048. doi:10.3389/fchem.2021.649048
- Gong, Y. H., Shu, M., Xie, J. H., Zhang, C., Cao, Z., Jiang, Z. z., et al. (2019). Enzymatic synthesis of PEG-poly(amine-co-thioether esters) as highly efficient pH and ROS dual-responsive nanocarriers for anticancer drug delivery. *J. Mat. Chem. B* 7 (4), 651–664. doi:10.1039/c8tb02882f
- Gulcin, I., and Alwasel, S. H. (2022). Metal ions, metal chelators and metal chelating assay as antioxidant method. *Processes* 10 (1), 132. doi:10.3390/pr10010132
- Gupta, M. K., Meyer, T. A., Nelson, C. E., and Duvall, C. L. (2012). Poly(PS-b-DMA) micelles for reactive oxygen species triggered drug release. *J. Control. Release* 162 (3), 591–598. doi:10.1016/j.jconrel.2012.07.042

Author contributions

MS, DB-A, DA contributed to the conception and design of the study. MS, DB-A, DA analyzed the data. MS, DB-A, DA wrote the first draft of the manuscript. All authors contributed to manuscript revision, read, and approved the submitted version.

Conflict of interest

The authors declare that the research was conducted in the absence of any commercial or financial relationships that could be construed as a potential conflict of interest.

Publisher's note

All claims expressed in this article are solely those of the authors and do not necessarily represent those of their affiliated organizations, or those of the publisher, the editors and the reviewers. Any product that may be evaluated in this article, or claim that may be made by its manufacturer, is not guaranteed or endorsed by the publisher.

- Herb, M., and Schramm, M. (2021). Functions of ROS in macrophages and antimicrobial immunity. *Antioxidants (Basel)* 10 (2), 313. doi:10.3390/antiox10020313
- Hu, P., and Tirelli, N. (2012). Scavenging ROS: Superoxide dismutase/catalase mimetics by the use of an oxidation-sensitive nanocarrier/enzyme conjugate. *Bioconjug. Chem.* 23 (3), 438–449. doi:10.1021/bc200449k
- Ikeda, Y., and Nagasaki, Y. (2018). Antioxidative biointerface: Biocompatible materials scavenging reactive oxygen species scavenging reactive oxygen species. *Biomed. Mat.* 13 (4), 044103. doi:10.1088/1748-605x/aab720
- Islam, B. U., Habib, S., Ahmad, P., Allarakha, S., and MoinuddinAli, A. (2015). Pathophysiological role of peroxynitrite induced DNA damage in human diseases: A special focus on poly(ADP-ribose) polymerase (parp). *Indian J. Clin. biochem.* 30 (4), 368–385. doi:10.1007/s12291-014-0475-8
- Ji, S., Cao, W., and Xu, H. (2013). A ROS eliminating nanocomposite film fabricated from diselenide-containing polymer micelles. *Part. Part. Syst. Charact.* 30, 1034–1038. doi:10.1002/ppsc.201300222
- Johnson, T. M., Yu, Z. X., Ferrans, V. J., Lowenstein, R. A., and Finkel, T. (1996). Reactive oxygen species are downstream mediators of p53-dependent apoptosis. *Proc. Natl. Acad. Sci. U. S. A.* 93 (21), 11848–11852. doi:10.1073/pnas.93.21.11848
- Joshi-Barr, S., de Gracia Lux, C., Mahmoud, E., and Almutairi, A. (2014). Exploiting oxidative microenvironments in the body as triggers for drug delivery systems. *Antioxid. Redox Signal.* 21 (5), 730–754. doi:10.1089/ars.2013.5754
- Jourd'heuil, D., Jour'dheuil, F. L., and Feelisch, M. (2003). Oxidation and nitrosation of thiols at low micromolar exposure to nitric oxide. Evidence for a free radical mechanism. *J. Biol. Chem.* 278 (18), 15720–15726. doi:10.1074/jbc.M300203200
- Kim, T., Suh, J., and Kim, W. J. (2021). Polymeric aggregate-embodied hybrid nitric-oxide-scavenging and sequential drug-releasing hydrogel for combinatorial treatment of rheumatoid arthritis. *Adv. Mat.* 33 (34), e2008793. doi:10.1002/adma.202008793
- Kollau, A., Gesslbauer, B., Russwurm, M., Koesling, D., Gorren, A. C., Schrammel, A., et al. (2018). Modulation of nitric oxide-stimulated soluble guanylyl cyclase activity by cytoskeleton-associated proteins in vascular smooth muscle. *Biochem. Pharmacol.* 156, 168–176. doi:10.1016/j.bcp.2018.08.009
- Liu, R., Xu, M., and Yan, Q. (2020). Nitric oxide-biosignal-responsive polypeptide nanofilaments. *ACS Macro Lett.* 9 (3), 323–327. doi:10.1021/acsmacrolett.0c00004
- Lu, C., Xiao, Y., Liu, Y., Sun, F., Qiu, Y., Mu, H., et al. (2020). Hyaluronic acid-based levofloxacin nanomicelles for nitric oxide-triggered drug delivery to treat bacterial infections. *Carbohydr. Polym.* 229, 115479. doi:10.1016/j.carbpol.2019.115479
- Luna-Velasco, A., Field, J. A., Cobo-Curiel, A., and Sierra-Alvarez, R. (2011). Inorganic nanoparticles enhance the production of reactive oxygen species (ROS) during the autoxidation of L-3, 4-dihydroxyphenylalanine (L-dopa). *Chemosphere* 85 (1), 19–25. doi:10.1016/j.chemosphere.2011.06.053
- Ma, N., Li, Y., Ren, H., Xu, H., Li, Z., and Zhang, X. (2010). Selenium-containing block copolymers and their oxidation-responsive aggregates. *Polym. Chem.* 1, 1609–1614. doi:10.1039/c0py00144a
- Martin, J. R., Gupta, M. K., Page, J. M., Yu, F., Davidson, J. M., Guelcher, S. A., et al. (2014). A porous tissue engineering scaffold selectively degraded by cell-generated reactive oxygen species. *Biomaterials* 35 (12), 3766–3776. doi:10.1016/j.biomaterials.2014.01.026
- Mittal, M., Siddiqui, M. R., Tran, K., Reddy, S. P., and Malik, A. B. (2014). Reactive oxygen species in inflammation and tissue injury. *Antioxid. Redox Signal.* 20 (7), 1126–1167. doi:10.1089/ars.2012.5149
- Movafagh, S., Crook, S., and Vo, K. (2015). Regulation of hypoxia-inducible factor-1 α by reactive oxygen species: New developments in an old debate. *J. Cell. Biochem.* 116 (5), 696–703. doi:10.1002/jcb.25074
- Napoli, A., Valentini, M., Tirelli, N., Müller, M., and Hubbell, J. A. (2004). Oxidation-responsive polymeric vesicles. *Nat. Mat.* 3 (3), 183–189. doi:10.1038/nmat1081
- Page, M. J., McKenzie, J. E., Bossuyt, P. M., Boutron, I., Hoffmann, T. C., Mulrow, C. D., et al. (2021). The PRISMA 2020 statement: An up-dated guideline for reporting systematic reviews. *BMJ* 372, n71. doi:10.1136/bmj.n71
- Phaniendra, A., Jestadi, D. B., and Periyasamy, L. (2015). Free radicals: Properties, sources, targets, and their implication in various diseases. *Indian J. Clin. biochem.* 30 (1), 11–26. doi:10.1007/s12291-014-0446-0
- Plater, M. J., Greig, I., Helfrich, M. H., and Ralston, S. H. (2001). The synthesis and evaluation of o-phenylenediamine derivatives as fluorescent probes for nitric oxide detection. *J. Chem. Soc. Perkin 1* 1, 2553–2559. doi:10.1039/b105953j
- Pu, H. L., Chiang, W. L., Maiti, B., Liao, Z. X., Ho, Y. C., Shim, M. S., et al. (2014). Nanoparticles with dual responses to oxidative stress and reduced pH for drug release and anti-inflammatory applications. *ACS Nano* 8 (2), 1213–1221. doi:10.1021/nn4058787
- Rathnasamy, G., Sivakumar, V., Rangarajan, P., Foulds, W. S., Ling, E. A., and Kaur, C. (2014). NF- κ B-mediated nitric oxide production and activation of caspase-3 cause retinal ganglion cell death in the hypoxic neonatal retina. *Invest. Ophthalmol. Vis. Sci.* 55 (9), 5878–5889. doi:10.1167/iov.13-13718
- Rendra, E., Riabov, V., Mossel, D. M., Sevastyanova, T., Harmsen, M. C., and Kzhyshkowska, J. (2019). Reactive oxygen species (ROS) in macrophage activation and function in diabetes. *Immunobiology* 224 (2), 242–253. doi:10.1016/j.imbio.2018.11.010
- Reshma, V. G., Syama, S., Sruthi, S., Reshma, S. C., Remya, N. S., and Mohanan, P. V. (2017). Engineered nanoparticles with antimicrobial property. *Curr. Drug Metab.* 18 (11), 1040–1054. doi:10.2174/1389200218666170925122201
- Ronzio, R. A. (2020). *Naturally occurring antioxidants. Textbook of natural medicine*. Fifth Edition. London, United Kingdom: Churchill Livingstone, 731–751. e12.
- Ryan, K. A., Smith, M. F., Jr, Sanders, M. K., and Ernst, P. B. (2004). Reactive oxygen and nitrogen species differentially regulate Toll-like receptor 4-mediated activation of NF- κ B and interleukin-8 expression. *Infect. Immun.* 72 (4), 2123–2130. doi:10.1128/iai.72.4.2123-2130.2004
- Sandalio, L. M., Rodríguez-Serrano, M., Romero-Puertas, M. C., and del Río, L. A. (2013). Role of peroxisomes as a source of reactive oxygen species (ROS) signaling molecules. *Subcell. Biochem.* 69, 231–255. doi:10.1007/978-94-007-6889-5_13
- Scarcello, E., Herpain, A., Tomatis, M., Turci, F., Jacques, P. J., and Lison, D. (2020). Hydroxyl radicals and oxidative stress: The dark side of Fe corrosion. *Colloids Surfaces B Biointerfaces* 185, 110542. doi:10.1016/j.colsurfb.2019.110542
- Schieber, M., and Chandel, N. S. (2014). ROS function in redox signaling and oxidative stress. *Curr. Biol.* 24 (10), R453–R462. doi:10.1016/j.cub.2014.03.034
- Shafiq, M., Chen, Y., Hashim, R., He, C., Mo, X., and Zhou, X. (2021). Reactive oxygen species-based biomaterials for regenerative medicine and tissue engineering applications. *Front. Bioeng. Biotechnol.* 9, 821288. doi:10.3389/fbioe.2021.821288
- Shim, M. S., and Xia, Y. (2013). A reactive oxygen species (ROS)-responsive polymer for safe, efficient, and targeted gene delivery in cancer cells. *Angew. Chem. Int. Ed. Engl.* 52 (27), 7064–7067. doi:10.1002/ange.201209633
- Snyder, C. M., Shroff, E. H., Liu, J., and Chandel, N. S. (2009). Nitric oxide induces cell death by regulating anti-apoptotic BCL-2 family members. *PLoS One* 4 (9), e7059. doi:10.1371/journal.pone.0007059
- Swami Vetha, B. S., Adam, A. G., and Aileru, A. (2021). Redox responsive copolyoxalate smart polymers for inflammation and other aging-associated diseases. *Int. J. Mol. Sci.* 22, 5607. doi:10.3390/ijms22115607
- Tao, W., and He, Z. (2018). ROS-responsive drug delivery systems for biomedical applications. *Asian J. Pharm. Sci.* 13 (2), 101–112. doi:10.1016/j.ajps.2017.11.002
- Troy, E., Tilbury, M. A., Power, A. M., and Wall, J. G. (2021). Nature-based biomaterials and their application in biomedicine. *Polym. (Basel)* 13 (19), 3321. doi:10.3390/polym13193321
- Turrens, J. F. (2003). Mitochondrial formation of reactive oxygen species. *J. Physiology* 552 (2), 335–344. doi:10.1113/jphysiol.2003.049478
- Vidrio, E., Jung, H., and Anastasio, C. (2008). Generation of hydroxyl radicals from dissolved transition metals in surrogate lung fluid solutions. *Atmos. Environ.* 42 (18), 4369–4379. doi:10.1016/j.atmosenv.2008.01.004
- Wang, L., Chang, Y., Feng, Y., Li, X., Cheng, Y., Jian, H., et al. (2019). Nitric oxide stimulated programmable drug release of nanosystem for multidrug resistance cancer therapy. *Nano Lett.* 19 (10), 6800–6811. doi:10.1021/acs.nanolett.9b01869
- Wang, L., Fan, F., Cao, W., and Xu, H. (2015). Ultrasensitive ROS-responsive coassemblies of tellurium-containing molecules and phospholipids. *ACS Appl. Mat. Interfaces* 7 (29), 16054–16060. doi:10.1021/acsami.5b04419
- Wilson, D. S., Dalmasso, G., Wang, L., Sitaraman, S. V., Merlin, D., and Murthy, N. (2010). Orally delivered thioketal nanoparticles loaded with TNF- α -siRNA target inflammation and inhibit gene expression in the intestines. *Nat. Mat.* 9 (11), 923–928. doi:10.1038/nmat2859
- Xu, Q., He, C., Xiao, C., and Chen, X. (2016). Reactive oxygen species (ROS) responsive polymers for biomedical applications. *Macromol. Biosci.* 16 (5), 635–646. doi:10.1002/mabi.201500440
- Yang, W., Yang, S., Jiang, L., Zhou, Y., Yang, C., and Deng, C. (2020). Tumor microenvironment triggered biodegradation of inorganic nanoparticles for

enhanced tumor theranostics. *RSC Adv.* 10 (45), 26742–26751. doi:10.1039/d0ra04651e

Yao, Y., Zhang, H., Wang, Z., Ding, J., Wang, S., Huang, B., et al. (2019). Reactive oxygen species (ROS)-responsive biomaterials mediate tissue microenvironments and tissue regeneration. *J. Mat. Chem. B* 7 (33), 5019–5037. doi:10.1039/c9tb00847k

Yeo, J., Lee, Y. M., Lee, J., Park, D., Kim, K., Kim, J., et al. (2019). Nitric oxide-scavenging nanogel for treating rheumatoid arthritis. *Nano Lett.* 19 (10), 6716–6724. doi:10.1021/acs.nanolett.9b00496

Yi, H., Lu, W., Liu, F., Zhang, G., Xie, F., et al. (2021). ROS-responsive liposomes with NIR light-triggered doxorubicin release for combinatorial therapy of breast cancer. *J. Nanobiotechnology* 19 (1), 134. doi:10.1186/s12951-021-00877-6

Yoboue, E. D., Sitia, R., and Simmen, T. (2018). Redox crosstalk at endoplasmic reticulum (ER) membrane contact sites (MCS) uses toxic waste to deliver messages. *Cell Death Dis.* 9 (3), 331. doi:10.1038/s41419-017-0033-4

Yu, S. S., Koblin, R. L., Zachman, A. L., Perrien, D. S., Hofmeister, L. H., Giorgio, T. D., et al. (2011). Physiologically relevant oxidative degradation of oligo(proline) cross-linked polymeric scaffolds. *Biomacromolecules* 12 (12), 4357–4366. doi:10.1021/bm201328k

Zhang, J., Hu, J., Sang, W., Wang, J., and Yan, Q. (2016). Peroxynitrite (ONOO[−]) redox signaling molecule-responsive polymersomes. *ACS Macro Lett.* 5, 919–924. doi:10.1021/acsmacrolett.6b00474

Zhao, C., Chen, J., Zhong, R., Chen, D. S., Shi, J., and Song, J. (2021). Oxidative-species-selective materials for diagnostic and therapeutic applications. *Angew. Chem. Int. Ed.* 60 (18), 9804–9827. doi:10.1002/anie.201915833

Zhao, H., Huang, J., Li, Y., Lv, X., Zhou, H., Wang, H., et al. (2020). ROS-scavenging hydrogel to promote healing of bacteria infected diabetic wounds. *Biomaterials* 258 (120286), 120286–129612. doi:10.1016/j.biomaterials.2020.120286

Frontiers in Bioengineering and Biotechnology

Accelerates the development of therapies,
devices, and technologies to improve our lives

A multidisciplinary journal that accelerates the
development of biological therapies, devices,
processes and technologies to improve our lives
by bridging the gap between discoveries and their
application.

Discover the latest Research Topics

[See more →](#)

Frontiers

Avenue du Tribunal-Fédéral 34
1005 Lausanne, Switzerland
frontiersin.org

Contact us

+41 (0)21 510 17 00
frontiersin.org/about/contact



Frontiers in
Bioengineering
and Biotechnology

